UC Santa Cruz

UC Santa Cruz Electronic Theses and Dissertations

Title

Understanding Atmospheres of Exoplanets and Brown Dwarfs with JWST

Permalink

https://escholarship.org/uc/item/6zz940mk

ISBN

9798293871827

Author

Mukherjee, Sagnick

Publication Date

2025-08-07

Peer reviewed|Thesis/dissertation

eScholarship.org Powered by the California Digital Library
University of California

UNIVERSITY OF CALIFORNIA
SANTA CRUZ

UNDERSTANDING ATMOSPHERES OF EXOPLANETS AND BROWN DWARFS WITH *JWST*

A dissertation submitted in partial satisfaction of the
requirements for the degree of

DOCTOR OF PHILOSOPHY

in

UNIVERSITY OF CALIFORNIA, SANTA CRUZ

by

Sagnick Mukherjee

September 2025

The Dissertation of Sagnick Mukherjee
is approved:

Professor Jonathan J. Fortney, Chair

Professor Andrew J. Skemer

Professor Rebecca Jensen-Clem

Dr. Natasha E. Batalha

Peter F. Biehl
Vice Provost and Dean of Graduate Studies

Copyright © by

Sagnick Mukherjee

2025

Table of Contents

List of Figures viii

List of Tables xxxvii

Abstract xxxix

Dedication xlii

Acknowledgments xliii

1 Introduction 1
- 1.1 Exoplanetary Atmospheres . . . 3
  - 1.1.1 Atmospheric Chemistry . . . 6
  - 1.1.2 Aerosols– Clouds and Hazes . . . 8
  - 1.1.3 Interior Structure . . . 11
- 1.2 Directly Imaged Exoplanets and Brown Dwarfs . . . 13
- 1.3 Transiting Exoplanets . . . 16
- 1.4 Observations from the *James Webb Space Telescope* . . . 17

I Brown Dwarfs and Directly Imaged Exoplanets 20

2 Probing Brown Dwarf Clouds with Polarization 21
- 2.1 Introduction . . . 21
- 2.2 Modeling Sub-stellar Atmospheres . . . 27
  - 2.2.1 General Circulation Models of Brown Dwarfs . . . 27
  - 2.2.2 Radiative Transfer with `ARTES` . . . 35
  - 2.2.3 Opacities and Scattering Matrices . . . 37
- 2.3 Results . . . 41
  - 2.3.1 Luhman 16 A . . . 41
  - 2.3.2 Luhman 16 B . . . 47
  - 2.3.3 Modeling of Polarization Signal with Band Models . . . 50

2.4 Discussion . . . 52
2.4.1 GCM Parameter Choices . . . 52
2.4.2 Spherical Cloud Particles . . . 54
2.4.3 Improvements to Radiative Transfer and Opacities . . . 55
2.5 Conclusions . . . 56

3 PICASO 3.0: A One-Dimensional Climate Model for Giant Planets and Brown Dwarfs 59
3.1 Model Setup of PICASO 3.0 . . . 65
3.1.1 Physics and Chemistry of Substellar Atmospheres . . . 68
3.1.2 Iteration Scheme And Model Convergence . . . 99
3.2 Benchmarking Analysis . . . 111
3.2.1 Benchmarking chemical equilibrium non-irradiated atmospheres . 111
3.2.2 Benchmarking chemical equilibrium irradiated atmospheres . . . 116
3.2.3 Benchmarking non-irradiated atmospheres with diseequilibrium chemistry . . . 116
3.3 Modeling Recommendations . . . 119
3.3.1 Choosing Model Pressure Grid . . . 119
3.3.2 Choosing the Initial Guess T(P) Profile . . . 121
3.3.3 Convergence . . . 122
3.4 Calculating Observables . . . 124
3.5 Future Improvements . . . 125
3.5.1 Clouds . . . 127
3.5.2 1D Chemical Kinetics Model . . . 127
3.5.3 Time Evolution Version . . . 128
3.6 Conclusions and Summary . . . 129

4 Probing the Extent of Vertical Mixing in Brown Dwarf Atmospheres with Disequilibrium Chemistry 131
4.1 Introduction . . . 131
4.1.1 Molecular abundances and non-equilibrium chemistry . . . 131
4.1.2 Modeling Approaches . . . 135
4.2 Modeling Sub-stellar Atmospheres . . . 139
4.2.1 Python Based implementation of EGP with Disequilibrium Chemistry . . . 140
4.3 Results . . . 145
4.3.1 Effect of Disequilibrium Chemistry on the $T(P)$ profile of brown dwarfs . . . 146
4.3.2 Quenching in the Radiative Zone or the Convective Zone ? . . . 154
4.3.3 Effect of Radiative and Convective Zone K_{zz} on Emission Spectra 164
4.3.4 Color Magnitude Diagrams . . . 173
4.3.5 Comparing to Spectroscopic Observations . . . 177
4.3.6 Constraining Radiative Zone K_{zz} with JWST . . . 191

4.4 Discussion . . . 194
4.4.1 PH_3 Quenching . . . 194
4.4.2 Clouds . . . 199
4.5 Summary and Conclusion . . . 200

5 The Sonora Substellar Atmosphere Models. 4. Elf Owl: Atmospheric Mixing and Chemical Disequilibrium with Varying Metallicity and C/O Ratios 204
5.1 Introduction . . . 204
5.1.1 Why is constraining K_{zz} important? . . . 205
5.1.2 Metallicity, C/O Ratio, and K_{zz} . . . 210
5.2 Atmospheric Modeling with `PICASO 3.0` . . . 213
5.3 The `Sonora` Model Series and why is `Elf Owl` important? . . . 220
5.4 Results . . . 221
5.4.1 Effect of K_{zz} on $T(P)$ Profiles Across Metallicities and C/O Ratios 223
5.4.2 Spectra Across Varying K_{zz}, Metallicity, and C/O Ratios . . . 235
5.5 Application . . . 247
5.5.1 Fitting Observed Spectrum with the `Sonora Elf Owl` Model grid 253
5.5.2 Trends in K_{zz} . . . 258
5.6 Discussion . . . 264
5.6.1 Clouds . . . 264
5.6.2 Constant K_{zz} with Pressure and Molecular Diffusion . . . 266
5.7 Summary and Conclusions . . . 267

II Transiting Exoplanets 272

6 Effects of Planetary Parameters on Disequilibrium Chemistry in Irradiated Planetary Atmospheres: From Gas Giants to Sub-Neptunes 273
6.1 Introduction . . . 273
6.2 Modeling . . . 282
6.2.1 1D Radiative–Convective Equilibrium Models . . . 282
6.2.2 Chemical Kinetics Modeling . . . 283
6.3 Results . . . 289
6.3.1 Exploring how abundances depend on K_{zz}, C/O, and $T_{\rm int}$ across different $T_{\rm eq}$ . . . 289
6.3.2 Exploring how abundances depend on K_{zz}, C/O, and $T_{\rm int}$ across different metallicities . . . 314
6.3.3 Chemical Transitions with $T_{\rm eq}$ . . . 318
6.3.4 Sensitivity of Transmission Spectrum to K_{zz} and $T_{\rm int}$ . . . 323
6.3.5 Precursors to Soot/Haze . . . 335
6.4 Discussion . . . 339
6.4.1 Radiative-convective-Photochemical-Equilibrium . . . 339

6.4.2 Dependence of Photochemical Calculations on the UV spectra of host stars . . . 343
6.4.3 Effect of Condensation on Chemical Kinetics Calculations . . . 346
6.4.4 Steady-State Convergence of Chemical Kinetics Model . . . 347
6.5 Conclusions . . . 348

7 A JWST Panchromatic Thermal Emission Spectrum of the Warm Neptune Archetype GJ 436b 352
7.1 Introduction . . . 352
7.2 Observations . . . 356
7.3 Data Analysis . . . 357
7.3.1 `tshirt` Reduction and Analysis . . . 357
7.3.2 `Eureka!` Reduction and Analysis . . . 360
7.3.3 Reduction Comparisons . . . 363
7.3.4 Calibrated Stellar Spectrum . . . 365
7.4 Results . . . 367
7.4.1 Atmospheric Retrievals . . . 367
7.4.2 Self-Consistent Models . . . 373
7.5 Discussion . . . 381
7.5.1 From *Spitzer* to *JWST* . . . 381
7.5.2 Transmission Spectrum of GJ 436b . . . 385
7.5.3 Day-side vs. Equilibrium Temperature . . . 387
7.6 Conclusions . . . 388
7.7 Appendix . . . 391
7.7.1 Observing Details . . . 391
7.7.2 Orbital Parameters from Broadband Fits . . . 392
7.7.3 NIRCam De-Trending Models . . . 392
7.7.4 Experiments with Moving the Field Point to Reduce 1/f Noise . 393
7.7.5 Comparison Across Separate Eclipses . . . 394
7.7.6 Correlated Noise in Eclipse Observations . . . 395
7.7.7 Comparison with Previous Spitzer Observations . . . 396
7.7.8 BOSZ model fits to stellar spectrum . . . 401
7.7.9 Posterior Distributions from Model Fits . . . 403
7.7.10 Contribution of Absorbers to the Best-fitting Self-consistent Model Spectra . . . 403

8 Cloudy Mornings and Clear Evenings in a Giant Extrasolar World 406
8.1 Asymmetric Limbs of a sub-Jovian Mass Planet . . . 410
8.2 Transmission Spectrum of the Morning and Evening Limbs . . . 411
8.3 A Cloudy Morning and Clear Evening– Aerosols composed of Clouds and not Hazes . . . 412
8.4 Temperature Differences and Day/Night Cloud Cycling . . . 414
8.4.1 Limb-to-Limb Temperature Difference . . . 414

8.4.2 Cloud Properties of each limb 415
8.4.3 Constraints on Circulation Timescales 416
8.5 Effect of Asymmetric Limbs on the Measured Composition of WASP-94A b417
8.6 Methods 419
8.6.1 Data Reduction 419
8.6.2 Modeling 430

9 Conclusions **475**
9.1 Where did we stand in 2020? 476
9.2 Where do we stand today? 479
9.3 Where do we go from here? 486

Bibliography **489**

List of Figures

1.1 Mass and radius of confirmed exoplanets is shown with black points. The density of the detected exoplanets in the mass-radius space is shown with the heat map. Solar system planets are also shown with colored solid circles. The mass of the exoplanet population is either mass (m), or $msin(i)/sin(i)$, or $msin(i)$ from higher to lower priority. 4
1.2 Schematic showing the various physical processes ongoing in an exoplanet atmosphere. 5
1.3 Theoretical evolutionary tracks for luminosity (left) and effective temperature (right) for objects with various masses between 0.5 to 83 Jupiter mass is shown. Evolution of objects classified as planets are shown with red lines. Brown dwarf evolution is shown with blue lines and evolution of stars have been shown with dashed black lines. The theoretical tracks are from the publicly available Sonora Diamondback grid (Morley et al. 2024) and were calculated using a evolutionary model developed as a part of this thesis. 14

2.1 The top panel shows the global temperature pattern from the GCM runs at a pressure of 0.23 Bars for Luhman 16 A (top left panel) and Luhman 16 B (top right panel). The bottom panels show the cloud mass mixing ratio (q_c) at a pressure of 0.1 Bars for Luhman 16 A (bottom left panel) and at a pressure level of 2 Bars for Luhman 16 B (bottom right panel). **Main Point** - The equator is hotter and more cloudy than the poles for Luhman 16 A; furthermore, the size of vortices in Luhman 16 A and B models are different due to these objects' different rotation rates. 30

2.2 The left panel shows the longitudinally averaged Temperature-Pressure (T-P) profiles for Luhman 16 A with solid lines. Various colored lines depict the average T-P profile of latitudinal bands each with a angular width of 20° starting from the equator (red) to the pole (blue). The black solid line shows the phase-boundary curve for enstatite from Visscher et al. (2010b) assuming solar abundance. The dotted colored lines depict the longitudinally averaged cloud particle sizes in μm from the equator to the poles. The right panel depicts the same for Luhman 16 B. 34
2.3 The top panel shows the cloud particle size distributions for different values of effective radius ($r_{\rm eff}$) and effective variance $v_{\rm eff}$. The solid lines depict the particle size distributions with $v_{\rm eff}$= 0.05 and $r_{\rm eff}$ of 0.1 μm (blue solid line), 1 μm (red solid line) and 10 μm (green solid line). The dashed lines show wider particle size distributions with $v_{\rm eff}$= 0.1 and $r_{\rm eff}$ of 0.1 μm (blue dashed line), 1 μm (red dashed line) and 10 μm (green dashed line). The bottom panel left vertical axis correspond to phase function ($P_{11}(\Theta)$). The solid lines show $P_{11}(\Theta)$ calculated from the particle size distributions shown in the top panel with the same colors. The percentage of linear polarization as a function of the scattering angle is shown with dashed lines for each of the particle distributions (right vertical axis). **Main Point**- Gas and clouds scatter infrared light very differently and single scattering polarizations are very sensitive to particle sizes. 39
2.4 The left panel shows the radiative transfer result for Luhman 16 A. The top left panel shows the surface brightness map for the object. The second panel in the left shows the variability of thermal flux at 1.6 μm with time as the object rotates with a period of 7 hours. The third left panel shows the linear polarization percentage vs. time with the solid red line. The solid black line and the shaded region shows the measured polarization for the object. The bottom left panel shows the variation of the angle of polarization of the object with time using the cyan line. The same plots for Luhman 16 B (5 hour period) has been shown in the right panels. **Main Point** - Our models match the degree of linear polarization well for both the objects but do not reproduce the observed optical variability amplitude of Luhman 16 B. 43
2.5 The top left, middle and right panel shows surface brightness map for Luhman 16 A if the typical cloud particle sizes were 1 μm (original GCM), 10 μm and 0.5 μm. The disk-integrated polarization for each case has been shown in the top right of each plot window. The bottom left, middle and right panel shows surface brightness map for Luhman 16 B if the typical cloud particle sizes were 5 μm (original GCM), 50 μm and 2.5 μm. Please note that the color scheme is inverted. **Main Point** - Luhman 16 A should have typical cloud particle sizes betwen 0.5-1 μm whereas Luhman 16 B should have cloud particle sizes of about 5 μm. . 49

2.6 Left panel shows the surface brightness map of the simple band model for Luhman 16 A along with the 1.6 μm disk-integrated polarization percentage denoted at the top in red. Right panel shows the same for the band model of Luhman 16 B. Please note that the color scheme is inverted. **Main Point**- Band models tend to overestimate polarization signal. 51

3.1 Schematic diagram of the radiative-convective model in `PICASO 3.0`. Solid outlines indicate required modules, while dashed outlines indicate optional models. 67

3.2 **Top left panel** shows the abundance map of CH_4 in the pressure-temperature chemistry grid used in the model with equilibrium chemistry described in the paper. Dashed red lines marked on the abundance map depict different converged $T(P)$ profiles of brown dwarfs from Marley et al. (2021) with $T_{\rm eff}$ between 300 K and 2300 K and log(g)=5. This grid is used for interpolation of chemical abundances during iteration of the atmospheric state in the code. The same for CO, H_2O, and NH_3 is shown in the **top right**, **bottom left** and **bottom right** panel. The abundances shown here are calculated for solar metallicity and C/O ratio. 85

3.3 **Left panel** shows the correlated-k opacity wavelength bins used in the radiative transfer calculations in our atmospheric model. The blackbody emission curves of temperatures of 1000 K, 2000 K and 300 K are also shown here. **Right panel** shows a zoomed version of the left panel with the wavelengths between 0.8-13 μm. The stellar spectrum from a solar metallicity PHOENIX model for a star with $T_{\rm eff}$= 5000 K is also shown in both the panels. 91

3.4 **Left panel** shows the high resolution opacity κ between 1 and 1.3 μm of a solar mixture of atmospheric gases at a temperature of 550 K and a pressure of 80 mbar. **Right panel** shows the k-distribution computed for the opacity shown in the left panel with the blue solid line. The black and red points are the Gauss points (from Table 3.2) overplotted on the k-distribution for this opacity window. These Gauss points are applicable for the double Gauss point method. The first set of 4 Gauss points are shown in black while the second set is shown with red points. 91

3.5 **Top left panel** shows the heat map of planck weighted molecular opacity in the pressure-temperature k-coefficient grid used in the model with equilibrium chemistry described in the paper. Dashed black lines marked on the cross-section map depict different converged $T(P)$ profiles of brown dwarfs from Marley et al. (2021) with $T_{\rm eff}$ between 300 K and 2300 K and log(g)=5. This grid is used for interpolation of opacities during iteration of the atmospheric state in the code. The same for the 3rd, 5th, and 7th Gauss points are also shown in the **top right**, **bottom left** and **bottom right** panel. 92

3.6 A heat map of the adiabatic lapse rate as a function of pressure and temperature is shown here. This grid is used to determine the lapse rate in atmospheric layers unstable against convection. 100
3.7 Three steps in the iteration towards a converged solution for a brown dwarf with $T_{\rm eff}$ of 1000 K and log(g) of 5 is shown here in each row. The first column shows the iteration of the $T(P)$ profile in red with the `SONORA BOBCAT` model shown in black dashed. The second columns show the lapse-rate from the $T(P)$ profiles in blue and the local adiabatic lapse rate in black. The third column shows the iterations in the volume mixing ratios of various gases. The fourth column shows the thermal spectrum emergent from the atmosphere of the object in each iteration. An animated gif of this figure can be found here 104
3.8 Three steps in the iteration towards a converged solution for an exoplanet around a sun like star with $T_{\rm int}$ of 300 K and log(g) of 3.4 is shown here in each row. The left-most column shows the iteration of the $T(P)$ profile in red with the `SONORA BOBCAT` model shown in black. The second left-most columns show the lapse-rate from the $T(P)$ profiles in blue and the local adiabatic lapse rate in black. The third column shows the iterations in the volume mixing ratios of various gases. The right-most column shows the thermal spectrum emergent from the atmosphere of the object in each iteration. An animated gif of this figure can be found here 105
3.9 Radiative and convective flux contributions compared to total net fluxes are shown for three $T(P)$ profiles in order to visualize the concept of "convergence". From left to right a representative brown dwarf, warm Jupiter, and hot Jupiter profile is shown. In each figure, the shaded blue region depicts the convective flux at each layer. The orange shaded region depicts the net radiative flux in each layer. The red dashed line shows the target flux for the brown dwarf in the left panel. For the brown dwarf (non-irradiated) this target flux is $\sigma {T_{\rm eff}}^4$. The red dashed line in the middle and the right panels shows the internal heat flux of the planets which is $\sigma {T_{\rm int}}^4$. Please note that the scale of the upper and lower X-axis are different in all the three panels. 107

3.10 Three steps in the iteration towards a converged solution with disequilibrium chemistry for a brown dwarf with $T_{\rm eff}$ of 700 K and log(g) of 5.25 is shown here in each row. The first column shows the iteration of the $T(P)$ profile with the red line and the `SONORA BOBCAT` chemical equilibrium is model shown in black dashed. The second column shows the lapse-rate from the $T(P)$ profiles in blue and the local adiabatic lapse rate in black. The third column shows the chemical timescales of various gases as a function of pressure with solid lines of different colors. The pressure dependant mixing timescale is shown in the third columns with the black dashed line. The fourth column shows the iterations of the volume mixing ratios of various gases. An animated gif of this figure can be found here 109
3.11 Benchmarking tests of the Python based-equilibrium chemistry developed in this work with the published chemical equilibrium models from Marley et al. (2021) and Phillips et al. (2020) are shown here. The benchmarking has been shown in the form of the converged $T(P)$ profiles predicted by each code for four different $T_{\rm eff}$ values at log(g)=5 in the left panels while the pressure-derivatives of the $T(P)$ profiles also have been shown in the right side panels for each case to show that the convective and radiative zones predicted by both the codes match excellently. 112
3.12 $T(P)$ profile computed using `PICASO 3.0` for WASP-25 b is shown with the red solid line compared with the `ATMO` models presented in Goyal et al. (2020) with dashed black lines. The left panel shows the comparison for sub-solar metallicity of 0.1×solar whereas the right panel shows comparisons between solar metallicity models. The same system parameters were used to compute both the models and they agree with each other with less than 3% differences. 113
3.13 Benchmarking tests of the Python based-Disequilibrium code used in this work by assuming K_{zz}= 0 with the published chemical equilibrium models from Marley et al. (2021) are shown here. The benchmarking has been shown in the form of the converged $T(P)$ profiles predicted by each code for four different $T_{\rm eff}$ values at log(g)=5 in the left panels while the pressure-derivatives of the $T(P)$ profiles also have been shown in the right side panels for each case to show that the convective and radiative zones predicted by both the codes match excellently. 114
3.14 Benchmarking tests of the Python based-Disequilibrium code used in this work by assuming non-zero K_{zz} values with the published chemical disequilibrium models from Phillips et al. (2020) are shown here. The benchmarking has been shown in the form of the converged $T(P)$ profiles predicted by each code for four different $T_{\rm eff}$ values and three different log(g) values in the three panels. The $T(P)$ profiles match well between the two independent models with different sets of opacities and totally different code methodologies. 115

3.15 Using our atmospheric model to calculate observables. **Top left** panel shows the converged $T(P)$ of an exoplanet calculated using our model with (blue) and without (black) disequilibrium chemistry. **Top right**, **bottom left** and **bottom right** panel shows the albedo spectrum, transmission spectrum, and thermal spectrum at a spectral resolution of R=300 of the exoplanet calculated using radiative transfer tools available in `PICASO`. 126

4.1 **Top panels** show the $\tau = 1$ pressure levels for specific gaseous absorbers in a model T-dwarf with $T_{\rm eff}$= 700 K and log(g) = 5.0 in the presence and absence of quenching due to vertical mixing. $\tau = 1$ pressure levels for H_2O, CH_4, CO, and NH_3 are shown in the first, second, third and fourth columns, respectively. The equilibrium chemistry pressure levels are shown in dashed lines whereas the disequilibrium chemistry pressure levels are shown in solid lines. The volume mixing ratio as a function of pressure of each gas in the presence (solid lines) and absence (dashed lines) of vertical mixing induced quenching are also shown with black lines in the top x-axis of each of the top four panels. **Bottom panels** shows the logarithm of the pressure ratio of these $\tau = 1$ levels with equilibrium chemistry and disequilibrium chemistry for the gaseous absorbers. The zero mark represents no change in these pressure levels. Positive values represents an increase in absorption in the disequilibrium chemistry models compared to equilibrium chemistry models. **Main Point** – Disequilibrium chemistry leads to large opacity changes in the atmosphere. 147

4.2 **Top left panel** $T(P)$ profile of brown dwarf models with log(g) = 5 and $T_{\rm eff}$ of 500, 700, and 1000 K. The solid $T(P)$ profiles assume disequilibrium chemistry self-consistently whereas the dotted profiles show equilibrium chemistry calculations. The convective zones are shown with thicker lines for each $T(P)$ profile. To differentiate the convective zones of the equilibrium chemistry models from the disequilibrium chemistry models, they are shown with much thicker lines compared to the convective zones of disequilibrium chemistry models. **Top right panel** Plotted are the CO volume mixing ratio profiles for these brown dwarf models. The solid lines show the mixing ratio with disequilibrium chemistry whereas the dotted lines show calculations from equilibrium chemistry. **Bottom panel** shows the normalized thermal emission spectra of these brown dwarfs. The solid lines show the disequilibrium chemistry results while dotted spectra represent the equilibrium chemistry calculations. The J, H, K', L', and M' bands are also shown as shaded regions of different colors. **Main Point**– Self- consistent treatment of disequilibrium chemistry leads to large changes in $T(P)$ profile, abundances, and thermal emission spectra. 151

4.3 **Left panel** shows the $T(P)$ profile of a brown dwarf with $T_{\rm eff}$ of 700 K and log(g) of 4.5. The dashed line is the $T(P)$ profile when chemical equilibrium is assumed whereas the solid line shows the $T(P)$ profile for disequilibrium chemistry. The convective zones are shown with darker and thicker lines. **Right panel** shows the wavelength dependant absorptivity of the different atmospheric layers for both the cases. The absorptivity is given by 1-e$^{-\tau}$. The absorptivity for the equilibrium chemistry model is shown with dashed lines whereas that for disequilibrium chemistry model are shown with solid lines. The local normalized blackbody spectrum is also shown for each layer with dashed and solid lines for equilibrium and disequilibrium chemistry models, respectively. The blue horizontal line for each layer shows the absorptivity corresponding to τ =1. **Main Point** – Opacity changes lead to large ($\sim$100 K) differences in $T(P)$ profiles between chemical equilibrium and disequilibrium models. 152

4.4 Model $T(P)$ profile, chemical and dynamical timescales, and chemistry for a brown dwarf with $T_{\rm eff}$ 700 K and log(g) = 4.5 is shown in the top panels whereas the same properties for a brown dwarf with $T_{\rm eff}$ 700 K and log(g) = 5.25 is shown in the bottom panels. $T(P)$ profile of the two brown dwarfs are shown in the **left panels** – one with a single deep convective zone while another with a deep "sandwiched" radiative zone between two deep convective zones. The **middle panels** show the comparison between the mixing timescale (black) and the chemical timescales of different gases like CO and NH_3 as a function of pressure for each of the $T(P)$ profiles shown in the left columns. The **right panels** show the volume mixing ratios of various molecules as a function of pressure for each atmosphere. **Main Point** – Gases can be quenched in a deeper "sandwiched" radiative zone in some brown dwarfs, where mixing timescales can be orders of magnitude larger than in convective zones. 156

4.5 Appearance of the 2nd radiative zone in the $T_{\rm eff}$ vs. log(g) parameter space in our grid is shown. The colors show the value of the quantity $\log_{10}(\rm P_{bot}/P_{top})$ where $\rm P_{bot}$ and $\rm P_{top}$ are the pressures at the bottom and top of the sandwiched radiative zone, respectively. The **top panel** shows this in case of equilibrium chemistry. The subsequent panels show the presence of the 2nd radiative zone if different vigor of K_{zz} is chosen keeping the convective zone mixing length fixed at H. Dark blue indicates no second convective zone at depth. 159

4.6 Appearance of the 2nd radiative zone in the $T_{\rm eff}$ vs. log(g) parameter space in our grid is shown. The colors show the value of the quantity $\log_{10}(\rm P_{bot}/P_{top})$ where $\rm P_{bot}$ and $\rm P_{top}$ are the pressures at the bottom and top of the sandwiched radiative zone, respectively. The **top panel** shows this in case of equilibrium chemistry. The subsequent panels show the presence of the 2nd radiative zone if different vigor of K_{zz} is chosen keeping the convective zone mixing length fixed at $0.1 \times H$. Dark blue indicates no second convective zone at depth. 160
4.7 **Top panel** shows the equilibrium chemistry abundance of CO at pressures where $T = T_{\rm eff}$ in our $T_{\rm eff}$ vs. gravity grid of chemical equilibrium models. The **second, third and last panels** depict the quenched CO abundance within the $T_{\rm eff}$ vs. gravity parameter space in our disequilibrium chemistry models. The second, third and last panels correspond models with radiative zone K_{zz} values of "Moses", "Moses×100", and "Moses/100", respectively while the convective zone mixing length L was fixed at the scale height H. Models where CO was quenched at the radiative zone are marked with black hatches. CO was quenched at a convective zone in the rest of the models. Models with radiative zone CO quenching show much smaller CO abundance compared to models with convective zone quenching. 165
4.8 Same as Figure 4.7 except with the mixing length in convective zones fixed at 0.1×H. In these models CO is mostly quenched in a radiative zone. 166
4.9 Same as Figure 4.7 but for quenching of CO_2. Given the different $t_{\rm chem}$ for CO_2, compared to CO, the quench levels are entirely different. . . . 167
4.10 Same as Figure 4.8 but for quenching of NH_3. Given the different $t_{\rm chem}$ for NH_3, compared to CO, the quench levels are entirely different. . . . 168
4.11 M-band Thermal emission spectra across a range of $T_{\rm eff}$ between 400 K and 1000 K with steps of 100 K are shown in each panel. log $(g) = 5.0$ is on the left and 5.5 is on the right. The colors are representative of the $T_{\rm eff}$. The models shown in the upper left and right panels assume the convective mixing length L to be H whereas the models shown in the lower left and right panels assume $L = 0.1 \times H$. The three line styles show different radiative zone K_{zz} parametrizations, including Moses (solid), Moses/100 (dashed), and Moses×100 (dash-dot). If quenching occurs in a convective zone the three spectra plot atop each other. The shaded region shows the wavelength range where CO is the most important absorber. . 169

4.12 H-band thermal emission spectra of models from our grid are shown in the top left and right panels whereas the bottom left and right panels show the K-band emission spectra. Models with log(g)=5 and different $T_{\rm eff}$ between 400-1000 K are shown in each panel. From bottom to top, spectra for $T_{\rm eff}$ values of 425 K, 700 K, 850 K, 900 K, and 1000 K are shown in all the panels. **Top left panel** shows the thermal emission spectra of models which have convective mixing length set at H but have different K_{zz} parametrizations like Moses, Moses/100, and Moses×100 which are represented by different line types in the panels like solid, dashed, and dashed-dotted. **Top right panel** shows the same but for models with convective mixing length set at $0.1 \times H$. **Bottom left and right panels** show the sensitivity of the K band spectrum to radiative zone K_{zz} when $L = H$ and $L = 0.1 \times H$, respectively. The shaded region shows the wavelength range where CH_4 is the most important absorber. 170

4.13 Thermal emission spectra of brown dwarfs between 3 and 3.5 μm are shown in the top left and right panels. Emission spectra of the same models in the L-band are shown in the bottom left and right panels. Models with log(g)=5 and different $T_{\rm eff}$ between 400-1000 K are shown in each panel. From bottom to top, spectra for $T_{\rm eff}$ values of 425 K, 700 K, 850 K, 900 K, and 1000 K are shown in all the panels. **Top left panel** shows the emission spectra of models which have convective mixing length set at H but have different K_{zz} parametrizations like Moses, Moses/100, and Moses×100 which are represented by different line types in the panels like solid, dashed, and dashed-dotted. **Top right panel** shows the same but for models with convective mixing length set at $0.1 \times H$. **Bottom left and right panels** show the sensitivity of the L-band spectrum to radiative zone K_{zz} when $L = H$ and $L = 0.1 \times H$, respectively. The shaded region shows the wavelength range where CH_4 is the most important absorber. 171

4.14 Color magnitude diagrams (CMD) of observed brown dwarfs in different filters are shown with overplotted equilibrium and disequilibrium chemistry model tracks with different strengths of convective and radiative zone vertical mixing. The top row shows the J vs. J-H where the models with convective zone mixing length of H and different radiative zone K_{zz} are shown with various linetypes of red. Models with convective zone mixing length of $0.1 \times H$ and different radiative zone K_{zz} are shown with various linetypes of blue and the equilibrium chemistry models are shown with dashed black lines. Each column shows the same data but the model tracks with different values of log(g). The second row shows the the $L^{'}$ vs $L^{'}$-$M^{'}$ whereas the third row shows the W1 vs. W1-W2. 174

4.15 The **top left panel** shows the observed M-band spectra of Gl 570D with red points, the 1-2.5 μm observations of Gl 570D with black points and the *Spitzer* IRS measurements with brown points.. The flux values sampled by the top 131 models with the least G_k parameter after fitting the M-band spectra only are shown with the shaded blue region. The **top right panel** shows the best-fit model obtained by fitting the M-band spectra, the 1-2.5 μm data, and the *Spitzer* 5-14 μm data for Gl 570D. The **bottom left panel** shows a comparison of the best-fit model with the M-band spectra only. The **bottom right panels** shows the $T(P)$ profile of the best fit model, the $t_{\rm mix}$ and $t_{\rm chem}$ of different quenched species as a function of pressure, and the rightmost panel shows the volume mixing ratios of CO, CH_4, NH_3, H_2O, CO_2 and PH_3. 179

4.16 The **top left panel** shows the observed M-band spectra of 2M 0415 with red points, the 1-2.5 μm observations of 2M 0415 with black points and the *Spitzer* IRS measurements with brown points. The flux values sampled by the top 101 models with the least G_k parameter after fitting the M-band spectra only are shown with the shaded blue region. The **top right panel** shows the best-fit model obtained by fitting the M-band spectra, the 1-2.5 μm data and the *Spitzer* 5-14 μm data for 2M 0415. The **bottom left panel** shows a comparison of the best-fit model with the M-band spectra only. The **bottom right panels** shows the $T(P)$ profile of the best fit model, the $t_{\rm mix}$ and $t_{\rm chem}$ of different quenched species as a function of pressure, and the rightmost panel shows the volume mixing ratios of CO, CH_4, NH_3, H_2O, CO_2 and PH_3. 180

4.17 The **left panel** shows a heat map of the χ^2 value calculated using model photometry and observed photometry (Miles et al. 2020) in various infrared bands as a function of model $T_{\rm eff}$ and log(g) for WISE 0313. The left panel indicates models where radiative K_{zz} is fixed at Moses and the convective mixing length is H. The **middle and right panels** also show the χ^2 heat maps using models with radiative K_{zz} of Moses/100 and Moses$\times$100, respectively. The best-fit $T_{\rm eff}$ is near 550 K. 183

4.18 The best-fit atmospheric models and their comparison with data are shown in this figure. **Each row** corresponds to a different object. The **left most column** shows the best-fit M-band spectra along with the observed data from Miles et al. (2020). The **second left column** shows the best-fit $T(P)$ profile for these objects from the grid of models presented in this paper. The **third column shows** the best-fit mixing timescale in blue along with the chemical timescale for CO in red as a function of pressure. The volume mixing ratios of various atmospheric gases are shown in the **fourth column** for each object. 185

4.19 The best fit quench K_{zz} of CO for each object is shown as a function of their best-fit $T_{\rm eff}$ with the red crosses. The median best-fit quench K_{zz} vs. $T_{\rm eff}$ inferred by Miles et al. (2020) with lower gravity models are shown with the faded red crosses. The inferred quench K_{zz} for NH_3, CO_2, HCN, and PH_3 from the best-fit models for each object are also shown as a function of their best-fit $T_{\rm eff}$. The black points show the theoretically maximum K_{zz} allowed from mixing length theory for these best-fit models. 188

4.20 Simulated data from JWST instruments are shown for one of our model brown dwarfs with $T_{\rm eff}$ of 700 K. The three colors in the simulated data correspond to models with different radiative zone K_{zz}. The **top left panel** shows the simulated NIRSpec spectra of a log (g)=5.5 object with an exposure time of 10 minutes while the **bottom left panel** shows a zoomed version of the top left panel to emphasize how JWST NIRSpec M-band observations can clearly distinguish between different K_{zz} in the radiative zones for these T-dwarfs. The **top right panel** shows the NIRSpec simulated data for a brown dwarf with $T_{\rm eff}$ of 700 K and log(g) of 4.5. The two colors represent different K_{zz} in the convective zone but the same K_{zz} in the radiative zone. The **bottom right panel** shows MIRI LRS simulated data for the same models shown in the top right panels. To compare the differences between the simulated data from different models to the typical JWST noise, the ratio of the flux differences (δF) between various models and the simulated JWST noise (N) is shown below each of these panels. This shows that both convective and radiative zone K_{zz} can be constrained with JWST. 192

4.21 Effect of PH_3 quenching on the spectrum has been shown by comparing them with disequilibrium chemistry model spectra where PH_3 is not quenched. Models with different $T_{\rm eff}$ values ranging from 400 K to 1000 K, with a step of 100 K, are shwon from bottom to top. All of these models have log(g)=5. 195

4.22 **Top panel** shows the equilibrium chemistry abundance of PH_3 at pressures where $T(P)= T_{\rm eff}$ in our $T_{\rm eff}$ vs. gravity grid of chemical equilibrium models. The **second, third and last panels** depict PH_3 abundance within the $T_{\rm eff}$ vs. gravity parameter space in our disequilibrium chemistry models. The second, third and last panels correspond models with radiative zone K_{zz} values of "Moses", "Moses×100", and "Moses/100", respectively while the convective zone mixing length L was fixed at the scale height H. Models where PH_3 was quenched in a radiative zone are marked with black hatches. PH_3 was quenched at a convective zone in the rest of the models. 196

5.1 The left panel shows self-consistently calculated K_{zz} profiles as a function of pressure for a series of solar composition model atmospheres with $T_{\rm eff}$ from 1500 K to 400 K and log(g)=5.0. The K_{zz} in the convective zone has been calculated with mixing length theory whereas the K_{zz} in the radiative atmosphere follows the parameterization in Moses et al. (2021). The right panel shows the K_{zz} profiles for a 700 K model with varying log(g) between 4.5 and 5.5. The black dashed lines depict the constant K_{zz} profiles used in this work for sampling the several orders of magnitude range in K_{zz} values covered by these model calculations. Some colder models in the left panel with $T_{\rm eff}$ between 500-800 K show a sharp drop and rise in K_{zz} in the deep atmosphere which is indicative of the presence of a detached radiative zone in their atmospheres. Similar behaviour is also present in low gravity models shown in the right panel. 208

5.2 The volume mixing ratio profiles of CH_4, CO, H_2O, CO_2, NH_3, and PH_3 are shown in the six panels for a 700 K object with log(g)=5.0 with solar composition atmosphere. Different colored lines represent models with different K_{zz} from 10^2 to 10^9 cm^{2}s^{-1}. The mixing ratio profiles from a chemical equilibrium model of the same object is shown with the black dashed lines. The mean photospheric pressure of the models is $\sim$ 2 bars, which is shown with the blue dashed line in all the panels. 222

5.3 The differences in $T(P)$ profiles between an atmosphere in thermochemical equilibrium and an atmosphere with vigorous mixing at different metallicities is shown by the three panels (top x-axis). All the atmospheric models shown here have $T_{\rm eff}$= 700 K, log(g) = 3.25, and solar C/O ratio. The $T(P)$ profile calculated with thermochemical equilibrium are shown as black dashed lines whereas the profile calculated by assuming K_{zz} = 10^9 cm^{2}s^{-1} are shown as green solid lines. The left panel, middle and right panels show the comparison at 0.1×, 1×, and 10 ×solar metallicities. The colored background (bottom x-axis) in each panel maps the difference in the pressure and wavelength-dependant optical depths between the chemical equilibrium and disequilibrium models with the quantity $\log_{10}(\tau_{\rm eq}/\tau_{\rm deq})$. A value $>$ 0 shows that the chemical equilibrium model is more opaque than the disequilibrium chemistry model at that particular wavelength and pressure whereas a negative value reflects the opposite scenario. The red horizontal line in each panel shows the pressure level at which CH_4, CO, and H_2O quench in each model atmosphere. The red dots on each $T(P)$ profile denotes the mean photospheric pressure levels of each case. Note that the quench pressure for NH_3/N_2 or CO_2 are different than depicted by the red horizontal line. 224

5.4 The differences in $T(P)$ profiles between an atmosphere in thermochemical equilibrium and an atmosphere with vigorous mixing at different C/O ratios is shown by the three panels (top x-axis). The atmospheric models shown here have $T_{\rm eff}$= 700 K and $\log(g)$ = 3.25 with solar metallicity. The $T(P)$ profile calculated with thermochemical equilibrium are shown as black dashed lines whereas the profile calculated by assuming K_{zz} = 10^9 cm^{2}s^{-1} are shown as green solid lines. The left panel, middle and right panels show the comparison at C/O = 0.22, 0.45, and 1.14, respectively. The colored background in each panel maps the same quantity as in Figure 5.3. The red horizontal line in each panel shows the pressure level at which CH_4, CO, and H_2O quench in each model atmosphere. The red dots on each $T(P)$ profile denotes the mean photospheric pressure levels of each case. Note that the quench pressure for NH_3/N_2 or CO_2 are different than depicted by the red horizontal line. 225

5.5 Sensitivity of the $T(P)$ profile to K_{zz} across a large range of $T_{\rm eff}$ values at different atmospheric metallicities and gravities are shown. Each panel shows $T(P)$ profiles for $T_{\rm eff}$ values of 2400 K, 2200 K, 2000 K, 1800 K, 1600 K, 1400 K, 1200 K, 900 K, 700 K, 500 K, and 300 K. The area shaded for the $T(P)$ profiles at each $T_{\rm eff}$ shows the sensitivity of the $T(P)$ profiles to variation in K_{zz} from 10^2 cm^{2}s^{-1} to 10^9 cm^{2}s^{-1}. Higher K_{zz} causes the $T(P)$ profiles to be colder than lower K_{zz} models. The top row shows models with 0.1×solar atmospheric metallicity while the middle and the bottom rows show models with solar and 10×solar atmospheric metallicity. The left row shows models at 31 ms^{-2} while the middle and right rows show models at 562 ms^{-2} and 1000 ms^{-2}, respectively. All models shown here have a C/O= 0.45. 230

5.6 Sensitivity of the $T(P)$ profile to K_{zz} across a large range of $T_{\rm eff}$ values at different atmospheric C/O and gravities are shown. Each panel shows $T(P)$ profiles for $T_{\rm eff}$ values of 2400 K, 2200 K, 2000 K, 1800 K, 1600 K, 1400 K, 1200 K, 900 K, 700 K, 500 K, and 300 K. The area shaded for the $T(P)$ profiles at each $T_{\rm eff}$ shows the sensitivity of the $T(P)$ profiles to variation in K_{zz} from 10^2 cm^{2}s^{-1} to 10^9 cm^{2}s^{-1}. The top row shows models with C/O= 0.22 while the middle and the bottom rows show models with C/O= 0.45 and C/O= 1.14. The left row shows models at 31 ms^{-2} while the middle and right rows show models at 562 ms^{-2} and 1000 ms^{-2}, respectively. All models shown here have solar metallicity. . 231

5.7 Effect of K_{zz} on the emission spectra between 0.8-12 μm of a 700 K object with log(g)=4.75 is shown in the top panel. The metallicity and the C/O are kept constant across all the models in the top panel. Effect of metallicity on the emission spectra between 0.8-12 μm of a 700 K object with log(g)=4.75 is shown in the middle panel. The K_{zz} and the C/O are kept constant across all the models in the top panel. Effect of C/O on the emission spectra between 0.8-12 μm of a 700 K object with log(g)=4.75 is shown in the bottom panel. The K_{zz} and the metallicity are kept constant across all the models in the top panel. Standard infrared photometric bands like J, H, K, L, and M are also depicted with the shaded region. . 236

5.8 The thermal emission spectra between 0.9-5.5 μm at varying $T_{\rm eff}$ from 2400 K to 275 K for metal-poor atmospheres with [M/H]=-0.5 and C/O=0.45 is shown here. All models shown here have the log(g)=4.75 (g= 562 ms^{-2}). At each $T_{\rm eff}$, the variation in the spectra due to K_{zz} is shown by shading the area between the spectra from models with K_{zz}=10^2 cm^{2}s^{-1} and K_{zz}=10^9 cm^{2}s^{-1}. The major absorption bands of CH_4 and CO are shown with pink and blue bands, respectively. 240

5.9 The thermal emission spectra between 0.9-5.5 μm at varying $T_{\rm eff}$ from 2400 K to 275 K for metal-rich atmospheres with [M/H]=+1.0 and C/O=0.45 is shown here. All models shown here have the log(g)=4.75 (g= 562 ms^{-2}). At each $T_{\rm eff}$, the variation in the spectra due to K_{zz} is shown by shading the area between the spectra from models with K_{zz}=10^2 cm^{2}s^{-1} and K_{zz}=10^9 cm^{2}s^{-1}. The major absorption bands of CH_4 and CO are shown with pink and blue bands, respectively. 241

5.10 The spectral strength metric S for the CH_4 feature at 3.3μm as a function of $T_{\rm eff}$ is shown in the panels in the left column. Each panel from top to bottom corresponds to a different metallicity, and each line represents the spectral strength from different K_{zz} values. The middle column shows the same metric for the CO feature between 4.5-4.8 μm, whereas the right column shows the metric for the 10-11 μm NH_3 feature. The black dashed line shows the $T_{\rm eff}$ value below which these features roughly appear in the spectra. 242

5.11 The left corner plot shows the posterior distributions for $T_{\rm eff}$, gravity, $\log_{10}K_{zz}$, [M/H], C/O (×Solar), and radius when various wavelength regions of a synthetic data set are fitted with the Bayesian grid fitting approach with the `Sonora Elf Owl` grid. The right corner plot shows posteriors when the same synthetic spectra is observed with various instrument modes of *JWST*. The six panels in Figure 5.12 show the synthetic dataset used for this analysis to obtain the posterior distributions shown in the corner plots. Left corner plot: The blue posteriors show when the synthetic spectra between 4.5-5 μm is fitted whereas the orange posteriors represent fitting the synthetic data between 5-14 μm. The green show results from fitting the 4-14μm regions, respectively. Right corner plot: The sky blue and crimson posteriors show results when synthetic data from *JWST* NIRSpec G395H and MIRI LRS is fitted, respectively. The brown posteriors show constraints obtained from synthetic Prism data. The posteriors obtained from the Prism data are too narrow for the range of the parameters shown in the corner plots. The black lines in the corner plot show the true parameter values used to produce the synthetic spectral data. 248
5.12 The six panels show the synthetic dataset used for this analysis to obtain the posterior distributions shown in the corner plots in Figure 5.11. The top left panel shows the synthetic spectra between 4.5-5 μm whereas the middle left panel shows the synthetic data between 5-14 μm. The bottom left panel show the 4-14μm region of the synthetic spectra. The top and middle right panels show the synthetic data from *JWST* NIRSpec Prism and *JWST* NIRSpec G395H, respectively. The bottom right panel shows the synthetic spectrum from *JWST* MIRI LRS. Each panel also shows the 1σ envelope on the spectra from the fitted posteriors. 249
5.13 *J* vs. *J-H* color magnitude diagram of the substellar object population is shown with gray circles. Our T-dwarf sample of 9 objects is shown with yellow circles and it uniformly spans almost the whole of the T- dwarf sequence except the L/T transition objects. All magnitudes shown in this diagram are MKO magnitudes. Data from Best et al. (2020). . . . 254

5.14 The observed spectra of 9 T-dwarfs from our sample are shown in the different panels. Observations from *AKARI* are shown with yellow circles, whereas *Spitzer* data are shown with green circles. For GL570D, ground-based data was also used, which is shown with pink circles. In each panel, spectra calculated from 100 random draws of parameters from their converged posterior distributions are also shown with the blue lines. At the top of each panel, the τ=1 pressure level for each gas from the best-fit model is shown as a function of wavelength. These pressure levels are only shown so that the spectral features in the data can be associated with the dominant atmospheric gaseous absorber in the best-fit model. The *AKARI* data was obtained from Sorahana & Yamamura (2012) and the *Spitzer* data from Suárez & Metchev (2022). The ground-based data for GL570D was obtained from Geballe et al. (2009). 255

5.15 The best-fit $\log(K_{zz})$ vs. $T_{\rm eff}$ is shown for our sample of 9 T- dwarfs. The green circles represent objects for which we have fit the spectra between 2.5-14 μm whereas the yellow triangles represent the objects for which 5-14 μm data was fit with our models. The colored lines show the expected model K_{zz} as a function of $T_{\rm eff}$ from mixing length theory assuming free convection in the deep convective atmosphere. Each line corresponds to a different $\log(g)$. The gray lines in the background show the actual grid points of the `Sonora Elf Owl` grid for $T_{\rm eff}$ and K_{zz} between which the grid was interpolated to obtain the results. 259

5.16 The trends in the $CO/CH_4/H_2O$ quenching in radiative or convective zone as a function of $T_{\rm eff}$ and $\log(g)$ is shown here from an extended version of the self-consistent model grid presented in Mukherjee et al. (2022). These models have K_{zz} varying across atmospheric depth instead of the constant K_{zz} approach used in the `Sonora Elf Owl` grid and have C/O ratio of 0.45. The colormap shows the quenched CO abundance as a function of $T_{\rm eff}$ and $\log(g)$ in both the panels. The left panel depicts models where the K_{zz} in the convective zone follows mixing length theory whereas the right panel shows models where the convective zone mixing length is smaller than the predictions from mixing length theory by a factor of a 10. The hatched regions depict parts of the parameter space where CO is quenched in a radiative zone instead of a convective zone. . 260

6.1 $T(P)$ profiles computed using 1D radiative–convective–equilibrium modeling at various $T_{\rm eq}$ and $T_{\rm int}$ values are shown. Each panel shows the model $T(P)$ profiles computed for a $T_{\rm eq}$ value at five different $T_{\rm int}$ values between 30 K and 500 K. The six panels correspond to $T_{\rm eq}$= 1600 K, 1400 K, 1100 K, 900 K, 800 K, and 600 K. The kink at 1 mbar and 1700 K in the hottest models ($T_{\rm eq}$=1600 K) is due to a small amount of TiO opacity. All the $T(P)$ profiles have been computed for a planet with gravity=4.5 ms^{-2} around a star with $T_{\rm eff}$= 5326.6 K, $log(g)$=4.38, and Radius=0.93$R_{\odot}$. 284

6.2 $T(P)$ profiles computed assuming radiative–convective–thermochemical equilibrium (RCTE) and radiative–convective–photochemical equilibrium (RCPE) are shown with dashed black lines and solid red lines, respectively. The assumed $T_{\rm eq}$, [M/H], and C/O of the model is 800 K, +1.0, and 1×solar, respectively. Each panel corresponds to a different $T_{\rm int}$ from 100 K to 500 K. The faded lines show the volume mixing ratios (top x-axis) of CH_4, NH_3, SO_2, and CO_2 in blue, green, orange, and brown, respectively. The dashed VMR profiles are from the RCTE models whereas the solid VMR profiles correspond to the RCPE models. The narrower panel accompanying each of the four panels shows the different in the $T(P)$ profile between the two modeling assumptions in each case as a function of pressure. 285

6.3 The dependence of chemical abundance profiles on K_{zz}, $T_{\rm int}$, and C/O are shown in the left, middle, and right columns, respectively. The upper row shows this dependence for CH_4 while the middle and lower rows show this dependence for SO_2 and CO_2, respectively. The pressure values typically probed by transmission spectra are shown with the red shaded region. . 290

6.4 The weighted abundance of CH_4 calculated using Equation 6.1 as a function of C/O and K_{zz} in each panel. Each row corresponds to a different $T_{\rm eq}$ value from 1100 K to 600 K from top to bottom. Each column correspond to a different $T_{\rm int}$ value between 30 K and 500 K from left to right. Note that the C/O is shown relative to an assumed solar value of 0.458 in this plot. 292

6.5 The weighted abundance of CO calculated using Equation 6.1 has been shown as a heat map as a function of C/O and K_{zz} in each panel. Each row corresponds to a different $T_{\rm eq}$ value from 1100 K to 600 K from top to bottom. Each column correspond to a different $T_{\rm int}$ value between 30 K and 500 K from left to right. Note that the C/O has been shown relative to the assumed solar value of 0.458 in this plot. 295

6.6 The weighted abundance of CO_2 calculated using Equation 6.1 has been shown as a heat map as a function of C/O and K_{zz} in each panel. Each row corresponds to a different $T_{\rm eq}$ value from 1100 K to 600 K from top to bottom. Each column correspond to a different $T_{\rm int}$ value between 30 K and 500 K from left to right. Note that the C/O has been shown relative to the assumed solar value of 0.458 in this plot. 296
6.7 **Left panel:** The $T(P)$ profiles of planets with $T_{\rm int}$= 30 K and $T_{\rm eq}$ between 1100 and 600 K are shown with the four solid lines. The black dashed line shows the CO=CH_4 equal abundance curve from chemical equilibrium calculations at [M/H]=+1.0 and C/O=1×solar. Equal abundance contours for CO and CH_4 are shown in blue and red, respectively. The four black markers on each $T(P)$ profile show the quench pressures of CO for 10^6, 10^8, 10^{10}, and 10^{12} $\rm cm^2s^{-1}$. **Right panel:** The $T(P)$ profiles of planets with $T_{\rm int}$= 200 K and $T_{\rm eq}$ between 1100 and 600 K are shown with the four solid lines, whereas the dashed lines show the models for $T_{\rm int}$= 30 K. Equal abundance contours for CO_2 from thermochemical equilibrium are shown in red. 299
6.8 The weighted abundance of H_2O calculated using Equation 6.1 has been shown as a heat map as a function of C/O and K_{zz} in each panel. Each row corresponds to a different $T_{\rm eq}$ value from 1100 K to 600 K from top to bottom. Each column correspond to a different $T_{\rm int}$ value between 30 K and 500 K from left to right. Note that the C/O has been shown relative to the assumed solar value of 0.458 in this plot. 304
6.9 The weighted abundance of NH_3 calculated using Equation 6.1 has been shown as a heat map as a function of C/O and K_{zz} in each panel. Each row corresponds to a different $T_{\rm eq}$ value from 1100 K to 600 K from top to bottom. Each column correspond to a different $T_{\rm int}$ value between 30 K and 500 K from left to right. Note that the C/O has been shown relative to the assumed solar value of 0.458 in this plot. 307
6.10 The weighted abundance of HCN calculated using Equation 6.1 has been shown as a heat map as a function of C/O and K_{zz} in each panel. Each row corresponds to a different $T_{\rm eq}$ value from 1100 K to 600 K from top to bottom. Each column correspond to a different $T_{\rm int}$ value between 30 K and 500 K from left to right. Note that the C/O has been shown relative to the assumed solar value of 0.458 in this plot. 308
6.11 The weighted abundance of SO_2 calculated using Equation 6.1 has been shown as a heat map as a function of C/O and K_{zz} in each panel. Each row corresponds to a different $T_{\rm eq}$ value from 1100 K to 600 K from top to bottom. Each column correspond to a different $T_{\rm int}$ value between 30 K and 500 K from left to right. Note that the C/O has been shown relative to the assumed solar value of 0.458 in this plot. 309

6.12 The top set of panels show the abundance of various Sulfur species at 1 mbar as a heat map as a function of C/O and $T_{\rm eq}$ in each panel. Each panel corresponds to a different S- bearing gas. All models shown here have $T_{\rm int}$=200 K and K_{zz}=$10^9 {\rm cm}^2{\rm s}^{-1}$. The lower panels show the abundance of the same species but at 0.1 bar instead. This is to show the abundance of S- bearing gases both at pressures probed by transmission and emission spectroscopy, respetively. 310
6.13 Each panel shows how X_w for a different gas varies with [M/H] and K_{zz} as a heat map. All the models shown here have $T_{\rm eq}$= 800 K, $T_{\rm int}$= 200 K, and C/O= 0.1×solar. 315
6.14 Each panel shows how X_w for a different gas varies with [M/H] and K_{zz} as a heat map. All the models shown here have $T_{\rm eq}$= 800 K, $T_{\rm int}$= 200 K, and C/O= 1×solar. 315
6.15 The variation of photospheric abundance of key atmospheric gases as a function of $T_{\rm eq}$ is shown here. Each column shows the variation for a different value of $T_{\rm int}$. The top row shows the evolution of CH_4 and CO abundance with $T_{\rm eq}$. The middle and last row shows the same for N_2-NH_3, and H_2S-SO_2-S, respectively. In each panel, the three colored lines shows the abundances for a three different values of K_{zz}. The C/O has been fixed to be 1×solar in these models. 319
6.16 The top panel shows the variation of transmission spectra with changing K_{zz} while the bottom panel shows the variation of the transmission spectra of the planet with changing $T_{\rm int}$. The models shown here are for $T_{\rm eq}$=800 K, [M/H]=+1.0, and C/O=1×solar. The $T_{\rm int}$ has been fixed at 200 K for the top panel while the K_{zz} has been fixed at $10^{10} {\rm cm}^2{\rm s}^{-1}$ in the bottom panel. Note that the transmission spectra have been renormalized in such a manner that the minimum transit depth of each model is set at zero. 322
6.17 Sensitivity of the transmission spectra to changing K_{zz} is shown here as a function of K_{zz} and wavelength. Each column corresponds to a different C/O value whereas each row shows models for different $T_{\rm int}$ values. All models shown here have $T_{\rm eq}$=800 K. A brighter red or a brighter blue color indicates that the transmission spectra is very sensitive to changing K_{zz} at that K_{zz} and wavelength value. 324
6.18 Sensitivity of the transmission spectra to changing K_{zz} is shown here as a function of K_{zz} and wavelength. Each column corresponds to a different $T_{\rm eq}$ value whereas each row shows models for different $T_{\rm int}$ values. All models shown here have C/O=1×solar. A brighter red or a brighter blue color indicates that the transmission spectra is very sensitive to changing K_{zz} at that K_{zz} and wavelength value. 325

6.19 Similar to Figure 6.17 but the sensitivity of transmission spectra to changing $T_{\rm int}$ is shown here as a function of $T_{\rm int}$ and wavelength, instead of K_{zz} in Figure 6.17. Each column corresponds to a different C/O value whereas each row shows models for different K_{zz} values. All models shown here have $T_{\rm eq}$=800 K. A brighter red or a brighter blue color indicates that the transmission spectra is very sensitive to changing $T_{\rm int}$ at that $T_{\rm int}$ and wavelength value. 329
6.20 Sensitivity of the transmission spectra to changing $T_{\rm int}$ is shown here as a function of $T_{\rm int}$ and wavelength. Each column corresponds to a different $T_{\rm eq}$ value whereas each row shows models for different K_{zz} values. All models shown here have C/O=1×solar. A brighter red or a brighter blue color indicates that the transmission spectra is very sensitive to changing $T_{\rm int}$ at that $T_{\rm int}$ and wavelength value. 330
6.21 The column density of haze precursors at pressures smaller than 10^{-3} bars has been shown as a heat map as a function of C/O and K_{zz} in each panel. Each row corresponds to a different $T_{\rm eq}$ value from 1100 K to 600 K from top to bottom. Each column correspond to a different $T_{\rm int}$ value between 30 K and 500 K from left to right. The abundance of gases– C_2H_2, C_2H_4, C_2H_6, C_4H_2, HCN, CH_3CN, and CS_2 were used to compute the column density of the haze precursor molecules. 333
6.22 The column density of haze precursors at pressures smaller than 10^{-3} bars has been shown as a heat map as a function of [M/H] and K_{zz} in each panel. The top row corresponds to $T_{\rm int}$= 30 K, while the bottom row shows models with $T_{\rm int}$= 200 K. The $T_{\rm eq}$ has been set to 800 K for all the panels. The left column shows models for C/O=0.1×solar while the right column shows models at C/O=1×solar. The abundance of gases– C_2H_2, C_2H_4, C_2H_6, C_4H_2, HCN, CH_3CN, and CS_2 were used to compute the column density of the haze precursor molecules. 334
6.23 Difference between the $T(P)$ profiles calculated using the RCPE model for three different K_{zz} values and the RCTE model is shown in the top left panel for a $T_{\rm int}$=100 K model. The same differences are shown for a $T_{\rm int}$=500 K model in the top right panel. The three bottom left panels show the abundance profiles for each model for CH_4, SO_2, and NH_3 at $T_{\rm int}$=100 K. The same quantities for the $T_{\rm int}$= 500 K model are shown in the three bottom right panels. All the models shown here are for $T_{\rm eq}$=800 K, [M/H]=+1.0, and C/O=1×solar. 339
6.24 The upper set of panels show the change in abundance profile of key molecules due to change in the X-ray/UV flux incident on the planet when K_{zz}=10^6cm^{2}s^{-1}. Profiles for SO_2, CH_4, NH_3, and CO_2 are shown from left to right, respectively. The black-dashed line shows the profile for the nominal case. The middle row compares the abundances when K_{zz}=10^{10}cm^{2}s^{-1}. The lower panel shows the X-ray/UV spectrum used to calculate each of these models. 341

6.25 This plot shows how the abundance of a certain gas changes at a given pressure when the UV flux at a given wavelength bin is increased by a factor of $\times 100$. This has been quantified with Y in Equation 6.2. This Y quantity has been plotted as a heat map in each panel for SO_2, CH_4, NH_3,H_2O, CO_2, SO, S_2, CS_2, and HCN. The X-axis in each panel is the wavelength of the UV flux and the Y-axis is pressure in the atmosphere. The wavelength bins used for boosting the UV fluxes are also shown as vertical lines at the bottom of each panel along with the nominal UV spectra incident on the planet. A positive value for Y at a given pressure and wavelength means that the molecular abundance has increased relative to the nominal case when UV flux at those wavelengths were boosted. A negative Y value corresponds to a decrease instead. 342

7.1 **Top panel** shows the panchromatic emission spectrum of GJ 436b observed with *JWST* using three instrument modes – NIRCam F322W2 (yellow points), NIRCam F444W (red points), and MIRI LRS (blue points). The NIRCam data shown here is from the `tshirt` reduction pipeline and the MIRI LRS data is from the `Eureka!` pipeline. The panchromatic spectrum is obtained from the weighted average of individual visits for each instrument mode. The pink diamonds, black diamonds, and green crosses also show photometry of the planet observed with *Spitzer* and analyzed by Stevenson et al. (2010), Morley et al. (2017a), and Lanotte et al. (2014), respectively. **Bottom panel** compares the F_p/F_s spectra derived from the *JWST* observations with two different data reduction pipelines – `tshirt` and `Eureka!`. 364

7.2 The **top panel** shows the median spectral model obtained from the free chemistry retrieval with the solid blue line compared with the *JWST* observations. The 1σ and 2σ envelopes on the model spectra are shown with dark and light blue shaded regions. The **middle panel** shows the residuals of the model fit divided by the errors in the data. The **bottom left** and **bottom right** panels show a zoomed in version of the top panel with comparison of the retrieved models with parts of the spectrum observed with NIRCam and MIRI, respectively. 368

7.3 The **top panel** shows the median spectrum obtained from the isothermal retrieval with the red solid line compared with the *JWST* spectrum of the planet. The 1σ and 2σ envelopes on the model spectra are shown with dark and light red shaded regions. The **middle panel** shows the residuals of the model fit divided by the errors in the data. The **bottom panel** shows the corner plot between Bond albedo (A_B) and heat recirculation parameter (ϵ) obtained by fitting the day-side blackbody temperature constrained from the isothermal retrieval with the methodology described in Cowan & Agol (2011). The dashed line show the median and 3σ constraints on each parameter. 372

7.4 The **top panel** shows the comparison of the best-fit clear equilibrium chemistry grid model (green line), clear disequilibrium chemistry grid model (red line), and cloudy equilibrium chemistry grid model (black line) with the *JWST* spectrum of GJ 436b. The **middle panel** shows the residuals of the model fits divided by the errors in the data. Similar to Figure 7.2, the **bottom left** and **bottom right** panels show a zoomed in version of the top panel with comparison of the best-fit grid models with parts of the spectrum observed with NIRCam and MIRI, respectively. The clear and cloudy equilibrium chemistry models are consistent with very elevated metallicities ($\geq$500$\times$solar and $\geq$300$\times$solar at 1σ, respectively), whereas the disequilibrium chemistry models are consistent with metallicities higher than 80$\times$solar. 377

7.5 The **left most panel** shows the $T(P)$ profile obtained from the clear free chemistry retrieval with the solid blue line along with the 1σ and 2σ envelopes on the $T(P)$ profile. The $T(P)$ profiles of the best-fit model from the clear equilibrium chemistry grid is shown with the green solid line. The $T(P)$ profile from the cloudy equilibrium chemistry grid and clear disequilibrium chemistry grid are also shown with black solid and red dot-dashed lines, respectively. The thermal contribution function from each of these models at 4 μm are also shown on the left side of the panel. The **second column** shows the cloud optical depth per atmospheric layer as a function of pressure at 4 μm for the best-fit cloudy equilibrium chemistry model. The **third column** shows the cloud mass mixing ratio as a function of pressure for the KCl and Na_2S cloud included in the cloudy best-fit model. The **forth column** shows the mean cloud particle sizes in the best-fit model as a function of pressure for KCl and Na_2S. 378

7.6 The **left panel** shows the corner plot obtained by fitting the *Spitzer* photometry of GJ 436b from Morley et al. (2017a) and Lanotte et al. (2014) with our clear disequilibrium chemistry model grid in blue. The corner plot obtained by fitting the *JWST* data with the same grid has been overplotted in red. The **right panel** compares the *Spitzer* photometry with the best-fit disequilibrium chemistry model in blue and the best-fit model to the *JWST* data in red. The model photometry derived from each model has been shown with blue and red dashes as well. Note that the C/O plotted here is relative to the solar value, where the assumed solar value is 0.458. 382

7.7 Comparison of the transmission spectrum computed from the various best-fit self-consistent models from this work with the HST/WFC3 transmission spectrum observations of GJ 436b. Green and black lines shows the clear and cloudy equilibrium chemistry models, respectively. The red line shows the best-fit clear disequilibrium chemistry model. 385

7.8 The ratio of planets' derived day-side effective/average brightness temperatures and equilibrium temperatures from their *JWST* emission spectroscopy or phase-curve measurements as a function of their equilibrium temperatures is shown. GJ 436b and GJ 1214b are the only two non-terrestrial planets where this ratio is less than or similar to 1. The faded black points show the ratio for the sample of planets presented in Deming et al. (2023). These ratios are computed using the brightness temperature derived from their *Spitzer* 3.6 μm flux in Deming et al. (2023). 387
7.9 *Top:* Example broadband NIRCam lightcurves for observation 1185-14 (F322W2, top left) and Observation 1185-15, (F444W, top right) before and after de-trending, as well as the residuals. In each time panel section, the data are plotted as blue points with error, and the model curve is plotted as an orange line for the raw lightcurve (top) and the de-trended lightcurve (middle). The bottom panel section shows the residuals and a set of 60 equally-spaced time-bins (4.8 minutes apart). *Bottom:* Broadband MIRI LRS lightcurve for Observation 1177-5. 394
7.10 Individual eclipse observations with NIRCam as reduced by `tshirt`. The errors, inflated by the Gaussian process fit, give largely consistent spectra. 395
7.11 Allan Variance Plots of the broadband lightcurves of the 8 observations analyzed by the `tshirt` pipeline (Top Left: F322W2, Top Right: F444W, Bottom: LRS). Significant levels of noise enter at the 100 ppm level, requiring a Gaussian process to mitigate systematics and ensure consistency across independent eclipse observations. The dotted lines ("White Noise Scaling") show the expectation for uncorrelated white noise, which follows $1/\sqrt{N}$ statistics for N data points. The dashed line shows the lightcurve residuals with the Gaussian Process component removed ("Before de-trending"). The solid lines show the lightcurve residuals with the Gaussian Process applied ("GP de-trended"). 397
7.12 Lomb Scargle Periodograms of the broadband lightcurves of the 8 observations analyzed by the `tshirt` pipeline (Top Left: F322W2, Top Right: F444W, Bottom: LRS). There can sometimes be broad periodicities near 80 and 130 minutes, which are mitigated by the Gaussian process. The solid lines show the periodogram of residuals with the Gaussian Process applied ("GP de-trended"). The solid lines show the periodogram of residuals without removing the GP correlated noise ("Before de-trending"). 398
7.13 We integrated the *JWST* NIRCam bandpass over the same wavelengths as *Spitzer* IRAC1 and IRAC2 bands. The bandpass-integrated photometry for three different eclipses observed with NIRCam F322W2 is considerably shallower than the observed 3.6 μm *Sptizer* photometry (gray posteriors), likely due to uncorrected correlated noise in the *Spitzer* lightcurves. While the *JWST* NIRCam observations contain their own systematics, the modeled eclipses are all in agreement at a much shallower eclipse depth. 399

7.14 Best-fit BOSZ stellar model compared with the flux calibrated stellar spectrum from *JWST* for GJ 436 is shown in the **top panel**. **Bottom panel** shows the ratio between the data and the best-fit model. Deviations of this ratio from 1 indicate missing or additional opacities present in the best-fit model compared to the observed stellar spectrum. 401
7.15 The corner plot from the clear free chemistry retrieval on the *JWST* data. 402
7.16 The corner plot obtained from the grid fitting exercise from the clear equilibrium chemistry grid is shown in the **left** panel. The corner plot from the cloudy equilibrium chemistry grid and clear disequilibrium chemistry grid are shown in the **middle** and **right** panels, respectively. Note that the C/O shown is relative to the solar value, where the assumed solar C/O is 0.458. 403
7.17 The contribution of gases and clouds in shaping the best-fit self-consistent model is shown here for the clear equilibrium chemistry scenario (**top panel**), cloudy equilibrium chemistry scenario (**middle panel**), and clear disequilibrium chemistry scenario (**bottom panel**). The best-fit model in each panel is shown with a solid line – green in the top panel, black in the middle panel, and red in the bottom panel. The contribution of each absorber is shown as the shaded region between the best-fit spectrum and best-fit model without that absorber. 405

8.1 **Transit light curves of WASP-94A b show limb asymmetry.** (**A**) shows the broadband light curve between 1.35-1.5 μm with black points. The asymmetric limb planet model fit to the light curve is shown with the blue line and the spherical planet model fit with the red line. The time period of ingress and egress are shown with the shaded gray region. The asymmetric limb model fits the light curve better at a 6σ significance. (**B**) shows the binned (larger points) and unbinned residuals of the asymmetric limb model fit to the data. The residuals are consistently zero. (**C**) shows the binned (larger points) and unbinned residuals of the spherical planet model fit to the data. The residuals are inconsistent with zero during ingress/egress. 454
8.2 **Transmission spectrum of the morning and evening limbs of WASP-94A b**. (**A**) shows the observing geometry of the two limbs of WASP-94A b and its host star (to scale). (**B**) shows the nightside cloud map of WASP-94A b predicted through a 3D general circulation model. (**C**) shows the observed transmission spectrum of the evening terminator of the planet with red points along with the best-fit model. The key atmospheric absorbers shaping the observed spectrum (H_2O, clouds, etc) are shown with the shaded colors. (**D**) shows the observed transmission spectrum of the morning terminator with blue points along with the best-fit model. The spectrum is mainly shaped by cloud scattering as has been shown with the gray shaded region. 455

8.3 **Constrained temperature and cloud structure of the morning and evening limbs.** (**A**) shows the median and 1σ envelopes on the retrieved temperature-pressure profile for the morning and evening terminators in blue and red, respectively. Condensation curves corresponding to $MgSiO_3$, Fe, and MnS clouds are shown with the red, green, and yellow dashed lines, respectively. The $T(P)$ profiles of the two terminators derived from the 3D general circulation model are also shown with dotted lines. The vertical solid red and blue lines show the range of pressures probed by the transmission spectrum of the evening and morning limbs, respectively. (**B**) and (**C**) shows the retrieved cloud optical depth as a function of pressure like (**A**) for the evening and morning terminators , respectively. (**D**) and (**E**) shows the retrieved cloud mass mixing ratio as a function of pressure for the evening and morning terminators, respectively. Mass mixing ratio of Fe, $MgSiO_3$, and MnS are shown with green, brown, and orange shaded regions in both panels, respectively. (**F**) and (**G**) shows the retrieved mean cloud particle radius as a function of pressure for the evening and morning terminators, respectively. Particle sizes of Fe, $MgSiO_3$, and MnS cloud are shown with green, brown, and orange shaded regions in both panels, respectively. (**B**)-(**G**) panels show the same pressure range in the y-axis as (**A**). 456

8.4 **Effect of limb asymmetry on inferred composition of WASP-94A b.** (**A**) shows a comparison of the observed transmission spectrum of the evening terminator of WASP-94A b in red with the 1D spectrum extracted assuming the planet is spherically symmetric in black. The red and black shaded regions show the 1σ envelope on the retrieved model spectrum in each case. The scale height of the spherical spectrum gets artificially muted relative to the scale height of the evening terminator spectrum by more than a factor of $\sim$2 due to very asymmetric limbs of the planet. (**B**) shows the effect of this muting on the inferred metallicity of the planet between the two cases. The metallicity inferred from the spherical spectrum (black) is biased at a 5σ level. (**C**) shows the bias on the posteriors of the inferred C/O ratio. (**D**) shows that the strength of the vertical mixing parameter K_{zz} also gets biased at 2σ level. (**E**) shows a comparison of the 1.4 μm H_2O feature amplitude for a population of exoplanets measured with the *HST*/WFC3 instrument with light gray points. The black point shows the H_2O feature amplitude measured from the spherical spectrum of WASP-94A b while the red and blue points show the H_2O amplitude for the evening and morning terminators, respectively. The red and blue solid lines and the black dashed lines show the H_2O amplitude from atmospheric models for a clear, very cloudy, and limb-asymmetry affected planet, respectively. This shows that these biases are likely to affect a much wider population of exoplanets other than just hot Jupiters. 457

8.5 **Observed and modeled white light curve**. (**A**) shows the observed white light curve of WASP-94A b from the FIREFLy reduction with black points and the best-fit asymmetric limb model from catwoman is shown with the blue line. (**B**) shows the binned and unbinned residuals of the fit, that have a median absolute deviation of 76 ppm. 458
8.6 **Observed and modeled spectroscopic light curves**. (**A**) shows the observed spectroscopic light curves as a heat map. (**B**) shows the model fits to the spectroscopic light curves as a heat map with FIREFLy. . . . 458
8.7 **Effect of limb darkening on the transmission spectrum**. (**A**) shows the u_+ parameter when fitted freely for each spectroscopic channel with black points. The u_+ parameter from a 3D stellar model with and without offset are shown with the blue lines. (**B**) shows the same for the u_- parameter. (**C**) and (**D**) show the measured transmission spectrum of the morning and evening limbs, respectively. The blue points in each panel show the spectrum when limb darkening is fitted freely and the red points show the spectrum when limb darkening parameters are fixed to the 3D stellar model+offset. 459
8.8 **Allan variance plots showing correlated noise behavior in spectroscopic light curves**. (**A**), (**B**), (**C**), and (**D**) show the Allan variance plots for four randomly selected spectroscopic channels. Each plot shows that neglegible correlated noise is present in the spectroscopic light curves. 460
8.9 **Alternative evidence of limb asymmetry in spectroscopic light curves.** (**A**) shows the mid-transit time (T_0) as a function of wavelength with black points, when all the spectroscopic light curves were fit with the spherical planet model allowing for an independently fitted T_0 for each channel. The fitted T_0 compensates for the limb asymmetry of the planet and thus shows molecular features in H_2O absorption bands. The T_0 spectrum calculated from the measured spectrum of the two limbs of the planet is shown with the green line. (**B**) shows a comparison of the average planet spectrum (green) derived from the spectrum of the two limbs (blue and red) with the spherical planet spectrum extracted with the spherical planet model (black). 461
8.10 **Contamination of the 2nd order trace.** Contamination of the 2nd order trace of the stellar spectrum is highlighted with red boxes on the detector image. The green box is the only small region from which we could reliably extract transmission spectrum. The wavelengths of each region of the 1st and 2nd order trace are marked on the blue line. . . . 461
8.11 **2nd order transmission spectrum.** Extracted 2nd order spectrum is shown with the star points and is compared with the 1st order spectrum of each planet limb (circular points). 462

8.12 **Comparison between spectrum of morning and evening limbs from different reduction pipelines.** (**A**) shows the comparison of the evening limb spectrum measured from three different reduction pipelines – FIREFLy, Eureka!, and Fu. (**B**) shows the same for the morning limb spectrum. (**C**) and (**D**) show the residuals between the spectrum derived from each pipeline for the evening and morning limbs, respectively. . . . 462
8.13 **Correlation between mid-transit time and difference in transit depths between limbs.** The difference in the transit depths between the morning and evening limbs at 1.4 μm from the three data reduction pipelines is shown as a function of the constrained mid-transit time from the white light curves from each pipeline. The difference between the mid-transit time from a pipeline and the mid-transit time from the Fu pipeline is plotted in the x-axis. Note that the uncertainty in the constrained T_0 from each pipeline is larger than the difference in T_0 between the pipelines. 463
8.14 **Comparison between spherical planet spectrum between pipelines.** (**A**) shows a comparison between the spectrum measured for the planet assuming a spherical planet model between the three pipelines. (**B**) shows the residuals between the pipelines. 463
8.15 **Retrieved spectrum for each planet limb**. The retrieved median spectrum for the evening and morning limbs along with their 1σ and 2σ envelopes are shown in red and blue, respectively. The observed evening and morning spectrum are also shown with red and blue points, respectively. 464
8.16 **Corner plot for simultaneous retrieval on both limbs**. The posterior distribution for each parameter along with their cross-correlations are shown for the 1.5D simultaneous retrieval on the spectrum of the evening and morning limbs of the planet. 465
8.17 **Contribution function for the evening and morning limb spectrum**. (**A**) shows the contribution function as a function of pressure and wavelength from the best-fit 1.5D retrieval model for the evening limb. The contribution function is derived from the derivative of the transmittance with pressure for each wavelength value. (**B**) shows the contribution function for the morning limb spectrum. 466
8.18 **Constraints on Chemical Abundances**. (**A**) shows the constraints on the chemical abundances of various atmospheric gases on the evening limb of the planet. (**B**) shows the constraints on the morning limb. Note that we detect H_2O from the spectrum but the chemical equilibrium assumption allows us to predict the abundance constraints on the other gases. 466
8.19 **Retrieved spectrum for the spherical planet spectrum**. The retrieved median spectrum for the spherical planet spectrum along with its 1σ and 2σ envelopes are shown in black. The measured spherical planet spectrum is shown with black points. 467

8.20 **Corner plot for 1D retrieval on the spherical spectrum of the planet**. The posterior distribution for each parameter along with their cross-correlations are shown for the 1D `PICASO` retrieval on the spherical spectrum of the planet. 468
8.21 **Results of the patchy 2D cloud retrieval with POSEIDON**. (**A**) shows the retrieved median spectrum along with the 1σ and 2σ regions in blue, along with the measured spherical planet spectrum as unfilled black points. (**B**), (**C**), and (**D**) shows histograms of the posterior for the planet's atmospheric metallicity, C/O ratio, and cloud coverage fraction, respectively. 469

, for the morning (blue) and evening (red) terminators. Condensation curves for $MgSiO_3$, Fe, and MnS are also shown with the dashed lines. (**C**) shows the zonal advective timescale at 1 mbar (colour scale) as a function of longitude and latitude. The wind direction is marked with white arrows. (**D**) shows the temperature (colour scale) for an isobaric surface at 1 mbar. All plots are generated with data corresponding to the final day of the simulation, horizontal wind vectors have been over-plotted to aid interpretation.470figure.8.22

8.23 **Vertical mixing and cloud properties from GCM simulations of WASP-94A b.** (**A**) shows a comparison of the global mean K_{zz} profile from the GCM (black dashed line) with the constraints on K_{zz} from the limb asymmetry observations shown as the blue shaded region. The measured K_{zz} profile for Jupiter from (Moses et al. 2005) is shown with the orange line. (**B**) shows the cloud optical depth map at 6 mbar obtained by post-processing the GCM with $MgSiO_3$, Fe, and MnS clouds using the `VIRGA` model. The morning terminator appears cloudy while the evening terminator is relatively clear. Wind vectors have been over-plotted to aid interpretation. 471
8.24 **Slope of morning limb spectrum.** The corner plot with panels (**A**), (**B**), and (**C**) show constraints obtained on the slope S of the morning limb transmission spectrum. Panel (**D**) shows the morning limb spectrum with blue points and 500 samples of the fitted parametric model with the blue lines. The order 2 spectrum of the morning limb, which was not used in the fitting, is also shown with the pink star points. 472
8.25 **Fit of the morning limb spectrum with various aerosol species.** The blue points show the spectrum of the morning limb. The different colored lines show the best-fit model with that aerosol species to the morning limb spectrum. The logarithm of the Bayesian evidence associated with each aerosol species is also shown in the legend. The cloud model provides the best-fit to the spectrum with the highest evidence. The pink star points show the 2nd order spectrum for the morning limb, which was not used in the fit. 473

8.26 **Detection of Helium outflow from WASP-94A b.** (**A**) shows the excess transit depth of WASP-94A b due to metastable He absorption at 1.083 μm with black points. The best-fit model of mass-loss from WASP-94A b's atmosphere is shown with the blue solid line. (**B**) compares the light curve within the He absorption band with the light curve just outside it, showing the excess transit depth at a light curve level. (**C**) compares the light curve within the He absorption band with the white light curve of WASP-94A b. 474

List of Tables

2.1 The brown dwarf parameters and their values used to model the three-dimensional circulation patterns for Luhman 16 A and Luhman 16 B are tabulated. The measured values of these parameters are also shown except for those parameters which are not yet measured but has been assumed in our modeling. 29

3.1 Gauss points and weights used for Gaussian quadrature integration of thermal flux over different angles. 75
3.2 Gauss points and weights used for calculation of the correlated-k opacities 80
3.3 Data used to compute correlated-K opacities. Correlated-K opacities are available at Lupu et al. (2021a) and detailed in Marley et al. (2021). . . 86

4.1 Results from fitting observed spectra of brown dwarfs with our model spectra. The radiative zone K_{zz} for models which do not quench at radiative zones are marked with a '–' as they couldn't be constrained. . 187

5.1 Parameters of the `Sonora Elf Owl` Atmospheric Model Grid and their ranges covered in this work. 216
5.2 References of gaseous opacities used for calculating the atmospheric models and resulting spectra in this work. Unless otherwise stated opacity calculations are detailed in Freedman et al. (2008, 2014a) 219
5.3 Summary of the best-fit parameters obtained in this analysis for various brown dwarfs. *AKARI* data used here is from Sorahana & Yamamura (2012) and *Spitzer* data is from Suárez & Metchev (2022). The M- band data for GL570D is from Geballe et al. (2009). 258

7.1 Summary of GJ 436b observations 392
7.2 Summary of GJ 436b Orbital Parameters 393

8.1 Constraints on system and planetary parameters from different reduction pipelines from fitting the white light curve for WASP-94A b with the catwoman transit model. The values which are denoted as "calculated" are not fit directly in that particular reduction pipeline but is derived from the median parameter values of related parameters. 421
8.2 Parameters in the PICASO atmospheric retrieval on the morning and evening limb transmission spectra with the combined morning/evening limb model along with applied priors and constraints. 433
8.3 Parameters in the PICASO atmospheric retrieval on the spherical transmission spectra with the 1D model along with applied priors and constraints. 435
8.4 WASP-94A b parameters used in the UM general circulation model simulations. 441
8.5 Comparison of model parameters and Bayesian evidences for various aerosol composition in the morning limb of WASP-94A b. Clouds are the most preferred aerosol. The mean radius r_{mean} reported here is in cm. 448
8.6 Isochrone- and spectroscopic-based stellar parameters for WASP-94 A. . 452
8.7 LTE and NLTE abundances from the spectroscopic analysis and key abundance ratios for WASP-94 A. 453

Abstract

Understanding Atmospheres of Exoplanets and Brown Dwarfs with *JWST*

by

Sagnick Mukherjee

We have entered a new era of detailed exoplanet and brown dwarf atmospheric characterization with the *James Webb Space Telescope (JWST)*, enabling very high signal-to-noise spectroscopic observations. This has allowed us to probe their atmospheres and interiors with unprecedented detail. This thesis introduces new constraints on previously uncertain processes such as atmospheric dynamics, cloud physics, and interior heat flux of transiting and self-luminous giant exoplanets, exo-Neptunes, and brown dwarfs, using newly developed advanced theoretical models and *JWST* observations.

Constraints on Aerosols– Using 3D general circulation models, we examine whether the unknown 3D cloud distribution in exoplanets and brown dwarfs can be probed by their disk-integrated polarized thermal radiation. Our findings show that the clouds predicted in 3D GCMs can replicate the observed thermal polarization of brown dwarfs Luhman 16 A and B. However, we also show that small-scale vortices and cloud particle radii can sufficiently alter the disk-integrated polarized signals from such objects. To probe the 3D distribution pattern of aerosols in giant transiting exoplanet atmospheres, we present limb-resolved transmission spectra of the morning and evening limbs of hot Jupiter WASP-94A b, obtained using *JWST*. We find the colder morning

limb of WASP-94A b is completely enshrouded in aerosols whereas the hotter evening limb is clear, showing prominent gas absorption features. We leverage these observations to show that aerosols in hot Jupiters can be primarily composed of condensate clouds instead of photochemical hazes. We also show that ignoring such aerosol-driven limb-to-limb differences can lead to severe ($\sim 5\sigma$) bias in their inferred composition, not only for hot Jupiters, but for the broader class of transiting exoplanets including smaller planets like sub-Neptunes.

Constraints on Atmospheric Dynamics– Atmospheric dynamics is one of the least understood and most poorly constrained aspects of substellar atmospheres. Atmospheric dynamics along the radial direction, or vertical mixing, is often represented by the K_{zz} diffusion parameter. Theoretical and empirical uncertainty on K_{zz} spans several orders of magnitude. To constrain K_{zz}, we introduce `PICASO 3.0`, an open-source Python-based 1D radiative-convective equilibrium model that self-consistently treats disequilibrium chemistry from vertical mixing. Using `PICASO 3.0`, we demonstrate that *JWST* data can precisely constrain K_{zz} in both radiative and convective atmospheric regions. Our models predict brown dwarfs with higher gravities and temperatures of 500-900 K should have a second "detached" radiative region, which makes them ideal targets for constraining the very uncertain K_{zz} in their radiative atmospheres. To explore how metallicity, C/O ratio, and K_{zz} together shape the spectra of directly imaged planets and brown dwarfs, we present the Sonora Elf Owl model grid, which has been calculated with the `PICASO` model. We show that metallicity and K_{zz} driven vertical mixing can have degenerate effects on their spectra at various wavelength ranges.

We use this model grid along with *AKARI* and *Spitzer* observations to show that free-floating brown dwarfs with temperatures between 500-900 K indeed have very low K_{zz} values, which agrees with our theoretical predictions of detached radiative regions in their deep atmospheres.

Constraints on Interior and Atmospheric Properties– To assess whether *JWST* can constrain vertical mixing and interior properties of transiting planets, including warm-to-hot sub-Neptunes and gas giants, we integrate photochemistry into `PICASO` using the *Photochem* model. We show that CH_4 is an ideal probe of K_{zz} in warm giants, while CO is better for warm sub-Neptunes. We also find that SO_2 is no longer the main S- bearing gas in planets with $T_{eq} \leq 700$ K or $T_{eq} \geq 1100$ K, with CS and CS_2 becoming dominant. Using this model and *JWST* data, we constrain the atmospheric and interior properties of Neptune-class exoplanet GJ 436 b. We present the panchromatic *JWST* eclipse spectrum of GJ 436 b, showing it differs significantly from previously published *Spitzer* photometry in the 3.6 μm band. We find weak evidence of CO_2 absorption in its spectrum. Using `PICASO` modeling, we find the planet's day-side is either covered with a thick layer of aerosols with a metallicity $\geq$300$\times$solar, or its interior is colder ($T_{int} \sim$ 60 K) with a metallicity $\geq$80$\times$solar. Future observations of the planet, preferably in transmission, are required to distinguish between these scenarios and constrain its interior properties more precisely.

To my parents and Namrata,

who sacrificed a lot for the string of sentences that follow.

Acknowledgments

I do not know if destiny is real or not, but maybe I was always destined to write a Ph.D thesis in some area of research or other. I want to start writing this by thanking the life experiences which makes me think so. The first thing I can remember growing up is my father trying to finish his own Ph.D thesis in his late thirties, while working on his full time job as a middle school biology teacher. Even before he started working on his thesis, it was perfectly clear to him that his Ph.D will not lead to his career growth and will also not allow him to change his career, as he was the sole bread earner for a family of three in an expensive city. He was pursuing scientific research purely to satiate his own curiosity and desire to contribute to insect biology. As a 4 year old, my weekends were often spent following a man in field research collecting insects in outskirts of Calcutta that was once a hideaway of British east company officers when Siraj-ud-Daulah expelled them from the Calcutta settlement in 1756. Roaming around with him in these jungles on the only days of the week he could have off from his 6 days a week day job taught me the two most important qualities to pursue research are relentless passion and hard work. I therefore want to thank my father, the scientist, who was almost demonstrating the difficult life of science and preparing me for it, right in front of me at an age when I was just gaining my consciousness. I also want to thank my father, the history lover, who very likely shaped my interest in all things old, forgotten, and broken during these field trips.

I don't think it is at all even possible to thank a mother, especially an ambitious

woman, whose life has been a string of sacrifices to see her son succeed in some form or other. These sacrifices came in the form of leaving several satisfying school teaching jobs, one after another, to take care of me and our family. One of my everlasting regrets is not being able to stop her from making those choices and I do not think any of my successes or achievements can ever be worth those sacrifices. Perhaps the best I can do today is to thank her for being the fierce advocate for my life choices, even at times when that meant compromising on her own life choices. Studying halfway around the world, such that you get to see each other only perhaps once a year has been a lot harder for my mother than on me in the past 5 years. I want to thank her for bearing with this pain, just so that I can write this thesis and achieve my dreams. I want to thank my mother, the teacher, who put all her energy to teach me. Lastly, I want to thank my mother, the mother, who always thinks more about my tiniest inconveniences instead of the bigger problems she might be facing herself. I am truly not worth so much, mom.

I could have perhaps expected that winning a fellowship to pursue summer research at UCSC for two months will be helpful for my career, but who would have thought that those two months in a beautiful coastal vacation town would turn my life upside down, in an amazing way. I still remember our hours long chat sitting on one of those wooden benches on the boardwalk on my first day in the US. It was like chatting with an old friend and a soulmate, with whom I had left a conversation in the middle just yesterday. Except, this was perhaps the first time we were chatting with each other just by ourselves, despite knowing vaguely about each other for several years. Seeing those chats and hikes grow into a friendship and then love and a beautiful marriage

while working on this thesis has been my most cherished and beautiful life experience. I want to thank Namrata for teaching me to smile for photos, for comforting my anxiety during postdoctoral applications, and everything that came in between. I want to thank Namrata, the partner, who found an amazing way to make me believe in my moments of intense doubts. I also want to thank Namrata, the graduate student, whose intense passion and relentless hard work reminded me of the importance of those virtues, in a time when I had forgotten about them. I also want to thank Namrata, the scientist, for those late night awe-filled astronomy discussions that were more inspiring than anything else for working on this thesis. So, thank you Namrata for being a soulmate, a guiding light in the darkest moments, an inspiration, a partner foodie, a fellow King Kohli and test cricket fan, and a patient sounding board for my absolutely horrible sense of humor. You are more than I ever wished for in a life partner– and then so much more.

I would also like to thank my in-laws who have taken care of me, cheered for me, fed me delicious plates of food, have been anxious for me, and have chatted with me for long hours. My sister-in-law's family, mishti doi, and my in-laws have been a great source of cheer, support, and inspiration through these years. I greatly appreciate their contribution to my career and life.

They say finding a compatible, supportive, understanding, and excellent thesis advisor requires a great deal of luck. In this regard, I have won the jackpot. Jonathan's kindness is perhaps the quality I appreciated the most while working with him on this thesis. His support for me came in many surprising ways in the past 5 years, but I think allowing me to move from Santa Cruz to Baltimore purely for my happiness, halfway

during my Ph.D has topped them all. I want to thank Jonathan, the person, for how empathetically he always dealt with me and for introducing me to smores in one of his many backyard gatherings. In terms of science, Jonathan always encouraged me to pursue my favorite science questions and instilled great confidence in me in tackling them. He always answered my unnecessarily long slack messages sent outside office hours, often about an idea which has been worked on years ago, explaining the literature patiently to me. I want to thank Jonathan, the advisor, who always made me feel like he was one message away no matter the problem I am facing and how busy he is. This thesis wouldn't be half of what it is today without Jonathan's excellent suggestions, ideas, feedback, and guidance. He is my scientific role model and I will consider myself lucky if I can emulate even half the scientist he is, a quarter the mentor he is, and carry forward his legacy as a ground-breaking researcher in the field of exoplanets. I also want to thank members of the Fortney research group at UCSC, sharing my science with whom was always a privilege. I want to specially mention Callie, Kazumasa, ZJ, Brianna, Aditya, Anna, and Evan who have contributed to my research and enriched my science by sharing their own amazing research with me.

Prof. David Sing had a huge impact on the science represented in this thesis. I want to thank David for welcoming me in his research group at JHU. I really found a scientific "home" in his group away from UCSC, when I moved to Baltimore in 2023. Collaborations with David, Guangwei, Zafar, Daniel, Stephen, Katie, Natalie, and others contributed significantly to several parts of this thesis. I want to thank David, the observer, for inspiring me to learn *JWST* data reduction, work with data on

my own, and lead a paper based on it. His guidance and support helped me become a better exoplanet researcher and write a better thesis. I also want to thank the `PICASO` development team. This thesis wouldn't be possible without their huge contribution on developing `PICASO`, documenting it, and debugging it. Each of these steps made `PICASO` extremely easy to use and considerably sped up the work for this thesis. Dr. Natasha Batalha's relentless work on making `PICASO` open-source and extremely easy to use has hugely inspired me to always strive towards making our science open, accessible, and making our results reproducible. She introduced me to exoplanet research during my undergrad days and her support and mentorship has helped me immensely to get here and also for working on this thesis. Dr. Mark Marley, Dr. Caroline Morley, Dr. Theodora Karalidi, and Jonathan's work on developing this model for decades set the perfect platform for this work. I would also like to thank Dr. Channon Visscher, Dr. Roxana Lupu, Dr. Ehsan Gharib-Nezhad, and Dr. Richard Freedman for their effort in making the `PICASO` modeling suite possible. I want to thank the whole MANATEE GTO collaboration, who provided me some amazing research opportunities to work on cutting-edge *JWST* observations of several planets. I want to particularly appreciate the support of Dr. Everett Schlawin, Dr. Taylor Bell, Dr. Luis Welbanks, Dr. Michael Line, and Dr. Thomas Greene, who supported me in making significant portions of the science presented in this thesis possible.

I am grateful for the immense support from incredible role-models, teachers, and mentors, I was lucky to find at the right times. I think the first turning point that brought me to astronomy was my physics teacher Bashab Bhattacharya. I was at the

brink of failing some of my physics courses in 11th standard, but when he brought out his cooking utensils to teach us the electric field at the center of a charged hemisphere, I couldn't help but fall in love with this beautiful subject. Bashab sir gifted me a new language to understand the world around me and that gift of language can only be topped by the gift of mother tongue. The next turning point was meeting Dr. Suchetana Chatterjee (SC) in the ground floor office of Baker laboratory of Presidency University. I still cannot forget the moment she showed me a composite image of a galaxy cluster from *Chandra*, *HST*, and radio observations to explain AGN feedback in galaxy clusters to me. She introduced me to scientific research and taught me what it means to do cutting-edge research. She gifted me her scientific philosophy and still is the happiest person to learn about the tiniest positives of my career and life. I want to thank SC, the mentor, for introducing me to research and the world of astronomy. Mentorship from Dr. Ritaban Chatterjee (RC) also meant the world for me. RC introduced me to astrophysical theoretical modeling and taught me computational physics, a skill that was of immense use for completing this thesis. Both RC and SC were the ones who saw me fitting right into the exoplanet field and I cannot thank both enough for believing in me and for being such visionaries. They gave their all to push me wherever I am today and this thesis wouldn't be ever possible without their effort, enthusiasm, support, and belief.

I want to thank the JBNSTS scholarship program for funding me for undergraduate research at Presidency University. I am thankful to the Indo-US Science and Technology Forum sponsored S. N. Bose Fellowship for sponsoring my summer research

at UCSC back in 2019. This summer research opportunity was transformative for my career and I want to thank Prof. Raja Guhathakurta for mentoring me during this summer. I am also thankful to Raja for giving me the opportunity to serve as a mentor in the SIP program during this summer. I am thankful for the UC Regents fellowship for funding me while writing this thesis. I also want to thank the John Templeton Foundation (JTF) for funding me through the Templeton Theory-Experiment (TEX) Cross Training Fellowship while working on this thesis. The TEX fellowship program supported me to explore observational studies of exoplanets, including my two year long stint as a visiting student at JHU to learn data reduction of *JWST* observations of transiting exoplanets. This support combined with David's mentorship helped me add several parts of this thesis, which wouldn't have been possible otherwise. Large parts of this thesis was also made possible due to funding support from various approved *JWST* programs. I am thankful to STScI and NASA for this funding which helped me pursue research in my favorite science areas. I am thankful to the OWL program hosted at UCSC which brought upon amazing collaborative opportunities for me. These opportunities shaped this thesis significantly. I am also thankful to the 51 Pegasi b fellowship funded by the Heising-Simons foundation for offering me a prized postdoctoral fellowship. I am thankful to Prof. Luis Welbanks for supporting me immensely through applying to postdoctoral jobs and agreeing to be my host at SESE, ASU for the 51 Pegasi b fellowship. I am looking forward to doing a lot of innovative science together and growing both as a scientist and a person while working at SESE with Luis, Mike, and the exoplanet group. I greatly appreciated the support of my thesis committee

including Dr. Rebecca Jensen-Clem and Dr. Andy Skemer. I am thankful to Becky for mentoring me while working on polarization signatures of brown dwarf and directly imaged exoplanets. I greatly enjoyed her support and guidance while working on the first project of my thesis. I also want to thank Becky for teaching the Adaptive Optics course, which was one of my favorite courses within the graduate school coursework. I also greatly appreciated Andy's very valuable suggestions during various important phases of working on this thesis over the past 5 years. These suggestions made me think deeply about the research areas I want to explore in this thesis and my research. I am also thankful to Andy for teaching the observational astronomy course at Lick Observatory. I never got to work or observe with a telescope during my undergrad. Therefore, this course was a complete revelation for me and taught me a lot about observational astronomy during that one week at Mt. Hamilton. Those lessons were of great use while working on the observational aspects of this thesis. I am also thankful to Prof. Xi Zhang for teaching the planetary atmospheres course at the EPS department. I had never taken a formal course on planetary atmospheres before and it helped me in understanding various concepts that were extremely relevant for the work presented in this thesis. I would also like to thank all the UCSC astronomy graduate students, postdocs, faculty, and the broader community, where I have always found encouragement, enthusiasm, help, and positivity. These were key ingredients that enriched my science and my life within this community in the last 5 years.

Life while working on this thesis would have been a lot more dull if not for my friends- Saugata, Anirban, Saurojit, Soumyadeep, Soumik, Arghyadeep, and Deep.

Even though we were separated by an ocean, Saugata was my exoplanet conference buddy during the thesis years. It was a privilege to share our experiences while both of us were working as exoplanet researchers. I was delighted when we got to work on a paper together. I hope our research and life partnership grows further in the coming years. Whenever life got stressful, reaching out to this group of friends would lift my spirits immediately. Those group video calls, cricket banter, and long threads of irrelevant messages greatly helped me to cope with the stresses of a Ph.D student's life. I am extremely grateful for this group of people in my life.

Even though I started this with the thought that writing this thesis was perhaps my destiny, by the time I finished this, I realized that reaching that destiny was only made possible by innumerable amazing people enriching my life with invaluable contributions. I have tried my best to capture some of them above but I am sure that I have missed a lot more than I have covered. But, reminiscing about how I got to this point helped me remind myself that our world is filled with really great people whose contributions can enhance our time on this planet by many folds. Looking ahead, I hope I, too, can have an impact on someone else's life like all these people had on mine. I conclude this section with a promise to continually strive towards that goal throughout my science career and beyond.

Chapter 1

Introduction

In humanity's pursuit of truth, understanding our place, origin, and journey in the universe has been an everlasting quest. The discovery of 1000s of extrasolar planets (or exoplanets) over the last three decades has been an extremely pivotal step towards that goal. We have found exoplanets with a much wider range of planetary properties like mass, radius, and orbital separation than expected before (e.g., Howard et al. 2010; Borucki et al. 2010; Mayor & Queloz 1995; Bean et al. 2021). Figure 1.1 shows the distribution of detected exoplanets in the mass–radius space, showing how we have detected exoplanets across a much wider parameter space than covered by the solar system planets. We have also found exoplanets in conditions thought to be non optimal for planet formation and survival (e.g., Vanderburg et al. 2020; Mullally et al. 2024). These discoveries have completely revolutionized our understanding of the possible diversity of planets, challenging several scientific ideas about planetary formation and evolution along the way (Bodenheimer et al. 2000; Mordasini & Burn

2024; Mordasini et al. 2016; Fulton et al. 2017; Alibert et al. 2005; Ida & Lin 2004). Echoing solar system exploration (Niemann et al. 2005; Bolton et al. 2017; Baines et al. 2009; Sromovsky et al. 2009), we as a community have now taken the great leap from detecting exoplanets to characterizing them in unprecedented detail. What are the chemical composition of these planets? How compositionally different/similar are they from their nearest solar system analog? What is the structure of their interior? How do they evolve over time? How similar are the chemical composition of these planets from their host stars or surrounding environment? Answers to these questions are now within our reach and will lead to a holistic understanding of the planetary formation process and shed light on its complexity. These still unsolved questions are, therefore, at the frontier of our centuries-old pursuit of understanding our origin.

A key point of difference between exoplanet exploration and solar system exploration is that we can only rely on remote sensing techniques to probe exoplanets as opposed to in-situ measurement techniques used often in solar system science. As a result, atmospheres are the most directly observable part of exoplanets. Atmospheres can bear crucial imprints from the formation and evolutionary history of exoplanets (Öberg et al. 2011; Mordasini et al. 2016; Mollière et al. 2022a). They can help reveal the chemical composition of planets and can also be affected by the structure of planetary interiors (Fortney et al. 2013; Agúndez et al. 2014; Fortney et al. 2020; Madhusudhan 2018). Atmospheres are also a key factor in deciding the habitability potential of a planet (McKay 2014; Abe et al. 2011; Ingersoll 1969). As a result, understanding exoplanetary atmospheres is a crucial link between detection of exoplanets and their use

to decipher the process of planetary formation, evolution, and habitability.

1.1 Exoplanetary Atmospheres

Planetary atmospheres are complex physical systems with several highly coupled ongoing physical processes affecting their state and observable properties (Marley & Robinson 2015; McKay et al. 1989, 1991; Manabe & Wetherald 1967; Somerville & Remer 1984; Spelman & Manabe 1984). Figure 1.2 shows a schematic representation of the various physical processes that might be playing a significant role in an exoplanetary atmosphere. Each of these processes are still active areas of investigation in solar system planets and moons despite more than half a century of dedicated solar system exploration both with in-situ experiments and remote observations (e.g., Baines et al. 2009; Zhang et al. 2012, 2015; Fletcher et al. 2023; Sromovsky et al. 2020; Sánchez-Lavega et al. 2020; Lavvas et al. 2021; Wong et al. 2017; Gladstone et al. 2016; Li et al. 2014; Ingersoll 2020; Atreya et al. 1999; Smith et al. 1981, 1982). This highlights the colossal challenge that exoplanet atmospheric characterization presents us with– understanding each of these processes to great detail from remote observations, which often might not spatially resolve the planet. But understanding these processes thoroughly is a necessity because of their coupled nature– uncertainty regarding one process leads to uncertainty about another (Marley & Robinson 2015; Drummond et al. 2016; Mukherjee et al. 2024c; Fortney et al. 2020; Morley et al. 2024; Steinrueck et al. 2023a; Somerville & Remer 1984). For example, a strong constraint on the chemical composition of an

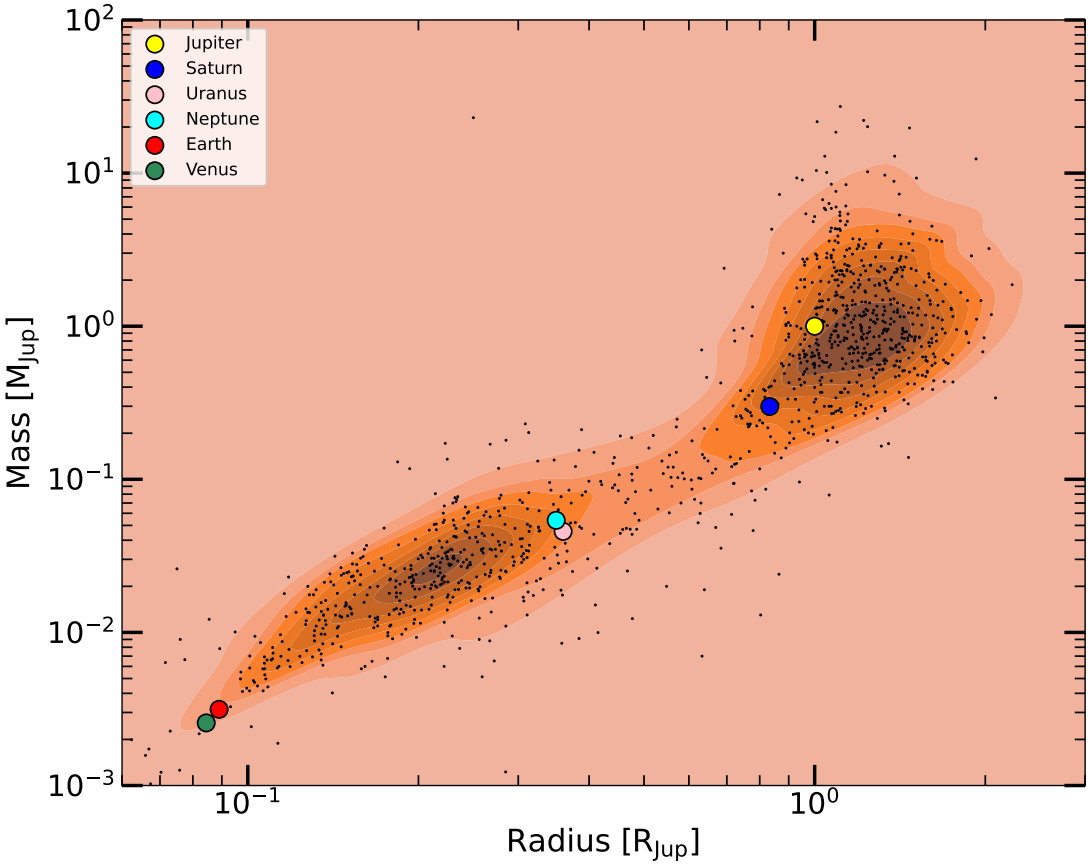

Figure 1.1: Mass and radius of confirmed exoplanets is shown with black points. The density of the detected exoplanets in the mass-radius space is shown with the heat map. Solar system planets are also shown with colored solid circles. The mass of the exoplanet population is either mass (m), or $msin(i)/sin(i)$, or $msin(i)$ from higher to lower priority.

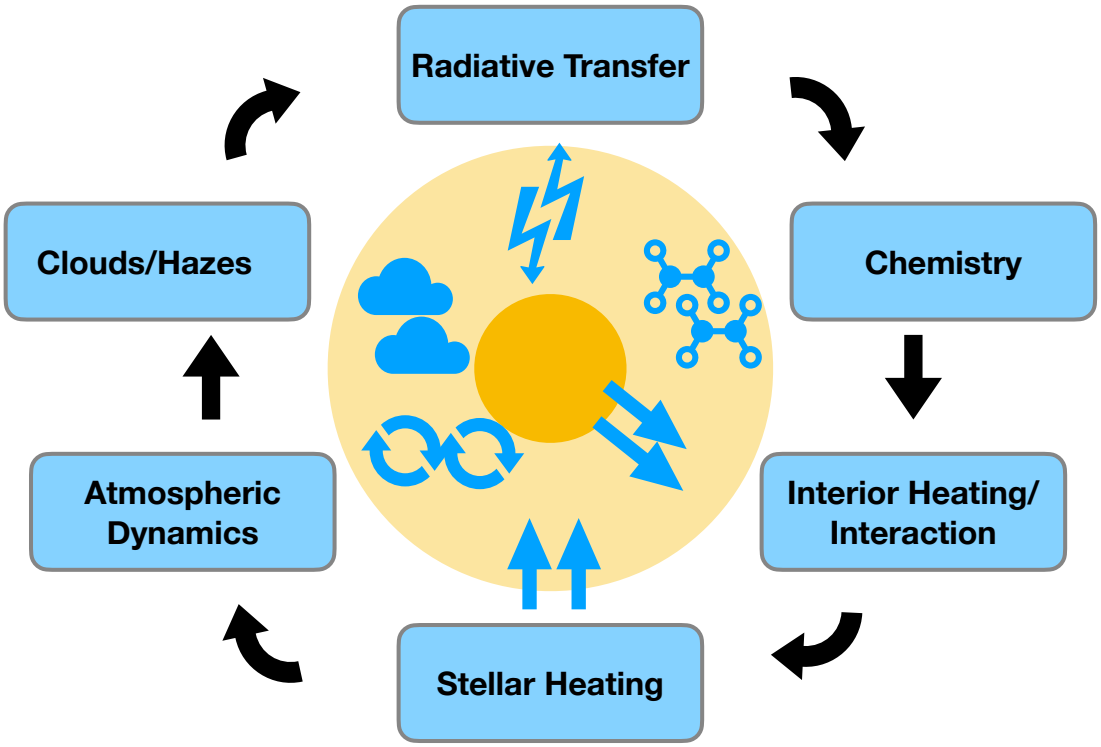

Figure 1.2: Schematic showing the various physical processes ongoing in an exoplanet atmosphere.

exoplanet atmosphere is not possible without constraints on atmospheric dynamics or cloud physics (Mukherjee et al. 2024a; Line & Parmentier 2016; Somerville & Remer 1984). Therefore, this thesis is dedicated towards constraining some of these key physical processes – mainly atmospheric chemistry, clouds/hazes, and interior properties, in the atmospheres of exoplanets and substellar objects, paving a path towards a more comprehensive understanding of planetary formation and evolution. A brief introduction to each of these atmospheric processes follows.

1.1.1 Atmospheric Chemistry

Due to their relatively lower temperatures and higher densities than stellar atmospheres, planetary atmospheres are predominantly molecular in nature (Burrows et al. 1997). Thousands of coupled chemical reactions are therefore a key physical process in planetary atmospheres. The chemical composition of a planetary atmosphere can be influenced by multiple physical processes. In the dense and hot parts of the atmosphere, thermochemical equilibrium is established, where the forward and backward reaction rates of all chemical reactions are equal (Visscher et al. 2006, 2010a,c; Burrows & Sharp 1999; Fegley & Lodders 1996). Such conditions are only met at the deepest and hottest reaches of planetary atmospheres, if at all. High energy photons from the host star or other sources incident on the top of the atmosphere can break down weakly bonded molecules and induce new chemical reactions in the atmosphere (Wildt 1937). This process called photochemistry can shape the upper atmospheric chemistry of planetary atmospheres, especially those with high levels of stellar irradiation (e.g.,

hot Jupiters) (Moses et al. 2011; Tsai et al. 2017, 2021; Allen et al. 1981). Atmospheric dynamics can also transport gases participating in chemical reactions across several atmospheric scale heights, to different pressure-temperature-density conditions (Griffith & Yelle 1999; Miles et al. 2020; Moses et al. 2011; Karalidi et al. 2021a; Visscher & Moses 2011; Allen et al. 1981; Prinn & Barshay 1977). As a result, atmospheric dynamics can disrupt the ongoing chemical reactions in the atmosphere, altering its chemical composition. Slower chemical reactions and their participant gases are especially susceptible to such atmospheric dynamics-driven changes. Gases can be exchanged between the interior and the atmosphere of planets as well (Kite et al. 2020, 2016; Robock 2000). This process becomes more crucial for planets with large "metal" enriched interiors that can potentially exchange gases with the atmosphere (e.g., sub-Neptunes or super-Earths). As measuring the chemical composition of exoplanetary atmospheres is necessary for deciphering their formation and evolutionary history, constraining each of these processes that influence atmospheric chemistry is crucial.

Owing to the vast ro-vibrational states accessible to gaseous molecules, their optical/infrared absorption cross-sections can vary over several orders of magnitude within a narrow wavelength range (Freedman et al. 2014b, 2008). Therefore, these molecular gases are dominant opacity sources in planetary atmospheres and they play a major role in shaping the observable spectrum of planets (Fortney et al. 2008a; Mollière et al. 2015; Goyal et al. 2018; Dickinson & Cicerone 1986; Manabe & Wetherald 1967; Kuiper 1947). As a result, each of these processes that influence atmospheric chemistry, altering abundances of various gaseous molecules, can leave distinct imprints on the ob-

servable spectrum of exoplanets (e.g., Moses et al. 2011; Agúndez et al. 2014; Mukherjee et al. 2024a; Phillips et al. 2020). Several parts of this thesis aims to constrain some of the least understood atmospheric processes like atmospheric dynamics, photochemistry, and thermochemical equilibrium (Chapters 3, 4, 5, & 6) by identifying and exploiting their distinct imprints on observables using newly developed state-of-the-art theoretical models and observations.

1.1.2 Aerosols– Clouds and Hazes

Aerosols are ubiquitous in solar system planets and moons (e.g., Baines et al. 2009; Sromovsky et al. 2020; Lavvas et al. 2021; Romani & Atreya 1988; Karkoschka & Tomasko 2011; Sagan & Thompson 1984; Smith et al. 1982, 1981). In addition to gaseous molecules, aerosols are also key sources of opacity in planetary atmospheres shaping their observable properties significantly by scattering or absorbing radiation (Fortney 2005; Ackerman & Marley 2001a; Pont et al. 2008; Steinrueck et al. 2023a; Parmentier et al. 2016; Morley et al. 2013, 2015). Aerosols can cause heating of the planet's atmosphere by trapping outgoing thermal radiation or they can also cause cooling by reflecting incident stellar radiation back to space (Marley & Robinson 2015; Steinrueck et al. 2023a; Morley et al. 2014a). Two distinct types of aerosols have been identified in solar system or exoplanetary atmospheres – condensate clouds (clouds hereafter) or photochemically produced hazes (hazes hereafter). Clouds are formed through direct condensation of gases through phase transition (e.g., water clouds in Earth's atmosphere) or through chemical reaction-driven condensation (e.g., condensation of silicates in brown dwarfs)

(Saumon & Marley 2008; Morley et al. 2014b, 2024; Gao & Benneke 2018a; Gao et al. 2020b; Sing et al. 2016). On the other hand, the photochemical process described above can lead to the growth of very large molecules or polymers often called hazes (Gao & Zhang 2020; Gao et al. 2017; Steinrueck et al. 2023a; Sagan & Thompson 1984; Khare et al. 1984). For exoplanets with temperatures similar to Earth and other solar system planets like Jupiter, gases like H_2O, CH_4, and NH_3 are expected to condense due to phase transition and form clouds (e.g., Morley et al. 2014b; Lewis 1969; West et al. 1986). However, for hotter exoplanets like warm or hot Jupiters, a large number of minerals and gases like silicates, sulfides, iron, oxides, etc can be expected to condense through phase transition or chemical reactions (e.g., Morley et al. 2024, 2012). Even though there is strong evidence pointing towards the presence of mineral clouds in exoplanet and substellar atmospheres, the mineral composition of such clouds is still relatively unknown. Evidence pointing towards the presence of photochemical hazes have been found in giant transiting exoplanets (e.g., Pont et al. 2008, 2013; Carter et al. 2020; Gao et al. 2023; Kawashima & Ikoma 2018). However, the exact chemical composition of such hazes and their production processes are extremely uncertain. Additionally, whether aerosols in hotter exoplanets like hot Jupiters is dominated by clouds or hazes is a long-lasting open question (e.g., Kempton et al. 2017; Steinrueck et al. 2021, 2023b). Parts of this thesis combines observations and theoretical models to answer this question for hot Jupiter exoplanets (Chapter 8).

In addition to uncertainties in the composition of aerosols, their distribution across the three-dimensional planetary atmosphere is also extremely uncertain (e.g.,

Steinrueck et al. 2021, 2023b; Fauchez et al. 2019). We can often spatially resolve the planetary disk of solar system planets using telescopic observations (e.g., Asay-Davis et al. 2009; Baines et al. 2007). We can directly image and track the 3D distribution of aerosols in their atmospheres but the inability to do so with exoplanets and substellar objects makes this a rather challenging but important problem. The 3D distribution of aerosols can have large direct or indirect influence on the observable properties of exoplanets (Line & Parmentier 2016; Webber et al. 2015a). Constraining them is therefore critical.

Like gas molecules, aerosol particles can be transported around the planet's atmosphere due to atmospheric dynamics (Ackerman & Marley 2001a; Parmentier et al. 2013a, 2016; Steinrueck et al. 2021). For condensate clouds, dynamics along the radial direction (vertical mixing hereafter) can cause lifting of condensible vapor across several atmospheric scale heights causing cloud particle formation (e.g., Gao & Benneke 2018a; Ackerman & Marley 2001a). These mixing processes are also responsible for keeping the formed cloud particles aloft in the atmosphere in addition to their growth and subsequent evaporation (e.g., Gao & Benneke 2018a). Dynamics along the horizontal direction can also transport aerosol particles across the atmosphere. In case of highly irradiated tidally-locked transiting planets, such horizontal transport can lead to large, but uncertain, asymmetries in the 3D aerosol distribution in their atmospheres (e.g., Kempton et al. 2017). The influence of horizontal transport on the 3D distribution of aerosols in planets and substellar objects which do not receive strong stellar irradiation and are also not expected to be tidally-locked to their host stars is unknown (e.g., Tan

& Showman 2021; Tan & Showman 2021, 2019). This thesis investigates both these regimes of aerosol distribution processes in transiting planets and substellar objects (Chapters 2 & 8) using new highly sensitive observations and theoretical models.

1.1.3 Interior Structure

Even though interiors of exoplanets cannot be directly probed through observations, they can greatly influence the thermal evolution of planets and substellar objects (e.g., Fortney et al. 2007; Marley et al. 2018a; Morley et al. 2024; Lopez & Fortney 2014; Hubbard 1977; Stevenson & Salpeter 1977; Hubbard et al. 1999). Planets and substellar objects are formed with a gravitational potential energy of formation. This causes their interiors to be extremely hot and their sizes to be large initially. As the planet cools and contracts over time, it loses this formation energy to outer space in the form of outgoing thermal radiation (Burrows et al. 1997; Saumon & Marley 2008; Phillips et al. 2020; Hubbard 1977; Fortney et al. 2007; Lunine et al. 1989). The density and opacity of the interior of planets and substellar objects are so high that this energy cannot be transferred radiatively through its interior (Stevenson 1991). Therefore, this energy is transferred convectively from the interior of the planet all the way to the atmosphere, until the atmosphere becomes transparent for radiative transfer of energy to be more efficient than convective transport (Burrows et al. 1997; Marley et al. 1996). Beyond this point, photons can freely stream to outer space as the atmosphere becomes tenuous enough for efficient radiative transport. As a result, the interior structure, its equation of state, and its connection to the atmosphere control the rate of cooling and

contraction of a planet with time (e.g., Marley et al. 2018b; Phillips et al. 2020; Hubbard 1977; Burrows et al. 1997; Chabrier et al. 2000; Baraffe et al. 2015).

The structure and composition of exoplanetary interiors can be partially probed by measuring planetary parameters such as mass, radius, and age. However, large uncertainties on important interior properties such as the fraction of metals in the interior remain with this approach (Thorngren et al. 2016; Bloot et al. 2023). These uncertainties hinder our understanding of planetary evolution. But planet interiors influence their observable atmospheres as well. The energy transported convectively through the planetary interior influences the thermal structure of the deep planetary atmosphere. The chemical reactions in the deep atmosphere respond to this energy flux from the interior causing sensitivity of the deep atmospheric chemical composition to interior properties (Fortney et al. 2020; Mukherjee et al. 2024a; Agúndez et al. 2014; Morley et al. 2017b). If processes like atmospheric dynamics can transport gases from this deep atmosphere to the observable atmosphere, then the planet interior can significantly shape its observable properties (e.g., spectrum) (Welbanks et al. 2024; Sing et al. 2024). Studying exoplanetary atmospheres can, therefore, be extremely useful in constraining interior properties and evolutionary history of exoplanets. Parts of this thesis focuses on leveraging this atmosphere-interior connection to understand the interior properties of exoplanets from their observed spectrum (Chapter 6).

1.2 Directly Imaged Exoplanets and Brown Dwarfs

Different observational techniques have been devised to find and study exoplanets. The direct imaging technique aims to detect photons emitted by the planet or substellar object directly. A major challenge in this technique is the host star itself, which can be much brighter than the planet. Advanced optical systems like adaptive optics and coronagraphs are often used to suppress the host star light and create enough contrast to detect the much fainter planet (Oppenheimer & Hinkley 2009; Currie et al. 2023). As a result, direct imaging is more likely to find planets that are well-separated (in terms of angular separation) from their host stars and planets that are bright due to their young age (Zurlo 2024). This population of planets are called directly imaged planets and their total emitted flux can be expressed as,

$$F = \sigma T_{\rm eq}^4 + \sigma T_{\rm int}^4 \tag{1.1}$$

where the first term represents the flux emitted due to heating of the planet from the host star irradiation and the second term represents the flux emitted from the planetary interior. Due to their typically large orbital separation from their host stars and their typically young ages, the second term dominates the energy budget of the directly imaged exoplanet population (e.g., Marley et al. 2018a; Morley et al. 2024; Phillips et al. 2020; Baraffe et al. 2015; Burrows et al. 1997). As a result, the directly imaged exoplanet population forms a compelling sample for testing the early stages of exoplanetary evolution and the nature of their atmospheres. Parts of this thesis have

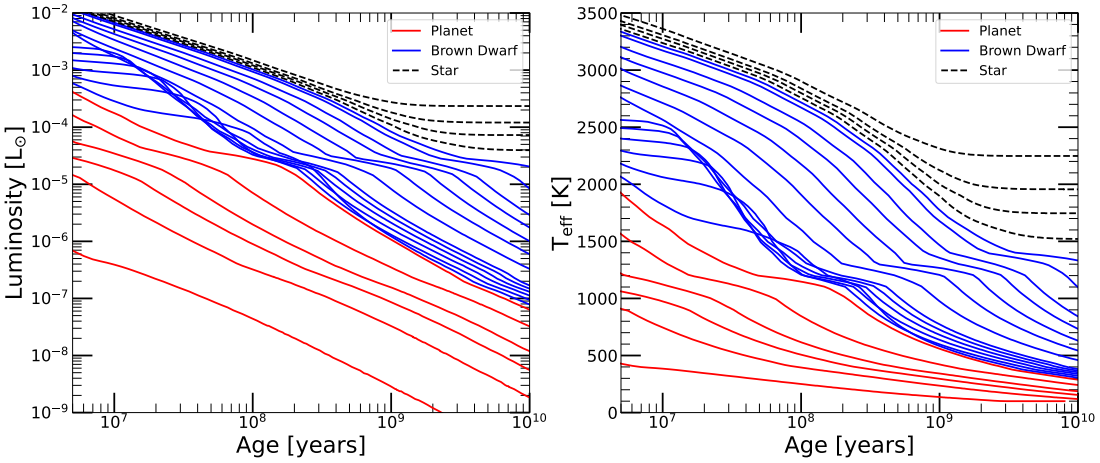

Figure 1.3: Theoretical evolutionary tracks for luminosity (left) and effective temperature (right) for objects with various masses between 0.5 to 83 Jupiter mass is shown. Evolution of objects classified as planets are shown with red lines. Brown dwarf evolution is shown with blue lines and evolution of stars have been shown with dashed black lines. The theoretical tracks are from the publicly available Sonora Diamondback grid (Morley et al. 2024) and were calculated using a evolutionary model developed as a part of this thesis.

developed atmospheric models to understand the composition, evolution, and formation mechanism of this population of exoplanets (Chapters 3, 4, and 5).

Another population that is highly analogous to the directly imaged exoplanet population in terms of their atmospheres but is often more easily observable are field brown dwarfs. A potential physical distinction between giant planets and brown dwarfs is made in terms of their ability to burn significant portions (50%) of their deuterium through nuclear fusion during their evolution (e.g., Spiegel & Burrows 2012). Objects with mass smaller than $\sim$ 12-13 Jupiter mass do not meet this criteria during their evolution and are classified as planets. However, objects with mass greater than this threshold burn a substantial fraction of their deuterium ($\geq$50%) within their lifetime and are classified as brown dwarfs. Figure 1.3 left panel shows this distinction between

the evolution of planets and brown dwarfs with their luminosity evolution over time from theoretical models from Morley et al. (2024). The black dashed lines in Figure 1.3 show that H-burning halts the luminosity evolution of these objects if their mass is greater than the Hydrogen-burning minimum mass (∼70-80 Jupiter mass) limit. These objects are classified as stars (Morley et al. 2024). Despite significant differences in mass and gravity, various physical aspects of the atmospheres of brown dwarfs and giant planets can be extremely similar. For example, the right panel of Figure 1.3 shows the evolution of the effective temperature ($T_{\rm eff}$) of planets (red lines) and brown dwarfs (blue lines) over time. The atmosphere of a young directly imaged giant exoplanet might have similar $T_{\rm eff}$ to that of an older massive field brown dwarf. Due to their similar H_2/He dominated chemical composition, both their atmospheres are also hosts to very similar chemical reactions and physical processes like cloud formation and large-scale atmospheric dynamics. Therefore, studying the atmospheres of freely floating field brown dwarfs with relatively higher signal-to-noise observations than directly imaged or transiting exoplanets can help us understand the uncertain physical processes ongoing in exoplanetery atmospheres in extraordinary detail. Several sections of this thesis have therefore leveraged observations of brown dwarfs to constrain extremely uncertain physical processes such as atmospheric dynamics (Chapters 4 & 5) and cloud physics (Chapters 2). Theoretical and observational results focused on directly imaged exoplanets and brown dwarfs will be presented in part I of this thesis.

1.3 Transiting Exoplanets

The transit method of detecting exoplanets has been extraordinarily successful in detecting a diverse population of planets that are relatively close to their host stars (Batalha 2014; Ricker et al. 2014). The stellar heating term of Equation 1.1 is much more important for this population than the directly imaged exoplanets (Fortney et al. 2020). This term can most often dominate the heat flux from the planetary interior for transiting exoplanets, unless the planet has a relatively large orbital separation and is very young (Fortney et al. 2020). Stellar irradiation can significantly influence the evolution and observable properties of transiting exoplanets (Fortney et al. 2007). Therefore, transiting exoplanets provide an excellent sample that can be studied to understand the formation and evolution of planets that exist in the strong stellar irradiation regime in contrast to the directly imaged exoplanet/ brown dwarf population, that are often subject to negligible stellar irradiation.

While theoretical models to understand the evolution of transiting exoplanets have been developed (e.g., Fortney et al. 2007; Lopez & Fortney 2014; Bloot et al. 2023; Thorngren et al. 2016), we need to probe their interior properties like the interior heat flux to observationally test these models. The influence of planetary interiors on their observable atmospheres described in §1.1.3 can be leveraged to probe their interiors. The atmospheres of transiting exoplanets can be studied using transmission spectroscopy or thermal emission spectroscopy. Transmission spectroscopy typically probes pressures between 0.001-10 mbars of the atmosphere, whereas emission spectroscopy probes deeper

pressures (e.g., Sing 2018; Kreidberg 2018). The transiting planet population is quite diverse, with planet radii varying from Earth sizes all the way to super-Jupiter sizes. A key question is how do the interiors of this diverse population impact their observable atmospheres? Is it easier to constrain the interior properties of hot Jupiters or warm sub-Neptunes? What are the most sensitive atmospheric signatures in each type of planet that can be leveraged to measure their interior properties? We use theoretical models to answer these questions in Chapter 6. We also present the panchromatic emission spectrum of a Neptune-like transiting exoplanet GJ 436b and use it to understand its atmospheric and interior properties in Chapter 7. We observationally probe the aerosol properties of transiting exoplanets as well, answering major questions about the composition of aerosols and their spatial distribution in Chapter 8.

1.4 Observations from the *James Webb Space Telescope*

The *James Webb Space Telescope (JWST)* was launched to space in December 2021, 1.5 years into the progress of this thesis. Since summer 2022, *JWST* has started a revolution in our understanding of exoplanets. A key reason behind this revolution is *JWST*'s unprecedented sensitivity at infrared wavelengths between 0.5-28 μm. Excellent sensitivity to infrared wavelengths is key for observing planetary atmospheres as the thermal emission of planets and brown dwarfs peak at infrared wavelengths owing to their colder temperatures than main-sequence stars. *JWST*'s infrared sensitivity has allowed us to study distant substellar objects that are colder than STP conditions on

Earth (e.g., Matthews et al. 2024). The gaseous components of planetary atmospheres also show higher degrees of interaction with infrared radiation than other parts of the electromagnetic spectrum. The range of spectral resolving power accessible to various *JWST* instrument configurations allows the detection and characterization of diverse atmospheric molecular features, each probing distinct atmospheric physics and chemistry (e.g., Schlawin et al. 2024a; Bell et al. 2023b; Sing et al. 2024; Welbanks et al. 2024; Miles et al. 2022; Bell et al. 2023c). *JWST*'s exceptional pointing stability also enhances its ability to observe transit light curves of exoplanets with extraordinary precision (e.g., Rustamkulov et al. 2023). These reasons among many other combine together to make *JWST* an exoplanet research powerhouse.

Understanding the physics of exoplanetary atmospheres and interiors with *JWST* observations has been a key focus of this thesis. Chapter 4 and 5 develops theoretical models to understand atmospheric dynamics in directly imaged exoplanets and brown dwarfs with *JWST* observations. The model developed in Chapter 3 was instrumental in making inferences from some of the first *JWST* observations of transiting exoplanet atmospheres (e.g., Rustamkulov et al. 2023; Ahrer et al. 2023; Feinstein et al. 2022; Alderson et al. 2022) and directly imaged exoplanets (e.g., Miles et al. 2022) through the transiting planets and direct imaging Early Release Science programs. These models continue to be utilized in understanding the atmospheres of a variety of exoplanetary and substellar atmospheres with *JWST* (e.g., Schlawin et al. 2024a; Gagnebin et al. 2024; Mukherjee et al. 2025; Thao et al. 2024; Inglis et al. 2024; Wallack et al. 2024; Gao et al. 2023). Chapter 6 develops theoretical models to probe

the interiors of transiting exoplanets from *JWST* observations of their atmospheres. Chapter 7 and 8 presents new *JWST* observations constraining their atmospheric and aerosol properties. This thesis presents observations with various *JWST* instrument configurations including observations from the NIRISS/SOSS mode, NIRCam mode, and the MIRI LRS mode.

Part I

Brown Dwarfs and Directly Imaged Exoplanets

Chapter 2

Probing Brown Dwarf Clouds with Polarization

2.1 Introduction

Infrared spectroscopy of brown dwarfs has revealed a great deal of information about the thermal and chemical structure of their atmospheres (Kirkpatrick 2005). These observations also have long suggested the presence of clouds in their atmospheres (Helling & Casewell 2014; Marley & Robinson 2015). However, cloud properties like their altitudes, vertical extent, and typical particle sizes are difficult to interpret from thermal spectroscopy or photometry. Moreover, time-series photometry and spectroscopy have often found these objects to be variable (Buenzli et al. 2015; Apai et al. 2021; Miles-Páez et al. 2015; Eriksson et al. 2019; Miles-Páez et al. 2017; Artigau et al. 2009; Radigan et al. 2012; Girardin et al. 2013; Radigan et al. 2014; Vos et al. 2019)

suggesting non-uniform cloud coverage, which further complicates the interpretation of these observations.

Additional observational and theoretical tools could potentially break important new ground in our understanding of substellar atmospheres. One such avenue is polarization. Thermal emission arising from substellar atmospheres may become partially linearly polarized due to scattering from the cloud/dust particles present in the atmosphere. Rayleigh scattering from gas molecules in the atmosphere can also give rise to significant polarization in optical wavelengths. However, this gets suppressed in the near infrared due to the sharp decline of Rayleigh scattering with increasing wavelength (Marley & Sengupta 2011). Therefore thermal polarized emission in near infrared wavelengths mainly arises from the Mie particle scattering of thermal photons by cloud particles that are present.

However, the observable disk-integrated polarization from perfectly spherical and uniformly cloudy objects cancels out to zero even though the local polarized surface brightness of the object might be non-zero. A detectable non-zero disk-integrated polarization can still arise if this symmetry is broken either by rotationally-induced oblateness of the object or non-uniformity of the cloud cover (Sengupta & Marley 2010; Marley & Sengupta 2011; Sengupta & Krishan 2001; de Kok et al. 2011). For self-luminous gas giant planets, cousins of brown dwarfs, the presence of circumplanetary disks (Stolker et al. 2017) or transiting exomoons (Sengupta & Marley 2016) can also break this symmetry for spherical objects and produce net disk-integrated polarized flux.

Sensitivity of the disk-integrated polarization signal to the rotationally induced oblateness, inclination of the spin-axis of the object, gravity, effective temperature and cloud particle sizes has been theoretically studied in detail for uniformly cloudy exoplanets and brown dwarfs (Sengupta & Marley 2010; Marley & Sengupta 2011; Sengupta & Krishan 2001; de Kok et al. 2011; Sanghavi et al. 2021; Sanghavi & West 2019; Sanghavi & Shporer 2018). Model calculations of disk-integrated polarization signals arising from non-uniform cloud coverage on exoplanets and brown dwarfs have been performed by de Kok et al. (2011) and Stolker et al. (2017), yielding polarization signal predictions typically $\geq$0.1% in the near-infrared wavelengths. At that level, near-infrared polarimetric and spectro-polarimetric observations of brown dwarfs can provide us with that additional diagnostic window into the nature of clouds in these atmospheres.

A number of observations of polarized emission from brown dwarfs have been published as well over the past two decades (Ménard et al. 2002; Manjavacas et al. 2017; Zapatero Osorio et al. 2005, 2011; Goldman et al. 2009; Tata et al. 2009; Miles-Páez et al. 2013; Millar-Blanchaer et al. 2020). Recently, upper limits on the polarized thermal emission have been determined for a large sample (23) of exoplanets and brown dwarf companions (Jensen-Clem et al. 2016; van Holstein et al. 2017; Jensen-Clem et al. 2020; van Holstein et al. 2021a; Millar-Blanchaer et al. 2015) using the Gemini Planet Imager (GPI,Macintosh et al. (2014)) and Spectro-Polarimetric High-contrast Exoplanet REsearch instrument (SPHERE, Beuzit et al. (2019)). van Holstein et al. (2021a) found that polarized thermal emission measurements from DH Tau B and GSC 6214-210 B hints towards the presence of circumsubstellar disks. Time-domain photometric

observations of some of the brown dwarf objects detected in polarized emission have additionally revealed significant variability in the thermal flux (Buenzli et al. 2015; Apai et al. 2021) and the polarized flux (Miles-Páez et al. 2015). This suggests not only the presence of clouds in these objects but might also hint towards non-uniformity in the cloud cover as well. However, no significant statistical correlation between the detection of polarized thermal emission and the presence of variability has been found yet. Nearly ∼40% of brown dwarfs near the L–T transition are found to be strongly variable (Eriksson et al. 2019) which suggests that these objects commonly have patchy cloud coverage, as had been suggested on theoretical grounds (Ackerman & Marley 2001b; Burgasser et al. 2002a).

Our nearest binary brown dwarf pair Luhman 16 A and B (Luhman 2013) is especially interesting in this context, as Luhman 16 A has a spectral type of L7.5 and Luhman 16 B is a T0.5 dwarf (Kniazev et al. 2013; Burgasser et al. 2013). As both of these objects are near the L–T transition, there is a good chance that they have non-uniform cloud cover (Saumon & Marley 2008). Two dimensional Doppler mapping of Luhman 16 B by Crossfield et al. (2014) found bright and dark regions across the globe which was indicative of cloud nonuniformity. Buenzli et al. (2015) have shown that the thermal spectra of both the objects can be adequately fit with the superposition of two models with different cloud properties and coverage fractions. Multiple time domain photometric studies have also found both the components to be variable (Buenzli et al. 2015; Apai et al. 2021) further hinting towards patchy cloud coverage.

Millar-Blanchaer et al. (2020) recently made the first detection of polarized

thermal emission from each of the components of the binary system Luhman 16 A and B. The H-band degree of linear polarization for Luhman 16 A and Luhman 16 B was measured to be 0.031% and 0.010%, respectively with a precision of 0.004%, thus providing 7.5 and 2.5 sigma detections. The angle of the polarization vector was also measured for both the objects. Atmospheric modeling by Millar-Blanchaer et al. (2020) of the disk-integrated polarization signal showed that the measured polarization signal from Luhman 16 B can arise from a uniformly cloudy oblate object or from a non-uniformly cloudy configuration. However, the polarization signal from Luhman 16 A could only be explained by non-uniform cloud coverage, for example multiple bands of relatively cloudy regions on the object (Millar-Blanchaer et al. 2020). This detection and the subsequent analysis emphasizes that non-uniformity in cloud cover should be considered while interpreting polarimetric (or even non-polarimetric) observations of brown dwarfs near the L–T transition.

An essential tool to understand three-dimensional phenomena in substellar atmospheres are general circulation models (GCMs). Such models couple fluid dynamics in three dimensions with radiative transfer, to understand energy transport throughout an atmosphere (Showman et al. 2020). A realization of the three-dimensional temperature and wind structure, when coupled with a treatment of cloud formation, yield physically-motivated predictions of substellar atmospheres. These GCMs provide the idealized basic structure of the atmosphere which can be post-processed with robust radiative transfer calculation codes like `ARTES`(Stolker et al. 2017) enabling direct comparisons with polarimetric observations.

Tan & Showman (2021) and Tan & Showman (2021) have recently developed 3D circulation models for brown dwarfs that include a variety of cloud phenomena, like condensation of clouds and cloud radiative feedback, in order to simulate the global circulation and cloud patterns of rotating brown dwarfs. This gives us the opportunity to model the polarization signals emitted from these physically motivated, inherently 3D and non-uniform cloud distributions, to test if they can match the observations of Luhmam 16 A and B. In this work, for the first time we use 3D circulation models and post-process them with vector Monte Carlo radiative transfer code `ARTES` to interpret the polarimetric data, focusing on the observations of Luhman 16 A and Luhman 16 B from Millar-Blanchaer et al. (2020). Despite the low statistical significance of the detection of polarization of Luhman 16 B, this object is of high interest to the astronomical community due to its proximity and significant variability, and we therefore consider it worthwhile to carry this modeling exercise on both A and B components. We specifically aim to explore and answer the following:

1. Can general circulation models with appropriate parameters for Luhman 16 A and Luhman 16 B be post-processed with a radiative transfer code like `ARTES` to match their observed polarization measurements?

2. Do these GCMs also match the observed photometric variability in Luhman 16 A and B?

3. Are the calculated polarization signal from circulation models of brown dwarfs sensitive to the spin-axis inclination relative to our line-of-sight of the objects?

4. How sensitive is the disk-integrated polarization signal arising from GCM of brown dwarfs to the typical cloud particle sizes?

5. Are cloud band models an adequate approximation when calculating polarization signals from objects which have non-uniform cloud covers including vortices of cloudy and clear regions?

We describe our modeling of the atmospheric circulation, cloud structures, and the polarized emission in §6.2, results in §7.4, discuss our findings in §7.5, and provide a summary and conclusion in §7.6.

2.2 Modeling Sub-stellar Atmospheres

2.2.1 General Circulation Models of Brown Dwarfs

We use the general circulation models (GCM) described and used in Tan & Showman (2021) and Tan & Showman (2021) to simulate the three-dimensional temperature and cloud structure for brown dwarfs Luhman 16 A and Luhman 16 B. The circulation models solve the fluid equations governing the horizontal momentum, mass continuity, hydrostatic balance and the energy transport of the substellar atmosphere in a rotating frame of reference. Two tracer equations are solved for the dynamics of the vapor and cloud components of the atmosphere. The radiative transfer for thermally emitted photons are computed using the gray atmosphere approximation in these models. The detailed physics and the governing equations of the GCM are fully described in Tan & Showman (2021). We use the temperature structures and cloud distributions

from these GCMs for calculating the disk-integrated polarized flux from Luhman 16 A and Luhman 16 B. Table 2.1 summarizes the physical input parameters used for simulating the circulation patterns for both the objects.

Of note, N_c in Table 2.1 denotes the cloud particle number per dry air mass for each object. The cloud material density used in the simulations corresponds to that of enstatite ($MgSiO_3$). N_c controls the mean cloud particle sizes in each radial bin in our GCM according to Equation 2.1 (see below) and the value of N_c for each object shown in Table 2.1 is such that Luhman 16 A and B has typically 1 μm and 5 μm sized cloud particles, respectively, near the base of their cloud decks. We explore the effect of having different size cloud particles on the disk-integrated polarization signal from these objects in §7.4.

The GCM models for Luhman 16 A use 60×190×384 grid cells corresponding to the r, θ, ϕ variables, respectively, where r is the radial dimension, θ is the polar dimension and ϕ is the azimuthal dimension. Models for Luhman 16 B use a 60×254×512 grid. The higher angular resolution used for Luhman 16 B is because it is a faster rotator, which requires following the dynamics on smaller length scales. The GCM model for both the objects evolve somewhat over time but here we use a time snapshot of the model after it reaches steady state. We now describe the modeled thermal and cloud structure from the GCM setups in §2.2.1.1 and §2.2.1.2.

Parameter	Model 16 A	Model 16 B	Measurement (16 A)	Measurement (16 B)
Rotation Period	7 Hours	5 Hours	6.94 Hours [1]	5.28 Hours ± 22% [2]
log(g)	4.5	5	4.5[3]	4.5-5 [4]
Radius	7×10^7 m	6.3×10^7 m	0.95 R_J[5]	0.8-0.93 R_J[6]
N_c	1×10^9 kg^{-1}	1×10^8 kg^{-1}	–	–
Cloud Material Density	3.19 g/cm^3	3.19 g/cm^3	–	–
Temperature (100 Bars)	4300 K	3500 K	–	–

Table 2.1: The brown dwarf parameters and their values used to model the three-dimensional circulation patterns for Luhman 16 A and Luhman 16 B are tabulated. The measured values of these parameters are also shown except for those parameters which are not yet measured but has been assumed in our modeling.

2.2.1.1 The 3D Temperature-Pressure Structure

The temperature patterns at a pressure level of $\sim$ 0.23 bars arising across the globe for both the brown dwarfs are shown in Figure 2.1. This is a representative pressure chosen to be within the enstatite cloud for both objects. The central band of comparatively hotter regions is very evident for Luhman 16 A whereas for Luhman 16 B such a distinct central hot band is missing at this pressure level. As Luhman 16 A has been assumed to be a slower rotator than Luhman 16 B, horizontal length scales of various vortices and features for Luhman 16 A are larger than Luhman 16 B. The Rossby deformation radius is inversely proportional to the coriolis parameter (f) and guides the typical length scales of vortices (Tan & Showman 2021) and as a result this difference in length scales of vortices arises in our models.

The longitudinally averaged temperature-pressure (T-P) profile for both Luh-

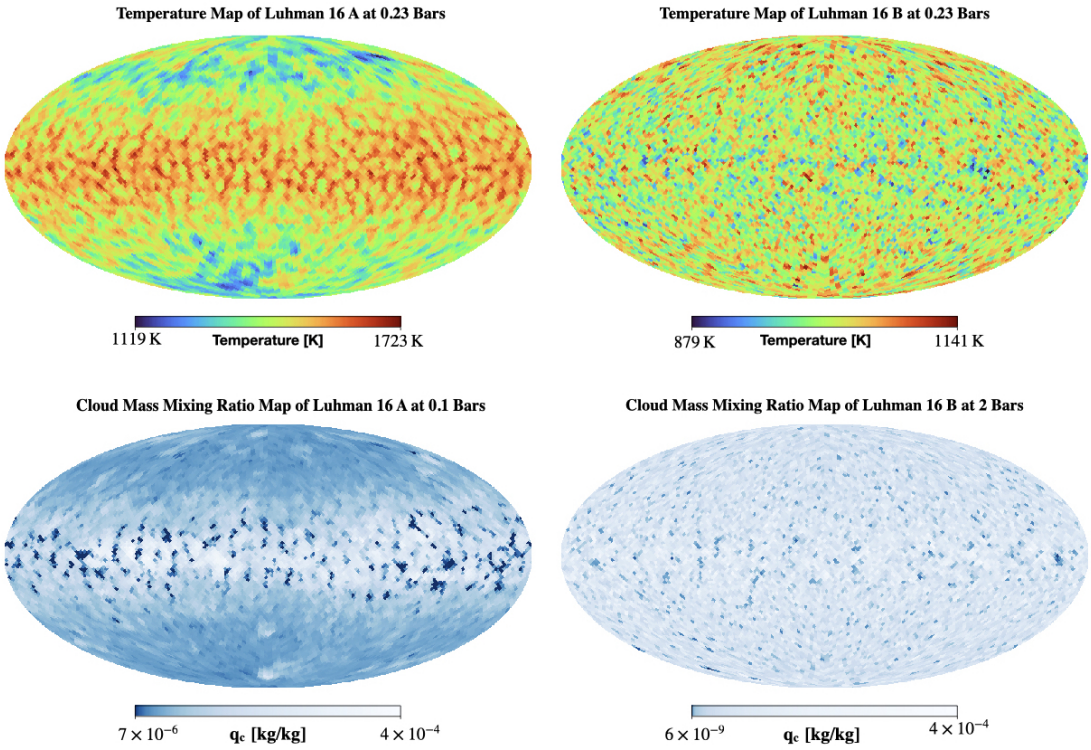

Figure 2.1: The top panel shows the global temperature pattern from the GCM runs at a pressure of 0.23 Bars for Luhman 16 A (top left panel) and Luhman 16 B (top right panel). The bottom panels show the cloud mass mixing ratio (q_c) at a pressure of 0.1 Bars for Luhman 16 A (bottom left panel) and at a pressure level of 2 Bars for Luhman 16 B (bottom right panel). **Main Point** - The equator is hotter and more cloudy than the poles for Luhman 16 A; furthermore, the size of vortices in Luhman 16 A and B models are different due to these objects' different rotation rates.

man 16 A and B is shown in Figure 2.2 with colored solid lines starting from the equatorial regions to the polar regions. The T-P profiles in the deep interior ($\geq$ 10 bars) all converge to the same adiabat due to the onset of convection at such high pressures in both the objects. For Luhman 16 A, the equatorial regions are hotter than the polar regions at lower pressures ($\leq$ 1 bars). This behaviour can be attributed to cloud radiative feedback. Equatorial regions for both the objects are relatively more cloudy than the polar regions as can be seen in Figure 2.1 left lower panel. Larger cloud opacities scatter and absorb more thermal flux and as a result heat up the atmospheric columns more in the equatorial regions than the polar regions.

The thermal structure of Luhman 16 B is more homogeneous compared to Luhman 16 A as can be seen in both Figure 2.1 and 2.2. This is related to the cloud optical depth variation for both the objects across the globe. Cloud particle sizes show higher variations across the globe in Luhman 16 A than Luhman 16 B which can be seen both in Figure 2.1 lower panels and Figure 2.2 (dotted lines). This causes the cloud radiative feedback on Luhman 16 B to be more homogeneous than Luhman 16 A leading to a compartively homogeneous thermal structure in Luhman 16 B than Luhman 16 A.

2.2.1.2 The 3D Cloud Structure

The GCMs treat the condensation and particle formation of $MgSiO_3$ (enstatite) for both the objects. $MgSiO_3$ is a dominant cloud species for objects with effective temperatures for Luhman 16 A and B and has been chosen here as a representative silicate. However, other species like Fe clouds might also be important sources of scattering in

the atmosphere but this is not expected to critically effect the cloud circulation patterns as long as the cloud opacities are greater than the gas opacities. We discuss this further in §7.5.

The condensing species in the GCM – enstatite, does not exist in the vapor phase. But it condenses through a chemical pathway involving a reaction between gaseous magnesium, water vapor and SiO (Visscher et al. 2010b). This reaction can only occur across a pressure-temperature curve which we refer to as the phase-boundary curve for enstatite. This phase-boundary curve for enstatite has been treated similarly to a condensation curve for species which condense directly from their vapor phase (like H_2O) in our GCM. The gaseous vapor phase Mg in our GCM condenses to enstatite cloud particles when the local mass mixing ratio of the condensible vapor is larger than the local saturation vapor mixing ratio (q_s). On the other hand, when the local cloud mixing ratio (q_c) exceeds the saturation vapor mixing ratio (q_s), it evaporates and turns back to vapor. The local saturation vapor mixing ratio q_s is determined by the temperature-pressure-dependent phase boundary curve of enstatite given by Visscher et al. (2010b) using solar abundance and has been shown in Figure 2.2 with black solid lines. The detailed implementation for condensates is the same as that in Tan & Showman (2019).

Figure 2.1 bottom left panel shows the q_c at 0.1 Bar pressure for our models of Luhman 16 A and the bottom right panel shows the q_c at 2 Bar pressure for our models of Luhman 16 B. The pressure levels are chosen here for highlighting the equator to pole trends of the cloud structure in the GCMs near the base of the cloud decks for

each object. The pressure dependence of the clouds and their equator to pole trends can be seen in Figure 2.2. The sizes of cloud vortices decrease from the equator towards the pole for both the objects due to the variation of the coriolis parameter f with ϕ across the globe. Also, Luhman 16 A has larger cloud patterns than Luhman 16 B due to the difference in their rotation periods, as has been discussed earlier in the context of temperature patterns.

We determine the mean cloud particle size of each layer using (Tan & Showman 2021),

$$r_c = \left(\frac{3q_c}{4\pi N_c \rho_c} \right)^{1/3} \tag{2.1}$$

where q_c is the cloud mass mixing ratio and ρ_c is the material density of our cloud species which has been specified in Table 2.1.

The longitudinally averaged cloud particle sizes are shown for different latitudes from the equator to the pole for Luhman 16 A (left) and Luhman 16 B (right) in Figure 2.2 with dotted lines. As has been noted in Tan & Showman (2021), faster rotation leads to vertically thinner cloud decks for Luhman 16 B compared to Luhman 16 A. The typical cloud particle sizes for the Luhman 16 A model is ~ 1 μm whereras that for Luhman 16 B is ~ 5 μm. This is analogous to a low value of f_{sed} – vertically thicker clouds with smaller particles (Luhman 16 A model) and higher value of f_{sed} – vertically thinner clouds with larger particles (Luhman 16 B model) – within the framework of the Ackerman & Marley (2001b) cloud model. Buenzli et al. (2015) found that spectroscopic variability data for the A component is best fit with a $f_{sed} = 2$ model whereas the B component data could be best fit with a superposition of a hotter

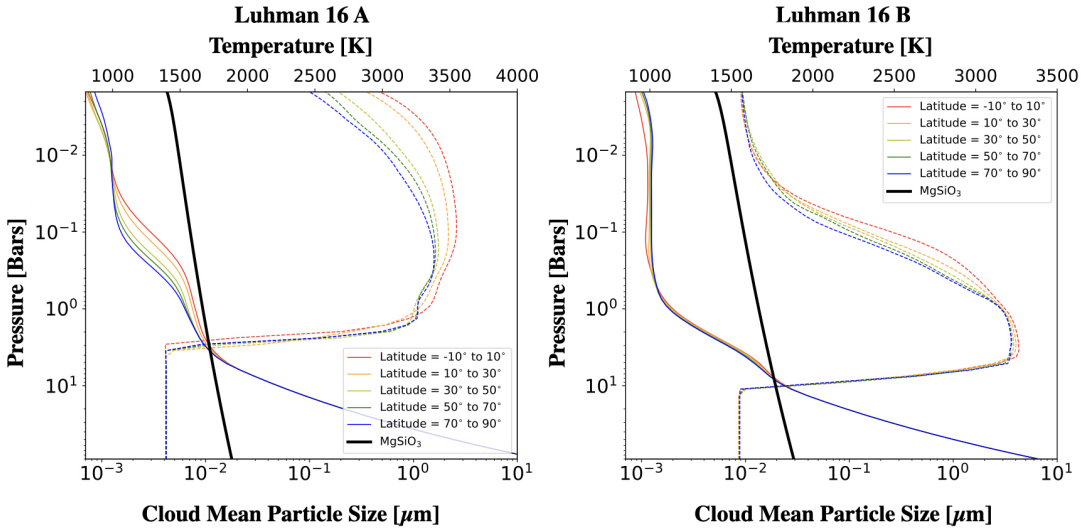

Figure 2.2: The left panel shows the longitudinally averaged Temperature-Pressure (T-P) profiles for Luhman 16 A with solid lines. Various colored lines depict the average T-P profile of latitudinal bands each with a angular width of 20° starting from the equator (red) to the pole (blue). The black solid line shows the phase-boundary curve for enstatite from Visscher et al. (2010b) assuming solar abundance. The dotted colored lines depict the longitudinally averaged cloud particle sizes in μm from the equator to the poles. The right panel depicts the same for Luhman 16 B.

model with thinner clouds of $f_{sed} = 3$ and a colder model with thicker clouds of $f_{sed} = 1$. In addition, our GCM finds that the cloud thickness decreases towards the pole from the equator due to variation of the coriolis parameter f with latitude. Table 2.1 shows that the number of cloud particles per dry air mass (N_c) which has been assumed to be larger for Luhman 16 A than Luhman 16 B as the former is classified to be a L dwarf and the later a T dwarf (Kniazev et al. 2013; Burgasser et al. 2013). This results in larger typical cloud particle sizes for Luhman 16 B than the Luhman 16 A model.

2.2.2 Radiative Transfer with ARTES

We use the publicly available 3D Monte Carlo radiative transfer code ARTES[7](Stolker et al. 2017) for post-processing the 3D atmospheric structure calculated from the GCMs. The radiative transfer formalism of ARTES involves emission of photon packages from each grid cell of the three dimensional atmosphere grid. These photons are stochastically absorbed or scattered as they travel through the atmosphere ultimately hitting the detector once they escape. The initial emission direction of the photons are sampled from a probability distribution function which is biased towards emitting photons in the radially outward direction. The probability distribution function (Stolker et al. 2017) p(ζ) is,

$$p(\zeta) = \frac{\sqrt{1-\epsilon^2}}{\pi(1+\epsilon\cos\zeta)} \tag{2.2}$$

where ζ is the emission direction and varies between 0 (radially downward) and π radians (radially outwards) and ϵ is the asymmetry parameter for the emission which varies between 0 and 1. A higher asymmetry parameter (ϵ) leads to a larger number of photons emitted initially towards the radially outwards direction. Since we are mainly concerned about the outgoing thermal emission from the atmosphere, we use ϵ= 0.8 for all our radiative transfer calculations. This is a valid approximation because scattering events which can change the direction of photons emitted to the radially downward directions to radially upward directions are possible but unlikely.

[7]https://github.com/tomasstolker/ARTES

Each photon has a stokes vector of the form,

$$S = \begin{pmatrix} I \\ Q \\ U \\ V \end{pmatrix} \tag{2.3}$$

where πI is the thermal flux. The degree of linear polarization (P) and angle of the polarization vector (χ) for each photon is given by,

$$P = \frac{\sqrt{Q^2 + U^2}}{I} \tag{2.4}$$

$$\chi = \frac{1}{2} \arctan\left(\frac{U}{Q}\right) \tag{2.5}$$

Each scattering event leads to the rotation of the stokes vector for each photon using a matrix multiplication operation involving the scattering matrix and a rotation matrix depending on the scattering direction of the photon. This operation is described in detail in Stolker et al. (2017). The final stokes parameters of the escaped photons are then projected on the detector. The additive nature of the stokes vectors allows the projected stokes vectors to be simply added to calculate the disk-integrated stokes vector of the object. This disk-integrated stokes vector is then used to calculate the disk-integrated flux, degree of linear polarization and angle of linear polarization using Equation 2.4 & 2.5.

We use 1×10^{11} photons for all of our calculations to maintain sufficient accuracy (≤ 10 % Monte Carlo error) in the calculated thermal and polarized flux. For com-

putational purposes, we regrid the GCM models into a 60×85×171 grid cells ($r \times \theta \times \phi$) for both Luhman 16 A and B. We assume a detector with 100×100 pixels for our calculations. We ensure that our resolution is high enough to preserve the overall circulation patterns of the original GCM runs described in §2.2.1 for both bodies.

2.2.3 Opacities and Scattering Matrices

We use the molecular and continuum opacity database available in open-source code `PICASO` (Batalha et al. 2019; Batalha et al. 2020c) for our calculations. Molecular opacities from H_2O (Barber et al. 2006; Tennyson & Yurchenko 2018), CH_4 (Yurchenko & Tennyson 2014; Yurchenko et al. 2013), NH_3 (Yurchenko et al. 2011), CO (Li et al. 2015), PH_3 (Sousa-Silva et al. 2014), H_2S (Azzam et al. 2016), CO_2 (Huang et al. 2014), Na & K (Ryabchikova et al. 2015), TiO (Schwenke 1998) and VO (McKemmish et al. 2016) are included. Collision-induced absorption opacities from H_2-H_2 (Abel et al. 2011), H_2-He, H_2-N_2, H_2-H, H_2-CH_4, H-electron bound-free, H-electron free-free and H_2-electron interactions are also included. We use the average T-P profile of the entire globe to calculate the molecular abundances and atmospheric opacities of these molecules assuming thermochemical equilibrium with solar values for C/O ratio and metallicity. For computational efficiency, we neglect the variation of the equilibrium molecular abundances due to the changing T-P profile across radial columns of the atmosphere. As we focus on polarization at a particular wavelength, rather than precision spectroscopy across a broad wavelength range, this simplification is warranted for this particular work. We discuss this further in §7.5.

We assume that the cloud particle sizes follow a gamma distribution (Hansen 1971; Stolker et al. 2017) although the GCM runs includes only single-sized particles. The cloud particle size distribution is given by,

$$n(r) = Cr^{(1-3v_{\rm eff})/v_{\rm eff}} e^{-r/v_{\rm eff} r_{\rm eff}} \tag{2.6}$$

where $r_{\rm eff}$, $v_{\rm eff}$ and C are the effective radius, effective variance and the normalization constant, respectively. Figure 2.3 top panels show the particle size distribution for various combinations of $r_{\rm eff}$ and $v_{\rm eff}$. The solid lines show the particle size distributions when $v_{\rm eff}$=0.05 and $r_{\rm eff}$ is 0.1 (blue), 1 (red) and 10 (green) μm. The dotted lines show the distributions when $v_{\rm eff}$=0.1 and $r_{\rm eff}$ is 0.1 (blue), 1 (red) and 10 (green) μm. Other cloud models like Ackerman & Marley (2001b) assume log-normal distribution of particle sizes. The gamma particle size distributions differ from log-normal distribution because of its asymmetry. It represents clouds where probability density is higher for larger particles near $r_{\rm eff}$ with a broader distribution of smaller particles.

For each (r, θ, ϕ) grid point we assume the $r_{\rm eff}$ to be the cloud particle radius from Equation 2.1 and $v_{\rm eff}$ to be 0.05. We then calculate the particle size distribution in 80 radial bins and calculate the absorption opacity, scattering opacity and the scattering matrix elements in each of these radial bins using Mie particle scattering theory. We obtain the complex refractive indices of amorphous magnesium silicates similar to enstatite in composition from Scott & Duley (1996) and use it for all our cloud opacity and scattering matrix calculations. These opacities and matrix elements are then integrated over the size distribution to obtain the total cloud opacities and scattering

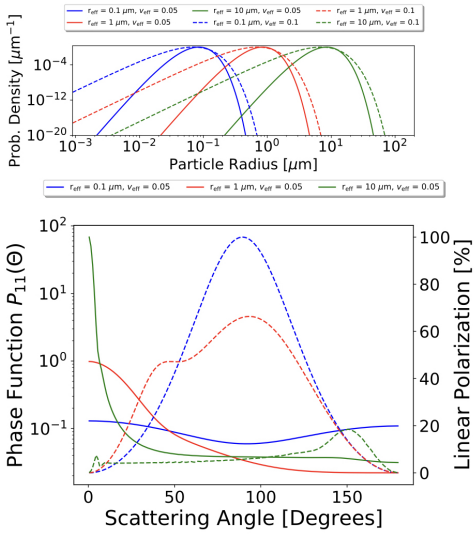

Figure 2.3: The top panel shows the cloud particle size distributions for different values of effective radius (r_{eff}) and effective variance v_{eff}. The solid lines depict the particle size distributions with v_{eff}= 0.05 and r_{eff} of 0.1 μm (blue solid line), 1 μm (red solid line) and 10 μm (green solid line). The dashed lines show wider particle size distributions with v_{eff}= 0.1 and r_{eff} of 0.1 μm (blue dashed line), 1 μm (red dashed line) and 10 μm (green dashed line). The bottom panel left vertical axis correspond to phase function ($P_{11}(\Theta)$). The solid lines show $P_{11}(\Theta)$ calculated from the particle size distributions shown in the top panel with the same colors. The percentage of linear polarization as a function of the scattering angle is shown with dashed lines for each of the particle distributions (right vertical axis). **Main Point**- Gas and clouds scatter infrared light very differently and single scattering polarizations are very sensitive to particle sizes.

matrix elements for that grid point. This calculaion is done using the Mie calculation module in `ARTES` (Stolker et al. 2017). The scattering matrices for the gas and cloud particles are calculated using the following form (Hansen & Travis 1974a; Stolker et al. 2017),

$$S = \begin{pmatrix} P_{11}(\Theta) & P_{12}(\Theta) & 0 & 0 \\ P_{12}(\Theta) & P_{22}(\Theta) & 0 & 0 \\ 0 & 0 & P_{33}(\Theta) & P_{34}(\Theta) \\ 0 & 0 & -P_{34}(\Theta) & P_{44}(\Theta) \end{pmatrix} \tag{2.7}$$

where Θ is the angle between the directions of the incident and the scattered light. The $P_{11}(\Theta)$ component represents the phase function of the scattering when normalized appropriately such that $\frac{1}{2\pi}\int_0^\pi P_{11}(\Theta) sin(\Theta)\, d\Theta = 1$. As the gas particle sizes are much smaller than infrared wavelengths, this matrix is calculated in the Rayleigh scattering regime for the gas particles where,

$$P_{11}(\Theta) = \frac{3\pi}{4}(1 + cos^2\Theta) \qquad P_{12}(\Theta) = \frac{3\pi}{4}(1 + cos^2\Theta)$$

$$P_{22}(\Theta) = P_{11}(\Theta) \qquad P_{33}(\Theta) = \frac{3\pi}{4}(2cos\Theta)$$

$$P_{44}(\Theta) = P_{33}(\Theta) \qquad P_{34}(\Theta) = 0$$

This Rayleigh scattering matrix represents a situation where the incident wavefront is scattered symmetrically in the forward and backward directions. Since the cloud particles scatter infrared photons in the Mie particle scattering regime, the cloud scattering matrix is calculated using the full Mie theory with the Mie calculation module

in ARTES. The Mie scattering matrix for micron sized cloud particles produces asymmetrically scattered wavefronts. This has been shown in Figure 2.3 bottom panel. The solid lines show the Mie particle scattering phase function ($P_{11}(\Theta)$) for a wavelength of 1.6 μm for the three particle size distributions shown in the top panel with solid lines corresponding to $v_{\rm eff}$=0.05 and $r_{\rm eff}$ is 0.1 (blue), 1 (red) and 10 (green) μm. The dotted lines show the polarization percentage from a single scattering event as a function of scattering angle. The phase function in solid blue shows that particles scatter light symmetrically in the forward and the backward direction with less light scattered at an angle of 90° when the $r_{\rm eff}$ is $\sim$ 0.1 μm. The polarization percentage for $\sim$ 0.1 μm particles peak at a scattering angle of 90° which is a typical Rayleigh scattering behaviour. Particle size distributions with typically larger particles like $r_{\rm eff}$ of 1 or 10 μm show much higher amounts of forward scattering compared to backward scattering. With increasing particle sizes, the degree of linear polarization also departs from the Rayleigh regime behaviour.

2.3 Results

2.3.1 Luhman 16 A

We first calculate the thermal flux and linear polarization percentage for Luhman 16 A at 1.6 μm. This choice of wavelength is motivated by the recent measurement of the polarization of Luhman 16 A in the H-band by Millar-Blanchaer et al. (2020). The measured polarization is 0.031$\pm$0.004%. For Luhman 16 A, we assume a rotation

period of 7 Hours (Apai et al. 2021) and a rotationally-induced oblateness of 0.003 which is expected from a Luhman 16 A like body with a rotational period of 7-8 hours (Millar-Blanchaer et al. 2020). We assume an inclination of 28° for our initial calculation (0° is equator-on hereafter). This is motivated by the recent measurements of inclination to be $\leq$ 28° for Luhman 16 A by Apai et al. (2021). We explore other inclinations closer to the equator-on view as well and describe the results from them. We calculate the polarization and flux signal from our Luhman 16 A GCM every 52.5 minutes as the object rotates for a total of one rotation period. This interval is chosen such that we repeat our calculation after every 45° rotation of the object along the spin axis. Figure 2.4 left panels show the surface brightness map of Luhman 16 A, thermal flux variability, linear polarization % variability and angle of polarization variability from top to bottom, respectively.

The surface brightness map for Luhman 16 A shows the thermal flux at 1.6 μm from each pixel at a single time snapshot as the object is rotating. The central relatively cloudy band is readily visible to be slightly off-centred in the image due to the assumed 28° inclination of the object. The cloudy regions emit less thermal flux and appear darker because they scatter/absorb more light compared to the clear regions. The flux variability of the object for one complete rotational period is shown with the yellow solid line. The peak-to-peak variability of the thermal flux is about 5% which mainly arises from the varying cloud patterns across the globe in our GCM. Buenzli et al. (2015) measured a 4% peak-to-peak variability of Luhman 16 A within the 0.8-1.15 μm wavelength range. Our results do not reproduce the Buenzli et al.

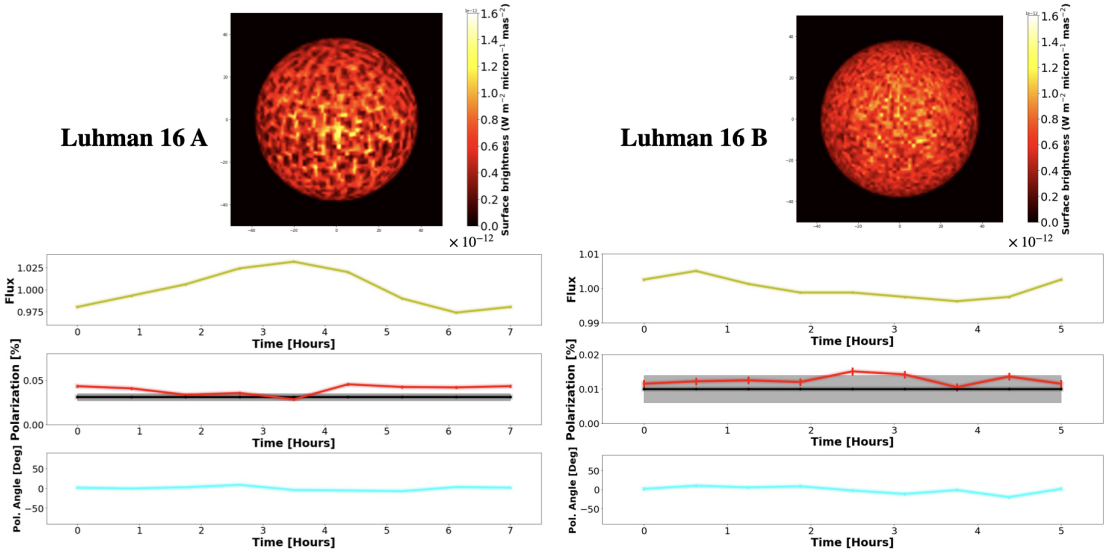

Figure 2.4: The left panel shows the radiative transfer result for Luhman 16 A. The top left panel shows the surface brightness map for the object. The second panel in the left shows the variability of thermal flux at 1.6 μm with time as the object rotates with a period of 7 hours. The third left panel shows the linear polarization percentage vs. time with the solid red line. The solid black line and the shaded region shows the measured polarization for the object. The bottom left panel shows the variation of the angle of polarization of the object with time using the cyan line. The same plots for Luhman 16 B (5 hour period) has been shown in the right panels. **Main Point** - Our models match the degree of linear polarization well for both the objects but do not reproduce the observed optical variability amplitude of Luhman 16 B.

(2015) measurement within the 1σ uncertainty. Our calculated flux variability is also larger than the measurements of Apai et al. (2021) who infer a typical peak-to-peak variability amplitude of 2.2% for Luhman 16 A using TESS light curves of the system in the wavelength range of 0.6-1.0 μm. But these differences can be due to difference in wavelength of our calculations (1.6 μm) and the observed wavelengths as the variability amplitude can vary strongly with wavelength (Buenzli et al. 2015). Biller et al. (2013) measured the H-band peak-to-peak amplitude for the unresolved Luhman 16 binary to be $\sim$ 4%. However, the H-band amplitude of the Luhman 16 A component alone remained below the detection limits of their observations. Differences in variability amplitudes can also arise if our circulation model is not capturing the 'true' cloud distribution and/or particle sizes in these objects.

The time varying modeled polarization signal is shown with the red solid line and is compared to the measured time averaged signal in black for Luhman 16 A (Millar-Blanchaer et al. 2020). The uncertainty in the measured polarization is shown with the shaded black region. The modeled polarization signal agrees well with the time averaged measurement. But importantly, the degree of polarization also shows significant variation within 0.03% to 0.045% within one rotational period.

Variability of linear polarization has been previously observed in cool M–dwarf stars (Miles-Páez et al. 2015) in optical wavelengths. However, the origin of those polarization signals are still unclear and can be due to the strong magnetic field of the cool dwarf, presence of a dusty disk around the star or presence of non-uniformly distributed dust grains in the stellar photosphere. de Kok et al. (2011) also found time

variable polarization signal from a brown dwarf model with a dusty hot spot in its atmosphere. We also simulate the polarization signals for more equator-on inclinations $\sim$20° and $\sim$0° (equator-on). The modeled time-averaged signal is $\sim$0.04% and $\sim$0.07% respectively for the two inclinations. Both these signals are much higher than the measured value. This indicates that inclination of Luhman 16 A is very close to 28° if our GCM represents its atmosphere correctly. We discuss this further in §7.5.

The disk-integrated polarization signal is also anti-correlated to the disk-integrated flux from the object. This is because scattering from cloud particles are primarily responsible for the polarized flux in infrared wavelengths, and hence a higher disk-integrated flux hints towards lower cloud coverage at that time instant and can give rise to lower disk-integrated signal.

The angle of linear polarization also varies significantly for Luhman 16 A as shown in the bottom left panel of Figure 2.4. The angle of polarization varies between -7° to 8° within one full rotational period. This kind of rotation of the plane of the polarization vector was also seen in models of brown dwarfs with a single dusty hot spot in de Kok et al. (2011). Our simulations suggest that the angle of polarization must show significant time variations if they arise from such circulation patterns. These polarization observations integrate over time scales of several hours which are comparable to the rotational period of these objects. We sum up the disk-integrated stokes parameters from each of our time steps to calculate the disk-integrated degree of linear polarization and angle of the polarization vector when time-integrated over one rotational period. We find that the time integrated degree of linear polarization is 0.038

% and the angle of the linear polarization is -0.28°. As has been outlined in Millar-Blanchaer et al. (2020) and Stolker et al. (2017), the polarization vector aligns itself with the spin axis if the disk-integrated polarization is dominated by equatorial bands of clouds and if oblateness dominates the polarization signal then the polarization vector is perpendicular to the spin axis. For Luhman 16 A, the polarization vector in all time steps as well as the disk-integrated polarization is aligned very close to the spin axis which suggests that our modeled polarization is mainly dominated by the equatorial bands of clouds in the GCM. The measured angle of linear polarization for Luhman 16 A by Millar-Blanchaer et al. (2020) is -32°±4° relative to the North direction on the sky. This angle is not comparable to our model results since the on-sky orientation of the spin-axis is unknown.

We check the sensitivity of the disk-integrated polarized signal to the typical cloud particle sizes of our GCM models. For Luhman 16 A, the typical cloud particle sizes are ~ 1 μm (we assume a gamma distribution of cloud particles) but we also simulate instances when the typical cloud particle sizes are ~ 10 μm and ~ 0.5 μm. Although changing the cloud particle sizes should also alter the circulation pattern in principle due to the dependence of cloud opacities on particle sizes, we neglect that subtlety here. Figure 2.5 shows the dependence of the disk-integrated polarization signal for both of our Luhman 16 A (top panels) and Luhman 16 B (bottom panels) models. The top left column shows the surface brightness map of the Luhman 16 A model when the typical cloud particle sizes are ~ 1 μm and the polarization percentage matches the observed polarization well. But when the particle sizes are increased to ~ 10 μm the

surface brightness increases but the polarization signal declines by about $\sim$ 10 times. The polarization signal increases slightly if the cloud particle sizes are taken to be about $\sim$ 0.5 μm. This indicates that the typical cloud particle sizes for Luhman 16 A, if the circulation patterns are representative of the reality, lies between $\sim$ 0.5-1 μm.

2.3.2 Luhman 16 B

The simulated surface brightness map of Luhman 16 B from the GCM models described in §2.2.1 is shown in Figure 2.4 top right panel. We have assumed an inclination of 26° for Luhman 16 B motivated by the results presented in Millar-Blanchaer et al. (2020). The time variability of thermal flux, degree of linear polarization and angle of linear polarization are shown in the right three panels from top to bottom, respectively. The modeled peak-to-peak variability for Luhman 16 B is about $\sim$ 1% which is much less than the observed Luhman 16 B typical H-band variability amplitude of about 13% measured by Biller et al. (2013). This shows that our GCM model is inadequate for explaining the variability of Luhman 16 B. This might happen due to the presence of a large cloud/cloudless feature on the globe of Luhman 16 B which is not present in our GCM run.

The variability of the disk-integrated polarization signal for the Luhman 16 B model matches well with the measured polarization of 0.010%±0.004% (Millar-Blanchaer et al. 2020) for an assumed inclination of 26° for the object. We explore the equator-on configuration for the Luhman 16 B model and find a disk-integrated polarization percentage of $\sim$0.03% which is $\sim$ 3 times larger than the measured value. So, our model

prefers an inclination of 26° for Luhman 16 B in contrast to a much more equator-on configuration suggested by the variability analysis in Apai et al. (2021). However, we take this opportunity to reiterate that the detection significance of the measurement is only 2.5-sigma.

The typical cloud particle sizes for Luhman 16 B GCM is ∼5 μm. The disk-integrated polarization signal at 1.6 μm for cloud particle sizes of ∼2.5 μm and ∼50 μm are found to be 0.0351% and 0.0001%, respectively. The calculated signal with particles of ∼50 μm sizes is ∼10 times lower than the measured signal whereas the signal with typically ∼2.5 μm clouds particles is ∼3 times higher than the measurement. This has been shown in Figure 2.5 lower panels. This suggests that the typical cloud particles sizes for Luhman 16 B is ∼5 μm.

The angle of linear polarization also varies significantly for Luhman 16 B between 10° and -20°. This suggests that our polarization calculations for Luhman 16 B are dominated by the equatorial band of clouds in our Luhman 16 B circulation model. We find the time-averaged degree of linear polarization from our Luhman 16 B model is 0.011 % by integrating the calculated signal over one rotation period of the object. This is in good agreement with the measured H–band polarization of 0.01 ± 0.004 % for Luhman 16 B. This time-integrated polarization vector projects an angle of -1.56° from the spin-axis of the object. The measured time averaged angle of the polarization vector is 73° (Millar-Blanchaer et al. 2020) relative to the North direction in the sky and hence is not directly comparable to our modeled angles since the on-sky orientation of the spin-axis is unknown.

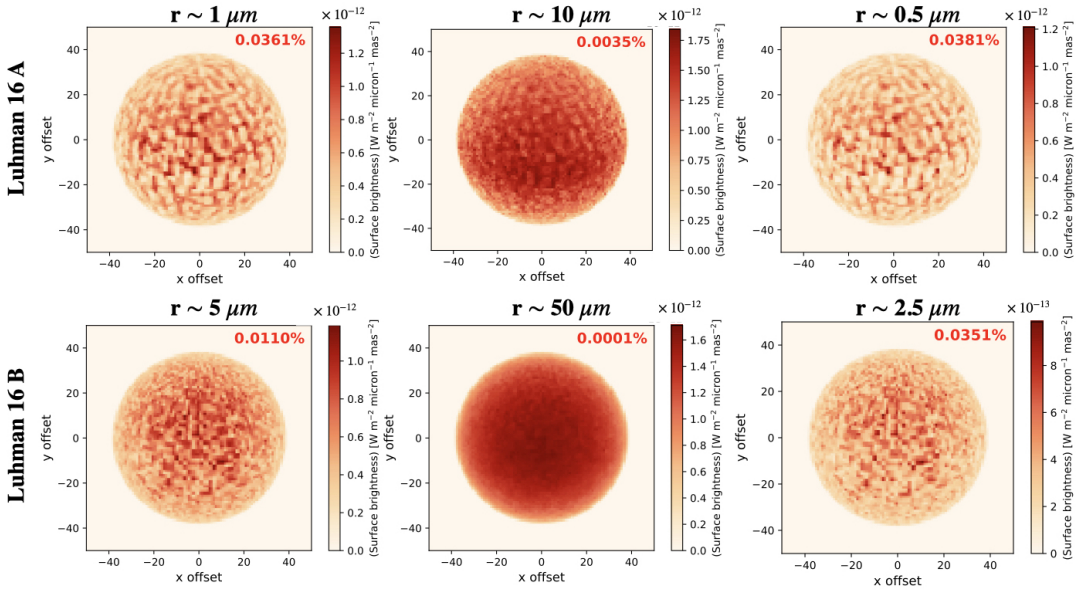

Figure 2.5: The top left, middle and right panel shows surface brightness map for Luhman 16 A if the typical cloud particle sizes were 1 μm (original GCM), 10 μm and 0.5 μm. The disk-integrated polarization for each case has been shown in the top right of each plot window. The bottom left, middle and right panel shows surface brightness map for Luhman 16 B if the typical cloud particle sizes were 5 μm (original GCM), 50 μm and 2.5 μm. Please note that the color scheme is inverted. **Main Point** - Luhman 16 A should have typical cloud particle sizes betwen 0.5-1 μm whereas Luhman 16 B should have cloud particle sizes of about 5 μm.

2.3.3 Modeling of Polarization Signal with Band Models

Single and multiple band models have often been used to model polarization signal from objects with non-uniformity in cloud coverage (Millar-Blanchaer et al. 2020; Stolker et al. 2017). These have been motivated by observed band-like cloud patterns in Jupiter. Here, we have tried to explore if such models are adequate for calculations of disk-integrated polarization signals from objects like those modeled by our GCM runs or if we need circulation models like the one used in this work for interpreting future polarization observations from non-uniformly cloudy objects. We first assume that the real nature of circulation on a brown dwarf/exoplanet is represented by our circulation models. We then create models with multiple bands of clouds ("band models") and test if they can reproduce the same polarization signal as we calculate from our GCM runs for Luhman 16 A and B. We assume that the cloud structure of our band models for Luhman 16 A and B is the same longitudinally averaged cloud structure shown in Figure 2.2. From the equator to the pole, each of the cloud profiles shown in Figure 2.2 left panel for Luhman 16 A forms a band with a latitude span of 20° in our band model for Luhman 16 A. Similarly, we construct our band model for Luhman 16 B with the averaged cloud profiles shown in Figure 2.2 right panel forming bands with latitude spans of 20°. The gas opacities used for the radiative transfer for the GCM are also used for the band models of the corresponding objects to ensure similarities in all conditions between the GCM models and the band models except for the detailed circulation patterns dominating the smaller length scales than the global jets. We compute the

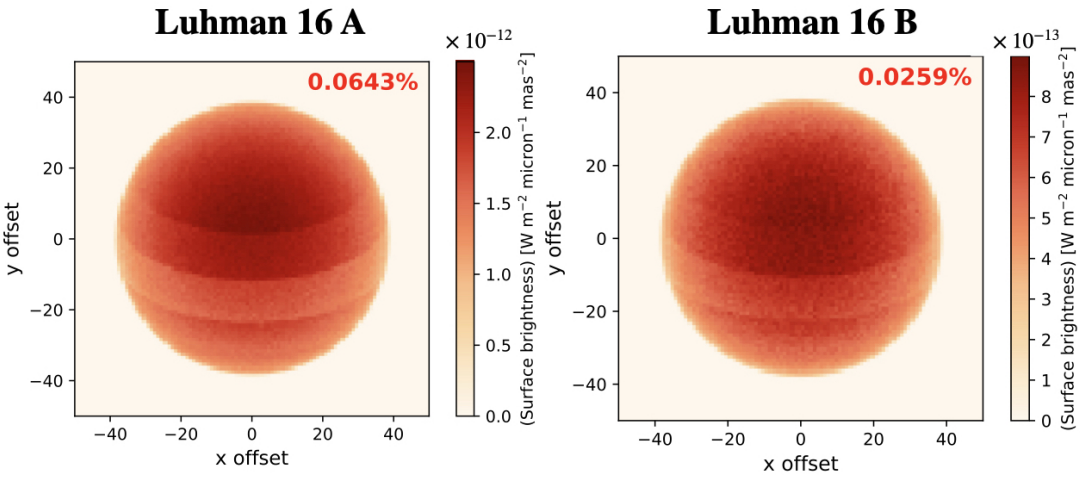

Figure 2.6: Left panel shows the surface brightness map of the simple band model for Luhman 16 A along with the 1.6 μm disk-integrated polarization percentage denoted at the top in red. Right panel shows the same for the band model of Luhman 16 B. Please note that the color scheme is inverted. **Main Point**- Band models tend to overestimate polarization signal.

polarization signal from the band models for Luhman 16 A and Luhman 16 B using the same oblateness and inclinations as has been used for the computations reported in §2.3.1 and 2.3.2.

Figure 2.6 shows the surface brightness map of the multiple band model for Luhman 16 A and the right panel shows the same for the multiple band model of Luhman 16 B. The disk-integrated polarization signal from this band model for Luhman 16 A is found to be 0.0643%. This is almost twice the signal which was calculated from the GCM for Luhman 16 A where the polarization was found to be ∼0.038%. For Luhman 16 B, the calculated polarization from the band model is 0.0259% in contrast to the circulation model polarization percentage of ∼0.011%. The linear polarization vectors from the band models of both the objects are aligned along the spin-axis as

has also been found from the GCM models. So in both the cases the band models overestimate the disk-integrated polarization compared with the GCM models even if other properties like inclination, oblateness, cloud optical properties, gas opacities and the thermal structure are almost alike between the band and the circulation models. This hints towards the significant influence of smaller scale vortices across the globe of these objects, which are present only in the circulation models, on the disk-integrated polarizations. Even if both Luhman 16 A and B circulation models have a central equatorial band of clouds, a band model with single or multiple cloud bands might still overestimate the polarization signal from the object. These smaller-scale vortices of cloudy and cloud free regions tend to decrease the overall disk-integrated polarization signal.

2.4 Discussion

We first discuss some of the caveats, implications and future follow up of our work and then summarize our findings in §7.6.

2.4.1 GCM Parameter Choices

Our circulation models use the computational framework described in Tan & Showman (2021), which necessarily involves some simplifications. For example, the GCM models and our subsequent radiative transfer calculations only consider the condensation of one cloud species (enstatite) which is an important cloud species in the temperature regime of our interest. Other cloud species like Fe and Olivine are also

suggested to be important sources of cloud opacity, and can alter the cloud radiative feedback, or cloud optical properties, for the object. The choice of the condensation species itself is not very critical as long as the cloud optical depths exceed the gaseous optical depths (Tan & Showman 2021). However, different cloud species like Fe might follow a different particle size distribution which can have an effect on the polarization signal calculations.

For our models presented here, we use a particular time snapshot of the circulation structure of these objects after they reach a quasi-steady state. However, these circulation patterns may continue to evolve further in time and therefore investigation of the long-term photometric and polarization variability may prove fruitful as well.

The circulation models used here can be sensitive to other assumptions as well, such as the drag strength deep in the brown dwarf atmosphere. The GCMs presented here have been calculated in the "strong drag" regime but this drag strength is highly uncertain as the interaction between the deeper interior and the atmosphere is not properly characterized to date (Tan & Showman 2021). This work uses these GCM runs for post-processing them with the comprehensive radiative transfer tool `ARTES` which allows us to make direct comparisons with observations but there remains ample scope for further exploration of the parameter space of the circulation models themselves. In future work, we will explore a wider range of GCM parameter space for Luhman 16 A and B, and generic brown dwarfs, to examine the sensitivity of our radiative transfer results to the assumptions outlined above. The combination of GCM outputs and post-processing for the calculation of polarization and spectra appears to be a powerful tool.

2.4.2 Spherical Cloud Particles

We assume cloud particles to be spherical throughout this study for simplicity, as it is typical in the field, and use Mie particle scattering theory for calculation of the cloud scattering properties. However, non-spherical particles can have significantly different scattering phase functions especially at back-scattering angles as has been investigated in detail by Mishchenko et al. (1997). However, they show that the difference in the cloud optical properties like optical depth, single scattering albedo and asymmetry parameter between a non-spherical and projected-area equivalent spherical distribution of particles is at maximum $\sim$ 10%. This suggests that considering non-spherical particles in our GCM will not significantly alter the cloud radiative forcing compared to the spherical particles assumed in this work.

Since the phase functions at back-scattering angles differ significantly between spherical and non-spherical distributions of particles (Mishchenko et al. 1997), they can affect the disk-integrated polarization signals calculated in this work. This has also been shown in Stolker et al. (2017) where the departure from spherical particles has been treated with the distribution of hollow spheres approach (Min et al. 2005). We use a spherical cloud particle shape assumption to avoid additional complexity at this time, in our already complex modeling. We defer treating non-spherical cloud particles for future work as more polarimetric observations are obtained in near future.

Lastly, optical constants for mineral aerosol particles can themselves be temperature dependent (Zeidler et al. 2015), which we ignore here. Neither the infrared

emission spectra or the polarimetric measurements of brown dwarfs are constrained enough at this point of time to investigate these effects.

2.4.3 Improvements to Radiative Transfer and Opacities

All our calculations are done at a single wavelength of 1.6 μm whereas the polarimetric measurements with which we compare our models are often done in a broader photometric wavelength bands (H–band for Luhman 16 A and Luhman 16 B). In this work, we do not perform our radiative transfer calculations for multiple wavelengths within the photometric wavelength band of observations for making our comparison with data in order to avoid the much larger computational time required. But integrating the disk-integrated polarization across a photometric band might change the predicted polarization signal from GCMs especially if there are sharp molecular absorption or emission windows within the photometric band in question.

In future modeling work over a broader wavelength range, to fit both emission spectroscopy as well as polarization, additional computational efforts should be put into opacity variations around the globe. Gaseous opacities depend on both the local temperature and pressure, and recall here that we use the gaseous opacities for the globally averaged T-P profile for our radiative transfer. We make this approximation because our main focus in this work is the calculation of the polarization signal and gas molecules are not important scattering sources in infrared wavelengths. The only way they effect the resultant infrared thermal polarized flux is with their absorption opacity. As the maximum fluctuation in temperature across the globe at a certain pressure level

for Luhman 16 A is about ∼200 K and that for Luhman 16 B is ∼20 K, the temperature dependance of gas opacity across the globe will be a small effect and will not affect the net-disk integrated polarization signal significantly, but may become important in future work.

2.5 Conclusions

We have coupled pioneering 3D GCM calculations for brown dwarfs Luhman 16 A and B with the vector Monte Carlo radiative transfer code `ARTES`, in order to calculate the polarization signal in three dimensions. We summarize our findings in the form of answers to the specific questions we promised to answer/explore in §7.1 here.

1. We find that General Circulation Models, with nearly global enstatite clouds, can be used to explain the observed H–band disk-integrated degree of linear polarization signals from cloudy brown dwarfs Luhman 16 A and Luhman 16 B. We calculate the degree of linear polarization for Luhman 16 A to be 0.038 % and the measured value is 0.031% ± 0.004%. For Luhman 16 B, our calculated degree of polarization is 0.011% and the measured polarization is 0.010% ± 0.004%.

2. The typical variability amplitude observed in Luhman 16 A is also reproduced from the thermal flux calculated from our GCM for Luhman 16 A. However, our Luhman 16 B GCM underestimates the variability amplitudes from the observations of Luhman 16 B. However, in all cases the observed variability for Luhman 16 A was not at 1.6 μm, the wavelength we model here.

3. If our circulation patterns are representative of the circulation patterns on these objects, then we find that the preferred spin-axis inclination for Luhman 16 A is $\sim 28^{\circ}$ whereas that for Luhman 16 B is $\sim 26^{\circ}$. We find that the disk-integrated polarization signals calculated from GCMs also decline as one moves from equator-on to pole-on configurations.

4. We also find that decreasing cloud particle sizes generally increases the disk-integrated polarization signal. For our GCM to match the observations for Luhman 16 A, we find that the typical cloud particle sizes should be within 0.5–1 μm. Whereas, for Luhman 16 B, cloud particles should be around 5 μm as both 2.5 μm or 50 μm overestimate and underestimate the disk-integrated polarization, respectively.

5. Simpler cloud band models with one or multiple bands have often been used to interpret polarization measurements from non-uniformly cloud covered objects. We find that even if we use cloud profiles very similar to the GCMs keeping every other important parameter such as oblateness and inclination the same, these band models tend to overestimate the disk-integrated polarization signal compared with the GCMs. This suggests that smaller scale vortices tend to decrease the disk-integrated polarizations in brown dwarfs and are important factors influencing the polarized emission. This also indicates that if the real cloud circulation of any object is like the GCMs then band models might not be adequate to interpret disk-integrated polarization measurements from them.

In our follow-up work we will expand to multi-wavelength polarization predictions, both for Luhman 16 A and B, and for brown dwarfs generally over a larger parameter phase space, given the larger data sets being accumulated (Jensen-Clem et al. 2020; van Holstein et al. 2021a). We will also explore a wider range of GCMs for Luhman 16 A and Luhman 16 B, to assess whether the observed broadband photometric variability in the visible and near infrared, as well as the polarization signal, can be interpreted in the framework of one model. Also, our cloudy GCMs for Luhman 16 A and B do not reproduce the multiple band like circulation patterns inferred by (Apai et al. 2021) for Luhman 16 B from TESS observations. Further exploration of our GCM parameter space for these objects and investigating the circulation patterns and the disk-integrated polarization signals arising from them will significantly progress our understanding of brown dwarf clouds.

Chapter 3

PICASO 3.0: A One-Dimensional Climate Model for Giant Planets and Brown Dwarfs

There are three broad categories of substellar atmosphere modeling frameworks: one-dimensional (1D) physically self-consistent models, three-dimensional (3D) General Circulation Models (GCMs) and atmospheric retrieval. Atmospheric models enable the understanding of physical and chemical processes driving the behaviour of substellar atmospheres. When combined with observational data, they can be used to infer the physical state of atmospheres. Additionally, the adiabat calculated by the atmospheric models provides the upper boundary conditions of the interior evolutionary models of substellar objects like giant planets and brown dwarfs (Hubbard 1977; Burrows et al. 1997; Chabrier et al. 2000; Saumon & Marley 2008). Although sub-

stellar atmospheres generally constitute a small fraction ($\sim 1\%$) of the total mass of their bodies, their radiative properties control the overall cooling of objects throughout their evolution. Therefore, atmospheric models are crucial for understanding both physical (e.g. climate and chemistry) and global properties of substellar objects (e.g. radius/luminosity evolution over time).

A variety of 1D radiative–convective–thermochemical equilibrium models of exoplanetary and brown dwarf atmospheres have been developed (e.g. Marley et al. 1996; Barman et al. 2001; Fortney et al. 2005, 2008a; Marley et al. 2021; Phillips et al. 2020; Piskorz et al. 2018; Goyal et al. 2020). These models originate both from stellar atmosphere modeling codes (e.g. Barman et al. 2001; Sudarsky et al. 2003; Seager & Sasselov 1998) and planetary atmospheric modeling codes (e.g. Marley et al. 1996; Baudino et al. 2015). These models rely on iterating to a self-consistent radiative-convective equilibrium (RCE) solution. Self-consistency here means that the model iterates on all components of the atmospheric structure simultaneously such that they are physically consistent with each other (e.g., chemical abundances are consistent with the current temperature profile). The models do not capture 3D dynamics, but instead are able to incorporate the effects of radiative/convective energy transport, chemistry, and clouds. These 1D models are also computationally efficient, which enhances their exploratory power significantly over 3D circulation models. For example, (e.g. Zhang et al. 2021a) used the `SONORA BOBCAT` grid of models, generated using the 1D RCTE model described in Marley et al. (2021), to infer the physical properties of 55 T-dwarfs in an uniform analysis. The computational speed of these 1D self-consistent models along

with their ability to treat atmospheric physics and chemistry self-consistently makes them a powerful tool for interpreting atmospheres of planets and brown dwarfs.

Besides the model used in Marley et al. (2021), several other independent 1D RCTE models have been widely used in the literature (e.g. Tremblin et al. 2015; Phillips et al. 2020; Gandhi & Madhusudhan 2017; Burrows et al. 2008; Marley et al. 2021; Malik et al. 2017). For example, the `GENESIS` code from Gandhi & Madhusudhan (2017) was used for the high significance detection of various Carbon and Nitrogen bearing species in the atmosphere of HD 209458b by Giacobbe et al. (2021). The `ATMO` model (Tremblin et al. 2015; Phillips et al. 2020) was used by Goyal et al. (2018) to perform a uniform fitting analysis of the transmission spectra of 10 hot Jupiters which led to important conclusions about their atmospheric composition. Despite the many insights gained from these models, their simplicity often makes them insufficient to explain a variety of atmospheric spectra (e.g. Noll et al. 1997; Oppenheimer et al. 1998; Saumon et al. 2003; Golimowski et al. 2004; Geballe et al. 2009; Sorahana & Yamamura 2012; Leggett et al. 2012; Miles et al. 2020). For example, Miles et al. (2020) found the presence of disequilibrium chemistry in a series of late T and early Y-dwarfs by measuring their significantly enhanced photospheric CO abundances. In another example, Zhang et al. (2021a) concluded that presence of clouds can lead to much better overall fit to the available infrared spectra of 55 brown dwarfs with a uniform analysis using the `SONORA` cloudless grid of models. This motivates adding physical complexity to 1D RCTE models in order to enable better interpretation of upcoming data, for example, from *JWST*.

Models for exoplanetary and brown dwarf atmospheres have been developed in

three-dimensions (3D) (e.g. Showman et al. 2008, 2020; Tan & Showman 2021; Menou & Rauscher 2009; Roman & Rauscher 2019; Wolf et al. 2022; Lee et al. 2021b) as well. The 3D models work to capture the detailed global dynamics like horizontal transport/winds in the atmospheres along with other atmospheric components like radiation and clouds. However, these models are computationally intensive which limits their power of exploration of the vast parameter space in question. Moreover, in order to make the models computationally feasible, they rely on approximations such as gray atmospheres in the radiative transfer calculations (e.g. Tan & Showman 2021; Tan & Showman 2019; Menou & Rauscher 2009; Tan 2022). As a result, 3D models are unable to resolve some atmospheric properties predicted by 1D models – like detached convective zones in brown dwarfs and giant planets.

Atmospheric retrievals are also widely used to interpret observational data. These studies aim to recover the atmospheric state of any planet/brown dwarf based on the observed spectral data in a Bayesian framework (e.g. Madhusudhan 2018; Line et al. 2017; Burningham et al. 2017). The free parameters of interest typically include the atmospheric temperature-pressure ($T(P)$) profile, chemical abundances and cloud properties (Line et al. 2017; Burningham et al. 2017, 2021; Mukherjee et al. 2021a; Taylor et al. 2021). The multi-dimensional parameter space of these free parameters is sampled by repeatedly calculating model observables (e.g., spectra) with simple and computationally fast forward models. Comparison of these modeled observables with the observed data helps in retrieving likelihood distributions for all the retrieved free parameters. However, these retrieved properties are often not required to have

physical constraints. For example, the retrieval analysis of hot Jupiter, WASP-18 b, was predicted to have a thermal inversion and relatively high metallicity (283×Solar), corresponding to a CO abundance of >10% (Sheppard et al. 2017). Later using a self-consistent grid of models, Arcangeli et al. (2018) showed that this planet is more likely to have a solar metallicity and hot dayside, which is more consistent with what is expected from a hot Jupiter with little heat redistribution. This means that even though retrieval studies are effective in inferring the various atmospheric properties like abundances and temperature structures, they are not equipped to provide the physical interpretations of why the atmosphere is in the retrieved state, and they often result in unphysical solutions. Therefore, physically motivated self-consistent models are required to understand the physical and chemical processes that drive the structure of planetary and substellar atmospheres.

In this work, we focus on 1D physically motivated radiative–convective equilibrium models for substellar atmospheres. In addition to include complexities like disequilibrium chemistry within these models, another important modification we must make to these codes, is to transform them to open sourced, "FAIR" codes (findable, accessible, interpretable, and reproducible). Doing so will enable the community to interpret the upcoming influx of data from missions like JWST (Pontoppidan et al. 2022). Currently, there are a handful of 1D climate models that are open source (e.g., `HELIOS` (Malik et al. 2017, 2019b), and `TLUSTY` (Hubeny 1988; Hubeny et al. 2003; Sudarsky et al. 2003)). `HELIOS` is a Python-based GPU dependent model and it has been used for modeling atmospheres of a variety of substellar objects (e.g. Fossati et al. 2021;

Malik et al. 2019a; Yan et al. 2022; Deline et al. 2022). TLUSTY is a stellar atmosphere model written in FORTRAN77. This code has been modified to be applied to substellar atmospheres as well and is called COOLTLUSTY (Hubeny et al. 2003). COOLTLUSTY also has been widely used for brown dwarfs and exoplanets (e.g. Burrows et al. 2006; Spiegel et al. 2010; **?**; Lacy et al. 2019; Lacy & Burrows 2020). In this work, we aim to add to develop a new open-source Python based one-dimensional radiative-convective equilibrium model for H-dominated substellar atmospheres – PICASO 3.0 that is both: 1) open source and 2) capable of including disequilibrium chemistry induced by vertical mixing self-consistently within the 1D radiative–convective equilibrium framework. PICASO 3.0 has been released publicly as an extension of the already open-source 1D and 3D radiative transfer tool PICASO (Batalha et al. 2019). It is also accompanied by detailed tutorials exploring all of its uses and limitations. Here, we focus on the description of the numerical techniques used in the code along with benchmarking to previous studies to demonstrate its functionality.

In §6.2, we discuss the methodology of PICASO 3.0, the new Python atmospheric model. We present the benchmarking of our model with other models in §3.2 followed by recommendations on how to use this model in §3.3. We briefly discuss ongoing and future improvements in §3.5 and conclude in §3.6.

3.1 Model Setup of PICASO 3.0

The heritage of our code is the Fortran based EGP sub-stellar atmospheric model. The EGP model has been used for substellar atmospheres including solar system planets – Titan and Uranus (McKay et al. 1989; Marley & McKay 1999), the L–T–Y brown dwarf sequence (e.g. Marley et al. 1996; Morley et al. 2014a, 2012; Marley et al. 2021; Karalidi et al. 2021a; Zhang et al. 2021a), cloudy atmospheres (e.g. Cushing et al. 2008; Stephens et al. 2009) and a wide variety of extrasolar planets (e.g. Fortney et al. 2005, 2007, 2008a; Marley et al. 2012; Fortney et al. 2020; Morley et al. 2015; Morley et al. 2017b) for over two decades. It has also been used as the primary radiative-transfer scheme in the SPARC GCM (Showman et al. 2009a). Briefly, this 1D model solves for the self-consistent temperature, chemical and cloud structure of H-dominated atmospheres under the assumption of radiative-convective equilibrium. The code structure of PICASO 3.0 is composed of Python classes [1] which generally include multiple Python functions. We refer to these classes and functions as modules here. In general, Python is significantly slower than Fortran. However, with the use of 'numba''s 'just-in-time' framework (Lam et al. 2015) to create on-the-fly compiled machine code, PICASO 3.0 has comparable run times to the original Fortran. Figure 3.1 shows a simplified schematic of PICASO 3.0's workflow.

First, the user provides an initial set of physical properties for the object to be modeled, shown within the red boxes at the top of Figure 3.1. The model supports both non-irradiated (e.g., brown dwarf) and irradiated (e.g., planets) calculations. Therefore,

[1] https://docs.python.org/3/tutorial/classes.html

we specify optional inputs with dashed outlines. For example, for modeling a field brown dwarf atmosphere, the user only must specify the $T_{\rm eff}$ ($T_{\rm int}$ in case of a planet), gravity, atmospheric metallicity and C/O ratio of the brown dwarf. For modeling an irradiated planet, the user must specify the internal temperature of the planet $T_{\rm int}$, planet gravity, atmospheric metallicity, C/O ratio, semi-major axis, and host star properties (e.g., stellar temperature, metallicity, and gravity). $T_{\rm int}$ represents the temperature obtained by converting the internal heat flow of the planet via the Stefan-Boltzmann law. Along with these inputs, the user must also specify an initial pressure-temperature profile ($T(P)$) guess, which is divided into plane-parallel logarithmically spaced pressure layers ($\sim$ 60-90). Then, through an iterative process, which we describe in §3.1.1, the model iterates through computing chemistry, opacities, and net upwelling and downwelling fluxes until a radiative-convective equilibrium threshold has been met. During this iteration, the model solves for both radiative and convective parts of the atmosphere and takes into account the possibility of multiple radiative and convective zones. Ultimately, the model produces the final atmospheric state of the object ($T(P)$ and associated chemistry). These can then be used to compute transmission, emission, and/or reflected light spectra used to compare with observations (see Figure 3.1). We discuss these physical and chemical aspects one by one in the following §3.1.1.

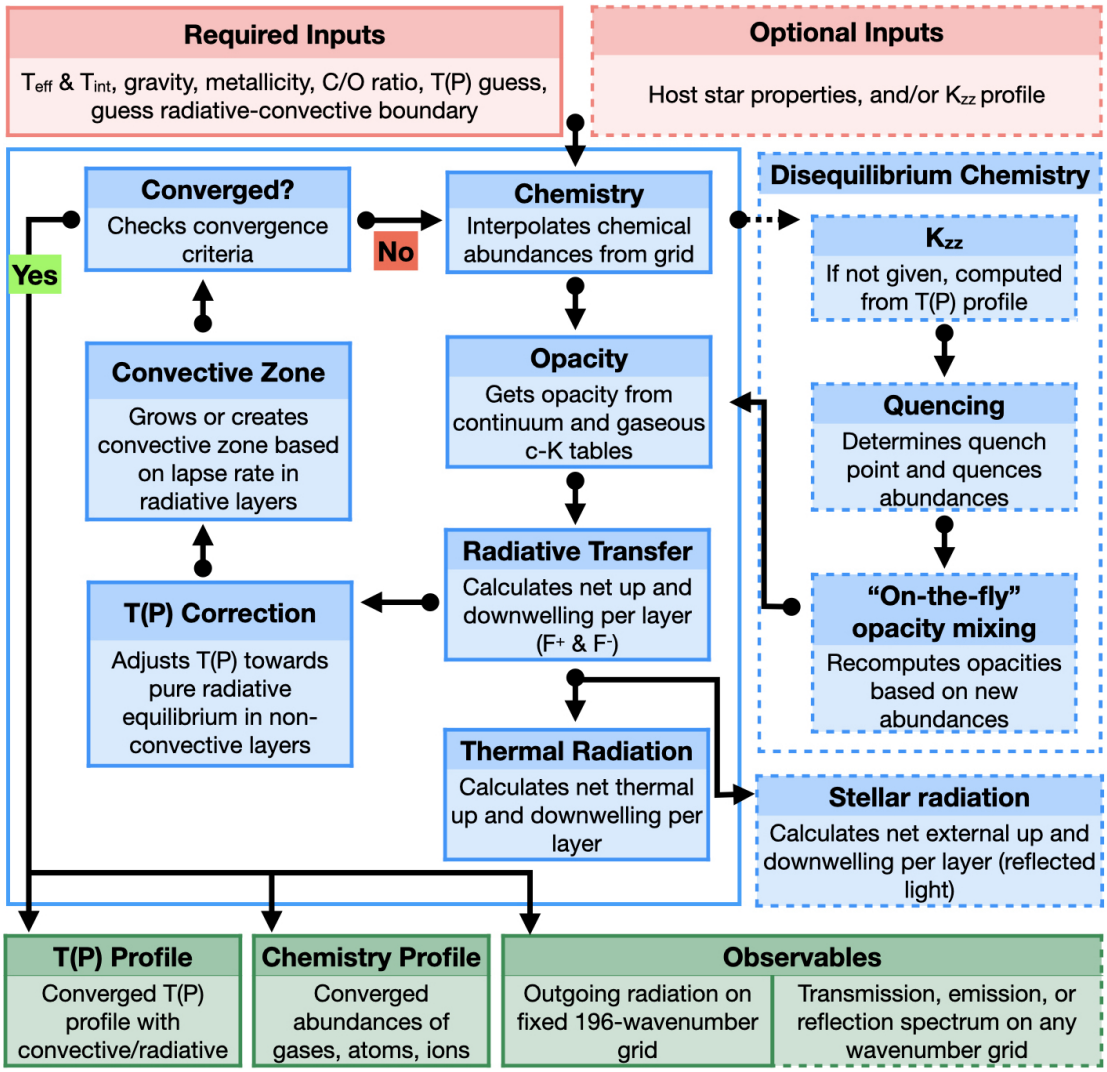

Figure 3.1: Schematic diagram of the radiative-convective model in `PICASO 3.0`. Solid outlines indicate required modules, while dashed outlines indicate optional models.

3.1.1 Physics and Chemistry of Substellar Atmospheres

3.1.1.1 Radiative-Convective Equilibrium

The key physical basis of this model is the assumption of radiative-convective equilibrium in substellar atmospheres. The radiative equilibrium represents the physical scenario where within each atmospheric layer the energy emitted must be balanced by the energy absorbed. This means that each atmospheric layer must allow the transfer of the same amount of radiative energy through it. Hubeny (2017) provides a detailed derivation of the radiative–convective equilibrium criteria. For completeness, we present some of the important steps here. Radiative equilibrium scenario is represented by:

$$\int_0^\infty (\chi_\nu J_\nu - \eta_\nu) d\nu = 0 \tag{3.1}$$

where χ_ν and η_ν are absorption and emission coefficients, respectively and J_ν is the first moment of the intensity field. Assumption of local thermodynamic equilibrium allows Equation 3.1 to be rewritten as:

$$\int_\nu \kappa_\nu (J_\nu - B_\nu) d\nu = 0 \tag{3.2}$$

where κ_ν is the wavelength dependent total absorption opacity of the layer and B_ν is the local Planck function of the layer. This is the integral form of the radiative equilibrium condition for each atmospheric layer. The integral form of the radiative–equilibrium condition (Equation 3.2) is applicable and numerically stable throughout the atmosphere. Another method of computing radiative-equilibrium condition, which

is used by our model, is referred to as the differential form. The differential form is numerically stable at optically thicker parts of the atmosphere and might become numerically unstable at parts of the atmosphere which are optically thin ($\tau << 1$). In practice, this instability only appears at parts of the atmosphere with low temperatures and very small optical depths. In our first release of the climate code, we stick to our original methodology of using the differential form, despite the instabilities pointed out by Hubeny (2017). In a later update we will explore and implement the integral form as well within our model to make our solutions more accurate at the optically thinner parts of the atmosphere.

The differential form can be derived by using Equation 3.2 along with the second moment of the radiative transfer equation,

$$\int_{\mu} \mu \frac{dI_\nu}{d\tau_\nu} d\mu = \int_{\mu} \mu (I_\nu - S_\nu) d\mu \tag{3.3}$$

which under local thermodynamic equilibrium leads to the form,

$$\frac{dH_\nu}{dz} = \kappa_\nu (J_\nu - B_\nu) \tag{3.4}$$

where H_ν is the wavelength dependent second moment of the specific intensity field. Comparing Equation 3.2 and 3.4 leads to the condition,

$$\int_{\nu} \frac{dH_\nu}{dz} d\nu = 0 \tag{3.5}$$

which means that the integral of the second moment of the intensity, H_ν, must be

constant at all layers. Mathematically, this can be written as:

$$\int_{\nu} H_{\nu} d\nu - \frac{\sigma_{sb} T_{\rm eff}^4}{4\pi} = 0 \tag{3.6}$$

where σ_{sb} is the Stefan–Boltzmann constant and $T_{\rm eff}$ is the effective temperature of the object. This calculation can be found in the `t_start` module in the code. The model tries to achieve this radiative equilibrium in all the atmospheric layers which are stable against convection.

Given Equation 3.6, which defines the radiative-equilibrium condition, the general procedure of the model is to start with an initial guess of the $T(P)$ profile of the atmosphere. This can be seen in the required inputs box at the top of Figure 3.1. Radiative fluxes through all the atmospheric layers are then calculated given a chemical state of the atmosphere. These radiative fluxes are used to compute the wavelength integrated flux carried by each layer $H(z)$. If the atmospheric layers are not in radiative equilibrium, this quantity $H(z)$ would not be equal to the target flux given by $\frac{\sigma_{sb} T_{\rm eff}^4}{4\pi}$, and the $T(P)$ solution would be perturbed until the convergence criteria set by Equation 3.6 is met. The methodology of the convergence is discussed further in §3.1.2.

3.1.1.2 Radiative Transfer

In order to compute radiative-convective equilibrium with Equation 3.6, radiative fluxes must be calculated for all atmospheric layers. The fundamental equation describing atmospheric radiative transfer is,

$$\mu \frac{dI_\nu(\mu, \tau_\nu, \phi)}{d\tau_\nu} = I_\nu(\mu, \tau_\nu, \phi) - S_\nu(\mu, \tau_\nu, \phi) - \frac{\omega_0}{4\pi} \int_0^{2\pi} \int_{-1}^{1} P_\nu(\mu, \mu', \phi, \phi') \cdot I_\nu(\mu', \tau_\nu, \phi') d\mu' d\phi' \tag{3.7}$$

where $\mu = \cos(i)$ where i is the incident angle of the ray, ϕ is the azimuthal angle, I_ν is the specific intensity, τ_ν is the frequency dependent optical depth, S_ν is the frequency dependent source function and P_ν is the scattering phase–function. The first term on the right–hand–side of Equation 3.7 describes the attenuation of the intensity with increasing optical depth. The source function S_ν is used to describe the emission of the atmosphere itself (e.g. thermal emission) or any external radiation source (e.g. incident stellar radiation). The third term in Equation 3.7 represents scattering of the intensity within the atmosphere where the phase–function $P_\nu(\mu, \mu', \phi, \phi')$ is the probability that intensity $I_\nu(\mu', \tau_\nu, \phi')$ will be scattered from the direction (μ', ϕ') to the direction (μ, ϕ).

In order to solve Equation 3.7, we follow the two-stream radiative transfer methodology described in Toon et al. (1989) for the calculation of radiative fluxes. The specific intensity $I_\nu(\mu, \tau_\nu, \phi)$ can be integrated over the azimuthal angle ϕ to calculate the azimuthally integrated intensity $I_\nu(\mu, \tau_\nu)$. The upward and downward fluxes can also be defined by,

$$\begin{aligned} F_\nu^+ &= \int_0^1 \mu I_\nu^+(\mu, \tau_\nu) d\mu \\ F_\nu^- &= \int_0^1 \mu I_\nu^-(\mu, \tau_\nu) d\mu \end{aligned} \tag{3.8}$$

where $I_\nu^+(\mu, \tau_\nu)$ is the azimuthally integrated intensity for upward values of μ and $I_\nu^-(\mu, \tau_\nu)$ is the azimuthally integrated intensity for downward values of μ. Equation

3.7 can be integrated to produce two separate coupled equations in terms of the upward and downward fluxes instead of the μ and ϕ dependent intensities. These equations for the upward and downward fluxes are[2],

$$\begin{aligned} \frac{\partial F_\nu^+}{\partial \tau_\nu} &= \gamma_1 F_\nu^+ - \gamma_2 F_\nu^- - S_\nu^+ \\ \frac{\partial F_\nu^-}{\partial \tau_\nu} &= \gamma_2 F_\nu^+ - \gamma_1 F_\nu^- + S_\nu^- \end{aligned} \tag{3.9}$$

where γ_1 and γ_2 are functions of the scattering properties of the medium and S_ν^+ and S_ν^- are modified versions of the source function. The radiative transfer calculation within our model is divided into two distinct parts: 1) the transfer of thermal emission through the atmosphere and 2) the transfer of the reflected external (e.g. stellar) radiation throughout the atmosphere. Equation 3.9 is applicable to both of these components but the functions γ_1, γ_2, S_ν^+, and S_ν^- are defined differently for each. A brief description of the radiative transfer of thermal radiation in our model is provided below followed by a discussion of the radiative transfer of external stellar radiation.

We use the two-stream source function technique described in Toon et al. (1989) to calculate the thermal upward and downward fluxes in each layer. The hemispheric mean approximation approach is used in this method where γ_1 is given by 2-$\omega_0(1+g)$ and γ_2 is $\omega_0(1+g)$. ω_0 and g are the single scattering albedo and the scattering asymmetry parameter of the atmospheric layer, respectively. This hemispheric mean approximation was used to obtain functional forms for the source functions S_ν^+ and S_ν^- in Toon et al. (1989) (see Table 3 and Equations 53 & 54 in Toon et al. (1989)).

[2]there is a typo in Eqn. 12 of Toon et al. (1989) which incorrectly swaps in S_ν^+ for S_ν^- in the negative partial flux

With these source functions, the upward azimuthally averaged intensities at the top ($I_n^+(0,\mu)$) and bottom ($I_n^+(\tau,\mu)$) of an atmospheric layer with optical depth τ can be written as,

$$\begin{aligned} I_n^+(0,\mu) =& I_n^+(\tau,\mu)e^{-\tau/\mu} + \frac{G}{\lambda\mu - 1}(e^{\lambda\tau}e^{-\tau/\mu} - 1) \\ &+ \frac{H}{\lambda\mu + 1}(1 - e^{-\lambda\tau}e^{-\tau/\mu}) + \alpha_1(1 - e^{-\tau/\mu}) \\ &+ \alpha_2(\mu - (\tau + \mu)e^{-\tau/\mu}) \end{aligned} \tag{3.10}$$

This calculation can be found in the `get_thermal_1d_gfluxi` module. Similarly the downward azimuthally averaged intensities at the top ($I_n^-(0,-\mu)$) and bottom ($I_n^-(\tau,-\mu)$) of the same atmospheric layer can be written as,

$$\begin{aligned} I_n^-(\tau,-\mu) =& I_n^-(0,-\mu)e^{-\tau/\mu} + \frac{K}{\lambda\mu - 1}(e^{-\tau/\mu} - e^{-\lambda\tau}) \\ &+ \frac{J}{\lambda\mu + 1}(e^{\lambda\tau} - e^{-\tau/\mu}) + \sigma_1(1 - e^{-\tau/\mu}) \\ &+ \sigma_2(\mu e^{-\tau/\mu} + \tau - \mu) \end{aligned} \tag{3.11}$$

and can also be found in the `get_thermal_1d_gfluxi` module. The functions G, H, K, I, α_1, α_2, σ_1, and σ_2 have been computed for the hemispheric-mean approximation in Toon et al. (1989) and are used in our calculation as well. Solving equations 3.10 and 3.11 also require boundary conditions for the diffuse flux at the top and bottom of the atmosphere. These boundary conditions are set using the thermal blackbody intensities at the top and bottom of the atmosphere using,

$$
\begin{aligned}
B_{\rm top} =& (1. - e^{-\tau^{'}/\mu_1}) B(T_{\rm top}) \\
B_{\rm bot} =& B(T_{\rm bot}) + \mu_1 \frac{B(T_{\rm bot}) - B(T_{\rm bot-1})}{\tau}
\end{aligned}
\tag{3.12}
$$

where $B(T)$ represents the blackbody function, $T_{\rm top}$ is the temperature of the top most atmospheric layer, $T_{\rm bot}$ is the temperature of the bottom most atmospheric layer, and τ is the optical depth of the bottom most atmospheric layer. μ_1 is assumed to be 0.5 due to the hemispheric-mean approximation. Note that the bottom boundary condition is valid only for gas giant atmospheres where the highest pressure grid point corresponds to the end of the user-defined grid and does not correspond to a "surface". `PICASO 3.0` does have the option to swap boundary conditions that are pertinent to the hard surfaces needed for terrestrial atmospheres, but it is not relevant for this work on gas giants and as such we do not discuss it here. $\tau^{'}$ is given by,

$$
\tau^{'} = \tau_{top} \frac{P_{\rm top}}{(P_{\rm top+1} - P_{\rm top})} \tag{3.13}
$$

This expression along with the top boundary condition in Equation 3.12 captures the downward thermal flux arising from the part of the atmosphere which has pressure less than the minimum pressure in the used atmospheric pressure grid. This formulation prevents arbitrary artificial cooling of the top-most atmospheric layer.

Equations 3.10 and 3.11 can be used to calculate the incidence angle (μ) dependent upward and downward – $I_n^+(\mu)$ and $I_n^-(\mu)$ intensity field in each atmospheric layer. But in order to use these radiative intensities ultimately for the convergence criteria in Equation 3.6, they need to be integrated with Equation 3.8 to calculate the

direction independent upward and downward fluxes – F_ν^+ and F_ν^-. In order to compute these disk-averaged, layer fluxes, the upward and downward thermal intensity for each atmospheric layer is calculated using Equation 3.10 and 3.11 at five incident angles. The cosine of these incident angles (μ) are determined using the Gaussian quadrature method with 5 points(Abramowitz & Stegun 1970). The choice of 5 Gauss points is the default setting in the code but other choices are also available in the `get_angles_1d` module. Table 3.1 shows the five default values of μ and the corresponding Gauss weights used for this Gaussian quadrature integration. The intensities at different incident angles are used to compute the integral in Equation 3.8 with the Gaussian-quadrature integration technique using the weights in Table 3.1. The module `get_thermal_1d_gfluxi` uses the formulation described above to calculate the wavelength dependent upward and downward thermal fluxes at the edges of each atmospheric layer.

θ(deg)	$\mu = cos(\theta)$	Gauss Weight
84.345	0.09853	0.015747
72.270	0.30453	0.073908
55.804	0.56202	0.146386
36.680	0.80198	0.167174
16.221	0.96019	0.096781

Table 3.1: Gauss points and weights used for Gaussian quadrature integration of thermal flux over different angles.

For the radiative transfer of the reflected stellar light, we use the quadra-

ture approximation. The calculation is performed for a single incidence angle of the stellar radiation beam ($60°, \mu_0$=0.5) unlike the 5 Gauss point method of the thermal counterpart. Under the quadrature approximation, γ_1 is $0.5\sqrt{3}(2 - \omega_0(1 + g))$, γ_2 is $\omega_0\sqrt{3}(1 - g)/2$, γ_3 is $(1 - \sqrt{3}g\mu_0)/2$, and γ_4 is 1-γ_3. These functions can be found in the `get_reflected_1d_gfluxv` module. The source functions S_ν^+ and S_ν^- for this component are,

$$\begin{aligned} S_\nu^+ &= \gamma_3 \pi F_s \omega_0 e^{-(\tau_c+\tau)/\mu_0} \\ S_\nu^- &= \gamma_4 \pi F_s \omega_0 e^{-(\tau_c+\tau)/\mu_0} \end{aligned} \tag{3.14}$$

where τ_c is the cumulative optical depth of all the atmospheric layers above the layer of calculation and τ is the optical depth of the layer itself. F_s here represents the stellar flux incident on the top of the atmosphere. F_s is interpolated from the `PHOENIX` grid of models (Allard et al. 2012a) available as a part of the `PySynPhot` (STScI Development Team 2013a) package. Using these functions, Equation 3.9 can be solved for the upward and downward fluxes for the n'th atmospheric layer as has been shown in Toon et al. (1989),

$$\begin{aligned} F_{\nu,n}^+ &= k_{1n} e^{\lambda_n \tau_n} + \Gamma_n k_{2n} e^{-\lambda_n \tau_n} + C_n^+ \\ F_{\nu,n}^- &= \Gamma_n k_{1n} e^{\lambda_n \tau_n} + k_{2n} e^{-\lambda_n \tau_n} + C_n^- \end{aligned} \tag{3.15}$$

where the quantities Γ_n, k_{1n}, k_{2n}, λ_n, C_n^+, and C_n^- are defined in Toon et al. (1989) (Equation 21, 22, 23, and 24). Equation 3.15 is solved in the `get_reflected_1d_gfluxv` module. However, an additional term needs to be added to the downward fluxes solved

from Equation 3.15 in this formulation. This term is,

$$F^{-}_{\nu,n} = F^{-}_{\nu,n} + \mu_0 F_s e^{-\tau_c/\mu_0} \tag{3.16}$$

Like the thermal component, complete solutions of Equation 3.15 also require boundary conditions on the diffuse flux at the top and bottom of the atmosphere. We use the boundary conditions,

$$\begin{aligned} F_{\rm top,st} &= 0 \\ F_{\rm bot,st} &= R_s \mu_0 F_s e^{-\tau_{\rm c,bot}/\mu_0} \end{aligned} \tag{3.17}$$

where $F_{\rm top,st}$ and $F_{\rm bot,st}$ are the diffuse flux at the top and bottom of the atmosphere, R_s denotes the reflectivity of the bottom surface and $\tau_{c,bot}$ is the cumulative optical depth of the deepest layer. The reflectivity of the bottom surface is typically assumed to be 1% in the model, but users should check that the bottom surface is not optically thin. This is further discussed in the §3.3. This formulation is used by the `get_reflected_1d_gfluxv` module to calculate the wavelength dependent upward and downward reflected stellar light fluxes at the edges of each atmospheric layer. But the calculation of both the thermal and reflected stellar light fluxes following the procedure described above requires another important parameter – the optical depth τ. The implemented τ calculation procedure in this model is described below.

Generally, two approaches are used for calculating the optical depth τ – 1) the line–by–line approach (e.g. Gandhi & Madhusudhan (2017),Burrows et al. (2008)) or 2) the correlated-k approach (e.g. Marley & McKay (1999), Malik et al. (2017), Fortney

et al. (2008a)). This model uses a correlated-k opacity approach for computationally efficient inclusion of gaseous opacities. In the correlated-k approach, each wavelength bin is represented by 8 distinct Gaussian quadrature points (g_i), each with its associated weight (w_i). Table 3.2 shows the Gauss points and the Gauss weights used for the 8 point correlated-k approach in the model. Each of these Gauss-points also have an optical depth τ_i associated with them. These "Gauss" points should not be confused with the "Gauss" points used to calculate the disk-integrated fluxes. This means that the radiative transfer equations for each wavelength bin must be computed 8 times, once for each value of optical depth τ_i corresponding to the i'th Gauss point. This calculation is done by calling `get_thermal_1d_gfluxi` and `get_reflected_1d_gfluxv` modules 8 times by the `climate` module. The 8 thermal and radiative upward and downward fluxes are then added together following,

$$F_n^{\pm}(\lambda) = \sum_{i=1}^{i=8} w_i F_{i,n}^{\pm}(\lambda, \tau_{i,n}) \tag{3.18}$$

where $F_{i,n}^{\pm}$ is the thermal/reflected light flux at the n'th atmospheric layer calculated with the optical depth $\tau_{i,n}$ corresponding to the i'th Gauss point. Our calculation of correlated-k opacities is described in more details in §3.1.1.4. This summation with Equation 3.18 within the `climate` module ultimately produces thermal/reflected wavelength dependent upward and downward fluxes in each atmospheric layer. These fluxes can now be used to calculate the convergence criteria in Equation 3.6. The net

thermal flux for the n'th layer can be simply obtained with,

$$\begin{aligned} F^n_{\text{thermal,net}} &= \int_\lambda (F^+_n(\lambda) - F^-_n(\lambda))d\lambda \\ F^n_{\text{stellar,net}} &= \int_\lambda (F^+_{n,s}(\lambda) - F^-_{n,s}(\lambda))d\lambda \end{aligned} \tag{3.19}$$

where $F^+_n(\lambda)$ represents the upward thermal flux from the n'th layer within the wavelength bin between λ and λ+dλ and $F^-_n(\lambda)$ is the downward thermal flux from the same layer within the same wavelength bin. $F^\pm_{n,s}$ also represent the same quantity for the reflected light component. The total net radiative flux in the n'th atmospheric layer can be calculated using,

$$F^n_{\text{net}} = r_{\text{th}} F^n_{\text{thermal,net}} + r_{\text{st}} F^n_{\text{stellar,net}} \tag{3.20}$$

where r_{th} is the contribution factor of the thermal radiation to the net flux and is generally fixed at 1 and r_{st} is the contribution factor of the stellar radiation to the net flux. Non-zero values of r_{st} is only relevant when the external irradiation on the atmosphere is non-zero. In the scenario when a user is computing a planet-wide average $T(P)$ profile, the stellar irradiation is contributing to 50% (one hemisphere) of the planet and as a result $r_{\text{st}} = 0.5$. If instead the goal is to compute a night-side average atmospheric state, r_{st} is set to be 0. On the other extreme, to compute the day-side atmospheric state of a tidally locked planet r_{st} should be set at 1.

This full net flux, F^n_{net}, is same as $4\pi \int_\nu H_\nu d\nu$ in Equation 3.6. Therefore, F^n_{net} can be used to check if the convergence criteria (Equation 3.6) is satisfied at all the radiative layers of the atmosphere. This check is done in the "Converged?" box of

the flow chart shown in Figure 3.1. Now that we have described the radiative transfer within our model, we will discuss other blocks of the model flow chart shown in Figure 3.1 starting with atmospheric chemistry.

Gauss Points (g_i)	Gauss Weights (w_i)
0.065960251992824	0.165231051440291
0.313509004297193	0.309768948559709
0.636490995702807	0.309768948559709
0.884039748007175	0.165231051440291
0.953471592210149	0.008696371128436358
0.966500473910379	0.01630362887156367
0.983499526089621	0.01630362887156367
0.996528407789851	0.008696371128436358

Table 3.2: Gauss points and weights used for calculation of the correlated-k opacities

3.1.1.3 Equilibrium Chemistry

As shown in Figure 3.1, in order to compute the radiative fluxes for checking the convergence criteria, as outlined in the previous §3.1.1.2, we first need a method to provide the chemical state of the atmosphere. This is required because the chemistry dictates the optical depth (τ) required for the radiative transfer calculations. In the simplest case, we determine the chemical state of the atmosphere using the $T(P)$ profile

of the atmosphere, atmospheric metallicity, and C/O ratio assuming chemical equilibrium. The atmospheric metallicity (M/H) is defined as the ratio of the abundances of all heavy elements to Hydrogen abundance in the atmosphere. Our climate model uses a pre-calculated grid of molecular abundances on a pressure vs. temperature vs. [M/H] vs. C/O grid. This chemistry grid is computed using the thermochemical equilibrium models presented in Gordon & McBride (1994); Lodders (1999, 2002); Visscher et al. (2006); Visscher et al. (2010) and using protosolar elemental abundances from Lodders (2010). The grid includes 73 temperature points between 75 K and 4000 K and 20 pressure points logarithmically spaced between 10^{-6} and 3000 bars. This corresponds to a pre-computed grid with 1460 grid points. The molecular abundances included in this grid are H_2, H, H^+, H^-, ${H_2}^-$, H_2^+, H_3^+, He, H_2O, CH_4, CO, CO_2, OCS, HCN, C_2H_2, C_2H_4, C_2H_6, NH_3, N_2, PH_3, H_2S, SiO, TiO, VO, Fe, FeH, MgH, CrH, Na, K, Rb, Cs, Li, LiOH, LiH, LiCl, and e-. The metallicities included in the grid are: [M/H] (relative to Solar)= -1, -0.75, -0.5, -0.3, -0.25, 0.0, 0.5, 0.7, 1.0, 1.5, 1.7 and 2. The C/O ratios included in the grid are: C/O (relative to Solar) = 0.25, 0.5, 1.0, 1.5, 2, and 2.5. In this way, Solar values are [M/H]=0 and C/O=1. In order to change the C/O ratio for a given atmospheric metallicity, both the elemental abundances ratios – C/H and O/H are increased/decreased slightly while maintaining a constant (C+O)/H. The version of `PICASO 3.0`, described in this work, does not allow to change other elemental ratios (e.g. S/H or N/H). Future releases will include this flexibility.

Figure 3.2 shows the pre-computed volume mixing ratios of four major atmospheric gases – CH_4, CO, H_2O, and NH_3 for a solar mixture of chemical elements.

Converged brown dwarf $T(P)$ profiles with log(g)=5 and multiple $T_{\rm eff}$ values between 300 K and 2300 K are also overplotted in the pressure-temperature space to depict parts of the parameter space relevant for objects with different $T_{\rm eff}$. There are a few important features that strongly influence the climates of sub-stellar atmospheres that are worth noting. First, the sharp drop in H_2O vapor abundance at T200 K which can be seen in Figure 3.2 lower left panel. This drop in H_2O vapor abundance is caused by the condensation of H_2O into cloud particles. A similar condensation effect can also be seen in the case of NH_3 at $T \leq$100 K. Condensation induced changes in the gaseous abundances are included in the pre-computed grid of gaseous abundances. Second, the most abundant carbon bearing gas in the atmosphere also changes from CO to CH_4 between temperatures of $\sim$ 1000 and 1200 K. Figure 3.2 top right panel shows that CO is the major carbon bearing gas above $\sim$ 1200 K but at temperatures cooler than 1200 K, CO abundance decreases rapidly and CH_4 abundance rises. This change can be understood by the net chemical reaction responsible for inter-conversion between CO and CH_4 under chemical equilibrium,

$$CH_4 + H_2O \leftrightarrow CO + 3H_2 \tag{3.21}$$

This reaction is favored in the forward direction for higher temperatures than $\sim$ 1200 K and as result CO is more dominant for such temperatures. The reverse reaction dominates for temperatures lower than $\sim$ 1200 K and CH_4 becomes the dominant C-bearing gas there. Many other similar interesting trends has been explored in the literature for several gases (e.g. Lodders 2002; Visscher et al. 2006, 2010b; Moses et al.

2005, 2011, 2013a). These trends can be directly explored from the available chemical grid within the model but we move on to another challenge of using a pre-computed chemistry grid – limited number of grid points.

Due to the finite number of grid points (1460 points), chemical abundances cannot be calculated exactly at any pressure–temperature point of interest. Therefore, each time the chemistry routine `premix_atmosphere` is called, the climate model uses an interpolation scheme to compute abundances at each pressure-temperature layer point. This interpolation is performed by the module `chem_interp`. The 2D interpolation scheme used relies on finding the four surrounding grid points namely $T_{\rm low}(P_{\rm low})$, $T_{\rm low}(P_{\rm high})$, $T_{\rm high}(P_{\rm low})$, and $T_{\rm high}(P_{\rm high})$. Then the abundances in these surrounding points represented by $\xi^i_{low,low}$, $\xi^i_{low,high}$, $\xi^i_{high,low}$, and $\xi^i_{high,high}$ are used to interpolate the abundance of each species in the $T(P)$ point. This interpolation is done using,

$$\begin{aligned}\ln \xi^i(T,P) = (1-t_{\rm int})(1-p_{\rm int})\ln \xi^i_{low,low} + \\ t_{\rm int}(1-p_{\rm int})\ln \xi^i_{high,low} + t_{\rm int}p_{\rm int}\ln \xi^i_{high,high} + \\ (1-t_{\rm int})p_{\rm int}\ln \xi^i_{low,high}\end{aligned} \tag{3.22}$$

where $t_{\rm int}$ and $p_{\rm int}$ are given by,

$$t_{\rm int} = \frac{1/T - 1/T_{low}}{1/T_{high} - 1/T_{low}} \tag{3.23}$$

$$p_{\rm int} = \frac{lnP - lnP_{low}}{lnP_{high} - lnP_{low}} \tag{3.24}$$

This interpolation can be found in the `chem_interp` module. In the case where the $T(P)$ moves outside the edges of this chemistry grid, a linear interpolation scheme is instead adopted within the range 50-5200 K. This allows some flexibility in the iteration scheme. However, beyond these values, the model is not valid. Note, choices in interpolation routines cause discrepancies in resulting abundances. For example, only using two nearest-neighbors causes instabilities in chemical profiles. The interpolation chosen here was tested in multiple chemical regimes to ensure stability. After computing the atmospheric chemistry, the next step in Figure 3.1 is the computation of the atmospheric opacities, which we describe next.

3.1.1.4 Pre-mixed Opacities

The chemical structure of the atmosphere dictates the optical depth ($\tau(\lambda)$) of each atmospheric layer which is necessary for solving the radiative transfer equations described in §3.1.1.2. This calculation of atmospheric optical depths occurs in the "Opacity" block of the model flow chart in Figure 3.1. As previously stated, we use the correlated-k approach to handle the molecular opacities in this model. An alternative approach is the line–by–line method which is more precise but comparatively speaking, more computationally expensive than the correlated-k approach at low resolution, and over large wavelength ranges. For completeness, we describe the general methodology of our approach here. However, the data were originally computed by Lupu et al. (2021a), available on Zenodo, and detailed in Marley et al. (2021). We include a table of the main reference data used to compute the pre-mixed opacities in Table 3.3.

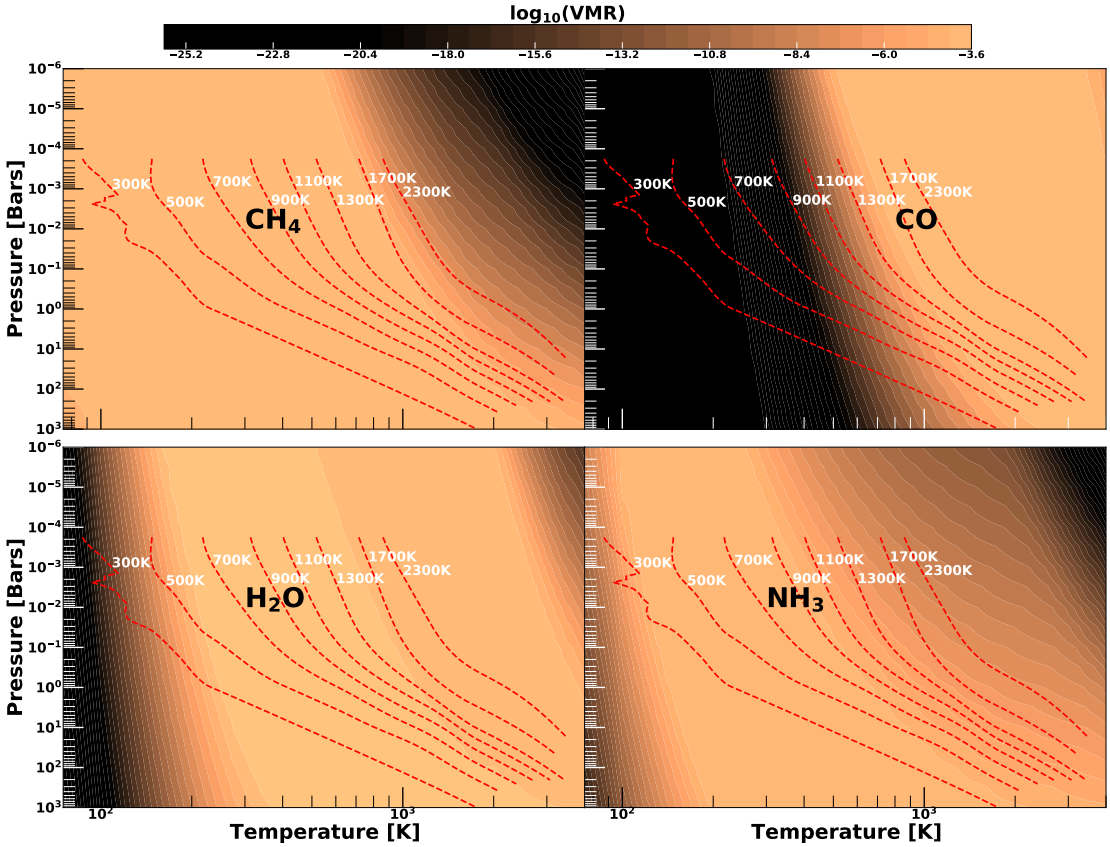

Figure 3.2: **Top left panel** shows the abundance map of CH_4 in the pressure-temperature chemistry grid used in the model with equilibrium chemistry described in the paper. Dashed red lines marked on the abundance map depict different converged $T(P)$ profiles of brown dwarfs from Marley et al. (2021) with $T_{\rm eff}$ between 300 K and 2300 K and log(g)=5. This grid is used for interpolation of chemical abundances during iteration of the atmospheric state in the code. The same for CO, H_2O, and NH_3 is shown in the **top right**, **bottom left** and **bottom right** panel. The abundances shown here are calculated for solar metallicity and C/O ratio.

C_2H_2	Rothman et al. (2013)
C_2H_4	Rothman et al. (2013)
C_2H_6	Rothman et al. (2013)
CH_4	Yurchenko et al. (2013); Yurchenko & Tennyson (2014)
CO	Rothman et al. (2010); Gordon et al. (2017); Li et al. (2015)
CO_2	Huang et al. (2014)
CrH	Burrows et al. (2002)
Fe	Ryabchikova et al. (2015); O'Brian et al. (1991); Fuhr et al. (1988); Bard et al. (1991); Bard & Kock (1994)
FeH	Dulick et al. (2003); Hargreaves et al. (2010)
H_2	Gordon et al. (2017)
H_3^+	Mizus et al. (2017)
H_2–H_2	Saumon et al. (2012) with added overtone from Lenzuni et al. (1991) Table 8
H_2–He	Saumon et al. (2012)
H_2–N_2	Saumon et al. (2012)
H_2–CH_4	Saumon et al. (2012)
H_2^-	Bell (1980)
H^- bf	John (1988)
H^- ff	Bell & Berrington (1987)
H_2O	Polyansky et al. (2018a)
H_2S	Azzam et al. (2016)
HCN	Harris et al. (2006); Barber et al. (2014a); Gordon et al. (2022)
LiCl	Bittner & Bernath (2018)
LiF	Bittner & Bernath (2018)
LiH	Coppola et al. (2011)
MgH	Yadin et al. (2012); GharibNezhad et al. (2013) assembled in Gharib-Nezhad et al. (2021a)
N_2	Rothman et al. (2013)
NH_3	Yurchenko et al. (2011); Wilzewski et al. (2016)
OCS	Gordon et al. (2017)
PH_3	Sousa-Silva et al. (2014)
SiO	Barton et al. (2013)
TiO	McKemmish et al. (2019) assembled in Gharib-Nezhad et al. (2021a)
VO	McKemmish et al. (2016) assembled in Gharib-Nezhad et al. (2021a)
Li,Na,K	Ryabchikova et al. (2015); Allard et al. (2007a,b, 2016, 2019)
Rb,Cs	

Table 3.3: Data used to compute correlated-K opacities. Correlated-K opacities are available at Lupu et al. (2021a) and detailed in Marley et al. (2021).

In the correlated-k approach, the relevant wavelength range for the radiative transfer is first divided to 196 wavelength bins. These carefully chosen wavelength bins are shown in Figure 3.3 and chosen to reflect the approximate spectral energy distributions of planetary atmospheres. The molecular opacity κ in any one of these wavelength bins has numerous individual molecular lines, as shown in Figure 3.4 left panel. The cumulative distribution function (CDF) of the opacity can be defined as $G(\kappa_0) = N(\kappa \leq \kappa_0)$ where N denotes the total number of instances when the condition $\kappa \leq \kappa_0$ is satisfied within the wavelength bin. The CDF $G(\kappa)$ of the opacity within each wavelength bin is computed. This function, $G(\kappa)$, is then inverted to obtain the "k-distribution". An example k-distribution for the the opacity window shown in the left panel in Figure 3.4, is shown in Figure 3.4 right panel. After computing a k-distribution for each of the 196 wavelength bins, the 8 Gauss points (g_i) shown in Table 3.2 are used to represent each distribution. Generally, the slope of k-distributions are shallow and slowly changing at lower Gauss point values (G) between 0 and 0.9. Then, the slope steepens rapidly between G= 0.9–1, as can be seen in Figure 3.4. To capture the complex shape of the k-distribution with just 8 Gauss points, a double-Gauss method is used for the integration. The first set of four Gauss points are shown in Figure 3.4 right panel with black points. These four Gauss points sparsely sample most of the k-distribution between G =0–0.95 whereas the last four Gauss points, shown with red points in Figure 3.4, sample the small, but rapidly changing, part of the k-distribution between G =0.95–1. The first and second set Gauss points and weights for this double-Gauss point method can be generated from sample points of the generally used Gauss-Legendre quadrature

(Abramowitz & Stegun 1970) using,

$$\begin{aligned} g_{i,1} &= f(g_i^{'} + 1)/2 \\ w_{i,1} &= f w_i^{'}/2 \\ g_{i,2} &= f + (1-f)(g_i^{'} + 1)/2 \\ w_{i,2} &= (1-f) w_i^{'}/2 \end{aligned} \tag{3.25}$$

where $g_{i,1}$ and $w_{i,1}$ represent the first set of our Gauss points (shown with black points in Figure 3.4) and $g_{i,2}$ and $w_{i,2}$ represents the second set (shown with red points in Figure 3.4), $g_i^{'}$ and $w_i^{'}$ are the sampling points for Gauss-Legendre quadrature of some order (4 in our case) defined within the interval [-1,1], and f is the adjustable parameter which sets the division in the values of G which will be sampled by the first and second set of Gauss points. For example, if $f = 0.8$ then $g_{i,1}$ will sample values between 0 and 0.8 while the rest will be sampled by $g_{i,2}$. For our purpose, this f is set at 0.95 which is a reasonable choice based on the typical shape of k-distributions as shown in Figure 3.4.

This double-Gauss method for calculating correlated k-coefficients has a large impact on the time and computational efficiency of the code as it reduces the number of Gauss points required for radiative transfer calculations but still maintains sufficient accuracy required for the model. It has been shown that the radiative transfer with double-Gauss method with 8 Gauss points is as accurate as a normal set of 20 Gauss points (Michael Line, priv. comm. as detailed in Marley et al. 2021). The choice of the wavelength-bins for the correlated-k opacities are also crucial for the model and are described next.

The 196 wavelength bins used span 0.2 μm – 227 μm to capture the general spectral energy distribution of planetary atmospheres. However, these wavelength bins are not all of equal wavelength width. These wavelength bins are shown in Figure 3.3 where three blackbody curves corresponding to temperatures of 300 K, 1000 K and 2000 K are also shown for comparison. The bins are narrow between 0.5-10 μm to capture the large number of molecular rovibrational bands in this range. At the tail ends of the blackbody distributions, larger bins help boost computational speed and maintain sufficient precision in radiative transfer calculations required for the application cases of this model.

As our model uses a pre-computed chemistry grid during iterations on the $T(P)$ profile, the k-coefficients are also pre-computed on the same pressure–temperature–metallicity–C/O ratio grid. For intermediately $T-P$ values, the molecular opacity is interpolated using the same formalism as has been described for the gas abundances in §3.1.1.3. Figure 3.5 shows heat maps of pre-computed Planck function and abundance weighted molecular cross-sections in the same pressure-temperature grid as Figure 3.2. For each $P-T$ point in the grid, the abundance weighted molecular cross-sections are integrated over all wavelengths using the Planck function (corresponding to the temperature T) as the integrating kernel (see Equation 2 in Freedman et al. (2014b)). Each panel corresponds to cross-sections at different Gauss points which we use in our models. Planck mean cross sections at only the first four Gauss points are shown here in the four panels. Dashed black lines marked on the cross-section maps depict different converged $T(P)$ profiles of brown dwarfs from (Marley et al. 2021) with $T_{\rm eff}$ between 300

K and 2300 K and log(g)=5. As the order of the Gauss points increases in Figure 3.5, the cross-sections become higher as higher order Gauss points trace higher opacity parts of the k-distribution. Achieving atmospheric convergence in regions of the $P-T$ space where the cross-section change rapidly with small changes in temperature or pressure can be difficult. Such an "opacity cliff" can be seen at T values between$\sim$ 900-1700 K in Figure 3.5. This cliff appears in the Planck mean cross-sections due to the overlap of the peak of the Planck function at 900-1700 K with large H_2O opacity bands between 1.5-3 μm. These "opacity cliffs" were also seen in Freedman et al. (2008, 2014b) with Rosseland-mean opacities. We discuss the effect of these cliffs on model convergence in more detail in §3.3.3.

In addition to molecular opacities, collision induced absorption (CIA) of H_2-H_2, H_2-H, H_2-He, H_2-N_2, H_2-CH_4, and continuum opacities such as H-bf, and H-ff are also accounted for. These are included separately from our correlated-k table. The CIA opacities are pre-calculated between temperatures of 75 K and 7000 K with 1000 wavelength bins and then interpolated to the correct $P-T$ combination with a spline. Note that even though the CIA temperatures are computed up to 7000 K, the temperature valid range of our model is still limited by the 1460 opacity grid.

We note that the pre-computed opacity grid used with this model is known to be incomplete with regards to atomic and ionic opacities, which are particularly important at the high temperature and low pressure parts of the atmosphere (e.g. Hoeijmakers et al. 2018, 2020). This limits, to some extent, the current code's ability to treat the "ultra-hot Jupiters" ($T_{\rm eq}$ $\geq\sim$2200 K). In a future update we will add these opacities to

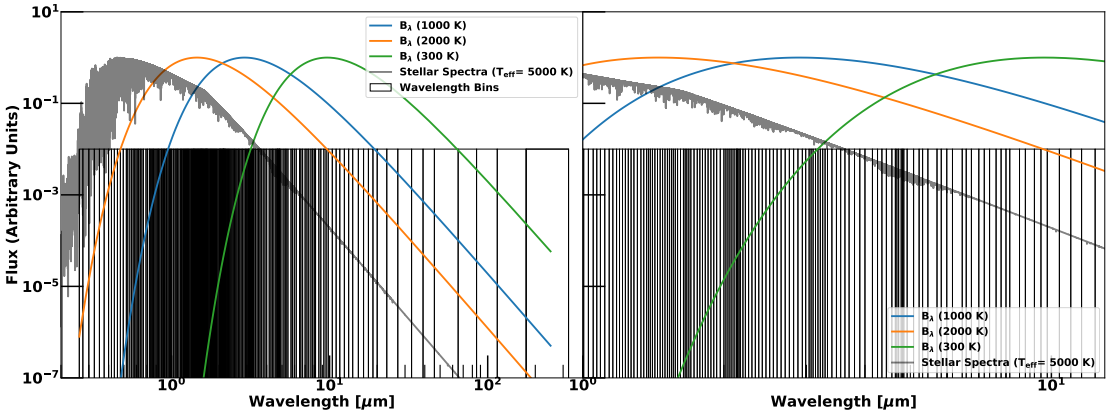

Figure 3.3: **Left panel** shows the correlated-k opacity wavelength bins used in the radiative transfer calculations in our atmospheric model. The blackbody emission curves of temperatures of 1000 K, 2000 K and 300 K are also shown here. **Right panel** shows a zoomed version of the left panel with the wavelengths between 0.8-13 μm. The stellar spectrum from a solar metallicity PHOENIX model for a star with $T_{\rm eff}$= 5000 K is also shown in both the panels.

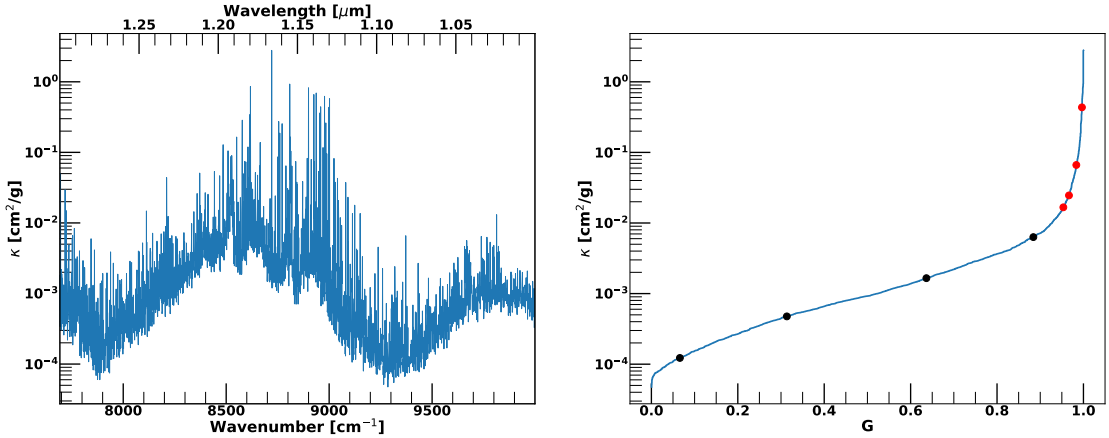

Figure 3.4: **Left panel** shows the high resolution opacity κ between 1 and 1.3 μm of a solar mixture of atmospheric gases at a temperature of 550 K and a pressure of 80 mbar. **Right panel** shows the k-distribution computed for the opacity shown in the left panel with the blue solid line. The black and red points are the Gauss points (from Table 3.2) overplotted on the k-distribution for this opacity window. These Gauss points are applicable for the double Gauss point method. The first set of 4 Gauss points are shown in black while the second set is shown with red points.

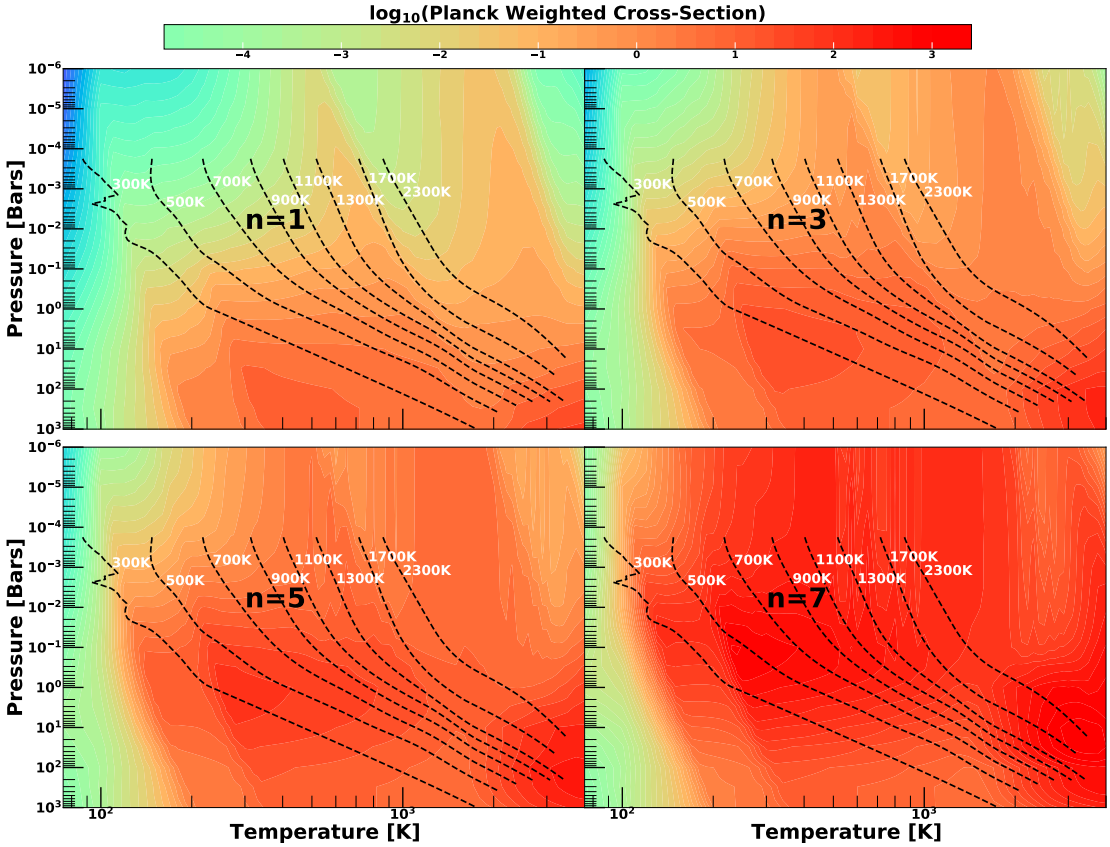

Figure 3.5: **Top left panel** shows the heat map of planck weighted molecular opacity in the pressure-temperature k-coefficient grid used in the model with equilibrium chemistry described in the paper. Dashed black lines marked on the cross-section map depict different converged $T(P)$ profiles of brown dwarfs from Marley et al. (2021) with $T_{\rm eff}$ between 300 K and 2300 K and log(g)=5. This grid is used for interpolation of opacities during iteration of the atmospheric state in the code. The same for the 3rd, 5th, and 7th Gauss points are also shown in the **top right**, **bottom left** and **bottom right** panel.

the correlated-K tables.

3.1.1.5 Disequilibrium Chemistry

A significant addition to this model is the capability to treat vertical mixing induced disequilibrium chemistry self-consistently within the radiative-convective equilibrium framework. This is an optional part of the model, as shown in Figure 3.1. In 1D models, vertical mixing is often parametrized as a diffusive process which is described by the eddy diffusion coefficient, K_{zz} (Allen et al. 1981). The mixing timescales of all relevant gases in each atmospheric layer is given by,

$$t_{\rm mix} = \frac{H^2}{K_{\rm zz}} \tag{3.26}$$

where H is the local scale height of that atmospheric layer. All thermochemical reactions within the atmosphere like $CO \leftrightarrow CH_4$ and $NH_3 \leftrightarrow N_2$ also proceed with a characteristic timescale – $t_{\rm chem}$. Zahnle & Marley (2014) parametrized the $t_{\rm chem}$ of several such gases using 1D chemical kinetics models. The parametrized $t_{\rm chem}$ from Zahnle & Marley (2014) and Visscher et al. (2006) are given by,

$$t_{\mathrm{CO,CH_4,H_2O}} = \frac{3 \times 10^{-6}}{P_{\mathrm{bar}}} exp\left(\frac{42000K}{T}\right)$$
$$t_{\mathrm{NH_3,N_2}} = \frac{10^{-7}}{P_{\mathrm{bar}}} exp\left(\frac{52000K}{T}\right)$$
$$t_{\mathrm{CO_2}} = \frac{10^{-10}}{\sqrt{P_{\mathrm{bar}}}} exp\left(\frac{38000K}{T}\right)$$
$$t_{\mathrm{HCN}} = \frac{1.5 \times 10^{-4}}{P_{\mathrm{bar}} m^{0.7}} exp\left(\frac{36000K}{T}\right)$$
$$t_{\mathrm{PH_3}} = \frac{1.9 \times 10^{12}}{[\mathrm{OH}]} exp\left(\frac{6013.6K}{T}\right)$$

where P_{bar} is the atmospheric pressure in bars, T is the temperature and m is the atmospheric metallicity relative to solar metallicity. t_{chem} is generally short at high pressure-high temperature regions of the atmosphere. As the atmosphere gets colder at lower pressures the t_{chem} rises exponentially and becomes large. The volume mixing ratios of CO, CH_4, NH_3, CO_2, H_2O and HCN are expected to follow equilibrium chemistry at pressures where $t_{\mathrm{mix}} >> t_{\mathrm{chem}}$ which happens in the deeper atmosphere. But as the atmosphere becomes colder with lowering pressure, t_{chem} may exceed t_{mix}. The pressure at which this occurs is called the "quench pressure". At pressures less than the "quench pressure", gases are expected to depart from chemical equilibrium and their mixing ratios become constant.

In this model, we include these disequilibrium chemistry effects for the 8 gas species shown in Eqn. 3.1.1.5: H_2O, CH_4, CO, CO_2, NH_3, N_2, HCN, and PH_3. The quench pressure is determined using the parametrized t_{chem} in Eqn. 3.1.1.5. The abundance then follows the equilibrium chemistry at pressures more than the quench level,

and is held constant at pressures less than the quench level.

The uncertain parameter in the disequilibrium modeling framework is the eddy diffusion parameter, K_{zz} (Phillips et al. 2020; Fortney et al. 2020; Karalidi et al. 2021a). Therefore, this model is flexible in assumptions regarding K_{zz}. Currently, there are two user-options for defining K_{zz} within a model run: 1) a fully user-defined K_{zz} value which is either constant or variable throughout the height of the atmosphere, but which does not change during the iterative climate solution (as was done in Karalidi et al. 2021a; Phillips et al. 2020), and 2) a model-predicted K_{zz}, which is calculated from the $T(P)$ profiles in the convective zones, using mixing length theory (Gierasch & Conrath 1985a), and in the radiative zones, using parametrizations (e.g. Moses et al. 2021). In the second case, along with the $T(P)$ profile, the K_{zz} will also change simultaneously with the iterations in the model. The K_{zz} in the convective zone can be calculated with mixing length theory and is given by (Gierasch & Conrath 1985a),

$$K_{zz} = \frac{H}{3}\left(\frac{L}{H}\right)^{4/3}\left(\frac{RF}{\mu\rho_a c_p}\right)^{1/3} \tag{3.27}$$

where H is the local scale height of the atmosphere, L is the turbulent mixing length, R is the universal gas constant, μ is the mean molecular weight of the atmosphere, ρ_a is the atmospheric density, c_p is the atmospheric specific heat at constant pressure and F is the convective heat flux. The convective heat flux can be calculated by the difference between the net thermal radiative flux and $\sigma {T_{\rm eff}}^4$ within the convective zones of the atmosphere. Therefore, $\sigma {T_{\rm eff}}^4$ is the maximum allowed value of F in this framework if the energy transport within the convective atmosphere is assumed to be

completely convective.

While various parametrizations of K_{zz} in the radiative zones of substellar atmospheres have been discussed in the literature (Wang et al. 2015; Zhang & Showman 2018a; Parmentier et al. 2013a; Tan 2022), we have included the parametrization from Moses et al. (2021) as a starting point. Further parametrizations of K_{zz} can easily be swapped in, in the future. The Moses et al. (2021) radiative zone K_{zz} is given by,

$$K_{zz} = \frac{5 \times 10^8}{\sqrt{P_{\rm bar}}} \left(\frac{H}{620{\rm km}} \right) \left(\frac{T_{\rm eff}}{1450{\rm K}} \right)^4 \tag{3.28}$$

where $P_{\rm bar}$ is the pressure of the radiative level in bars and H is the atmospheric scale height. Both Equation 4.2 and 4.3 can be found in the `get_kzz` function. As the $T(P)$ profile iterates towards the converged solution, the quench levels of various gases change as well. This means that the abundances of quenched species will depart from chemical equilibrium, and the pre-computed k-coefficient tables described in §3.1.1.4 are no longer valid. The methodology to remix the k-coefficients with updated abundances and recompute resulting optical depth calculation during the convergence process, is referred to "on–the–fly" mixing, and is described in the following §3.1.1.6.

3.1.1.6 Mixing Opacities "on–the–fly"

With disequilibrium chemistry, the atmospheric chemistry depends on the quench pressures, which again depend on the $T(P)$ profile of the atmosphere. Therefore, because the chemistry of the atmosphere cannot be pre-determined, the atmospheric opacities also need to be calculated "on–the–fly".

We mix the correlated-k opacities of individual gases using the methodology of Amundsen et al. (2017) called the resort-rebin technique. Currently, in this model we focus on the quenching of CO, CH_4, H_2O, NH_3, CO_2, N_2, HCN and PH_3. However, the major opacity sources among these gases are mainly CO, CH_4, H_2O, and NH_3. Meaning, the contribution of N_2, HCN and PH_3 on the total gas opacity is negligible for the relatively small departures from the chemical equillibrium with $\log(M/H) \leq 2.5$ explored in this analysis. Therefore, we mix the correlated-k opacities of CO, CH_4, H_2O, and NH_3 with the correlated-k opacities of all the other sets of background gases which follow equilibrium chemistry as the volume mixing ratio of these gases evolve due to quenching with the $T(P)$ profile of the atmosphere. Should the motivation to include more gases in the "on–the–fly" methodology present themselves in future observations, they can be included in a future code release.

One of the drawbacks of "on–the–fly mixing" outlined in Amundsen et al. (2017) is the dependence of the accuracy of the technique on the spectral resolution of the correlated-k opacities. This effect has been well explored in Karalidi et al. (2021a). Specifically, it was found that the 196 wavelength bins, traditionally used in the chemical equilibrium version of `EGP` and this new python version, is not sufficiently high to use with the resort-rebin technique. Karalidi et al. (2021a) found that 661 wavelength bins in the correlated-k opacities are required to counteract the inaccuracies in the resort-rebin technique. Therefore, when disequilibrium calculations are requested by the user, `PICASO` automatically switches to 661 wavelength bins.

With the opacities and mixing routines described, the final module, shown in

Figure 3.1 is the computation of the convective zones, which we outline in the following §3.1.1.7.

3.1.1.7 Convective Zones

As the $T(P)$ profile iterates towards radiative equilibrium, parts of the atmosphere will become unstable against convection, and energy transport will be expected to occur via convection instead of radiation. These parts of the atmosphere are forced to follow the local adiabat. Figure 3.6 shows a heat map of the adiabatic lapse-rate, dlnT/dlnP, used in `PICASO`. This grid is pre-computed assuming a solar H–He mixture with He mass fraction of Y=0.28. This includes $H_2 \leftrightarrow 2H$ dissociation and a detailed accounting of the molecular vibrational and rotational levels[3]. The calculations for this grid was done by Didier Saumon as described in Marley et al. (2021). The pre-computed grid has 53 temperature points between 10 K and 3981 K and 26 pressure points between 10^{-2} and 10^{3} bars. The lapse-rate of parts of the profile which become unstable against convection are interpolated from this grid. For every atmospheric layer, the lapse-rate, dlnT/dlnP, is first calculated from the $T(P)$ profile. The grid of adiabatic lapse-rates shown in Figure 3.6 is then used to interpolate the local adiabatic lapse rate for each atmospheric layer. This interpolation is done using 2D interpolation similar to the technique described in §3.1.1.3.

If the ratio between the lapse-rate obtained from the $T(P)$ profile and the interpolated, lapse rate, ∇ is greater than $\sim$1 (numerically set to 0.98) in any of the layers,

[3]Raw grid can be found in GitHub file specific_heat_p_adiabat_grad.json

then these layers are considered convective and are forced to follow the interpolated local adiabatic lapse rate according to the following equation,

$$T^{i+1} = \exp\left(T^i + \nabla ln\left(\frac{P^{i+1}}{P^i}\right)\right) \tag{3.29}$$

where T^i and P^i are the temperature and pressure of the i'th convective layer and T^{i+1} and P^{i+1} are the temperature and pressure of the i+1'th convective layer starting from below the radiative-convective boundary layer. We should note that this convective adjustment is done for one layer at a time followed by a iteration of the entire $T(P)$ as this adjustment for each layer, in principle, would lead to temperature changes in all the other layers. This approach used in this model is different from forcing all the layers which are unstable against convection to be convective at once. The `t_start` module implements this convective adjustment of the $T(P)$ profile. This methodology is used to develop and grow convective zones in the atmosphere with the `find_strat` module during the iterations of the model. Note that this module is designed to always form or grow convective zones and not shrink or remove them. We discuss the important implications of this for the user in §3.3.

3.1.2 Iteration Scheme And Model Convergence

Each required and optional physical component of the model shown in Figure 3.1 has been described separately in §3.1.1. But as our model is iterative in nature, a description of the iterative scheme of the model along with its convergence criteria is a necessary component. We provide a brief outline of the model iterative scheme for both

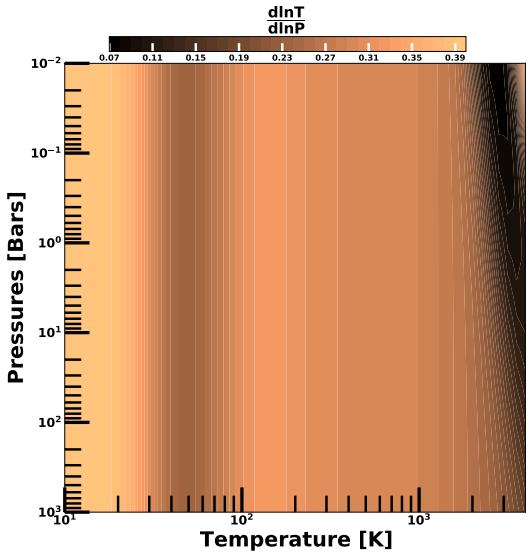

Figure 3.6: A heat map of the adiabatic lapse rate as a function of pressure and temperature is shown here. This grid is used to determine the lapse rate in atmospheric layers unstable against convection.

the chemical equilibrium and disequilibrium runs separately below.

3.1.2.1 Iterative Scheme for Chemical Equilibrium

This model aims to achieve radiative-convective equilibrium using the Newton-Rhapson iterative scheme. As a first step, the chemistry and the correlated-k opacities of the atmosphere for the first given guess $T(P)$ profile are calculated as detailed in §3.1.1.3 and 3.1.1.4. Then, the methodology described in §3.1.1.2 is used to compute the net radiative fluxes in all atmospheric layers. The temperature of each layer is then perturbed by a small arbitrary dT, historically set at 0.01% of the current layer temperature, while keeping the other layer temperatures fixed. The radiative fluxes in all layers are then recomputed after this perturbation. These two sets of radiative fluxes

are used to compute the Jacobian A_{ij} which quantifies the change in radiative flux in layer i due to perturbed temperature in layer j. The Jacobian is given by (e.g. Hubeny 2017),

$$A_{ij} = \frac{F_{i,p}^{j} - F_i}{dT_j} \tag{3.30}$$

where F_i is the net radiative flux in layer i before the perturbation and $F_{i,p}^{j}$ is the perturbed net radiative flux in layer i due to a change in temperature dT_j in layer j. The ultimate temperature correction, δT, needed to ensure radiative equilibrium (in the radiative zones) is then solved using the equation,

$$A\delta T = \sigma {T_{\rm eff}}^4 - F(T(P)) \tag{3.31}$$

where A is the Jacobian and $F(T(P))$ are the net radiative fluxes in each layer with the current atmospheric state. This process continues iteratively until a tolerance of maximum allowed radiative flux difference from $\sigma {T_{\rm eff}}^4$ is reached in all the radiative layers of the atmosphere. This convergence criteria can be expressed as,

$$\left| \frac{F_{\rm net}^{n} - \sigma T_{\rm eff}^4}{\sigma T_{\rm eff}^4} \right| \leq \epsilon \tag{3.32}$$

where ϵ denotes the tolerance parameter, set at 5×10^{-3} in our model. This equation is a numerical version of Equation 3.6. The model is also considered to be converged if the maximum fractional temperature correction among all the radiative layers $|\delta T/T|$, calculated from Equation 3.31, during any iteration is smaller than ϵ. It is important to note that the model satisfies the convergence criteria in Equation 3.32 in the mid-point of each atmospheric layer while the temperature at the edges of each atmospheric layer

(levels) is iterated. For example, if the optical depths at the bottom and top (edges) of the i'th atmospheric layer are τ_i and τ_{i-1}, then the model aims to satisfy Equation 3.32 in this layer for an optical depth of $(\tau_i + \tau_{i-1})/2$. But, the iteration of the temperature profile is done to the temperature at the bottom and top (or edges) of this atmospheric layer. This is important for the stability of the iterative process.

As the iteration progresses, the stability of each atmospheric layer against convective mixing is also checked using the technique described in §3.1.1.7. If layers unstable against convection are found, the temperature of these convectively unstable layers are forced to a H_2-He gas mixture adiabat from the grid shown in Figure 3.6. Once the convergence criteria of Equation 3.32 is met, the model run stops and it produces the outputs outlined by the green boxes in Figure 3.1. Outputs such as the converged $T(P)$ profile, chemical abundances and outgoing radiative fluxes in the 196 wavelength grid are always returned to the user after model converges. These outputs can further be optionally used for calculating various observables such as transmission, emission or reflected light spectra with `PICASO`.

For a deeper understanding of the iteration scheme of this model, three atmospheric iteration steps for a brown dwarf with $T_{\rm eff}$ of 1000 K and log(g)=5 are shown in Figure 3.7 and iterations for an irradiated planet at a distance of 0.1 AU from a sun like star with $T_{\rm int}$ of 300 K and log(g)=3.4 are shown in Figure 3.8. In Figure 3.7 and 3.8, each row corresponds to the atmospheric state in a certain iteration of the model. The first column shows the $T(P)$ profile of the atmosphere in each iterative step of this model with the red solid line whereas `SONORA` $T(P)$ profile for this case is shown as a

black dashed line. The second column shows the lapse-rate of the $T(P)$ profile as a function of pressure in each iteration with the solid blue line and the adiabatic lapse-rate is shown with a black solid line. The third column shows the volume mixing ratio profiles of four gases – H_2O, CH_4, NH_3, and CO as a function of pressure and the fourth column shows the emergent thermal spectrum from the top of the atmosphere. In Figure 3.7, the first row shows a simple initial isothermal guess profile of 500 K and the last row shows the final converged solution. For our initial guess, the bottom four layers of the atmosphere have been assumed to be convective. The initial thermal emission spectrum resembles a blackbody because the atmosphere is isothermal. As the model iterates, the isothermal $T(P)$ profile is perturbed to reach an atmospheric state such that Equation 3.32 is satisfied for all radiative layers of the atmosphere. In the iteration shown in the middle row, the bottom of the atmosphere becomes unstable against convection and therefore in the final solution the lapse-rate in that part of the atmosphere is forced to follow the local adiabatic lapse-rate. As the model iterates towards the converged solution, the $T(P)$ profile becomes more complex and leads to a redistribution of flux in each wavelength bin. This leads to molecular absorption lines becoming more evident in the thermal spectrum with each iteration. The final converged solution matches well with the `SONORA BOBCAT` grid of models (shown as black dashed line). For the irradiated planet convergence shown in Figure 3.8, the initial guess is an isothermal profile with $T = 700$ K and the iterations continue until Equation 3.32 is satisfied.

A second helpful method of visualizing a converged run is to look at the contribution of radiative and convective fluxes as compared to the target flux in brown dwarfs

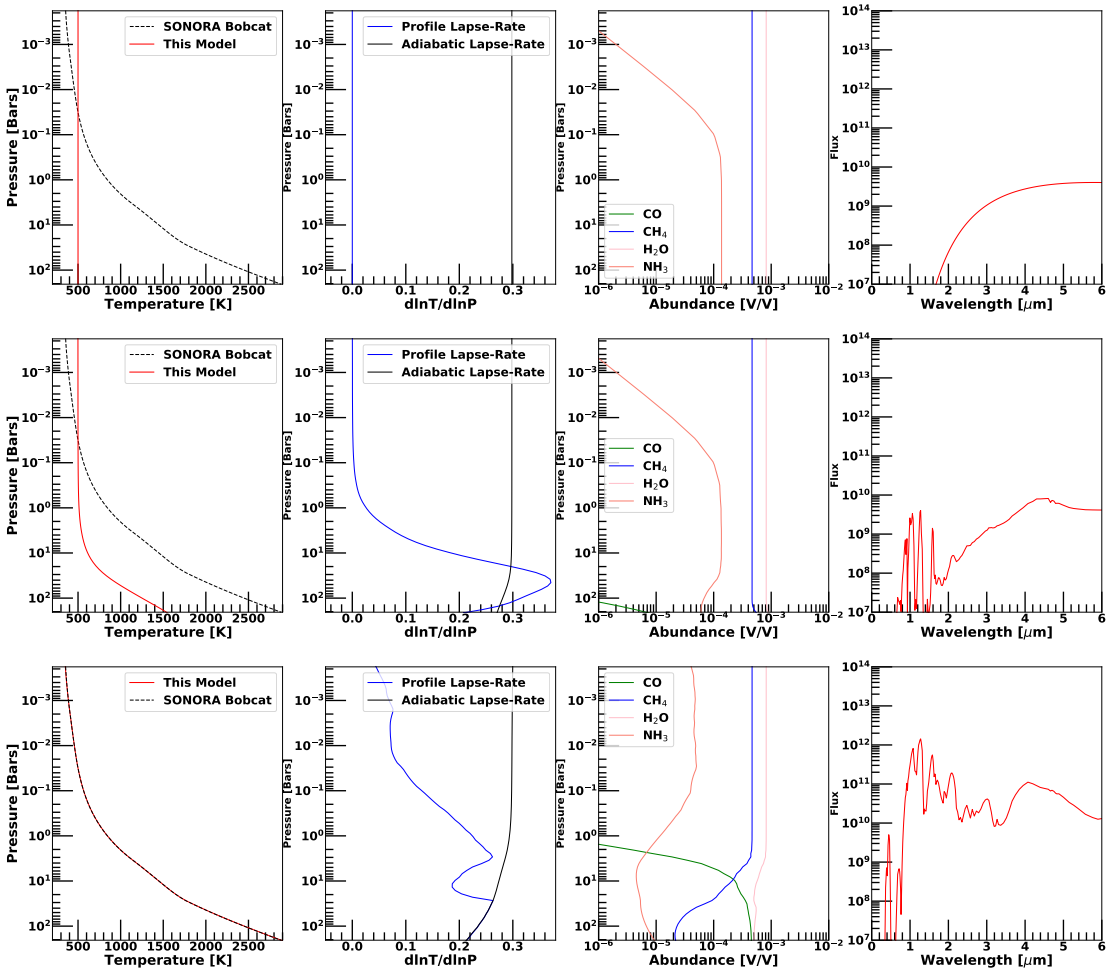

Figure 3.7: Three steps in the iteration towards a converged solution for a brown dwarf with $T_{\rm eff}$ of 1000 K and log(g) of 5 is shown here in each row. The first column shows the iteration of the $T(P)$ profile in red with the `SONORA BOBCAT` model shown in black dashed. The second columns show the lapse-rate from the $T(P)$ profiles in blue and the local adiabatic lapse rate in black. The third column shows the iterations in the volume mixing ratios of various gases. The fourth column shows the thermal spectrum emergent from the atmosphere of the object in each iteration. An animated gif of this figure can be found here

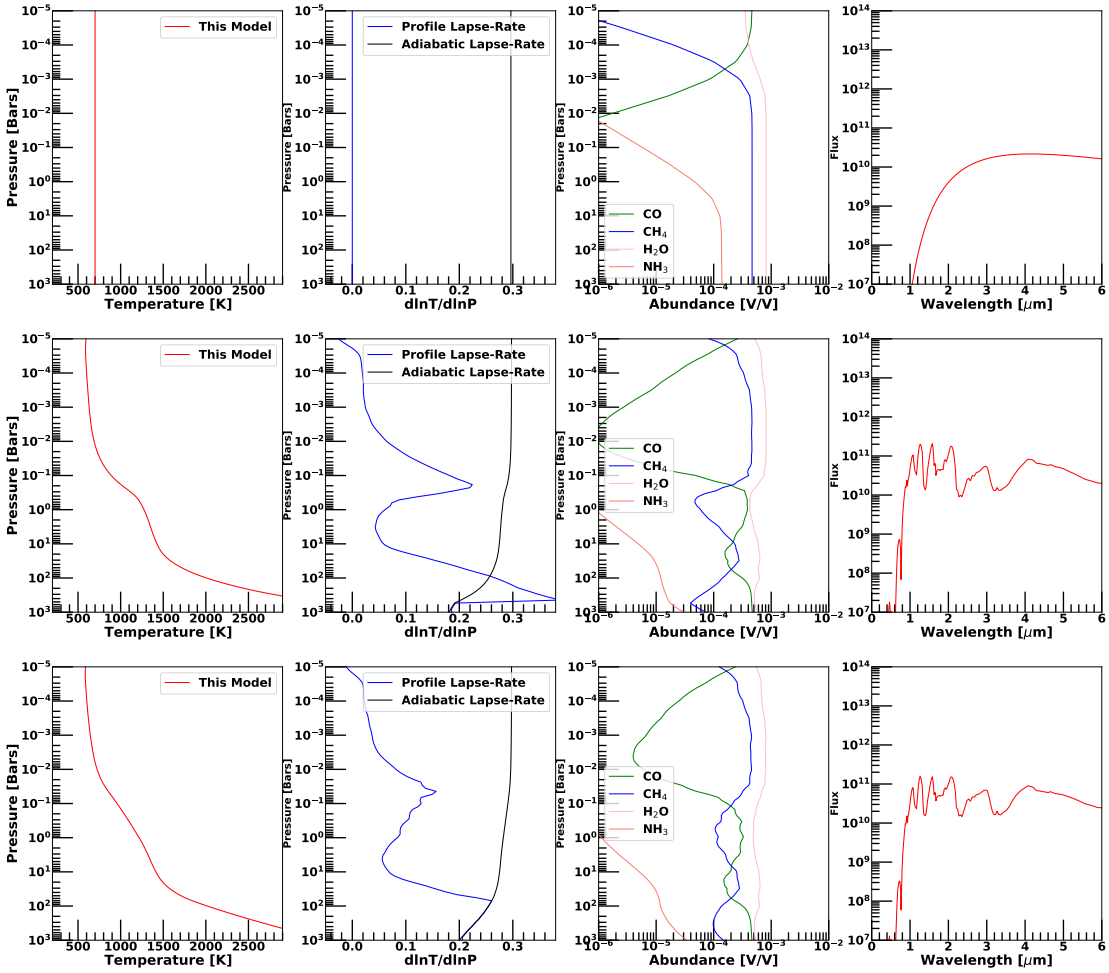

Figure 3.8: Three steps in the iteration towards a converged solution for an exoplanet around a sun like star with $T_{\rm int}$ of 300 K and log(g) of 3.4 is shown here in each row. The left-most column shows the iteration of the $T(P)$ profile in red with the `SONORA BOBCAT` model shown in black. The second left-most columns show the lapse-rate from the $T(P)$ profiles in blue and the local adiabatic lapse rate in black. The third column shows the iterations in the volume mixing ratios of various gases. The right-most column shows the thermal spectrum emergent from the atmosphere of the object in each iteration. An animated gif of this figure can be found here

given by $\sigma T_{\rm eff}{}^4$ or the internal heat flux for planets given by $\sigma T_{\rm int}{}^4$. Figure 3.9 shows these layer–by–layer radiative and convective fluxes for converged models of a representative brown dwarf (left panel), warm Jupiter (middle panel), and hot Jupiter (right panel). The net radiative flux in each layer is shown with the orange shaded region. The shaded blue region depicts the convective flux at each layer. The red dashed line shows the target flux for the brown dwarf – $\sigma T_{\rm eff}{}^4$. This converged brown dwarf model has two convective and radiative zones as can be seen from its $T(P)$ profile shown in black. As a result, the convective flux (blue) peaks at the location of these convective zones. The net radiative flux decays rapidly at the deeper convective zone and convection carries the majority of the energy in these deep convective layers. The proof that this is a converged model and Equation 3.32 is satisfied lies in the fact that the sum of the net radiative and convective fluxes is equal to the target flux at all atmospheric layers. For the planet case where there is an additional energy flux from the host star, we show the additional energy with black hatched shading (2nd and 3rd column of Figure 3.9). This incident flux is downward, compared to the thermal radiative and convective fluxes, which is upward. Therefore, the upper atmosphere needs larger quantities of upward thermal radiative fluxes to balance this downward stellar flux. Ultimately, the goal is to maintain a summed flux of $\sigma T_{\rm int}{}^4$ (red dashed line) at all the atmospheric layers of the planet. Therefore, the upper atmosphere of irradiated planets, with a given $T_{\rm int}$, is pushed toward hotter temperatures when compared to a brown dwarf with a comparable $T_{\rm eff}$.

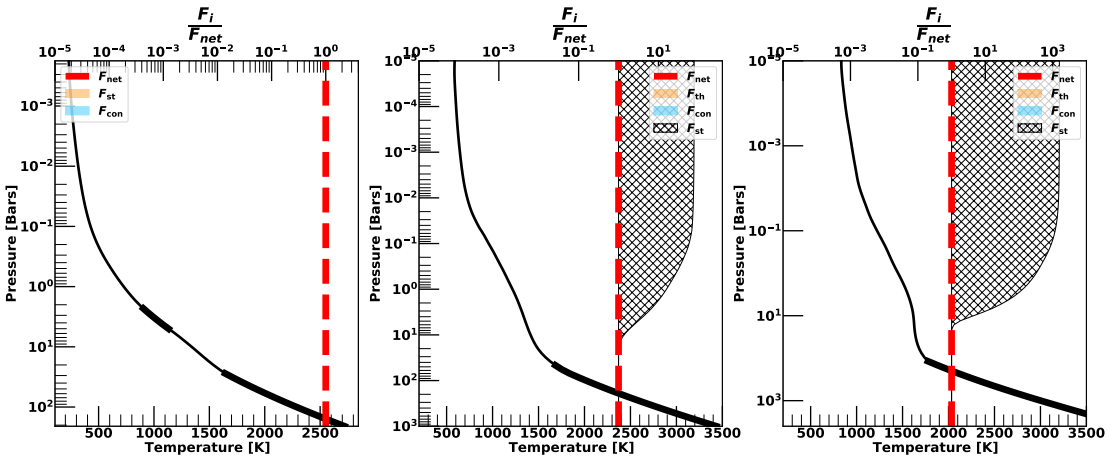

Figure 3.9: Radiative and convective flux contributions compared to total net fluxes are shown for three $T(P)$ profiles in order to visualize the concept of "convergence". From left to right a representative brown dwarf, warm Jupiter, and hot Jupiter profile is shown. In each figure, the shaded blue region depicts the convective flux at each layer. The orange shaded region depicts the net radiative flux in each layer. The red dashed line shows the target flux for the brown dwarf in the left panel. For the brown dwarf (non-irradiated) this target flux is $\sigma {T_{\rm eff}}^4$. The red dashed line in the middle and the right panels shows the internal heat flux of the planets which is $\sigma {T_{\rm int}}^4$. Please note that the scale of the upper and lower X-axis are different in all the three panels.

3.1.2.2 Iteration Scheme for Chemical Disequilibrium

The primary difference in the iterative scheme of the disequilibrium model is that it uses a two-step convergence method. With the user specified input parameters, the code first uses the basic chemical equilibrium model (§3.1.2.1) to converge to a chemical equilibrium atmospheric solution. This atmospheric solution is then used as the initial guess to the disequilibrium chemistry model in the second step of the iterative process. Of particular importance, is the need to recalculate the convective zones when disequilibrium chemistry is turned on. This is important because recent work has shown that there are major differences in the location, extent and number of convective zones between the equilibrium chemistry and disequilibrium chemistry atmospheric solutions (Mukherjee et al. (2022 submitted)). The general procedure is to partially reset the convective zones before moving to disequilibrium solver. First, any upper convective zones are removed. Next, the upper boundary of the deepest convective zone is reset to slightly higher pressures (usually $\sim$5 levels in a 91-level atmosphere from 10^{-4} to 200 bars). This enables the convective zones in the presence of vertical mixing to be re-calculated because we cannot assume there will be minor perturbations from the equilibrium chemistry solutions.

In order to highlight the convergence of a brown dwarf disequilibrium chemistry model, a few atmospheric iterations are shown in Figure 3.10 for a brown dwarf with $T_{\rm eff}$ of 700 K and log(g)=5.25. The figure is similar to Figure 3.7 except here the third column now shows the mixing (black dashed line) and chemical timescales (solid colored

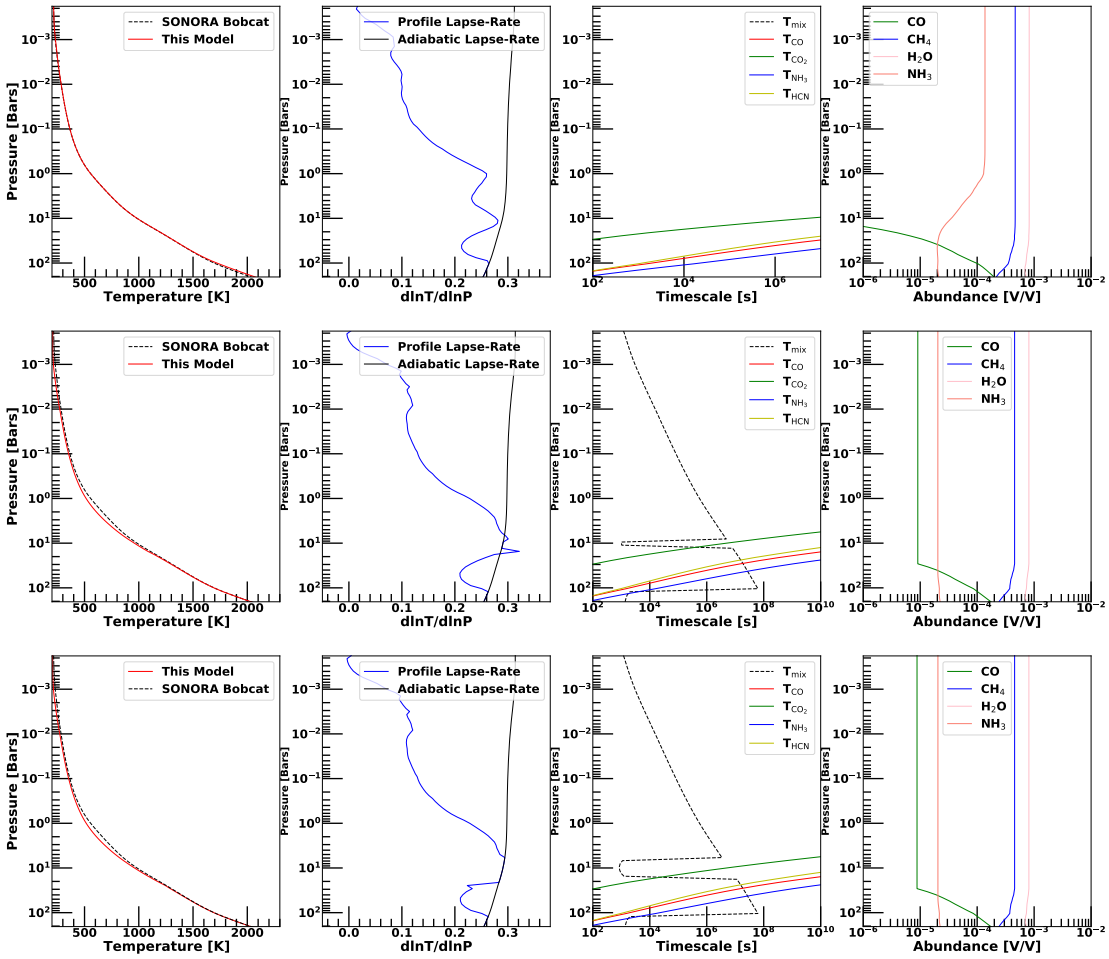

Figure 3.10: Three steps in the iteration towards a converged solution with disequilibrium chemistry for a brown dwarf with $T_{\rm eff}$ of 700 K and log(g) of 5.25 is shown here in each row. The first column shows the iteration of the $T(P)$ profile with the red line and the `SONORA BOBCAT` chemical equilibrium is model shown in black dashed. The second column shows the lapse-rate from the $T(P)$ profiles in blue and the local adiabatic lapse rate in black. The third column shows the chemical timescales of various gases as a function of pressure with solid lines of different colors. The pressure dependant mixing timescale is shown in the third columns with the black dashed line. The fourth column shows the iterations of the volume mixing ratios of various gases. An animated gif of this figure can be found here

lines) as a function of pressure and the fourth column shows the volume mixing ratio profiles of various gases. The first row shows the atmospheric state reached after the first step of the convergence process, where a converged chemical equilibrium solution is achieved. The last row shows the final converged solution with disequilibrium chemistry. The chemical equilibrium solution from the `SONORA` grid is shown with the black dashed line in the first column. As the model iterates, chemical equilibrium $T(P)$ profile is perturbed to reach an atmospheric state where the $T(P)$ profile is visibly colder than the chemical equilibrium solution. This is a result of different atmospheric optical depths as a result of quenching of several gases in the deeper atmosphere. The chemical equilibrium solution has a single deep convective zone for this brown dwarf. However, in the iteration shown in the middle row and last row, a second convective zone also develops when disequilibrium chemistry is treated self-consistently. This shows that chemical disequilibrium also impacts the location and number of convective zones in the atmosphere. As a second convective zone develops in the middle and the third row, a decrease in mixing timescale can also be seen in that pressure range of the convective zone because convective zones are assumed to be much more efficient in mixing and thus have higher K_{zz} and lower $t_{\rm mix}$ than radiative zones. Comparing the fourth column in the first and the last row shows that mixing causes several orders of magnitude change in the abundance of CO in the upper atmosphere when compared to chemical equilibrium solutions. With these examples, we conclude our detailed discussion on the methodology of the model and move on to the model benchmarking analysis.

3.2 Benchmarking Analysis

We have benchmarked this model in four ways in order to ensure all the described methodology is functioning as expected: 1) `PICASO 3.0` chemical equilibrium non-irradiated functionality vs. `SONORA BOBCAT` grid from Marley et al. (2021), 2) `PICASO 3.0` chemical equilibrium non-irradiated functionality vs. `ATMO 2020` code from Phillips et al. (2020), 3) `PICASO 3.0` chemical equilibrium irradiated functionality vs. `ATMO` code from (Goyal et al. 2020), and 4) `PICASO 3.0` chemical disequilibrium non-irradiated functionality vs. `ATMO 2020` code from Phillips et al. (2020).

3.2.1 Benchmarking chemical equilibrium non-irradiated atmospheres

Figure 3.11 shows the comparison between the three chemical equilibrium non-irradiated models. The models described in this paper are shown in red, the `BOBCAT` models are shown with a black dashed line, and the blue dot-dashed line show the models from Phillips et al. (2020). The left columns show a comparison between the $T(P)$ profiles of the three models. The right column shows a comparison between the lapse-rate of the profiles. Included in the benchmarking is four different log(g) = 5 brown dwarf models with $T_{\rm eff}$ values of 600 K, 700 K, 800 K, and 1000 K, which covers significant chemical transitions of carbon species. `PICASO 3.0` and the models from (Marley et al. 2021) match well with $T(P)$ profiles differences smaller than 0.1%. The lapse-rates from this model also match excellently with those from Marley et al. (2021). Given `PIASO`'s heritage in the EGP model used to compute the grid in Marley et al. (2021),

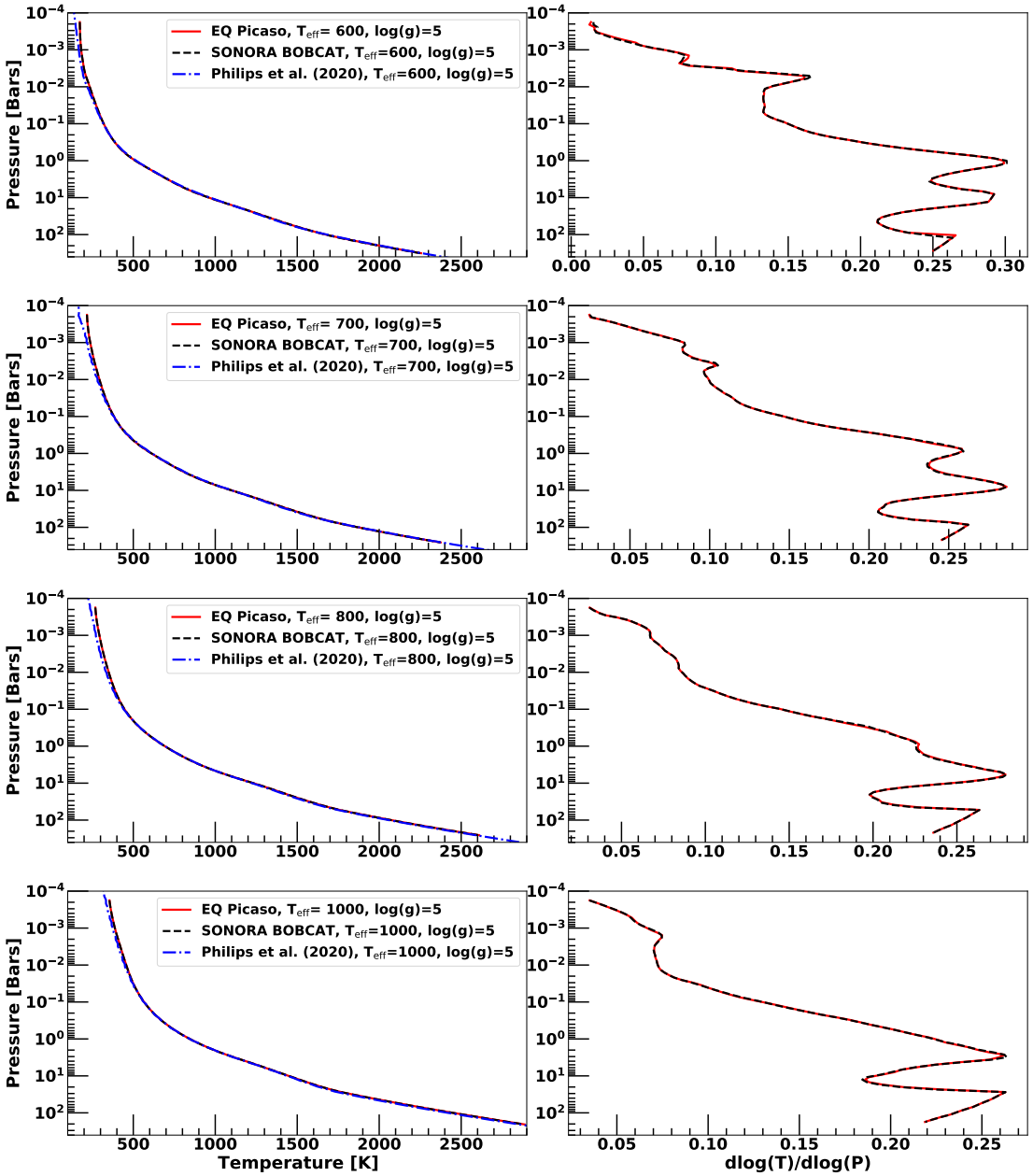

Figure 3.11: Benchmarking tests of the Python based-equilibrium chemistry developed in this work with the published chemical equilibrium models from Marley et al. (2021) and Phillips et al. (2020) are shown here. The benchmarking has been shown in the form of the converged $T(P)$ profiles predicted by each code for four different $T_{\rm eff}$ values at log(g)=5 in the left panels while the pressure-derivatives of the $T(P)$ profiles also have been shown in the right side panels for each case to show that the convective and radiative zones predicted by both the codes match excellently.

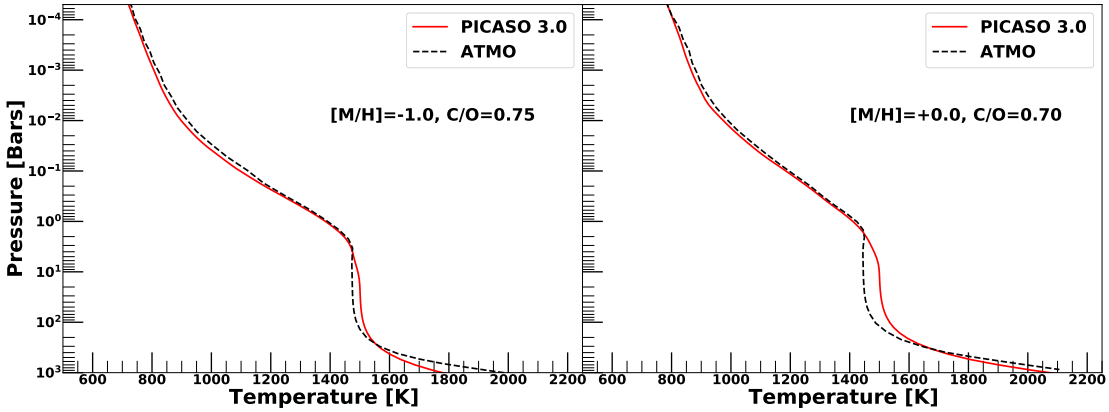

Figure 3.12: $T(P)$ profile computed using `PICASO 3.0` for WASP-25 b is shown with the red solid line compared with the `ATMO` models presented in Goyal et al. (2020) with dashed black lines. The left panel shows the comparison for sub-solar metallicity of 0.1×solar whereas the right panel shows comparisons between solar metallicity models. The same system parameters were used to compute both the models and they agree with each other with less than 3% differences.

this is validation that the update to Python from Fortran did not introduce numerical issues. The disagreement between `PICASO 3.0` and the chemical equilibrium models from the `ATMO 2020` grid are typically smaller than 1% in the deeper atmosphere below 10 mbars. At pressures less than 10 mbars, the differences between the two models are between 1% to 5%. These differences are considered minor given the independent code setup, opacity calculations, and chemistry routines. For example, models presented in Phillips et al. (2020) use the "on–the–fly" opacity mixing method described in §3.1.1.6 even when modeling atmospheres with chemical equilibrium whereas `PICASO 3.0` uses interpolations of pre-mixed opacities for iterations of chemical equilibrium models. Differences such as these along with differences in opacity line lists used by the two models could account for the 1% to 5% differences in $T(P)$ profiles in the upper atmosphere.

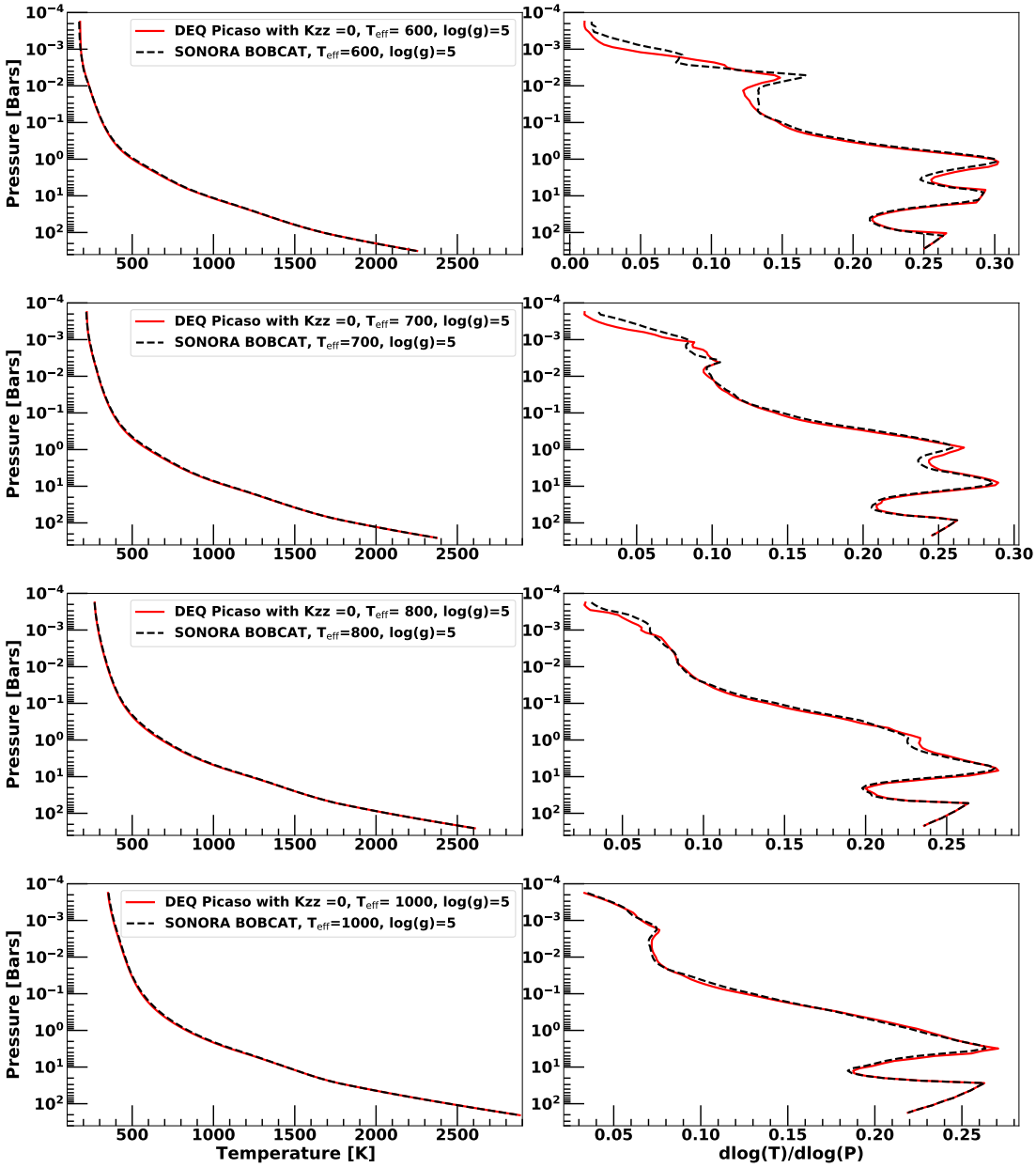

Figure 3.13: Benchmarking tests of the Python based-Disequilibrium code used in this work by assuming K_{zz}= 0 with the published chemical equilibrium models from Marley et al. (2021) are shown here. The benchmarking has been shown in the form of the converged $T(P)$ profiles predicted by each code for four different $T_{\rm eff}$ values at log(g)=5 in the left panels while the pressure-derivatives of the $T(P)$ profiles also have been shown in the right side panels for each case to show that the convective and radiative zones predicted by both the codes match excellently.

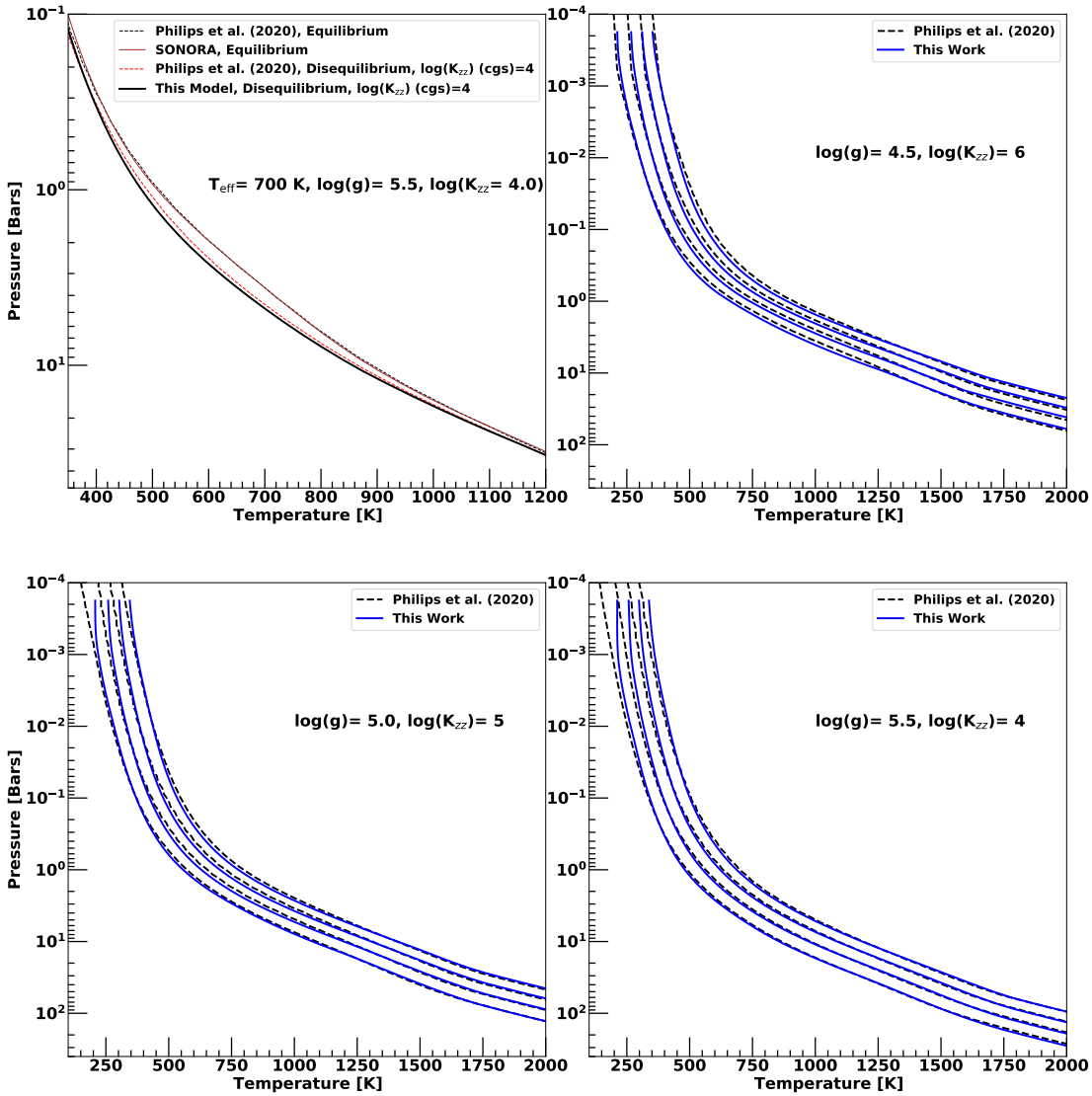

Figure 3.14: Benchmarking tests of the Python based-Disequilibrium code used in this work by assuming non-zero K_{zz} values with the published chemical disequilibrium models from Phillips et al. (2020) are shown here. The benchmarking has been shown in the form of the converged $T(P)$ profiles predicted by each code for four different $T_{\rm eff}$ values and three different log(g) values in the three panels. The $T(P)$ profiles match well between the two independent models with different sets of opacities and totally different code methodologies.

3.2.2 Benchmarking chemical equilibrium irradiated atmospheres

We also benchmark the equilibrium chemistry version of the code by comparing models of irradiated exoplanets calculated using `PICASO 3.0` with the published `ATMO` models presented in Goyal et al. (2020). We use the RCTE models for WASP-25 b (Enoch et al. 2011; Southworth et al. 2014) presented in (Goyal et al. 2020) to perform this benchmarking. WASP-25 b is a hot Saturn with an estimated equilibrium Temperature of $\sim$ 1210 K (assuming 0 albedo) (Enoch et al. 2011; Southworth et al. 2014). We use the same system parameters for WASP-25 b as are used in the models presented in Goyal et al. (2020) and detailed in the Appendix section of their article. Figure 3.12 shows the comparison between the two models at sub-solar and solar metallicities with a super-solar C/O ratio. The models generally agree for both the metallicities. For the sub-solar metallicity models, the agreement is better than 1% across all the pressures. For the solar metallicity models, the maximum disagreement between the models is $\sim$ 3%. These minor differences were also found between the `PICASO 3.0` and `ATMO 2020` models for brown dwarfs. As described above, these minor differences can be attributed to different opacities and numerical methodologies used.

3.2.3 Benchmarking non-irradiated atmospheres with diseequilibrium chemistry

In order to benchmark the version of the model with disequilibrium chemistry we have done two types of comparisons. First, we set $K_{zz} = 0$ in our disequilibrium chemistry model and compare to the results of our equilibrium chemistry model from the

SONORA grid. Second, we benchmark our disequilibrium chemistry model with results from the ATMO 2020 grid.

In the first test, if K_{zz} is assumed to be zero, $t_{\rm mix}$ becomes infinitely large according to Equation 4.1. Therefore, in principle, none of the gases will be quenched and their volume mixing ratios will follow equilibrium chemistry throughout the atmosphere. Therefore, a disequilibrium chemistry model run with $K_{zz} = 0$ must produce the same result as the equilibrium chemistry models. Of particular importance, this test checks if our "on–the–fly" mixing routines, and double-iterative routine are performing as expected. Figure 3.13 shows the benchmarking between our disequilibrium chemistry model with $K_{zz} = 0$ and the equilibrium chemistry models from the SONORA BOBCAT grid. The left column shows the comparison of the $T(P)$ profiles between the two models and the right column shows the comparison of the lapse-rates between the two models. Each row from the top to bottom shows log(g) = 5.0 brown dwarf models with $T_{\rm eff}$ of 600, 700, 800, and 1000 K. The two models match with differences $\leq 1\%$ level. The small $\leq 1\%$ deviations are due to the slight inaccuracies in the "on–the–fly" mixing technique (Amundsen et al. 2017), which is sensitive to number of wavenumber bins, versus the pre-weighted technique (see §3.1.1.6).

In the second test, we directly benchmark our disequilibrium chemistry model with disequilibrium chemistry models from Phillips et al. (2020). Disequilibrium chemistry models in Phillips et al. (2020) assume a constant-with-pressure K_{zz} for the atmospheres. Therefore, we use a constant K_{zz} in our benchmarking test and show the results in Figure 3.14. For a brown dwarf with $T_{\rm eff}$ of 700 K and log(g) of 5.5, the

top left panel in Figure 3.14 shows: 1) the differences that arise in the $T(P)$ profiles when disequilibrium is turned on for both the models from Phillips et al. (2020) and `PICASO 3.0`, and 2) the differences that arise between Phillips et al. (2020) and `PICASO 3.0`. Both the equilibrium chemistry and disequilibrium chemistry models show excellent matches with among themselves which is an excellent benchmarking demonstration of our methods and codes. Additionally, this also shows the impact of disequilibrium chemistry on the $T(P)$ profiles of this representative brown dwarfs, which results in $\sim$50 K colder $T(P)$ profiles compared to equilibrium chemistry models.

The rest of the panels in Figure 3.14 show comparisons between various disequilibrium chemistry $T(P)$ profiles with different K_{zz} and gravity values produced with our model with the grid of models from Phillips et al. (2020). Our disequilibrium models generally agree well within 5% levels in the deeper atmosphere with models from Phillips et al. (2020). However, the disagreements are higher in the much lower pressure upper atmosphere which was also the case for the equilibrium chemistry model comparisons. The small disagreements between the models are mainly due to two reasons – 1) Phillips et al. (2020) use chemical kinetics models for calculation of quenched abundances whereas we use the "quench-time" approximation (§3.1.1.5) to do so and 2) differences between the accuracy of the "on–the–fly" mixing method used between the two models due to differences in number of wavelength bins used. These disagreements show the uncertainty in state–of–the–art models which perhaps can be explained in future with comparisons with high signal-to-noise data.

3.3 Modeling Recommendations

The code is generally well-behaved across the parameter space of interest for brown dwarfs and exoplanets. However, iterative schemes are sometimes notoriously tricky to converge. Therefore, here we outline recommendations regarding the use of code such that users can get meaningful and accurate results. These recommendations are implemented in the publicly available code tutorials available via the `PICASO` documentation page [4].

3.3.1 Choosing Model Pressure Grid

We recommend using typically 50-90 atmospheric pressure layers, corresponding to 51-91 pressure levels. In general, higher number of pressure layers increases the computational time required for convergence substantially and lower number of layers makes the atmospheric grid too coarse for an accurate calculation. The maximum and minimum values of the pressure grid are also ultimately chosen by the user. While the choice of the minimum pressure can be made somewhat arbitrarily, we recommend that the model not be run at pressures lower than 10^{-6}. This is the lowest pressure for which chemistry and opacities are computed (shown in Figure 3.2 and 3.5). Another uncertainty from the double-Gauss correlated-k approach can arise from running the model at very low pressures ($\leq 10^{-4}$ bars). As the molecular lines become very narrow at such low pressures, most of the opacities resides at very high values of $G(\kappa)$ (e.g. between 0.995-1.0) in the k-distribution. Therefore, these opacities are not taken into

[4] https://natashabatalha.github.io/picaso/tutorials.html released with publication acceptance

account even with the double-Gauss method. This can make the radiative transfer at such low pressures inaccurate.

The maximum pressure of the atmospheric model needs to chosen carefully in the case of giant planet atmospheres and brown dwarfs. If the maximum pressure of the atmospheric model is too low, then the model can become transparent to the deepest atmospheric layer, especially in wavelengths with little gaseous opacities (e.g. optical wavelengths 1μm). This would result in an inaccurate $T(P)$ profile. A good way to check if the profile was run with low maximum pressure is to plot the wavelength dependent brightness temperature of the converged model along with the converged temperature of the deepest atmospheric layer. If the brightness temperature at any wavelength exceeds the brightness temperature associated with the bottom temperature, then the pressure grid is not well-suited for the calculation. However, if the brightness temperature is smaller than this bottom temperature at all wavelength, then the pressure grid is well-suited for the calculation. In the first scenario, the pressure grid needs to be extended to higher pressures. The problem with this approach to choose a pressure-grid is that it can only be done after running the model once. A more practical alternative to this approach is to find a comparable model from the `SONORA BOBCAT` [5] to the temperature, gravity parameter space wanted and use the maximum pressure corresponding to that model. Also, the highest pressure for which chemistry and opacities are computed (shown in Figure 3.2 and 3.5) is 3000 bars. Therefore, runs with pressure grids extending to higher pressures than this will be inaccurate as they would require linear extrapolation of both

[5] Link to published SONORA BOBCAT models

gas abundances and opacities.

When computing disequilibrium chemistry runs, the user must take another aspect into consideration while choosing the maximum pressure of the atmospheric pressure grid: the quench levels of various gases. If the maximum pressure of the atmospheric grid is too low such that gases are expected to quench at deeper parts of the atmosphere than the pressure grid, then the model run will be incorrect. Therefore, users must check the quench levels of various gases after performing a disequilibrium chemistry calculation with the model. If the quench levels of any of the gases are at the last pressure level, then the user needs to increase the maximum pressure of the run to get a correct converged solution.

3.3.2 Choosing the Initial Guess T(P) Profile

Climate models that leverage an iterative scheme require a first guess of the $T(P)$ profile. This guess $T(P)$ profile is then iterated to reach the converged solution. Even though we used isothermal $T(P)$ profiles as our first guess in both Figure 3.7 and 3.8, it is usually preferable to start with an initial guess that is close to the expected solution. Using simple profiles like isothermal profiles can lead to significant increase in run times and in the worst cases also lead to solutions which do not converge. A far better alternative to isothermal profiles, are publicly available model grids like `SONORA BOBCAT` or the Phillips et al. (2020) models. For exoplanets, we recommend using parametrized $T(P)$ profiles from, for example Guillot (2010), as a first guess. Functionalities to browse these profiles directly are already available in `PICASO`, via the

guillot_pt(), and sonora() functions [6].

Another first guess required to run the model is the extent of the deepest convective zone. Specifically, the user needs to specify a guess of the pressure level of the radiative-convective boundary in the atmosphere which the code will then modify using methods described in §3.1.1.7. Even though this guess is modified within the iteration, we recommend always setting the bottom 3-5 levels to be convective first. If the user sets too many layers to be convective, the converged solutions may be inaccurate because the model is only equipped to grow and merge convective zones, not shrink them. Therefore, the best practice is to start with 3-5 bottom convective levels. If the code runs into convergence issues after doing so, we recommended increasing this number slowly to check if it helps converge the solution.

3.3.3 Convergence

In most cloud-free cases, the code will converge. However, there are a few known cases where extra steps are needed to reach a converged solution. For equilibrium chemistry brown dwarf models with $T_{\rm eff}$ between 1500 K–1700 K, an oscillating behaviour is seen in the iterations of the $T(P)$ profile. In these cases, the $T(P)$ profile oscillates between two profiles with a constant temperature offset. This behaviour is not unexpected and is caused by the sharp "cliff" in gaseous opacity at these effective temperatures. This can be seen in the cross-section maps in Figure 3.5. All the four panels in Figure 3.5 show a sharp change in gaseous opacity around the 900 K–1700

[6] also see various tutorials e.g. Download and Query from Sonora Profile Grid, and Accessing the pressure-temperature profile parameterizations

K temperature range. The overlap of this cliff with the converged brown dwarf $T(P)$ profile at $T_{\rm eff}$=1700 K can also be seen in Figure 3.5. As already mentioned in §3.1.1.4, this sharp opacity "cliff" makes the convergence difficult around this temperature range. In order to overcome this, we recommend performing multiple runs for the same object by recycling the unconverged final $T(P)$ profile of each run as an initial guess profile for the next run until a converged solution is reached.

A similar convergence issue also occurs for objects with $T_{\rm eff} < 300$ K. Figure 3.2 bottom left panel shows how H_2O abundance in the vapor phase falls drastically due to H_2O condensation at such low temperatures. This sharp drop in the H_2O abundance causes the $T(P)$ profiles of these cold objects at the low pressure regions to oscillate between multiple possible solutions. This behaviour can be seen in the upper parts of the $T_{\rm eff}$=300 K $T(P)$ profile in Figure 3.5. We recommend two solutions to this problem: 1) either set the minimum pressure of the model pressure grid to no less than 1 mbar, or 2) use a `SONORA` profile as an initial guess and recycle the unconverged profile multiple times ($\sim$ 4 times) to reach a converged state. The first recommendation helps the user exclude the part of the $T(P)$ profile which causes the instability in the convergence. As these objects are cold, the excluded pressure region is extremely cold ($<$ 120 K), which means that there is practically no contribution to the observables (e.g. total emergent flux).

3.4 Calculating Observables

After using the radiative-convective equilibrium model to calculate the atmospheric structure of a brown dwarf or an exoplanet, the user may want to compute various observables. `PICASO` has been updated to include the capability of calculating the 1D and 3D thermal emission spectrum, the 1D transmission spectrum, and the 1D and 3D reflection spectroscopy, and phase curves. With a 1D $T(P)$ profile, users will likely want to produce 1D higher resolution thermal emission spectra, reflection spectra, and/or transmission spectra of the planet or brown dwarf. These calculated observables can be directly compared with observational data.

Figure 3.15 shows an example of this with an exoplanet. The exoplanet has been assumed to be a Jupiter mass and size planet with $T_{\rm int}$=300 K at a distance of 0.1 AU around a Sun like star. The radiative-convective equilibrium model described in this work has been used to calculate the planet-wide average atmospheric structure of this hypothetical planet once with chemical equilibrium and then again with chemical disequilibrium. The top left panel in Figure 3.15 shows the $T(P)$ profile of this planet in each case. It is clear that self-consistent treatment of disequilibrium chemistry also impact the $T(P)$ profile of irradiated planets compared to equilibrium chemistry models. We have then used the 1D radiative transfer routines of `PICASO` to compute the reflection albedo spectrum of this exoplanet. This albedo spectrum has been shown in Figure 3.15 top right panel. The planet is not very reflective after 0.5 μm, after which brightness from Rayleigh scattering tapers off. The transmission spectra of the planet is also

modeled with PICASO and is shown in Figure 3.15 bottom left panel. This panel shows that the presence of disequilibrium chemistry can be clearly detected for a hot Jupiter like this with its transmission spectra between 3-5 μm. The thermal spectra are shown in the bottom right panel and the presence of disequilibrium chemistry in hot Jupiters also can be easily detected with their thermal spectra in the M-band, or in various NIRSpec and/or NIRCam JWST modes. Note that for this illustrative example, we have used the planet-wide average computed $T(P)$ profile for all these viewing geometries. However, a more self-consistent method to compute these viewing geometries would be to compute a day-side averaged profile for use in the zero-phase reflection and thermal spectrum, and a planet-wide average for the transmission spectrum.

PICASO has also been equipped with simple modules to couple the atmospheric models produced from this code with the evolutionary models from Marley et al. (2021) to calculate absolute Vega magnitudes of the modeled object in any filter of choice. The atmospheric model presented in this paper used with these radiative transfer tool are already available in PICASO and can be immensely helpful in modeling or planning observations using models.

3.5 Future Improvements

Currently, our publicly released model has the capability to model non-cloudy brown dwarfs and exoplanets with equilibrium chemistry and disequilibrium chemistry. However, several future improvements of the model are needed to enhance its capability

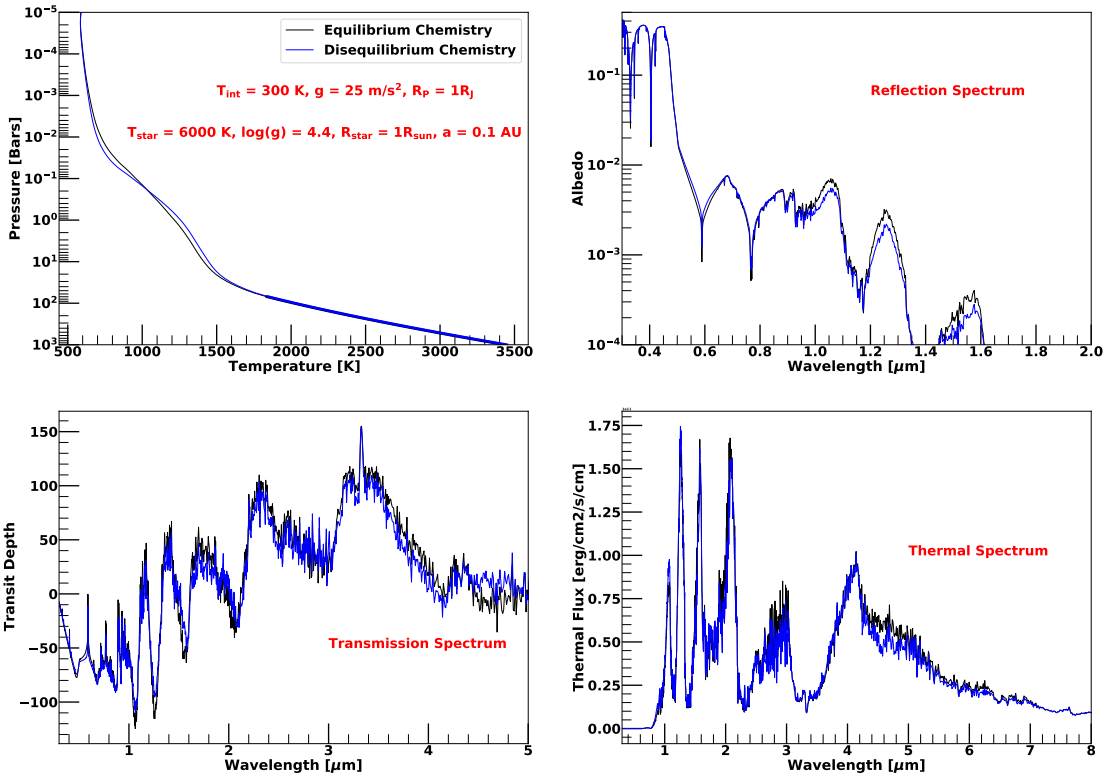

Figure 3.15: Using our atmospheric model to calculate observables. **Top left** panel shows the converged $T(P)$ of an exoplanet calculated using our model with (blue) and without (black) disequilibrium chemistry. **Top right**, **bottom left** and **bottom right** panel shows the albedo spectrum, transmission spectrum, and thermal spectrum at a spectral resolution of R=300 of the exoplanet calculated using radiative transfer tools available in `PICASO`.

to capture a larger parameter space. Here we briefly discuss these needed future improvements. We note that all PICASO development is public, and open to community involvement.

3.5.1 Clouds

Our iterative climate model currently does not include the capability to treat atmospheric clouds self-consistently. The EGP code already includes condensation clouds with the Ackerman & Marley (2001b) model and has been used to model cloudy L-dwarf atmospheres (e.g. Cushing et al. 2008; Stephens et al. 2009). Clouds can become important opacity sources in brown dwarf and exoplanetary atmospheres due to their strong scattering tendencies. This also has large effects on the $T(P)$ profile of these atmospheres (Morley et al. 2014a, 2012). We plan to couple this model with the Python-based cloud model VIRGA (Batalha et al. 2020a). Recently, VIRGA has been updated to include variable sedimentation efficiency (f_{sed}) with height (Rooney et al. 2021). We will couple this updated VIRGA model with our model so that our models can be used to model hotter L-dwarfs which are generally assumed to be cloudy and also much colder Y-dwarfs with H_2O clouds. This improvement will also enable us to apply our model to cloudy exoplanets and brown dwarfs.

3.5.2 1D Chemical Kinetics Model

We use the quench time approximation to model the effects of vertical mixing on the chemical abundance profiles in this model. This approximation is based on

the parametrized mixing timescales from Zahnle & Marley (2014) outlined in §3.1.1.5. However, more robust 1D chemical kinetics models of treating disequilibrium chemistry caused by vertical mixing are now open-sourced like the `VULCAN` model (Tsai et al. 2017, 2021). We plan to couple our Python model with the `VULCAN` chemical kinetics model to increase the flexibility of our model. This will make our disequilibrium chemistry models more robust. Moreover, `VULCAN` also includes the capability to treat stellar irradiation induced photochemistry. This will lead to a significant improvement for applicability of our model to irradiated exoplanets where photochemistry can largely impact atmospheric chemistry especially at lower pressures. This update will allow us to explore the impact of photochemistry on the atmospheric structure of exoplanets. We have already made progress for this coupling but still need to test and benchmark several aspects of the coupled code before this update is publicly available for use.

3.5.3 Time Evolution Version

Recently, Mayorga et al. (2021); Robinson & Marley (2014) enhanced the `EGP` model to `EGP+` by including a time-stepping version of the code which can model the dynamic temporal response of the atmosphere to time-varying physical conditions like stellar irradiation changing with time. This is especially relevant to planets with highly eccentric orbits as the stellar irradiation can change by a large amount within one orbital time-period for these planets. We plan to adapt this improvement within our code in the near future as well. Studying the atmospheres of eccentric exoplanets is a promising research area and a subject of future JWST observing campaigns.

3.6 Conclusions and Summary

We presented a new open-source Python based 1D radiative–convective equilibrium model as part of the `PICASO` package. This code derives its heritage from the `EGP` code developed by Marley & McKay (1999) based upon a Titan atmosphere model developed by McKay et al. (1989). The `EGP` code has been used to model brown dwarf and exoplanetary atmospheres for almost three decades now. The model is applicable to H-dominated atmospheres of both brown dwarfs and irradiated exoplanets. The model includes the capability to do calculations with both equilibrium chemistry and disequilibrium chemistry due to vertical mixing. The model includes options to use K_{zz} values constant with height while performing disequilibrium chemistry runs. We have also included the capability to use self-consistent prescriptions of K_{zz} within the model where the K_{zz} will also iterate along with the $T(P)$ profile and atmospheric chemistry to ultimately reach a converged atmospheric state.

We have benchmarked this model with publicly available models from the `SONORA BOBCAT` grid and also with results from an independent model used by Phillips et al. (2020) to produce the `ATMO 2020` atmospheric grid. For irradiated planets, the `PICASO 3.0` models were benchmarked against the `ATMO` grid presented in Goyal et al. (2020), using the hot Saturn WASP 25-b as a test case. The chemical equilibrium version of the model was benchmarked both with models from the `SONORA` grid, `ATMO 2020`, and the `ATMO` models for WASP 25-b. The chemical disequilibrium models were benchmarked against models from the disequilibrium chemistry atmospheric models from the `ATMO`

2020 grid of models. This benchmarking analysis showed excellent agreement with PICASO.

Our model is open-source and publicly available for the community (we include several in text links to code throughout this manuscript). Additionally, we outlined many recommendations in this work for proper usage of the model. This includes recommendations on choosing the atmospheric pressure grid for a science object, choosing the initial guess $T(P)$ profile for a particular run and also the various parts of the parameter space where the model is known to face convergence issues. We also included ways of resolving these convergence issues.

We also released tutorials to apply this model for various science cases with the code. We plan to actively develop this model further to include clouds, couple it with 1D chemical kinetics codes for better robustness and also include time dependent effects like variable stellar irradiation within our model.

Chapter 4

Probing the Extent of Vertical Mixing in Brown Dwarf Atmospheres with Disequilibrium Chemistry

4.1 Introduction

4.1.1 Molecular abundances and non-equilibrium chemistry

The astronomical community is now ready to observe the atmospheres of a diverse range of exoplanets and brown dwarfs in unprecedented detail with the *James Webb Space Telescope* (JWST) (Gardner et al. 2006; Pontoppidan et al. 2022). These atmospheres are complex systems with a range of physical processes like radiative/convective energy transport, chemical reaction networks, clouds/haze formation, and dynamical processes like vertical mixing. Upcoming high signal–to–noise (SNR) spectra from

JWST for these substellar atmospheres will provide us with a unique opportunity to probe these physical and chemical processes and compare to state–of–the–art theoretical models. Therefore, it is crucial to develop and update these models by including necessary complex processes and assessing how uncertainties in physical and chemical parameters affect the structure, abundances, and spectra of these atmospheres.

One such complex process in substellar atmospheres is atmospheric dynamics. Dynamics is a three-dimensional process. In the case of solar system planets, atmospheric dynamics can be directly studied with spatially and time resolved imaging or spectroscopy. Although, we cannot spatially resolve brown dwarfs and exoplanets, dynamical processes can still be studied by their impact on molecular abundances and condensate clouds, which affect their spectra and lightcurves. Surface inhomogeneities can be probed via rotationally modulate lightcurves (Metchev et al. 2015; Cushing et al. 2016; Karalidi et al. 2015; Vos et al. 2022), often in two dimensions when observed at a single wavelength. Spectra, which probe a range of atmospheric pressures, provide a potential view of dynamics in the additional dimension of atmosphere depth. Processes like convection, the breaking of gravity waves, and convective overshoot can impact both the chemical and cloud structure of these atmospheres by causing net vertical transport of atmospheric gases and particles across many atmospheric scale heights (Freytag et al. 2010; Parmentier et al. 2013a; Bordwell et al. 2018; Tan 2022).

Dynamical processes can also alter the abundances of atmospheric gases in the visible atmosphere by transporting gas molecules through several scale heights, on a timescale faster than chemical reactions are able to locally equilibrate to their new

surroundings. This leads to departures from the chemical equilibrium, often assumed as a starting point in exoplanet and brown dwarf atmosphere models (e.g., Marley et al. 2021). The dynamics induced transport of gases and particles along the radial dimension of these atmospheres is called "vertical mixing". Vertical mixing can lead to disequilibrium chemical abundances in substellar atmospheres for gases like CO, CH_4, H_2O, NH_3, CO_2, PH_3, and HCN (Fortney et al. 2020; Tsai et al. 2017, 2021; Moses et al. 2011). Because most of these gases are major sources of opacities in substellar atmospheres (H_2O, CH_4, CO, etc.), their spectra can be altered significantly.

Vertical mixing also directly affects cloud formation through it's effect on molecules like H_2O in Y-dwarfs and colder exoplanets (Morley et al. 2014b; Ackerman & Marley 2001b; Gao et al. 2020c). Vertical mixing transports condensable vapor from the deeper atmosphere to lower pressures and temperatures, where they condense. Moreover, mixing counteracts gravitational settling, and therefore helps to dictate the size of cloud particles that can remain aloft. As a result, the atmospheric vertical mixing significantly impacts the cloud opacity by controlling the cloud vertical extent and particle size distribution. As both the chemical and cloud structure of these atmospheres impact radiative and convective energy transport, vertical mixing also affects the temperature structure of substellar atmospheres.

There is already decades-deep literature on observations and modeling of disequilibrium chemistry in Jupiter and Saturn (Beer 1975; Larson et al. 1978; Prinn & Barshay 1977; Larson et al. 1977; Fegley & Prinn 1985; Visscher et al. 2010c), and in T-dwarfs and early Y-dwarfs (Fegley & Lodders 1996; Noll et al. 1997; Oppenheimer

et al. 1998; Saumon et al. 2003; Golimowski et al. 2004; Hubeny & Burrows 2007; Geballe et al. 2009; Sorahana & Yamamura 2012; Leggett et al. 2012; Visscher et al. 2010a; Visscher & Moses 2011; Zahnle & Marley 2014; Miles et al. 2020). We briefly summarize the key developments in the field in §4.1.2. But, more recently, Miles et al. (2020) obtained M-band spectra of four late T and early Y-dwarfs and used archival M-band spectra of two T-dwarfs and a Y-dwarf to infer the strength of vertical mixing in their atmospheres as a function of $T_{\rm eff}$. They determined the CO abundance in each of these objects by fitting models to spectra. 1D brown dwarf atmospheric models with equilibrium chemistry were post-processed to include the effect of disequilibrium chemistry due to vertical mixing to interpret the observed CO abundances and infer the vigor of vertical mixing in these atmospheres. This demonstrated that measurements of chemical abundances of various gases along with 1D forward models can be used to constrain vertical mixing in substellar atmospheres. However, disequilibrium chemistry can lead to significant changes in the atmospheric state of these objects compared to equilibrium chemistry calculations due to the feedback of the modified chemical abundances of gases on the atmospheric temperature structure (Hubeny & Burrows 2007; Karalidi et al. 2021a; Phillips et al. 2020).

The Miles et al. (2020) paper and new modeling work points to the possibility of using upcoming high SNR JWST spectra of brown dwarfs to probe their atmospheric structure and atmospheric chemistry in a much more detailed way. The rationale of our study here is to specifically examine how differences in the strength of vertical mixing, and how it is typically parametrized in convective and radiative atmospheric regions,

gives rise to distinct differences in model spectra. Comparison with measured spectra now and in the future can then be used to assess the mixing speed in convective and radiative regions, yielding novel constraints on atmospheric physics.

4.1.2 Modeling Approaches

Mixing in substellar atmospheres is a 3-dimensional process. Both 2D and 3D models have been used to study vertical mixing in hotter brown dwarfs and hot Jupiters (Tan 2022; Tan & Showman 2021; Parmentier et al. 2013a; Freytag et al. 2010; Bordwell et al. 2018). However, a full exploration of the relevant parameter space of brown dwarf mixing properties, is currently not feasible with 3D models. Moreover, these 3D models often include simplified or gray radiative transfer, so in detail the calculated temperature structures yield model spectra that are not yet an adequate match to measured spectra (Tan & Showman 2021; Mukherjee et al. 2021b). Chemical equilibrium is also often assumed in GCMs (e.g., Lee et al. 2021a; Showman et al. 2009b) but some models also treat chemical species within a passive transport framework (e.g., Parmentier et al. 2013a; Komacek et al. 2019; Tan 2022) to explore the effects of atmospheric mixing on chemical structure of substellar atmospheres.

1D self-consistent models, which iterate to a radiative-convective equilibrium (RCE) solution, given specified atmospheric physics and chemistry, include many of the complex physical processes of real atmospheres and can be used to produce high SNR model observables. Given the relatively fast computational times, they are important in exploring wide ranges of parameter space (e.g. Marley et al. 1996; Burrows et al.

1997; Marley & McKay 1999; Burrows et al. 2003; Fortney et al. 2008a; Morley et al. 2014b; Gandhi & Madhusudhan 2017; Malik et al. 2017; Marley et al. 2021). Although such models only include one dimension, the effects of dynamics can still be included. This is typically done by approximating vertical mixing as a diffusive process, and parameterizing this diffusive "speed' with a single vertical eddy diffusion coefficient – K_{zz} (Allen et al. 1981) which has dimensions of $[L]^2/[T]$, where [L] and [T] represent length and time, respectively. However, theoretical and observational constraints of K_{zz}, and its dependence on temperature and pressure, is uncertain by several orders of magnitude today (Fortney et al. 2020; Miles et al. 2020; Phillips et al. 2020).

The vigor of vertical mixing could well have a complex behavior, even within the atmosphere of a single object. Brown dwarf atmospheres have convective and radiative zones. In the convective zones mixing is expected to be comparatively efficient with higher values of K_{zz}, compared to the radiative zones which are stable to convection. Theoretically, K_{zz} has been approximated with mixing length theory in the convective zones of these atmospheres (e.g., Ackerman & Marley 2001a; Smith 1998; Gierasch & Conrath 1985b). However, this approximation is still uncertain due to uncertainties in key parameters in the mixing length theory like the mixing length itself. Theoretical understanding of K_{zz} is even more primitive in the case of radiative zones. Typically, K_{zz} is varied by a factor of a *million* or more, with its effects on the temperature structure and atmospheric abundances inadequately explored. This poor knowledge of K_{zz} leaves large gaps in our understanding of vertical mixing on chemistry, clouds, and temperature structure.

Previously, several authors computed RCE models that treated non-equilibrium chemical abundances self-consistently with the atmospheric temperature structure (e.g. Hubeny & Burrows 2007; Phillips et al. 2020; Karalidi et al. 2021a). However, these models were all computed either within the framework of a constant K_{zz} value in the atmosphere, with an exploration of K_{zz} varied across many orders of magnitude (e.g. Karalidi et al. 2021a; Phillips et al. 2020), or with K_{zz} computed using mixing length theory in the convective zones and constant K_{zz} in the radiative zones (e.g. Hubeny & Burrows 2007). We build on these works, but aim for a more precise assessment of how a changing K_{zz} within a given atmosphere, due to convective- and radiative-zone mixing, alters atmospheric abundances and spectra. The output from 3D GCMs show that K_{zz} can vary by several orders of magnitude with pressure in a substellar atmosphere (Freytag et al. 2010; Parmentier et al. 2013a; Tan 2022), but this has not yet been implemented within a self-consistent RCE model.

Observations from Miles et al. (2020) showed that T-dwarfs with $T_{\rm eff}$ between 400–800 K have much smaller K_{zz} than expected from convective mixing. They also found a factor of 100 *increase* in the inferred K_{zz} in these brown dwarfs when $T_{\rm eff}$ *decreased* below $\sim$ 400 K. Miles et al. (2020) suggested an explanation for this behavior if in the warm objects with $T_{\rm eff}$ between 400-800 K, gases are "quenched" within a radiative part of the atmosphere (lower K_{zz}), but in a convective part of the atmosphere in objects with $T_{\rm eff}<$ 400K. Therefore, already available observations demand models with higher complexity than a constant K_{zz} approach. This is especially needed to prepare these models adequately to interpret the much higher quality data expected

from JWST.

In this work, we enhance the models presented in Karalidi et al. (2021a) by inclusion of temperature- and pressure- dependant K_{zz} profiles within the 1D RCE framework. We use this model to explore the complex interconnections between K_{zz}, the temperature structure, molecular abundances, and spectra in late T and early Y-dwarfs. We use this model and already available ground-based spectroscopic data of six brown dwarfs to address the following questions,

1. How does a self-consistent treatment of vertical mixing affect the $T(P)$ profile?

2. Does a self-consistent treatment of K_{zz} cause changes in the radiative and convective zone locations and depths in brown dwarfs compared to equilibrium chemistry models?

3. In what objects can we expect quenching of gases like CO, CH_4 and NH_3 to occur in radiative zones instead of convective zones?

4. Is photometry and spectroscopy of brown dwarfs between 1-14 μm sensitive to the K_{zz} in the radiative and convective zone?

5. How much can we learn about the atmospheric properties of late T-dwarfs by applying self-consistent disequilibrium chemistry models on already available infrared spectral data?

6. Can JWST be used to accurately infer the vertical mixing strength in radiative zones and convective zones of brown dwarfs?

We briefly discuss our new Python based atmospheric model in §6.2. We present our results in §6.3 followed by discussion of our results in §7.5 and conclude in §4.5

4.2 Modeling Sub-stellar Atmospheres

We have adapted the Fortran based `EGP` sub-stellar atmospheric model to Python. This new Python version of the `EGP` code is open-source and available as a part of the widely used Python exoplanet atmospheric modeling tool `PICASO` (Batalha et al. 2019), as a part of the `PICASO 3.0` (Mukherjee et al. 2023) release. The numerical and functional details of the code along with a series of benchmarks with previously available models are presented in Mukherjee et al. (2023). The `EGP` model has been used by our group for substellar atmospheres for over two decades (Marley et al. 1996; Marley et al. 2012; Fortney et al. 2005, 2007, 2008a; Morley et al. 2014b; Marley et al. 2021; Karalidi et al. 2021a). Recently, Karalidi et al. (2021a) updated the Fortran based `EGP` code with the capability to include constant K_{zz} and its impact on chemistry self-consistently. We have converted this version of the code in Python and have modified it by including the capability to treat pressure-dependent variable K_{zz} in substellar atmospheres. Here we briefly describe the model methodology used in this work and we refer the reader to Mukherjee et al. (2023) for a more detailed discussion of the numerical methodology of our models.

4.2.1 Python Based implementation of EGP with Disequilibrium Chemistry

We divide the 1D model atmosphere in 90 pressure layers (91 layer boundaries or levels) with logarithmically-spaced pressure values. From an initial guess temperature-pressure ($T(P)$) profile, the model iterates on the $T(P)$ profile, atmospheric chemistry, and radiative/convective energy transport using a Newton-Rhapson method, yielding temperature corrections at each pressure level. These iterations continue until it finds the converged atmospheric state in which radiative-convective equilibrium is satisfied throughout the atmosphere. Self-consistent modeling of effects like disequilibrium chemistry due to vertical mixing requires simultaneous calculation of gas abundances and opacities with the iteration on the $T(P)$ profile instead of interpolation on a precomputed grid.

Each chemical reaction in the atmosphere proceeds with a characteristic timescale $t_{\rm chem}$ which is a strong function of temperature, pressure, and the chemical composition of the atmosphere. Zahnle & Marley (2014) used 1D chemical kinetics models to parameterize $t_{\rm chem}$ expression for the major O-, C-, H-, and N-bearing reactions in substellar atmospheres. These reactions often are a part of a large network of chemical reactions with many chemical species but still can be represented by simpler net reactions between a few species of interest. The net chemical reactions between O-, C-, H- and N-bearing gases we consider here are,

$$CH_4 + H_2OCO + 3H_2$$

$$CO + H_2OCO_2 + H_2$$

$$2NH_3N_2 + 3H_2$$

$$CH_4 + NH_3HCN + 3H_2$$

$$2CO + N_2 + 3H_2 2HCN + 2H_2O$$

$$CO + NH_3HCN + H_2O$$

Vertical mixing in the atmosphere also proceeds with a typical timescale, which is associated with the eddy diffusion coefficient K_{zz},

$$t_{\rm mix} = \frac{H^2}{K_{\rm zz}} \tag{4.1}$$

where H is the local scale height of that atmospheric layer. $t_{\rm chem}$ is generally much shorter than $t_{\rm mix}$ in high pressure, high temperature regions of the atmosphere where gas abundances are expected to follow chemical equilibrium. But as the atmosphere gets colder at lower pressures $t_{\rm chem}$ rises exponentially and becomes much longer than $t_{\rm mix}$. The pressure at which the intersection between the two timescales occurs is called the "quench pressure" or "quench level." At all pressure levels lower than the quench pressure (higher up the atmosphere) atmospheric abundances for the relevant chemical compounds take on the abundances at the relevant quench pressure, rather than those of equilibrium chemistry at the local P and T. In the brown dwarf context this behavior

was first predicted by Fegley & Lodders (1996) and observed by Noll et al. (1997).

Within our model, the $T(P)$ profile is used to calculate the K_{zz} as a function of each model layer's pressure. K_{zz} in the convective zone is calculated with mixing length theory (Gierasch & Conrath 1985b),

$$K_{zz} = \frac{H}{3}\left(\frac{L}{H}\right)^{4/3}\left(\frac{RF}{\mu\rho_a c_p}\right)^{1/3} \tag{4.2}$$

where H is the local scale height of the atmosphere, L is the turbulent mixing length, R is the universal gas constant, μ is the mean molecular weight of the atmosphere, ρ_a is the atmospheric density, c_p is the atmospheric specific heat at constant pressure and F is the convective heat flux. The convective heat flux is given by the difference between $\sigma {T_{\rm eff}}^4$ and the radiative flux at each layer within the convective zones of the atmosphere. The maximum convective heat flux would then be $\sigma {T_{\rm eff}}^4$. Here the convective heat flux is calculated self-consistently in each layer. The turbulent mixing length L is set to be equal to the scale height (H) in our models. But in order to explore scenarios where convective mixing is less effective, we also simulate cases where the mixing length is smaller than the atmospheric scale height H by a factor of 10. Note that this turbulent mixing length (L) was only changed in Equation 4.2 and not in Equation 4.1. The mixing length in Equation 4.1 remained the same as the local atmospheric scale height throughout this study. For further background, we refer the reader to previous work (e.g. Visscher & Moses 2011; Smith 1998; Bordwell et al. 2018; Bézard et al. 2002; Visscher et al. 2010c) exploring the relationship between mixing length and the scale height in Equation 4.1.

Over the past several years various parameterizations of K_{zz} in the radiative zones of substellar atmospheres have been discussed in the literature (e.g., Wang et al. 2015; Zhang & Showman 2018a; Parmentier et al. 2013a). As a starting point, we use the parametrization from Moses et al. (2021),

$$K_{zz} = \frac{5 \times 10^8}{\sqrt{P_{bar}}} \left(\frac{H_{1\mathrm{mbar}}}{620\,\mathrm{km}} \right) \left(\frac{T_{\mathrm{eff}}}{1450\,\mathrm{K}} \right)^4 \tag{4.3}$$

where P_{bar} is the pressure in bars and $H_{1\mathrm{mbar}}$ is the atmospheric scale height at 10^{-3} bars. The $5{\times}10^8/\sqrt{P}$ dependence was estimated by Parmentier et al. (2013a) using tracer transport in 3D GCM for hot Jupiter HD209458b. This dependence was found to be valid for this object between 10^{-6}-1 bars. The $\mathrm{P}^{-0.5}$ dependence captures the increase of K_{zz} with lowering pressure in the radiative zone as mixing can be efficient in low pressure ($\mathrm{P} \sim 10^{-4}$ bars) parts of the radiative atmosphere due to mechanisms like gravity wave breaking (Freytag et al. 2010). The factor $H_{1\mathrm{mbar}}T_{\mathrm{eff}}^4$ was also included in the parametrization as this factor shows good correlation with the measured K_{zz} (via photochemical models) of solar system planets (including Jupiter, Saturn, Uranus, Neptune, Earth, and Venus) and exoplanets (Moses et al. 2005; Zhang & Showman 2018a; Moses et al. 2021). But, as the $T(P)$ structure of brown dwarfs can be quite different from irradiated planets, we also explore deviations from this parametrization where this relation is increased or decreased by factors of 100 to explore the relevant parameter space. As the $T(P)$ profile iterates towards the converged solution, the K_{zz} in convective zones, given by Equation 4.2 and the K_{zz} in radiative zones, given by Equation 4.3, evolve as well. The mixing timescale in each atmospheric layer is then

calculated in every iteration from this K_{zz} using Equation 4.1. The quench pressures of each of these chemical species are found by comparing $t_{\rm mix}$ with $t_{\rm chem}$ expressions from Zahnle & Marley (2014). The abundances of CO, CH_4, NH_3, CO_2, H_2O and HCN are allowed to follow equilibrium chemistry at pressures higher than their relevant "quench pressure" and their abundances are quenched above the quench pressure level. But as the $T(P)$ profile iterates to the converged solution, the quench pressure of various gases also change at each step as both the $t_{\rm chem}$ and $t_{\rm mix}$ are dependent on the $T(P)$ profile of the atmosphere. This requires the RCE model to include "on–the–fly" calculations of both chemistry and opacities in order to include disequilibrium chemistry self-consistently in the calculations.

As in Karalidi et al. (2021a) we use the "on–the–fly mixing" method of opacities following the methodology of Amundsen et al. (2017). In this work we focus on the quenching of CO, CH_4, H_2O, NH_3, N_2, HCN and PH_3. Of these, only CO, CH_4, H_2O, and NH_3 are major opacity sources. Therefore, we mix the correlated-k opacities of CO, CH_4, H_2O, and NH_3 with the correlated-k opacities of all the other sets of gases which follow equilibrium chemistry as the volume mixing ratio of these gases evolve due to quenching with the $T(P)$ profile of the atmosphere. As in Karalidi et al. (2021a), given inaccuracies inherent in the flexible Amundsen et al. (2017) resort-rebin approach necessitates the use of a denser grid of 661 wavelength bins, compared to the 196 used for our equilibrium chemistry models (Marley et al. 2021).

We benchmark the code in two ways: 1) by setting K_{zz}= 0 and finding that the on–the–fly mixing method still converges to the equilibrium chemistry solutions from

Marley et al. (2021), and 2) by testing the resulting models against results obtained by Phillips et al. (2020) with non-zero but constant K_{zz} values. The benchmarking results are presented in Mukherjee et al. (2023). The code results matches well with both models. In future work the code will be further enhanced via coupling with 1D chemical kinetics model `VULCAN` (Tsai et al. 2017, 2021) so that it can self-consistently treat both vertical mixing and photochemistry. This Python based code will be open-sourced as a part of the `PICASO 3.0` package. Next, we discuss results obtained by applying this code to model disequilibrium chemistry and characterize mixing strengths in late T and early Y-dwarf atmospheres.

4.3 Results

We performed a detailed four dimensional parameter space exploration of how varied vigor of vertical mixing in brown dwarf atmospheres affects the atmospheric state and spectra. We produced a grid of models by varying four physical parameters – $T_{\rm eff}$, gravity, radiative zone K_{zz}, and convective zone mixing length L. The gravity has been varied across five values 316, 562, 1000, 1780 and 3160 ms^{-2} ($\log(g)$ from 4.5 to 5.5 with an interval of 0.25 dex). The $T_{\rm eff}$ range is 400 K to 1000 K with an interval of 25 K.

To explore the role of radiative zone K_{zz}, in our grids we multiply Equation 4.3 by a multiplicative factor of $\times$ 100, $\times$ 1, and $\times$ 0.01. We refer to these parameter values as "Moses$\times$100", "Moses", and "Moses/100", respectively, after Moses et al. (2021). The mixing length parameter in the convective zones (L in Equation 4.2) has

been varied between the scale height H and $0.1 \times H$ to explore scenarios where mixing in the convective zone is less efficient than the typically assumed mixing length theory in 1D models. Furthermore, for reasons discussed in §7.5, we ran two sets of models – one where PH_3 is quenched given its appropriate $t_{\rm chem}$ and another where PH_3 follows equilibrium chemistry while other molecules are quenched. This parameter space has a total of 5×25×3×2×2=1500 self-consistent radiative-convective equilibrium models. All of these models are cloud free and assume solar metallicity and C/O ratio, following Marley et al. (2021). We haven't included clouds in our models as at the temperature range of our grid (400 – 1000 K), clouds are not expected to be a significant opacity source in the upper atmosphere. We present our key findings from this grid of models below beginning with the feedback of disequilibrium chemistry on $T(P)$ profiles of brown dwarfs.

4.3.1 Effect of Disequilibrium Chemistry on the $T(P)$ profile of brown dwarfs

Disequilibrium chemistry leads to enhanced CO, depleted CH_4, NH_3, and H_2O abundances in T and Y-dwarfs. This leads to major changes in the wavelength-dependent optical depths in the atmosphere. The top four panels of Figure 4.1 shows the $\tau = 1$ pressure levels, for specific gases, for a T-dwarf with $T_{\rm eff}$ = 700 K and log(g) = 5.0 in the presence and absence of quenching due to vertical mixing. These $\tau = 1$ pressure levels are strongly wavelength dependent. Here K_{zz} has been assumed to follow Equation 4.2 in the convective zones and Equation 4.3 in radiative zones. The

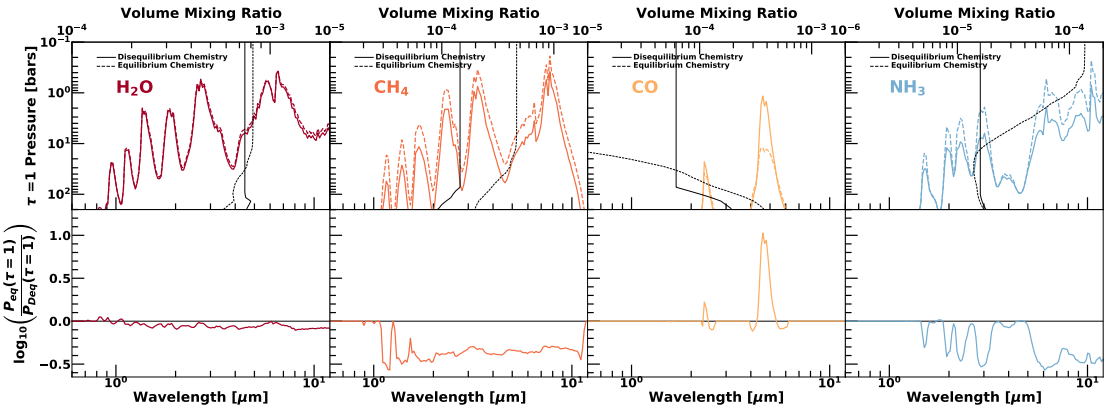

Figure 4.1: **Top panels** show the $\tau = 1$ pressure levels for specific gaseous absorbers in a model T-dwarf with $T_{\rm eff}$= 700 K and log(g) = 5.0 in the presence and absence of quenching due to vertical mixing. $\tau = 1$ pressure levels for H_2O, CH_4, CO, and NH_3 are shown in the first, second, third and fourth columns, respectively. The equilibrium chemistry pressure levels are shown in dashed lines whereas the disequilibrium chemistry pressure levels are shown in solid lines. The volume mixing ratio as a function of pressure of each gas in the presence (solid lines) and absence (dashed lines) of vertical mixing induced quenching are also shown with black lines in the top x-axis of each of the top four panels. **Bottom panels** shows the logarithm of the pressure ratio of these $\tau = 1$ levels with equilibrium chemistry and disequilibrium chemistry for the gaseous absorbers. The zero mark represents no change in these pressure levels. Positive values represents an increase in absorption in the disequilibrium chemistry models compared to equilibrium chemistry models. **Main Point** – Disequilibrium chemistry leads to large opacity changes in the atmosphere.

disequilibrium chemistry pressure levels are shown in solid lines and the corresponding equilibrium chemistry levels are shown as dotted lines. The pressure-dependant volume mixing ratios of these gases under chemical equilibrium and disequilibrium are also shown in the top x-axis in each of the top four panels with dashed and solid black lines, respectively.

The bottom panels in Figure 4.1 depicts the log of the ratio in the $\tau = 1$ pressure level between these two models. Values greater than zero represent shallower depth probed, due to an increase in an absorber of interest, for instance CO in yellow

in the third column, in particular at 4.5-5 μm. There are also significant changes due to depleted NH_3 and CH_4. There is a more modest effect on H_2O. Overall, since major opacity sources H_2O, NH_3, CH_4 are depleted, and they absorb across a broad wavelength range, one sees deeper, to a higher pressure, in a disequilibrium chemistry model.

A manifestation of these effects are shown in Figure 4.2, which shows temperature structure (upper left), CO mixing ratios (upper right), and spectra (bottom) three models at $T_{\rm eff}$ = 500, 700, and 1000 K and log(g) = 5. Solid lines include induced quenching and dashed lines represent equilibrium chemistry. The K_{zz} for these models evolved self-consistently following mixing length theory in the convective zones and followed Equation 4.3 in the radiative zones.

Disequilibrium abundances mainly lead to colder $T(P)$ profiles compared to equilibrium chemistry models as can be seen in Figure 4.2. In the overall optically thinner disequilibrium chemistry atmosphere (see Figure 4.1) one must see down to a higher pressure to obtain a given T. This effect was also seen in Karalidi et al. (2021a) for constant K_{zz} models.

Volume mixing ratio profiles of CO for each of these models are shown in the top right panel of Figure 4.2. As described earlier, disequilibrium chemistry greatly enhances the CO abundances above quench level. However, even deep down, below the quench level, there are important CO abundance differences due to differences in the converged $T(P)$ profile. As equilibrium chemistry models have hotter $T(P)$ profiles, at a given pressures, than disequilibrium chemistry models, they also have higher CO abundances. This drives home the point that a self-consistent treatment of disequilibrium chemistry

(as in §4.2.1) is needed rather than post-processing self-consistent equilibrium chemistry models with quenched abundances. Even if one obtains the correct quench pressures during post-processing equilibrium chemistry models, one would calculate a physically inconsistent and higher abundance of CO at the upper atmospheres than self-consistent disequilibrium chemistry models.

The thermal emission spectra of these models are shown in Figure 4.2 bottom panel. The flux from these objects were normalized by their maximum flux and are plotted from the hottest model ($T_{\rm eff}$=1000 K) at the top to the coldest model ($T_{\rm eff}$=500 K) at the bottom. Large differences in outgoing thermal flux can be seen in the H, K, L and M bands between the equilibrium chemistry and disequilibrium chemistry model spectra. Comparing these differences with the differences in the $\tau = 1$ pressure levels in Figure 4.1 makes it clear that the differences in the H, K, and L bands arises due to changes in the CH_4 abundance profiles. Another major difference is in M-band. CO enhancement and modest H_2O depletion leads to a major suppression of thermal flux between 4.5-5 μm in the disequilibrium models.

Although NH_3 abundances show large changes between equilibrium chemistry and disequilibrium chemistry models, it still is not the major opacity source at the shorter IR wavelengths. It becomes a major opacity source at 11 μm and causes a distinct feature in the spectra. Figure 4.2 bottom panels show a significant change in this NH_3 feature due to disequilibrium chemistry. Quenching of NH_3 causes this feature to become slightly less prominent compared to chemical equilibrium models.

Other carbon and nitrogen bearing molecules like HCN, N_2 and CO_2 are also

quenched due to K_{zz}. But these molecules do not have readily apparent absorption features in the infrared at these spectral resolutions in a solar metallicity mixture. N_2 is essentially transparent in solar metallicity mixtures and detecting CO_2 is very difficult from the ground but JWST, like AKARI (Sorahana & Yamamura 2012), can detect disequilibrium abundances of CO_2 in brown dwarf with higher metallicity. As our models have solar metallicity, we do not specifically discuss these signatures here.

Of particular interest to our work here are the changes in $T(P)$ structure, and the locations of radiative and convective zones show in Figure 4.2. We examine the causes for these differences in more detail in Figure 4.3 for a brown dwarf with $T_{\rm eff}$ = 700 K and $\log(g)$ of 4.5. The left panel in Figure 4.3 shows the $T(P)$ profile of this brown dwarf under equilibrium chemistry with the dashed line and the $T(P)$ profile of the brown dwarf with chemical disequilibrium is shown with the solid line. The radiative zones are shown with narrower lines whereas the convective zones are shown with thicker lines.

There are significant changes in the location and number of radiative and convective zones in the two profiles, with the disequilibrium model having one convective zone at depth and radiative zone at lower pressure. However, the equilibrium models finds two convective zones and two radiative zones. To examine why, the right panel in Figure 4.3 shows the wavelength dependent absorptivity in several layers of these atmospheres with dashed (equilibrium chemistry) and solid (disequilibrium chemistry) lines. The absorptivity is given by A=(1-e$^{-\tau}$). A high absorptivity (close to 1) corresponds to an opaque wavelength whereas a low absorptivity corresponds to a transparent wave-

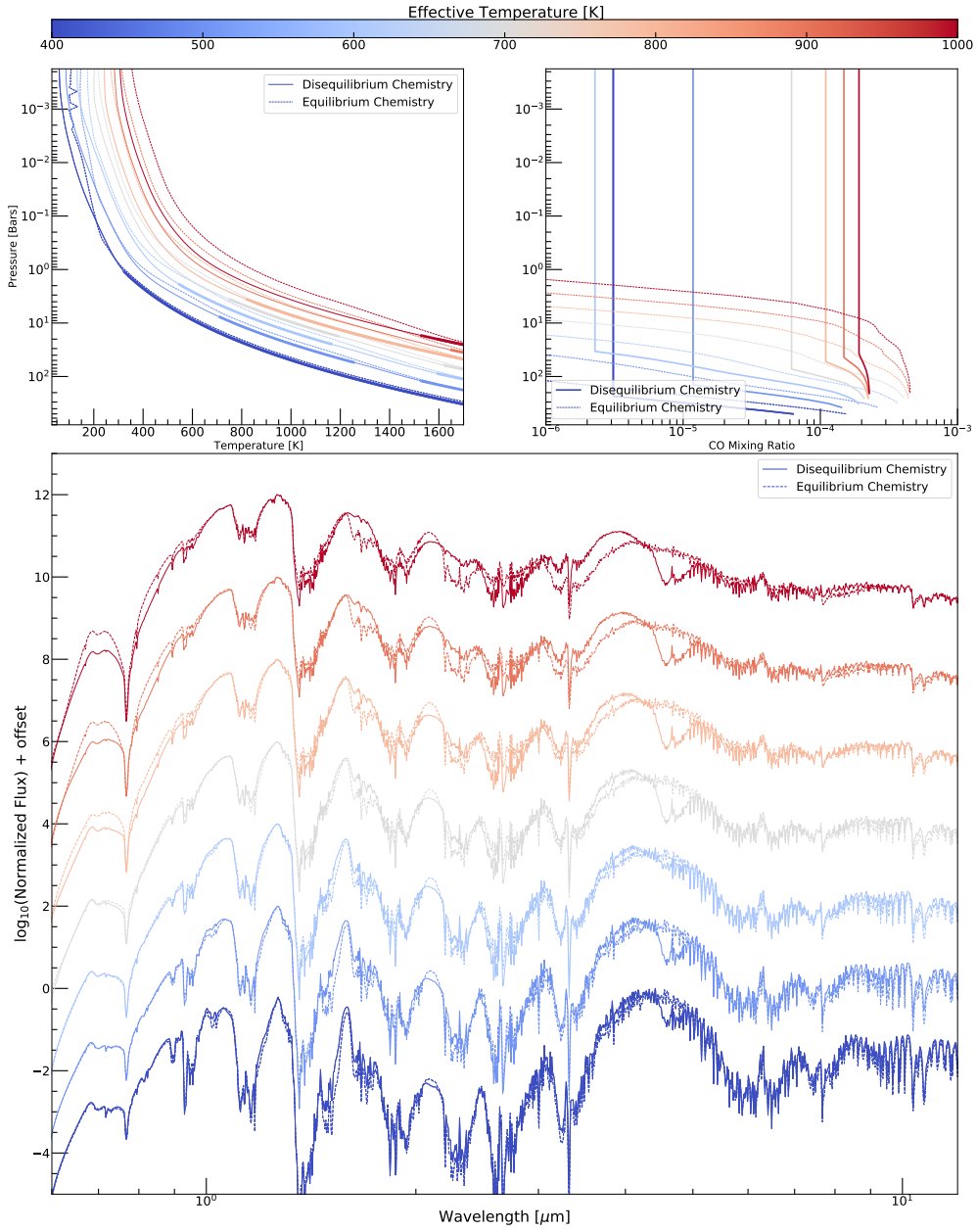

Figure 4.2: **Top left panel** $T(P)$ profile of brown dwarf models with log(g) = 5 and $T_{\rm eff}$ of 500, 700, and 1000 K. The solid $T(P)$ profiles assume disequilibrium chemistry self-consistently whereas the dotted profiles show equilibrium chemistry calculations. The convective zones are shown with thicker lines for each $T(P)$ profile. To differentiate the convective zones of the equilibrium chemistry models from the disequilibrium chemistry models, they are shown with much thicker lines compared to the convective zones of disequilibrium chemistry models. **Top right panel** Plotted are the CO volume mixing ratio profiles for these brown dwarf models. The solid lines show the mixing ratio with disequilibrium chemistry whereas the dotted lines show calculations from equilibrium chemistry. **Bottom panel** shows the normalized thermal emission spectra of these brown dwarfs. The solid lines show the disequilibrium chemistry results while dotted spectra represent the equilibrium chemistry calculations. The J, H, K', L', and M' bands are also shown as shaded regions of different colors. **Main Point**– Self- consistent treatment of disequilibrium chemistry leads to large changes in $T(P)$ profile, abundances, and thermal emission spectra.

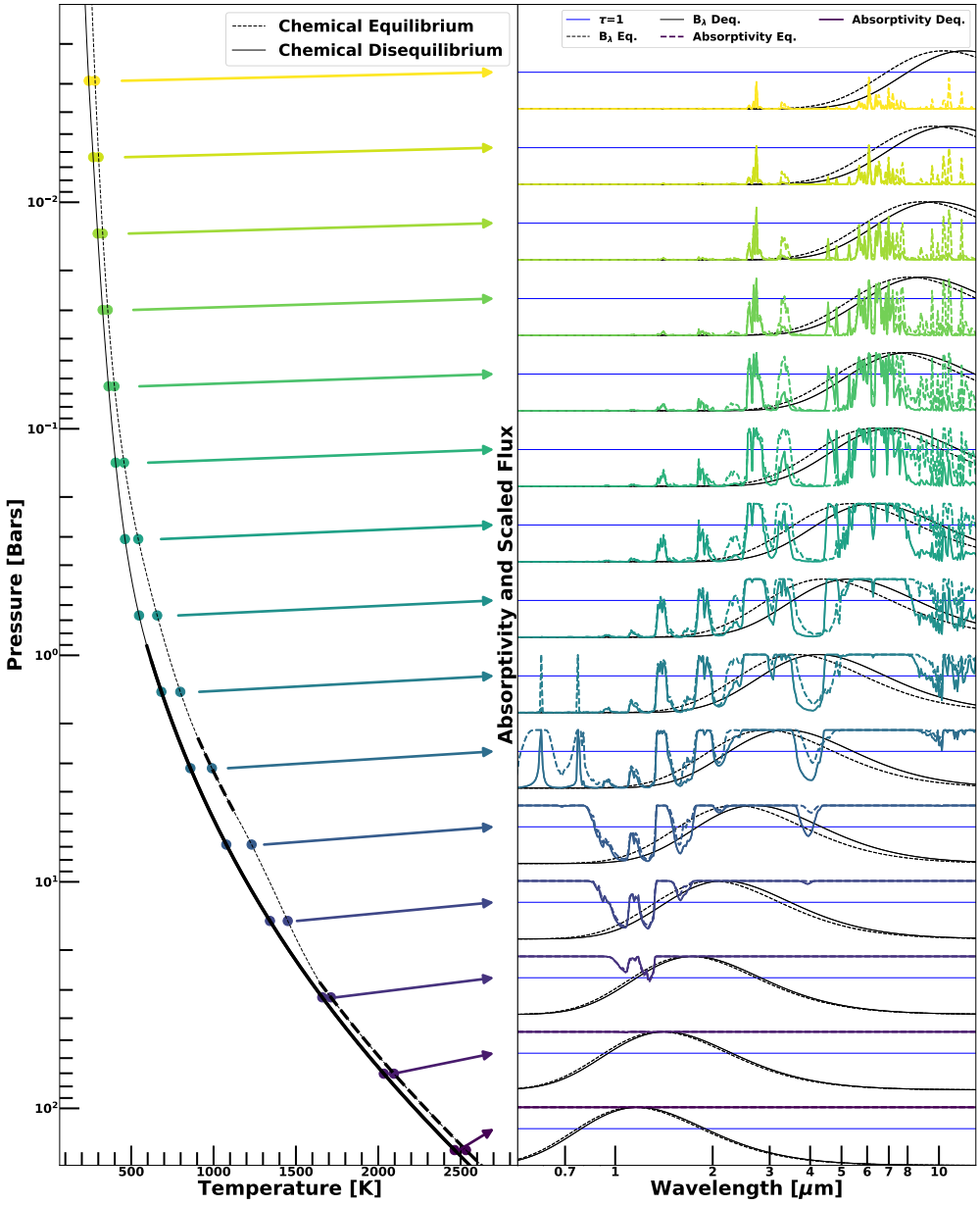

Figure 4.3: **Left panel** shows the $T(P)$ profile of a brown dwarf with $T_{\rm eff}$ of 700 K and log(g) of 4.5. The dashed line is the $T(P)$ profile when chemical equilibrium is assumed whereas the solid line shows the $T(P)$ profile for disequilibrium chemistry. The convective zones are shown with darker and thicker lines. **Right panel** shows the wavelength dependant absorptivity of the different atmospheric layers for both the cases. The absorptivity is given by 1-e$^{-\tau}$. The absorptivity for the equilibrium chemistry model is shown with dashed lines whereas that for disequilibrium chemistry model are shown with solid lines. The local normalized blackbody spectrum is also shown for each layer with dashed and solid lines for equilibrium and disequilibrium chemistry models, respectively. The blue horizontal line for each layer shows the absorptivity corresponding to τ =1. **Main Point** – Opacity changes lead to large (∼100 K) differences in $T(P)$ profiles between chemical equilibrium and disequilibrium models.

length window. The normalized local blackbody Planck function B_λ is also plotted for each layer for the equilibrium (dashed black line) and disequilibrium chemistry (solid black line) models for comparison with the absorptivity. We follow Marley & Robinson (2015) for the explanation of this phenomenon below.

As the atmosphere becomes colder with lower pressure in both models, the peak of the local B_λ shifts to longer wavelengths. In the deep atmosphere $\sim$ 100 bar, gaseous optical depths are very high which causes the absorptivity to be very close to 1 across all wavelength ranges for both cases. The atmosphere is opaque to radiative energy transport in these pressure layers for both cases, and convection ensues at these pressure levels. This is the case at pressures higher than $\sim$ 40 bars for both models. At about 20 bars some transparent windows start to appear. Since the equilibrium chemistry model is hotter than the disequilibrium chemistry model, the peak of its local blackbody emission coincides more closely in wavelength with the transparent opacity windows between 0.8-1 μm in the atmosphere at these pressures. This causes the equilibrium chemistry model to be radiative in these pressure ranges whereas the disequilibrium chemistry model is still convective as its local blackbody emission still peaks at longer wavelengths where the atmosphere is opaque at $\sim$ 20 bars pressure. As the atmosphere gets colder with lower pressure, large transparent windows develop between 0.5-2 μm but as these layers are much colder, their blackbody peaks are at wavelengths greater than 2 μm.

At $\sim$ 2 bars, the blackbody peak of the chemical equilibrium model hits another opaque range between 2-3 μm. This causes it to develop another, detached, convective

zone at these pressures. At pressures lower than this range, a large transparent opacity window develops between 3.5-5 μm in both the models. The disequilibrium model is more transparent than the equilibrium model between 3.5-4.5 μm (due to less CH_4 and H_2O) but is more opaque than the equilibrium model between 4.5-5 μm (due to more CO). As the local blackbody function of both models also peaks between 3.5-5 μm in these pressure layers, these differences in transparency between the two atmospheres causes a large change ($\sim$ 150 K) between their $T(P)$ profiles in these pressures. As the cooler local blackbody peak of the disequilibrium model more closely overlaps with the opaque window in the disequilibrium model between 4.5-5 μm, its atmosphere is still convective in these pressures, while the equilibrium model is radiative. At pressures lower than $\sim$ 0.8 bars, both atmospheres are radiative as more transparent windows start appearing in longer wavelengths with decreasing pressure. With these differences in the $T(P)$ profile and convective/radiative zones between models with chemical equilibrium and disequilibrium, the next important question to be investigated is whether gases like CO, NH_3, and H_2O are quenched in the radiative or convective zones of models with chemical disequilibrium. Results from our model grid on this question are presented next.

4.3.2 Quenching in the Radiative Zone or the Convective Zone ?

Quenching of gases can occur in convective zones or radiative zones. Vertical mixing in convective zones is expected to be very efficient, yielding a high K_{zz} and correspondingly low $t_{\rm mix}$. The top three panels of Figure 4.4 show the $T(P)$ profile of a

brown dwarf with $T_{\rm eff}$ of 700 K and log(g) of 4.5 (left panel), the mixing and chemical timescales ($t_{\rm mix}$ and $t_{\rm chem}$) for the same brown dwarf (middle panel), and the volume mixing ratios of various molecules (right panel) in the brown dwarf atmosphere. This brown dwarf has a single convective and radiative zone. The mixing timescale $t_{\rm mix}$ is shown in dashed black whereas the $t_{\rm chem}$ for CO and other chemical reactions are shown with different colors of dashed lines. The $t_{\rm mix}$ profile has been calculated using mixing length theory in the convective zone and with Equation 4.3 in the radiative zone. The mixing timescales in radiative zones are expected to be longer at depth, due to the lack of efficient dynamical mixing processes. However, as briefly described in §6.2, the mixing timescale is expected to be short in the much lower pressure regions (P $\sim 10^{-4}$ bars) due to the presence of gravity wave breaking mechanisms (Freytag et al. 2010; Moses et al. 2005, 2011).

$t_{\rm mix}$ is much longer than $t_{\rm chem}$ at pressures $>$ 100 bars and therefore CO and CH_4 are expected to follow chemical equilibrium in these high pressure high temperature parts of the atmosphere. But the $t_{\rm chem}$ for CO$\leftrightarrow$CH$_4$ reaction is a very strong function of both temperature and pressure (Zahnle & Marley 2014). Therefore, it increases by 12 orders of magnitudes within one order of magnitude in pressure and a change of 500 K in temperature. As a result, the two timescales cross each other at about $\sim$ 30 bars at the quench pressure ($P_{\rm Q}$). The abundances of both of these molecules, and H_2O, are quenched to constant values above P_Q as a result, as shown in the Figure 4.4 top right panel. As different net chemical reactions proceed at different rates and have *different* $t_{\rm chem}$, their P_Q will also be different.

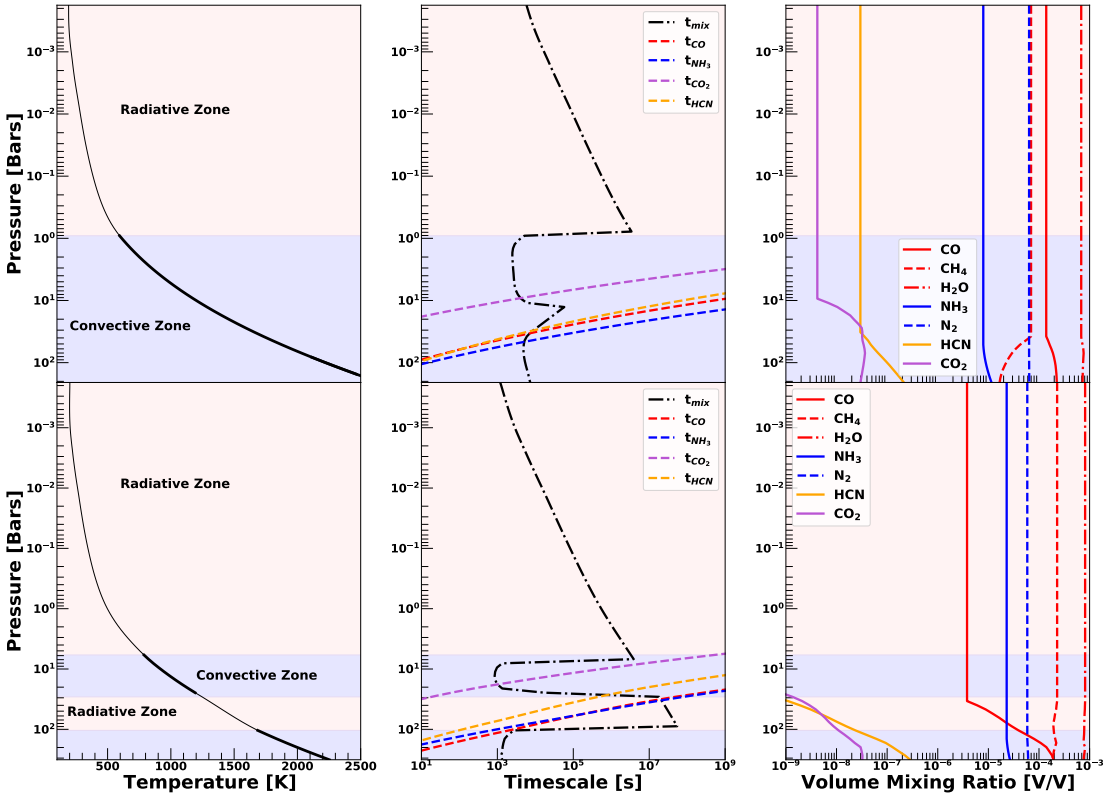

Figure 4.4: Model $T(P)$ profile, chemical and dynamical timescales, and chemistry for a brown dwarf with $T_{\rm eff}$ 700 K and log(g) = 4.5 is shown in the top panels whereas the same properties for a brown dwarf with $T_{\rm eff}$ 700 K and log(g) = 5.25 is shown in the bottom panels. $T(P)$ profile of the two brown dwarfs are shown in the **left panels** – one with a single deep convective zone while another with a deep "sandwiched" radiative zone between two deep convective zones. The **middle panels** show the comparison between the mixing timescale (black) and the chemical timescales of different gases like CO and NH_3 as a function of pressure for each of the $T(P)$ profiles shown in the left columns. The **right panels** show the volume mixing ratios of various molecules as a function of pressure for each atmosphere. **Main Point** – Gases can be quenched in a deeper "sandwiched" radiative zone in some brown dwarfs, where mixing timescales can be orders of magnitude larger than in convective zones.

Self-consistent chemical equilibrium models of T-dwarfs with $T_{\rm eff}$ within the range of 400–800 K have shown the presence of an upper detached convective zone in addition to the deeper convective zone (Burrows et al. 1997; Marley et al. 2021), with a radiative zone in between. The $T(P)$ profile in this scenario is shown in Figure 4.4 bottom left panel for a brown dwarf with $T_{\rm eff}$ of 700 K (as above) but with a log(g) of 5.25. This detached zone appears when the $T(P)$ profile of the atmosphere is such that the radiative energy transport in the deeper atmosphere becomes efficient due to the opening of a molecular opacity window at near infrared wavelengths (Marley & Robinson 2015), as shown in Figure 4.4. The resulting "sandwiched radiative zone" is very likely to have a much slower rate of vertical mixing (longer $t_{\rm mix}$) compared to the convective zones. As these radiative zones appear at high pressures (P $\geq$ 10 bars), it is possible that molecules like CO, CH_4 and NH_3 are quenched in the radiative zone instead of the convective zone. Note that the mixing timescale profile in the upper middle panel in Figure 4.4 shows a "kink" like structure in $t_{\rm mix}$ values between 10-30 bars. This kink is due to the decrease in the convective heat flux (F in Equation 4.2) in the convective zone around that region. This can happen in convective regions where a non-negligible, but smaller than the convective heat transport, amount of energy transfer in a convective zone still occurs via radiation. This leads to a smaller convective heat flux in these regions.

The bottom middle panel of Figure 4.4 shows this scenario. Within our modeling framework, the $t_{\rm mix}$ is low (high K_{zz}) in the deep convective zone and $t_{\rm mix}$ is high (low K_{zz}) in the deep sandwiched radiative zone. The P_Q for CO in this case is within

the sandwiched radiative zone. Therefore, if one is trying to probe the K_{zz} of this hypothetical object with constant K_{zz} models (e.g. Miles et al. 2020), one would infer a much lower K_{zz} than what is expected from Equation 4.2. However, the reason for this is is not because of sluggish mixing in the convective zone but rather quenching is occurring in a radiative zone where mixing is expected to be sluggish.

Such a scenario was suggested in fits to observations presented in Miles et al. (2020). They inferred the K_{zz} for several late T and early Y-dwarfs and found that the K_{zz} for objects with $T_{\rm eff}$ between 400-800 K are much smaller than expectations from mixing length theory. Although equilibrium chemistry models find the sandwiched radiative zone between $T_{\rm eff}$ of 400–800 K (e.g. Marley et al. 2021; Allard et al. 2012b), it is not clear if the self-consistent treatment of disequilibrium chemistry preserves these sandwiched radiative zones and also if molecules like CO or NH_3 actually quench in these sandwiched radiative zones. Next, we investigate this scenario in more detail.

We can expand the modeling work shown in Figure 4.4 over a range in $T_{\rm eff}$ and log (g) to assess under what conditions a sandwiched radiative zone occurs in self-consistent non-equilibrium models. Figure 4.5 shows the appearance of the sandwiched radiative zones across this phase space in the presence and absence of vertical mixing. The colors shown in Figure 4.5 represents $\log_{10}(\mathrm{P_{bot}}/\mathrm{P_{top}})$ where $\mathrm{P_{bot}}$ and $\mathrm{P_{top}}$ are the pressures at the bottom and top of the sandwiched radiative zone, respectively. If the model does not find a sandwiched radiative zone, this number will be zero. The top panel in Figure 4.5 shows the sandwiched radiative zones in chemical equilibrium models. The other three panels show the appearance of the second radiative zone

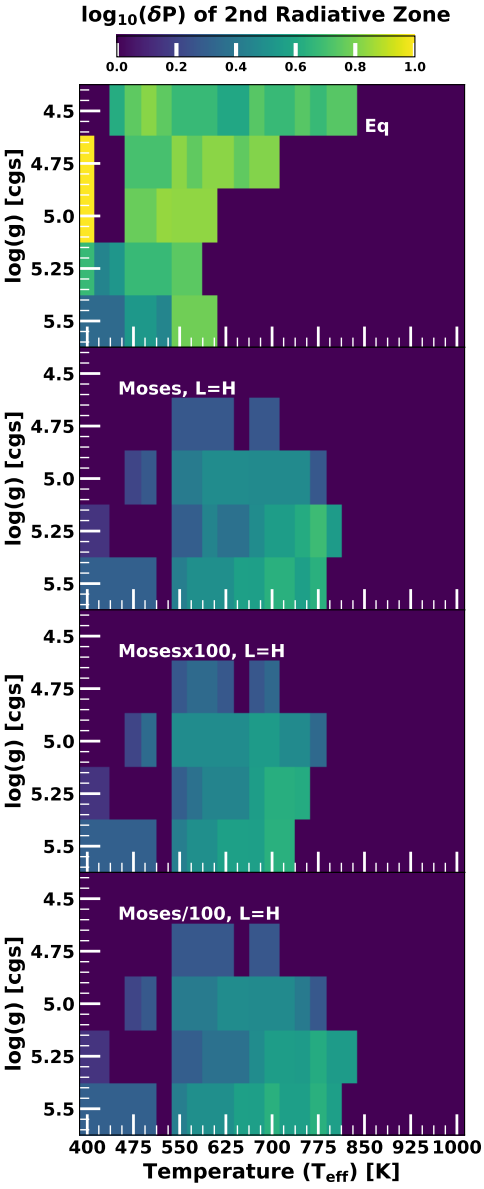

Figure 4.5: Appearance of the 2nd radiative zone in the $T_{\rm eff}$ vs. log(g) parameter space in our grid is shown. The colors show the value of the quantity $\log_{10}(\mathrm{P_{bot}}/\mathrm{P_{top}})$ where $\mathrm{P_{bot}}$ and $\mathrm{P_{top}}$ are the pressures at the bottom and top of the sandwiched radiative zone, respectively. The **top panel** shows this in case of equilibrium chemistry. The subsequent panels show the presence of the 2nd radiative zone if different vigor of K_{zz} is chosen keeping the convective zone mixing length fixed at H. Dark blue indicates no second convective zone at depth.

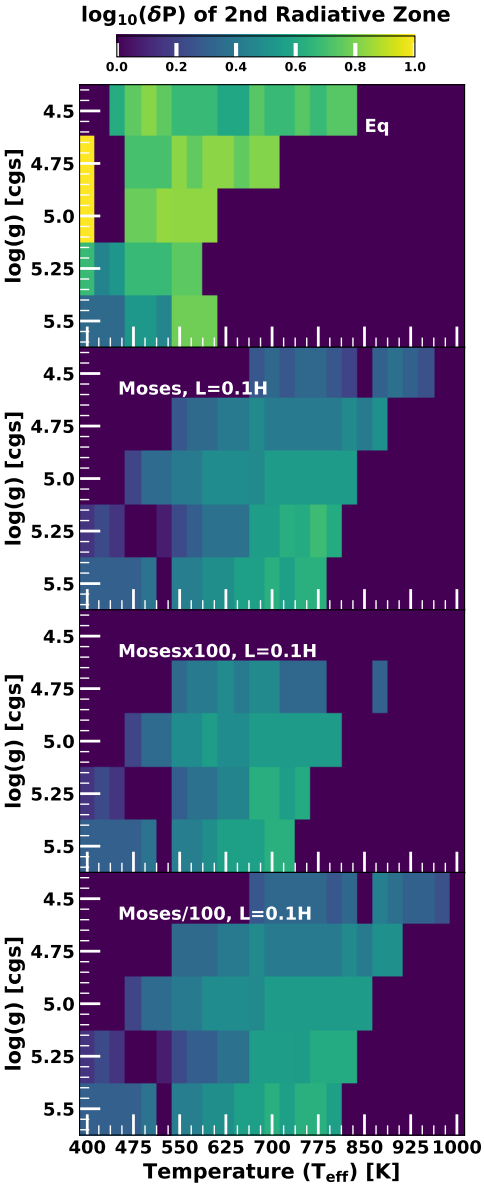

Figure 4.6: Appearance of the 2nd radiative zone in the $T_{\rm eff}$ vs. log(g) parameter space in our grid is shown. The colors show the value of the quantity $\log_{10}(\mathrm{P_{bot}}/\mathrm{P_{top}})$ where $\mathrm{P_{bot}}$ and $\mathrm{P_{top}}$ are the pressures at the bottom and top of the sandwiched radiative zone, respectively. The **top panel** shows this in case of equilibrium chemistry. The subsequent panels show the presence of the 2nd radiative zone if different vigor of K_{zz} is chosen keeping the convective zone mixing length fixed at $0.1 \times H$. Dark blue indicates no second convective zone at depth.

with three different magnitudes of mixing in the radiative zone, all assuming the mixing length L is H in the convective region. Under the assumption of equilibrium chemistry it is clear that the sandwiched radiative zones appear between $T_{\rm eff}$ of 450-800 K for a log(g) of 4.5. However, for objects with log(g) of 4.75 and higher, the sandwiched radiative zones only appear between 450-600 K in chemical equilibrium models. For models with disequilibrium chemistry, the models that show the presence of this sandwiched radiative zone appear at a different set of $T_{\rm eff}$ and log(g) values. As can be seen in Figure 4.5 (second, third, and fourth panels), high gravity models with log(g) of 5.0 and greater have this sandwiched radiative zone between $T_{\rm eff}$ of $\sim$ 500-800 K. For models with log(g) of 4.75 the sandwiched radiative zone appears between 500-750 K. However, for models with log(g) of 4.5, the sandwiched radiative zone is non-existent when quenching due to vertical mixing is taken into account. The thickness of these zones is typically smaller, too, as can be seen from the shading that is less yellow.

Figure 4.6 shows the appearance of this sandwiched radiative zone if the convective mixing length L is smaller, only $0.1 \times H$. The second, third, and fourth panels in Figure 4.6 show that larger number of models now develop this sandwiched radiative zone compared to models with $L = H$ shown in Figure 4.5. The sandwiched radiative zone does indeed appear at low gravity (log(g) = 4.5) when $L = 0.1 \times H$. Additionally, the radiative zones tend to appear at higher $T_{\rm eff}$ than for $L = H$ models. This shows that the strength of vertical mixing in both the radiative and convective zone can influence the presence and absence of multiple convective zones.

The effect of radiative and convective K_{zz} on the chemical abundances is more

complex than it may appear. The presence of a sandwiched radiative zone does not guarantee that quenching occurs *in* the radiative zone. Furthermore, radiative zone quenching can also occur in atmospheres with a single radiative zone and single convective zones. We investigate the resulting photospheric CO abundances in $T_{\rm eff}$ vs. log(g) space in Figure 4.7. The top panel shows the CO abundance in models in chemical equilibrium. The second, third, and fourth panels show models with disequilibrium chemistry. Each of these panels represents models with different values of K_{zz} in the radiative zone while the mixing length in the convective zone is fixed to H. Models where CO, CH_4, and H_2O are quenched in radiative zones are marked with black hatches. The rest of the models still have CO quenching, but in the convective zones instead.

The CO abundances in these models with radiative zone CO quenching also show large differences from CO abundances in models with convective zone quenching. These differences appear as discontinuities in the CO abundance heat map shown in the second, third, and fourth panels of Figure 4.7. The reason behind these discontinuities is mainly the smaller P_Q of CO in models with radiative zone quenching compared to models with convective zone quenching.

However, Figure 4.8 shows that CO abundances over $T_{\rm eff}$ and log(g) will change if the mixing length in the convective zone is smaller. Here, again, $L = 0.1 \times H$, leading to smaller K_{zz} values, and longer $t_{\rm mix}$ in the convective zone. This causes quenching to often occur in the top or sandwiched radiative zone in a significantly larger fraction of the $T_{\rm eff}$ and log(g) parameter space compared to the nominal $L = H$ scenario in Figure 4.7. For models with log(g)=4.75 and greater, all models with $T_{\rm eff} \geq 550$ K show

radiative zone quenching of CO and CH_4 in this case. Both Figure 4.7 and 4.8 makes it clear that the chemical properties of brown dwarfs that will have either radiative zone or convective zone quenching depends on the vigor of mixing in both of these types of zones.

Furthermore, since $t_{\rm chem}$, and hence the P_Q, of different gaseous species are different, this means that models where CO quenches in radiative zones are not necessarily models where CO_2 or NH_3 also quenches in the radiative zone. This effect can be clearly seen in Figure 4.9, which shows the same set of models in Figure 4.7, but now with the CO_2 abundances and its radiative/convective quench behavior. Because the $t_{\rm chem}$ for the thermochemical equilibrium of CO_2 is orders of magnitude shorter than for CO and CH_4, the models where CO_2 quenches in the radiative zone are also different than those where CO/CH_4 quenches in the radiative zone. If the mixing length in the convective zone is H, CO_2 radiative zone quenching occurs mostly in models that are hotter than 700 K and have gravity higher than log(g) of 5. The same effect for quenching of NH_3 has been shown in Figure 4.10 in models with $L = 0.1 \times H$. Comparing Figure 4.10 with 4.8 shows that the radiative zone quenching of NH_3 occurs in only a small subset of lower temperature (500–800 K) models with radiative zone quenching of CO , when $L = 0.1 \times H$. The $t_{\rm chem}$ for the reaction between $N_2 \leftrightarrow NH_3$ is the slowest among the other reactions described in §4.2.1. As a result, if $L = H$, NH_3 always gets quenched in the deep convective zone in the parameter space explored by our grid. Even if the convective mixing length is smaller ($L = 0.1 \times H$), NH_3 gets quenched in the convective zone of the majority of the models except in some where deeper "sandwiched" radiative

zones develop. But in order to measure these quenched abundances observationally and infer the K_{zz} profile of the atmosphere, we need to investigate the effect of K_{zz} on observables, such as the emission spectra of these brown dwarfs, which we discuss next.

4.3.3 Effect of Radiative and Convective Zone K_{zz} on Emission Spectra

We have established in §4.3.2 that gases like CO, CH_4 and CO_2 can be quenched in the sandwiched radiative zones or single radiative zones in a subset of late T and early L-dwarfs. In Figures 4.11, 4.12, and 4.13, we show how thermal emission spectra are sensitive to the vigor of vertical mixing in the radiative zone of these objects. These spectra, with a spectral resolution of 600, are calculated using the thermal emission calculation module of `PICASO` (Batalha et al. 2019), using the same opacities that were used for model convergences to RCE. Sources of these opacities can be found in Marley et al. (2021).

The thermal emission spectra between 4.2-5.0 μm, across a range of $T_{\rm eff}$ between 400 K and 1000 K with steps of 100 K, are shown for log(g) values of 5 and 5.5 in the two upper panels of Figure 4.11. The choice of the wavelength range focuses on the role of CO, which has significant impacts on the spectrum in M-band between 4.4-5 μm. H_2O is the primary absorber between 4.0-4.4 μm. These models assume $L = H$ in the convective zones. Figure 4.11 lower panels shows the spectrum from the same set of models except $L = 0.1 \times H$. Spectra arising from different vigors of vertical mixing in the radiative zones are shown with different line dashes in all the panels.

Sensitivity of the M-band spectrum to radiative zone K_{zz} values is more com-

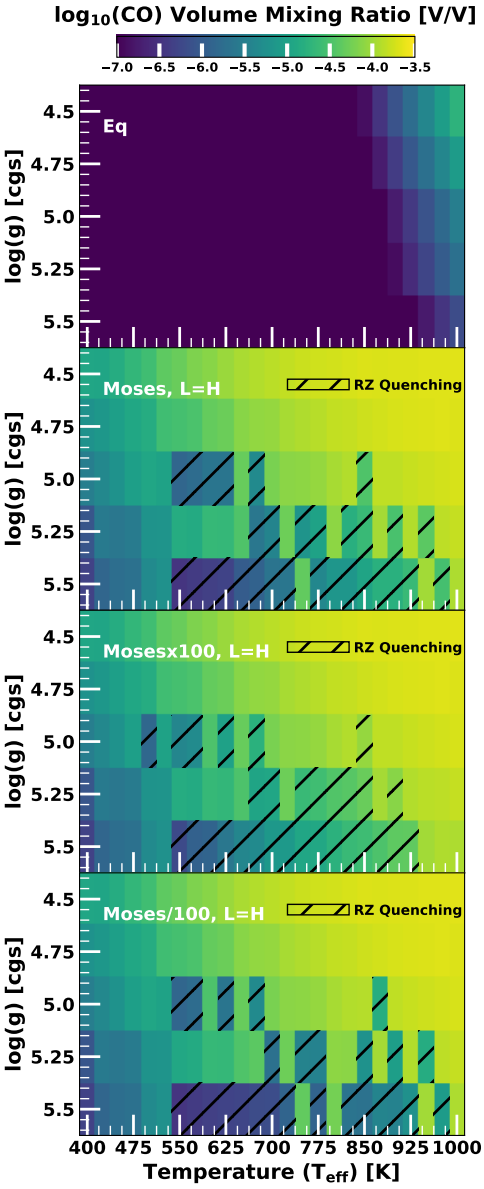

Figure 4.7: **Top panel** shows the equilibrium chemistry abundance of CO at pressures where $T = T_{\rm eff}$ in our $T_{\rm eff}$ vs. gravity grid of chemical equilibrium models. The **second, third and last panels** depict the quenched CO abundance within the $T_{\rm eff}$ vs. gravity parameter space in our disequilibrium chemistry models. The second, third and last panels correspond models with radiative zone K_{zz} values of "Moses", "Moses×100", and "Moses/100", respectively while the convective zone mixing length L was fixed at the scale height H. Models where CO was quenched at the radiative zone are marked with black hatches. CO was quenched at a convective zone in the rest of the models. Models with radiative zone CO quenching show much smaller CO abundance compared to models with convective zone quenching.

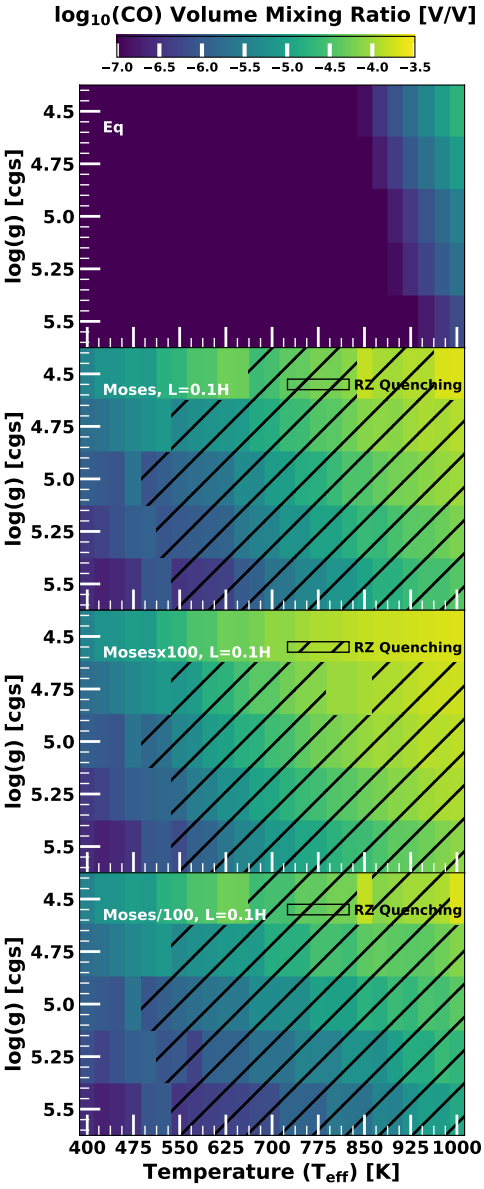

Figure 4.8: Same as Figure 4.7 except with the mixing length in convective zones fixed at 0.1×H. In these models CO is mostly quenched in a radiative zone.

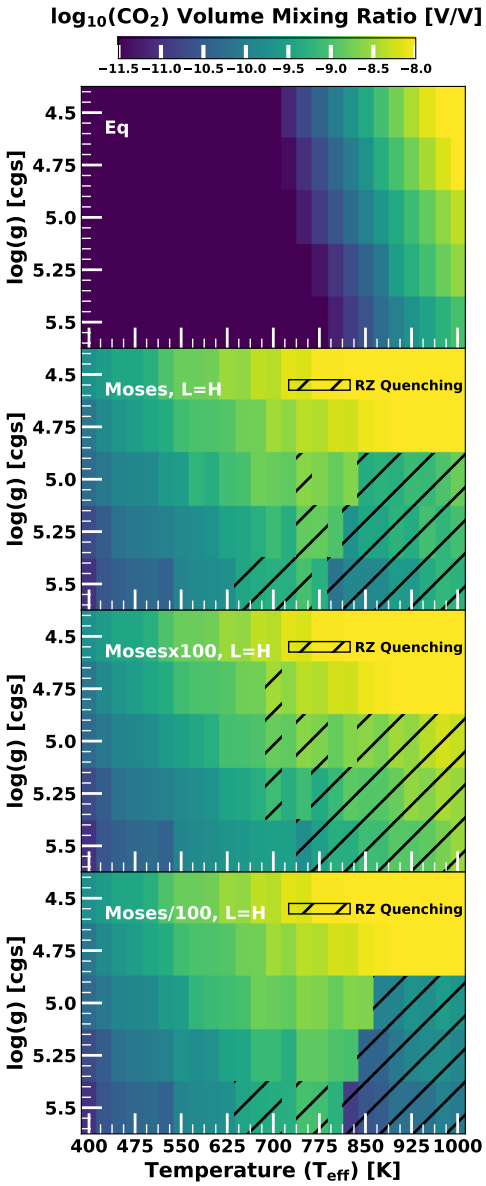

Figure 4.9: Same as Figure 4.7 but for quenching of CO_2. Given the different $t_{\rm chem}$ for CO_2, compared to CO, the quench levels are entirely different.

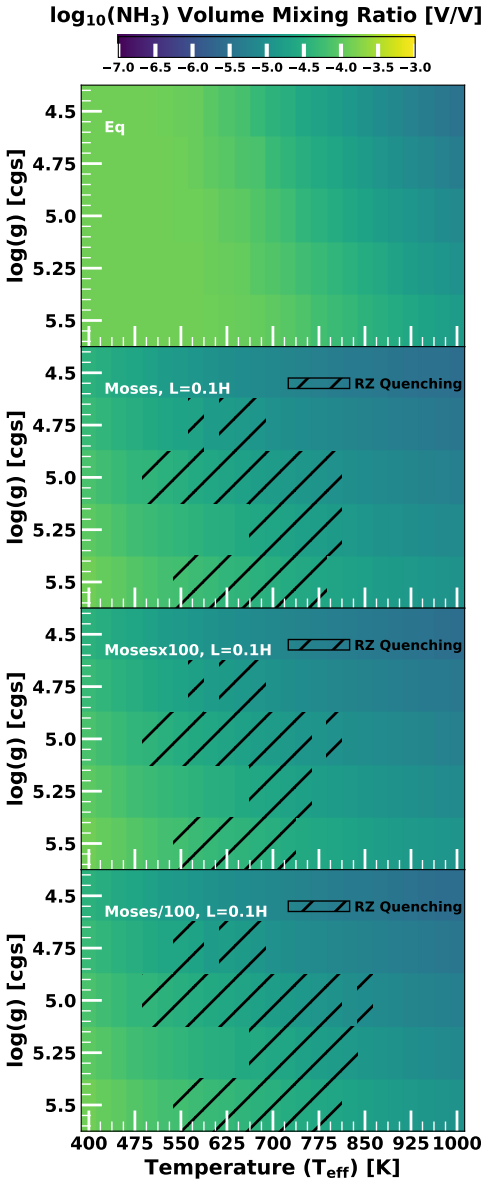

Figure 4.10: Same as Figure 4.8 but for quenching of NH_3. Given the different $t_{\rm chem}$ for NH_3, compared to CO, the quench levels are entirely different.

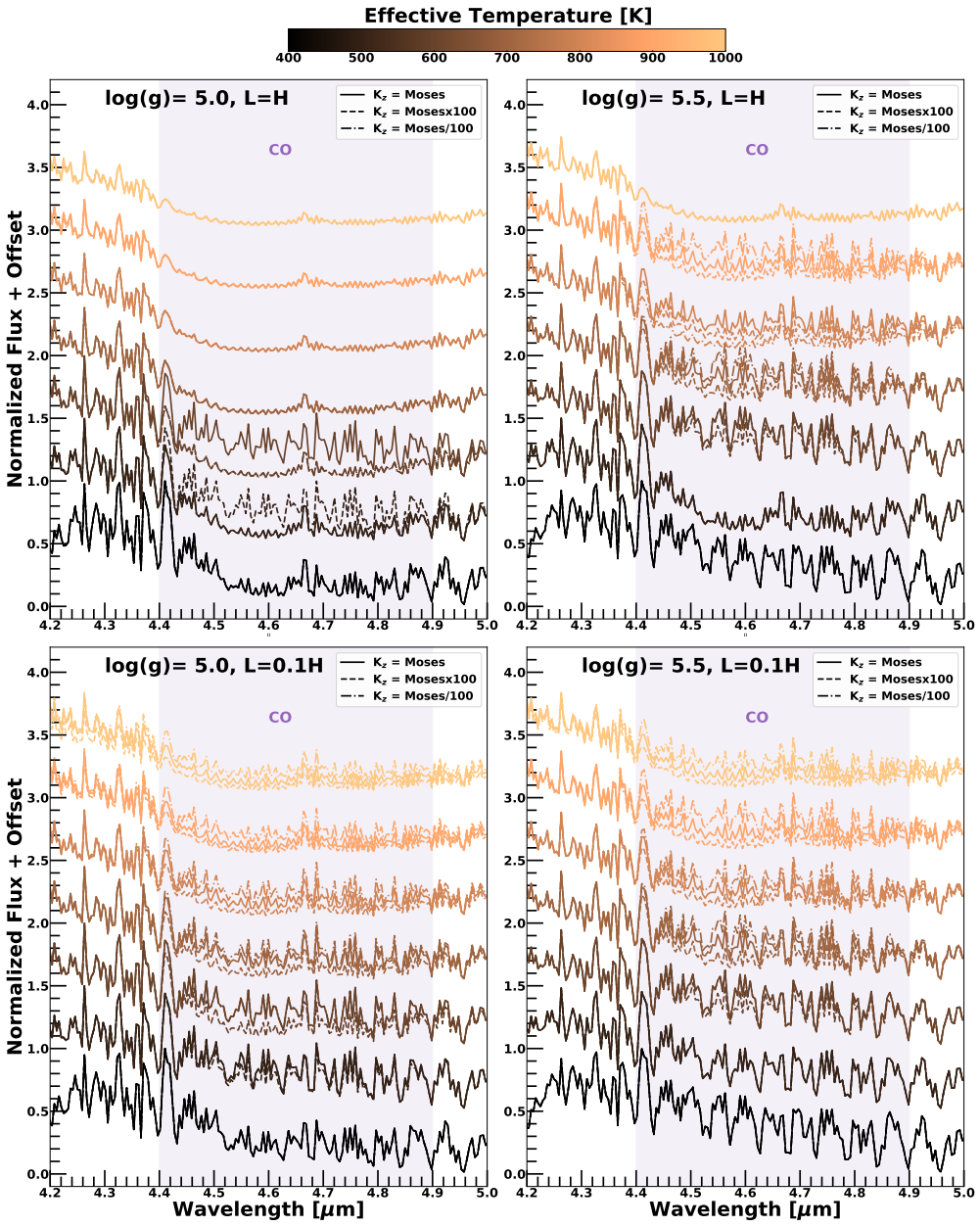

Figure 4.11: M-band Thermal emission spectra across a range of $T_{\rm eff}$ between 400 K and 1000 K with steps of 100 K are shown in each panel. log (g) = 5.0 is on the left and 5.5 is on the right. The colors are representative of the $T_{\rm eff}$. The models shown in the upper left and right panels assume the convective mixing length L to be H whereas the models shown in the lower left and right panels assume $L = 0.1 \times H$. The three line styles show different radiative zone K_{zz} parametrizations, including Moses (solid), Moses/100 (dashed), and Moses×100 (dash-dot). If quenching occurs in a convective zone the three spectra plot atop each other. The shaded region shows the wavelength range where CO is the most important absorber.

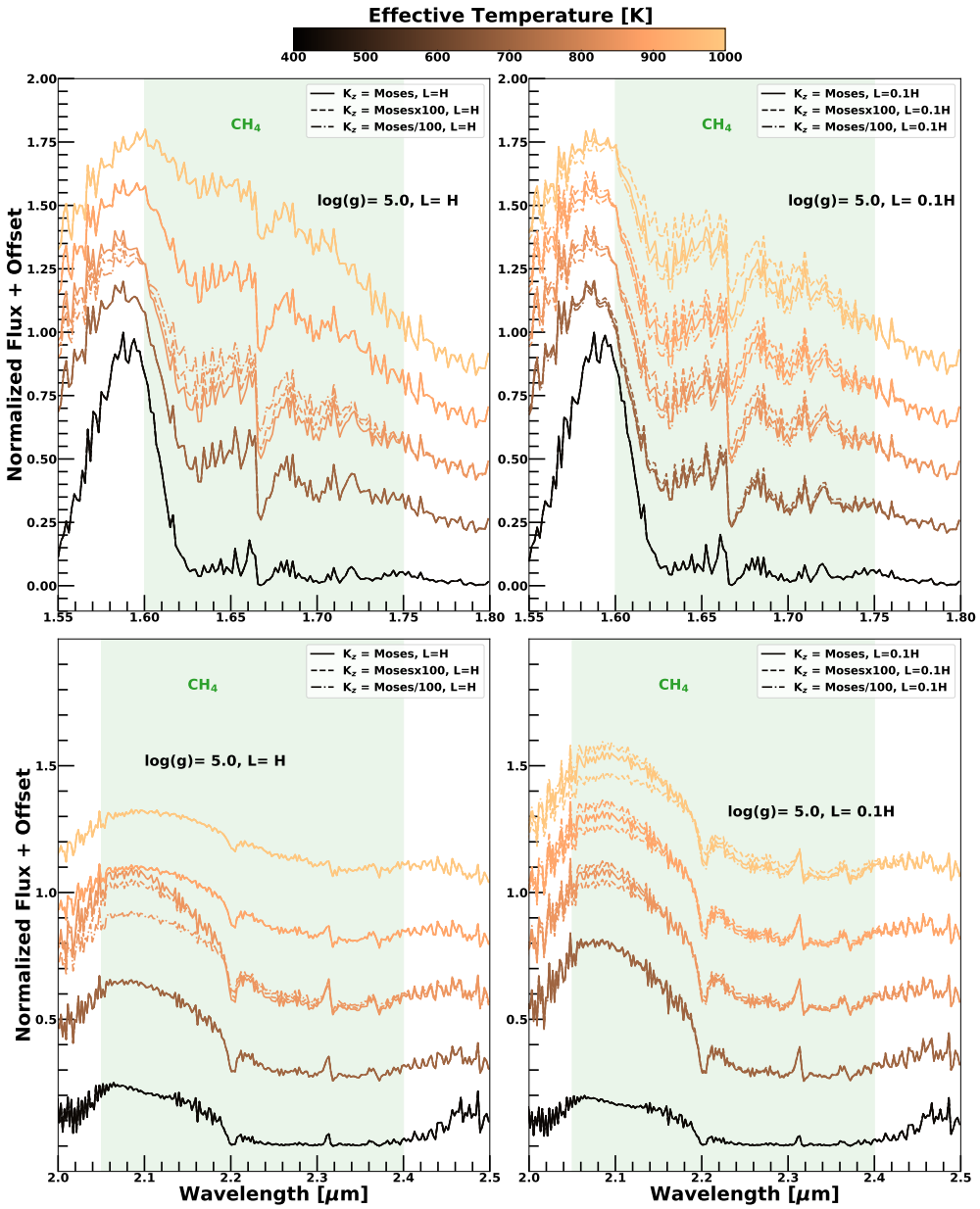

Figure 4.12: H-band thermal emission spectra of models from our grid are shown in the top left and right panels whereas the bottom left and right panels show the K-band emission spectra. Models with log(g)=5 and different $T_{\rm eff}$ between 400-1000 K are shown in each panel. From bottom to top, spectra for $T_{\rm eff}$ values of 425 K, 700 K, 850 K, 900 K, and 1000 K are shown in all the panels. **Top left panel** shows the thermal emission spectra of models which have convective mixing length set at H but have different K_{zz} parametrizations like Moses, Moses/100, and Moses×100 which are represented by different line types in the panels like solid, dashed, and dashed-dotted. **Top right panel** shows the same but for models with convective mixing length set at $0.1 \times H$. **Bottom left and right panels** show the sensitivity of the K band spectrum to radiative zone K_{zz} when $L = H$ and $L = 0.1 \times H$, respectively. The shaded region shows the wavelength range where CH_4 is the most important absorber.

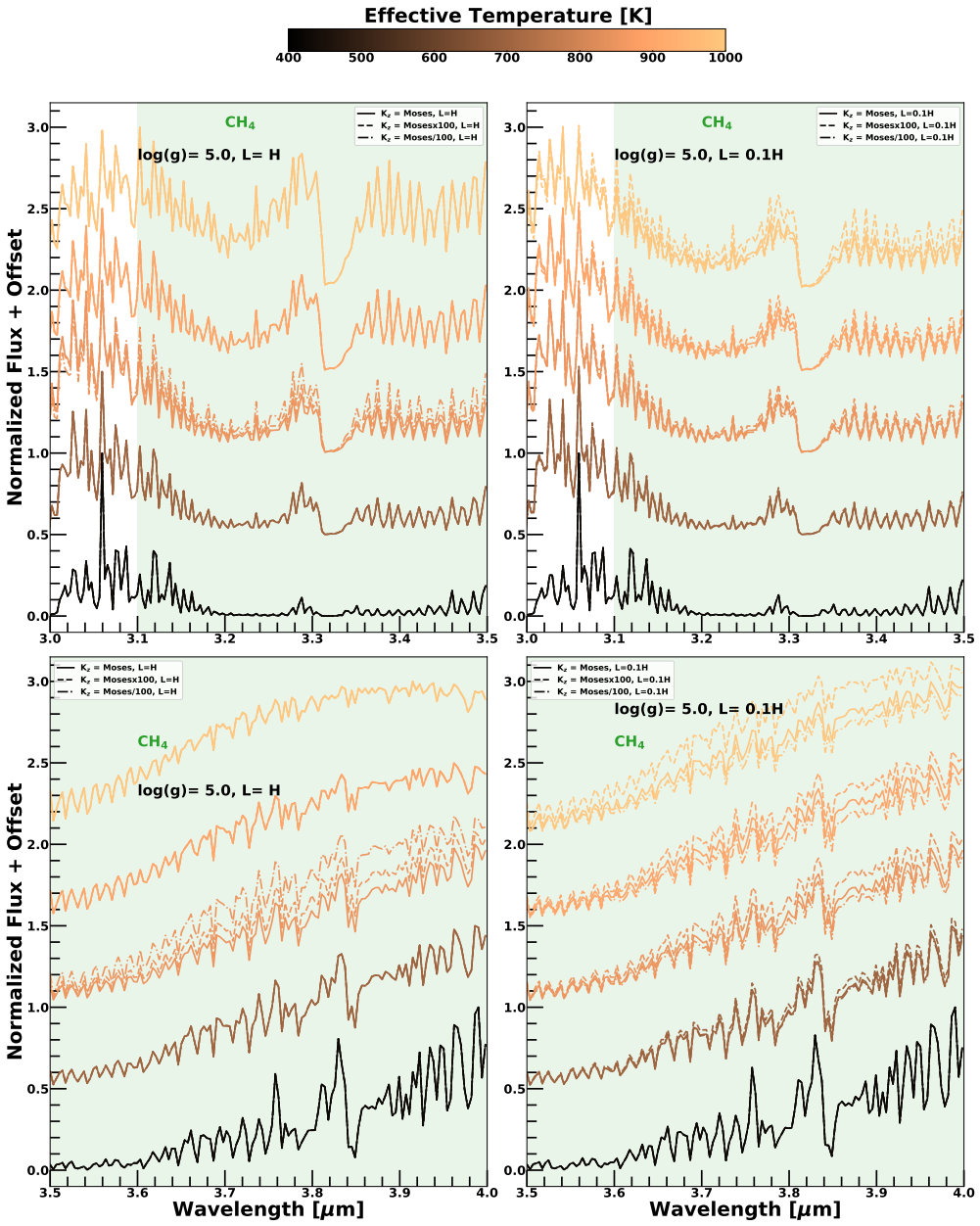

Figure 4.13: Thermal emission spectra of brown dwarfs between 3 and 3.5 μm are shown in the top left and right panels. Emission spectra of the same models in the L-band are shown in the bottom left and right panels. Models with log(g)=5 and different $T_{\rm eff}$ between 400-1000 K are shown in each panel. From bottom to top, spectra for $T_{\rm eff}$ values of 425 K, 700 K, 850 K, 900 K, and 1000 K are shown in all the panels. **Top left panel** shows the emission spectra of models which have convective mixing length set at H but have different K_{zz} parametrizations like Moses, Moses/100, and Moses×100 which are represented by different line types in the panels like solid, dashed, and dashed-dotted. **Top right panel** shows the same but for models with convective mixing length set at $0.1 \times H$. **Bottom left and right panels** show the sensitivity of the L-band spectrum to radiative zone K_{zz} when $L = H$ and $L = 0.1 \times H$, respectively. The shaded region shows the wavelength range where CH_4 is the most important absorber.

mon for higher gravity objects with log(g) of 5.0 and 5.5. If the convective mixing length is H, then this sensitivity appears between models with $T_{\rm eff}$ 550- 700 K for log(g) of 5. However, if the convective mixing length is $0.1 \times H$, then this sensitivity appears much more commonly between models with $T_{\rm eff}$ of 500-1000 K for log(g)= 5.0. At higher gravity, log(g) of 5.5, the sensitivity of M-band spectra to radiative zone K_{zz} appears at both convective mixing lengths of H and $0.1 \times H$. In Figure 4.11 upper right panel, this sensitivity appears between 500-900 K whereas in Figure 4.11 lower right panel this sensitivity appears between 500-1000 K.

While the M-band shows the greatest sensitivity to K_{zz} in the radiative and convective zones, smaller differences in the spectra arise in other wavelengths as well. Figure 4.12 top panels shows the sensitivity of the H-band spectra to the radiative zone K_{zz} across various values of $T_{\rm eff}$ for brown dwarf models with log(g)=5.0. The top left panel shows models with $L = H$ whereas the top right panel shows models with $L = 0.1 \times H$. The sensitivity mainly appears between 1.69 μm and 1.75 μm in models where CH_4 is quenched in the radiative zone as it is the main opacity source at these wavelengths. CH_4 is also the main opacity source between 2–2.2 μm, 3.2-3.5 μm, and 3.5–4 μm. As a result, the spectra at these wavelength ranges also show some sensitivity to the radiative zone K_{zz} of the deep atmosphere. This sensitivity between 2–2.2 μm, 3.2-3.5 μm, and 3.5–4 μm is shown in Figure 4.12 bottom panels and Figure 4.13 top and bottom panels, respectively. Examining different spectral regions for a given object, that are sensitive to both CH_4 and CO, will help in constraining the radiative zone K_{zz}, as both gas species abundances can be used as probes. Apart from the emission spectra

itself, other observables like broadband IR colors and magnitudes of brown dwarfs are also known to be sensitive to K_{zz} (e.g. Saumon et al. 2003; Karalidi et al. 2021a), which we explore next.

4.3.4 Color Magnitude Diagrams

Coupling our atmospheric model grid with brown dwarf evolutionary models from Marley et al. (2021) enables us to generate color magnitude diagrams (CMDs) of these brown dwarfs. These evolutionary models track the $T_{\rm eff}$, log(g) and bolometric luminosity as a function of age for each brown dwarf mass. The procedure is the same as in Marley et al. (2021), although our models here are slightly not self-consistent, as the upper boundary condition for the Marley et al. (2021) cooling tracks assume equilibrium chemical abundances.

Figure 4.14 shows the observed CMD of brown dwarfs in various standard infrared filter combinations. We show J vs. J-H, MKO L$'$ vs. L$'$-M$'$, and WISE W1 vs. W1-W2 in the first, second and third rows, respectively. The mid-infrared wavelengths are most sensitive to disequilibrium chemistry effects. Model tracks for three different log(g) (4.5, 5.0 and 5.5) values are shown in the three columns for each combination of filters. The database maintained by Trent Dupuy [1] (Dupuy & Liu 2012; Dupuy & Kraus 2013; Liu et al. 2016) has been used for the observational data. The red model tracks in all the panels represents models with convective mixing length set at H whereas the blue tracks represents models with convective mixing length set at $0.1 \times H$.

[1] http://www.as.utexas.edu/ tdupuy/plx

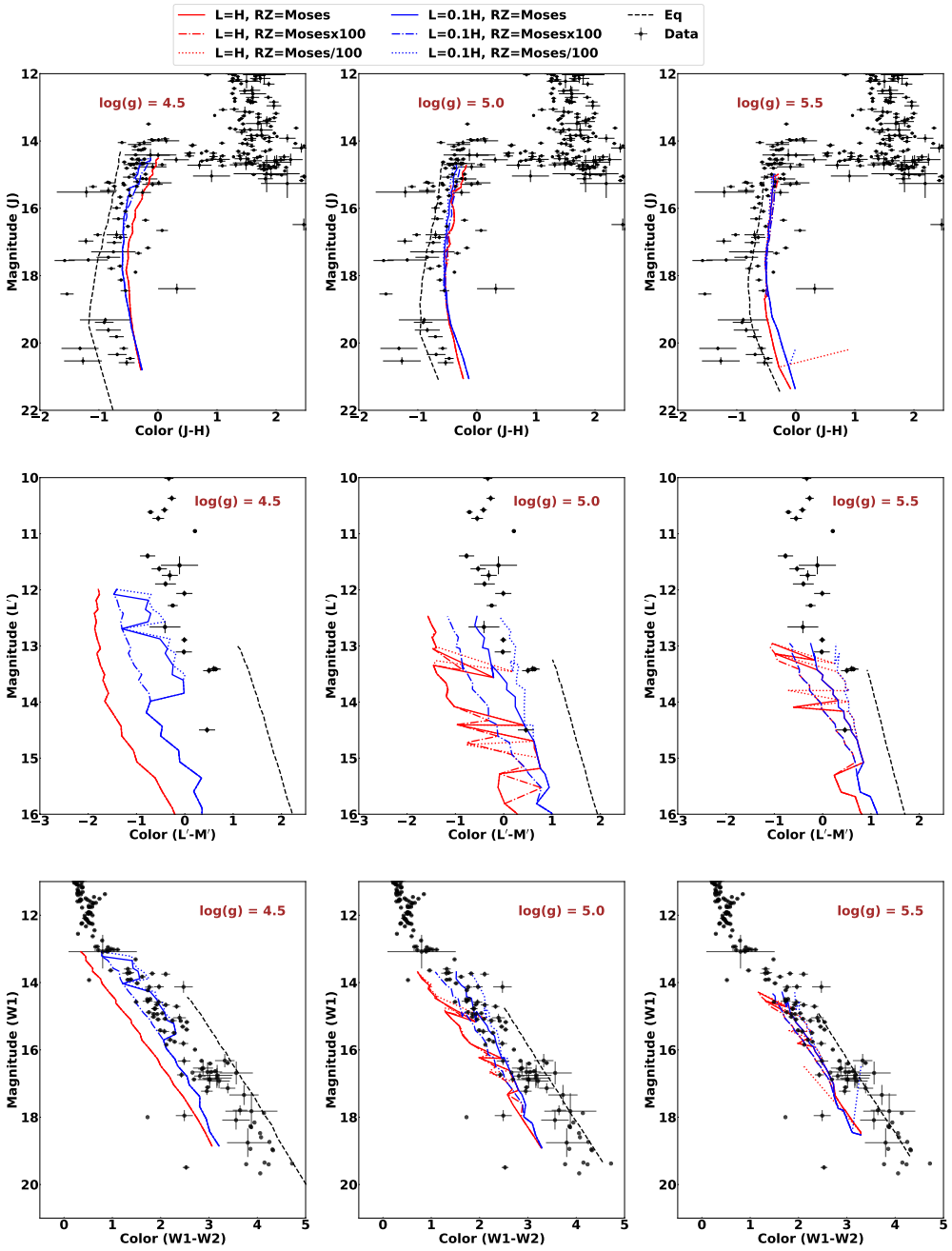

Figure 4.14: Color magnitude diagrams (CMD) of observed brown dwarfs in different filters are shown with overplotted equilibrium and disequilibrium chemistry model tracks with different strengths of convective and radiative zone vertical mixing. The top row shows the J vs. J-H where the models with convective zone mixing length of H and different radiative zone K_{zz} are shown with various linetypes of red. Models with convective zone mixing length of $0.1 \times H$ and different radiative zone K_{zz} are shown with various linetypes of blue and the equilibrium chemistry models are shown with dashed black lines. Each column shows the same data but the model tracks with different values of log(g). The second row shows the the $L^{'}$ vs $L^{'}$-$M^{'}$ whereas the third row shows the W1 vs. W1-W2.

Each line type (solid, dotted, and dash-dotted) in both of these colors represents models with the different radiative zone K_{zz} values "Moses×100", "Moses", and "Moses/100," respectively. The black dashed lines represents CMD tracks from equilibrium chemistry models.

In the J vs. J-H filter combination CMD, it appears that models treating disequilibrium chemistry self-consistently provide a slightly better fit to the observed photometry than the equilibrium chemistry, for models at log(g) of 5.0-5.5, representative of the field sample. The disequilibrium chemistry models with different convective mixing lengths shown by the blue and red tracks almost fall on top of each other as the J and H band fluxes are not particularly sensitive to CO abundance but has some sensitivity to CH_4 abundance.

The chemical equilibrium model CMD tracks follow a much redder sequence in the MKO $L^{'}$ vs. $L^{'}$-$M^{'}$ CMDs compared to the observed photometry. The disequilibrium chemistry models are comparatively much bluer. As discussed in the previous sections, enhanced CO abundance in disequilibrium chemistry model causes the M′-band and the W2-band fluxes to be fainter than equilibrium chemistry models. On the other hand, depleted CH_4 abundance in disequilibrium chemistry models causes higher fluxes in the L′ and W1 bands. Both of these effects causes the disequilibrium model tracks (shown with red and blue lines) to be significantly bluer than the equilibrium chemistry model tracks (shown with black line) in the $L^{'}$ vs. $L^{'}$-$M^{'}$ and W1 vs. W1-W2 CMD.

It is interesting to note the non-monotonic behavior. At higher gravity (log(g) = 5.0 and 5.5) some disequilibrium chemistry models show radiative zone quenching

instead of convective zone quenching. As a result, these atmospheres have lower photospheric CO compared to disequilibrium chemistry with convective quenching, but a much higher CO abundance compared to the equilibrium chemistry models. Therefore, the models with radiative zone quenching are redder than disequilibrium chemistry models with convective zone quenching but bluer than equilibrium chemistry models, "jutting out" to the red for some models.

The second and third rows in Figure 4.14 also show that disequilibrium models with $L = H$ with convective zone quenching of CO are much bluer than the observed sequence. However, disequilibrium models with $L = 0.1 \times H$ provide a generally better fit to the mid-IR photometry. This suggests that longer $t_{\rm mix}$ values in the deeper atmosphere provide a better fit to the photometry from the T and Y dwarf population, than the $t_{\rm mix}$ calculated from assumptions like free convection. However, this result is empirical in nature and needs further validation from 3D tracer transport models like in Bordwell et al. (2018). Coupling our models with 1D chemical kinetics models will also help us in interpreting these trends better, which is something we will address in future studies. It seems clear that even lower K_{zz} values for the faintest models may be necessary, as the data are generally more consistent with equilibrium chemistry models at log (g) of 5.0-5.5 We also note that we have not included clouds within our models and they might have some impact on the model magnitudes presented here especially for the faintest end of these tracks as H_2O clouds are expected to form in the colder objects ($T_{\rm eff} \leq 450$ K) (Morley et al. 2014b).

4.3.5 Comparing to Spectroscopic Observations

We use our grid of atmosphere models to compare with ground-based spectral observations of six late T and early Y-dwarfs. We aim to determine the atmospheric properties of brown dwarfs – Gleise 570 D (Burgasser et al. 2000), 2MASS J0415-0935 (Burgasser et al. 2002a), WISE 0313 (Kirkpatrick et al. 2011), UGPS 0722 (Cushing et al. 2011), WISE 2056 (Schneider et al. 2015), and WISE 1541 (Schneider et al. 2015) with our models. Although Miles et al. (2020) had the Y-dwarf WISE 0855 in their sample, we exclude this object from our analysis as it is expected to have optically thick water clouds in its atmosphere due to its cold $T_{\rm eff}$ ($\sim$ 250 K) and our model grid only extends to a $T_{\rm eff}$ = 400 K. As noted in §6.3, this choice for the lower bound on $T_{\rm eff}$ in our model grid was made because our models lack a self-consistent treatment of clouds with disequilibrium chemistry, currently.

For comparing our models with observational data, which includes both near-infrared and M-band spectra, we use the goodness of fit parameter – G_k defined as (Cushing et al. 2008),

$$G_k = \frac{1}{n-m} \sum_{i=1}^{n} w_i \left(\frac{f_i - C_k F_i^k}{\sigma_i} \right)^2 \tag{4.4}$$

where n is the number of observational data points, m is the number of free parameters being fit, w_i are the weights of fitting i'th data point, f_i is the i'th observed flux, F_i^k is the i'th model flux point of the k'th model, and σ_i is the error in the i'th observed flux. The factor C_k is a renormalization factor for the model fluxes. If the observed fluxes are flux calibrated then C_k represents the factor R^2/D^2 but if the observed fluxes

are not flux calibrated then C_k represents the factor $\alpha R^2/D^2$ where $1/\alpha$ represents the unknown flux normalization of the observed flux. The C_k factor is given by (Cushing et al. 2008),

$$C_k = \frac{\sum_{i=1}^{n} w_i f_i F_i^k/\sigma_i^2}{\sum_{i=1}^{n} w_i (F_i^k)^2/\sigma_i^2} \tag{4.5}$$

Since there is no reported bias in any of the datasets we use, w_i is always fixed at 1 for our analysis.

4.3.5.1 Gliese 570 D and 2MASS J0415-0935

Gliese 570 D is a T7.5 dwarf (Burgasser et al. 2006) which has a measured spectrum in the M-band with two different instruments – AKARI (Sorahana & Yamamura 2012) and GEMINI/NIRI (Geballe et al. 2009). We used the M-band spectra of Gliese 570 D reported in (Geballe et al. 2009) because it has a higher SNR ratio. We also use the NIRC 1-2.5 μm spectra of Gliese 570 D (Gl 570D) reported in Burgasser et al. (2002a) and *Spitzer* Infrared Spectrograph (IRS) 5-14 μm spectra of Gliese 570 D reported in Suárez & Metchev (2022). We adopt the methodology described in Sorahana & Yamamura (2012) for fitting the spectrum of Gl 570D with our grid of models. Firstly, we use our grid of models to calculate C_k using only the M-band GEMINI/NIRI data for Gl 570D. Using this set of calculated C_k, we calculate the G_k parameter using our models and the M-band GEMINI/NIRI data for Gl 570D. Then we select all the models with values of the G_k parameter between $min(G_k)$ and $min(G_k)$ +1. This step gave us 131 models which best-fits the M-band GEMINI/NIRI data for Gl 570D. The

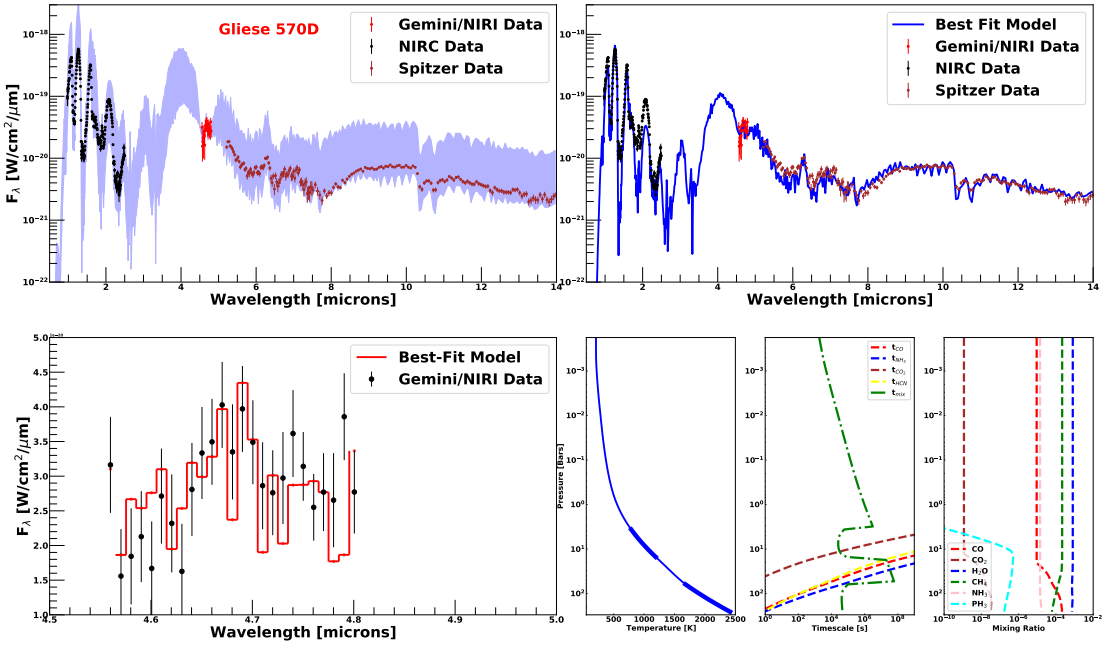

Figure 4.15: The **top left panel** shows the observed M-band spectra of Gl 570D with red points, the 1-2.5 μm observations of Gl 570D with black points and the *Spitzer* IRS measurements with brown points.. The flux values sampled by the top 131 models with the least G_k parameter after fitting the M-band spectra only are shown with the shaded blue region. The **top right panel** shows the best-fit model obtained by fitting the M-band spectra, the 1-2.5 μm data, and the *Spitzer* 5-14 μm data for Gl 570D. The **bottom left panel** shows a comparison of the best-fit model with the M-band spectra only. The **bottom right panels** shows the $T(P)$ profile of the best fit model, the $t_{\rm mix}$ and $t_{\rm chem}$ of different quenched species as a function of pressure, and the rightmost panel shows the volume mixing ratios of CO, CH_4, NH_3, H_2O, CO_2 and PH_3.

G_k parameter for these 131 models are distributed between 0.9899 and 1.9550.

The top left panel of Figure 4.15 shows the observed M-band spectrum of Gl 570 D (Geballe et al. 2009) with red points, the observed NIRC spectrum of Gl 570 D (Burgasser et al. 2002a) with black points, and the *Spitzer* IRS spectrum (Suárez & Metchev 2022) with brown points. The range of fluxes covered by the 131 best-fitting models to the M-band spectra only, are shown with the blue shaded region in the top left panel of Figure 4.15. All of these models fit the M-band spectrum well but

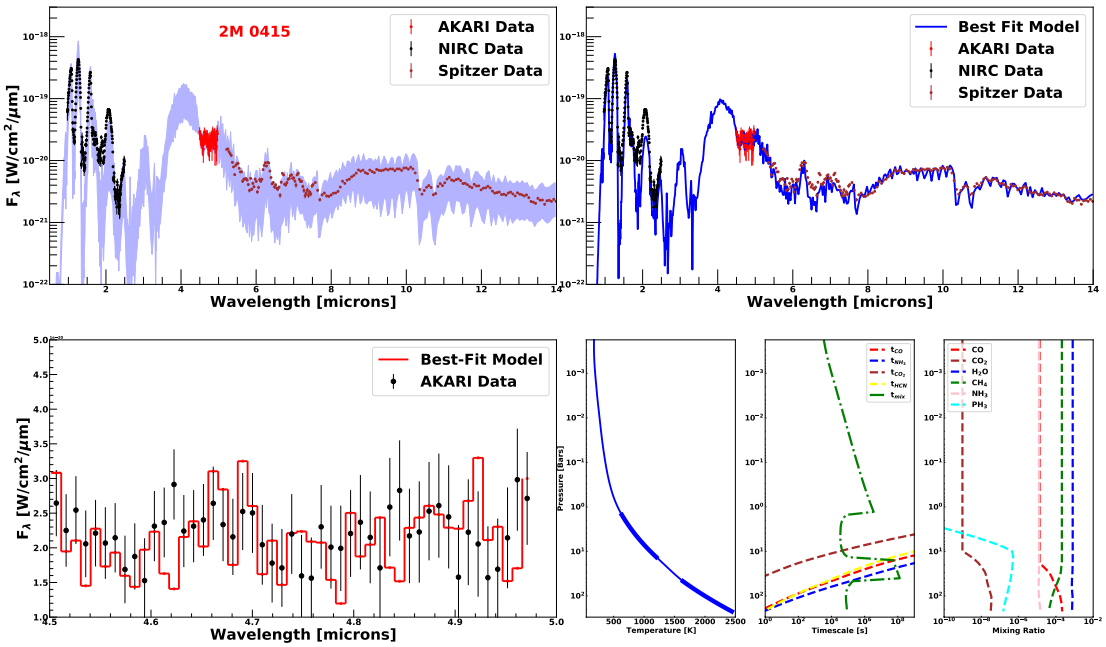

Figure 4.16: The **top left panel** shows the observed M-band spectra of 2M 0415 with red points, the 1-2.5 μm observations of 2M 0415 with black points and the *Spitzer* IRS measurements with brown points. The flux values sampled by the top 101 models with the least G_k parameter after fitting the M-band spectra only are shown with the shaded blue region. The **top right panel** shows the best-fit model obtained by fitting the M-band spectra, the 1-2.5 μm data and the *Spitzer* 5-14 μm data for 2M 0415. The **bottom left panel** shows a comparison of the best-fit model with the M-band spectra only. The **bottom right panels** shows the $T(P)$ profile of the best fit model, the $t_{\rm mix}$ and $t_{\rm chem}$ of different quenched species as a function of pressure, and the rightmost panel shows the volume mixing ratios of CO, CH_4, NH_3, H_2O, CO_2 and PH_3.

differ significantly in their fluxes in the shorter and longer wavelengths. We calculate a new set of G_k parameter for these 131 models but now with the NIRC and *Spitzer* IRS data only. The set of C_k parameters for each model, determined by fitting the M-band spectra already, are re-used for this, following the methodology of Sorahana & Yamamura (2012). The model among these 131 models that fits this shorter and longer wavelength data as well (has the least G_k) is taken to be the overall best-fit model from the grid. This model spectra is shown in Figure 4.15 top right panel and it has a G_k value of 669.06. This large difference between the G_k values from M-band data and the NIRC+IRS data is mainly because of the large difference in the uncertainties in the fluxes from these two sets of observations.

The best-fit model has a $T_{\rm eff}$ of 725 K and a log(g) of 5.0. The K_{zz} in the radiative zone for this model is Moses and the convective mixing length is $0.1 \times H$. The M-band spectra of this model compared to the M-band data for Gl 570D is also shown in the bottom left panel. The $T(P)$ profile, mixing timescale and chemical timescales, as well as the mixing ratio profiles of various gases in this model are shown in the three bottom right panels. The $T(P)$ profile and the $t_{\rm mix}$ profile both show that this model has two convective zones. The $t_{\rm chem}$ and $t_{\rm mix}$ shown in the middle panel of the bottom right part of Figure 4.15 also show that CO, CH_4, H_2O, HCN, and NH_3 are quenched in the sandwiched radiative zone for this best-fit model whereas CO_2 is quenched in the upper detached convective zone. The C_k value of this best-fit model is 1.72×10^{-19}. The measured parallax of Gl 570D is 171.22 mas (Dupuy & Liu 2012). This corresponds to a distance (D) of 5.84 pc. We get a radius of 1.04 R_J for Gl 570D combining these

values together. The radius of a brown dwarf with $T_{\rm eff}$=725 K and log(g)=5.0 can also be interpolated from evolutionary grids like the `SONORA BOBCAT` models (Marley et al. 2021). We find this interpolated radius to be 0.89 R_J which is somewhat smaller than our calculated radius. But as we also note in §4.3.4, these evolutionary tracks were computed assuming chemical equilibrium.

We use the same technique for fitting the AKARI M-band spectrum (Sorahana & Yamamura 2012) and the NIRC + *Spitzer* IRS spectrum (Burgasser et al. 2002a; Suárez & Metchev 2022) of 2MASS J0415-0935 (2M 0415). The top left panel of Figure 4.16 shows the M-band spectra of 2M 0415 with red points, the NIRC measurements are shown with black points, and the *Spitzer* IRS measurements are shown with brown points. The $min(G_k)$ obtained by fitting the M-band spectra only is 0.8755 and the flux range covered by all the models with G_k between 0.8755 and 1.8583 is shown with the blue shaded region in the top left panel. These models were then used to obtain the best-fitting model with the low and high wavelength data. The best-fit model has a G_k of 514.28. This model has a $T_{\rm eff}$ of 675 K and a log(g) of 4.75. The K_{zz} in the radiative zone for this model is Moses and the convective mixing length is $0.1 \times H$. The measured parallax of 2M 0415 is 175.2 mas (Dupuy & Liu 2012) which corresponds to a distance of 5.707 pc. Combining this with the best-fit model C_k value ($1.84{\times}10^{-19}$) provides a radius of 1.05 R_J for 2M 0415. The interpolated radius from the `SONORA BOBCAT` grid for this object is 0.98 R_J. This shows much better agreement with the calculated radius of the object compared to Gl 570D. The M-band spectrum of this best-fit model compared to the M-band data for 2M 0415 is also shown in the bottom

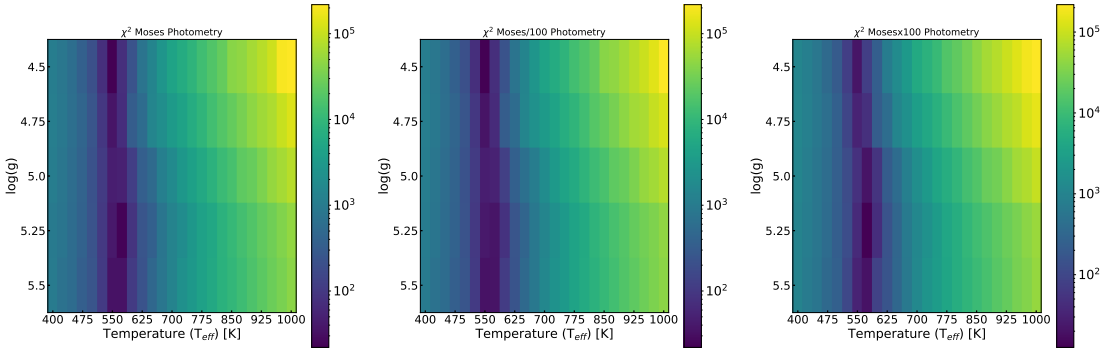

Figure 4.17: The **left panel** shows a heat map of the χ^2 value calculated using model photometry and observed photometry (Miles et al. 2020) in various infrared bands as a function of model $T_{\rm eff}$ and log(g) for WISE 0313. The left panel indicates models where radiative K_{zz} is fixed at Moses and the convective mixing length is H. The **middle and right panels** also show the χ^2 heat maps using models with radiative K_{zz} of Moses/100 and Moses×100, respectively. The best-fit $T_{\rm eff}$ is near 550 K.

left panel. Atmospheric properties of the best-fit model are shown in the three bottom right panels. This best-fit model has a second sandwiched radiative zone and CO, CH_4, H_2O, and HCN are quenched in this sandwiched radiative zone whereas CO_2 is quenched in the upper detached convective zone.

4.3.5.2 WISE 0313, UGPS 0722, WISE 2056 and WISE 1541

Miles et al. (2020) has obtained M-band observations of the late T and early Y-dwarfs WISE 0313, UGPS 0722, WISE 2056, and WISE 1541. However, these M-band spectra are not flux calibrated. Using photometry collected from various studies and the `SONORA` evolutionary tracks, Miles et al. (2020) found ranges of $T_{\rm eff}$ and log(g) values for these objects. We use our models along with these photometry datasets (see Table 2 in Miles et al. (2020) for photometry obtained from Skrutskie et al. (2006); Kirkpatrick et al. (2011); Lucas et al. (2010); Leggett et al. (2013); Schneider et al. (2015); Geballe

et al. (2001); Knapp et al. (2004); Leggett et al. (2015); Golimowski et al. (2004); Leggett et al. (2017); Patten et al. (2006); Kirkpatrick et al. (2012); Cutri et al. (2021); Luhman & Esplin (2016); Schneider et al. (2016); Wright et al. (2014); Esplin et al. (2016)) to find a similar range of $T_{\rm eff}$ values for each of these sources. Figure 4.17 shows the map of χ^2 values in a $T_{\rm eff}$ vs. log(g) parameter space obtained by comparing our models with observed photometry of WISE 0313. It is clear that the χ^2 values are sensitive to the $T_{\rm eff}$ of models but there is not much sensitivity to the log(g) of the models. This method helps us in identifying a range (δT = 100 K) of $T_{\rm eff}$ values for each object. Then using models within this $T_{\rm eff}$ range we try to determine the best-fit atmospheric model by comparing our model spectra shapes with the shape of the M-band spectra of these four objects. We use the same metric G_k and C_k defined in Equations 4.4 and 4.5 for finding the best-fit models. However, as the observed spectra lacks flux calibration, the C_k now includes the α parameter as well where $1/\alpha$ represents the unknown flux calibration of the observed spectrum. For each object, we use the models within the determined $T_{\rm eff}$ ranges and allow all the other parameters such as log(g), radiative zone K_{zz} and mixing length L to vary while calculating the G_k and C_k values of the models using the M-band spectrum. Then the model with the least G_k value is chosen as the best-fit model for the object.

Figure 4.18 shows the results of this fitting exercise for all the four objects. The four rows in Figure 4.18 shows the results for WISE 0313, UGPS 0722, WISE 2056, and WISE 1541, respectively. The left columns show the best-fit spectra compared with the observational data for each object. The second column from left shows the best-fit

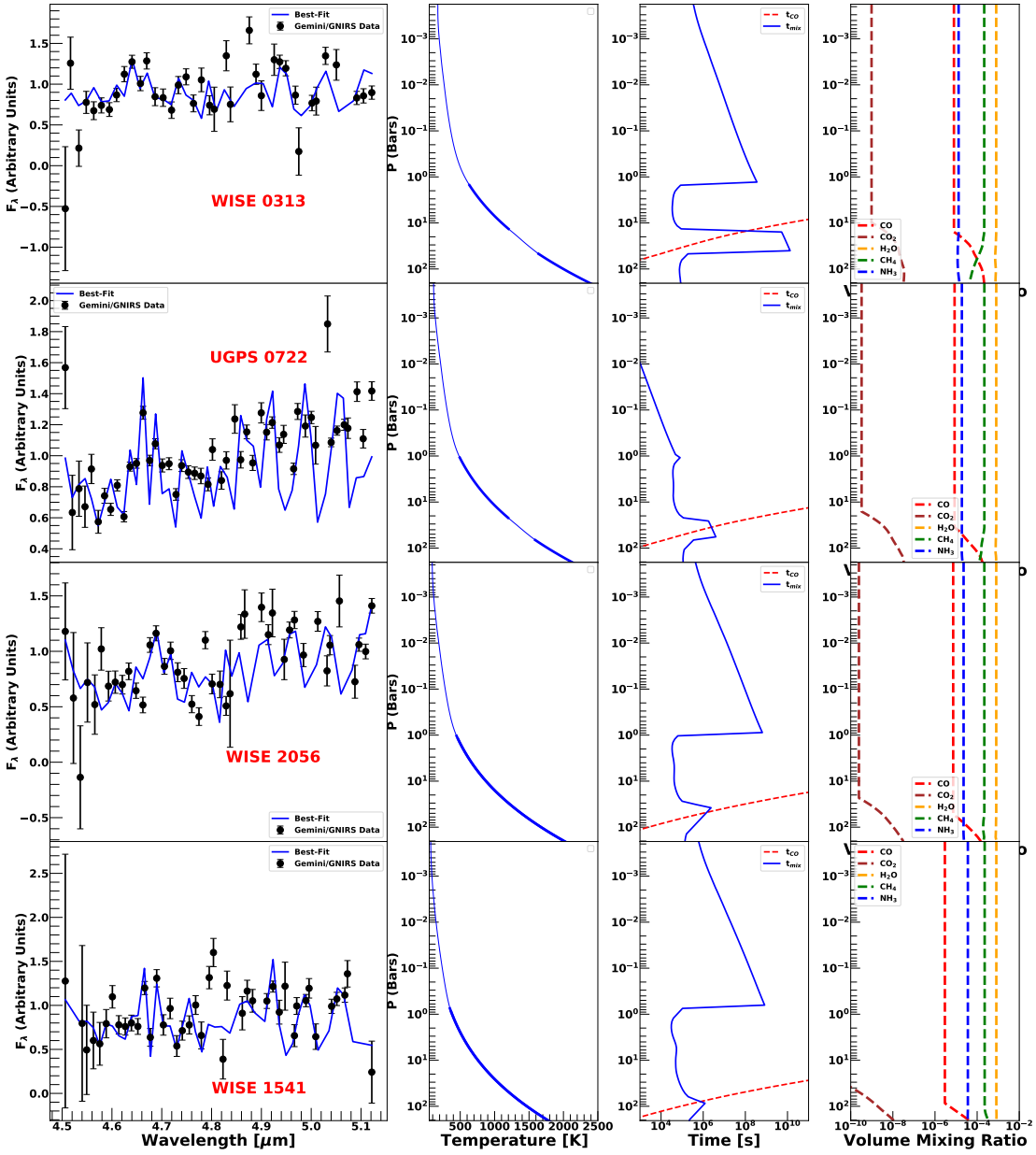

Figure 4.18: The best-fit atmospheric models and their comparison with data are shown in this figure. **Each row** corresponds to a different object. The **left most column** shows the best-fit M-band spectra along with the observed data from Miles et al. (2020). The **second left column** shows the best-fit $T(P)$ profile for these objects from the grid of models presented in this paper. The **third column shows** the best-fit mixing timescale in blue along with the chemical timescale for CO in red as a function of pressure. The volume mixing ratios of various atmospheric gases are shown in the **fourth column** for each object.

$T(P)$ profile for each object. The third column shows the best-fit mixing timescale and chemical timescale for CO as a function of pressure for these objects and the fourth columns depicts the best-fit volume mixing ratios for each object.

We find that the best-fit model describing the WISE 0313 and UGPS 0722 data have radiative zone quenching of CO/CH_4 whereas the best-fit models describing the WISE 2056 and WISE 1541 data has CO quenching in the convective zone. Table 4.1 shows the values of all the parameters relevant to fitting the spectral data for all of these objects. We note that the best-fit log(g) values obtained in this work are not from fitting any spectral shape/feature directly. As can be seen in Figure 4.5, log(g) controls the presence/absence of a sandwiched radiative zone which in turn dictates whether gases can be quenched in regions with low or high K_{zz}. These effects of log(g) on atmospheric chemistry lead to preference of certain log(g) values over others while fitting the data.

We choose our best-fit model to be the model with the least G_k value but we also find that there are quite a few models which have G_k values only differ from the minimum only by a small amount. This shows the presence of degeneracy in our models with the current precision of available data for these objects. This degeneracy will be broken with much higher precision flux calibrated M-band and shorter wavelength spectra expected from JWST which we discuss in §4.3.6.

Source	$T_{\rm eff}$ Range[K]	Best-Fit $T_{\rm eff}$[K]	Best-Fit log(g)	Radiative K_{zz}	Convective L	M-band G_k	J–H–K+*Spitzer*IRS G_k	C_k
Gl 570D	700–800	725	5.0	Moses	$0.1 \times H$	1.414	669.06	1.72×10^{-19}
2M 0415	600–700	675	4.75	Moses	$0.1 \times H$	0.925	514.28	1.84×10^{-19}
WISE 0313	575–675	675	4.75	Moses/100	$0.1 \times H$	3.849	–	6.477
UGPS 0722	500–600	575	4.75	Moses×100	$0.1 \times H$	23.884	–	11.636
WISE 2056	450–550	525	4.75	–	$0.1 \times H$	6.651	–	14.575
WISE 1541	400–450	450	4.75	–	$0.1 \times H$	5.243	–	20.275

Table 4.1: Results from fitting observed spectra of brown dwarfs with our model spectra. The radiative zone K_{zz} for models which do not quench at radiative zones are marked with a '–' as they couldn't be constrained.

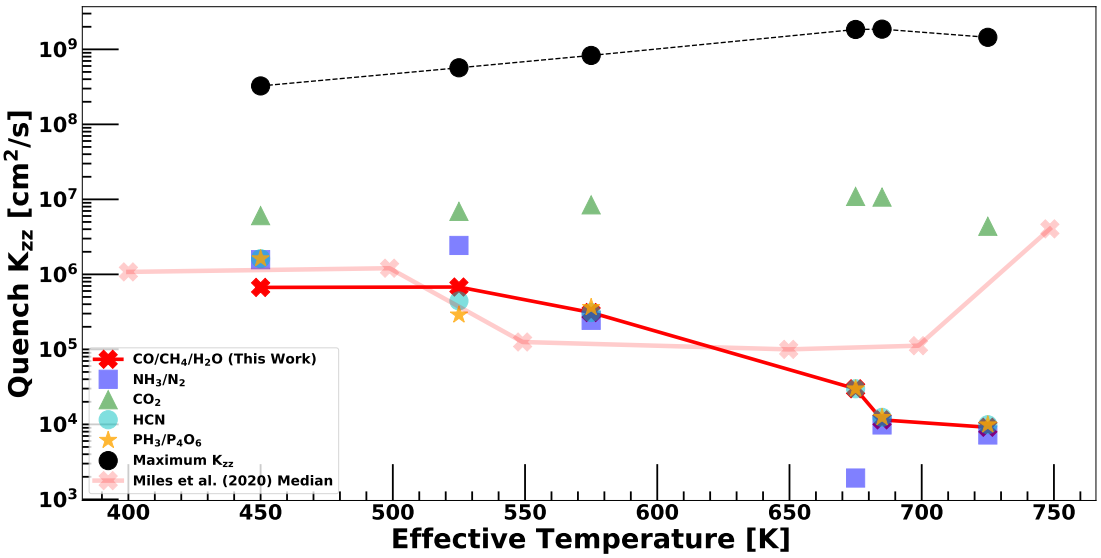

Figure 4.19: The best fit quench K_{zz} of CO for each object is shown as a function of their best-fit $T_{\rm eff}$ with the red crosses. The median best-fit quench K_{zz} vs. $T_{\rm eff}$ inferred by Miles et al. (2020) with lower gravity models are shown with the faded red crosses. The inferred quench K_{zz} for NH_3, CO_2, HCN, and PH_3 from the best-fit models for each object are also shown as a function of their best-fit $T_{\rm eff}$. The black points show the theoretically maximum K_{zz} allowed from mixing length theory for these best-fit models.

4.3.5.3 Trends in Quench Timescales

We present the trend of the best-fit K_{zz} at P_Q for CO in these sources in Figure 4.19. As we mainly fit the M-band spectra of these objects in our analysis, we are only sensitive to CO and H_2O abundances and therefore we can only fit the quench K_{zz} of CO. Our best-fit quench K_{zz} for CO as a function of the best-fit $T_{\rm eff}$ for each object are shown with red crosses in Figure 4.19. The best-fit quench K_{zz} determined by Miles et al. (2020) are shown with faded red crosses as a function of the best-fit $T_{\rm eff}$ obtained by Miles et al. (2020) for each object. Although the overall trend of much lower CO quench K_{zz} than the theoretical maximum in objects with $T_{\rm eff}$ between 600–800 K, found by Miles et al. (2020), still stands in this analysis, there are some differences in the best-fit K_{zz} and $T_{\rm eff}$ values between the two studies. These differences are due to multiple factors which we discuss briefly here.

Our work uses RCE models that include disequilibrium chemistry self-consistently to fit the data while equilibrium chemistry RCE models were post-processed by Miles et al. (2020) to include quenching of gases to fit the data. Figure 4.2 top left panel shows that including disequilibrium chemistry self-consistently can lead to large changes in the $T(P)$ profile of brown dwarfs compared to equilibrium chemistry models. This can be the reason behind the $\sim$ 50 K differences in the $T_{\rm eff}$ values for these objects between the two studies. For 5 of the 6 analyzed objects in this work, our assessment of CO quench K_{zz} are somewhat smaller than previously found. As some of our best-fit models have higher $T_{\rm eff}$ than the best-fit models of Miles et al. (2020), CO is more abundant in the

deeper atmosphere of our best-fit models than those of Miles et al. (2020). Figure 4.2 shows that CO abundance falls very rapidly with decreasing pressure in the deep atmosphere (which is under chemical equilibrium) in these colder brown dwarfs. Therefore colder best-fit models in Miles et al. (2020) need to quench CO deeper in the atmosphere than our hotter best-fit models. So, the best-fit models presented in Miles et al. (2020) need higher CO quench K_{zz} compared to our best-fit models to produce the same CO abundance in the upper well mixed atmosphere of these brown dwarfs. Additionally, the best-fit K_{zz} presented in Miles et al. (2020) has been shown to be dependant on the gravity of the model used for fitting the data. In this work, we allowed gravity to be a free parameter while fitting the data and compared our best-fit K_{zz} in Figure 4.19 with the median K_{zz} obtained by Miles et al. (2020) by trying out various values of log(g).

We can use our best-fit models with CO quenching to infer the quench K_{zz} of other quenched gases like CO_2, NH_3 or HCN in these best-fit models. The inferred quench K_{zz} values for the other gases in these objects are also shown in Figure 4.19. As each gas has a different $t_{\rm chem}$, they also are quenched at different depths of the brown dwarf atmosphere as shown in Figure 4.7 and 4.9 for CO and CO_2. This means that measuring the abundance of each gas can help us in measuring the height dependant K_{zz} profile in these brown dwarf atmospheres. For example, in Figure 4.19, the inferred quench K_{zz} for CO_2 are very different than the inferred quench K_{zz} of CO (or NH_3) as CO_2 is quenched at different pressures (having different mixing strengths) compared to CO. But inferring the height dependant K_{zz} profile of a single brown dwarf by using different gases as probes of K_{zz} at different pressures is only possible with self-consistent

disequilibrium chemistry models with height dependant K_{zz} profiles such as the model grid presented in this work.

The theoretical maximum limit on convective zone K_{zz} for each best-fit model is also shown with black points in Figure 4.19. This maximum limit on convective K_{zz} was calculated using Equation 4.2 with the convective heat flux fixed at $\sigma {T_{\rm eff}}^4$ and the mixing length L fixed at the scale height of the atmosphere. It is clear from Figure 4.19 that all the gases in all these objects quench at lower K_{zz} than this theoretical limit. But even though all the objects analyzed in this work have much smaller CO quench K_{zz} than the maximum convective limit shown with the black line, this does not mean that all these "quenchings" occurred in the radiative zones in our models. For Gl 570D, 2M 0415, W0313, and UGPS 0722, CO is quenched in the radiative zones in our best-fit models but for W 2056 and W 1541 CO along with all the other molecules are quenched in the convective zone with a much smaller mixing length than the scale height of the atmosphere as was also suggested by the CMD analysis detailed in §4.3.4. Finally, we note that our best-fit models, especially for objects which lack flux-calibrated spectra, are often degenerate with the present data, and better data from observatories like JWST will be instrumental in giving us better constraints on the K_{zz} of these objects, which we discuss next.

4.3.6 Constraining Radiative Zone K_{zz} with JWST

An important takeaway from Miles et al. (2020) and our work is that detailed analysis of atmospheric abundances can constrain K_{zz} in brown dwarf atmospheres.

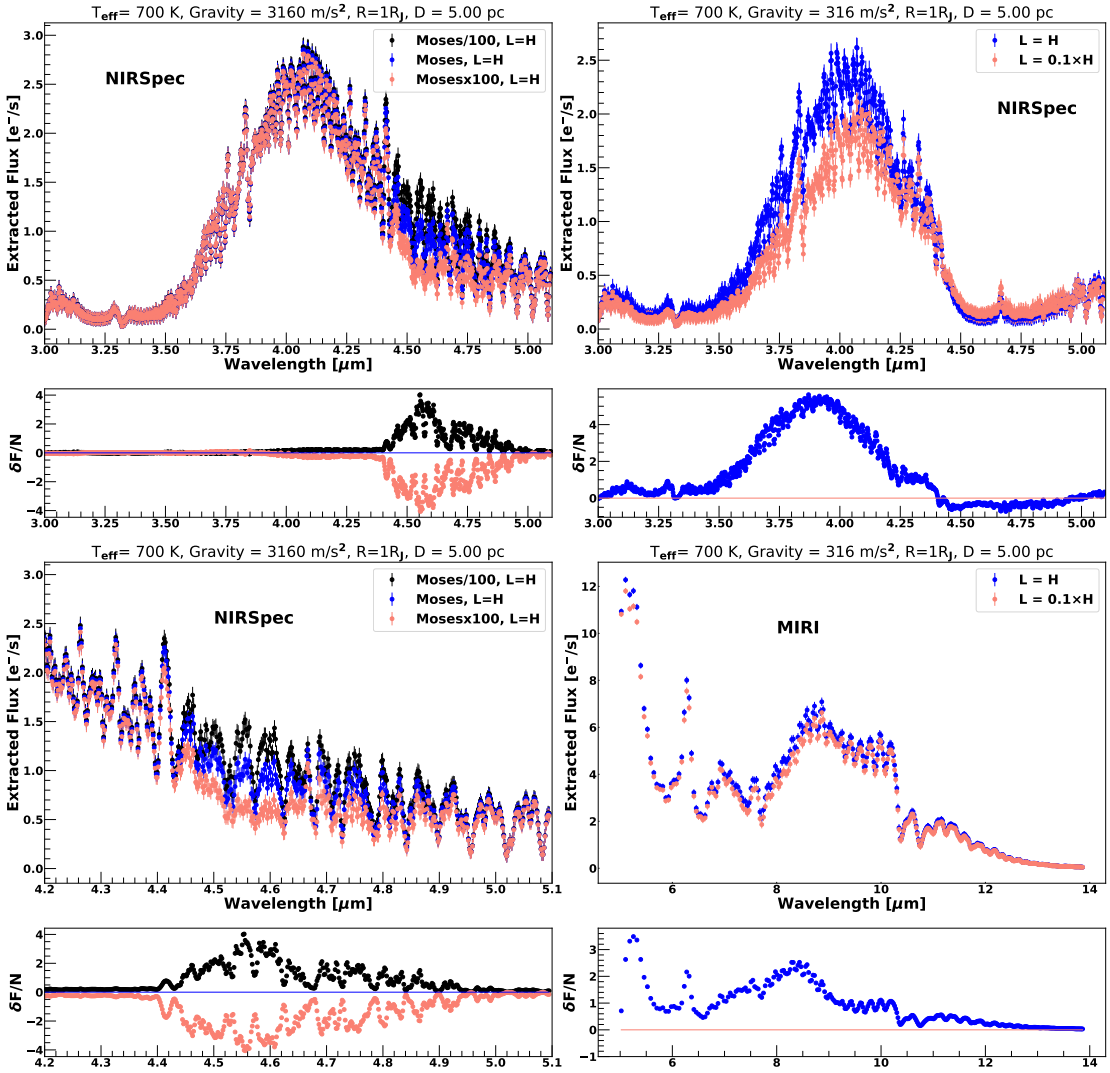

Figure 4.20: Simulated data from JWST instruments are shown for one of our model brown dwarfs with $T_{\rm eff}$ of 700 K. The three colors in the simulated data correspond to models with different radiative zone K_{zz}. The **top left panel** shows the simulated NIRSpec spectra of a log (g)=5.5 object with an exposure time of 10 minutes while the **bottom left panel** shows a zoomed version of the top left panel to emphasize how JWST NIRSpec M-band observations can clearly distinguish between different K_{zz} in the radiative zones for these T-dwarfs. The **top right panel** shows the NIRSpec simulated data for a brown dwarf with $T_{\rm eff}$ of 700 K and log(g) of 4.5. The two colors represent different K_{zz} in the convective zone but the same K_{zz} in the radiative zone. The **bottom right panel** shows MIRI LRS simulated data for the same models shown in the top right panels. To compare the differences between the simulated data from different models to the typical JWST noise, the ratio of the flux differences (δF) between various models and the simulated JWST noise (N) is shown below each of these panels. This shows that both convective and radiative zone K_{zz} can be constrained with JWST.

There is strong evidence for mixing orders of magnitude weaker than expectations from free convection with $L = H$. The launch of JWST begs the question of whether JWST data will be able to give us better constraints on the vigor of vertical mixing in these atmospheres. We can provide a test by simulating the JWST spectra using the JWST Exposure Time Calculator (Pontoppidan et al. 2016) with some of the emission spectra from our model grid. As an illustrative example, we use the spectrum of a 700 K object. In the left panels of Figure 4.20 we examine three models at log(g) of 5.5, where the radiative zone K_{zz} is "Moses×100", "Moses", and "Moses/100" and $L = H$. We assume that the source has a radius of $1 R_J$ and is at a distance of 5 pc. The temperature and distance chosen for this exercise are somewhat representative of objects like Gl 570D and 2M 0415.

The NIRSpec panels (which is 3 of the 4 figures) assume fixed slit mode with the G395M grating and the F290LP filter for these simulations. The results are impressive, with only a total of 10.39 minutes exposure time, simulated with 10 groups per integration, 2 integration per exposure, and 5 exposures. It is clear from the top left panel that the radiative zone K_{zz} can be constrained with high precision with about a total $\sim$ 10 minutes exposure time per object in this JWST observing mode. This time includes all the 5 exposures used for this simulation. In order to emphasize the difference arising in the synthetic counts from the three models in the 4.5-5 μm range, the bottom left panel shows a zoomed in view of the 4.3-5 μm wavelength range, focusing on CO absorption, where the main sensitivity of the data to radiative zone K_{zz} lies. The top right panel shows a lower-gravity model (log (g)=4.5), where a lower pressure

photosphere favors CO at the expense of CH_4. Here the blue model is simulated from a model where the convective mixing length $L = H$ whereas the salmon colored data is simulated from a model where the convective mixing length is $L = 0.1 \times H$. The radiative zone K_{zz} of both the cases in this panel are "Moses×100". Both of these models have the quenching of all relevant gases occurring in the convective zone. The large differences in the synthetic counts between the two models in the 3.5–4.25 μm range shows that JWST data can also be used to probe differences in the convective zone K_{zz} with exposure times of $\sim$ 10 minutes.

Radiative and convective zone K_{zz} can be probed with other wavelengths as well. The bottom right panel in Figure 4.20 shows the simulated spectrum of the two cases shown in the top right panel but when observed by the MIRI instrument. The MIRI LRS mode was used for this data simulation along with a 60 minutes exposure time. Differences between the two model spectra arise between 5–9 μm. A comparison with Figure 4.1 shows that these differences mainly arise from different CH_4, H_2O and NH_3 abundances due to differences in the convective zone K_{zz}.

4.4 Discussion

4.4.1 PH_3 Quenching

Under chemical equilibrium conditions the major phosphorus-bearing molecule PH_3 is expected to be removed by oxidation at low temperatures in the visible atmospheres of giant planets and colder brown dwarfs. A number of oxidation products

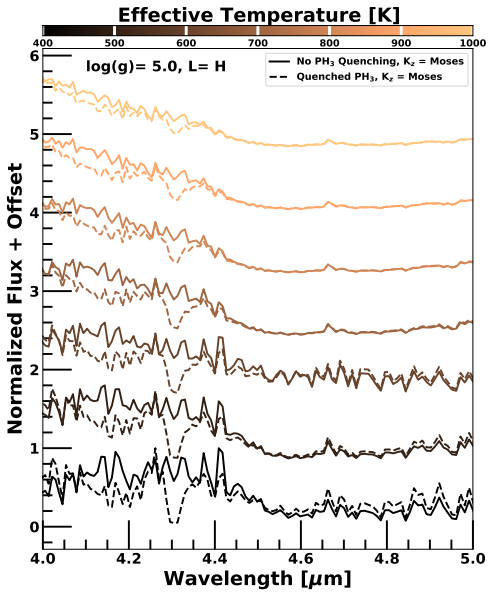

Figure 4.21: Effect of PH_3 quenching on the spectrum has been shown by comparing them with disequilibrium chemistry model spectra where PH_3 is not quenched. Models with different $T_{\rm eff}$ values ranging from 400 K to 1000 K, with a step of 100 K, are shwon from bottom to top. All of these models have log(g)=5.

have been considered (see Visscher 2020), including P_4O_6 (e.g., Fegley & Lodders 1994; Visscher et al. 2006), P_4O_{10} (Borunov et al. 1995), H_3PO_4 (Wang et al. 2016), or condensation of $NH_4H_2PO_4$ (Fegley & Lodders 1994; Visscher et al. 2006; Morley et al. 2018). Following the work of Visscher & Fegley (2005); Visscher et al. (2006); Miles et al. (2020), as a representative example of PH_3 oxidation we may consider the conversion of PH_3 into P_4O_6 via the net thermochemical reaction,

$$P_4O_6 + 12H_24PH_3 + 6H_2O \tag{4.6}$$

However, the $t_{\rm chem}$ of $PH_3 \rightarrow P_4O_6$ is such that it can be quenched in the deeper atmosphere, leading to a large enhancement of PH_3 in the photosphere. This effect makes PH_3 the major phosphorus bearing gas in atmospheres of Jupiter and Saturn (Lodders

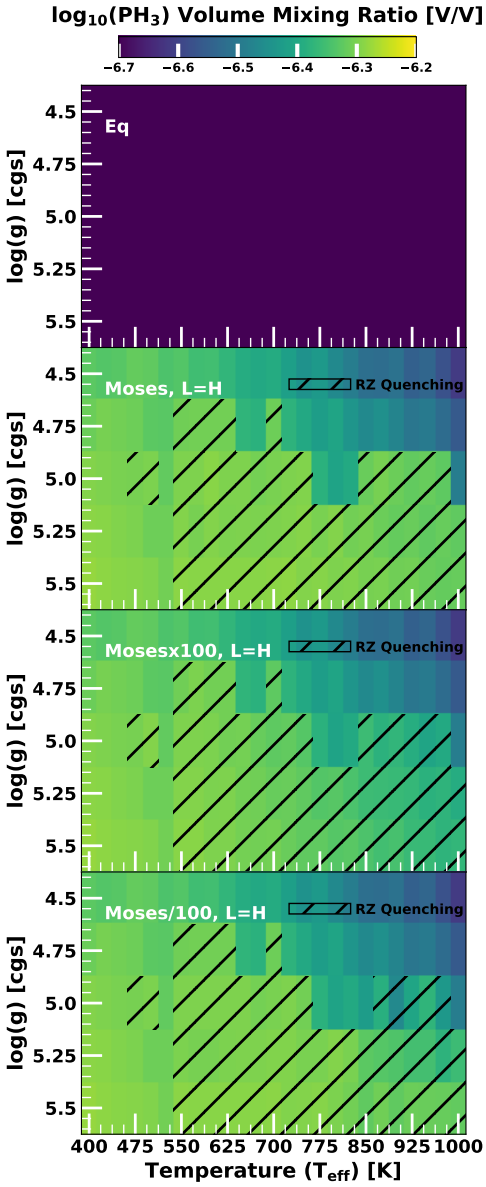

Figure 4.22: **Top panel** shows the equilibrium chemistry abundance of PH_3 at pressures where $T(P)= T_{\rm eff}$ in our $T_{\rm eff}$ vs. gravity grid of chemical equilibrium models. The **second, third and last panels** depict PH_3 abundance within the $T_{\rm eff}$ vs. gravity parameter space in our disequilibrium chemistry models. The second, third and last panels correspond models with radiative zone K_{zz} values of "Moses", "Moses×100", and "Moses/100", respectively while the convective zone mixing length L was fixed at the scale height H. Models where PH_3 was quenched in a radiative zone are marked with black hatches. PH_3 was quenched at a convective zone in the rest of the models.

2004; Visscher & Fegley 2005). PH_3 is expected to be found in colder brown dwarfs as well (Visscher et al. 2006; Morley et al. 2018).

Due to expected small affect of P-bearing molecules on brown dwarf temperature structures, we did not include PH_3 as a molecule to be mixed on–the–fly for converging to a final atmospheric state. However, in order to test the effect of PH_3 on the emergent thermal emission spectra, we post-process our converged disequilibrium chemistry model with quenched PH_3 abundance. The $t_{\rm chem}$ for $PH_3 \rightarrow P_4O_6$ is given by Visscher & Fegley (2005),

$$t_{\rm chem} = \frac{1.9 \times 10^{12}}{[\rm OH]} \exp\left(\frac{6013.6}{T}\right) \rm s \tag{4.7}$$

where [OH] represents the number density of OH molecules in units of $\rm cm^{-3}$. With our converged disequilibrium chemistry modules, we calculate the mixing ratio of OH molecules using Visscher & Fegley (2005),

$$X_{\rm OH} = \frac{K X_{\rm H_2O} \sqrt{X_{\rm H_2}}}{\sqrt{P}} \tag{4.8}$$

where $X_{\rm OH}$, $X_{\rm H_2O}$, and $X_{\rm H_2}$ represent the volume mixing ratios of each of these components and P represents the pressure in bars. The constant K is temperature dependant and based on fits to thermodynamic data, and is given by,

$$K = 3.672 - \frac{14791}{T} \tag{4.9}$$

where T is the temperature in K. Using Equations 4.7, 4.8, and 4.9 we determine the

$t_{\rm chem}$ of PH_3 for all our converged models. Then using our converged $t_{\rm mix}$ profiles we determine P_Q for PH_3 and quench it creating another set of our models which has quenched PH_3 abundances. Using these modified chemical compositions, we create another set of thermal emission spectra models with quenched PH_3 abundances. Figure 4.21 compares the differences in spectra caused by the quenching of PH_3 with disequilibrium models where PH_3 is not quenched. This quenching of PH_3 increases the PH_3 volume mixing ratios dramatically, from $\leq 10^{-30}$ under chemical equilibrium, to $\sim 10^{-6}$ to 10^{-7} due to quenching. The main impact of this increase appears between 4-4.5 μm in the thermal emission spectrum as shown in Figure 4.21. This also suggests that PH_3 may become an important enough atmospheric opacity source to have a small effect on their $T(P)$ profiles as well, which we will aim to explore in future work.

Figure 4.22 shows the parameter space of models where PH_3 quenches at the radiative zone and convective zones for different levels of radiative zone K_{zz} when the convective mixing length is H. This also shows that depending on the properties of the object in question, PH_3 can also be used as a probe for determining radiative or convective zone K_{zz}. The region around 4.0-4.4 μm is difficult to probe from the ground (Miles et al. 2020), but it is clear from Figure 4.21 that these PH_3 should be readily detectable with *JWST*. Interestingly, Morley et al. (2018) didn't detect PH_3 between 4.0-4.4 μm in WISE 0855 even though it is expected to be present in it's atmosphere theoretically. Determining the strength of these features, or their absence, will have important implications in understanding K_{zz} and phosphorus chemistry.

4.4.2 Clouds

The models presented in this work are cloud-free. However, H_2O condensation in the upper atmospheres of objects can begin at $T_{\rm eff} \leq 450$ K (Morley et al. 2014b) and these clouds can start becoming an important opacity source colder than ~ 400 K (Morley et al. 2014b). Once water clouds become optically thick, they can change the overall energy balance of the atmosphere impacting the $T(P)$ profile. The presence of disequilibrium chemistry causes a cooling down of the upper atmosphere, compared to equilibrium chemistry, but the opacity of clouds has the opposite effect of heating up the $T(P)$ profile.

Importantly, the cloud particle size and vertical extent are also quite sensitive to the mixing parameter K_{zz} as mixing helps to keep cloud particles aloft against their gravitational settling (Ackerman & Marley 2001a). Cloud particle sizes are an extremely important parameter in dictating their scattering properties (Mukherjee et al. 2021b; Ackerman & Marley 2001a) and hence K_{zz} has a large effect on the cloud opacities in these atmospheres. Therefore, it is clear that information gleaned on K_{zz} from disequilibrium chemistry studies will be important in improving cloud models. Future studies should aim for a self-consistent treatment of disequilibrium chemistry and cloud formation with a self-consistent treatment of K_{zz} within a given model atmosphere. Recently, Mang et al. (2022) showed that water clouds have a large impact on the M-band spectra of colder Y-dwarfs, with $T_{\rm eff} \leq 400$ K, just below the lower T edge of our study. Somewhat different than this work, Mang et al. (2022) calculated the radiative

zone K_{zz}, needed for cloud modeling, by setting the mixing length to one–tenth of the scale height in the radiative zones. This approach also leads to smaller K_{zz} in the radiative zones compared to the convective zones. When we extend our disequilibrium chemistry model to colder objects, inclusion of clouds in this framework is an important milestone.

4.5 Summary and Conclusion

In this work, we have used a newly developed Python–based 1D radiative-convective equilibrium model with the capability to self-consistently capture disequilibrium chemistry in brown dwarf and exoplanet atmospheres. Using this model we have created a self-consistent grid of brown dwarf models between $T_{\rm eff}$ of 400-1000 K with an increment of 25 K and log(g) of 4.5-5.5 with an increment of 0.25. Instead of using a constant K_{zz} prescription throughout the entire atmosphere as done in earlier work (e.g. Karalidi et al. 2021a; Phillips et al. 2020) or self-consistent K_{zz} in the convective zones and constant K_{zz} in the radiative zones (e.g. Hubeny & Burrows 2007), we use a self-consistent $T(P)$ structure dependant K_{zz} profile for the entire atmosphere for our grid. In the convective zone, we use mixing length theory with two different mixing lengths whereas in the radiative zones we use various multiples of a T and P-dependent K_{zz} prescription. The idea behind these models was to assess whether disequilibrium chemical abundance can be used as a probe for temperature structure and mixing processes below the visible atmosphere in brown dwarfs. With this grid in hand, we conclude on

the following points.

1. As found by others, a self-consistent treatment of disequilibrium chemistry causes cooling of $T(P)$ profiles, especially in the upper atmospheres of late T and early Y-dwarfs.

2. Post-processing equilibrium chemistry models by quenching various molecules instead of using self-consistent models with disequilibrium chemistry should be avoided because this can lead to significant errors in the calculated abundances of molecules like CO, CH_4 and NH_3. This can also lead to incorrect $T(P)$ profiles. Both of these results are especially relevant in the JWST era with significantly higher S/N mid-infrared data.

3. Self-consistent models including disequilibrium chemistry also show a large change in the location, depths, and number of radiative and convective zones in brown dwarfs compared to self-consistent models with equilibrium chemistry.

4. Depending on the strengths of radiative zone K_{zz} and convective mixing length, gases like CO, CH_4, NH_3, CO_2 and PH_3 can be quenched in the radiative zones of brown dwarfs in a large fraction of the $T_{\rm eff}$ and log(g) parameter space.

5. Since different molecules have different $t_{\rm chem}$ values, which leads them to quench at different pressure levels. This means that some molecules may quench in radiative zones, while other may quench in convective zones, in the same atmosphere, such that different molecules may be quenched by very different K_{zz} values.

6. The M-band thermal spectra of objects where radiative zone quenching occurs, is very sensitive to the K_{zz} in the radiative zones. This can lead to non-monotonic behavior in the CO abundance and spectra as a function of $T_{\rm eff}$. This is especially exciting because it provides an avenue to observationally constrain the highly uncertain radiative zone K_{zz} in these objects.

7. The mid-infrared photometric bands – MKO L$^{'}$ and MKO M, and WISE 1 and 2, are quite sensitive to the K_{zz} in the radiative zone. We also find that our models provide a better fit to the infrared photometry of these objects than chemical equilibrium models.

8. We use our models to fit the M-band spectra of 6 brown dwarfs – Gleise 570 D, 2MASS J0415-0935, WISE 0313, UGPS 0722, WISE 2056, and WISE 1541. We determine the best-fit atmospheric state for these objects including the quench level K_{zz} of quenched gases in these objects. Similar to Miles et al. (2020), we also find that these objects have K_{zz} much smaller than the theoretical convective mixing limit. We also see that the best fit quench K_{zz} in these objects are very low between $T_{\rm eff}$ of 675-800 K while it shows an increase with lowering $T_{\rm eff}$ for objects with $T_{\rm eff}$ below 575 K.

9. By performing some signal–to–noise calculations for JWST, we conclude that short exposure time observations can provide us with excellent measurements of the radiative and convective zone K_{zz} in brown dwarfs.

10. We also expect JWST to find clearly detectable disequilibrium PH_3 abundances

in the atmospheres of these objects.

The non-monotonic behaviour of atmospheric chemistry, as a function of $T_{\rm eff}$ and log(g), found in this work indicates the need to explore these effects with even finer grid spacing than this work in parameters like $T_{\rm eff}$ (25 K in this work), log(g) (0.25 dex in this work), and K_{zz} (factor of 100 in this work). This remains the focus of a future model grid release. The model presented in this work will be updated to include self-consistent clouds in the near future. Additional future work will couple the code to the chemical kinetics model `VULCAN` (Tsai et al. 2017, 2021) which would enable a more rigorous self-consistent treatment of disequilibrium chemistry in our models. This will also allow us to include effects like the feedback of the disequilibrium abundances of gases like CH_4 on the entire chemical network of the atmosphere within our models, self-consistently. This will also allow us to explore the empirical trends we find in this work, like probable slower convective mixing than typically calculated assuming free convection, more robustly. Moreover, such a coupling opens up the possibility to explore both photochemistry and vertical mixing together self-consistently, which is more relevant for irradiated exoplanets. This updated model will then be used to explore effects of vertical mixing and photochemistry for warm transiting giant planets and find additional observables to constrain K_{zz} in such planets, an important comparison sample to the non-irradiated objects explored here.

Chapter 5

The Sonora Substellar Atmosphere Models. 4. Elf Owl: Atmospheric Mixing and Chemical Disequilibrium with Varying Metallicity and C/O Ratios

5.1 Introduction

Exoplanet and brown dwarf atmospheres are primarily molecular due to their low temperatures and high pressures. The chemical composition of these atmospheres is dictated by the interplay between temperature- and pressure-dependant chemical reactions and atmospheric dynamical mixing processes.. The rates of molecular reactions

are influenced by the atmospheric pressure-temperature structure and the inventory of chemical elements in the atmosphere. The atmosphere is said to be in chemical equilibrium if its chemistry is determined by thermochemical reactions based on the local pressure and temperature conditions. But processes like dynamical mixing can cause substellar atmospheres to deviate from chemical equilibrium (Fegley & Lodders 1996; Noll et al. 1997; Moses et al. 2011; Zahnle & Marley 2014; Tsai et al. 2021; Lee et al. 2023) if mixing timescales are faster than the timescales of chemical reactions. However, dynamical mixing remains one of the most uncertain and poorly understood aspect of substellar atmospheres.

Dynamical mixing and its effects on atmospheric chemistry is a well-studied process in Solar System planetary atmospheres (e.g., Prinn & Barshay 1977; Yung et al. 1988; Bjoraker et al. 1986; Zhang & Showman 2018b; Zhang et al. 2012; Allen et al. 1981; Nair et al. 1994; Moses et al. 2005; Li et al. 2014; Visscher et al. 2010c; Visscher & Moses 2011; Wong et al. 2017). However, as most brown dwarfs and strongly irradiated exoplanets belong to a very different temperature–pressure regime, dynamical processes in their atmospheres are still poorly understood.

5.1.1 Why is constraining K_{zz} important?

Atmospheric dynamics can transport gases and clouds/dust particles across several pressure scale-heights in the radial direction of substellar atmospheres (e.g., Parmentier et al. 2013a; Tan 2022; Freytag et al. 2010). This process is often called vertical mixing. Under this *assumption* that this mixing can be modeled as a diffusion

process, it is typically parameterized by the vertical eddy diffusion parameter – K_{zz} [cm^2/s]. K_{zz} is influenced by the rate of atmospheric turnover and heuristically K_{zz} can be understood as the product of the lengthscale over which mixing is occurring and the mixing velocity (Chamberlain & Hunten 1987). A high value of K_{zz} represents a very dynamically active atmosphere, whereas a low value represents a scenario with slow, inefficient mixing. In the convective parts of the atmosphere, the rate of mixing is expected to be linked with the convective energy flux, and indeed mixing length theory (MLT) provides estimates for K_{zz} (e.g., Gierasch & Conrath 1985b; Ackerman & Marley 2001a). In the radiative atmospheres, other dynamical processes, such as the breaking of atmospheric waves, can control the mixing and as a result, influence the value of K_{zz}.

A complete understanding of atmospheric dynamical mixing thus requires constraints on K_{zz} both in the convective and radiative parts of the atmosphere. Currently, K_{zz} in brown dwarf and exoplanet atmospheres remains uncertain by more than a factor of a million (Lacy & Burrows 2023; Mukherjee et al. 2022; Karalidi et al. 2021a; Phillips et al. 2020; Fortney et al. 2020; Zahnle & Marley 2014; **?**; Barman et al. 2015). Theoretical estimates of K_{zz} profiles for a series of brown dwarf atmospheres with changing $T_{\rm eff}$ from Mukherjee et al. (2022) are shown in Figure 5.1, left panel. The right panel of Figure 5.1 shows the dependence of theoretical K_{zz} profiles on $\log(g)$. These theoretical estimates show that K_{zz} can vary by orders of magnitude due to changes in both of these parameters. Moreover, in the same atmosphere, K_{zz} can vary by several orders of magnitude depending on whether a particular part of the atmosphere is radiative or convective in nature. Such variation of K_{zz} across radiative or convective regions is

also seen in stellar models (e.g., Varghese et al. 2023). Figure 5.1 also shows that the position of convective and radiative zones can also be a strong function of both $T_{\rm eff}$ and $\log(g)$.

Constraining K_{zz} is crucial to understand the physical nature of atmospheric dynamics operating in the deep atmospheres of brown dwarfs and exoplanets, as well as the implications for atmospheric chemistry and clouds, both of which have large imprints on the observed spectra of these objects. Atmospheric mixing dredges up gases from the deep atmosphere to the upper, visible atmosphere. If these gases are chemically destroyed faster than the typical timescale of mixing, then the atmosphere remains in thermochemical equilibrium. However, if the mixing process is faster than the chemical reaction timescales, then the upper atmosphere no longer remains in thermochemical equilibrium (Moses et al. 2011; Tsai et al. 2017, 2021; Zahnle & Marley 2014; Visscher & Fegley 2005; Visscher et al. 2006; Visscher & Moses 2011). This causes large changes in the chemical composition and optical depths of the observable photosphere thus changing the observable spectrum of the object (e.g., Phillips et al. 2020; Tremblin et al. 2015; Lacy & Burrows 2023; Karalidi et al. 2021a; Mukherjee et al. 2022; **?**; Lee et al. 2023).

Vertical mixing can also transport gaseous vapor from the deeper atmosphere to the colder atmosphere where they can condense and form clouds (e.g., water clouds in Y-dwarfs, Fe clouds in L-dwarfs) (e.g., Ackerman & Marley 2001a; Morley et al. 2014a, 2012; Saumon & Marley 2008; Woitke et al. 2020; Lacy & Burrows 2023; Freytag et al. 2010; Allard et al. 2012b; Helling et al. 2017; Lee et al. 2016; Gao & Benneke 2018a;

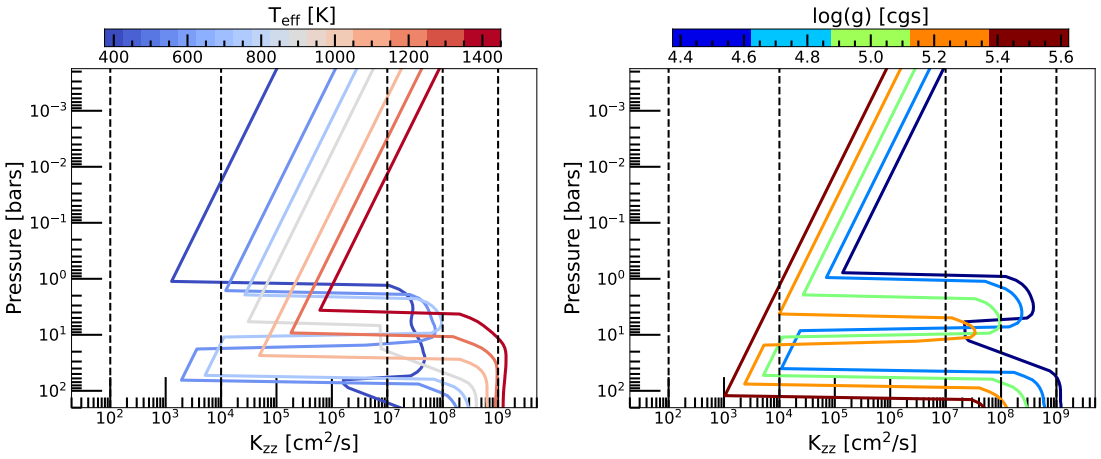

Figure 5.1: The left panel shows self-consistently calculated K_{zz} profiles as a function of pressure for a series of solar composition model atmospheres with $T_{\rm eff}$ from 1500 K to 400 K and log(g)=5.0. The K_{zz} in the convective zone has been calculated with mixing length theory whereas the K_{zz} in the radiative atmosphere follows the parameterization in Moses et al. (2021). The right panel shows the K_{zz} profiles for a 700 K model with varying log(g) between 4.5 and 5.5. The black dashed lines depict the constant K_{zz} profiles used in this work for sampling the several orders of magnitude range in K_{zz} values covered by these model calculations. Some colder models in the left panel with $T_{\rm eff}$ between 500-800 K show a sharp drop and rise in K_{zz} in the deep atmosphere which is indicative of the presence of a detached radiative zone in their atmospheres. Similar behaviour is also present in low gravity models shown in the right panel.

Charnay et al. 2018; Cooper et al. 2003; Helling et al. 2001). Moreover, mixing can keep these cloud particles lofted in the photosphere by counteracting their gravitational settling. These lofted cloud particles "redden" the spectrum of substellar objects with their absorption and scattering opacities and also tend to heat up the deeper atmosphere by absorbing additional thermal radiation (e.g., Saumon & Marley 2008; Morley et al. 2012, 2014a; Luna & Morley 2021; Gao et al. 2020c; Mang et al. 2022; Lee et al. 2016; Tan 2022). Even though it is highly uncertain, K_{zz} plays a major role in influencing the key atmospheric components of substellar objects like atmospheric chemistry, clouds, and the temperature–pressure ($T(P)$) structure (e.g., Drummond et al. 2016). With highly sensitive and stable instruments like *JWST*, previous studies have shown that the dependence of atmospheric chemistry and clouds on K_{zz} can be leveraged to constrain K_{zz} itself (e.g., Miles et al. 2020; Karalidi et al. 2021a; Mukherjee et al. 2022; Phillips et al. 2020).

Theoretical models have studied the effects of K_{zz} on the atmospheric chemistry and spectra previously for brown dwarfs and directly imaged planets with solar atmospheric composition. Karalidi et al. (2021a) and **?** have probed these effects with pressure-independent constant K_{zz} profiles for solar composition substellar atmospheres, whereas Phillips et al. (2020) have studied these effects at solar metallicity with pressure-independent but gravity dependant K_{zz} profiles. K_{zz} in the radiative regions can vastly differ from K_{zz} in the convective regions due to the completely separate turnover mechanisms operating in each regime. Mukherjee et al. (2022) explored the $T_{\rm eff}$-$\log(g)$ parameter space of solar-composition brown dwarf atmospheres and iden-

tified ways to measure K_{zz} in the radiative as well as convective atmosphere of these objects with *JWST*. Lacy & Burrows (2023) explored a self-consistent treatment of both water clouds and disequilibrium chemistry due to mixing for Y-dwarfs with solar and slightly sub- or supersolar metallicities. Using ground-based spectroscopic observations and solar composition atmospheric models, Miles et al. (2020) measured K_{zz} in a series of late T- and early Y- dwarfs and observed a sharp increase in K_{zz} at $T_{\rm eff}\sim$ 400 K. It was hypothesized in Miles et al. (2020) that this low to high K_{zz} transition is due to the presence of "sandwiched" radiative zones in the deep atmospheres of objects with $T_{\rm eff}$ between 400-800 K, which was later theoretically confirmed in Mukherjee et al. (2022). This was a great demonstration of how constraining the uncertain K_{zz} can help us in gaining fundamental insights into the atmospheres of brown dwarfs and planets. However, not all brown dwarf atmospheres are expected to be of solar composition (e,g, Line et al. 2017; Zalesky et al. 2019; Zalesky et al. 2022; Meisner et al. 2023; Beiler et al. 2023; Hoch et al. 2023), and mixing-induced disequilibrium chemistry in non-solar composition atmospheres hasn't been sufficiently explored.

5.1.2 Metallicity, C/O Ratio, and K_{zz}

Bayesian retrieval studies of a growing population of brown dwarfs have revealed non-solar composition atmospheres. These range from very metal-poor atmospheres (e.g., Meisner et al. 2023; Zhang et al. 2021b; Line et al. 2017; Zalesky et al. 2019; Zalesky et al. 2022; Burgasser et al. 2023) to objects with enhanced atmospheric metallicities (e.g., Zhang et al. 2021b; Line et al. 2017; Zalesky et al. 2022; Zalesky

et al. 2019; Zhang et al. 2023). Significant scatter in the atmospheric carbon–to–oxygen (C/O) from sub-solar to super-solar values has also been established in the literature (e.g., Calamari et al. 2022; Zalesky et al. 2022; Zalesky et al. 2019; Line et al. 2017; Hoch et al. 2023). Published *JWST* observations of objects like VHS 1256b and HD 19467b already reveal strong signatures of chemical disequilibrium (Miles et al. 2022; Greenbaum et al. 2023; Beiler et al. 2023) in addition to ground-based and space-based observations of brown dwarfs obtained in the past two decades (e.g., Noll et al. 1997; Oppenheimer et al. 1998; Sorahana & Yamamura 2012; Miles et al. 2020; Madurowicz et al. 2023). Available and upcoming *JWST* data from brown dwarfs and directly imaged planets are expected to show the presence of both vertical mixing induced disequilibrium chemistry and deviations from solar composition atmospheres.

Vertical mixing induces large changes in the photospheric abundances of gases like CO, CH_4, NH_3, CO_2, N_2, PH_3, and H_2O by quenching their abundances in the deeper atmospheres. These gases are particularly affected due to vertical mixing as they have very long chemical reaction timescales. For example, the conversion of N_2 to NH_3 or CO to CH_4 requires the breaking of strong molecular bonds. However, the abundances of all these gases are also sensitive to atmospheric metallicity and the C/O ratio. Elevated atmospheric metallicity leads to an increase in all these gases in the atmosphere to varying degrees, in particular for "metal-dominated" molecules like CO and CO_2. The C/O ratio changes the relative abundance of various C- and O- bearing gases (e.g., Madhusudhan 2012; Moses et al. 2013b). For example, a high C/O ratio increases the CH_4 abundance and decreases the abundance of O- bearing

gases like H_2O in the atmosphere. Apart from changing the atmospheric chemistry, the metallicity, C/O ratio, and K_{zz} also have impacts on the atmospheric $T(P)$ profile due to enhanced or diminished atmospheric optical depths. Therefore, in order to constrain the metallicity, C/O ratio, and K_{zz} simultaneously from *JWST* observations of brown dwarfs and directly imaged exoplanets, theoretical "self-consistent" radiative-convective models that include variations in K_{zz}, metallicity, and C/O ratios are needed. Such atmospheric models are crucial for this purpose as all these three parameters impact the atmospheric $T(P)$ profile. This can only be captured by self-consistent radiative–convective atmospheric models that calculate the chemistry, radiative transfer, and $T(P)$ profile of atmospheres simultaneously by taking all the physical connections between these processes into account (e.g., Mukherjee et al. 2023; Phillips et al. 2020; Barman et al. 2001, 2011; **?**; Lacy & Burrows 2023).

In this work, we have used the open-sourced `PICASO 3.0`[1] atmospheric model (Mukherjee et al. 2022; Batalha et al. 2019) to simulate the `Sonora Elf Owl` grid of self-consistent cloud-free model atmospheres with vertical mixing induced chemical disequilibrium for directly imaged planets and brown dwarfs. Apart from the range in $T_{\rm eff}$ and $\log(g)$ values captured within the grid, it includes variation in K_{zz} across 7 orders of magnitude, variation in atmospheric metallicity from 0.1×solar to 10×solar values, and a variation of C/O ratio from 0.22 to 1.14. The range of variation in K_{zz} values is motivated by the large change in K_{zz} estimates from theoretical models between the radiative and convective zones in an atmosphere and also the large variation in theoretical

[1] https://natashabatalha.github.io/picaso/

K_{zz} estimates with both $T_{\rm eff}$ and $\log(g)$ (Figure 5.1).

Using this grid of models and by comparing it with existing space-based observational data from 9 sources, we address the following questions in this work:

1. What is the impact of K_{zz} on the $T(P)$ profile of directly imaged planets and brown dwarfs at different metallicities and C/O ratios?

2. How does K_{zz} impact the spectra of L-type, T-type, and Y-type objects at sub-solar, solar, and super-solar metallicities and C/O ratios?

3. How do the absorption signatures of key gaseous absorbers like CH_4, CO, NH_3, and CO_2 vary with $T_{\rm eff}$, $\log(g)$, K_{zz}, metallicity, and C/O ratio?

4. How do the measured K_{zz} from the available infrared spectroscopy of substellar objects vary with $T_{\rm eff}$?

We describe our model in §6.2. We present the key results from our model grid in §6.3 followed by application of this grid in §5.5. Our conclusions and discussions are presented in §5.6 and §5.7, respectively.

5.2 Atmospheric Modeling with `PICASO 3.0`

We use the open-sourced Python-based `PICASO 3.0` atmospheric model (Mukherjee et al. 2023) to calculate the `Sonora Elf Owl` model grid. `PICASO 3.0` has been widely used to model exoplanet and brown dwarf atmospheres (e.g., Rustamkulov et al. 2022b; Alderson et al. 2022; Feinstein et al. 2022; Ahrer et al. 2022; Miles et al. 2022;

Greenbaum et al. 2023; Mukherjee et al. 2022; Beiler et al. 2023). This model has legacy from the well known `EGP` model (Marley et al. 1996; Marley & McKay 1999; Marley et al. 2002; Saumon & Marley 2008; Fortney et al. 2005, 2008a, 2007; Morley et al. 2014a; Karalidi et al. 2021a). We only describe the latest upgrades of the model which are relevant to this work here and refer the reader to Mukherjee et al. (2023) for a detailed description of the full self-consistent atmospheric model.

The `Sonora Elf Owl` grid is five dimensional with varying $T_{\rm eff}$, $\log(g)$, K_{zz}, [M/H], and C/O ratios. Each model atmosphere is divided into 90 plane-parallel pressure layers (i.e., 91 levels or grid points) for computing the atmospheric structure in our models. The pressure corresponding to these layers are logarithmically spaced from the minimum to the maximum pressure of the model. The maximum pressure of each model is chosen carefully such that the atmosphere is opaque ($\tau(\lambda)$ >1) at all wavelengths at pressures less than the maximum pressure of the model. As atmospheric gaseous optical depths are inversely proportional to gravity, higher gravity models have higher maximum pressure values than lower gravity models. Therefore, the exact upper and lower bounds of atmospheric pressure varies across our grid.

We use the quench time approximation to model the effect of K_{zz} on atmospheric chemistry (Prinn & Barshay 1977). The mixing timescale in each atmospheric layer is determined by,

$$\tau_{\rm mix} = \frac{H^2}{K_{\rm zz}} \tag{5.1}$$

where H is the atmospheric pressure scale height of that atmospheric layer which is calculated using the layer temperature, layer pressure, mean molecular weight, and

object gravity. We consider the quenching of CH_4, CO, CO_2, NH_3, N_2, HCN, PH_3, and H_2O in our models. The net chemical reactions of these gases are (Zahnle & Marley 2014; Mukherjee et al. 2022),

$$CH_4 + H_2OCO + 3H_2$$

$$CO + H_2OCO_2 + H_2$$

$$2NH_3N_2 + 3H_2$$

$$CH_4 + NH_3HCN + 3H_2$$

$$2CO + N_2 + 3H_22HCN + 2H_2O$$

$$CO + NH_3HCN + H_2O$$

$$P_4O_6 + 12H_24PH_3 + 6H_2O$$

For each of these net chemical reactions, we use the chemical timescale approach ($t_{\rm chem}$) presented in Zahnle & Marley (2014). For $PH_3 \leftrightarrow P_4O_6$, we use the chemical timescale approximation from Visscher & Fegley (2005) and Visscher et al. (2006). However, we note that large uncertainties in our understanding of phosphorus chemistry still remain today which will ultimately lead to uncertainties on its reaction timescales (e.g., Wang et al. 2016; Visscher 2020; Bains et al. 2023). We assume that these reaction timescales are independent of metallicity and C/O ratio for simplicity. We think that this is a valid assumption because the uncertainty in quench pressures of various gases is mainly driven by the very large uncertainty in K_{zz} currently. The

Parameter	**Range**	**Increment/Values**
$T_{\rm eff}$	275 K to 2400 K	Increment- 25 K between 275-600 K Increment- 50 K between 600-1000 K Increment- 100 K between 1000-2400 K
log(g)	3.25 to 5.5	Increment- 0.25 dex
$\log_{10}(K_{zz})$	2 to 9 (cgs)	Values- 2,4,7,8, and 9
[M/H]	-1.0 to +1.0 (cgs)	Values- -1.0,-0.5,+0.0 Values- +0.5,+0.7,+1.0
C/O	0.22 to 1.14	0.22,0.458, 0.687, and 1.12

Table 5.1: Parameters of the `Sonora Elf Owl` Atmospheric Model Grid and their ranges covered in this work.

variations of chemical timescales of these gases with metallicity and C/O varying from slightly sub-solar to super-solar values are expected to be much smaller than this current uncertainty.

The $t_{\rm chem}$ of the above-listed reactions are compared to the layer $t_{\rm mix}$ for each atmospheric layer. The abundances of all the gases are allowed to follow chemical equilibrium values for all the deep pressure layers where $t_{\rm chem} \leq t_{\rm mix}$. However, the abundances of the constituent gases are "quenched" at pressures smaller than the quench pressure ($\rm P_Q$). The $\rm P_Q$ of each net chemical reaction is defined as the pressure at which $t_{\rm chem}$ of the relevant reaction is equal to $t_{\rm mix}$. The abundances of the participating gases remain constant at the quenched value at pressures smaller than $\rm P_Q$. Gases other

than CH_4, CO, CO_2, NH_3, N_2, HCN, PH_3, and H_2O are allowed to follow chemical equilibrium throughout the atmosphere in all the models.

We use the equilibrium chemistry calculations presented in Lupu et al. (2021b) for calculating the abundance of gases in thermochemical equilibrium. Equilibrium chemistry calculations at [M/H] values -1.0, -0.5, +0.0, +0.5, +0.7, and +1.0 were used for our grid, where [M/H]=0.0 corresponds to solar metallicity.

At each metallicity equilibrium chemistry tables corresponding to four C/O ratios – 0.22, 0.45, 0.687, and 1.14 – were used as inputs in our models (Solar C/O is assumed to be 0.458 (Lodders et al. 2009)). The solar elemental abundances from Lodders et al. (2009) are used as elemental abundances for the solar composition atmosphere. We note that the solar elemental abundances have been since updated by Lodders (2019). For consistency with our prior work for now we continue to use the Lodders et al. (2009) values. To change the C/O ratio, we keep C+O fixed while the ratio of C and O are changed relative to their solar values. Then, to account for change in metallicity, all elemental abundances are multiplied with the metallicity factor. This makes sure that a changing C/O doesn't also change the atmospheric metallicity. The chemistry of all the gases at pressures larger than their P_Q are interpolated from these precalculated equilibrium chemistry tables.

We assume five different K_{zz} values ranging from $10^2\,cm^2\,s^{-1}$ to $10^9\,cm^2\,s^{-1}$ for our models. Unlike Mukherjee et al. (2022), but similar to Karalidi et al. (2021a), the K_{zz} profiles here do not vary with atmospheric pressure. Figure 5.1 shows that this is a simplification of the more realistic case where K_{zz} varies substantially with atmospheric

pressure depending on whether the atmosphere is locally radiative or convective. But as both the convective and radiative K_{zz} are very uncertain, we adapt this simplification here to explore trends in the atmospheric response to K_{zz}. We further discuss the effect of this assumption in §5.6.

To capture the effect of quenched gaseous abundances on the $T(P)$ profile self-consistently, we mix the individual correlated-k opacities of all the atmospheric gases "on–the–fly" using the resort-rebin technique detailed in Amundsen et al. (2017). The correlated-k opacities of the following gases are weighted according to their equilibrium/quenched abundances during the model iterations and mixed "on–the–fly" – CO, CH_4, H_2O, NH_3, N_2, CO_2, HCN, H_2, PH_3, C_2H_2, Na, K , TiO, VO, and FeH. Each model atmosphere is iterated until a predetermined convergence criterion described in Mukherjee et al. (2023) is met. The sources of various gaseous opacities used for calculating the grid are listed in Table 5.2. The opacity data incorporated into these models are computed using the most recent updates from both laboratory and ab initio studies. The temperature and broadening coefficients are relevant to the objects under study. For an in-depth discussion regarding the accuracy of these line lists and their comparison to other versions, we refer the reader to Gharib-Nezhad et al. (2021a). The thermal emission spectra between 0.5 and 30 μm is computed from the converged atmospheric model with the radiative transfer routines in `PICASO` (Batalha et al. 2019). These spectra are computed at a spectral resolution (R) of 5000.

Our five dimensional atmospheric model grid includes 43,200 distinct models.

All these models are publicly available for download at [2,3,4] accompanied by modeling and analysis tutorial scripts. Table 5.1 summarizes the five parameters which have been varied in our model grid along with the ranges and increments used for each parameter. The chosen ranges and increments in most of the parameters are kept similar to the previous set of `Sonora` grids (e.g., Marley et al. 2021; Karalidi et al. 2021a).

Species	Line list/opacity References
C_2H_2	Rothman et al. (2013)
C_2H_4	Rothman et al. (2013)
C_2H_6	Rothman et al. (2013)
CH_4	Yurchenko et al. (2013); Yurchenko & Tennyson (2014) (CK) Hargreaves et al. (2022) (Hi-Res)
CO	Rothman et al. (2010); Gordon et al. (2017); Li et al. (2015)
CO_2	Huang et al. (2014)
CrH	Burrows et al. (2002)
Fe	Ryabchikova et al. (2015); O'Brian et al. (1991); Fuhr et al. (1988); Bard et al. (1991); Bard & Kock (1994)
FeH	Dulick et al. (2003); Hargreaves et al. (2010)
H_2	Gordon et al. (2017)
H_3^+	Mizus et al. (2017)
H_2–H_2	Saumon et al. (2012) with added overtone from Lenzuni et al. (1991) Table 8
H_2–He	Saumon et al. (2012)
H_2–N_2	Saumon et al. (2012)
H_2–CH_4	Saumon et al. (2012)
H_2^-	Bell (1980)
H^- bf	John (1988)
H^- ff	Bell & Berrington (1987)
H_2O	Polyansky et al. (2018a)
H_2S	Azzam et al. (2016)
HCN	Harris et al. (2006); Barber et al. (2014a); Gordon et al. (2022)
LiCl	Bittner & Bernath (2018) computed by Gharib-Nezhad et al. (2021c)
LiF	Bittner & Bernath (2018) computed by Gharib-Nezhad et al. (2021c)
LiH	Coppola et al. (2011) computed by Gharib-Nezhad et al. (2021c)
MgH	Yadin et al. (2012); GharibNezhad et al. (2013) computed by Gharib-Nezhad et al. (2021a)
N_2	Rothman et al. (2013)
NH_3	Yurchenko et al. (2011); Wilzewski et al. (2016)
OCS	Gordon et al. (2017)
PH_3	Sousa-Silva et al. (2014)
SiO	Barton et al. (2013)
TiO	McKemmish et al. (2019) computed by Gharib-Nezhad et al. (2021a)
VO	McKemmish et al. (2016) computed by Gharib-Nezhad et al. (2021a)
Li,Na,K	Ryabchikova et al. (2015); Allard et al. (2007a,b, 2016, 2019)
Rb,Cs	

Table 5.2: References of gaseous opacities used for calculating the atmospheric models and resulting spectra in this work. Unless otherwise stated opacity calculations are detailed in Freedman et al. (2008, 2014a)

[2] https://zenodo.org/records/10381250
[3] https://zenodo.org/records/10385821
[4] https://zenodo.org/records/10385987

5.3 The Sonora Model Series and why is Elf Owl important?

Multiple editions of the Sonora models such as Sonora Bobcat and Sonora Cholla have been published previously (Marley et al. 2021; Karalidi et al. 2021a). The Sonora Bobcat models assumed thermochemical rainout equilibrium across the whole $T_{\rm eff}$ parameter space from 200 K to 2400 K. It also included sub-solar ([M/H]=-0.5) to super-solar metallicities ([M/H]=+0.5) and C/O ratios. Building on these models, Karalidi et al. (2021a) developed the Sonora Cholla models which includes a self-consistent treatment of disequilibrium chemistry but only for solar composition atmospheres. These models included variation in K_{zz} across several orders of magnitude and also covered $T_{\rm eff}$ from 500-1300 K. The Elf Owl models present further developments in three main areas –

1. The Elf Owl models include effects of mixing-induced disequilibrium chemistry beyond just solar–composition atmospheres by including metallicities ranging from [M/H]=-1.0 to [M/H]=+1.0. This enhances its applicability to a wider range of objects including metal-poor brown dwarfs to metal-enriched giant planets.

2. It also includes departures from the solar C/O ratio varying it from 0.22 to 1.14.

3. The Elf Owl models almost captures the same vast $T_{\rm eff}$-$log(g)$ parameter space as the Sonora Bobcat models but with chemical disequilibrium. This means it can be used to study early Y- dwarfs as well in contrast to Sonora Cholla which

stops at $T_{\rm eff}$= 500 K.

Another methodological difference between the `Cholla` models and the `Elf Owl` models is that the `Cholla` models were computed by mixing only the gaseous opacities of CO,CH_4,NH_3, and H_2O "on–the–fly" even though it included calculations for chemical disequilibrium for CO,CH_4,NH_3,H_2O,CO_2, N_2, and HCN. As already described in §6.2, `Elf Owl` models were computed by mixing the opacities of all atmospheric gases "on–the–fly" which further enhances the self-consistency of these models as there is no pre-assumed mixed opacity grid. This improvement is necessary as it is very important to mix a gas like CO_2 "on–the–fly" at super-solar metallicities or a gas like HCN at high C/O ratios. Additionally, the `Elf Owl` models have been computed with the latest updated opacities which have been improved since the previous generations of `Sonora` models.

5.4 Results

Quenching of gases due to K_{zz} can lead to orders of magnitude changes in their photospheric abundances. Figure 5.2 shows the effect of quenching on the abundance profiles of some key atmospheric gases like CH_4, CO, H_2O, CO_2, NH_3, and PH_3 for a 700 K solar composition object with log(g)=5. The different solid colored lines trace different abundances associated with different K_{zz} values from K_{zz}= 10^2 cm^{2}s^{-1} to K_{zz}= 10^9 cm^{2}s^{-1} while the abundance profiles predicted from equilibrium chemistry are shown with the black dashed lines. The range in K_{zz} chosen here reflects the typical

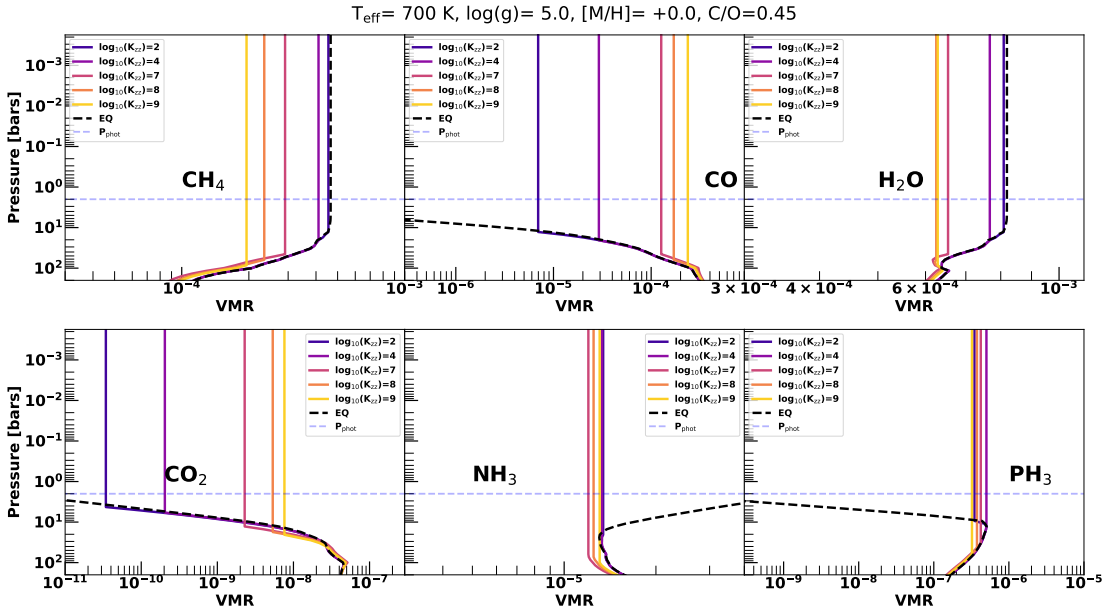

Figure 5.2: The volume mixing ratio profiles of CH_4, CO, H_2O, CO_2, NH_3, and PH_3 are shown in the six panels for a 700 K object with $\log(g)$=5.0 with solar composition atmosphere. Different colored lines represent models with different K_{zz} from 10^2 to 10^9 cm^2s^{-1}. The mixing ratio profiles from a chemical equilibrium model of the same object is shown with the black dashed lines. The mean photospheric pressure of the models is $\sim$ 2 bars, which is shown with the blue dashed line in all the panels.

K_{zz} uncertainty in brown dwarf and exoplanet atmospheres. The mean photospheric pressure is $\sim$ 2 bars and is depicted with the blue solid line in Figure 5.2. Figure 5.2 shows that variation in K_{zz} can cause variations in the photospheric CH_4 and CO by a factor of $\sim$ 10. This variation is similar to the findings in Visscher & Moses (2011). CO_2 and PH_3 abundances can vary by several orders of magnitude due to variation in K_{zz} whereas the dependence of NH_3 abundance on K_{zz} is minimal for this particular combination of $T_{\rm eff}$ and $\log(g)$. These large changes in the photospheric chemistry due to K_{zz} can have a large and complex impact on the atmospheric $T(P)$ structure and observable spectra. Figure 5.2 also shows that different gases quench at different pressures. For example, CH_4, CO, and H_2O quench at a higher pressure than CO_2 (cf. Visscher et al. 2010c). This difference in quench pressures is due to different chemical timescales associated with the CO_2 and CH_4-CO-H_2O reaction kinetics.

5.4.1 Effect of K_{zz} on $T(P)$ Profiles Across Metallicities and C/O Ratios

As quenched gaseous abundances affect the layer-by-layer optical depth of the atmosphere, they impact the radiative fluxes in each atmospheric layer. The affected radiative fluxes also lead to a change in the atmospheric $T(P)$ profile relative to the $T(P)$ profile computed by assuming thermochemical equilibrium. This effect has been previously studied in solar-composition atmospheres by Mukherjee et al. (2022); Karalidi et al. (2021a); Phillips et al. (2020); **?**); Lacy & Burrows (2023). These studies have established that these effects can bring changes to the $T(P)$ profile of the order of $\sim$

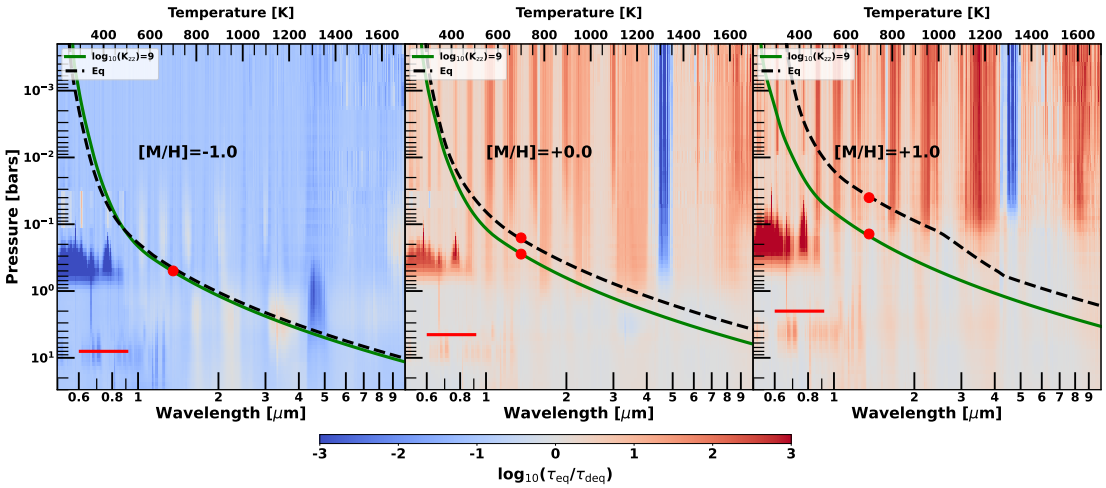

Figure 5.3: The differences in $T(P)$ profiles between an atmosphere in thermochemical equilibrium and an atmosphere with vigorous mixing at different metallicities is shown by the three panels (top x-axis). All the atmospheric models shown here have $T_{\rm eff}$= 700 K, $\log(g) = 3.25$, and solar C/O ratio. The $T(P)$ profile calculated with thermochemical equilibrium are shown as black dashed lines whereas the profile calculated by assuming $K_{zz} = 10^9$ cm^{2}s^{-1} are shown as green solid lines. The left panel, middle and right panels show the comparison at 0.1×, 1×, and 10 ×solar metallicities. The colored background (bottom x-axis) in each panel maps the difference in the pressure and wavelength-dependant optical depths between the chemical equilibrium and disequilibrium models with the quantity $\log_{10}(\tau_{\rm eq}/\tau_{\rm deq})$. A value > 0 shows that the chemical equilibrium model is more opaque than the disequilibrium chemistry model at that particular wavelength and pressure whereas a negative value reflects the opposite scenario. The red horizontal line in each panel shows the pressure level at which CH_4, CO, and H_2O quench in each model atmosphere. The red dots on each $T(P)$ profile denotes the mean photospheric pressure levels of each case. Note that the quench pressure for NH_3/N_2 or CO_2 are different than depicted by the red horizontal line.

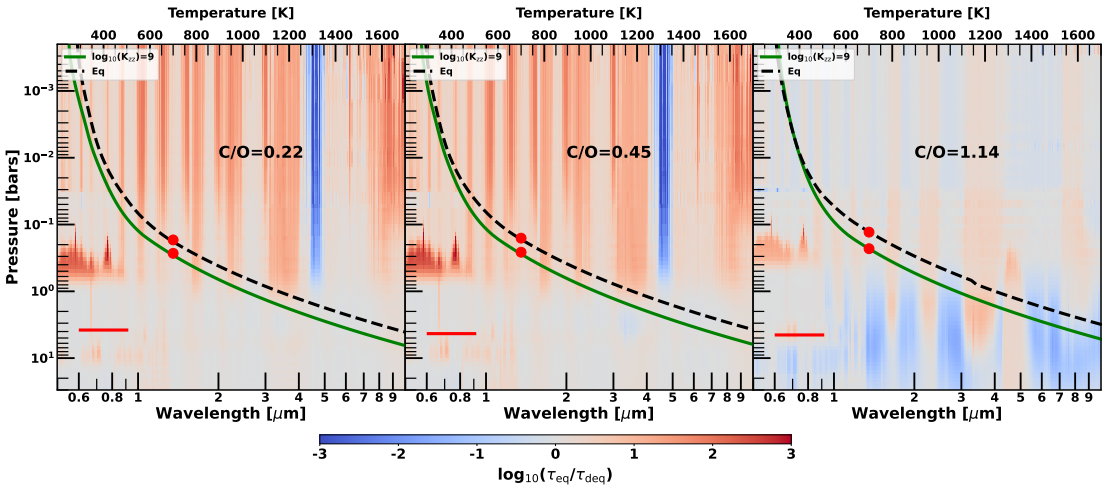

Figure 5.4: The differences in $T(P)$ profiles between an atmosphere in thermochemical equilibrium and an atmosphere with vigorous mixing at different C/O ratios is shown by the three panels (top x-axis). The atmospheric models shown here have $T_{\rm eff}$= 700 K and $\log(g) = 3.25$ with solar metallicity. The $T(P)$ profile calculated with thermochemical equilibrium are shown as black dashed lines whereas the profile calculated by assuming $K_{zz} = 10^9$ cm^{2}s^{-1} are shown as green solid lines. The left panel, middle and right panels show the comparison at C/O = 0.22, 0.45, and 1.14, respectively. The colored background in each panel maps the same quantity as in Figure 5.3. The red horizontal line in each panel shows the pressure level at which CH_4, CO, and H_2O quench in each model atmosphere. The red dots on each $T(P)$ profile denotes the mean photospheric pressure levels of each case. Note that the quench pressure for NH_3/N_2 or CO_2 are different than depicted by the red horizontal line.

100 K at solar metallicity and C/O ratio (e.g., Mukherjee et al. 2023; Karalidi et al. 2021a; Mukherjee et al. 2022). However, metal-enriched atmospheres (relative to the sun) will contain higher mixing ratios of CH_4, CO, H_2O, NH_3, CO_2, etc. all of which are quite sensitive to K_{zz}. Therefore, depending on the $T_{\rm eff}$ and $\log(g)$, quenching of these gases in super-solar metallicity atmospheres can have a more significant effect on the atmospheric $T(P)$ profile compared to the effect found in solar composition atmospheres. On the other hand, atmospheres with sub-solar metallicity will contain a smaller amount of these gases, and the dependence of the $T(P)$ profile on K_{zz} is expected to be relatively more minor than the solar composition atmospheres.

5.4.1.1 K_{zz}, Atmospheric Optical Depths, and $T(P)$ Profiles

Figure 5.3 shows the effect of K_{zz} on the atmospheric $T(P)$ profile by comparing $T(P)$ profiles obtained with chemical equilibrium with $T(P)$ profiles calculated using $K_{zz} = 10^9$ cm^{2}s^{-1} at three different metallicities for an object with $T_{\rm eff}$= 700 K and $\log(g)$= 3.25 (g=17 ms^{-2}). This choice of gravity is representative of a young version of a Jupiter like planet. The left panel in Figure 5.3 shows the comparison for a metal-poor object with [M/H] = -1.0. The black-dashed line shows the $T(P)$ profile computed with thermochemical equilibrium whereas the green solid line shows the $T(P)$ profile computed with $K_{zz} = 10^9$ cm^{2}s^{-1}. The colored map in the background shows the quantity $\log_{10}(\tau_{\rm eq}/\tau_{\rm deq})$, which compares the wavelength and pressure-dependent optical depths in the thermochemical equilibrium and $K_{zz} = 10^9$ cm^{2}s^{-1} models. A value greater than 0 indicates that the thermochemical equilibrium model is more opaque than the K_{zz} =

10^9 cm^{2}s^{-1} model at that particular wavelength and pressure. In contrast, a negative value reflects the opposite scenario.

For the [M/H] = -1.0 case shown in the left panel of Figure 5.3, most of the optical depths are similar between the thermochemical equilibrium and $K_{zz} = 10^9$ cm^{2}s^{-1} cases and as a result, $\log_{10}(\tau_{\rm eq}/\tau_{\rm deq})$ is within an order of magnitude of 0 at most wavelengths across all the pressures. This causes the thermochemical equilibrium and disequilibrium $T(P)$ profiles to be very close to each other at [M/H] = -1.0. The blue strip between 4.5-4.8 μm in all three panels of Figure 5.3 is due to enhanced CO abundance due to quenching whereas the differences between the 0.6-1 μm region originate from the pressure-broadened Na and K absorption. The enhanced CO causes the atmospheres with chemical disequilibrium to be more opaque than atmospheres in chemical equilibrium in these wavelengths.

However, at solar metallicity (middle panel), the thermochemical equilibrium model is more opaque compared to the $K_{zz} = 10^9$ cm^{2}s^{-1} model, especially above 1 bar. This is because the high value of K_{zz} in the disequilibrium chemistry model causes CH_4 to be quenched in the deeper hotter atmosphere leading to a lower CH_4 abundance in the upper atmosphere making the atmosphere more transparent than the CH_4 rich chemical equilibrium atmosphere. Since CH_4 absorbs across the near-infrared, the lower abundance of the gas allows more efficient radiative cooling from deeper in the atmosphere and the $T(P)$ profile of the $K_{zz} = 10^9$ cm^{2}s^{-1} model is consequently colder by $\sim$ 100 K than the chemical equilibrium model at solar metallicity. The same effect gets amplified to a greater extent at [M/H]= +1.0 shown in the right panel in Figure

5.3. This causes the $K_{zz} = 10^9$ cm^{2}s^{-1} model to be colder by about $\sim$ 300-400 K than the chemical equilibrium model at 10$\times$ solar metallicity. The quench pressures for CO, CH_4, and H_2O in the atmospheres with vertical mixing is denoted with red horizontal lines in all three panels of Figure 5.3.

The atmospheric C/O ratio can also influence how K_{zz} impacts the atmospheric $T(P)$ profile. For the same atmospheric metallicity, the C/O ratio controls the relative abundances of C- bearing and O- bearing gases like CH_4, H_2O, CO, etc. Under chemical equilibrium, gases like H_2O, CO, and CO_2 are abundant in O- rich atmospheres (low C/O). However, if the atmosphere becomes C- rich, C- bearing gases like CH_4 and HCN become abundant, and O- bearing gases like H_2O and CO_2 become less abundant.

Figure 5.4 shows the impact of atmospheric C/O ratio on the $T(P)$ profile of a $T_{\rm eff}$= 700 K object with log(g)=3.25 at solar metallicity. The left panel shows the difference in the $T(P)$ profiles between the thermochemical model and the $K_{zz} = 10^9$ cm^{2}s^{-1} model in an O- rich atmosphere with C/O= 0.22. Like Figure 5.3, the quench pressures for CO, CH_4, and H_2O in the atmospheres with vertical mixing are denoted with red horizontal lines in Figure 5.4 as well. At pressures less than $\sim$ 1 bar, Figure 5.4 left panel shows that both the short and long wavelength optical depths in the chemical equilibrium atmospheres are larger than the $K_{zz} = 10^9$ cm^{2}s^{-1} atmosphere. This causes the chemical equilibrium $T(P)$ profile to be hotter than the $K_{zz} = 10^9$ cm^{2}s^{-1} atmosphere at all pressures.

The middle panel shows the difference at C/O =0.45. The chemical equilibrium atmosphere is more opaque than the $K_{zz} = 10^9$ cm^{2}s^{-1} model at short wavelengths

($\lambda \leq 1$ μm), however the difference in the transparency of the two models at longer wavelengths ($\lambda \geq 1$ μm) is smaller than what is seen in the low C/O model in the left panel. The deeper hotter atmosphere emits at shorter wavelengths whereas the upper colder atmosphere emits at longer wavelengths. As the C/O= 0.45 chemical equilibrium model is more opaque than the chemical disequilibrium model at shorter wavelengths, this causes larger differences between the $T(P)$ profile of the models in the deep atmosphere. But as the difference in the long wavelength optical depths are relatively smaller between the two models, the $T(P)$ profile in their upper atmospheres are also similar to each other. At C/O= 1.14 (Figure 5.4 right panel), the atmosphere becomes CH_4 dominated due to lower abundances of O- bearing gases like H_2O and CO_2. This causes the difference in the optical depths between the chemical equilibrium and the $K_{zz} = 10^9$ cm^{2}s^{-1} models to be mainly caused by quenching of CH_4 only. Figure 5.4 right panel shows the differences between optical depths of the two models at longer wavelengths is smaller compared to the middle and left panels. This causes the $T(P)$ profiles of the two models to be almost identical at pressures less than $\sim$ 0.01 bars. However, due to the remaining differences between the transparency of the atmospheres at shorter wavelengths, the $T(P)$ profiles at the deeper pressures show significant differences. Figure 5.3 and 5.4 shows the impact of K_{zz} at a fixed $T_{\rm eff}$ and $\log(g)$. But atmospheric chemistry changes strongly with $T_{\rm eff}$ and $\log(g)$ as well.

5.4.1.2 Impacts of K_{zz} on $T(P)$ profiles across $T_{\rm eff}$ and $\log(g)$

$T_{\rm eff}$ and $\log(g)$ lead to large changes in atmospheric chemistry. For example, L-

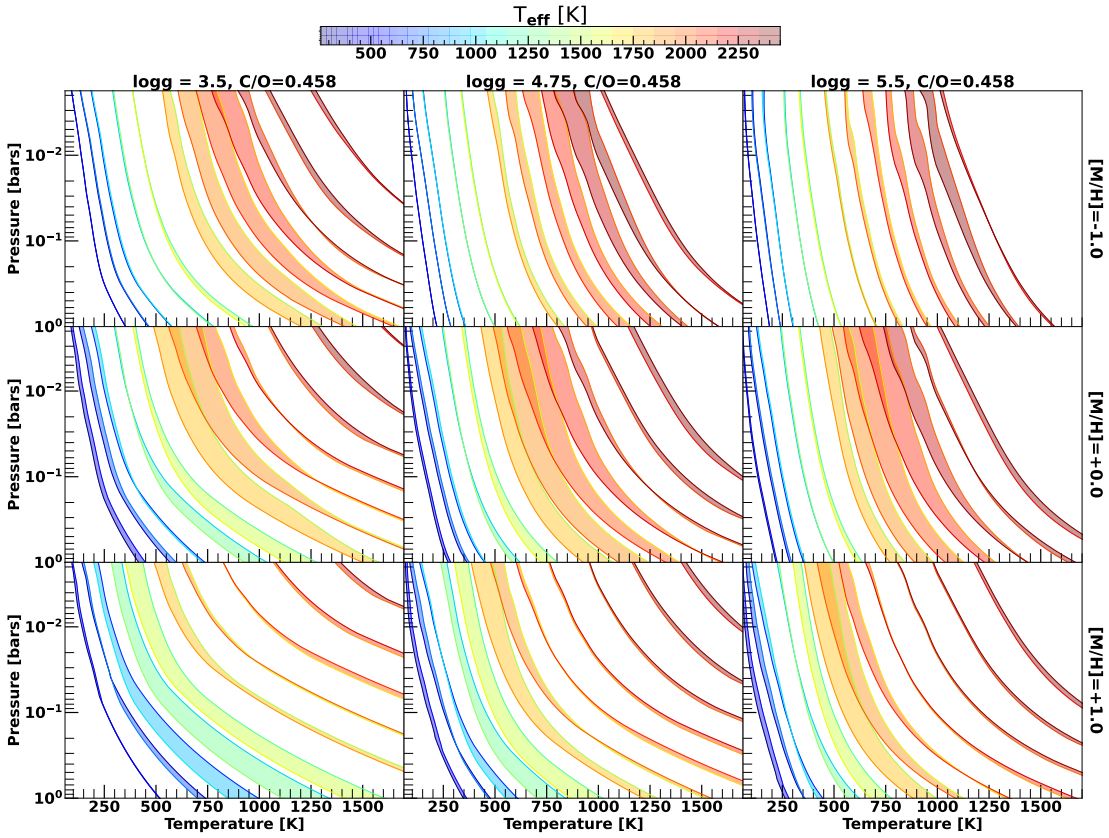

Figure 5.5: Sensitivity of the $T(P)$ profile to K_{zz} across a large range of $T_{\rm eff}$ values at different atmospheric metallicities and gravities are shown. Each panel shows $T(P)$ profiles for $T_{\rm eff}$ values of 2400 K, 2200 K, 2000 K, 1800 K, 1600 K, 1400 K, 1200 K, 900 K, 700 K, 500 K, and 300 K. The area shaded for the $T(P)$ profiles at each $T_{\rm eff}$ shows the sensitivity of the $T(P)$ profiles to variation in K_{zz} from 10^2 cm^{2}s^{-1} to 10^9 cm^{2}s^{-1}. Higher K_{zz} causes the $T(P)$ profiles to be colder than lower K_{zz} models. The top row shows models with 0.1×solar atmospheric metallicity while the middle and the bottom rows show models with solar and 10×solar atmospheric metallicity. The left row shows models at 31 ms^{-2} while the middle and right rows show models at 562 ms^{-2} and 1000 ms^{-2}, respectively. All models shown here have a C/O= 0.45.

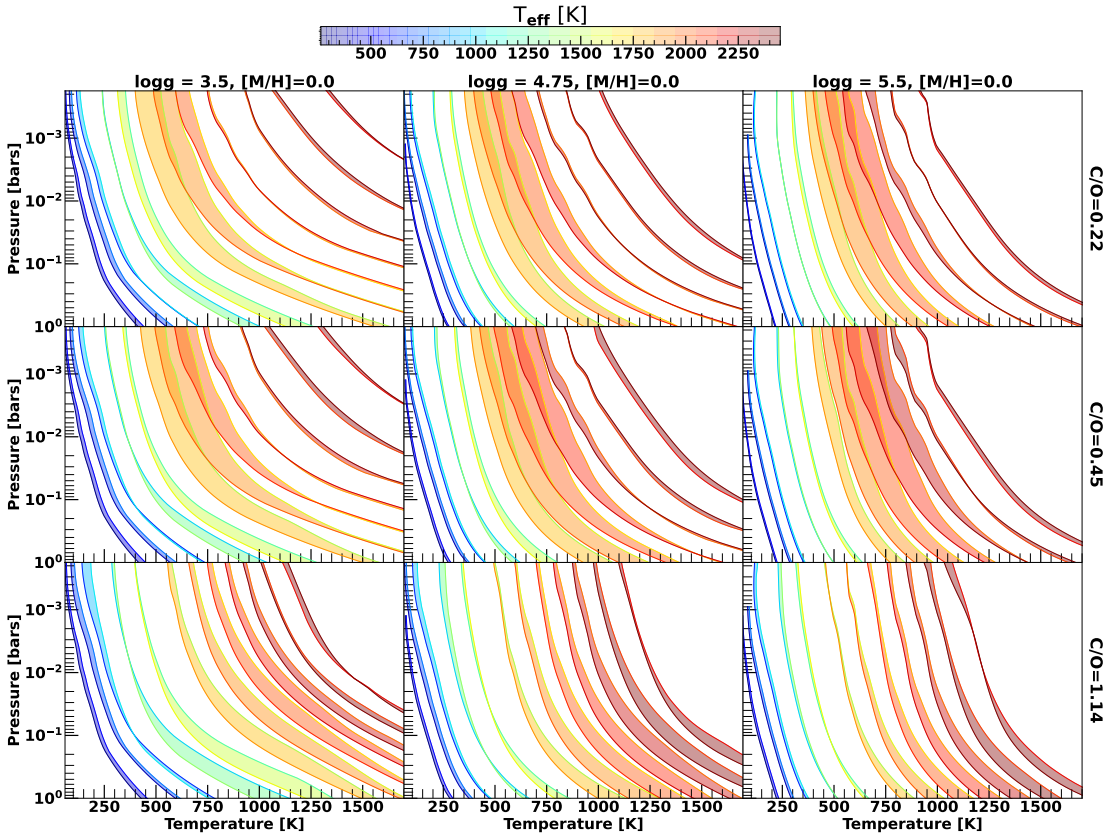

Figure 5.6: Sensitivity of the $T(P)$ profile to K_{zz} across a large range of $T_{\rm eff}$ values at different atmospheric C/O and gravities are shown. Each panel shows $T(P)$ profiles for $T_{\rm eff}$ values of 2400 K, 2200 K, 2000 K, 1800 K, 1600 K, 1400 K, 1200 K, 900 K, 700 K, 500 K, and 300 K. The area shaded for the $T(P)$ profiles at each $T_{\rm eff}$ shows the sensitivity of the $T(P)$ profiles to variation in K_{zz} from 10^2 cm^{2}s^{-1} to 10^9 cm^{2}s^{-1}. The top row shows models with C/O= 0.22 while the middle and the bottom rows show models with C/O= 0.45 and C/O= 1.14. The left row shows models at 31 ms^{-2} while the middle and right rows show models at 562 ms^{-2} and 1000 ms^{-2}, respectively. All models shown here have solar metallicity.

type objects with $T_{\rm eff}$ larger than $\sim$ 1500 K are expected to be CH_4 poor with gases like CO carrying most of the C- atoms under chemical equilibrium. But a rapid transition from CO dominated to CH_4 dominated atmospheres occurs as the $T_{\rm eff}$ cools down below 1200-1500 K. A similar transition from N_2 dominated atmospheres (higher $T_{\rm eff}$) to NH_3 dominated atmospheres (lower $T_{\rm eff}$) is also expected to occur under chemical equilibrium. The object's gravity, on the other hand, leads to large changes in the $T(P)$ profile of atmospheres as well because the atmospheric optical depths are inversely proportional to gravity. Therefore, as both $T_{\rm eff}$ and $\log(g)$ strongly affects atmospheric chemistry, investigating how K_{zz} affects the $T(P)$ profile at different $T_{\rm eff}$ and $\log(g)$ is crucial.

Figure 5.5 shows how K_{zz} impacts the $T(P)$ profile at $T_{\rm eff}$ values ranging from 300 K to 2400 K. Each column corresponds to a different $\log(g)$ value with the left column showing models at $\log(g)$= 3.5, middle column showing models at $\log(g)$= 4.75, and the right column showing models at $\log(g)$= 5.5. The top row in Figure 5.5 shows this effect at [M/H]= -1.0 while the middle and bottom row shows the effect at [M/H]= +0.0 and [M/H]= +1.0, respectively. The shaded area around the $T(P)$ profile for each $T_{\rm eff}$ value represents the variation in the $T(P)$ profile due to K_{zz} varying from 10^2 $\rm cm^2 s^{-1}$ to 10^9 $\rm cm^2 s^{-1}$. Higher K_{zz} causes the $T(P)$ profiles to be colder than the lower K_{zz} cases.

At sub-solar metallicity (Figure 5.5 top row), the variation in the $T(P)$ profile largely occurs for $T_{\rm eff}$ values which are greater than $\sim$ 1200 K. K_{zz} affects this temperature range the most because low metallicity leads to colder $T(P)$ profiles compared to solar or super-solar atmospheres. As a result, CH_4 becomes a dominant gaseous ab-

sorber below relatively high $T_{\rm eff}$ values close to $\sim$ 1800 K for low gravity models shown in the top left row in Figure 5.5. For higher gravity atmospheres, CH_4 becomes a dominant absorber below a slightly higher $T_{\rm eff}$ values than 1800 K. As the CH_4 abundance is very sensitive to K_{zz}, mixing impacts the $T(P)$ structure heavily at these $T_{\rm eff}$ values in very metal-poor atmospheres. But as the $T_{\rm eff}$ goes below $\sim$ 1200 K for $\log(g)$ 3.5 and 4.75 models, the CH_4 abundance in the atmosphere becomes high, and it loses its high sensitivity to K_{zz}. As a result, the $T(P)$ profile also becomes less sensitive to K_{zz} below $T_{\rm eff} \approx$ 1200 K for $\log(g)$ 3.5 and 4.75 atmospheres. For higher gravity metal-poor objects (top right panel), this loss of sensitivity to K_{zz} appears at an even higher $T_{\rm eff}$ value than 1200 K. This is because higher gravity objects have even colder $T(P)$ profiles than lower gravity objects. As a result, the atmospheres become CH_4 dominated at even higher $T_{\rm eff}$ than 1800 K and also loose their sensitivity to K_{zz} at higher $T_{\rm eff}$ than 1200 K.

The middle and bottom row in Figure 5.5 shows the same effect for solar and super-solar metallicity atmospheres. Due to higher metallicity, the $T(P)$ profiles at these metallicities are relatively hotter than the profiles at sub-solar metallicity. These hotter atmospheres start to become CH_4 dominated at a lower $T_{\rm eff}$ of $\sim$ 1600 K for the solar metallicity atmospheres and near $\sim$ 1200 K for the 10$\times$solar metallicity atmospheres. Moreover, with increasing metallicity CO is increasingly favored as a C- carrying gas compared to CH_4 according to thermochemical equilibrium (Lodders 2002). This effect also leads to lower CH_4 abundance in high $T_{\rm eff}$ atmospheres at higher metallicities compared to the low metallicity atmospheres with similar $T_{\rm eff}$. As a result, Figure 5.5

shows that the L/T transition and early T- type (900 K$\leq T_{\rm eff} \leq$1600 K) objects are expected to have the most K_{zz} sensitive $T(P)$ profiles at solar metallicity. At 10$\times$solar metallicity, the most sensitive $T(P)$ profiles appear for the early to late T- type objects with $T_{\rm eff}$ between 500-1200 K. The same trend of higher gravity objects showing smaller sensitivity of the $T(P)$ profile to K_{zz} remains for solar and super-solar metallicities as well.

Figure 5.4 shows that C/O ratio also has a large impact on the atmospheric $T(P)$ profile when atmospheres have strong vertical mixing. Figure 5.6 explores this effect with solar metallicity atmospheres for a similar range of $T_{\rm eff}$ and $\log(g)$ values as in Figure 5.5. The top row in Figure 5.6 shows how K_{zz} impact the $T(P)$ profile in O-rich atmospheres with C/O= 0.22. The middle and bottom rows in Figure 5.6 shows the effect at C/O= 0.45 and C/O= 1.14, respectively.

Figure 5.6 shows that there is not much variation in the effect of K_{zz} on the $T(P)$ profile between C/O= 0.22 (top row) and C/O= 0.45 (middle row). At both of these C/O ratios, the effect is qualitatively similar to the solar metallicity behaviour seen in the middle row of Figure 5.5. However, at higher C/O ratio of 1.14 (bottom row), the impact of K_{zz} on the $T(P)$ profile changes. The $T(P)$ profiles appear to be relatively less sensitive to K_{zz} in these C- rich atmospheres. But for the low gravity cases (left row), a lower level of sensitivity to K_{zz} persists between $700 \leq T_{\rm eff} \leq 2000$ K. For the moderate and high gravity cases shown in the middle and the right rows, the sensitivity of the $T(P)$ profile to K_{zz} is even smaller. For a $\log(g)$ of 4.75, the sensitivity persists between $900 \leq T_{\rm eff} \leq 2400$ K. K_{zz} impacts the $T(P)$ profile between $1200 \leq T_{\rm eff} \leq 2400$ K

for the high gravity case (log(g)= 5.5, right row) in these C- rich atmospheres. CH_4 is a major carrier of C- atoms in these C- rich atmospheres and therefore the CH_4 abundance shows less sensitivity to variations in K_{zz}. This is the main reason behind the diminished sensitivity of the $T(P)$ profiles to K_{zz} in C- rich atmospheres with C/O greater than unity.

This section has shown how K_{zz}, metallicity, and C/O ratio affect the atmospheric $T(P)$ profiles. This gives us intuition for our next discussion which focuses on synthetic emission spectra from these models.

5.4.2 Spectra Across Varying K_{zz}, Metallicity, and C/O Ratios

In this section we present our trends in spectra in two ways. First, we inspect the spectral trends caused by K_{zz}, metallicity, and C/O at a fixed $T_{\rm eff}$ and log(g) value corresponding to a T- type object. This helps us in identifying the degeneracies and distinguishing effects of each of these parameters on the emission spectra of substellar objects. We follow this by presenting the trends of particular spectral features as a function of $T_{\rm eff}$, which helps us in focusing on model trends across the L-, T-, and Y- spectral sequences.

5.4.2.1 How does K_{zz}, metallicity, and C/O Impacts Spectra of a T- type Object: A Case Study

Figure 5.7 shows the impact of K_{zz}, metallicity, and C/O on the emission spectra of a $T_{\rm eff}$= 700 K and log(g)= 4.75 object. The top panel shows the variation

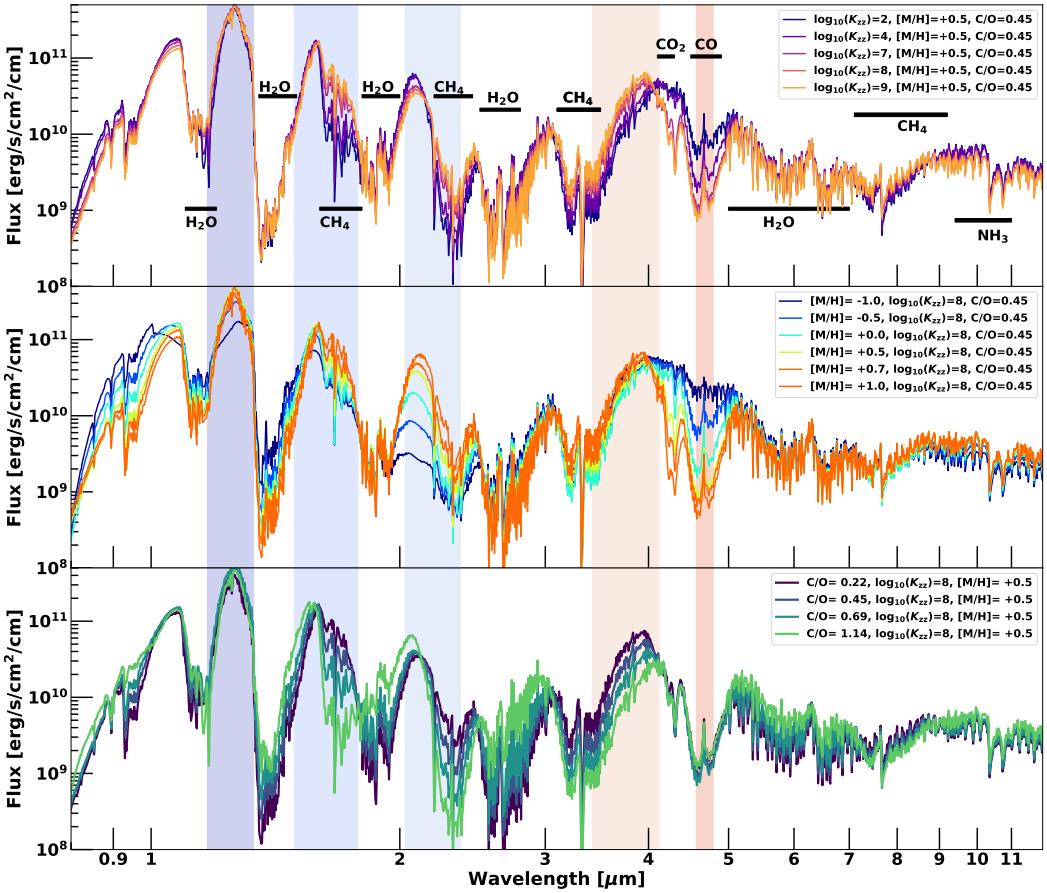

Figure 5.7: Effect of K_{zz} on the emission spectra between 0.8-12 μm of a 700 K object with log(g)=4.75 is shown in the top panel. The metallicity and the C/O are kept constant across all the models in the top panel. Effect of metallicity on the emission spectra between 0.8-12 μm of a 700 K object with log(g)=4.75 is shown in the middle panel. The K_{zz} and the C/O are kept constant across all the models in the top panel. Effect of C/O on the emission spectra between 0.8-12 μm of a 700 K object with log(g)=4.75 is shown in the bottom panel. The K_{zz} and the metallicity are kept constant across all the models in the top panel. Standard infrared photometric bands like J, H, K, L, and M are also depicted with the shaded region.

of the emission spectra with K_{zz} varying from 10^2 cm^2s^{-1} to 10^9 cm^2s^{-1} while the metallicity and the C/O ratio are kept constant at 3× solar and 0.45, respectively. Large spectral variation due to K_{zz} occurs in the CH_4 absorption bands between 1.6-1.8 μm, 2.1-2.5 μm, and 3-4 μm. The CO absorption band between 4.5-4.8 μm also is sensitive to K_{zz}. The H_2O bands between 1.10-1.20 μm, 1.35-1.45 μm, and 1.8-2 μm and the NH_3 features between 10-11 μm show very little variation with K_{zz}. The high K_{zz} models show smaller Y- band peaks than the low K_{zz} models. The decreased CH_4 abundance in high K_{zz} models allows more flux to be emitted in the H- band and the L- band than the low K_{zz} models. The CO_2 and PH_3 absorption bands between 4-4.5 μm also are strongly influenced by K_{zz} at 3× solar metallicity.

The middle panel in Figure 5.7 shows the impact of varying metallicity on the emission spectra of the same object while the K_{zz} and C/O are kept constant. Higher metallicity models show fainter flux in the Y- band but higher flux in the J-band compared to lower metallicity models. However, the higher metallicity models are brighter in the H- and K- bands compared to the lower metallicity model. The CH_4 absorption bands between 1.6-1.8 μm, 2.1-2.5 μm, and 3-4 μm are deeper in the lower metallicity models than the higher metallicity models. On the other hand, the CO band between 4.5-4.8 μm and the CO_2 band between 4-4.5 μm are stronger for the metal-enriched objects than the metal-poor ones. Comparing Figure 5.7 middle and top panels near the M- band (4.5-5.0) μm shows a potential degeneracy between K_{zz} and metallicity as both of these parameters have similar effects on the CO feature. The CO_2 feature shows a strong metallicity dependence and weak K_{zz} dependence due to

the dependence of CO_2 abundance on metallicity. Therefore, the CO_2 feature can help break this degeneracy. The CO_2 feature is inaccessible from ground-based observations due to the high concentration of CO_2 in Earth's atmosphere, so space-based observations from *JWST* can help in constraining both K_{zz} and metallicity. Comparing Figure 5.7 middle panel with the top panel also shows that the H_2O absorption bands between 1.10-1.20 μm, 1.35-1.45 μm, and 1.8-2 μm are more sensitive to atmospheric metallicity than K_{zz} with increasing H_2O band strengths with increasing metallicity.

The dependence of the emission spectra on atmospheric C/O with constant K_{zz} and metallicity is shown in Figure 5.7 bottom panel. For $T_{\rm eff}$= 700 K atmosphere, the C/O= 0.22, C/O= 0.45, and C/O = 0.68 spectra look qualitatively similar throughout most of the wavelength range shown in Figure 5.7. The CH_4 feature in the C/O= 0.22 model is shallower than the CH_4 features in the C/O= 0.45 model, which is expected as the smaller C/O leads to an atmosphere poorer in C- atoms. However, the C/O= 1.14 spectra is very different than the three other models shown in Figure 5.7 bottom panel. The C- rich spectra have shallower H_2O features and stronger Y- and J- band peaks compared to the other two O- rich models. However, the CH_4 bands in the H-, K- and L- bands are deeper than the O- rich spectra as the C/O= 1.14 atmospheres are very CH_4 rich. The rapid change in atmospheric chemistry and spectra near the C/O $\sim$1 part of the parameter space suggests that users should be cautious about interpolating spectra around this region. The CO and the CO_2 features are practically insensitive to atmospheric C/O, which makes the 4-5 μm region very useful for breaking the metallicity and K_{zz} degeneracy.

Figure 5.7 shows that the 1-5 μm spectra of imaged planets or brown dwarfs are influenced by all the three parameters - K_{zz}, metallicity, and C/O to similar extents. For example, the M- band spectra between 4.5-5 μm, which has been used to place constraints on K_{zz} with solar composition models, is similarly influenced by both K_{zz} and metallicity for a fixed $T_{\rm eff}$ and $\log(g)$. On the other hand, the CH_4 bands in the spectra are influenced by all the three parameters – metallicity, K_{zz}, and C/O. Other parts of the spectra like the H_2O bands and the CO_2 band are more sensitive to atmospheric metallicity than K_{zz} or C/O. The NH_3 feature between 10-11 μm shows very little sensitivity to all these three parameters. Figure 5.7 makes it clear that while fitting precise observational spectral data of imaged exoplanets and brown dwarfs (e.g., from *JWST*), fitting for all these three parameters simultaneously and self-consistently is crucial.

5.4.2.2 Trends in Spectral Features across L-, T-, and Y- type Disequilibrium Chemistry Models

Figure 5.5 and 5.6 establishes that atmospheric chemistry and $T(P)$ profiles are sensitive to $T_{\rm eff}$ as well, in addition to parameters like atmospheric metallicity, C/O, and K_{zz}. Here, we present the spectral trends as a function of $T_{\rm eff}$ for various metallicity, C/O, and K_{zz} values.

Figure 5.8 shows the 0.9-5.5 μm emission spectral sequence from $T_{\rm eff}$= 2400 K to $T_{\rm eff}$ = 275 K at a sub-solar atmospheric metallicity of 0.3$\times$ solar and C/O= 0.45. All the models shown here are for a $\log(g)$= 4.75 (g= 562 ms^{-2}). For each spectrum shown

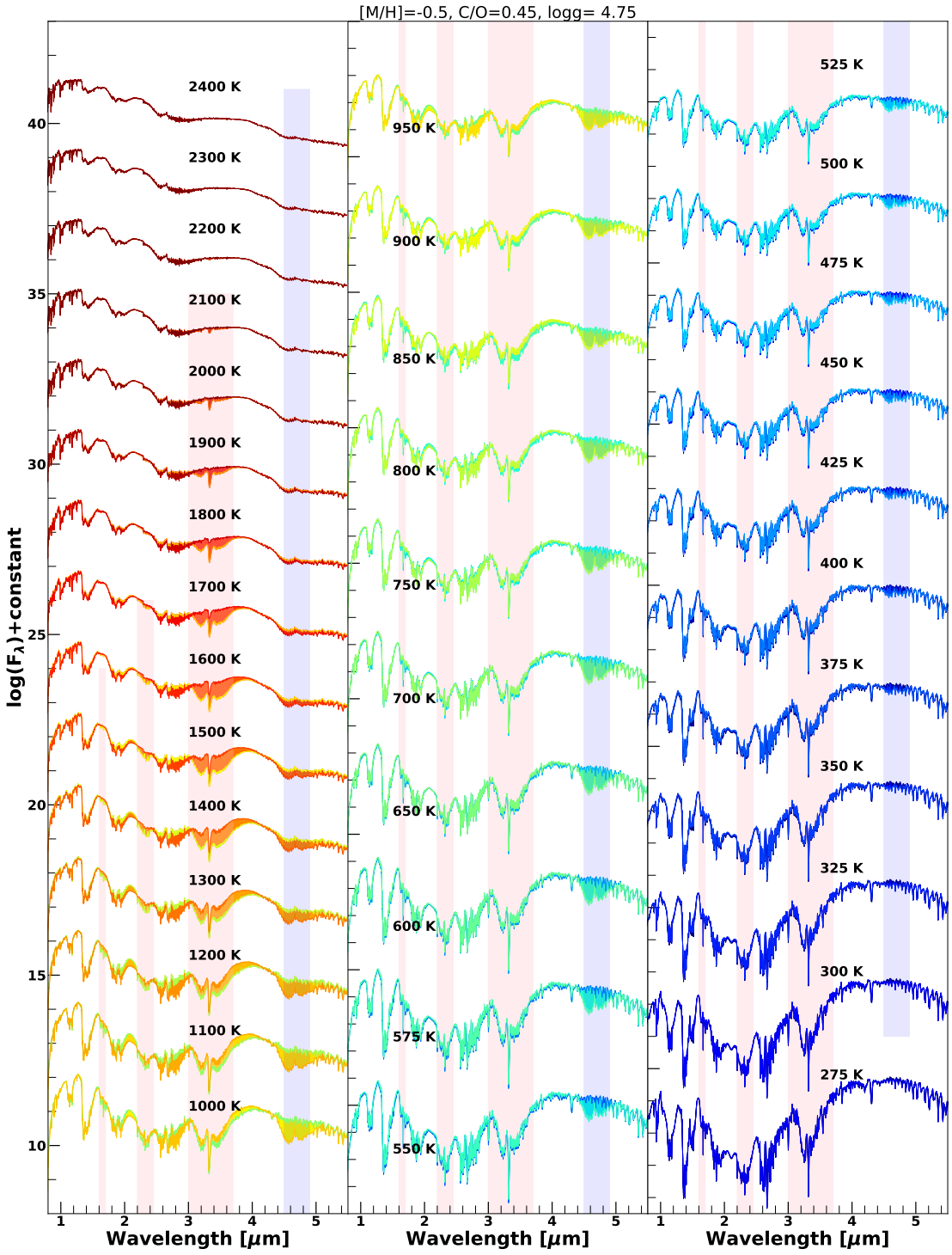

Figure 5.8: The thermal emission spectra between 0.9-5.5 μm at varying $T_{\rm eff}$ from 2400 K to 275 K for metal-poor atmospheres with [M/H]=-0.5 and C/O=0.45 is shown here. All models shown here have the $\log(g)$=4.75 (g= 562 ms^{-2}). At each $T_{\rm eff}$, the variation in the spectra due to K_{zz} is shown by shading the area between the spectra from models with K_{zz}=10^2 cm^{2}s^{-1} and K_{zz}=10^9 cm^{2}s^{-1}. The major absorption bands of CH_4 and CO are shown with pink and blue bands, respectively.

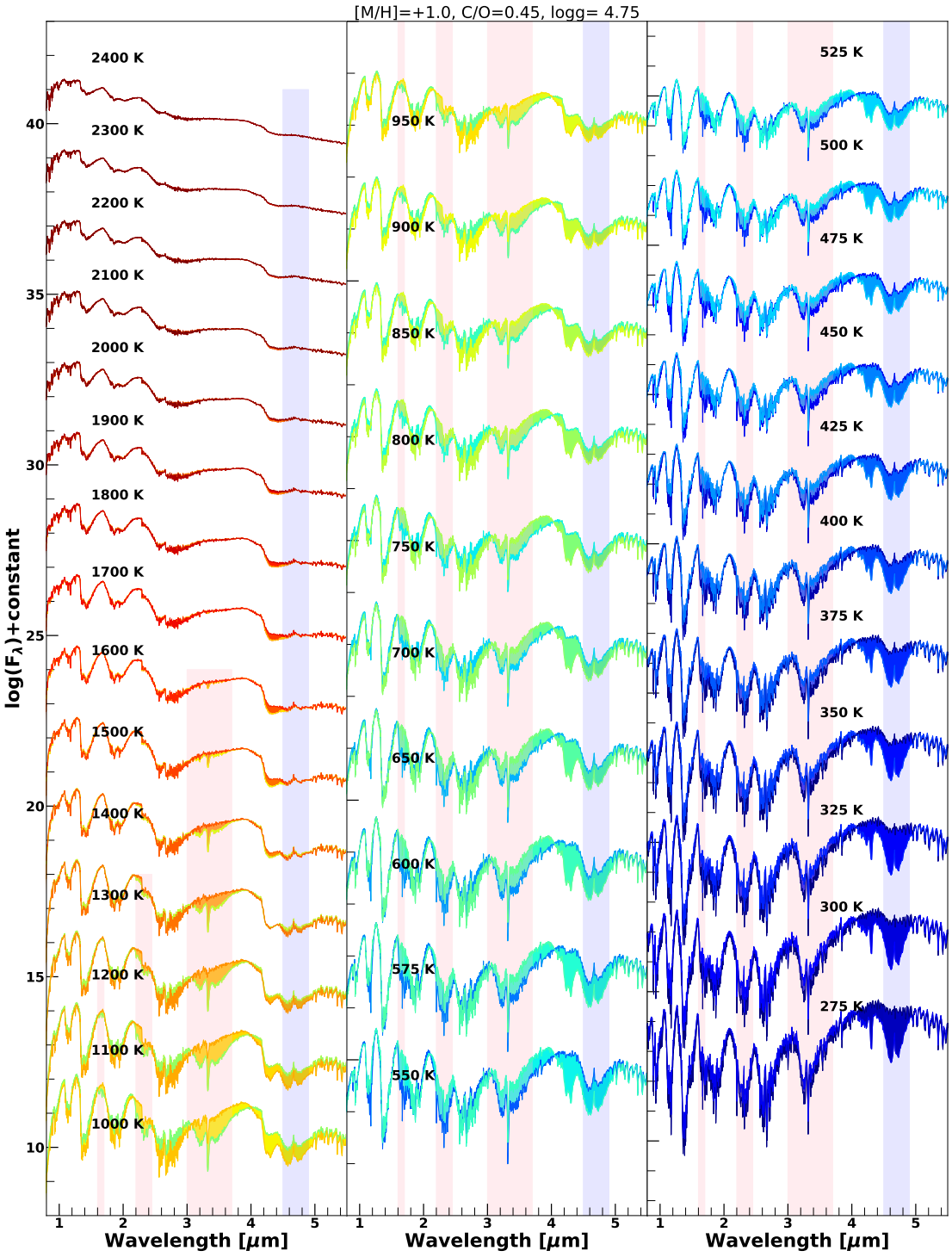

Figure 5.9: The thermal emission spectra between 0.9-5.5 μm at varying $T_{\rm eff}$ from 2400 K to 275 K for metal-rich atmospheres with [M/H]=+1.0 and C/O=0.45 is shown here. All models shown here have the log(g)=4.75 (g= 562 ms^{-2}). At each $T_{\rm eff}$, the variation in the spectra due to K_{zz} is shown by shading the area between the spectra from models with K_{zz}=10^2 cm^{2}s^{-1} and K_{zz}=10^9 cm^{2}s^{-1}. The major absorption bands of CH_4 and CO are shown with pink and blue bands, respectively.

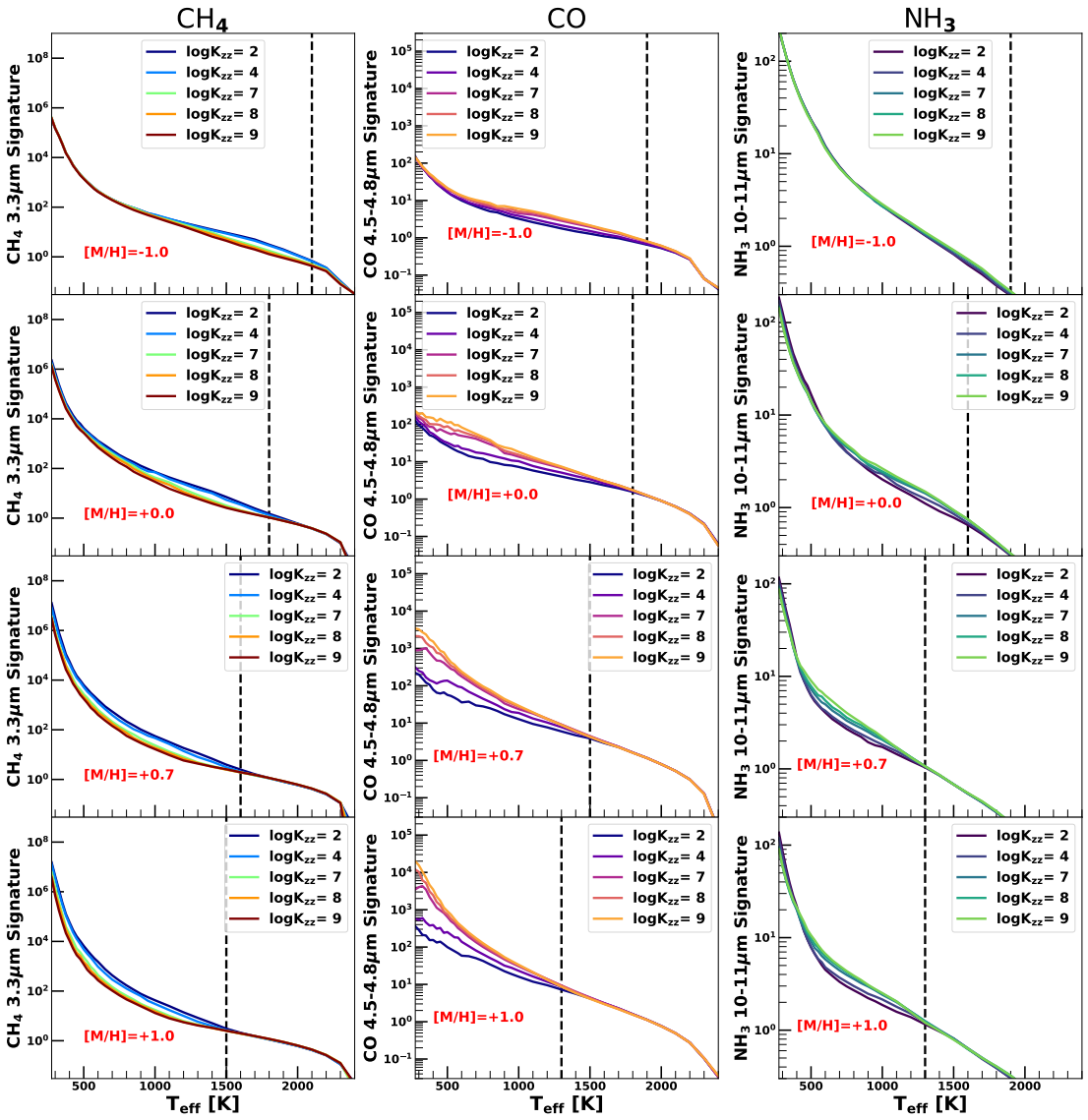

Figure 5.10: The spectral strength metric S for the CH_4 feature at 3.3μm as a function of $T_{\rm eff}$ is shown in the panels in the left column. Each panel from top to bottom corresponds to a different metallicity, and each line represents the spectral strength from different K_{zz} values. The middle column shows the same metric for the CO feature between 4.5-4.8 μm, whereas the right column shows the metric for the 10-11 μm NH_3 feature. The black dashed line shows the $T_{\rm eff}$ value below which these features roughly appear in the spectra.

in Figure 5.8, the area between the spectral model with the lowest vertical mixing (K_{zz}= 10^2 cm^{2}s^{-1}) and the highest vertical mixing (K_{zz}= 10^9 cm^{2}s^{-1}) is shaded to depict the variation in spectral features due to changes in K_{zz} at each $T_{\rm eff}$. Figure 5.9 shows the same spectral sequences but for super-solar metallicity atmospheres (10$\times$ solar).

The evolution of some notable spectral features across $T_{\rm eff}$ can be readily seen in Figure 5.8 and 5.9. For example, the CH_4 feature at 3.3 μm starts to appear in the spectrum at $T_{\rm eff}\approx$ 2100 K for the metal-poor atmospheres represented in Figure 5.8. The main reason behind the appearance of CH_4 at such high $T_{\rm eff}$ values is the low atmospheric metallicity which causes the atmospheric $T(P)$ to be colder than what is expected from solar or super-solar metallicity atmospheres. This can be seen in Figure 5.5 as well. The opposite effect is operating in Figure 5.9 which depicts super-solar atmospheric spectra. In this case, the 3.3 μm CH_4 signature only starts to appear in models which are colder than $T_{\rm eff}\approx$ 1500 K. These high metallicity atmospheres have hotter $T(P)$ profiles which means that the $T_{\rm eff}$ needs to be lower in these atmospheres for it to build up enough CH_4 so that the CH_4 signatures appear in the spectra. Moreover, in such metal-rich atmospheres, CO/CH_4 ratio is higher than in metal-poor atmospheres. The 3.3 μm CH_4 feature shows the most sensitivity to K_{zz} for $T_{\rm eff}$ between 1900 K and 450 K for the metal-poor objects in Figure 5.8. Below $T_{\rm eff}\sim$ 450 K, the atmospheres of these objects are so cold that they are very rich in CH_4, so much so that the CH_4 signature becomes insensitive to K_{zz}. For the metal-rich objects shown in Figure 5.9, the sensitivity of the CH_4 band remains in place for $T_{\rm eff}$ as cold as 275 K.

The evolution of the 4.5-4.8 μm CO band across the $T_{\rm eff}$ range can also be

seen in Figure 5.8 and 5.9. For the subsolar metallicity models shown in Figure 5.8, the CO band between 4.5-4.8 μm starts to show dependence on K_{zz} at $T_{\rm eff}$ lower than 1600 K. With decreasing $T_{\rm eff}$ below 1600 K, the sensitivity of the CO band to K_{zz} increases and this sensitivity peaks around $T_{\rm eff} \sim$ 700 K. Objects that are cooler than $T_{\rm eff}\sim$700 K, progressively lose the sensitivity of the CO band to K_{zz} with declining $T_{\rm eff}$ at sub-solar metallicity atmospheres. This behavior can be explained with the $T(P)$ profiles at sub-solar metallicity, which are colder than the $T(P)$ profiles calculated from solar or super-solar metallicity atmospheres. Below $T_{\rm eff}\sim$425 K, the deeper atmosphere of these metal-poor objects is expected to be so cold that they do not have enough CO in the deep atmosphere to be transported to the photosphere via mixing. The comparatively lower CO/CH_4 ratio in metal-poor objects than in metal-rich atmospheres also is a significant reason behind this trend. On the other hand, the CO band remains extremely sensitive to K_{zz} until $T_{\rm eff}$= 275 K for super-solar metallicity spectra shown in Figure 5.9. The higher CO/CH_4 ratio in metal-rich objects than in metal-poor atmospheres causes CO to be a prominant C- carrying gas even in very cold metal-rich objects. Moreover, the $T(P)$ profiles at these elevated metallicities are hotter than the $T(P)$ profiles calculated for solar or sub-solar metallicity atmospheres, which causes the deeper atmospheres of these objects to be still very rich in CO even at cold $T_{\rm eff}$ values like 275 K. This CO abundance is mixed to the photosphere due to mixing and causes the CO band to very extremely sensitive to K_{zz} even in these metal-rich Y- type objects.

The PH_3 feature at 4.2 μm appears in the spectra in objects colder than $T_{\rm eff}$ $\sim$1000 K in the metal-poor atmospheric spectra shown in Figure 5.8. However,

its sensitivity to K_{zz} remains very low in these sub-solar metallicity models. On the other hand, CO_2 becomes the dominant absorber between 4-4.5 μm at $T_{\rm eff}\leq$2200 K in super-solar metallicity models shown in Figure 5.9. CO_2 abundance is very sensitive to metallicity leading to very high CO_2 abundance at super-solar metallicities. The CO_2 feature in Figure 5.9 also shows sensitivity to K_{zz} as well across all $T_{\rm eff}$ values colder than 1500 K in these metal-rich models.

To better visualize these spectral feature trends, we design a metric that probes the strength of the 3-4 μm CH_4 feature, 4.5-4.8 μm CO feature, and the 10-11 μm NH_3 features. We define this metric relative to a reference spectrum. We define the metric as,

$$S = max\left(\frac{abs(F(\delta\lambda) - F_{ref}(\delta\lambda))}{max(F(\delta\lambda))}\right) \tag{5.2}$$

where $F(\delta\lambda)$ represents the flux values within the wavelength range of the absorption feature of interest. For example, for the CH_4 feature at 3.3 μm, $F(\delta\lambda)$ would represent the spectra between 3.2-3.4 μm. The numerator term in Equation 5.2 represents the depth of the absorption feature relative to the reference spectra, whereas the denominator is a normalizing term to account for the difference in the absolute levels of emitted fluxes between the spectra of interest and the reference spectra. To use this metric to assess the strength of a particular feature, the reference spectra must have the weakest feature of interest. Therefore, to assess the strength of various features, we chose the $T_{\rm eff}$= 2400 K spectra with 0.1$\times$solar metallicity, C/O=0.45, and K_{zz}= 10^2 $\rm cm^2 s^{-1}$ as the reference spectra.

Figure 5.10 shows the variation of three spectral features across $T_{\rm eff}$ values for different K_{zz} and metallicity values by plotting the metric S. The left column shows the variation in the CH_4 feature at 3.3 μm relative to the reference spectra defined above, where each row corresponds to a different atmospheric metallicity. The different colored lines in each panel show the variation in CH_4 strength for different K_{zz} values. The second column of Figure 5.10 shows the variation in the CO feature between 4.5-4.8 μm relative to the reference spectra, while the third column shows the variation in the NH_3 doublet feature between 10-11 μm.

Figure 5.8 and 5.9 already showed that the onset $T_{\rm eff}$ value for the appearance of CH_4 features on spectra is a function of atmospheric metallicity. This phenomenon is further highlighted in Figure 5.10 left column. The black dashed vertical line in each left panel marks the $T_{\rm eff}$ value at which the 3.3 μm CH_4 feature first appears in the spectra of a certain metallicity. It can be seen that this CH_4 onset $T_{\rm eff}$ value varies strongly from 2100 K at sub-solar metallicity atmospheres to 1500 K at super-solar metallicity atmospheres. The sensitivity of the CH_4 feature to K_{zz} also is a strong function of $T_{\rm eff}$ as well.

The strength of the 4.5-4.8 μm CO feature as a function of $T_{\rm eff}$ is shown in the middle column of Figure 5.10 for various atmospheric metallicities. A higher value of K_{zz} increases the strength of the CO feature at all metallicities. Similar to the trends seen in the CH_4 feature, the onset $T_{\rm eff}$ at which the CO feature becomes sensitive to K_{zz} also varies with metallicity. The strength of the NH_3 feature between 10-11 μm is shown in the right column of Figure 5.10. The sensitivity of the NH_3 feature strength

on K_{zz} is very low. This lack of sensitivity to K_{zz} is because the constant abundance curves of NH_3 from equilibrium chemistry have similar slopes expected from H_2-He adiabats (Saumon et al. 2006; Fortney et al. 2020; Zahnle & Marley 2014; Ohno & Fortney 2023a). As a result, the NH_3 abundance predicted from thermochemical equilibrium doesn't show much variation with pressure or temperature in the convective parts of the deeper atmosphere. Therefore, the quenched NH_3 abundance becomes almost independent of the quench pressure when the quench pressure lies in or near convective regions of the atmosphere. Even though small, Figure 5.10 right column shows that there is still some dependence of the NH_3 feature on K_{zz}. This small dependence comes from the self-consistent nature of our models. As K_{zz} influences the radiative $T(P)$ profile, it can cause the deeper adiabat of the atmosphere to have a small but non-negligible dependence on K_{zz} as well. As the NH_3 abundance in the deeper atmospheres is dependent on the deep atmospheric adiabat, the NH_3 feature also shows small dependence on K_{zz}.

5.5 Application

We use the `Sonora Elf Owl` grid to fit the infrared spectra of a series of early to late T-dwarfs to constrain their $T_{\rm eff}$, $\log(g)$, K_{zz}, [M/H], and C/O. We use the Python `SciPy` based `RegularGridInterpolator` function to perform a multi-dimensional linear interpolation of the spectra at each wavelength point. We use this interpolated function in a Bayesian framework to fit the observed spectra of several brown dwarfs. The

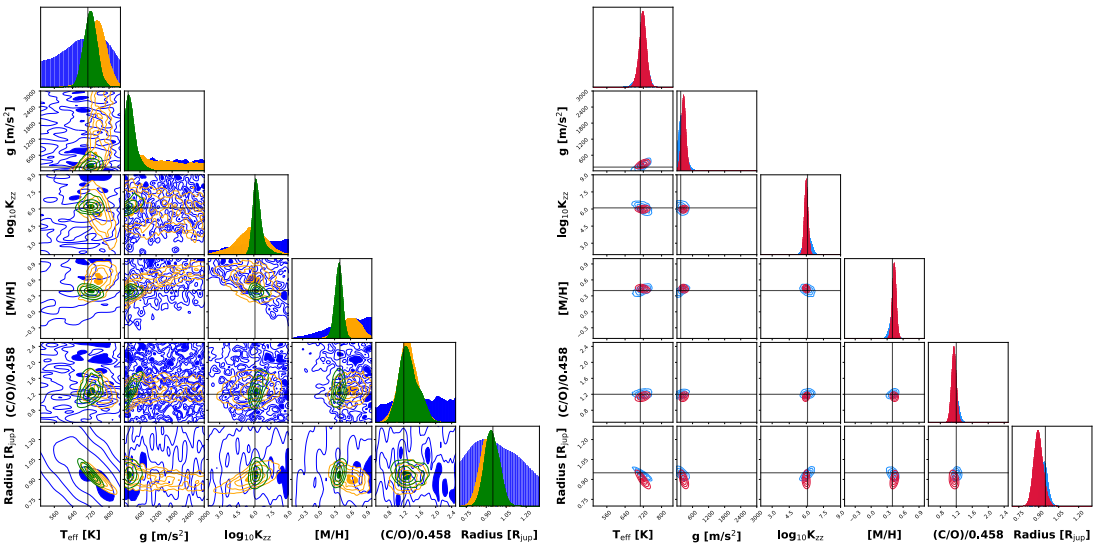

Figure 5.11: The left corner plot shows the posterior distributions for $T_{\rm eff}$, gravity, $\log_{10}K_{zz}$, [M/H], C/O (×Solar), and radius when various wavelength regions of a synthetic data set are fitted with the Bayesian grid fitting approach with the `Sonora Elf Owl` grid. The right corner plot shows posteriors when the same synthetic spectra is observed with various instrument modes of *JWST*. The six panels in Figure 5.12 show the synthetic dataset used for this analysis to obtain the posterior distributions shown in the corner plots. Left corner plot: The blue posteriors show when the synthetic spectra between 4.5-5 μm is fitted whereas the orange posteriors represent fitting the synthetic data between 5-14 μm. The green show results from fitting the 4-14μm regions, respectively. Right corner plot: The sky blue and crimson posteriors show results when synthetic data from *JWST* NIRSpec G395H and MIRI LRS is fitted, respectively. The brown posteriors show constraints obtained from synthetic Prism data. The posteriors obtained from the Prism data are too narrow for the range of the parameters shown in the corner plots. The black lines in the corner plot show the true parameter values used to produce the synthetic spectral data.

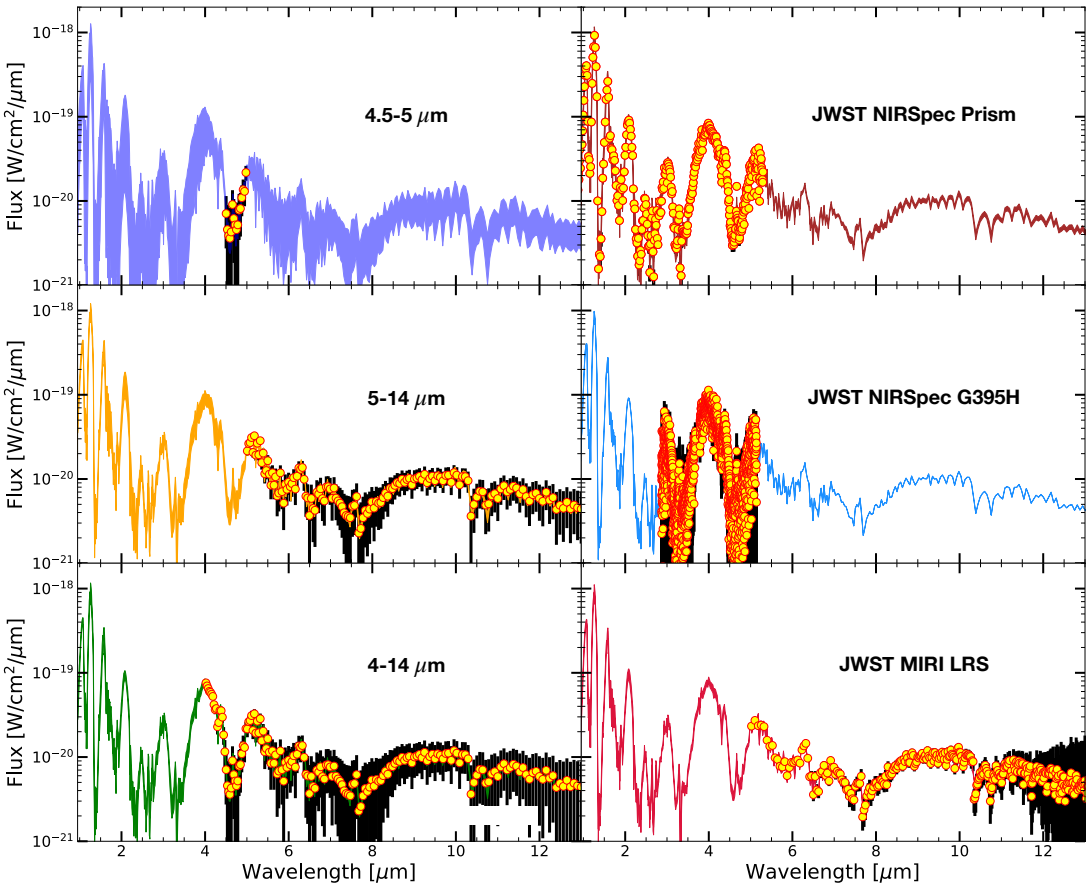

Figure 5.12: The six panels show the synthetic dataset used for this analysis to obtain the posterior distributions shown in the corner plots in Figure 5.11. The top left panel shows the synthetic spectra between 4.5-5 μm whereas the middle left panel shows the synthetic data between 5-14 μm. The bottom left panel show the 4-14μm region of the synthetic spectra. The top and middle right panels show the synthetic data from *JWST* NIRSpec Prism and *JWST* NIRSpec G395H, respectively. The bottom right panel shows the synthetic spectrum from *JWST* MIRI LRS. Each panel also shows the 1σ envelope on the spectra from the fitted posteriors.

dynamic nested sampling code `DYNESTY` (Speagle 2020) was used as a Bayesian sampler for this purpose. Uniform priors on $T_{\rm eff}$, $\log(g)$, $\log(K_{zz})$, [M/H], and C/O ratio were used for fitting the data.

First, we demonstrate how the choice of different wavelength ranges and instruments leads to varying degrees of constraints on atmospheric parameters like K_{zz} or $T_{\rm eff}$. Typically, the 4.5-5 μm wavelength region (M- band) has been used to constrain the very uncertain K_{zz} in brown dwarf atmospheres (e.g., Miles et al. 2020; Mukherjee et al. 2022). However, such efforts have often ignored the effect of varying metallicity or C/O in addition to varying K_{zz} on the spectrum in this wavelength window. Figure 5.7 top and middle panels show how the M- band spectrum shows degeneracy between varying metallicity and K_{zz}. Therefore, using our grid, we examine the extent to which only M- band spectrum of a brown dwarf can constrain K_{zz}.

As an example object, we generate a synthetic spectrum of an object with $T_{\rm eff}$= 707 K, $\log(g)$= 4.2, $\log_{10}(K_{zz})$=6.1, [M/H]= +0.4, C/O= 1.2×solar (C/O=0.5496), and Radius= $0.95 R_{\rm J}$ from our interpolated grid. This example object represents a slightly metal-rich late T- dwarf with moderate atmospheric mixing. We test six different observational scenarios with this synthetic spectrum. To represent some of the ground-based or space-based observations of brown dwarfs with instruments like *AKARI* and *Spitzer*, we simulate a synthetic observed spectrum by decreasing the spectral resolution of our interpolated spectra to R=100 and artificially adding noise to the data by maintaining a signal–to–noise ratio (SNR) of 5 at 5 μm of the synthetic spectrum. We use this synthetic spectrum to examine how constraints on these parameters depend on the

wavelength ranges by fitting this synthetic spectra in different wavelength windows – 4.5-5 μm, 5-14 μm, and 4-15 μm. Even though the 5-14 μm and 4-15 μm choices do not differ much in terms of wavelength coverage, the additional 4-5 μm wavelengths have absorption features from CO and CO_2 both of which are sensitive to K_{zz} and metallicity. To represent *JWST* observations of brown dwarfs, we assume the brown dwarf is at a distance of 5 pc and use the *JWST* Exposure Time Calculator to simulate the signal-to-noise on the spectrum if observed for a total exposure time of 30 minutes with the NIRSpec Prism mode, NIRSpec G395H mode, and the MIRI LRS mode. Figure 5.11 shows the results of fitting the synthetic spectra in these six different scenarios. The synthetic observed spectrum along with the best fit models for each scenario is shown in Figure 5.12. The synthetic data fitted in each case is shown with yellow points along with the synthetic noise. The 1σ envelopes of the model spectra drawn from the Bayesian posteriors obtained by fitting each wavelength region are also overplotted in these panels of Figure 5.11 with different line colors.

Figure 5.11 shows a compilation of all the corner plots obtained by fitting each of these wavelength regions of the synthetic spectra. The corner plots shown in the left side show posterior distributions from fitting the synthetic data which are representative of the typical ground-based/*AKARI*/*Spitzer* scenario. The right corner plot shows posteriors obtained by fitting various types of observations possible with *JWST*. The true parameters from which the synthetic spectra were created are marked with solid black lines in the corner plots.

The blue posteriors in the left corner plot show the results of fitting only the

4.5-5 μm (M- band) part of the synthetic spectra. The posteriors on $T_{\rm eff}$, log(g), K_{zz}, [M/H], and C/O obtained from the M- band show large uncertainties. Most importantly, K_{zz} remains unconstrained along with [M/H], C/O, and log(g) with the M-band data. The orange posteriors overplotted in the left corner plot are the results of fitting the 5-14 μm window of the synthetic spectra. The constraints on all the parameters are significantly better with this wavelength range compared to fits of the M- band data only. Unlike the M- band data, this wavelength region can constrain K_{zz}, [M/H], C/O, and $T_{\rm eff}$. However, like the M- band, this wavelength window can still not constrain log(g). A significant improvement in the constraints on all the parameters is achieved by fitting the data from 4-14 μm. These posteriors are shown with green color. This wavelength range allows all the parameters to be constrained, including log(g). The posteriors on all the parameters are both more precise and accurate compared to the M- band (blue) and 5-14 μm (green) posteriors.

The sky blue colored posteriors in the right corner plot in Figure 5.11 were obtained by fitting the synthetic *JWST* NIRSpec G395H spectra of the same object. Due to the higher spectral resolution and higher signal-to-noise of such observations, the constraints obtained from it are more precise than the scenarios discussed above. Constraints on the parameters from fitting the MIRI LRS synthetic spectra are shown with crimson colors and are similar in precision as those obtained from NIRSpec G395H data. The posteriors estimated from fitting the NIRSpec Prism data are also shown in the right corner plots but are too narrow and precise for the range in parameter values plotted in Figure 5.11. The high precision of the constraints achievable with *JWST*

NIRSpec Prism observations is because of the higher signal-to-noise that is achieved within the same exposure time with this instrument mode compared to the other two *JWST* instrument modes explored here. The broad wavelength coverage of *JWST* NIRSpec Prism also is a major factor behind the precise constraints achievable with this mode.

Figure 5.11 shows that fitting the M- band data at R $\sim$ 100 alone does not yield constrained atmospheric parameters. Although, this result is only valid if no additional priors are available on the different parameters from other observations like photometry. Fitting the spectra between 5-14 μm provides meaningful constraints on $T_{\rm eff}$, K_{zz}, [M/H], and C/O but log(g) still remains unconstrained. Fitting the spectra between 4-14 μm can constrain all the atmospheric parameters studied here, including log(g), with tighter posteriors on the other parameters. Such constraints can be obtained by fitting *AKARI* and *Spitzer* data together. Figure 5.11 also shows that constraints achievable with *JWST* data are tighter than those from these other instruments. We use these findings from our synthetic spectra fitting exercise to apply our models to a small sample of brown dwarfs with archival infrared spectroscopic data.

5.5.1 Fitting Observed Spectrum with the `Sonora Elf Owl` Model grid

We fit the spectra of 9 early to late T-dwarfs with the `Elf Owl` model grid to asses their atmospheric parameters. The sample is shown in the J vs. J-H color-magnitude diagram shown in Figure 5.13 and was chosen such that it spans the entire T-dwarf spectral type starting from early to late T- dwarfs. Our grid covers the parameters

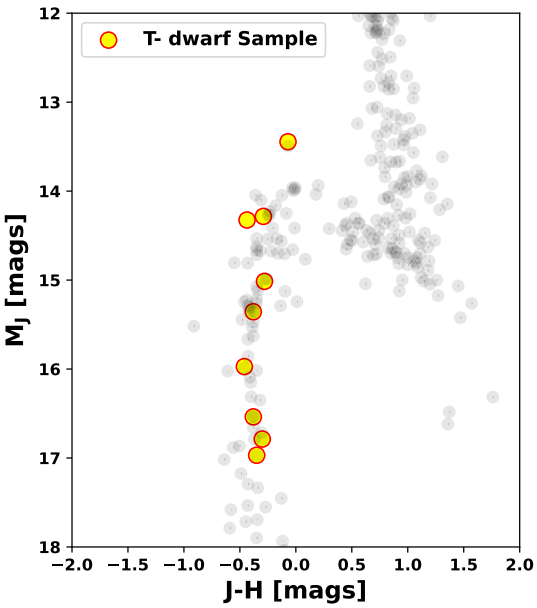

Figure 5.13: J vs. J-H color magnitude diagram of the substellar object population is shown with gray circles. Our T-dwarf sample of 9 objects is shown with yellow circles and it uniformly spans almost the whole of the T- dwarf sequence except the L/T transition objects. All magnitudes shown in this diagram are MKO magnitudes. Data from Best et al. (2020).

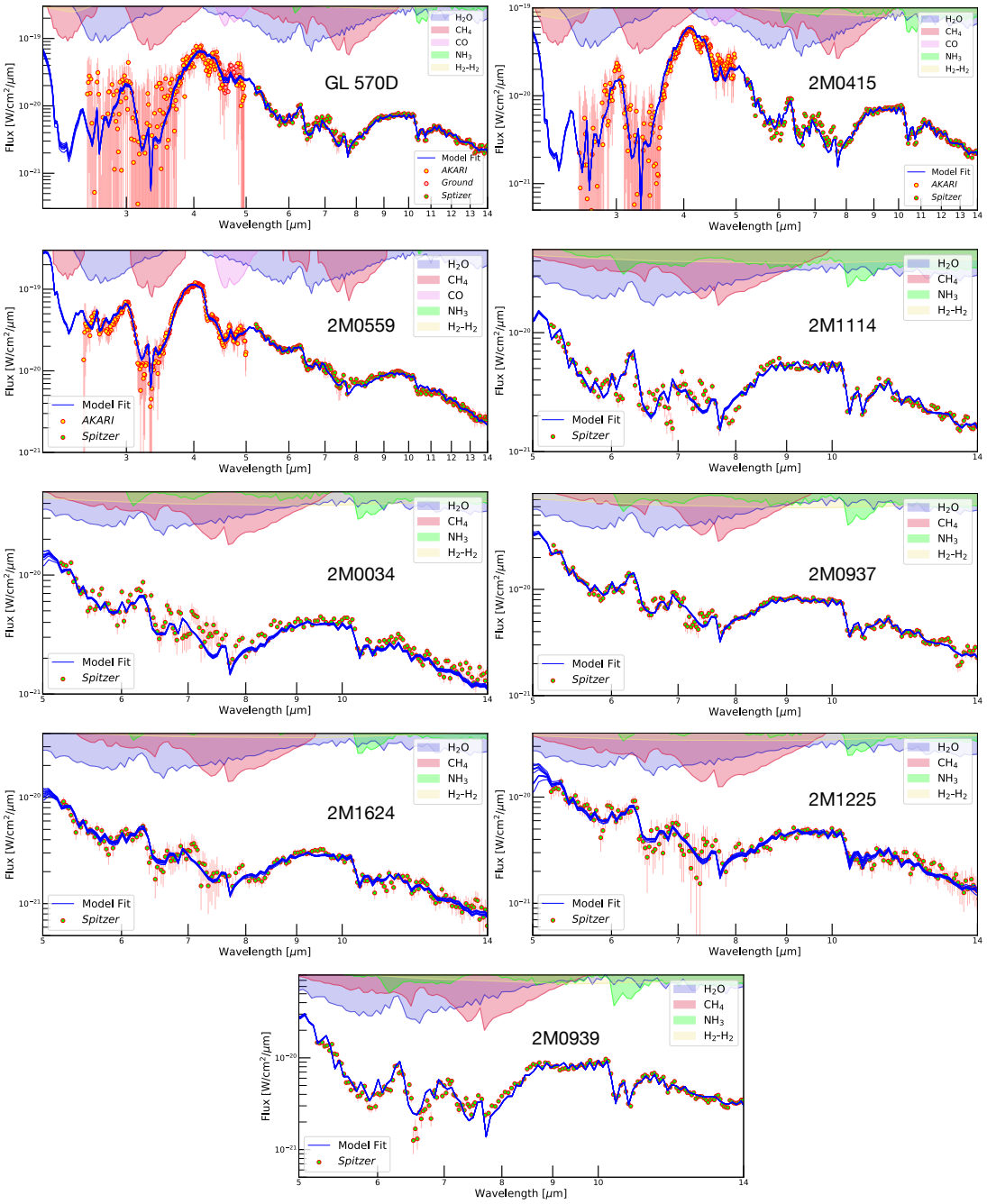

Figure 5.14: The observed spectra of 9 T-dwarfs from our sample are shown in the different panels. Observations from *AKARI* are shown with yellow circles, whereas *Spitzer* data are shown with green circles. For GL570D, ground-based data was also used, which is shown with pink circles. In each panel, spectra calculated from 100 random draws of parameters from their converged posterior distributions are also shown with the blue lines. At the top of each panel, the τ=1 pressure level for each gas from the best-fit model is shown as a function of wavelength. These pressure levels are only shown so that the spectral features in the data can be associated with the dominant atmospheric gaseous absorber in the best-fit model. The *AKARI* data was obtained from Sorahana & Yamamura (2012) and the *Spitzer* data from Suárez & Metchev (2022). The ground-based data for GL570D was obtained from Geballe et al. (2009).

for all the spectral classes from L to Y- type objects, but we choose this spectral type to fit our grid as clouds in T- dwarf atmospheres are expected to be well below the observable photosphere. We exclude L/T transition objects from our sample because they too might have optically thick clouds in their photospheres and the `Elf Owl` grid is cloudless.

We only use available space-based spectroscopy measurements of these objects except GL570D, as ground-based spectroscopy of substellar atmospheres can often be contaminated by absorption from Earth's own atmosphere, especially in the molecular absorption bands. For GL570D, the available ground-based 4.5-5 μm spectra from Geballe et al. (2009) has a significantly higher signal–to–noise than the *AKARI* spectrum in that wavelength window. Therefore, we replace the *AKARI* data with the ground-based data for GL570D only between 4.5-5 μm. Based on the results shown in Figure 5.11, we fit the 2.5-14 μm spectra of objects for which both the *AKARI* and *Spitzer* observations are available. We only fit the 5-14 μm *Spitzer* spectra of other objects for which M- band observations are not publicly available. We use uniform priors on all the atmospheric parameters similar to §5.5. The sampling for $\log_{10}(K_{zz})$, [M/H], and C/O were allowed to go slightly beyond the boundaries of our atmospheric grid e.g., $\log_{10}(K_{zz})$ was allowed to vary between 0.5 to 9.5 (in cgs) even though the grid boundaries are 2-9 for $\log_{10}(K_{zz})$. In our analysis, we also do not consider any systematic offsets which might be caused by differences in flux calibration across different instruments like *AKARI* and *Spitzer*.

Figures 5.14 show the observed spectra along with the best-fitting spectral

models for each object in each panel. Data from different instruments are shown with different colored markers in each panel. 100 randomly drawn models from the converged posteriors of each object is shown with blue lines in all the panels of Figure 5.14. To identify the dominant atmospheric gaseous absorbers at each wavelength region, we also show the τ =1 pressure level as a function of wavelength for the dominant gaseous components in the best-fit atmospheric model of each object. These τ=1 pressure levels are for illustrative purposes and are shown with an inverted pressure y-axis on the top of each panel. For example, for GL570D in Figure 5.14, we find that the dominant absorber between 7-9 μm is CH_4 (shaded crimson red), between 4.5-4.8 μm is CO (shaded pink), between 5-7 μm is H_2O (shaded blue), and between 10-11 μm is NH_3 (shaded green). We obtain a corner plot for all these objects similar to the corner plot shown in Figure 5.11.

Table 5.3 lists the objects analyzed in this work and the best-fit atmospheric parameters obtained by fitting their spectra between 2.5-14 or 5-14 μm data. The errors quoted in each of these estimated parameters are the 1σ bounds on the posteriors of the parameters obtained from our fitting process. We note that the error bars on the parameters obtained by our fitting procedure ignores the uncertainty due to spectral interpolations in our grid. Such errors are known to be significant, especially for higher resolution or higher signal–to–noise spectral data (e.g., Zhang et al. 2021b). However, the datasets we fit have a typical spectral resolution of R $<$ 100 and a typical maximum signal–to–noise of about 100. Therefore, for simplicity, we ignore these interpolation errors in this work while a follow-up work which implements these errors with the `Elf`

`Owl` grid using the `STARFISH` tool is under preparation (Zhang et al., in prep). We now examine the trends we find among fitted parameters.

Object ID	**Used ID**	Instrument	$T_{\rm eff}$ [K]	*log(g)* [cgs]	$\log_{10} K_{zz}$ [cgs]	[M/H]	C/O	Radius [$R_{\rm Jup}$]
GL570D	GL570D	*Spitzer & Akari*	$813.0^{+27.0}_{-25.0}$	$3.64^{+0.47}_{-0.29}$	$1.57^{+0.42}_{-0.43}$	$-0.12^{+0.06}_{-0.07}$	$0.24^{+0.11}_{-0.05}$	$0.8^{+0.02}_{-0.02}$
2M0415	2M0415	*Spitzer & Akari*	$737.0^{+9.0}_{-9.0}$	$3.67^{+0.04}_{-0.05}$	$2.71^{+0.17}_{-0.17}$	$0.11^{+0.03}_{-0.03}$	$0.18^{+0.0}_{-0.0}$	$0.83^{+0.01}_{-0.01}$
2M0559	2M0559	*Spitzer & Akari*	$1154.0^{+16.0}_{-12.0}$	$3.66^{+0.18}_{-0.12}$	$1.07^{+0.41}_{-0.36}$	$0.28^{+0.05}_{-0.05}$	$0.48^{+0.04}_{-0.02}$	$1.12^{+0.01}_{-0.01}$
2M1114	2M1114	*Spitzer*	$772.0^{+13.0}_{-15.0}$	$4.62^{+0.1}_{-0.17}$	$4.5^{+0.25}_{-0.27}$	$0.34^{+0.06}_{-0.05}$	$0.19^{+0.02}_{-0.0}$	$0.72^{+0.01}_{-0.01}$
2M0034	2M0034	*Spitzer*	$974.0^{+28.0}_{-42.0}$	$4.16^{+0.41}_{-0.65}$	$2.83^{+2.17}_{-1.53}$	$-0.25^{+0.29}_{-0.23}$	$0.38^{+0.16}_{-0.11}$	$0.88^{+0.03}_{-0.03}$
2M0937	2M0937	*Spitzer*	$965.0^{+18.0}_{-20.0}$	$4.56^{+0.2}_{-0.14}$	$1.29^{+1.06}_{-0.76}$	$-0.3^{+0.1}_{-0.07}$	$0.2^{+0.04}_{-0.01}$	$0.83^{+0.02}_{-0.02}$
2M1624	2M1624	*Spitzer*	$1030.0^{+44.0}_{-54.0}$	$4.38^{+0.81}_{-0.88}$	$1.3^{+2.34}_{-0.76}$	$-0.11^{+0.44}_{-0.4}$	$0.26^{+0.23}_{-0.08}$	$0.78^{+0.05}_{-0.04}$
2M1225	2M1225	*Spitzer*	$983.0^{+47.0}_{-52.0}$	$4.75^{+0.64}_{-1.1}$	$3.57^{+2.94}_{-2.9}$	$0.05^{+0.7}_{-0.5}$	$0.61^{+0.23}_{-0.32}$	$1.27^{+0.09}_{-0.08}$
2M0939	2M0939	*Spitzer*	$592.0^{+5.0}_{-4.0}$	$3.23^{+0.06}_{-0.02}$	$2.25^{+0.43}_{-0.41}$	$-0.17^{+0.03}_{-0.03}$	$0.18^{+0.0}_{-0.0}$	$1.15^{+0.01}_{-0.02}$

Table 5.3: Summary of the best-fit parameters obtained in this analysis for various brown dwarfs. *AKARI* data used here is from Sorahana & Yamamura (2012) and *Spitzer* data is from Suárez & Metchev (2022). The M- band data for GL570D is from Geballe et al. (2009).

5.5.2 Trends in K_{zz}

Figure 5.15 shows the inferred K_{zz} in our analysis as a function of the determined $T_{\rm eff}$. The objects for which these parameters were estimated using both *AKARI* and *Spitzer* data are shown with green markers, whereas objects for which only *Spitzer* data were used are shown with yellow markers. Figure 5.15 shows that the inferred K_{zz} are between 10^1-10^4 cm^{2}s^{-1} in the $T_{\rm eff}$ range of $\sim$ 550-1150 K.

This behavior of low K_{zz} between 500-800 K has been previously seen in brown dwarfs (e.g., Miles et al. 2020; Mukherjee et al. 2022) and low K_{zz} in objects between 800-1000 K had been predicted by theoretical models as well (Mukherjee et al. 2022). Miles et al. (2020) used ground-based and space-based M- band spectra of a series of late T- dwarfs and found that the estimated K_{zz} is low between 500-800 K with

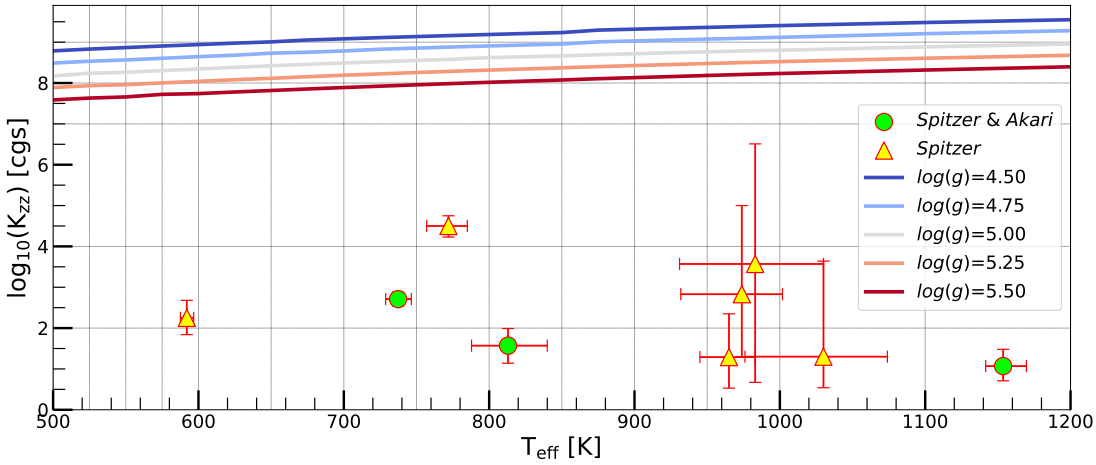

Figure 5.15: The best-fit $\log(K_{zz})$ vs. $T_{\rm eff}$ is shown for our sample of 9 T- dwarfs. The green circles represent objects for which we have fit the spectra between 2.5-14 μm whereas the yellow triangles represent the objects for which 5-14 μm data was fit with our models. The colored lines show the expected model K_{zz} as a function of $T_{\rm eff}$ from mixing length theory assuming free convection in the deep convective atmosphere. Each line corresponds to a different $\log(g)$. The gray lines in the background show the actual grid points of the `Sonora Elf Owl` grid for $T_{\rm eff}$ and K_{zz} between which the grid was interpolated to obtain the results.

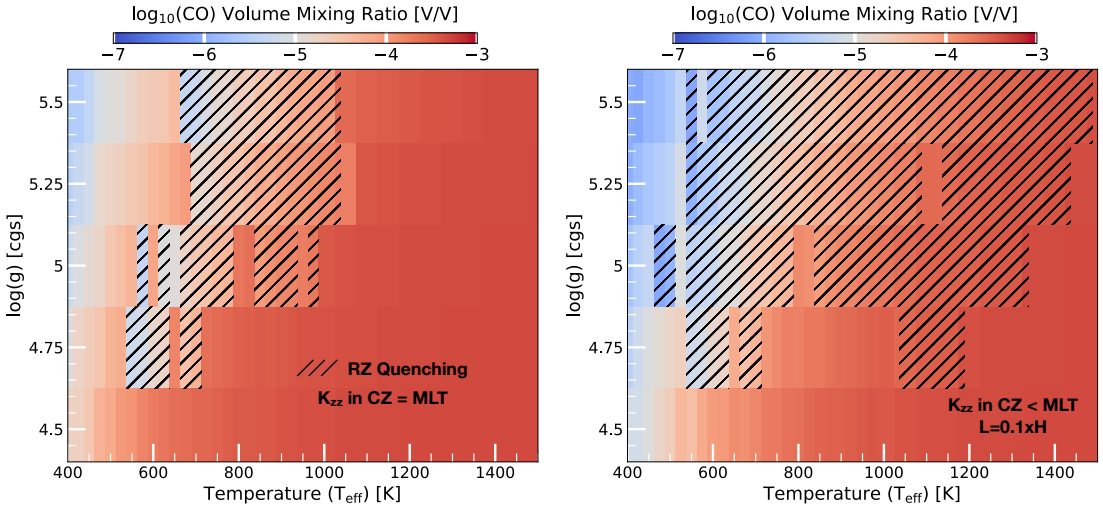

Figure 5.16: The trends in the $CO/CH_4/H_2O$ quenching in radiative or convective zone as a function of $T_{\rm eff}$ and $\log(g)$ is shown here from an extended version of the self-consistent model grid presented in Mukherjee et al. (2022). These models have K_{zz} varying across atmospheric depth instead of the constant K_{zz} approach used in the `Sonora Elf Owl` grid and have C/O ratio of 0.45. The colormap shows the quenched CO abundance as a function of $T_{\rm eff}$ and $\log(g)$ in both the panels. The left panel depicts models where the K_{zz} in the convective zone follows mixing length theory whereas the right panel shows models where the convective zone mixing length is smaller than the predictions from mixing length theory by a factor of a 10. The hatched regions depict parts of the parameter space where CO is quenched in a radiative zone instead of a convective zone.

the K_{zz} showing a large increase with decreasing $T_{\rm eff}$ below 500 K. Miles et al. (2020) hypothesized that the drop in K_{zz} between 500-800 K was a result of the gases quenching in a deep sandwiched radiative zone around these $T_{\rm eff}$ values while gases quench in the convective zones of the colder objects. Mukherjee et al. (2022) used self-consistent models to show that the sandwiched radiative zones indeed appear between $T_{\rm eff} \sim$ 500-900 K when disequilibrium chemistry is treated self-consistently. Mukherjee et al. (2022) also showed that gases could quench in these sandwiched radiative zones in this $T_{\rm eff}$ range leading to low K_{zz} estimates. They also found that for $T_{\rm eff}$ higher than 900 K and lower than 500 K, gas quenching occurs in convective zones with high K_{zz}. However, the upper bound in $T_{\rm eff}$ below which radiative region quenching can occur depends also on the vigor of mixing in the deep convective atmosphere (Mukherjee et al. 2022).

The analysis of both Miles et al. (2020) and Mukherjee et al. (2022) used only solar composition models. Using the metallicity, C/O, and K_{zz} dependant `Sonora Elf Owl` grid, Figure 5.15 shows that objects with $T_{\rm eff}$ between 550-1150 K still show low K_{zz}. This strongly suggests that the quenching of gases like CO and CH_4 occurs in a deep radiative zone in this entire $T_{\rm eff}$ range.

Numerical models presented in Mukherjee et al. (2022) show that *if* the mixing timescale in the convective zones follows predictions from mixing length theory, T-dwarfs tend to show convective zone quenching of CH_4/CO/H_2O above $T_{\rm eff}$ of $\sim$ 900 K. But if the mixing in the convective zone is slower, then CH_4/CO/H_2O can continue quenching in the radiative zone at least up to $T_{\rm eff}$ of 1000 K, which was the boundary of their modeling grid. To test the limits of radiative zone quenching beyond the grid

boundaries of Mukherjee et al. (2022), we extend their self-consistent model grid to a higher $T_{\rm eff}$ of 1500 K. Both panels of Figure 5.16 show the quenched CO abundance as a function of $T_{\rm eff}$ and $\log(g)$ as a color map. The left panel shows models where mixing in the convective zones follows mixing length theory, whereas the right panel shows models where mixing in the convective zones is slower than the predictions from the mixing length theory. In this case, this has been achieved by reducing the mixing length in the convective zone by a factor of 10 less than mixing length theory.

The hatched regions in both panels show the part of the parameter space where CO quenches in a radiative zone instead of a convective zone. As previously found in Mukherjee et al. (2022), Figure 5.16 left panel shows that radiative zone quenching of CO occurs between $\sim$ 500-1000 K for high gravity objects, if K_{zz} in the convective zone follows mixing length theory. But if the convective K_{zz} is smaller than mixing length theory predictions, Figure 5.16 shows that radiative zone quenching of CO occurs between $\sim$ 500 and 1200 K or more depending on the gravity of the object. This second scenario readily explains the very low K_{zz} found in this work across a range of 550 K - 1150 K seen in Figure 5.15 is a result of CO/CH_4/H_2O quenching in the radiative zone at these $T_{\rm eff}$. Figure 5.16 right panel also shows that the mixing in the convective zone needs to be less vigorous than predictions from mixing length theory for the K_{zz} probed with spectra to be very low beyond $\sim$ 1000 K. However, the Mukherjee et al. (2022) models and our extensions to that grid are applicable only to solar metallicity atmospheres. This work shows that metallicity can become a very important factor in setting these ranges in $T_{\rm eff}$. The higher SNR data obtained by *JWST* for a larger

sample of T- dwarfs combined with these self-consistent models will help reassess this trend with higher precision on both $T_{\rm eff}$ and K_{zz}.

The very low radiative zone K_{zz} constraints for these objects can have significant implications for cloud physics in objects with $T_{\rm eff}$ near the L/T transition boundary. If the very low K_{zz} values ($\log K_{zz} \sim 2$ [cgs]) found for these colder objects ($T_{\rm eff} < 1150$ K) are indeed due to radiative zone quenching, then this implies that mixing in radiative regions of these objects is very slow. In such a scenario, it might be very difficult to keep cloud particles of condensates such as silicates aloft near the photospheres of these objects. This mechanism, in addition to the cloud condensation points moving deeper with lower $T_{\rm eff}$, can accelerate the clearing of the atmospheres of brown dwarfs as they cool below the L/T transition boundary. The right panel of Figure 5.16 also predicts a sharp jump in probed K_{zz} when the $T_{\rm eff}$ is higher than 1200 K or more (depending on $\log(g)$) due to a switch from quenching of CH_4/CO in the radiative atmosphere for colder objects to the convective atmosphere in hotter objects. But the possible presence of photospheric clouds complicates the interpretation of K_{zz} from chemistry alone for these hotter objects. We discuss this further in §5.6.1.

Figure 5.16 also predicts a strong dependence of the radiative zone vs. convective zone quenching behaviour of gases like CO and CH_4 on the gravity of the object. This implies that for directly imaged exoplanets with lower gravity, unlike brown dwarfs, we should be probing the convective K_{zz} throughout the T- sequence $T_{\rm eff}$ range and expect to see higher values of K_{zz} in their atmospheres. We should either not at all expect to see any sharp increase and decrease of quench K_{zz} across $T_{\rm eff}$ or we should see the

sharp change but for a colder and narrower $T_{\rm eff}$ range for such objects. Observations of young directly imaged planets along with brown dwarfs will be instrumental in testing these model predictions.

5.6 Discussion

5.6.1 Clouds

We have not included any effects of clouds in our model grid or while fitting the observational data in this work. Clouds are known to be present in brown dwarf atmospheres, and the pressures at which they form and their optical depths are critical parameters that decide whether they would affect the spectrum of a brown dwarf (e.g., Morley et al. 2012, 2014a; Ackerman & Marley 2001a; Marley et al. 2002; Saumon & Marley 2008; Barman et al. 2011; Burrows et al. 2006; Gao et al. 2020c; Lacy & Burrows 2023; Charnay et al. 2018; Cooper et al. 2003). Infrared and optical colors have already shown that L- dwarf objects with $T_{\rm eff}$ values higher than $\sim$ 1400 K have photospheric silicate clouds and iron clouds (e.g., Saumon & Marley 2008; Marley et al. 2010; Miles et al. 2022; Morley et al. 2012; Gao et al. 2020c). Objects which are colder than $T_{\rm eff}$ of 400 K are also expected to have H_2O clouds (e.g., Morley et al. 2014a; Lacy & Burrows 2023). Therefore, the part of our grid above 1400 K and below 400 K might not be sufficient to fit the spectra of such objects unless they are unusually cloud-free or have very optically thin clouds in their photospheres or where the cloud opacity only affects the optical/near-infrared part of the object's spectrum.

Self-consistency is another very important aspect of cloudy models. Clouds tend to trap the outgoing radiation in the atmosphere in shorter wavelengths, causing an overall "reddening" of observable spectra (e.g., Marley et al. 2002; Saumon & Marley 2008; Morley et al. 2012, 2014b). This also causes the deeper atmosphere to be heated up. This behavior is opposite from the effect of K_{zz} on the $T(P)$ profile of the atmosphere, which causes atmospheric $T(P)$ profiles to cool down (e.g., Figure 5.3 & 5.4) (Karalidi et al. 2021a; Mukherjee et al. 2022; Phillips et al. 2020). Therefore, even in objects with clouds forming below their photospheres, the deeper parts of the $T(P)$ profile can be heated up. This can lead to changes in the abundance of gases like CH_4 in the deep atmosphere. As K_{zz} dredges up the gases from the deeper atmosphere, a change in the deep atmosphere chemistry due to clouds can lead to changes in the quenched photospheric abundances of various gases. In these scenarios, even though clouds do not directly affect the strength of spectral features, they could indirectly affect them by heating up the deeper atmosphere. The models in our grid have ignored these effects as well for simplicity in this work. Figure 5.16 predicts a sharp rise in observable K_{zz} across $T_{\rm eff}$ of $\sim$1200 K. But verifying this observationally from L/T transition objects with a cloudless grid of models is perhaps inappropriate due to these indirect but large effects of clouds. To address these gaps in the modeling literature, we are already developing a set of models for brown dwarfs and exoplanets which treat both clouds and disequilibrium chemistry self-consistently.

5.6.2 Constant K_{zz} with Pressure and Molecular Diffusion

The `Sonora Elf Owl` grid assumes a constant value of K_{zz} throughout the atmosphere for each model. This constant value is varied across a large range. However, a more realistic scenario would have a K_{zz} variable with atmospheric pressure, similar to Figure 5.1 and like what is seen in solar System planet atmospheres (e.g., Zhang & Showman 2018a; Moses et al. 2005; Visscher & Fegley 2005). In this more practical scenario, the K_{zz} is expected to be high in the convective parts of the atmosphere and low in the radiative parts of the atmosphere. Such a scenario and its implications have already been explored by Mukherjee et al. (2022) for solar composition atmospheres. One important and useful consequence of such a scenario is different gas abundances tracing K_{zz} at different pressures. For example, if CO_2 quenches at a different pressure than CO, then the CO_2 abundance should constrain the K_{zz} at a different pressure than the CO or CH_4 abundance. Although the prospect of measuring the variation of K_{zz} with altitude is very exciting for upcoming *JWST* observations, how K_{zz} varies with the $T(P)$ profile in the radiative zone is still uncertain (Mukherjee et al. 2022; Parmentier et al. 2013a; Moses et al. 2021; Komacek et al. 2019). Therefore, to make the `Sonora Elf Owl` grid more flexible for fitting observations, we ignore the variation of K_{zz} with $T(P)$ profile in this work.

The last simplification of a constant K_{zz} approach is the effect on diffusion. Depending on the value of K_{zz}, at pressures less than the homopause pressure, molecular diffusion becomes the dominant process guiding atmospheric chemistry instead of

mixing (Tsai et al. 2017, 2021; Zahnle & Marley 2014). The scale height for each gas in the atmosphere starts to depend on its molecular mass instead of the atmospheric mean molecular mass at pressures less than the homopause pressure. If the K_{zz} is low (e.g., 10^2 cm^{2}s^{-1}) then the homopause might occur at higher pressures near the photosphere of the atmosphere (Zahnle & Marley 2014; Tsai et al. 2017). However, in a more realistic scenario the K_{zz} in the upper atmosphere is expected to increase due to dynamical processes like gravity wave-breaking pushing the homopause at lower pressures (Parmentier et al. 2013a; Zhang & Showman 2018a; Mukherjee et al. 2022; Freytag et al. 2010; Tan 2022). Therefore, in the `Sonora Elf Owl` grid we ignore this molecular diffusion effect even in the low K_{zz} models.

5.7 Summary and Conclusions

We present the `Sonora Elf Owl` grid in this work, which includes self-consistent cloud-free disequilibrium chemistry cloud-free atmospheric models which cover a large parameter space of $T_{\rm eff}$, $\log(g)$, K_{zz}, [M/H], and C/O ratio. These models were calculated using the open-source atmospheric modeling code `PICASO` and apply to H-dominated directly imaged exoplanet and brown dwarf atmospheres. The grid captures variations in $T_{\rm eff}$ from 275 - 2400 K and $\log(g)$ from 3.25-5.5. The grid also includes variations in K_{zz} from 10^2- 10^9 cm^{2}s^{-1} in subsolar to supersolar metallicity atmospheres with metallicity varying from 0.1×solar to 10×solar values. Additionally, we vary the C/O ratio from 0.229 to 1.14. Previous work has analyzed how K_{zz} impacts atmospheric

structure and spectra of substellar objects with self-consistent atmospheric models (e.g., ?Karalidi et al. 2021a; Mukherjee et al. 2022; Phillips et al. 2020; Lacy & Burrows 2023). However, these effects were studied mostly in solar composition atmospheres. But apart from K_{zz}, atmospheric metallicity and C/O ratio also play important roles in shaping the chemical composition of a planet or a brown dwarf. This grid was created to examine how K_{zz}, metallicity, and C/O ratio interplay to shape the $T(P)$ profile, chemical composition, and spectrum of substellar objects across different $T_{\rm eff}$ and C/O ratio. We conclude with the following points by using and analyzing this vast grid of atmospheric models.

1. We analyze the effect of disequilibrium chemistry on atmospheric $T(P)$ profiles for various subsolar to supersolar metallicities. As seen in previous work, K_{zz} causes $T(P)$ profiles to cool down relative to models which assume thermochemical equilibrium. With our self-consistent modeling, we show that the cooling of the $T(P)$ profile is a strong function of atmospheric metallicity in Figure 5.3.

2. We find that the cooling of the $T(P)$ profile due to K_{zz} also depends on the atmospheric C/O ratio but to a lesser extent than its dependence on atmospheric metallicity (Figure 5.4). We have linked this cooling of $T(P)$ profiles with the differences in atmospheric optical depths between atmospheres in chemical equilibrium and disequilibrium due to quenching of gases like CH_4, H_2O, and CO.

3. We find that the $T_{\rm eff}$ value around which the $T(P)$ profile shows the maximum sensitivity to changes in K_{zz} depends strongly on the atmospheric metallicity. For

metal-poor atmospheres, $T(P)$ profiles between 1200-1800 K shows the maximum sensitivity to changes in K_{zz}. However, for metal-rich atmospheres, the $T(P)$ profiles between 500-1200 K show the maximum sensitivity to K_{zz} (Figure 5.5). We conclude that this trend is related to the appearance of CH_4 in the atmosphere.

4. We examine how the spectra of substellar objects are sensitive to K_{zz}, metallicity, and C/O ratio in Figure 5.7. We find that the 3-5 μm spectra show the highest sensitivity to both changing K_{zz} and changing metallicity. This can lead to degeneracies between K_{zz} and metallicity when a very small wavelength region is analyzed and also when models do not consider varying metallicity and C/O in addition to K_{zz} while fitting available observational data and data from very sensitive instruments like *JWST*.

5. Atmospheric metallicity also controls the sensitivity of the spectra to K_{zz} at various $T_{\rm eff}$ values, as shown in Figures 5.8 & 5.9. For example, for 0.3×solar metallicity objects, the CH_4 absorption feature in the L- band shows high sensitivity to K_{zz} between $T_{\rm eff}$ values of 1900 K to 450 K. But for 10×solar metallicity objects, the CH_4 absorption band shows sensitivity to K_{zz} between 1400 K to 275 K. A similar behavior is also seen in the dependence of the 4.5-4.8 μm CO band to K_{zz}.

6. We use the `Sonora Elf Owl` grid to test how different spectral wavelength ranges lead to constraints on different atmospheric parameters. We find that constraining K_{zz}, metallicity, and C/O is difficult by fitting low-resolution M- band spectra only. However, Figure 5.11 shows that fitting other wavelength ranges like 4-14

μm and 5-14 μm, or *JWST* observations can lead to very tight constraints on these parameters.

7. We use these models to fit the 2.5-14 μm or 5-14 μm observed *AKARI* and *Spitzer* spectra of 9 T- dwarfs sampling the T- type spectral sequence. We constrain the $T_{\rm eff}$, log(g), K_{zz}, [M/H], and C/O of these objects. For objects with $T_{\rm eff}$ between 550-1150 K, the K_{zz} values determined are very low, lying in the 10^1 to 10^4 cm^{2}s^{-1} range, shown in Figure 5.15.

8. Our constraints on K_{zz} in the 550-1150 K $T_{\rm eff}$ range are similar to the findings of Miles et al. (2020), but now with a wider $T_{\rm eff}$ range. Mukherjee et al. (2022) attributed this low K_{zz} to gases quenching in a radiative zone in these $T_{\rm eff}$ values with self-consistent modeling. We extend the modeling grid from Mukherjee et al. (2022) with depth-dependant K_{zz} to $T_{\rm eff}$= 1500 K and find that more sluggish convective zone K_{zz} than from mixing length theory can explain this radiative zone quenching at $T_{\rm eff}$ as high as $\sim$ 1200 K (Figure 5.16).

This work demonstrates that the interplay between K_{zz}, metallicity, and C/O to control the atmospheric chemistry of directly imaged exoplanets and brown dwarfs is very complex. We try to explore these complexities and examine how each of these parameters influence the observables. The atmospheric grid presented in this work will be very useful to constrain all these atmospheric properties from high signal–to–noise and high-resolution data from telescopes like *JWST*. However, all the models presented here are cloud-free, which limits the applicability of these models only to relatively

cloud-free objects. As a future work, we aim to upgrade the `PICASO` code to simulate clouds and disequilibrium chemistry simultaneously across different metallicities and C/O. Additionally, the strong influence of metallicity, K_{zz}, and C/O on the $T(P)$ profile and its deeper adiabat suggests that these results will also have strong implications for evolutionary calculations of brown dwarfs and directly imaged exoplanets. This is expected since the deeper atmospheric adiabat controls the cooling of the interior of such objects, as their interiors are expected to be fully convective in nature. As *JWST* is expected to measure the most precise luminosities of brown dwarfs and imaged exoplanets till date (e.g., Miles et al. 2022; Beiler et al. 2023; Greenbaum et al. 2023), we will follow up this work with a new generation of `Sonora Elf Owl` evolutionary models, which are consistent with atmospheres in chemical disequilibrium across various metallicities and C/O ratios.

Part II

Transiting Exoplanets

Chapter 6

Effects of Planetary Parameters on Disequilibrium Chemistry in Irradiated Planetary Atmospheres: From Gas Giants to Sub-Neptunes

6.1 Introduction

Major goals of characterizing exoplanet atmospheres are to understand the formation and evolutionary history of planets. This process involves observing exoplanetary atmospheres and intrepreting these observations to estimate some key bulk planetary parameters, like metal enrichment of the atmosphere, which can be used to understand their formation scenario and evolutionary history. However, our interpretation of observational data of exoplanetary atmospheres requires a robust understanding

of the various physical and chemical processes ongoing in the planet's atmosphere. In this work, we explore how a series of atmospheric processes can affect our interpretation of exoplanet atmospheric observations. We explore how these atmospheric processes specifically impact atmospheric chemistry, which is a crucial link between understanding exoplanetary atmospheres and constraining their formation and evolutionary processes.

There has been a considerable amount of modeling work revolving around the idea that planets retain some amount of information about their formation scenario and subsequent evolution in their current state (e.g., Öberg et al. 2011; Mollière et al. 2022a; Mordasini et al. 2016). This information can be retained within important planetary parameters like the planetary radius, bulk metal enrichment, elemental abundance ratios, internal heat flux of the planet, etc. (e.g., Madhusudhan 2012; Fortney et al. 2007; Öberg et al. 2011; Mollière et al. 2022a). For transiting planets, parameters like planetary mass and radius are directly measurable. But other critical parameters like bulk metal-enrichment, bulk elemental abundance ratios, and internal heat flux of planets need to be inferred by observing and understanding their atmospheres. As planetary atmospheres are quite complex, drawing inferences about their bulk properties requires a detailed understanding of the multiple interconnected physical processes at play.

JWST observations have opened a new era of precision chemical analysis of transiting planet atmospheres (e.g., Rustamkulov et al. 2022b; Ahrer et al. 2022; Alderson et al. 2022; Feinstein et al. 2022; Tsai et al. 2023b; Kirk et al. 2024; Thao et al. 2024; Welbanks et al. 2024; Sing et al. 2024; Beatty et al. 2024a; Bell et al. 2023c; Grant et al. 2023; Fu et al. 2024; Radica et al. 2023; August et al. 2023a; Schlawin et al. 2024a; Xue

et al. 2024; Inglis et al. 2024; Bean et al. 2023; Gagnebin et al. 2024). This is especially interesting because the atmospheric chemistry of planets with H/He atmospheres (from giant planets down to sub-Neptunes) is sensitive to three key planetary parameters – 1) bulk metal-enrichment (or metallicity), 2) bulk elemental abundance ratios, and 3) internal heat flux of planets (e.g., Fortney et al. 2020; Mollière et al. 2015).

The metallicity of a planet's atmosphere is defined as $(X/H)_{planet}/(X/H)_{sun}$, where X represents the number of atoms of a certain element (like C-, O-, S-, etc) in the object and H is the number of hydrogen atoms. Therefore a planet with higher metallicity will have significantly different atmospheric chemical composition than one with lower metallicity. Two planets with the same metallicity might have the "metals" distributed differently among various elements. For example, one planet can have a higher C/H ratio and lower O/H ratio than the other and yet maintain the same bulk metallicity (e.g., Madhusudhan 2012; Moses et al. 2013b). These abundance ratios are important potential markers of the formation location of planets because of the presence of various ice lines in propoplanetary disks (e.g., Öberg et al. 2011; Mollière et al. 2022a; Mordasini et al. 2016). It is clear and well-studied how both of these bulk parameters can affect atmospheric chemistry especially if the atmosphere is in thermochemical equilibrium throughout (e.g., Visscher & Fegley 2005; Visscher et al. 2006; Goyal et al. 2018; Mollière et al. 2015; Lodders 2004, 2002). However, studies of solar system giant planets and brown dwarf atmospheres have shown that disequilibrium chemical processes in addition to thermochemistry can play a significant role across planetary atmospheres (e.g., Zhang 2020; **?**; Karalidi et al. 2021a; Mukherjee et al. 2023;

Miles et al. 2020; Phillips et al. 2020; Tsai et al. 2017; Moses et al. 2011; Mukherjee et al. 2024c; Venot et al. 2012; Drummond et al. 2016).

The chemical structure of a planet's atmosphere is shaped by a number of other physical processes too, namely – 1) atmospheric mixing, 2) photochemistry, 3) condensation, and 4) molecular diffusion. As a result, the photospheric abundance of a gas like CH_4 is not only controlled by the metallicity, C/O ratio, and heat flux from the deep interior of the planet but also by parameters like the stellar UV flux incident on the planet along with atmospheric properties like strength of vertical and horizontal dynamics in the atmosphere (e.g., Tsai et al. 2021, 2023c; Moses et al. 2011; Fortney et al. 2020; Tsai et al. 2023a). Molecular diffusion is an important process controlling the chemical nature of atmospheres at very low pressures but the importance of this process is often overshadowed by photochemical processes, especially in highly irradiated giant exoplanets (e.g., Tsai et al. 2021). Atmospheric mixing, photochemistry, condensation, and internal heat flux of exoplanets remain the least understood/constrained processes/parameters in exoplanet atmospheres. We briefly explain these processes here.

Atmospheric Mixing – Atmospheres of planets are dynamic, not static, in nature. This dynamics can play out in three dimensions causing both vertical and horizontal bulk transport of gases and aerosols in atmospheres (e.g., Showman et al. 2009b; Menou & Rauscher 2009; Steinrueck et al. 2019; Roth et al. 2024). As a result, photospheric abundances of gases such as CH_4, CO, NH_3 can be significantly altered depending on the strength of dynamics in the atmosphere (Cooper & Showman 2006; Drummond et al. 2016; Steinrueck et al. 2019; Mendonça et al. 2018; Drummond et al.

2018, 2020a; Zamyatina et al. 2023; Lee et al. 2023). 3D models of tidally locked close-in giant exoplanets have revealed three major types of transport operational in their atmospheres – 1) vertical transport, 2) day-to-night transport, and 3) pole-to-equator transport. Vertical transport can lift gases and aerosols from the deeper parts of the atmosphere across several pressure scale-heights, while the day-to-night winds can transport gases from the hotter day-side of the planet to their colder night-side. Clearly, a full understanding of the role of atmospheric dynamics on planet-wide chemistry requires the use of 3D models to explore vast swathes of the multidimensional parameter space involved. This vast parameter space includes dimensions like the stellar flux incident on the planet, the planet's gravity, atmospheric composition, rotational period, interior properties such as interior heat flux, cloud composition, etc. The computational run times involved in 3D atmospheric models often prohibit a full scale parameter space exploration.

However, 1D models can somewhat capture the vertical transport operating in these atmospheres by simplifying the transport as a diffusive process, parametrized with the 1D eddy diffusion coefficient– K_{zz}. K_{zz} is defined as $v_{\rm mix} L_{\rm mix}$, where $v_{\rm mix}$ is the typical velocity of transport and $L_{\rm mix}$ is the typical length-scale at which this bulk transport is operational (Allen et al. 1981). But, observational constraints on K_{zz} are very weak. Recently, several studies have constrained K_{zz} to a certain extent in brown dwarf atmospheres with ground-based and space-based data (e.g., Miles et al. 2020; Mukherjee et al. 2022; Madurowicz et al. 2023; Beiler et al. 2023; Mukherjee et al. 2024c; Kothari et al. 2024) but we have only started to constrain it for irradiated planets

(e.g., Sing et al. 2024; Welbanks et al. 2024; Kawashima & Min 2021). Various 3D and 2D modeling efforts have found a large range of K_{zz} values in model atmospheres (e.g., Tan 2022; Parmentier et al. 2013a; Komacek et al. 2019; Tsai et al. 2023c; Freytag et al. 2010; Menou 2019), keeping the parameter uncertain by several orders of magnitude in irradiated planets. It is important to especially mitigate this uncertainty due to the influence of K_{zz} on key gas abundances that are used to infer bulk properties of planets such as C/O or metallicity.

Internal Heat Flux – As planets evolve, they slowly lose their gravitational heat of formation to space. This energy is carried from the deep interior through convection to the deep atmosphere up to the point where the atmosphere is opaque at all wavelengths (e.g., Fortney et al. 2007). Beyond that, the heat is lost to space via radiation in the partially or fully optically thin radiative atmosphere. Therefore, detailed properties of the atmosphere, such as its composition and thermal structure, control the rate of cooling of the whole planet over its entire lifetime. This rate of cooling, in turn, also controls the contraction of the planet over time. Additionally, external energy sources like tidal heating can also deposit energy to the deep interior of the planet, the extent of which depends on various orbital and bulk planet properties.

The internal heat flux cannot be measured directly through transmission and emission spectroscopy of close-in exoplanet atmospheres because it typically only alters the temperature structure of the planet where its atmosphere is optically thick, leading to little or no affect on its photospheric temperatures. However, internal heat flux can indirectly affect the photospheric chemical abundances due to the vertical mixing

phenomenon discussed previously (e.g., Fortney et al. 2020; Agúndez et al. 2014). If gases are mixed up to the photospheres of the planets from the deep optically thick atmosphere, where internal heat flux affects chemistry, then they can alter the observable photospheric chemistry of the planet and let us infer the internal heat flux of the planet as well. This works for gases which are stable for long times and not chemically destroyed in the photosphere immediately after being transported. Gases such as CO and N_2 fit into this category as destroying them chemically at low temperature photospheres and converting them to gases like CH_4 and NH_3 is generally energetically prohibitive. Therefore, photospheric abundances of such gases are strongly influenced by the internal heat flux of the planet. Recently, *JWST* transmission spectroscopy observations of WASP-107b were used to constrain its internal heat flux by Welbanks et al. (2024) and Sing et al. (2024). Both of these analysis revealed a high $T_{\rm int}$ ($\geq$345 K), which was interpreted as evidence for tidal heating of the planet's interior. Similar constraints on other transiting planets have also been obtained using *HST* (e.g., Barat et al. 2024). These studies are an excellent example of how understanding atmospheric chemistry can reveal details of close-in giant planet evolution.

The internal heat flux of a planet at a given age depends on the mass of the planet. For example, at a similar age, a more massive planet is expected to have a hotter interior than a less massive planet, if there are no external perturbations on the planet such as tidal heating. However, interior temperatures also depend on aspects of atmospheric physics. For example, the strength of vertical mixing plays a major role in affecting both atmospheric clouds and chemistry. Both of these things can

delay/accelerate the cooling of planets over time (e.g., Morley et al. 2024; Saumon & Marley 2008).

Photochemistry – Planets can have significant X-ray and UV photons incident on them from their host stars. These photons can cause the photolysis of weakly bonded molecules such as CH_4, NH_3, H_2S, etc. in the upper atmosphere (e.g., Moses et al. 2011; Tsai et al. 2021, 2023c,a; Wogan et al. 2023; Hu 2021; Venot et al. 2012; Moses et al. 2016). This can trigger a whole new set of chemical reactions altering photospheric composition. The first concrete evidence of a photochemical by-product was confirmed with *JWST* in WASP-39b by the presence of photochemically produced SO_2 in its upper atmosphere (Tsai et al. 2023c; Ahrer et al. 2022; Alderson et al. 2022; Rustamkulov et al. 2022b). While significant modeling work on understanding photochemistry in close-in planets has been done previously (e.g., Moses et al. 2011; Tsai et al. 2021, 2023c,a; Crossfield 2023; Zahnle et al. 2009; Venot et al. 2012), this *JWST* work demonstrated that photochemistry cannot be neglected while modeling the photospheric chemical nature of planets and using abundances to infer planetary properties.

Additionally, photolysis of gases like CH_4 and NH_3 can lead to the production of C- and N- bearing molecules like C_2H_2 and HCN. These gases in the upper atmospheres of H_2/He-rich atmospheres can act as precursors for further reactions to form photochemical hazes (e.g., Morley et al. 2013, 2015; Fortney et al. 2013; Gao et al. 2020). The optical properties of these hazes are such that they can play a significant role in shaping the observable spectra of exoplanet atmospheres (e.g., Lavvas & Koskinen 2017; Kawashima & Ikoma 2018; Ohno & Kawashima 2020; Steinrueck et al. 2023b; Arfaux

& Lavvas 2022; Morley et al. 2015).

The discussion above shows that the observational data from transiting planets today is at a stage where its chemistry can be leveraged to not only understand atmospheric elemental compositions of planets but also should be leveraged to understand exoplanetary atmospheric processes better as well. These include constraining key atmospheric processes such as atmospheric dynamics and parameters like internal heat flux of planets. Therefore, it is necessary to explore how atmospheric dynamics and internal heat flux can influence the photospheric abundance of gasses in exoplanets with varying bulk properties such as equilibrium temperature, C/O ratio, metallicity, and varying amounts of incident UV flux. It is also important to identify the key molecules that can produce the best constraints on very uncertain parameters like K_{zz} in different parts of this vast parameter space.

This paper presents a broad parameter space study to address these questions. Our work is applicable to a wide variety of planets. In terms of internal heat flux, this includes sub-Neptune mass planets with lower internal heat fluxes, to Jupiter mass giant planets with much hotter interiors. In terms of planetary temperatures, we explore planets between cold giant planets ($T_{\rm eq}\sim$ 400 K) to hot Jupiters ($T_{\rm eq}\sim$ 1600 K). We also explore the atmospheric chemistry of planets with varying C- and O- abundances. We also investigate the effects of a wide range of the atmospheric mixing parameter K_{zz} and atmospheric metallicity on the chemistry of these planets.

We describe our modeling setup in§6.2 followed by the results presented in §6.3. We discuss the limitations and caveats in this analysis in §7.5 followed by summarizing

our key conclusions in §7.6.

6.2 Modeling

The aim of the modeling presented in this work is to explore a significant parameter space of properties that can influence atmospheric chemistry of transiting planets with H/He atmospheres. The parameters we consider in this study are the equilibrium temperature ($T_{\rm eq}$), interior heat flux through the parameter $T_{\rm int}$, strength of vertical mixing parameterized with K_{zz}, C/O ratio, and metallicity. The modeling setup to achieve this parameter space exploration can be divided into two different components – 1) 1D radiative–convective atmospheric modeling, and 2) chemical kinetics modeling. We describe each component in detail below.

6.2.1 1D Radiative–Convective Equilibrium Models

We use the 1D radiative–convective equilibrium model `PICASO` (Mukherjee et al. 2023; Batalha et al. 2019) to generate atmospheric temperature–pressure ($T(P)$) profiles for irradiated planets. We generate the $T(P)$ profiles for a planet with gravity= 4.5 ms^{-2} around a star with $T_{\rm eff}$=5327 K, $log(g)$=4.38, [M/H]= -0.03, and Radius= 0.932 R$_{\odot}$. These system parameters are chosen to be the same as WASP-39b. We divide the planet atmosphere into 91 plane-parallel levels (90 layers) logarithmically spaced in pressure between 10^{-6} to 100/5000 bars. We generate the $T(P)$ profiles using the heat recirculation factor `rfacv`= 0.5, which corresponds to the case of full heat redistribution across the planet. We place the planet at different distances from the star

such that the $T_{\rm eq}$ of the planet (assuming 0 albedo) are 1600 K, 1400 K, 1100 K, 900 K, 800 K, 600 K, and 400 K. For each of these cases, we generate 5 different cases with different $T_{\rm int}$ values of 30 K, 100 K, 200 K, 300 K, and 500 K. The lowest value, 30 K, is representative of Gyr+ old sub-Neptunes (Lopez & Fortney 2014). Jupiter's value today is 100 K. More massive, younger, or inflated gas giants (such as by tidal heating or other factors) would have larger $T_{\rm int}$ values (Fortney et al. 2020). The equilibrium chemistry calculation and gaseous opacities used for computing these $T(P)$ profiles are the same as used in Mukherjee et al. (2024c). Figure 6.1 shows these generated $T(P)$ profiles where each panel corresponds to a different $T_{\rm eq}$ case. Note that these radiative–convective–thermochemical–equilibrium (RCTE) models were calculated by including TiO and VO opacities, which are known to cause thermal inversions in atmospheres which have $T_{\rm eq}\geq$ 1600 K. We generate these $T(P)$ profiles at 10×solar metallicity and solar C/O ratio (C/O= 0.458 (Lodders et al. 2009)) assuming thermochemical equilibrium throughout the atmosphere.

6.2.2 Chemical Kinetics Modeling

To simulate disequilibrium chemistry within our model atmospheres, we use the python wrapped *Photochem*[1] chemical kinetics model (Wogan et al. 2023, 2024). We use the $T(P)$ profiles computed using the method described in the previous section as inputs in the *Photochem* package. In addition to the *Photochem* package, we use the *Cantera* software (Goodwin et al. 2023) to simulate thermochemical equilibrium in the

[1]https://github.com/Nicholaswogan/photochem

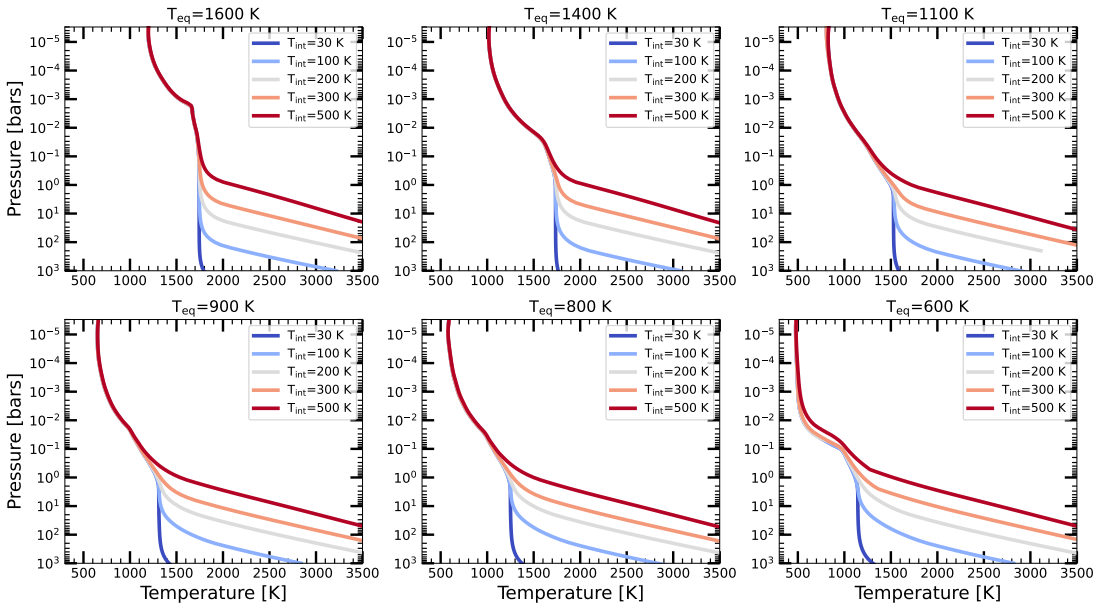

Figure 6.1: $T(P)$ profiles computed using 1D radiative–convective–equilibrium modeling at various $T_{\rm eq}$ and $T_{\rm int}$ values are shown. Each panel shows the model $T(P)$ profiles computed for a $T_{\rm eq}$ value at five different $T_{\rm int}$ values between 30 K and 500 K. The six panels correspond to $T_{\rm eq}$= 1600 K, 1400 K, 1100 K, 900 K, 800 K, and 600 K. The kink at 1 mbar and 1700 K in the hottest models ($T_{\rm eq}$=1600 K) is due to a small amount of TiO opacity. All the $T(P)$ profiles have been computed for a planet with gravity=4.5 ms^{-2} around a star with $T_{\rm eff}$= 5326.6 K, $log(g)$=4.38, and Radius=0.93$R_{\odot}$.

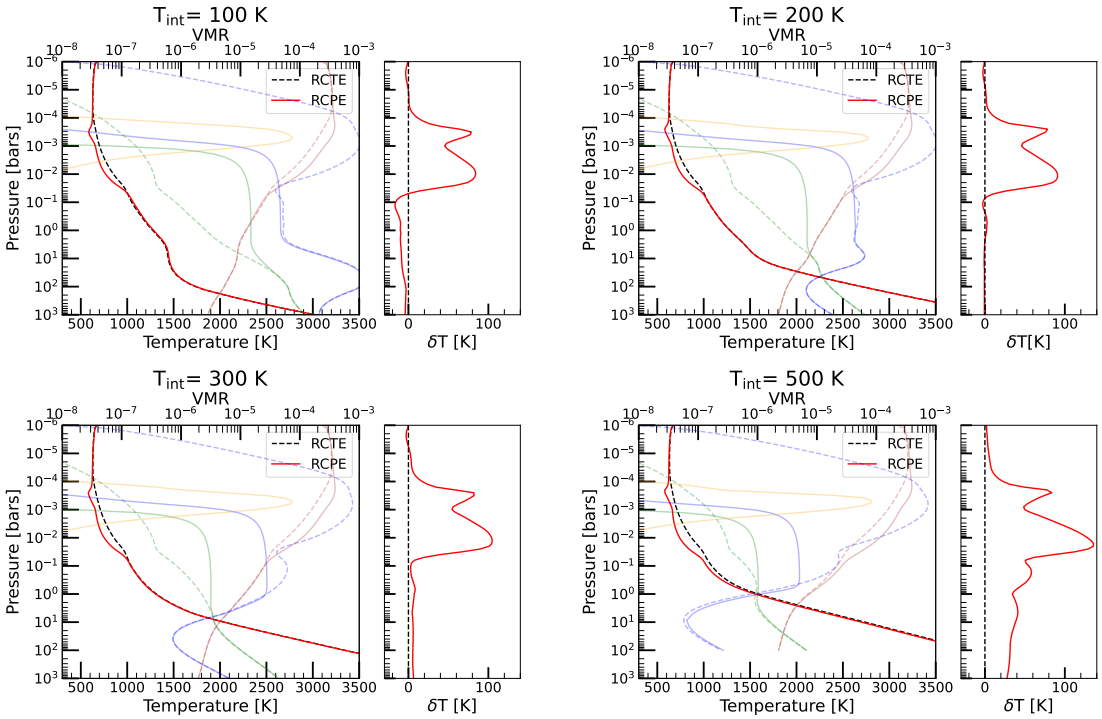

Figure 6.2: $T(P)$ profiles computed assuming radiative–convective–thermochemical equilibrium (RCTE) and radiative–convective–photochemical equilibrium (RCPE) are shown with dashed black lines and solid red lines, respectively. The assumed $T_{\rm eq}$, [M/H], and C/O of the model is 800 K, +1.0, and 1×solar, respectively. Each panel corresponds to a different $T_{\rm int}$ from 100 K to 500 K. The faded lines show the volume mixing ratios (top x-axis) of CH_4, NH_3, SO_2, and CO_2 in blue, green, orange, and brown, respectively. The dashed VMR profiles are from the RCTE models whereas the solid VMR profiles correspond to the RCPE models. The narrower panel accompanying each of the four panels shows the different in the $T(P)$ profile between the two modeling assumptions in each case as a function of pressure.

very deep atmosphere of the model planet atmospheres. For each model, we use the quench time approximation with chemical timescales from Zahnle & Marley (2014) to determine the quench pressures of key gases like CH_4, NH_3, CO_2, etc. At atmospheric levels with pressures much greater than the highest quench pressures among these gases (5-8 atmospheric levels deeper than the highest quench pressure), we use *Cantera* to calculate the thermochemical equilibrium state of the atmospheres. At pressures smaller than this pressure level we use *Photochem* to simulate chemical disequilibrium with its kinetics calculations. The convergence criteria used in our photochemistry modeling is presented in §6.4.4. This modeling setup helps us in calculating photochemical models significantly quicker than using the chemical kinetics calculation for all the pressure layers in the atmosphere including the very high pressure and high temperature deep atmosphere where chemical reactions are expected to be very fast. The setup saves computational time by preventing the kinetics model from taking extremely small time steps to model the very rapid chemical reactions in the very deep atmosphere, which is bound to remain in thermochemical equilibrium anyway. To maintain sufficient accuracy in the 1D chemical kinetics calculations, we interpolate the atmospheric $T(P)$ profiles with 91 pressure levels to a finer grid of pressures with 180 pressure levels before ingesting them within *Photochem*.

For a given metallicity, we scale the C/H, O/H, N/H, S/H from the solar values with the metallicity factor in our model. To change the C/O ratio for a given metallicity, we change both the C/H and O/H such that (C+O)/H remains the same. This is crucial to maintain the same atmospheric metallicity while changing the C/O ratio of

the atmosphere. To account for O- atoms locked up in various expected condensates such as silicates, we remove 20% of the O from the atmospheric gas phase.

`PICASO` and *Photochem* can be fully and iteratively coupled, instead of `PICASO` using pre-computed equilibrium chemistry tables (e.g., Marley et al. 2021; Fortney et al. 2007; Morley et al. 2013; Mukherjee et al. 2023; Morley et al. 2014b; Fortney et al. 2005, 2008b), or using on-the-fly non-equilibrium chemistry due to mixing implemented using quench time approximation (e.g., Mukherjee et al. 2022, 2024c). Figure 6.2 illustrates the difference in the $T(P)$ profile between a fully self-consistent treatment of photochemistry within the climate model and a profile computed assuming radiative–convective–thermochemical equilibrium (RCTE) for the same set of physical parameters – $T_{\rm eq}$= 800 K, [M/H]=+1.0, and C/O=1×solar. The radiative–convective–photochemical equilibrium (RCPE) (e.g., Bell et al. 2023c; Welbanks et al. 2024) model was computed by combining the *Photochem* kinetics model (Wogan et al. 2023) calculations within the `PICASO` climate calculation framework. Each panel of Figure 6.2 illustrates the difference between the $T(P)$ profiles for four different $T_{\rm int}$ values of 100 K, 200 K, 300 K, and 500 K with K_{zz}=10^9cm^{2}s^{-1}. The RCTE (dashed) and RCPE (solid) chemical profiles for CH_4 (blue), NH_3 (green), and SO_2 (orange) are also shown in each panel. It is clear that for lower values of $T_{\rm int}$, the maximum difference in the $T(P)$ profile is typically around $\sim$ 100 K in the 0.1 mbar to 0.1 bar range. Whereas as the $T_{\rm int}$ increases, small differences of the order of $\sim$ 20 K remain in the profiles, even at deeper pressures till around 100 bars. This shows that the corrections in the $T(P)$ profiles due to radiative feedback from the changed atmospheric chemistry due to vertical mixing or photochemistry is

an important effect, especially for high $T_{\rm int}$ values. This will be especially relevant for interpreting emission spectra of planets. Even though this work focuses on modeling disequilibrium chemistry effects, we choose not to use the RCPE approach for our $T(P)$ profile calculations mainly because this can vastly increase the computational time involved in running a 1D model. We make this choice because we focus on transmission spectroscopy in this paper where temperature has a relatively small effect compared to emission spectroscopy. Moreover, in our parameter space exploration, we vary both metallicity and C/O ratio but we do not self-consistently include the variation of the $T(P)$ profile with metallicity and C/O in our models. We discuss the effect of these approximations further in §7.5.

Our parameter space exploration (§6.3.1) is focused on investigating roles of C/O and K_{zz} across planets with different $T_{\rm eq}$ and $T_{\rm int}$. For this, we run photochemical models for 13 different C/O values between a range of C/O ratios starting from 0.0458 to 1.125 with a step size of 0.0916, exploring the very O- rich to very C- rich atmospheres at 10×solar metallicity. We also vary the K_{zz} parameter between 10^6 to 10^{13} cm^{2}s^{-1} with steps of 1 in the $\log_{10}(K_{zz})$ space. This range reflects the huge range of uncertainty on this parameter covering cases of very slow vertical mixing to rapid mixing. Therefore, in the first parameter space exploration we compute chemical kinetics models for each $T(P)$ profile shown in Figure 6.1 for a range of C/O and K_{zz}. For each model, we use the X-ray/UV spectra for WASP-39b used in Tsai et al. (2023c). Note that we *do not* scale the UV flux incident on the planet as we move the planet closer or further away from the star to change its $T_{\rm eq}$. We make this choice as we want to explore the chemical trends

in atmospheres as a function of varying $T_{\rm eq}$ with a uniform X-ray/UV flux incident on the planet. This is to avoid changing this additional parameter while we sweep the $T_{\rm eq}$ parameter space. Our second part of the parameter space exploration (§6.3.2) is focused on exploring the role of metallicity, C/O, K_{zz}, and $T_{\rm int}$ on the photospheric abundances but at a fixed $T_{\rm eq}$. We present the trends in photospheric abundance with varying $T_{\rm eq}$ in §6.3.3 and the sensitivity of the transmission spectra to various planetary parameters in §6.3.4. We also present trends in our estimates of photochemical precursors to haze/soot across the parameter space in §6.3.5.

6.3 Results

6.3.1 Exploring how abundances depend on K_{zz}, C/O, and $T_{\rm int}$ across different $T_{\rm eq}$

In this section, we present the variation of key molecular abundances at the pressures typically probed by transmission spectroscopy for transiting planets. The top three panels of Figure 6.3 shows an example of how CH_4 abundance profiles change with changing K_{zz}, $T_{\rm int}$, and C/O, respectively for a planet with $T_{\rm eq}$= 800 K. The middle and bottom three panels of Figure 6.3 shows the same but for SO_2 and CO_2, respectively. The approximate pressure range probed by transmission spectroscopy is shown with the red shaded region in each panel. It is clear that $T_{\rm int}$, K_{zz}, and C/O can cause significant changes to the photospheric abundance of gases like CH_4 but Figure 6.3 also shows that not all gases are equally sensitive to all of these parameters.

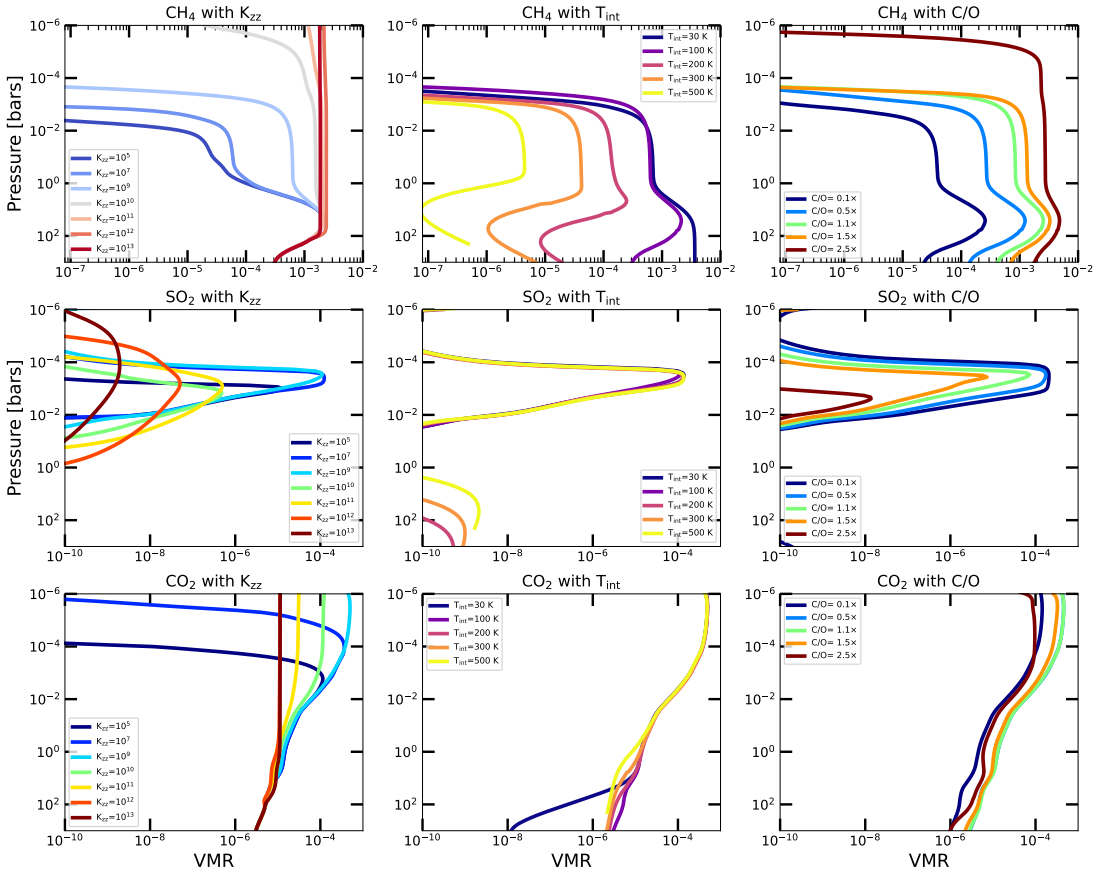

Figure 6.3: The dependence of chemical abundance profiles on K_{zz}, $T_{\rm int}$, and C/O are shown in the left, middle, and right columns, respectively. The upper row shows this dependence for CH_4 while the middle and lower rows show this dependence for SO_2 and CO_2, respectively. The pressure values typically probed by transmission spectra are shown with the red shaded region.

In order to present the trends in photospheric abundance of gases with variations in these parameters, we use a box-shaped kernel between 10 mbar and 0.1 mbar which is also the region shaded in Figure 6.3. For each gas abundance profile, we calculate the logarithm of the average photospheric abundance using,

$$log_{10}(X_{\rm w}) = \frac{\int_{P_1}^{P_2} \log_{10}(X(p))dp}{\int_{P_1}^{P_2} dp} \tag{6.1}$$

where $X(P)$ is the volume mixing ratio profile of gas X, p_1 is 10 mbar, and p_2 is 0.1 mbar. This range covers a typical pressure range probed by transmission spectroscopy. We present the trends in $X_{\rm w}$ for various gases in the following sections.

6.3.1.1 Trends in CH_4, CO, H_2O, and CO_2

CH_4

CH_4 is one of the major C-bearing gases in giant planet atmospheres. Figure 6.4 shows the quantity $X_{\rm w}$ for CH_4 with a heat map as a function of K_{zz} and C/O at various $T_{\rm eq}$ and $T_{\rm int}$ values. Each row in Figure 6.4 corresponds to a different $T_{\rm eq}$ from 1100 K to 600 K, while each column corresponds to a different $T_{\rm int}$ from 30 K to 500 K. We do not show the heat maps computed for $T_{\rm eq}$ of 1400 and 1600 K here as they are qualitatively similar to the 1100 K case. The left most part of each sub-figure shows the trend in CH_4 $X_{\rm w}$ in the case of thermochemical equilibrium.

Figure 6.4 shows that for $T_{\rm eq} \geq 1100$ K, CH_4 only becomes abundant in the photosphere when the atmosphere is very C- rich with C/O $>$ 2$\times$solar or when K_{zz}

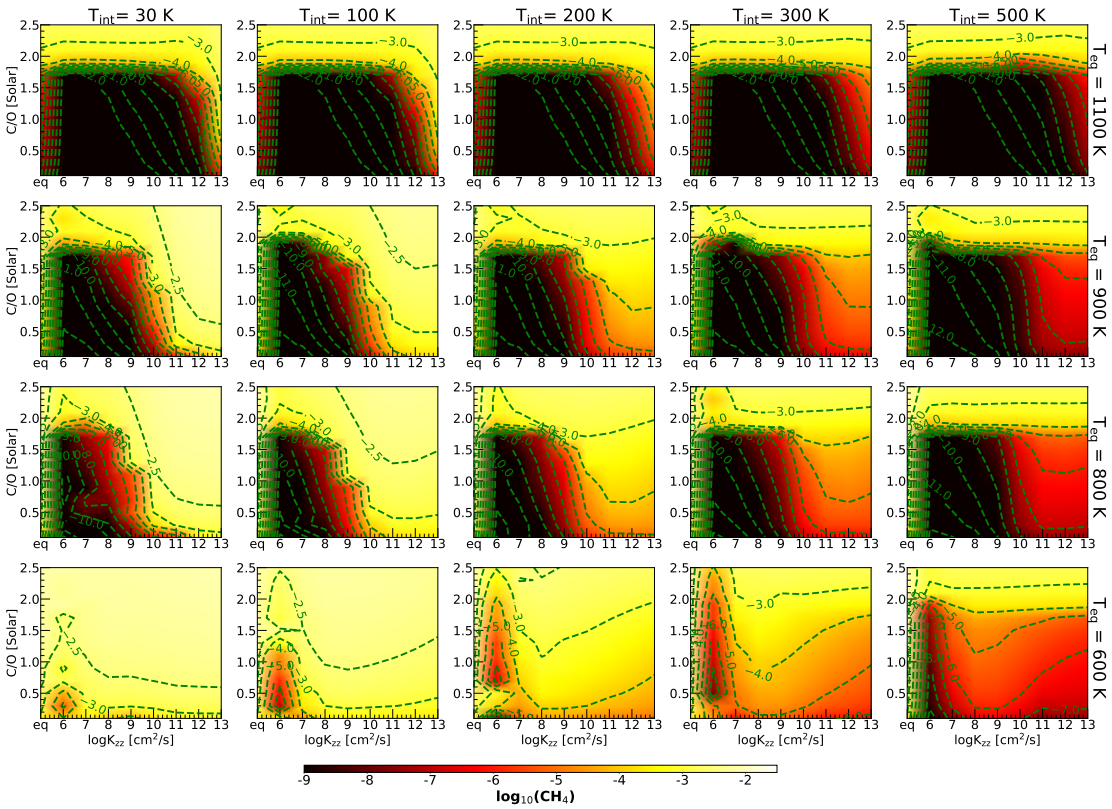

Figure 6.4: The weighted abundance of CH_4 calculated using Equation 6.1 as a function of C/O and K_{zz} in each panel. Each row corresponds to a different $T_{\rm eq}$ value from 1100 K to 600 K from top to bottom. Each column correspond to a different $T_{\rm int}$ value between 30 K and 500 K from left to right. Note that the C/O is shown relative to an assumed solar value of 0.458 in this plot.

$\geq 10^{12}$ cm^{2}s^{-1}. Madhusudhan (2012) found very similar C/O dependence for CH_4, albeit their calculations assumed thermochemical equilibrium. The amount of CH_4 in the photosphere for these hotter planets shows some $T_{\rm int}$ dependence when the vertical mixing is extremely vigorous with $K_{zz} \geq 10^{12}$ cm^{2}s^{-1}. In these cases, a colder interior planet (e.g., $T_{\rm int}$= 30 K or 100 K) shows higher amount of photospheric CH_4 than planets with much hotter interior (e.g., $T_{\rm int}$= 500 K). This shows that the $T_{\rm int}$ parameter, which mostly affects the $T(P)$ and chemistry in the deep atmosphere, already starts to affect the CH_4 abundance at much smaller pressures at $T_{\rm eq}$=1100 K, when mixing is vigorous.

Figure 6.4 shows that for a given C/O, $T_{\rm int}$, or K_{zz}, the CH_4 abundance is much higher in the $T_{\rm eq} \leq$ 900 K planets than the $T_{\rm eq} \geq$ 1100 K planets. For $T_{\rm eq}$= 900 K, Figure 6.4 shows that the CH_4 abundance varies very strongly with K_{zz}. For a given C/O, the photospheric CH_4 abundance shows 6-7 orders of magnitude increase with the K_{zz} increasing by 7 orders of magnitude. The abundance of photospheric CH_4 is much lower than the expectations from thermochemical equilibrium for $K_{zz} \leq 10^{11}$cm^{2}s^{-1} when $T_{\rm int} \leq$ 200 K. For stronger vertical mixing, the amount of CH_4 rises to thermochemical equilibrium expectations for these colder interior planets. Whereas, the CH_4 abundance is always lower than the expected amount from thermochemical equilibrium for hotter interiors for all the K_{zz} values explored in Figure 6.4. Equal abundance contours plotted on Figure 6.4 $T_{\rm eq}$=900 K panels are nearly vertical which suggests that the variation of CH_4 abundance with changing K_{zz} is stronger than its variation with C/O. For a given C/O and K_{zz}, the CH_4 abundance typically decreases by 3-4 orders of magnitude with the $T_{\rm int}$ increasing from 30 K to 500 K for $T_{\rm eq}$=900

K. Figure 6.4 shows that the qualitative behavior shown by the CH_4 abundance is very similar between T_{eq}=900 K and T_{eq}=800 K panels except the CH_4 abundances are higher in the T_{eq}=800 K panels than the T_{eq}=900 K panels for a given C/O, T_{int}, and K_{zz} value.

The last row in Figure 6.4 shows CH_4 abundances for T_{eq}= 600 K. For these cold T_{eq} values, CH_4 abundance shows a significant increase compared to the T_{eq}= 800 K cases. This increase is especially high for $K_{zz} \leq 10^{10} cm^2 s^{-1}$. Also, the equal abundance contours for T_{eq}= 600 K, are nearly horizontal which shows that the CH_4 abundance is much more sensitive to C/O than K_{zz} for these cold planets. At T_{eq}= 600 K, for a given C/O and K_{zz} value, the CH_4 abundance shows a 2-3 orders of magnitude decrease with T_{int} increasing from 30 K to 500 K. The equal abundance contours shown in Figure 6.4 show that while interpreting the C/O of a planet from its measured CH_4 abundance, one should be particularly careful in parts of the parameter space where the contours in Figure 6.4 are not horizontal. This means that the same photospheric CH_4 abundance can be a result of a wide range C/O in these parts of the parameter space. This also suggests that the CH_4 abundance, if detected, can be a good diagnostic of K_{zz} in parts of the parameter space where the equal abundance contours are nearly vertical. Figure 6.4 suggests that CH_4 becomes a favorable marker of vertical transport when T_{eq} is between 800–900 K, which is slightly colder than the 'sweet-spot' identified in the 3D models presented in Zamyatina et al. (2023). Note that we have shown these trends at a fixed metallicity (i.e., 10×solar).

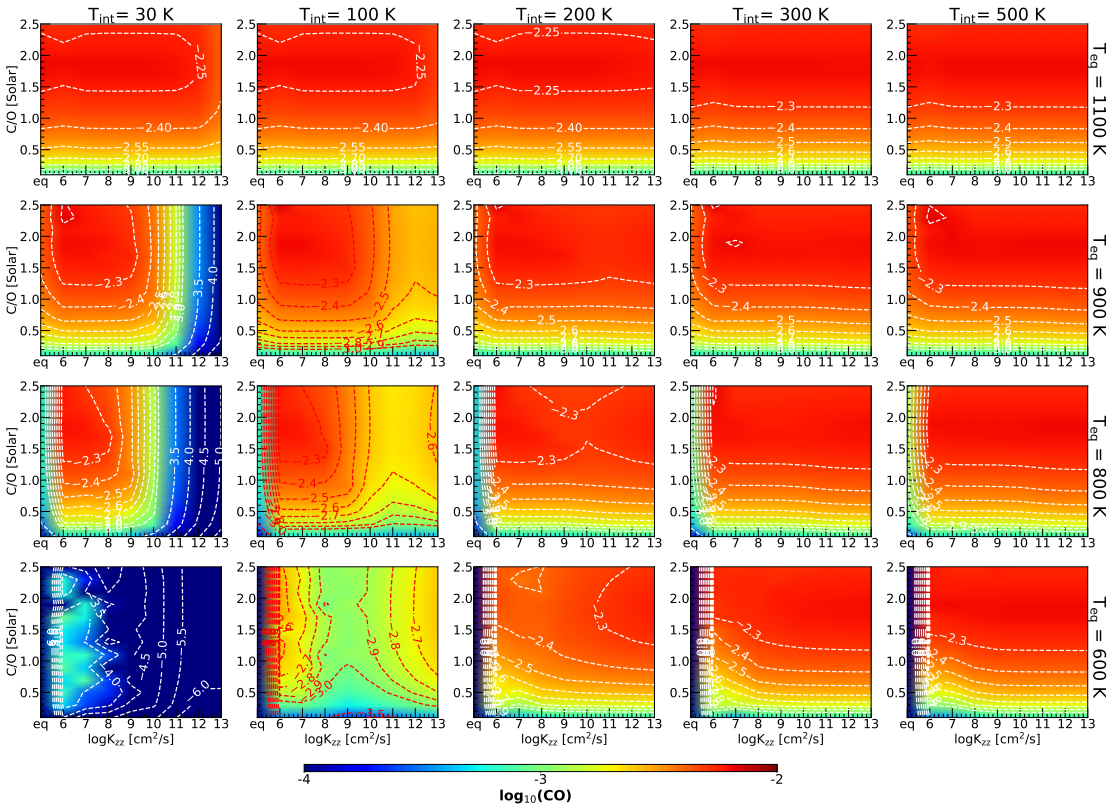

Figure 6.5: The weighted abundance of CO calculated using Equation 6.1 has been shown as a heat map as a function of C/O and K_{zz} in each panel. Each row corresponds to a different $T_{\rm eq}$ value from 1100 K to 600 K from top to bottom. Each column correspond to a different $T_{\rm int}$ value between 30 K and 500 K from left to right. Note that the C/O has been shown relative to the assumed solar value of 0.458 in this plot.

CO

Figure 6.5 presents the X_w for CO across different C/O ratios and K_{zz}. Again, each panel corresponds to a different $T_{\rm eq}$ and $T_{\rm int}$ combination. **For $T_{\rm eq}$= 1100 K, Figure 6.5 shows that the CO abundance shows some weak sensitivity to C/O showing an increase with increasing C/O around C/O∼0.3×solar. Figure 6.5**

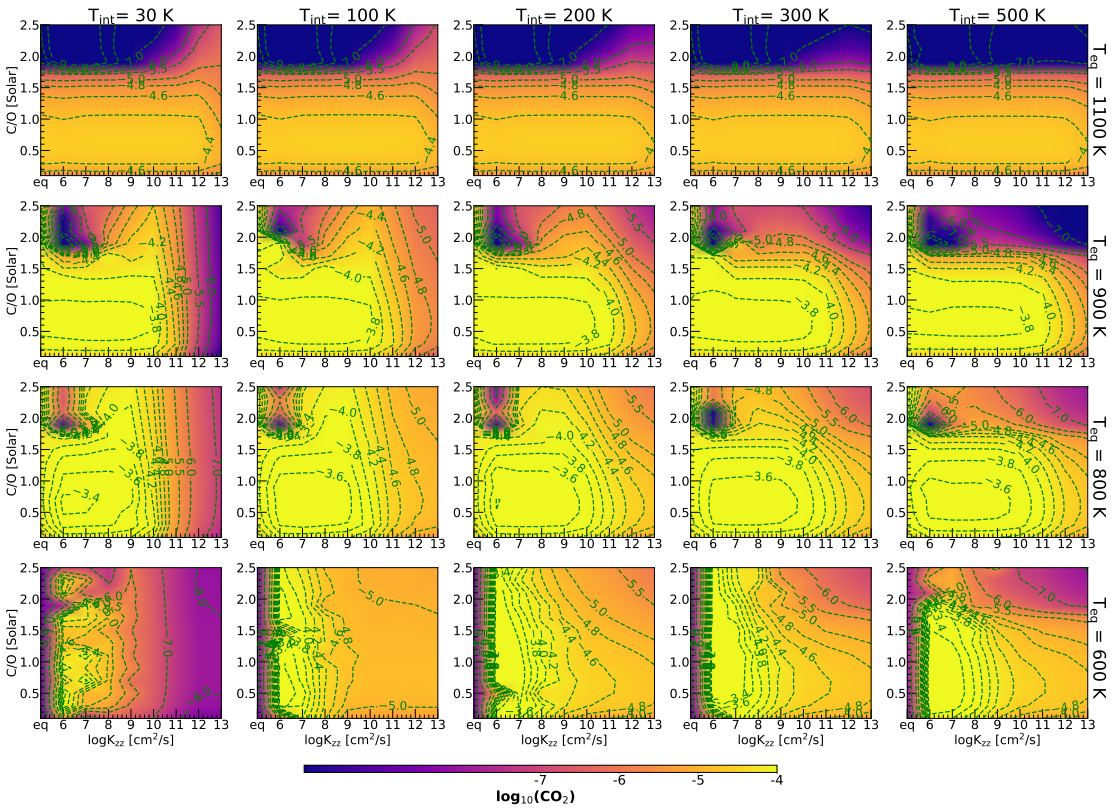

Figure 6.6: The weighted abundance of CO_2 calculated using Equation 6.1 has been shown as a heat map as a function of C/O and K_{zz} in each panel. Each row corresponds to a different $T_{\rm eq}$ value from 1100 K to 600 K from top to bottom. Each column correspond to a different $T_{\rm int}$ value between 30 K and 500 K from left to right. Note that the C/O has been shown relative to the assumed solar value of 0.458 in this plot.

suggests that the CO gas cannot be a great tracer of K_{zz} for planets with $T_{\rm eq}$ $\geq$ 1100 K irrespective of the strength of K_{zz}. The CO abundane for a given C/O also shows almost no $T_{\rm int}$ dependence for $T_{\rm eq}\geq$1100 K. The difference in CO abundance between the thermochemical equilibrium and disequilibrium chemistry at $T_{\rm eq}$= 1100 K and 900 K is almost negligible. However, some K_{zz} dependence of CO abundance appears at $T_{\rm eq}$= 900 K, when $T_{\rm int}\leq$ 100 K. For these cases, CO shows a decrease with increasing K_{zz} when $K_{zz}\geq 10^9 {\rm cm}^2{\rm s}^{-1}$. This decrease of CO abundance with increasing K_{zz} beyond $10^9 {\rm cm}^2{\rm s}^{-1}$ is much more pronounced when $T_{\rm int}$=30 K than the case of $T_{\rm int}$= 100 K. Similar behavior is also shown by the $T_{\rm eq}$= 800 K models, where the K_{zz} dependence of CO abundance for cold interior planets ($T_{\rm int}\leq$ 100 K) sets in at a slightly lower K_{zz} of $10^8 {\rm cm}^2{\rm s}^{-1}$. This suggests that for planets with $T_{\rm eq}$ at 800 K or 900 K and hot interiors ($T_{\rm int} \geq$ 200 K), CO can weakly trace the C/O, irrespective of K_{zz} and with minimal dependence on $T_{\rm int}$ as well. But for such planets with cold interiors $T_{\rm int} \leq$ 100 K, CO abundance can show a strong dependance on the strength of K_{zz}.

The same behavior is not only shown but enhanced further in $T_{\rm eq}$= 600 K planets shown in the last row of Figure 6.5. The CO abundance mainly depends on K_{zz} only in these cases for $T_{\rm int} \leq$ 100 K and shows a weak dependence on C/O for $T_{\rm int} \geq$ 200 K. This suggests that for planets with colder $T_{\rm eq}$ ($\leq$ 900 K) and cold interiors ($T_{\rm int} \leq$ 100 K), CO abundance can be a tracer of K_{zz}, whereas for all the other cases of hotter planets or hotter interiors, CO abundance can weakly trace the atmospheric C/O. We note that the weak dependence of CO abundance on C/O might not be measurable with the current precision of atmospheric observations of transiting planets.

The CO abundance in planets with cold interiors and colder $T_{\rm eq}$ values shows a decrease with increasing K_{zz}, beyond a certain K_{zz} value, because their $T(P)$ profiles straddle the CO=CH_4 equal abundance curve (Fortney et al. 2020). This has been shown in Figure 6.7 left panel, where the black dashed curve shows the CO=CH_4 equal abundance curve and the solid $T(P)$ profiles represent $T_{\rm int}$=30 K models with $T_{\rm eq}$ lying between 1100 K and 600 K. CO abundance decreases in the bottom left direction of the figure and CH_4 abundance decreases towards the top right direction of the plot. The black points on each $T(P)$ profile show the quench points for CO, when the K_{zz} is 10^6, 10^8, 10^{10}, and 10^{12} $\rm cm^2s^{-1}$. The CO abundance remains almost constant with changing K_{zz} if the quench pressure lie in the CO dominated region, which is the top right part above the CO=CH_4 equal abundance curve. If quenching happens in this region, the quenched CO abundance is expected to be insensitive to K_{zz}. However, if CO is quenched in the lower left half, where CO abundance is rapidly decreasing, then the CO abundance shows a rapid decrease with increasing K_{zz}. This decrease is sharper because of the isothermal nature of the $T(P)$ profile, which are far from being parallel to the equal abundance contours of CO in this part of the $T-P$ space.

Another important behavior reflected in Figure 6.5 is that the photospheric CO abundance remains the same between thermochemical equilibrium and chemical disequilibrium for $T_{\rm eq} \geq 900$ K, but for colder planets, the CO abundance in the thermochemical equilibrium cases are smaller than the models with low K_{zz} values ($K_{zz} \leq 10^7 \rm cm^2s^{-1}$), irrespective of $T_{\rm int}$. This suggests that even though the CO abundance can act as a weak tracer of C/O (without any K_{zz} dependence) in planets with hot interiors,

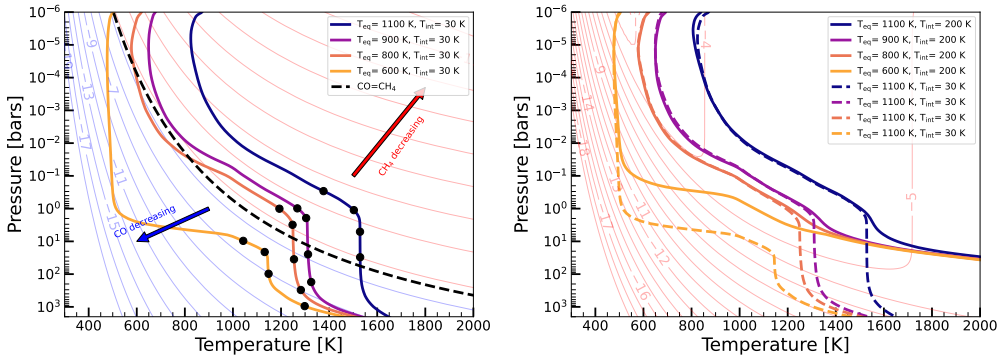

Figure 6.7: **Left panel:** The $T(P)$ profiles of planets with $T_{\rm int}$= 30 K and $T_{\rm eq}$ between 1100 and 600 K are shown with the four solid lines. The black dashed line shows the CO=CH_4 equal abundance curve from chemical equilibrium calculations at [M/H]=+1.0 and C/O=1×solar. Equal abundance contours for CO and CH_4 are shown in blue and red, respectively. The four black markers on each $T(P)$ profile show the quench pressures of CO for 10^6, 10^8, 10^{10}, and 10^{12} $\rm cm^2 s^{-1}$. **Right panel:** The $T(P)$ profiles of planets with $T_{\rm int}$= 200 K and $T_{\rm eq}$ between 1100 and 600 K are shown with the four solid lines, whereas the dashed lines show the models for $T_{\rm int}$= 30 K. Equal abundance contours for CO_2 from thermochemical equilibrium are shown in red.

disequilibrium chemistry calculations must still be used to interpret the correct C/O of a planet from its measured CO abundance. This behavior is a direct effect of the shape of the $T(P)$ profiles of these planets, when their $T_{\rm eq}$ is $\leq$ 800 K and can also be understood with the left panel of Figure 6.7. The $T(P)$ profiles of planets with $T_{\rm eq}\leq$800 K transition from the CO-dominated to the CH_4 dominated regions in the $T-P$ space, as shown in Figure 6.7. This leads to a sharp decrease in photospheric CO in these objects. However, even for low K_{zz} values (e.g., 10^6 $\rm cm^2 s^{-1}$), the CO gets quenched at much deeper pressures, where their $T(P)$ profiles cross equal abundance contours corresponding to higher CO abundance than the low photospheric CO abundance expected from thermochemical equilibrium. As the CO abundance becomes roughly constant on the top right side of the CO=CH_4 line, this doesn't happen when $T_{\rm eq}\geq$900 K.

CO_2

Figure 6.6 shows the X_w for CO_2. At $T_{\rm eq}$= 1100 K, the CO_2 abundance shows a sharp decrease when C/O $\geq$ 1.9×solar. This behaviour is unlike CO, which doesn't show such a sharp change in its abundance when C/O is $\geq$ 1.9×solar as shown in the top panels of Figure 6.5. CO_2 shows this sharp decline beyond C/O $\geq$ 1.9×solar due to the unavailability of enough O- atoms to form CO_2 when the C/O is approaching 1. At this $T_{\rm eq}$, CO_2 remains practically independent of K_{zz} across all $T_{\rm int}$ values, except for some slight K_{zz} sensitivity for $K_{zz}\geq 10^{12}{\rm cm^2 s^{-1}}$. However, Figure 6.6 also shows that the photospheric CO_2 abundance doesn't show much change with changing C/O between 0.3×solar$\leq$C/O$\leq$1.2×solar across all $T_{\rm int}$ values. This might limit the utility of CO_2 as a C/O diagnostic for this range of C/O values. This suggests the CO_2 can be a good tracer for C/O in these $T_{\rm eq} \geq$ 1100 K planets, except for very high strengths of vertical mixing or for 0.3×solar$\leq$C/O$\leq$1.2×solar. CO_2 also doesn't show much dependence on $T_{\rm int}$ at this $T_{\rm eq}$.

CO_2 has a larger K_{zz} dependence for planets with $T_{\rm eq}\leq$ 900 K. For $T_{\rm eq}$= 900 K and $T_{\rm int}$= 30 K, the CO_2 remains insensitive to K_{zz} for $K_{zz}\leq 10^{9}{\rm cm^2 s^{-1}}$. However, the CO_2 shows very strong sensitivity to K_{zz} for higher values of K_{zz} causing the CO_2 abundance to drop by two orders of magnitude with K_{zz} increasing by four orders of magnitude. This behavior is present for hotter $T_{\rm int}$ models as well, albeit with a slower decrease of CO_2 abundance with increasing K_{zz}. With increasing $T_{\rm int}$, the K_{zz} value

at which CO_2 transitions from being insensitive to sensitive to K_{zz} also shifts slowly towards higher value. The $T_{\rm eq}$= 800 K models shown in the third row of Figure 6.6, also show the same qualitative behavior as the $T_{\rm eq}$ =900 K models, but with an even stronger dependence of CO_2 abundance on K_{zz} once the K_{zz} value is higher than the "transition" K_{zz} value. This behavior can be readily understood with the right panel of Figure 6.7, which shows the $T(P)$ profiles for $T_{\rm int}$= 200 K and 30 K models with solid and dashed lines, respectively. Each profile corresponds to a different $T_{\rm eq}$. The equal abundance contours for CO_2 from thermochemical equilibrium are shown with the red lines. For planets with hotter $T_{\rm eq}$ or hotter $T_{\rm int}$, most of the $T(P)$ profile lie in parts of the $T-P$ space where the CO_2 equal abundance contours appear less dense. This suggests that a large change in quench pressure of CO_2 due to changing K_{zz} will only cause a small change in the quenched CO_2 abundance for such $T(P)$ profiles. However, for planets with colder $T_{\rm eq}$ or colder $T_{\rm int}$, the $T(P)$ profiles traverse a denser region of equal abundance contours of CO_2. For these models, a change in quench pressure of CO_2 due to changing K_{zz} will produce a much more pronounced effect on the quenched CO_2 abundance. These models suggest that for $T_{\rm eq}$=800 and 900 K planets, irrespective of $T_{\rm int}$, the CO_2 abundance remains sensitive to K_{zz} to varying degrees if K_{zz} is higher than a "transition" value which is typically somewhere between 10^9-10^{10}cm^{2}s^{-1}. Other than the coldest interior case of $T_{\rm int}$=30 K, the CO_2 abundance doesn't show very strong dependence on $T_{\rm int}$.

Although for $T_{\rm eq}\geq$800 K, the photospheric CO_2 abundances between thermochemical equilibrium and low K_{zz} values are nearly the same, this breaks down for $T_{\rm eq}$=

600 K. The CO_2 abundance shows a sharp increase between thermochemical equilibrium models and K_{zz}=10^6cm^{2}s^{-1} for these models. This effect can be understood with the interplay between the 'U' shaped CO_2 equal abundance contours and the $T(P)$ profiles shown in the right panel of Figure 6.7. Most of the $T(P)$ profiles of planets with $T_{\rm eq}$≥800 K remain in the $T-P$ space where the CO_2 contours are less dense and nearly vertical. As a result, the equilibrium abundance of CO_2 monotonically and slowly increases with decreasing pressure in these objects. Therefore, there is generally not a large difference between the quenched abundance and chemical equilibrium abundance of CO_2 in these objects. However, the $T_{\rm eq}$= 600 K model has a complex shape with a nearly horizontal region traversing the densely packed contours, where the chemical equilibrium CO_2 abundance decreases rapidly. If the CO_2 abundance is quenched in this region, the quenched abundance will be significantly higher than expected equilibrium chemistry abundance of CO_2 in the photosphere. Moreover, at $T_{\rm eq}$=600 K, CO_2 depends almost solely depends on K_{zz}, and not C/O, for $T_{\rm int}$≤100 K. Some C/O dependence of the photospheric CO_2 abundance sets in for higher $T_{\rm int}$ values. This suggests that near $T_{\rm eq}$=600 K, the CO_2 abundance can be a good tracer of K_{zz} for planets with cold interiors ($T_{\rm int} \leq 100$ K) but for planets with hotter interiors, it can be quite degenerate between K_{zz} and C/O.

H_2O

The X_w for H_2O is shown in Figure 6.8. The range of variation in X_w for

H_2O is much lower when compared with other gases shown in Figures 6.4, 6.5, and 6.6. H_2O shows strong sensitivity to C/O when $T_{\rm eq}$= 1100 K without much dependence on K_{zz}. At $T_{\rm eq}$= 900 K, when the $T_{\rm int}\geq$ 200 K, this behaviour of H_2O abundance being only dependant on C/O continues. The dependence of H_2O abundance on $T_{\rm int}$ is also extremely weak in these cases. H_2O starts to show some K_{zz} dependence when $K_{zz} \geq 10^{10}{\rm cm^2 s^{-1}}$ for $T_{\rm int} \leq$ 100 K at $T_{\rm eq}$= 900 K. This behaviour continues for $T_{\rm int}\leq$ 100 K at $T_{\rm eq}$= 800 K as well, except the K_{zz} dependence of H_2O abundance sets in a lower value of $K_{zz}\geq 10^{9}{\rm cm^2 s^{-1}}$. The H_2O abundance shows an increase with K_{zz} beyond this value which is also accompanied by a sharp decrease in CO and CO_2 abundance seen in this part of the parameter space in Figures 6.5 and 6.6, especially at $T_{\rm int}$= 30 K. The H_2O abundance shows a decrease between thermochemical equilibrium and the $K_{zz}=10^{6}{\rm cm^2 s^{-1}}$ chemical disequilibrium calculations for models with $T_{\rm eq}\leq$800 K. This decrease is particularly strong for C/O$\geq$1.7$\times$solar for $T_{\rm eq}$= 800 K models. This decrease in H_2O abundance between thermochemical equilibrium and $K_{zz}=10^{6}{\rm cm^2 s^{-1}}$ is also seen for $T_{\rm eq}$=600 K models. However, the amount of decrease seen in these models increases with increasing $T_{\rm int}$ at this $T_{\rm eq}$. This highlights that for these hotter $T_{\rm int}$ values ($T_{\rm int} \geq$ 200 K) at $T_{\rm eq} \leq$ 900 K, H_2O can still be a good tracer of C/O but chemical disequilibrium calculations must still be carried out to interpret the C/O from H_2O abundance accurately. The $T_{\rm eq}$=600 K models shown in the last row of Figure 6.8 show much less sensitivity to K_{zz} compared to the $T_{\rm eq}$=900 K and 800 K models. This behavior is similar to the smaller sensitivity shown by CH_4 abundance to K_{zz} in Figure 6.4 at $T_{\rm eq}$= 600 K.

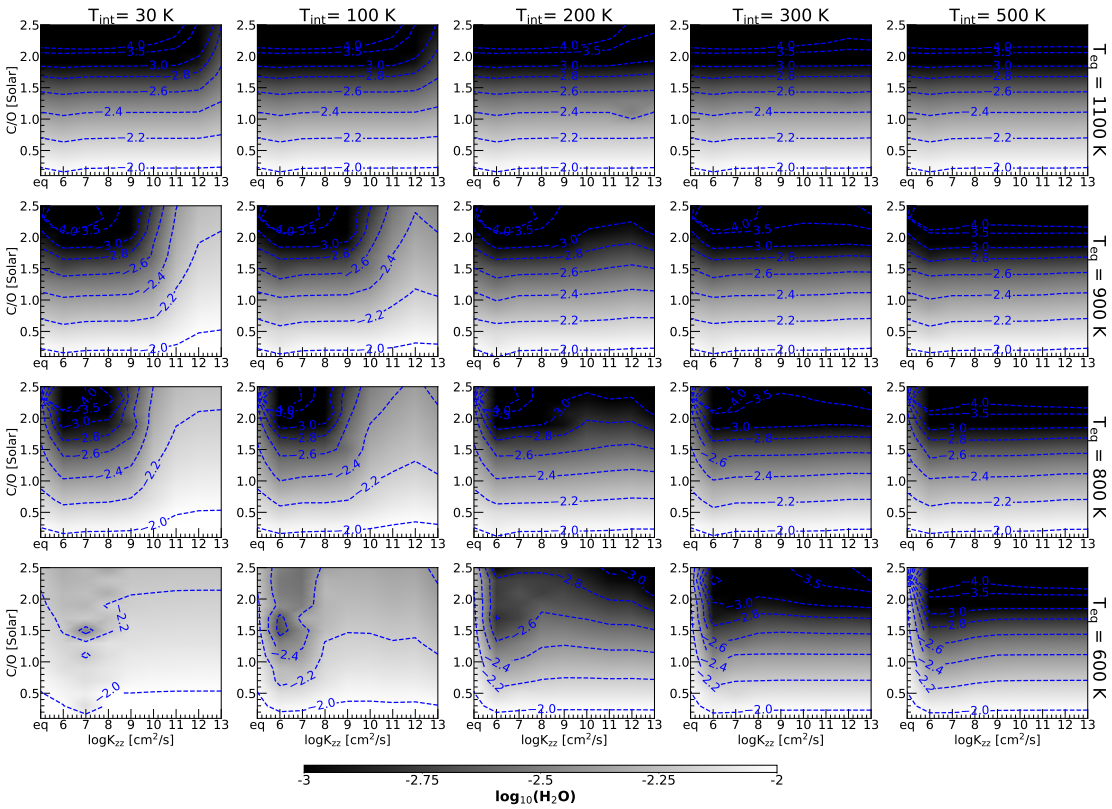

Figure 6.8: The weighted abundance of H_2O calculated using Equation 6.1 has been shown as a heat map as a function of C/O and K_{zz} in each panel. Each row corresponds to a different $T_{\rm eq}$ value from 1100 K to 600 K from top to bottom. Each column correspond to a different $T_{\rm int}$ value between 30 K and 500 K from left to right. Note that the C/O has been shown relative to the assumed solar value of 0.458 in this plot.

6.3.1.2 Trends in NH_3 and HCN

NH_3

Figure 6.9 shows the X_w metric for NH_3. NH_3 neither contains C- or O- and therefore is expected to not depend strongly on C/O. All panels of Figure 6.9 reflect this behavior. At $T_{\rm eq}$= 1100 K, the photospheres are very NH_3 poor. For $T_{\rm eq}$= 900 K, the photospheric NH_3 abundance slowly starts to rise, much more for the colder $T_{\rm int}$ models. The vertical equal abundance contours in Figure 6.9 show that NH_3 is very sensitive to K_{zz} in addition to high sensitivity to $T_{\rm int}$. Similar to the CH_4 behavior seen in the previous section, NH_3 abundance monotonically increases with K_{zz}. For the coldest interior of $T_{\rm int}$= 30 K at $T_{\rm eq}$= 900 K or 800 K, NH_3 abundance increases by 7 orders of magnitude between K_{zz} of $10^6 {\rm cm^2 s^{-1}}$ and $10^{13} {\rm cm^2 s^{-1}}$. The equal abundance curves for NH_3 are known to be nearly parallel to the adiabats for H_2/He gas mixture in the deep atmosphere (Zahnle & Marley 2014; Fortney et al. 2020; Ohno & Fortney 2023b). This means that if NH_3 is quenched in the deep convective atmosphere, its photospheric abundance will not be very sensitive to K_{zz}. NH_3 can become more sensitive to K_{zz} if it is quenched in the radiative atmosphere in irradiated planets, where the lapse rate of the $T(P)$ profile is very different than the adiabatic lapse rate. The photodissociation of NH_3 due to the incident UV radiation also depends on K_{zz}. A low K_{zz} in the upper atmosphere causes the NH_3 abundance to be depleted very rapidly with decreasing pressure. The depletion of NH_3 with decreasing pressure is much less if the K_{zz} in

the upper atmosphere is high. Both of these effects shape the K_{zz} dependence of the NH_3 abundance shown in Figure 6.9 in the pressures typically probed by transmission spectroscopy.

At $T_{\rm eq}$≤900 K, the NH_3 abundance also declines by several orders of magnitude as $T_{\rm int}$ rises from 30 K to 500 K. Similar to the findings of Ohno & Fortney (2023b), we also find that when $T_{\rm int} \leq 200$ K, the photospheric NH_3 abundance shows a very sharp rise with $T_{\rm eq}$ below $T_{\rm eq}$=800 K when vertical mixing is slow (K_{zz}≤10^8cm^{2}s^{-1}). But when vertical mixing is faster, the photospheric NH_3 abundance shows a much more gradual rise with $T_{\rm eq}$, as was also found by Ohno & Fortney (2023b). Even though detecting NH_3 has proven to be a difficult task so far with *JWST* (Welbanks et al. 2024), its abundance can be of great use for reducing the degeneracies discussed in the previous section arising from just fitting CH_4 abundances and measuring K_{zz} and $T_{\rm int}$, especially for warm planets.

HCN

HCN is a molecule which is quenched due to K_{zz} as well as produced photochemically. Moreover, unlike NH_3, it has C- and therefore should be sensitive to C/O. Figure 6.10 shows the X_w calculated for HCN. As expected, photospheric HCN shows sensitivity to both C/O and K_{zz}, and also depends on $T_{\rm int}$. Figure 6.10 shows that the disequilibrium chemistry abundance of HCN is much higher than the expected thermochemical equilibrium abundance. The equal abundance contours in the top row for $T_{\rm eq}$=

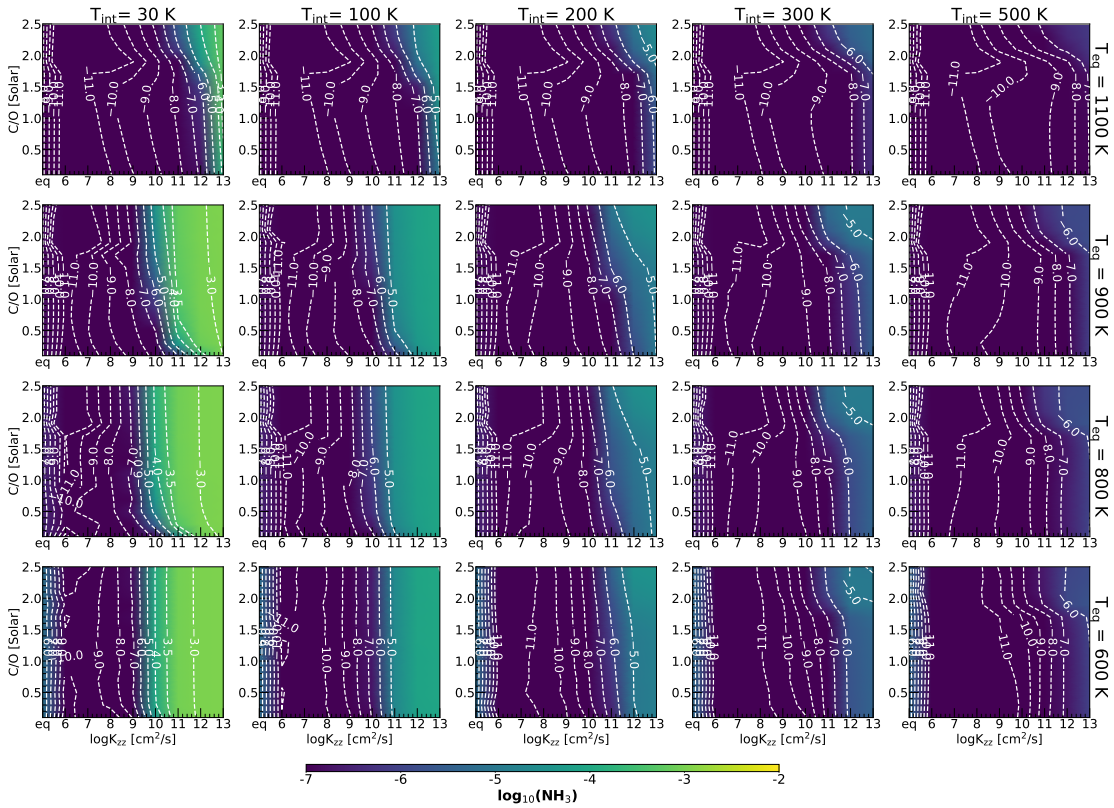

Figure 6.9: The weighted abundance of NH_3 calculated using Equation 6.1 has been shown as a heat map as a function of C/O and K_{zz} in each panel. Each row corresponds to a different $T_{\rm eq}$ value from 1100 K to 600 K from top to bottom. Each column correspond to a different $T_{\rm int}$ value between 30 K and 500 K from left to right. Note that the C/O has been shown relative to the assumed solar value of 0.458 in this plot.

1100 K run diagonally which shows that same HCN abundance can be very degenerate corresponding to a wide range of C/O ratios and K_{zz} for these hotter planets. At $T_{\rm eq}$= 900 K ,800 K and 600 K, the HCN abundance is mostly sensitive to K_{zz} and not much to C/O if K_{zz} is either low or very high. The HCN abundance is not sensitive to either K_{zz} or C/O for intermediate values of K_{zz}.

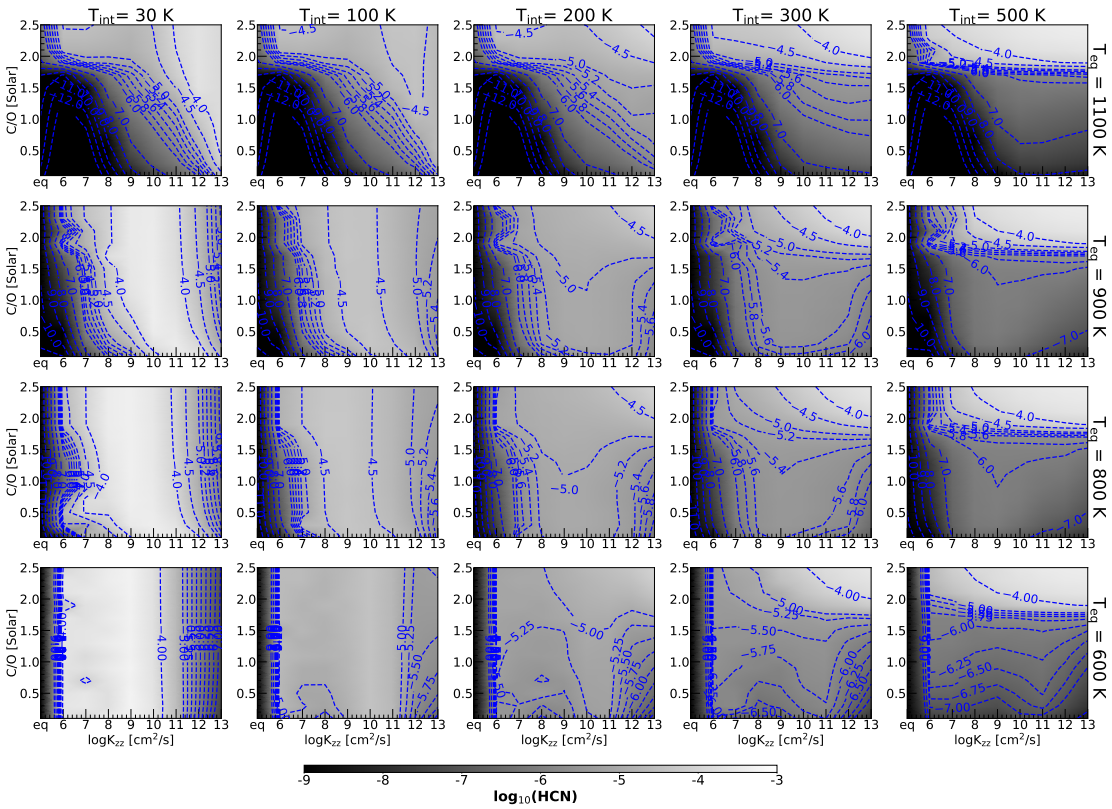

Figure 6.10: The weighted abundance of HCN calculated using Equation 6.1 has been shown as a heat map as a function of C/O and K_{zz} in each panel. Each row corresponds to a different $T_{\rm eq}$ value from 1100 K to 600 K from top to bottom. Each column correspond to a different $T_{\rm int}$ value between 30 K and 500 K from left to right. Note that the C/O has been shown relative to the assumed solar value of 0.458 in this plot.

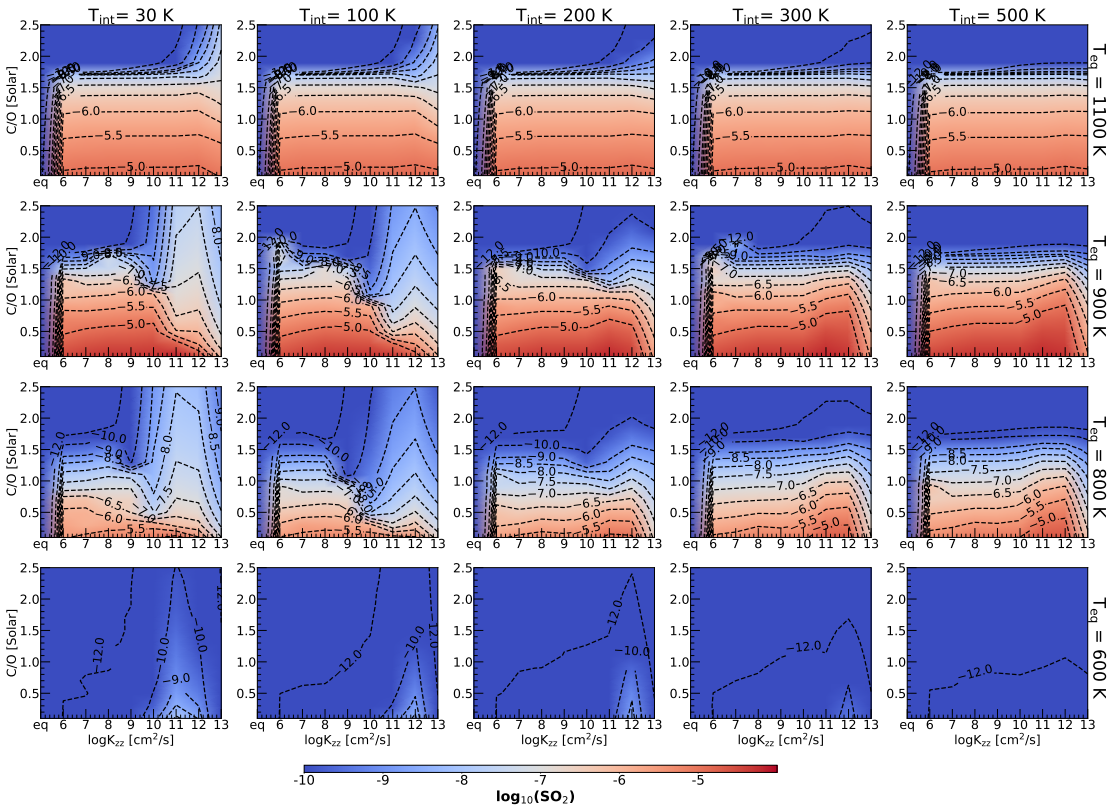

Figure 6.11: The weighted abundance of SO_2 calculated using Equation 6.1 has been shown as a heat map as a function of C/O and K_{zz} in each panel. Each row corresponds to a different $T_{\rm eq}$ value from 1100 K to 600 K from top to bottom. Each column correspond to a different $T_{\rm int}$ value between 30 K and 500 K from left to right. Note that the C/O has been shown relative to the assumed solar value of 0.458 in this plot.

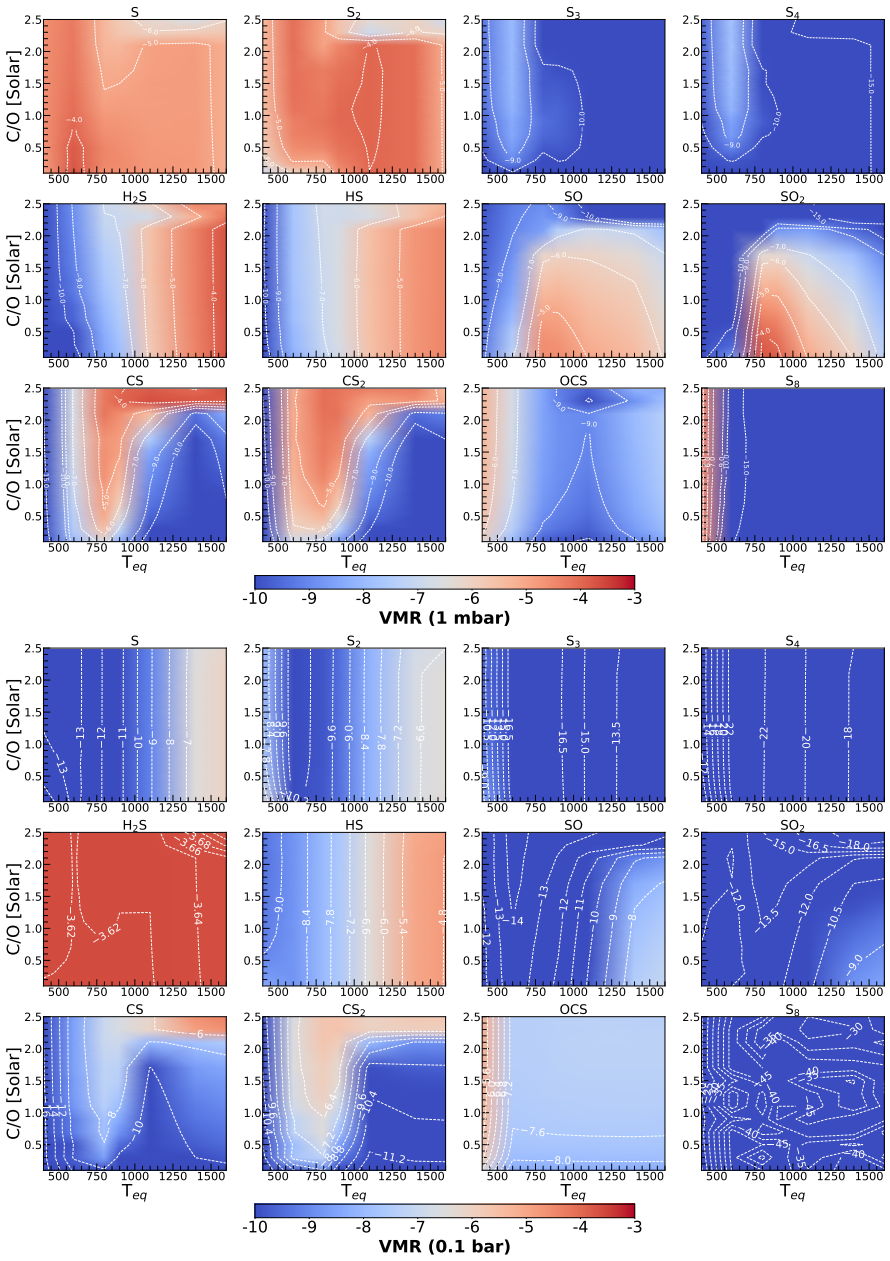

Figure 6.12: The top set of panels show the abundance of various Sulfur species at 1 mbar as a heat map as a function of C/O and $T_{\rm eq}$ in each panel. Each panel corresponds to a different S- bearing gas. All models shown here have $T_{\rm int}$=200 K and K_{zz}=10^9cm^{2}s^{-1}. The lower panels show the abundance of the same species but at 0.1 bar instead. This is to show the abundance of S- bearing gases both at pressures probed by transmission and emission spectroscopy, respetively.

6.3.1.3 Trends in Sulfur Species

The detection of SO_2 in WASP-39b has garnered great interest in the community due to its photochemical origin. Figure 6.3 shows how SO_2 is produced in a narrow pressure region in the upper atmosphere. But as transmission spectra of gas giant planets probes this particular pressure region as well, SO_2 features can be easily observed in transmission spectroscopy. Figure 6.11 shows the X_w for SO_2. At all $T_{\rm eq}$ values except for 600 K, SO_2 shows a sharp increase from thermochemical equilibrium to disequilibrium chemistry cases. For $T_{\rm eq}$= 1100 K, the SO_2 abundance only depends on C/O and shows a small dependence on K_{zz}. For lower C/O values than 1.7×solar, the SO_2 abundance increases very slowly with increasing K_{zz} for $K_{zz} \leq 10^{12}{\rm cm^2 s^{-1}}$ followed by a small decrease for higher K_{zz} values. The nearly horizontal equal abundance contours in the top row of Figure 6.11 shows that the SO_2 abundance is much more sensitive to C/O than K_{zz} at $T_{\rm eq}$=1100 K. The SO_2 abundance shows a gradual decrease with increasing C/O, which is expected as the SO_2 molecule contains two O-atoms and no C- atoms. The decrease of SO_2 with increasing C/O is particularly rapid when C/O≥1.7×solar for these hot planets, similar to CO_2. This is again because of the lack of enough O- atoms to form SO_2 in these very C- rich atmospheres. For these hotter planets, SO_2 also remains independent of $T_{\rm int}$.

For 800 K≤$T_{\rm eq}$≤ 900 K, the SO_2 abundance is overall higher than the $T_{\rm eq}$=1100 K. The SO_2 abundance starts to show strong dependence on K_{zz} at this $T_{\rm eq}$, especially for high K_{zz} values. This dependence particularly sets in when the K_{zz} is higher than

another "transition" value of K_{zz}. Below this transition value, the SO_2 shows little to no dependence on K_{zz}, but once the K_{zz} is higher than this value, SO_2 abundance shows a rapid decline with increasing K_{zz}. Figure 6.11 second row shows that this transition K_{zz} depends on both C/O and $T_{\rm int}$. For example, at $T_{\rm eq}$=900 K, this "transition" K_{zz} can be identified to be around $10^{10}{\rm cm}^2{\rm s}^{-1}$ when $T_{\rm int}$=30 K. But this "transition" K_{zz} is higher at K_{zz}=$10^{12}{\rm cm}^2{\rm s}^{-1}$ for $T_{\rm int}$=300 K. Qualitatively similar behavior is also exhibited in the $T_{\rm eq}$=800 K models. SO_2 shows another interesting behavior for $T_{\rm int}\leq$200 K where the SO_2 shows a rapid increase with K_{zz} when C/O$\geq$1.5$\times$solar and K_{zz} is between 10^{10}-$10^{12}{\rm cm}^2{\rm s}^{-1}$. The SO_2 abundance then declines rapidly when K_{zz} is increased further, which is the effect discussed just above. This rapid increase of SO_2 with increasing K_{zz} before showing a decline occurs for C/O$\geq$1.0$\times$solar in the $T_{\rm eq}$=800 K models shown in the third row of Figure 6.11.

The SO_2 abundance in the photosphere of the $T_{\rm eq}$= 600 K models declines by several orders of magnitude than the $T_{\rm eq}$=800 K models. This decline is close to 6-7 orders of magnitude for values of K_{zz} lower or higher than a narrow range of K_{zz} between $10^{10}\leq K_{zz}\leq 10^{12}{\rm cm}^2{\rm s}^{-1}$, when $T_{\rm int}$=30 K. For this narrow range of K_{zz} values, the decline is only about by $\sim$ 1-2 order of magnitudes. For higher $T_{\rm int}$ values, this narrow range of K_{zz} where SO_2 is still relatively more abundant than the rest of the parameter space, still exists. However, this region of the parameter space shrinks progressively along both the C/O and K_{zz} direction with increasing $T_{\rm int}$. This shows that below $T_{\rm eq}\leq$600 K, it is very difficult to photochemically produce a detectable amount of SO_2, unless the atmospheric metallicity is much higher than 10$\times$ solar. The depletion

of SO_2 at cool T_{eq} is consistent with previous work and is attributed to the depletion of OH radicals that are needed to form SO_2 (Tsai et al. 2023c).

SO_2 is not the only important S- bearing molecule in these atmospheres. Figure 6.12, upper set of panels, shows the volume mixing ratio of various S-bearing molecules as a function of T_{eq} and C/O at a fixed K_{zz}=$10^9 cm^2 s^{-1}$ and T_{int}=200 K. The volume mixing ratios at 1 mbar are shown. The right-most panel in the middle row of Figure 6.12 shows that the SO_2 abundance in the photosphere declines sharply when $T_{eq} \leq$ 600 K or C/O $\geq$2×solar. The same behaviour is also shown by SO. Figure 6.12 also shows that SO is an almost equally abundant product of photochemistry expected in the same part of the parameter space as SO_2. Comparing the SO and SO_2 panels in Figure 6.12 also shows that SO declines slower with increasing T_{eq} compared to SO_2. As both SO and SO_2 decline at high C/O$\geq$2×solar, most of the S- in the photosphere goes into CS instead. With the decline of SO and SO_2 at $T_{eq} \leq$ 600 K, CS and CS_2 also start to carry a large fraction of the S- inventory. This is particularly interesting in the context of the recent tentative detection of CS_2 in the atmosphere of TOI-270 d with *JWST* (Benneke et al. 2024; Holmberg & Madhusudhan 2024), which has a T_{eq} between 350-380 K but is inferred to be much more metal rich than 10×solar.

Among the other S_x kind of molecules S_2 seems the most abundant. Molecules like S_3 and S_4 are at least 4-6 orders of magnitude less abundant than S_2. Interestingly, the abundance of S_8 is almost negligible for $T_{eq} \geq$600 K, but Figure 6.12 shows that S_8 and OCS shows a very sharp increase in abundance for $T_{eq} \leq$400 K. Figure 6.12 shows that among the H_xS gases, H_2S is more abundant than HS at 1 mbar, especially for $T_{eq} \geq$

1200 K. We note that S- polymerization kinetics is still not very well understood (e.g., Zahnle et al. 2016) and there is also significant uncertainty in the OCS recombination rates (e.g., Ranjan et al. 2020; Tsai et al. 2021).

Figure 6.12, lower set of panels, shows the abundance of the same gases but at 0.1 bar instead. It is clear that almost all of the S- is present in the form of H_2S with a minor amount in the form of HS in the deeper atmospheres. The abundance of gases like SO, SO_2, and CS, which are the dominant S- bearers near the pressures probed by transmission spectroscopy, are much lower at these deeper pressures. This is expected as these gasses are photochemically enhanced at the smaller pressures. Interestingly, even though CS is more abundant than CS_2 in the upper atmosphere probed by transmission spectroscopy, CS_2 appears to be more abundant molecule in the deeper atmosphere probed by emission spectroscopy. The most abundant S- carrying gas after H_2S in the deeper atmosphere is HS for $T_{\rm eq}\geq$1000 K. But below $T_{\rm eq}\leq$1000 K, CS_2 becomes the second-most abundant S- carrying gas after H_2S in the deep atmosphere. For $T_{\rm eq}$ lower than 500 K, OCS replaces CS_2 as the second most S- carrying gas after H_2S.

6.3.2 Exploring how abundances depend on K_{zz}, C/O, and $T_{\rm int}$ across different metallicities

Metallicity scales the abundance of C-, O-, N-, and S- relative to H in our modeling framework. §6.3.1 showed that C/O can be degenerate with K_{zz} and $T_{\rm int}$ for most gases at small or big parts of the parameter space. Here, we explore how atmospheric metallicity influences photospheric abundance of gases across the same

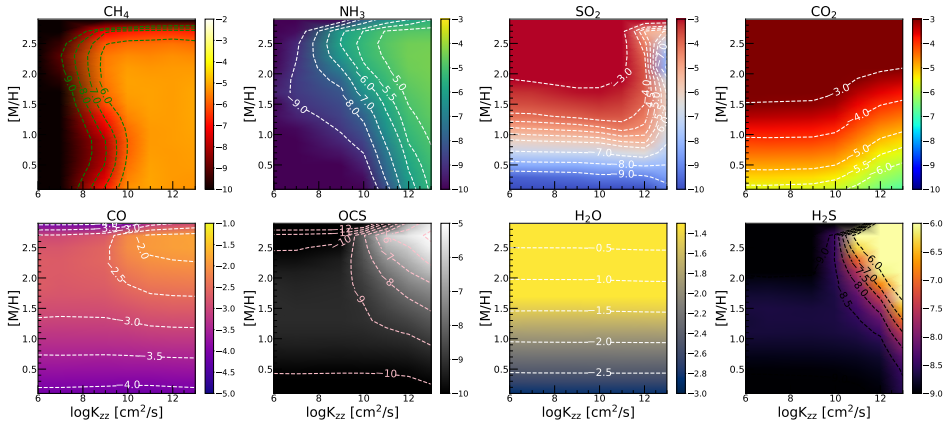

Figure 6.13: Each panel shows how X_w for a different gas varies with [M/H] and K_{zz} as a heat map. All the models shown here have $T_{\rm eq}$= 800 K, $T_{\rm int}$= 200 K, and C/O= 0.1×solar.

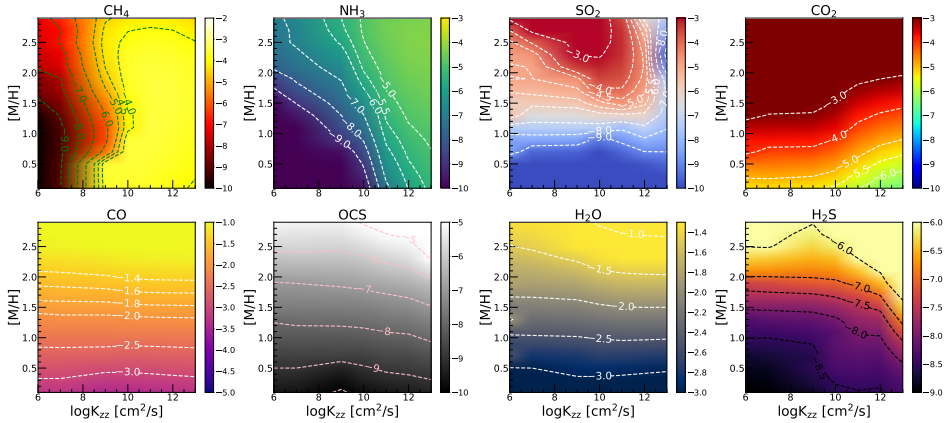

Figure 6.14: Each panel shows how X_w for a different gas varies with [M/H] and K_{zz} as a heat map. All the models shown here have $T_{\rm eq}$= 800 K, $T_{\rm int}$= 200 K, and C/O= 1×solar.

parameter space. We use models for a planet with $T_{\rm eq}$= 800 K for this purpose with a $T_{\rm int}$=200 K.

Figure 6.13 shows X_w for CH_4, NH_3, SO_2, CO_2, CO, OCS, H_2O, and H_2S as a function of [M/H] and K_{zz} in the different panels. These models are shown for a very O-rich atmosphere with C/O=0.1× solar whereas Figure 6.14 shows the same quantities but for C/O=1×solar. The CH_4 panel of Figure 6.13 shows that at C/O=0.1×solar, increasing K_{zz} leads to increase in CH_4 when $K_{zz}\leq 10^{10}$cm^{2}s^{-1}. This holds true at C/O=1×solar in Figure 6.14 too. The overall CH_4 abundances are much lower in the C/O=0.1×solar than the C/O=1×solar, as expected. The equal abundance contours for CH_4 in the C/O=0.1×solar case (Figure 6.13) are nearly vertical which suggests that the photospheric CH_4 abundance varies a lot with changing K_{zz}, but not much with [M/H]. This holds true at C/O=1×solar as well (Figure 6.14) but only for [M/H]≤+0.5 and [M/H]≥+1.0. For intermediate metallicities, Figure 6.14 shows that CH_4 abundance can depend both on [M/H] and K_{zz}, increasing as both of these parameters are increased. For metallicities higher than [M/H]=+2.5, CH_4 abundance starts to decrease rapidly with increasing metallicity for the very O- rich case shown in Figure 6.13. This behavior is also present but to a smaller extent in the solar C/O models in Figure 6.14. Note that our models do not account for graphite saturation (Moses et al. 2013c), which could draw down the CH_4 concentration and impact other carbon-bearing species in Figure 6.14 for high metallicities ([M/H] > 2).

NH_3 abundance in Figures 6.13 and 6.14 also show increase with increasing K_{zz}. The equal abundance contours of NH_3 are along the diagonal direction, which

suggests that the NH_3 abundance shows a dependence on both [M/H] and K_{zz}. For a given K_{zz}, higher [M/H] values produces more photospheric NH_3 than lower [M/H] values, except for [M/H]$\geq$+2.5 models with C/O=0.1$\times$solar. Both SO_2 and CO_2 show much stronger [M/H] dependence than K_{zz} dependence, unlike CH_4 and NH_3. This is expected as both SO_2 and CO_2 require one C- or S- and two O- atoms per molecule. It is interesting that for very O- rich atmospheres (Figure 6.13), the rate of increase of SO_2 with increasing [M/H] slows down considerably for high [M/H] values. This behavior also happens in the C/O=1$\times$solar atmospheres in Figure 6.14, but not to the extent present in Figure 6.13. The metallicity dependence of SO_2 only dissappears when the K_{zz} is higher than a threshold value. Beyond this value, the SO_2 abundance shows a sharp decline with increasing K_{zz} without much [M/H] dependence. In Figure 6.13, this threshold appears to be close to 10^{12}cm^{2}s^{-1}, whereas in Figure 6.14, the threshold is near 10^{11}cm^{2}s^{-1}. The CO_2 abundance also shows some K_{zz} dependence for high K_{zz} values, but not to the extent of the sharp change shown by SO_2. For a given [M/H], the CO_2 abundance shows a slight increase with increasing K_{zz} when the K_{zz} is higher than 10^{11}cm^{2}s^{-1}. For lower K_{zz} values, the CO_2 abundance solely depends on [M/H] (for a fixed C/O).

Like CO_2, CO shows little to no dependence on K_{zz} and strong dependence on metallicity. The main reason behind this is the relatively higher $T_{\rm int}$=200 K of these models. Interestingly, CO abundances in Figure 6.13 are generally lower than the CO abundances in Figure 6.14. This is the case as CO contains equal numbers of C- and O- atoms, so its abundance is diminished in a very O- rich and C- poor atmosphere.

CO also shows some minor dependance on K_{zz} in the very O- rich atmospheres (Figure 6.13) when [M/H]$\geq$+2.0. OCS also shows a similar behavior as CO, where its abundance is diminished in the very O- rich/C- poor atmospheres compared to solar C/O atmospheres. The OCS abundance seems to primarily depend on atmospheric [M/H] unless K_{zz} is high. For high K_{zz}, the OCS abundance starts to increase with increasing K_{zz} and this increase is particularly rapid for significantly metal-enriched atmospheres. This behavior is also mimicked by H_2S, where its much less abundant in the O- rich/C- poor atmosphere than the solar C/O atmosphere. The photospheric abundance of H_2S also shows a rapid increase with increasing K_{zz} beyond a threshold value, particularly in high [M/H] atmospheres. Figures 6.13 and 6.14 show that H_2O abundance in the photosphere only depends on [M/H], with almost no K_{zz} dependence at all.

6.3.3 Chemical Transitions with $T_{\rm eq}$

Fortney et al. (2020) and Ohno & Fortney (2023b) presented how fundamental chemical transitions in the atmosphere, like from being CO rich to CH_4 rich, can depend on both $T_{\rm int}$ and K_{zz} in addition to $T_{\rm eq}$. Recently, Bell et al. (2023c) reported the discovery of CH_4 in the atmosphere of WASP-80b detected in both transmission and emission spectroscopy of the planet with *JWST*. There have been efforts to measure the $T_{\rm eq}$ value below which CH_4 first starts to appear in observations of exoplanetary atmospheres. But this can be a complex function of $T_{\rm int}$, K_{zz}, C/O, and [M/H] (e.g., Fortney et al. 2020).

Figure 6.15 presents these transitions/behavior from our photochemical 1D

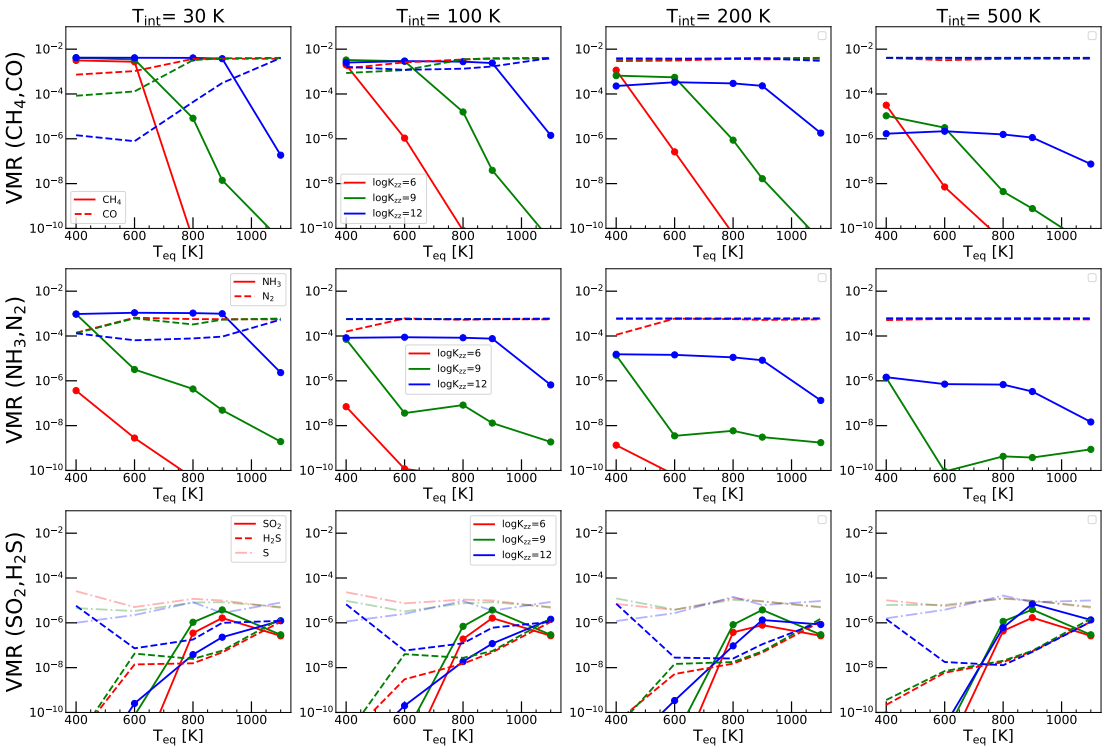

Figure 6.15: The variation of photospheric abundance of key atmospheric gases as a function of $T_{\rm eq}$ is shown here. Each column shows the variation for a different value of $T_{\rm int}$. The top row shows the evolution of CH_4 and CO abundance with $T_{\rm eq}$. The middle and last row shows the same for N_2-NH_3, and H_2S-SO_2-S, respectively. In each panel, the three colored lines shows the abundances for a three different values of K_{zz}. The C/O has been fixed to be 1×solar in these models.

chemical kinetics grid for three pairs of molecules – CO-CH_4, N_2-NH_3, and H_2S-SO_2-S at [M/H]=+1.0. The top row panels in Figure 6.15 shows how CO and CH_4 photospheric abundance change with decreasing $T_{\rm eq}$ for $T_{\rm int}$=30 K, 100 K, 200 K, and 500 K from left to right, respectively. Each panel in Figure 6.15 shows three colored solid lines denoting the CH_4 abundance for three different K_{zz} values, whereas the dotted lines indicate the CO abundance in each case. It is clear that the upper atmosphere probed by transmission spectroscopy can only have $CH_4 \geq$CO in planets with cold interiors $T_{\rm int}$ $\sim$ 100 K or lower. For hotter interiors, CO always remains the majority C- carrier molecule with higher abundance than CH_4. This transition was seen to be happening at or below $T_{\rm int}$=150 K too by Fortney et al. (2020), even though they used quench-time approximation for approximating the effect of K_{zz} on chemistry and also did not treat photochemistry in their models. We note that this threshold of $T_{\rm int}$=150 K was found at 3×solar metallicity in Fortney et al. (2020) instead of the 10×solar metallicity assumed in our analysis. Figure 6.15 also shows that the $T_{\rm eq}$ value where this transition from CO rich to CH_4 rich occurs is a very strong function of K_{zz}. When K_{zz}=10^{12}cm^{2}s^{-1}, this transition happens near $T_{\rm eq}$= 1000 K for atmospheres with $T_{\rm int} \leq$100 K. But, for K_{zz}=10^9cm^{2}s^{-1} or K_{zz}=10^6cm^{2}s^{-1} , atmospheres can remain CO rich for $T_{\rm eq}$ above 600 K. When $T_{\rm int}$= 500 K, shown in the right most column of Figure 6.15, the CH_4 abundance is still an order of magnitude lower than CO even for $T_{\rm eq}$= 400 K.

The second row of Figure 6.15 shows the same quantities as the first row but for NH_3 (solid lines) and N_2 (dashed lines) instead. Figure 6.15 second row shows that the NH_3 can only become the major N- carrier if the $T_{\rm int}$ is 30 K. Even for such cold

interior, the mixing needs to be high to make NH_3 carry most of the N- atoms in the photosphere. For example, the NH_3 in the photosphere still remains almost two orders of magnitude lower than that of N_2 abundance if K_{zz}=10^6cm^{2}s^{-1}, even if $T_{\rm int}$=30 K. This result is also consistent with the findings of both Fortney et al. (2020) and Ohno & Fortney (2023b). Ohno & Fortney (2023a) found that NH_3 can become the dominant carrier of N- atoms in giant planets only in a small parameter space where the planet has a low mass and is very old, such that the interior is sufficiently cool and vertical mixing can dredge the NH_3 up to the upper atmosphere.

The last row of Figure 6.15 shows the behavior of the abundance of three major S- carrying species – H_2S (dashed lines), SO_2 (solid lines), and S (faded dash-dotted lines) as a function of $T_{\rm eq}$. The notable thing in Figure 6.15 is that neither SO_2 or H_2S carries majority of the S- inventory of the atmosphere, not atleast at [M/H]=+1.0. Instead, neutral S- atoms form a much more substantial fraction of the total S- inventory in the upper atmosphere than SO_2. These are shown with the faded dash dotted lines in all the panels and the same phenomenon is also shown in Figure 6.12. This was seen in previous work (e.g., Tsai et al. 2023c,b) as well. Figure 6.15 also shows how the SO_2 abundance peaks near $T_{\rm eq}$= 900 K but gradually decreases when the $T_{\rm eq}$ increases further. But the decrease of SO_2 with decreasing $T_{\rm eq}$ is much more rapid as was also seen in Figure 6.12.

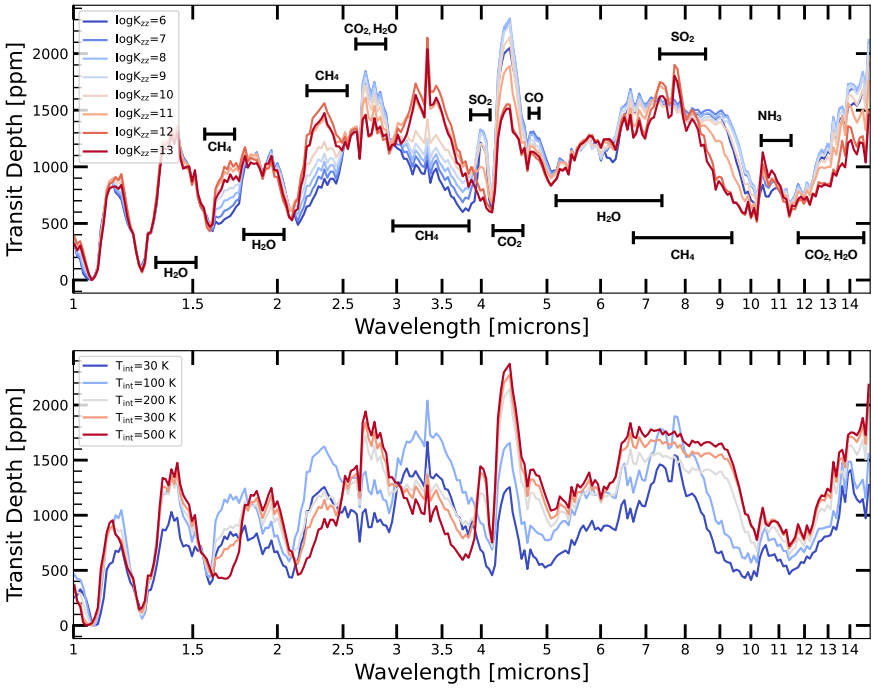

Figure 6.16: The top panel shows the variation of transmission spectra with changing K_{zz} while the bottom panel shows the variation of the transmission spectra of the planet with changing $T_{\rm int}$. The models shown here are for $T_{\rm eq}$=800 K, [M/H]=+1.0, and C/O=1×solar. The $T_{\rm int}$ has been fixed at 200 K for the top panel while the K_{zz} has been fixed at $10^{10}{\rm cm}^2{\rm s}^{-1}$ in the bottom panel. Note that the transmission spectra have been renormalized in such a manner that the minimum transit depth of each model is set at zero.

6.3.4 Sensitivity of Transmission Spectrum to K_{zz} and $T_{\rm int}$

While we have presented our results on the detailed chemical abundances at different parts of the parameter space till now, here we present how this chemistry affects the observable – the transmission spectra. The top panel of Figure 6.16 shows the transmission spectra computed from the $T_{\rm eq}$= 800 K, $T_{\rm int}$= 200 K, C/O=1.1×solar, and [M/H]=+1.0 models for a range of different K_{zz} values. It is clear that certain parts of the transmission spectra are quite sensitive to K_{zz} while others are not as much. For example, the CH_4 band between 3-3.5 μm, and the SO_2 band at 4μm and 7-10 μm are quite sensitive to K_{zz}. On the other hand, the H_2O bands between 1-1.5 μm does not show as much sensitivity to K_{zz}.

The lower panel in Figure 6.16 shows the sensitivity of the transmission spectrum to $T_{\rm int}$ with a fixed K_{zz}=10^{10}cm^{2}s^{-1}. The $T_{\rm int}$ has been varied from 30 K to 500 K. It is clear that the spectra is very CH_4 dominated for cold interiors with $T_{\rm int}$=30 K and 100 K. As the $T_{\rm int}$ increases further, the effect of CH_4 on the spectra slowly decreases. Looking at Figure 6.16, it is not exactly clear at how the transmission spectrum responds to changing K_{zz} and $T_{\rm int}$ in different parts of the vast parameter space explored in this work. Therefore, we present those trends in the upcoming section by computing the differential of the transmission spectra at each wavelength bin with changing K_{zz} and $T_{\rm int}$.

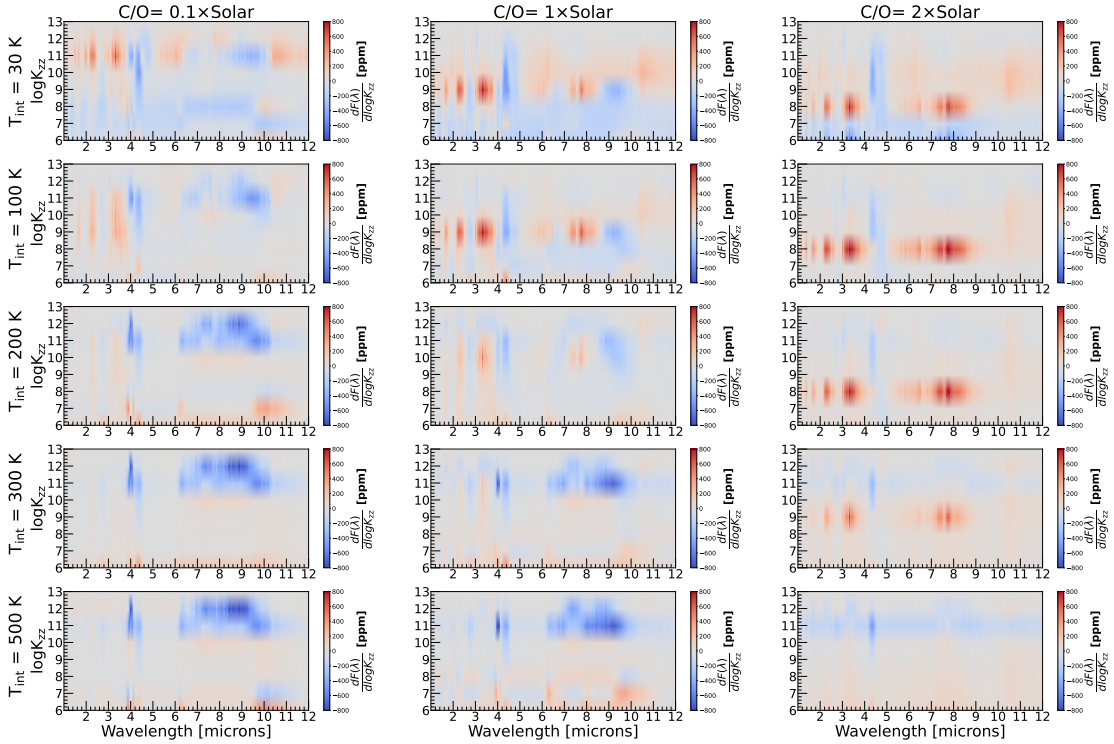

Figure 6.17: Sensitivity of the transmission spectra to changing K_{zz} is shown here as a function of K_{zz} and wavelength. Each column corresponds to a different C/O value whereas each row shows models for different $T_{\rm int}$ values. All models shown here have $T_{\rm eq}$=800 K. A brighter red or a brighter blue color indicates that the transmission spectra is very sensitive to changing K_{zz} at that K_{zz} and wavelength value.

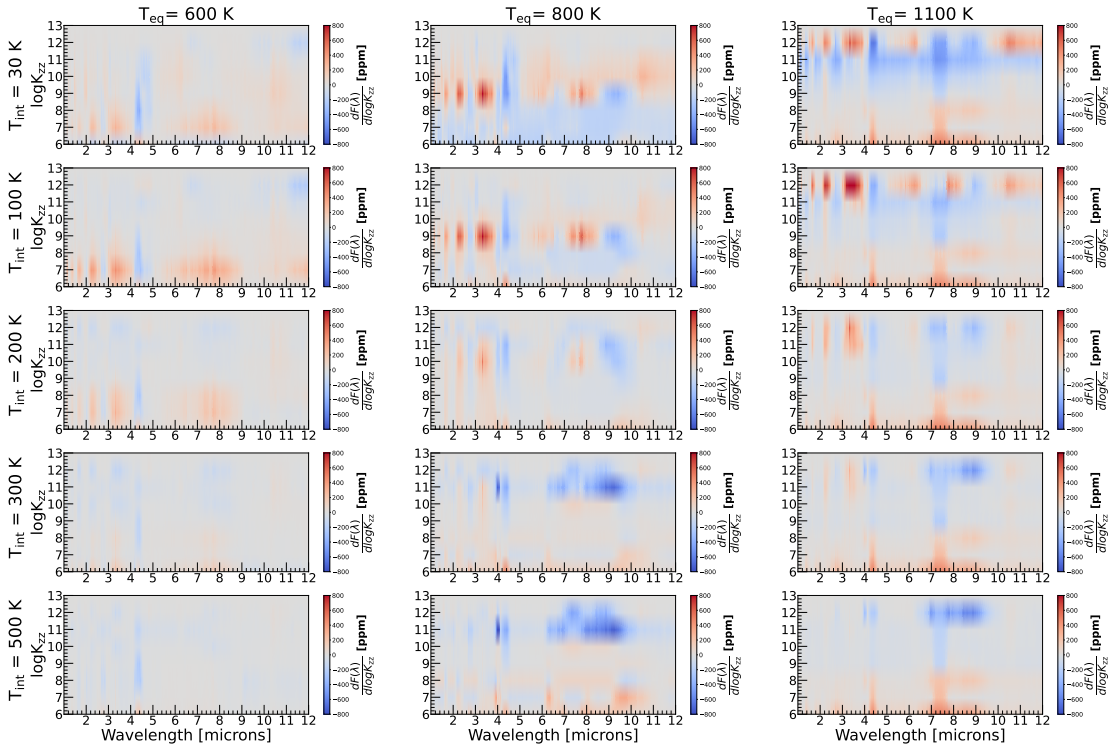

Figure 6.18: Sensitivity of the transmission spectra to changing K_{zz} is shown here as a function of K_{zz} and wavelength. Each column corresponds to a different $T_{\rm eq}$ value whereas each row shows models for different $T_{\rm int}$ values. All models shown here have C/O=1×solar. A brighter red or a brighter blue color indicates that the transmission spectra is very sensitive to changing K_{zz} at that K_{zz} and wavelength value.

6.3.4.1 Dependence of spectra on K_{zz}

To highlight the wavelength ranges where the transmission spectra changes the most when a parameter like K_{zz} is changed, we first renormalise all the transmission spectra across our grid such that the minimum transit depth of each transmission spectra is zero. Then, we calculate the change in the renormalised transit depth within each wavelength bin from one grid point to the next grid point. For example, to highlight which part of the transmission spectra changes the most with a change in K_{zz} near $T_{\rm int}$=30 K, $T_{\rm eq}$=800 K, C/O=0.1×solar, [M/H]=+1.0, and K_{zz}=$10^8 {\rm cm}^2{\rm s}^{-1}$, we calculate $dF(\lambda)/dlogK_{zz}$= ($F(\lambda,K_{zz}=10^8)$- $F(\lambda,K_{zz}=10^7)$)/($log_{10}(10^8)$-$log_{10}(10^7)$), where F denotes the renormalized transmission spectra at the above mentioned grid point parameters. We plot this quantity $dF(\lambda)/dlogK_{zz}$ in the top left panel of Figure 6.17 as a function of K_{zz} with a color map. Each row in Figure 6.17 shows the same quantity for a different $T_{\rm int}$ value while each column corresponds to a different C/O for a fixed $T_{\rm eq}$= 800 K. The $dF(\lambda)/dlogK_{zz}$ quantity shows how the transit depth in a given wavelength change in parts-per-million (ppm) in a particular part of the parameter space if K_{zz} is changed by one order of magnitude there. We note that the $dF(\lambda)/dlogK_{zz}$ quantity is sparsely sampled in the K_{zz} direction, and as a result the trends shown in Figure 6.17 and 6.18 may appear smoother than expected. This quantity helps us to identify which are the best wavelength range or molecular features to constrain K_{zz} in a particular part of the parameter space.

Figure 6.17 top row shows that if the interior of the planet has $T_{\rm int}$=30 K, the

CH_4 and CO_2 bands near 3.3 μm and 4.2-4.3μm, respectively, show the most sensitivity to changing K_{zz}. However, it is clear that the maximum change on the spectra due to changing K_{zz} appears at different K_{zz} values depending on the C/O. For example, in the C/O=0.1×solar panel on the top left, the maximum change in the CH_4 feature appears at high K_{zz} values near 10^{10}cm^{2}s^{-1}. This region of maximum sensitivity of the CH_4 band shifts to lower K_{zz}=10^8cm^{2}s^{-1} value when the C/O is 1×solar and to even lower K_{zz}= 10^7cm^{2}s^{-1} when the C/O is 2×solar in the top row. However, Figure 6.17 top row shows that the CO_2 band near 4.2-4.3 μm remains quite sensitive to K_{zz} for almost all K_{zz} values in this cold interior scenario.

As the $T_{\rm int}$ is increased from 30 K to 500 K (moving from the top towards the bottom row in Figure 6.17), the sensitivity of the CH_4 bands to K_{zz} slowly diminishes while the SO_2 bands near 4μm and 7-9 μm become increasingly sensitive to changing K_{zz}. This happens only in the C/O = 0.1× and 1×solar columns. The sensitivity of the SO_2 bands set in particularly for high values of K_{zz} above 10^{10}cm^{2}s^{-1}. The rest of the transmission spectra still remains sensitive to K_{zz} but to a smaller degree. When C/O=2×solar, the CH_4 bands remain the most sensitive parts of the transmission spectra till $T_{\rm int}\leq$300 K. The sensitivity of the 4.2-4.3 μm CO_2 slowly diminishes in this case as the interior warms up from a $T_{\rm int}$ of 30 K to 500 K.

Next, we present the trends in $dF(\lambda)/dlogK_{zz}$ at three different $T_{\rm eq}$ values in Figure 6.18, instead of the three different C/O values shown in Figure 6.17. Each column in Figure 6.18 shows the trends for $T_{\rm eq}$= 600 K, 800 K, and 1100 K while the C/O has been fixed at 1×solar. Figure 6.18 shows that transit depths at $T_{\rm eq}$= 600 K are

much less sensitive to K_{zz} than those at $T_{\rm eq}$= 800 K and $T_{\rm eq}$= 1100 K. At $T_{\rm eq}$= 600 K, most of the sensitivity of the spectrum arises in the CO_2 bands (4.2-4.3 μm) and CH_4 bands (3-4 μm and others) at low values of $T_{\rm int}$. The CH_4 bands show some sensitivity but only when K_{zz} is low whereas the CO_2 band shows sensitivity for a larger range of K_{zz} values. When the $T_{\rm int} \geq$ 300 K, there is reduced sensitivity to K_{zz} across the transmission spectrum at $T_{\rm eq}$=600 K.

The trends in the middle column of Figure 6.18 and the middle panel of Figure 6.17 represent the same set of models, so we don't describe them again here. The $T_{\rm eq}$=1100 K models shown in the right columns of Figure 6.18 show that the CH_4 bands (between 3-4μm and others) are particularly sensitive to K_{zz}, especially at high K_{zz} values but this sensitivity diminishes slowly with increasing $T_{\rm int}$ value. The CO_2 feature (4.2-4.3 μm) shows high sensitivity to K_{zz} across all K_{zz} values, but this sensitivity slowly diminishes with increasing $T_{\rm int}$ at $T_{\rm eq}$=1100 K. While the 4 μm SO_2 feature doesn't show much sensitivity to K_{zz} for this $T_{\rm eq}$ value, but the 7-9 μm SO_2 is very sensitive to K_{zz} throughout all $T_{\rm int}$ and K_{zz} values for the $T_{\rm eq}$=1100 K case. As it is not possible to present these trends for the whole suite of models within this paper in a wavelength resolved manner, we now move on to showing sensitivity of the transmission spectra to changing $T_{\rm int}$ instead of changing K_{zz}.

6.3.4.2 Dependence of spectra on $T_{\rm int}$

Figure 6.19 presents the sensitivity of the transmission spectra to changing $T_{\rm int}$ when the $T_{\rm int}$ changes within our five $T_{\rm int}$ grid points of 30 K, 100 K, 200 K,

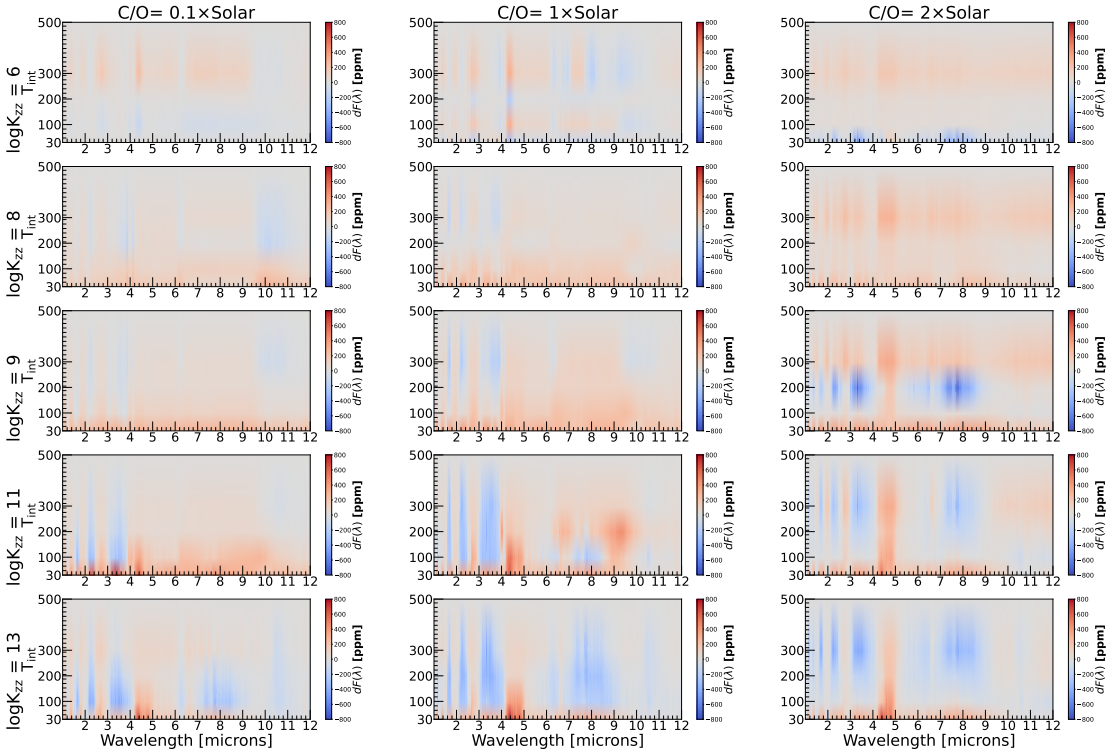

Figure 6.19: Similar to Figure 6.17 but the sensitivity of transmission spectra to changing $T_{\rm int}$ is shown here as a function of $T_{\rm int}$ and wavelength, instead of K_{zz} in Figure 6.17. Each column corresponds to a different C/O value whereas each row shows models for different K_{zz} values. All models shown here have $T_{\rm eq}$=800 K. A brighter red or a brighter blue color indicates that the transmission spectra is very sensitive to changing $T_{\rm int}$ at that $T_{\rm int}$ and wavelength value.

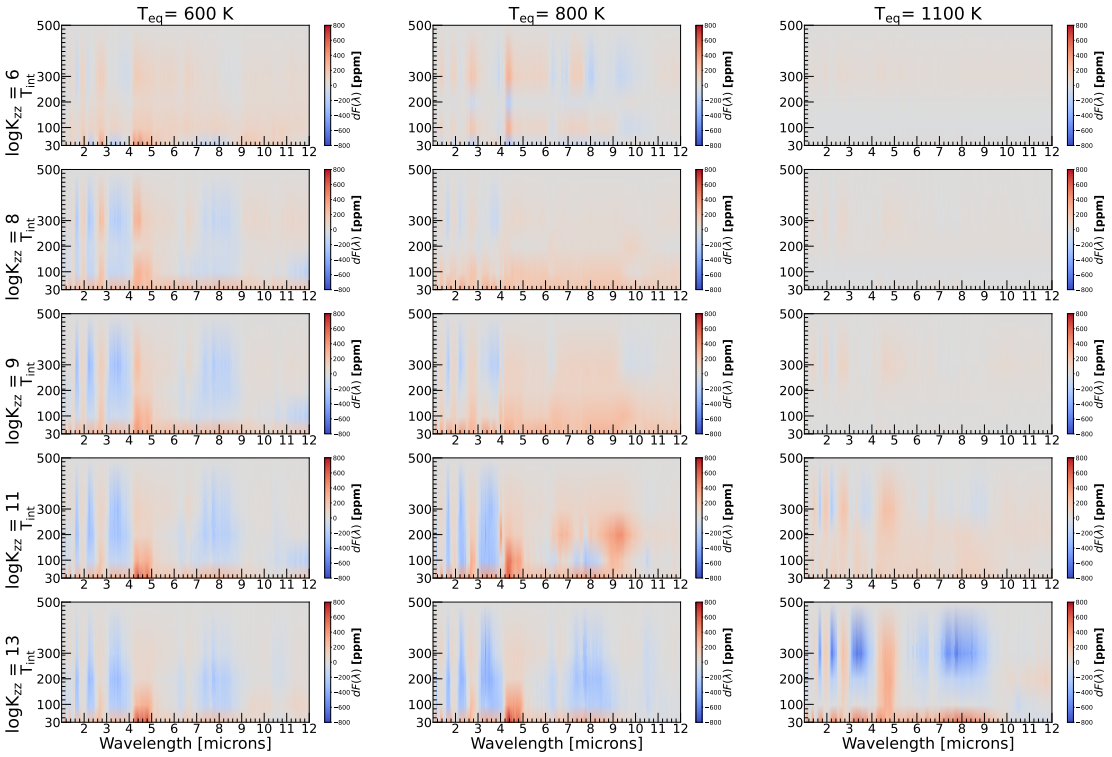

Figure 6.20: Sensitivity of the transmission spectra to changing $T_{\rm int}$ is shown here as a function of $T_{\rm int}$ and wavelength. Each column corresponds to a different $T_{\rm eq}$ value whereas each row shows models for different K_{zz} values. All models shown here have C/O=1×solar. A brighter red or a brighter blue color indicates that the transmission spectra is very sensitive to changing $T_{\rm int}$ at that $T_{\rm int}$ and wavelength value.

300 K, and 500 K. As our $T_{\rm int}$ grid points are non-uniformly spaced, unlike for K_{zz}, we plot the quantity $dF(\lambda)$ here, which is simply the difference in the renormalized transit depths between two $T_{\rm int}$ values. Like Figure 6.17, each column of Figure 6.19 also represents different C/O values. But unlike Figure 6.17, each row of Figure 6.19 represents a different value of K_{zz} with K_{zz} increasing from the top to the bottom row. It is clear that for the very O- rich case of C/O=0.1×solar shown in the left columns, the sensitivity of the transmission spectra is very subtle to changing $T_{\rm int}$, especially for low K_{zz} values. But as the K_{zz} values increase, the CH_4 band between (3-4 μm) starts to show high sensitivity to changing $T_{\rm int}$.

The C/O=1×solar models shown in middle column of Figure 6.19 show a relatively higher level of sensitivity to changing $T_{\rm int}$ value compared to the C/O=0.1×solar models, especially for $K_{zz}\geq 10^9 {\rm cm}^2{\rm s}^{-1}$. Most of the sensitivity here is shown in the CH_4 bands (3-4 μm and others) and the sensitivity of the CH_4 bands to changing $T_{\rm int}$ increases with increasing K_{zz} at this C/O value. The CO_2 absorption bands also show high sensitivity to changing $T_{\rm int}$ values, especially for higher K_{zz} values. For the C/O=2×solar models shown in Figure 6.19, most of the sensitivity of the transit depth is mainly seen in the CH_4 bands (3-4μm and others) and the the CO_2 band between 4.2-4.3 μm.

Figure 6.20 shows the sensitivity of the transmission spectra at three different $T_{\rm eq}$ values shown in each column for 600 K, 800 K, and 1100 K from left to right, respectively. The C/O ratio has been fixed to 1×solar for this purpose. It is clear that the overall sensitivity of the transmission spectra to changing $T_{\rm int}$ diminishes with

increasing $T_{\rm eq}$. For $T_{\rm eq}$=600 K, the CH_4 and CO_2 bands show the most sensitivity to changing $T_{\rm int}$. This sensitivity increases progressively from low K_{zz} to high K_{zz} at $T_{\rm int}$=600 K. The $T_{\rm eq}$=1100 K models shown in the right column show much lower sensitivity of the transit depths to changing $T_{\rm int}$ than the $T_{\rm eq}$=600 K and $T_{\rm eq}$=800 K models. This is especially true for $K_{zz}\leq 10^9 {\rm cm}^2{\rm s}^{-1}$. However, when K_{zz} is higher than this value, some $T_{\rm int}$ sensitivity starts to appear in the spectrum. This sensitivity appears primarily in the CH_4, CO_2 and CO bands (4.5-4.8 μm) in the K_{zz}=10^{11} and $10^{13}{\rm cm}^2{\rm s}^{-1}$ cases.

Our sensitivity analysis of the transmission spectra reveals that the different wavelength regions in the transmission spectra show complex sensitivity with changing K_{zz} and $T_{\rm int}$ in different parts of the C/O, $T_{\rm eq}$, K_{zz}, and $T_{\rm int}$ parameter space. This suggests that the precision to which parameters like $T_{\rm int}$ and K_{zz} can be constrained for giant transiting planets depends on where that planet lands in this multi-dimensional parameter space. This kind of analysis can also be used to carefully design the wavelength region and the required signal-to-noise to achieve a certain science goal (like constraining $T_{\rm int}$ to a certain precision) with instruments like *JWST*. We avoid presenting similar analysis for eclipse spectroscopy as we chose to ignore the disequilibrium chemistry processes self-consistently within our $T(P)$ profile calculation and that would matter for emission spectra of these planets to a much larger extent than the transmission spectra analysis presented here.

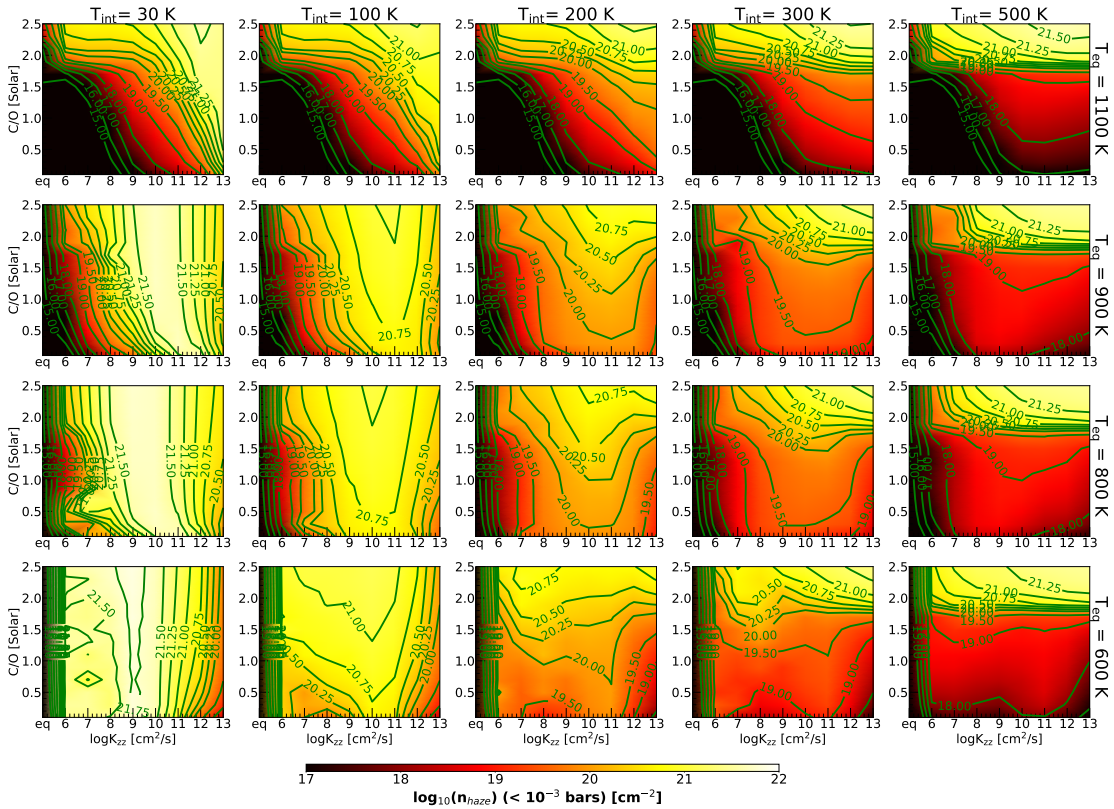

Figure 6.21: The column density of haze precursors at pressures smaller than 10^{-3} bars has been shown as a heat map as a function of C/O and K_{zz} in each panel. Each row corresponds to a different $T_{\rm eq}$ value from 1100 K to 600 K from top to bottom. Each column correspond to a different $T_{\rm int}$ value between 30 K and 500 K from left to right. The abundance of gases– C_2H_2, C_2H_4, C_2H_6, C_4H_2, HCN, CH_3CN, and CS_2 were used to compute the column density of the haze precursor molecules.

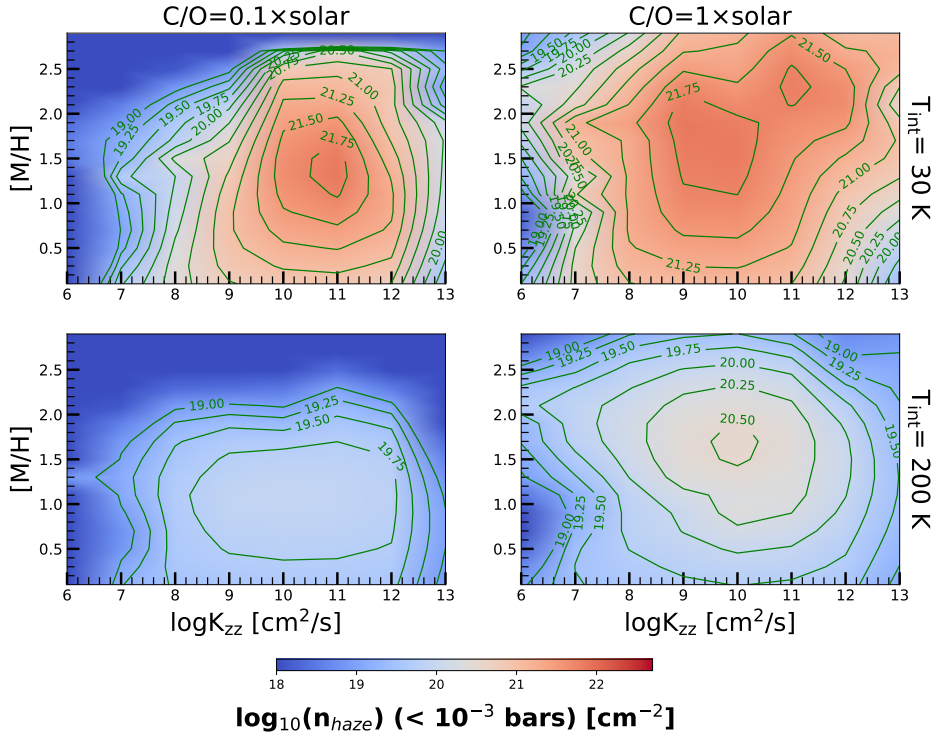

Figure 6.22: The column density of haze precursors at pressures smaller than 10^{-3} bars has been shown as a heat map as a function of [M/H] and K_{zz} in each panel. The top row corresponds to $T_{\rm int}$= 30 K, while the bottom row shows models with $T_{\rm int}$= 200 K. The $T_{\rm eq}$ has been set to 800 K for all the panels. The left column shows models for C/O=0.1×solar while the right column shows models at C/O=1×solar. The abundance of gases– C_2H_2, C_2H_4, C_2H_6, C_4H_2, HCN, CH_3CN, and CS_2 were used to compute the column density of the haze precursor molecules.

6.3.5 Precursors to Soot/Haze

Photolysis of C- bearing gases (e.g., CH_4) in the upper atmospheres of gas giants can lead to formation of gases like C_2H_2, C_2H_4, C_2H_6, etc, which in turn can act as precursors to haze/soot creation, if the conditions are favorable to further polymerization of these gases (e.g., Fortney et al. 2013; Morley et al. 2013, 2015). This polymerization can be enabled by the reducing nature of the upper atmosphere of these planets. Hazes can have large impact on the observed transmission, reflection, and emission spectra of exoplanets (e.g., Morley et al. 2013; Fortney et al. 2013; Morley et al. 2015; Ohno & Kawashima 2020; Sing et al. 2016). While the *Photochem* kinetics model doesn't track the growth of these hydrocarbons to large polymers, we can still quantitatively estimate the abundances of these haze precursors across the vast parameter space explored in this work. We adopt the methodology presented in Morley et al. (2015) to estimate the column density of haze precursors above 10^{-3} bars. Following Morley et al. (2015) and Tsai et al. (2021), we include the following C- bearing molecules to estimate the abundance of haze/soot precursors– C_2H_2, C_2H_4, C_2H_6, C_4H_2, HCN, CH_3CN, and CS_2. We calculate the column density of these gases at pressures smaller than 10^{-3} bars across our model grid.

Each panel of Figure 6.21 shows the logarithm of the column density of these precursors as a function of C/O and K_{zz}. Similar to Figure 6.4, each column represents a value of $T_{\rm int}$ while each row represents a different value of $T_{\rm eq}$. Figure 6.21 shows that the abundance of haze precursors can be very strongly dependant on K_{zz} in planets with

$T_{\rm int}$≤100 K. This sensitivity of the haze precursor column density to K_{zz} diminishes with increasing $T_{\rm int}$ at all $T_{\rm eq}$ values. For $T_{\rm eq}$≤900 K models with $T_{\rm int}$=30 K, the abundance of haze precursors increases first as a function of increasing K_{zz} before reaching a peak, beyond which it decreases with increasing K_{zz}, for a fixed C/O. The value of K_{zz} where this peak in haze precursor abundance occurs is a strong function of $T_{\rm eq}$. For $T_{\rm eq}$=1100 K and $T_{\rm int}$=30 K, this peak happens at or beyond K_{zz}=10^{13}cm^2/s, whereas at $T_{\rm eq}$=800 K and $T_{\rm int}$=30 K, this peak occurs at K_{zz}=10^{10}cm^2/s. At $T_{\rm eq}$=600 K, the peak occurs near K_{zz}=10^{8}cm^2/s, when $T_{\rm int}$=30 K. Similar to the findings of Fortney et al. (2013); Morley et al. (2015), we also find that the abundance of haze precursors shows an increase with decreasing $T_{\rm eq}$ between $T_{\rm eq}$=1100 K and $T_{\rm eq}$= 900 K for a fixed C/O and K_{zz}. Below $T_{\rm eq}$=900 K, for models with $T_{\rm int}$≤100 K, whether the column density of precursors increases or decreases with decreasing $T_{\rm eq}$ depends largely on the K_{zz} and C/O. However, when the $T_{\rm int}$≥200 K, the column density of the precursors do not show much change with decreasing $T_{\rm eq}$ below $T_{\rm eq}$= 900 K, for a given C/O and K_{zz} value.

Above $T_{\rm int}$≥100 K, C/O starts to influence the column density of haze precursors significantly, in addition to K_{zz}. Figure 6.21 shows that the influence of C/O on the precursors becomes stronger with increasing $T_{\rm int}$ for all $T_{\rm eq}$. For planets with $T_{\rm int}$ ≥ 300 K, the precursor column density shows a sharp increase when C/O ≥ 2×solar. In these very C- rich atmospheres with hot interiors, the abundance of the precursors mostly remain independent of K_{zz}. For a given value of C/O and K_{zz}, Figure 6.21 also shows that the abundance of the precursors show an overall decline with increasing $T_{\rm int}$ for all $T_{\rm eq}$ values. This can be seen in the overall fading of the brightness of the panels

in Figure 6.21 as one goes from left to right. Figure 6.21 proves that the precursors to larger haze molecules in the upper atmosphere of H_2/He rich atmospheres show very complex dependence on K_{zz}, $T_{\rm int}$, C/O, and $T_{\rm eq}$. For planets with hotter interiors both C/O and K_{zz} influence the availability of haze precursors in the upper atmosphere, but for planets with low $T_{\rm int}$, K_{zz} almost solely influences the column density of these precursors in the upper atmosphere. This suggests that for low mass planets at old ages, C/O might not be very correlated to the abundance of hazes in their atmospheres. However, these results are only for 10×solar metal enrichment.

Figure 6.22 shows the how the column density of the haze precursors vary with metallicity and K_{zz}. The top rows show models with $T_{\rm int}$=30 K while the bottom row shows models with $T_{\rm int}$= 200 K. The left and right columns show models at C/O= 0.1×solar and C/O=1×solar, respectively. All the models shown in Figure 6.22 are for $T_{\rm eq}$=800 K. Figure 6.22 shows that the amount of haze precursors in the upper atmosphere generally depends both on [M/H] and K_{zz}, to varying degrees, in all the four panels. When $T_{\rm int}$=30 K and C/O=0.1×solar (top left panel), the amount of haze precursor starts to show some [M/H] dependence when the K_{zz} is between 10^9 and $10^{12}{\rm cm^2 s^{-1}}$. At K_{zz} values lower or higher than this range, the abundance of haze precursors shows strong dependence on K_{zz}. For C/O=1×solar and $T_{\rm int}$=30 K models shown in the top right panel, the abundance of haze precursors show [M/H] dependence when $10^8 \leq K_{zz} \leq 10^{10}{\rm cm^2 s^{-1}}$. For K_{zz} outside this range, the haze precursor column density becomes very sensitive to mixing with little to no dependence on [M/H]. When the $T_{\rm int}$ is higher (bottom panels), the sensitivity of the haze precursors to [M/H] and

K_{zz} are also different.

At $T_{\rm int}$=200 K, the C/O=0.1× cases show dependence of the precursor column density to [M/H] when $10^8 \leq K_{zz} \leq 10^{12}$ cm^{2}s^{-1}. But even when K_{zz} lies in between these values, the variation of the precursor abundances with changing [M/H] is much less rapid in this hotter interior model compared to the top panel. However, outside this range of K_{zz} values, the precursor show strong dependence on K_{zz}. When the atmosphere becomes more C- rich in these hotter interior models (bottom right panel), the haze precursor abundance shows greater metallicity dependence. For these models, the haze precursors become sensitive to K_{zz} for $K_{zz} \geq 10^{12}$ cm^{2}s^{-1} and $K_{zz} \leq 10^8$ cm^{2}s^{-1}.

The maximum abundance of haze precursors occurs between $+1.0 \leq$[M/H]$\leq +1.5$ for the top left panel, while the bottom left panel shows maximum precursors between $+0.5 \leq$[M/H]$\leq +1.5$. For the top and bottom right panels, maximum precursor abundances are reached between $+1.3 \leq$[M/H]$\leq +2.5$ and $+1.5 \leq$[M/H]$\leq +2.0$, respectively. The top right panel, with C/O=1×solar and $T_{\rm int}$= 30 K, also shows that the maximum haze precursor abundance extends to higher metallicities (e.g., [M/H]=+2.5), if K_{zz} is high. All the panels show that the haze precursor abundances can be very low if mixing is not vigorous enough. Comparing the top to the bottom panel in both the columns of Figure 6.22 shows that planets with lower $T_{\rm int}$ show enhanced levels of haze precursors at all [M/H], K_{zz}, and C/O values compared to planets with hotter interiors. Both Figure 6.21 and Figure 6.22 therefore suggest that the atmospheres of lower mass planets at older ages might have a higher haze content than higher mass planets. However, this only holds true if their interiors have not been heated through external perturbations.

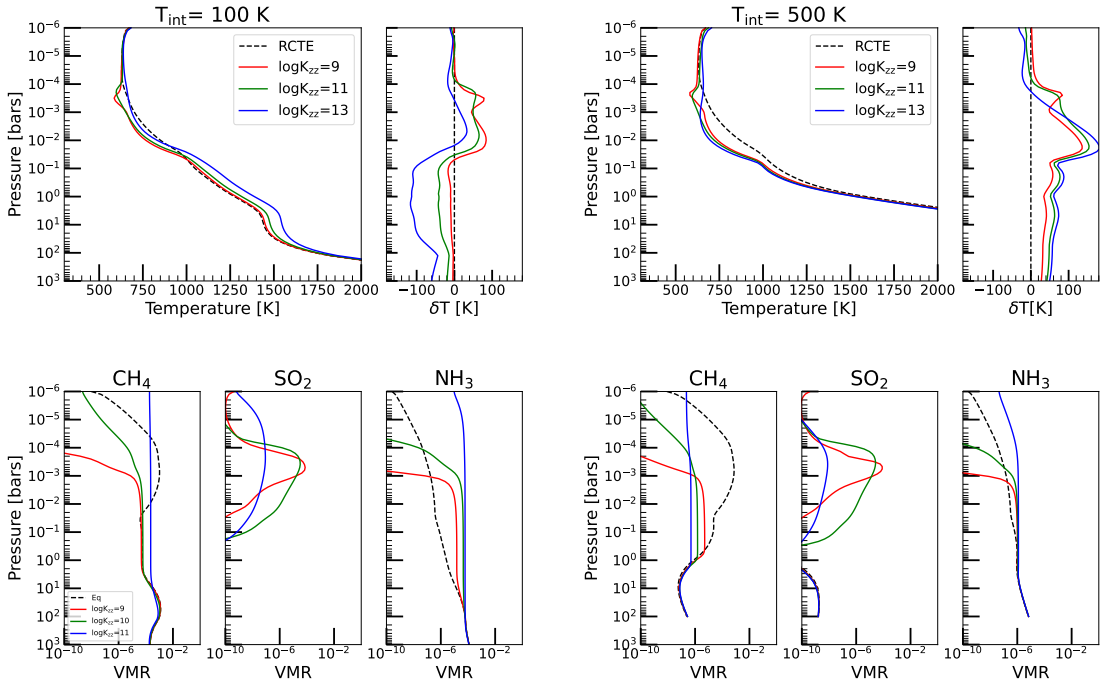

Figure 6.23: Difference between the $T(P)$ profiles calculated using the RCPE model for three different K_{zz} values and the RCTE model is shown in the top left panel for a $T_{\rm int}$=100 K model. The same differences are shown for a $T_{\rm int}$=500 K model in the top right panel. The three bottom left panels show the abundance profiles for each model for CH_4, SO_2, and NH_3 at $T_{\rm int}$=100 K. The same quantities for the $T_{\rm int}$= 500 K model are shown in the three bottom right panels. All the models shown here are for $T_{\rm eq}$=800 K, [M/H]=+1.0, and C/O=1×solar.

6.4 Discussion

6.4.1 Radiative-convective-Photochemical-Equilibrium

Figure 6.2 has already established that there can be significant differences in the $T(P)$ structure calculated using RCTE and RCPE models. This has been shown in previous studies as well (e.g., Drummond et al. 2016; Bell et al. 2023c; Welbanks et al. 2024). This self-consistency between disequilibrium chemistry and $T(P)$ profiles has been found to be important for atmospheric models used to interpret the emission

spectra of brown dwarfs and directly imaged planets (Mukherjee et al. 2023, 2022; Lacy & Burrows 2023; Phillips et al. 2020; Karalidi et al. 2021a; Mukherjee et al. 2024c). For the high signal-to-noise spectra of these objects, these atmospheric details matter.

However, we have ignored the self-consistent approach for the bulk of this work as it is not expected to matter much in a parameter space exploration and identification of major trends in chemistry, which is the main focus of this work. The correction of $T(P)$ profile due to RCPE calculations relative to RCTE models will typically be dependant on K_{zz}. Figure 6.23 shows the $T(P)$ profiles computed with RCPE modeling for three different K_{zz} values for a $T_{\rm eq}$=800 K object with [M/H]=+1.0 and solar C/O. We calculate these RCPE profiles for two $T_{\rm int}$ values of 100 K and 500 K, which are shown in Figure 6.23 along with the RCTE $T(P)$ profiles computed in each case. The chemical abundances in each model for CH_4, NH_3, and SO_2 are also shown. It is clear that the correction on the $T(P)$ profiles relative to RCTE models is quite a strong function of both K_{zz} and $T_{\rm int}$. For example, the absolute δT in the $T_{\rm int}$=500 K cases are larger but not very K_{zz} dependant, whereas the absolute δT is relatively lower but much more K_{zz} dependant in the $T_{\rm int}$=100 K. Moreover, we also find that the RCPE models have slightly different radiative-convective boundaries from the RCTE models too. This sensitivity can have modest effects on the absolute abundances presented in this work but does not appear to be strong enough to alter the trends presented here.

We have also made this simplification because here we only explore the effect of the planetary parameters on *transmission spectra* of planets. Drummond et al. (2016) has shown that the effect of the difference between the RCTE and RCPE calculations

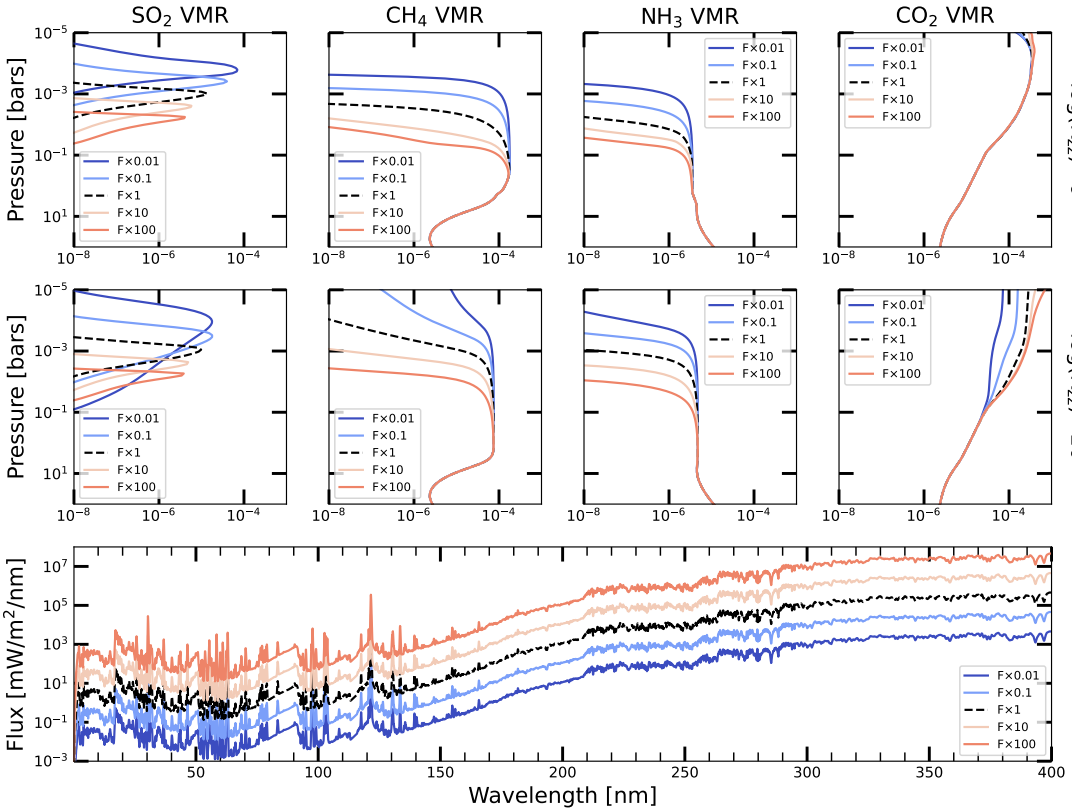

Figure 6.24: The upper set of panels show the change in abundance profile of key molecules due to change in the X-ray/UV flux incident on the planet when K_{zz}=10^6cm^{2}s^{-1}. Profiles for SO_2, CH_4, NH_3, and CO_2 are shown from left to right, respectively. The black-dashed line shows the profile for the nominal case. The middle row compares the abundances when K_{zz}=10^{10}cm^{2}s^{-1}. The lower panel shows the X-ray/UV spectrum used to calculate each of these models.

is much stronger for *eclipse spectroscopy*. Figure 6.23 reiterates this point and suggests that RCPE models should be used when eclipse spectroscopy data of warm and cold transiting planets are interpreted.

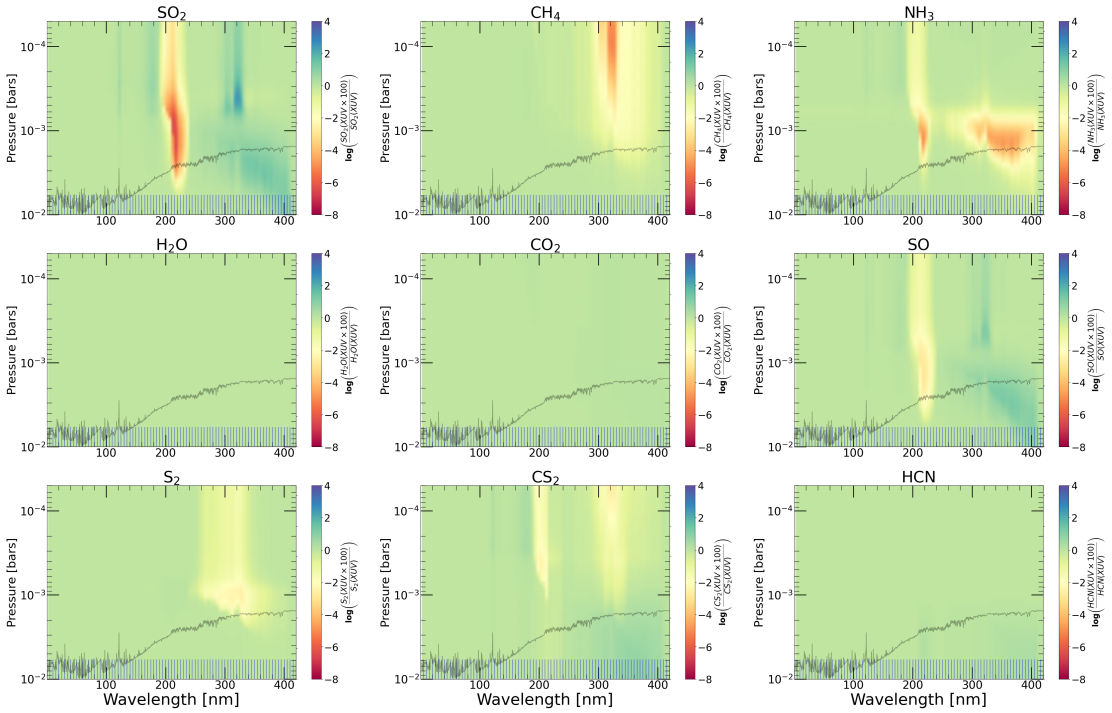

Figure 6.25: This plot shows how the abundance of a certain gas changes at a given pressure when the UV flux at a given wavelength bin is increased by a factor of $\times 100$. This has been quantified with Y in Equation 6.2. This Y quantity has been plotted as a heat map in each panel for SO_2, CH_4, NH_3,H_2O, CO_2, SO, S_2, CS_2, and HCN. The X-axis in each panel is the wavelength of the UV flux and the Y-axis is pressure in the atmosphere. The wavelength bins used for boosting the UV fluxes are also shown as vertical lines at the bottom of each panel along with the nominal UV spectra incident on the planet. A positive value for Y at a given pressure and wavelength means that the molecular abundance has increased relative to the nominal case when UV flux at those wavelengths were boosted. A negative Y value corresponds to a decrease instead.

6.4.2 Dependence of Photochemical Calculations on the UV spectra of host stars

Figure 6.3 shows that photochemistry shapes a significant portion of the abundance profiles of gases like CH_4 and SO_2 in/near the pressures typically probed by transmission spectroscopy. Therefore, another planetary parameter which can be influential on the photospheric abundances of gases in irradiated giant planets is the host star X-ray/UV spectra incident on the planetary atmosphere.

The black-dashed line in the bottom panel of Figure 6.24 shows the nominal UV spectra used for the parameter space exploration presented in §6.3. The other colored lines show the same UV spectra multiplied with different factors of 100×, 10×, 0.1×, and 0.01×. The top panels in Figure 6.24 show the chemical abundance profiles calculated for the same planet but with these different incident UV fluxes on the planet. We use the $T_{\rm eq}$= 800 K, $T_{\rm int}$= 300 K, K_{zz}= $10^6 {\rm cm}^2{\rm s}^{-1}$, and C/O= 1.1×solar case for all results presented in this section. Abundance profiles for SO_2, CH_4, NH_3, and CO_2 are shown from top left to right, respectively. It is clear that changes in the whole UV flux by five orders of magnitude does not cause the peak SO_2 abundance to change much, but instead has a significant impact on the pressure where it is produced, which can change by two orders of magnitude. For CH_4 and NH_3, that same change in UV flux can cause the pressure at which they are photochemically depleted to change by a factor of 10. On the other hand, the UV flux has almost no effect on the CO_2 abundance profiles. The middle panels in Figure 6.24 show the effect of UV flux on the abundances when

K_{zz}=10^{10}cm^{2}s^{-1}. The effect of the UV flux on the abundances are more pronounced in this case compared to the lower K_{zz} case shown in the top panel. Additionally, CO_2 shows much stronger variation in the upper atmosphere with changing UV flux when the mixing is strong. This exercise shows that having constraints on the overall flux levels of UV photons incident on giant planets is important for interpreting abundances of some gases like SO_2 or CH_4 from observations.

We further explore the sensitivity of atmospheric chemistry to different wavelength regions of the UV spectrum. We take the nominal UV spectra from Figure 6.24 and divide it into a large number of wavelength bins. Then, we boost the flux at each wavelength bin by a factor of 100× and recalculate the chemistry while keeping the rest of the fluxes in other wavelength bins the same. Figure 6.25 shows the results from this exercise. The nominal UV spectra are shown in the three panels in light gray, and the many vertical lines at the bottom of each panel depict the wavelength bins that we use. Each panel shows the quantity,

$$Y = log\left(\frac{X(F(w)\times 100)}{X(F(w))}\right) \tag{6.2}$$

as a heat map, where $X(F(w) \times 100)$ is the abundance of a gas X calculated when the UV flux at wavelength w has been boosted by a factor of 100. $X(F(w))$ is the abundance of the same gas calculated using the nominal UV flux. When Y in Equation 6.2 is greater/lower than zero, it means that the boost in UV flux in that wavelength bin causes an increase/decrease in the abundance of molecule X relative to the abundance calculated using the nominal UV flux.

The top left most panel in Figure 6.25 shows Y for SO_2. It shows that the SO_2 abundance near 0.1 to 3 mbar shows a decrease if the UV flux between 200 to 240 nm is boosted by a factor of 100. This sensitivity is due to the high UV cross-section of SO_2 between 200-240 nm shown in Figure **??** in Appendix §7.7. It also shows that the SO_2 abundance is slightly enhanced between 1-10 mbar if the UV flux near 350-400 nm is boosted. The SO_2 also shows a small increase near the 0.1 mbar level if the UV flux between 300-340 nm is increased. Both of these enhancements in SO_2 are linked with the additional destruction of S_2 and CS_2 when the flux between 300-400 nm is increased. This can be seen in the bottom left and bottom middle panels of Figure 6.25. This enhanced destruction of S_2 and CS_2 is due to the strong UV cross-sections of S_2 and CS_2 between 300-400 nm and 300-350 nm, respectively. Interestingly, the Y map for H_2O in the bottom left panel shows the opposite behavior than SO_2 when fluxes in the same wavelength ranges are boosted. But this is not visible in the plot as we choose to keep the same color scale across all panels in Figure 6.25 so that the sensitivity of each gas to changing UV flux can be compared with the rest.

The top middle panel in Figure 6.25 shows Y for CH_4. CH_4 abundance shows a small decrease near 0.1-3 mbar region when fluxes between 350-400 nm are boosted. CH_4 also shows a sharp decrease near the 0.1-0.6 mbar level when flux between 300-350 nm is increased by a factor of 100. Like SO_2, NH_3 abundance also shows a sharp decrease between 0.1-3 mbar when flux between 200-240 nm is increased. This is also related to the high UV cross-section of NH_3 (see Figure **??**) between 200-240 nm. Between 0.8-2 mbar, NH_3 shows a depletion when UV fluxes at wavelengths higher than 300 nm are

boosted. Comparing Figure 6.24 and Figure 6.25 shows that determining the level of UV flux incident on the whole planet in very broad wavelength bands is much more important than determining the very detailed nature of the UV SED to interpret the chemical abundances in irradiated planet atmospheres and connecting them to planetary bulk properties. However, we note that photochemical kinetics calculations are highly non-linear in nature and our calculations have several simplifications. For example, a more comprehensive approach where the incident flux is varied within randomly selected wavelength bins simultaneously and $T - P$ dependant UV cross-sections might provide additional insights.

6.4.3 Effect of Condensation on Chemical Kinetics Calculations

Our photochemical model does not track alkali metals and other condensibles relevant to the deep portions of gas-giant atmospheres. In reality, species like Na_2S and MnS, which we do not model, should condense at relatively high pressures and temperatures which may prevent some amount of sulfur from reaching the upper atmosphere (e.g., Morley et al. 2012). Therefore, our omission of these species should cause our simulations to over-predict the abundance of sulfur gases (e.g., SO_2) in the upper atmosphere. However, we expect our over-prediction to be small and inconsequential, because sulfur should be far more abundant than the alkali metals. For example, the Sun has $\sim 10\times$ more sulfur atoms than sodium atoms (Lodders et al. 2009), meaning Na_2S condensation could, at most, only sequester about 5% of the available sulfur. In summary, we expect the lack of condensibles in our photochemical model to cause our

results to over-estimate the sulfur in the upper atmosphere by an amount that does not effect our overall conclusions which is based on order-of-magnitude trends in sulfur bearing species.

6.4.4 Steady-State Convergence of Chemical Kinetics Model

To achieve a photochemical steady-state, the *Photochem* code integrates the photochemical equations forward in time until the atmosphere ceases to change. Our code identifies convergence to such a steady-state with the following criteria:

$$\Delta y_{\max} = \max \left| \frac{f_{ij}(t_n) - f_{ij}(t_n/2)}{f_{ij}(t_n)} \right| \tag{6.3}$$

$$\frac{\Delta y_{\max}}{\Delta t} = \frac{\Delta y_{\max}}{t_n/2} \tag{6.4}$$

Here, f_{ij} is the mixing ratio of species i in layer j, and t_n is the current integration time, making $\Delta y_{\max}$ the maximum relative change over the last $t_n/2$ seconds. We assume a steady-state is achieved when $\Delta y_{\max} < 0.05$ and $\frac{\Delta y_{\max}}{\Delta t} < 10^{-4}$. From testing, these criteria appear appropriate over a wide parameter space. Furthermore, the VULCAN photochemical code (Tsai et al. 2017) uses similar convergence requirements that have proved reliable for warm gas-rich planets (e.g., Tsai et al. (2023c)).

Photochem, like many other chemical kinetics models (e.g., VULCAN (Tsai et al. 2021)), computes the atmospheric chemistry in a grid of atmospheric altitudes instead of the pressure space used in the `PICASO` climate model. As a result, as the chemistry of the atmosphere evolves in the chemical kinetics model, the mean molecular weight of the atmosphere also changes. So, when the altitudes are converted back to

pressures after the kinetics models have converged, the $T(P)$ profile effectively becomes ever so slightly different than the input $T(P)$ profile. To avoid this, the *Photochem* code adaptively re-grids and adjusts the temperature profile during integration as to ensure the $T(P)$ profile matches the input `PICASO` $T(P)$ profile. This approach is particularly very important for the RCPE models we have presented in this work, where the chemical kinetics model is iteratively coupled directly with the climate model.

6.5 Conclusions

We have explored the variation of atmospheric chemistry in close-in giant transiting exoplanets across a vast parameter space of bulk planetary properties like $T_{\rm eq}$, $T_{\rm int}$, [M/H], and C/O. Our exploration includes chemical disequilibrium processes such as vertical mixing and photochemistry and is applicable for a wide variety of planets in terms of their mass, age, and proximity to their host stars. We have arrived at the following conclusions from this exploration,

1. We have shown that the the photospheric abundances of gases like CH_4 can be sensitive to just the K_{zz} parameter or just the C/O ratio or can also be quite degenerate between the two depending on the bulk properties of the planet like $T_{\rm int}$ or $T_{\rm eq}$ and also atmospheric properties like the vigor of vertical mixing. We have identified these trends in this work at different parts of the parameter space.

2. We have shown that CO is a weak tracer of the C/O ratio and remains largely independent of K_{zz}, unless the $T_{\rm int}$ of the planet is $\leq$ 100 K. For these cold interior

planets, CO can become a strong tracer of K_{zz}.

3. CO_2 on the other hand shows strong sensitivity to K_{zz} if the $T_{\rm eq}$≤900 K. This sensitivity is particularly enhanced for cold interiors. We also show that NH_3 is an excellent tracer of K_{zz}, without much dependence on C/O, as expected.

4. Photochemically produced SO_2 on the other hand depends quite strongly on the C/O of the planet unless the K_{zz} exceeds high values like $\sim 10^{11}{\rm cm^2 s^{-1}}$. We also show that SO_2 abundance shows a very sharp decline once the $T_{\rm eq}$≤600 K. For these colder $T_{\rm eq}$ planets, we find that the S- content of the photosphere is carried by other gases like CS, CS_2, and S_8. We also find that atomic S is a major carrier of S- near the photosphere irrespective of $T_{\rm eq}$.

5. We also explore how the abundances of some key gases in the atmosphere behave in the [M/H] vs. K_{zz} space. Among other trends, we find that other S- carriers like OCS and H_2S can show a rapid increase with K_{zz} in the photosphere, especially for metal enriched objects.

6. In order to explore the major chemical transitions in the atmosphere with $T_{\rm eq}$, we explore the $T_{\rm eq}$ vs. abundance trends of gas combinations like CO-CH_4, NH_3-N_2, and SO_2-H_2S-S. Our findings on these key transitions reflect the findings from previous work (Fortney et al. 2020; Ohno & Fortney 2023a,b; Baxter et al. 2021; Hobbs et al. 2021; Polman et al. 2023). Interestingly, we find that even in the photosphere, atomic S can carry a significant fraction of the S- inventory along with H_2S and SO_2.

7. In order to explore how sensitive is the transmission spectra to parameters like K_{zz} and $T_{\rm int}$ in different parts of the parameter space, we present a wavelength resolved sensitivity analysis of the transmission spectra to these parameters. We find that the sensitivity of the transmission spectra to these parameters is quite complex. In some parts of the parameter space, the CH_4 absorption bands might show great sensitivity to K_{zz}, while in some parts the CO_2 or SO_2 bands might show the highest sensitivity to changing K_{zz} or $T_{\rm int}$.

8. We calculate the column number density of molecules like C_2H_x, HCN, etc, which can act as precursors to photochemical hazes in the upper atmosphere. We find that these precursors molecules show very strong dependence on K_{zz} and almost no dependence on C/O for planets with cold interiors ($T_{\rm int}\leq$100 K) at 10$\times$solar metallicity. We also find that planets with low $T_{\rm int}$ are likely to have significantly higher abundance of haze precursors in the upper atmosphere compared to planets with hotter interiors. This is especially relevant to older low mass planets with no external heating.

There are several aspects of our modeling of giant planet atmospheric chemistry which can be improved in the near future. These include inclusion of more elements in our chemical kinetics calculations and inclusion of condensation and rainout chemistry within our chemistry calculation as well. We think that the assumptions made in our modeling approach are sufficient for the typical quality of transmission spectra obtained with *JWST*, especially in the near-future. But these kind of improvements might lead

to new avenues of characterizing the physics and chemistry of giant planet atmospheres and also their bulk properties.

Chapter 7

A JWST Panchromatic Thermal Emission Spectrum of the Warm Neptune Archetype GJ 436b

7.1 Introduction

The exoplanet field's goal to characterize and understand the composition and formation mechanisms of smaller exoplanets, like exo-Neptunes and sub-Neptunes, has gained significant momentum over the years with the launch of *JWST* (e.g., Benneke et al. 2024; Beatty et al. 2024b; Kempton et al. 2023; Gao et al. 2023; Madhusudhan et al. 2023; Piaulet-Ghorayeb et al. 2024; Schlawin et al. 2024c; Wallack et al. 2024; Radica et al. 2024). Owing to their lower mass, these planets are expected to be significantly more "polluted" by planetesimal accretion than giant exoplanets (Fortney et al. 2013). The atmospheres of these smaller planets are theoretically expected to

reflect this compositional difference with elevated atmospheric metallicities. Several studies in the past decade have tried to characterize the atmosphere of these smaller exoplanets observationally using transmission and emission spectroscopy (e.g., Knutson et al. 2014b; Stevenson et al. 2010; Morley et al. 2017a; Ehrenreich et al. 2014; Benneke et al. 2019; Kreidberg et al. 2014; Brande et al. 2024).

Characterizing the atmosphere of Neptune-sized or smaller exoplanets has often been challenging on multiple fronts. The small size of these planets creates signal-to-noise (SNR) challenges for both transmission and emission spectroscopy. For transmission spectroscopy, observations have focused on planets around smaller and nearby stars to mitigate this challenge. For emission spectroscopy, the hotter small exoplanets around cooler, smaller, and nearby stars can boost the expected SNR. Another challenge originates from the expectation that the atmospheres of these planets might be very rich in "metals". This effect increases the mean molecular weight of the atmosphere, reducing the scale height and thus reducing the size of features that can be observed in transmission. Enhanced metallicities can also lead to very optically thick clouds and hazes, which can further mute gaseous absorption features in both transmission and emission. A proposed investigation strategy in this scenario has been to select targets with the highest transmission and/or emission spectroscopy metrics (TSM/ESM) (Kempton et al. 2018), and then observe several transits/eclipses to enhance the SNR of the planet spectrum. This process is expected to reveal the gaseous features in the spectrum, enabling estimation of the atmospheric and bulk composition of these smaller planets.

GJ 436b is a nearly Neptune-like exoplanet with a reported mass of $0.08 M_{\rm jup}$ (25.43 $M_{\oplus}$) and a radius of $0.36 R_{\rm jup}$ ($\sim$4.03$R_{\rm earth}$) (Lanotte et al. 2014). The host-star is an M-dwarf at a distance of 9.7532±0.0089 pc. GJ 436b has the highest emission spectroscopy metric among planets which are smaller than or similar in size to Neptune, making it one of the ideal targets for atmospheric characterization with emission spectroscopy. The planet was the first detected exo-Neptune and was discovered with the radial velocity method (Butler et al. 2004). GJ 436b was later found to be transiting its host star by Gillon et al. (2007). The planet has an orbital period of 2.64389803±0.00000025 days, and its semi-major axis is 0.030±0.001 AU. It also has an eccentric orbit with $e = 0.1616^{+0.0041}_{-0.0032}$ (e.g., Lanotte et al. 2014; Wright et al. 2007; Maness et al. 2007; Knutson et al. 2014b; Bourrier et al. 2018; Rosenthal et al. 2021). GJ 436b's "warm" equilibrium temperature and its non-zero eccentricity makes it a very interesting target for atmospheric characterization. The eccentricity of its orbit despite its small orbital separation from its host star suggests the possibility of still ongoing tidal energy dissipation in the planet's interior. Processes like disequilibrium chemistry at these planetary temperatures can be very useful for directly probing such tidal dissipation processes by measuring the interior heat flux and composition of this Neptune-like exoplanet (e.g., Fortney et al. 2020; Morley et al. 2017a; Madhusudhan & Seager 2011; Line et al. 2011; Moses et al. 2013b; Agúndez et al. 2014; Stevenson et al. 2010; Sing et al. 2024; Welbanks et al. 2024; Beatty et al. 2024b; Barat et al. 2024).

Efforts to characterize the atmosphere of GJ 436b have been ongoing since the *Spitzer* era. Demory et al. (2007) and Deming et al. (2007) observed the secondary

eclipse of GJ 436b with the *Spitzer* IRAC instrument in the 8 μm band. These observations helped confirm the non-zero eccentricity of the planet and also provided an estimate of the planet's day-side brightness temperature. Stevenson et al. (2010) observed GJ 436b in the 3.6, 4.5, 5.8, 8.0, and 16 μm *Spitzer* bands. This was the first multi-band photometry performed for the planet, and the data hinted at the presence of disequilibrium chemistry in the planet's atmosphere. This conclusion was primarily driven by the very high 3.6 μm flux and very low 4.5 μm flux. At the equilibrium temperature of the planet, this could only be explained by the suppression of CH_4 and enhancement of CO due to quenching driven by vertical mixing. Atmospheric retrieval studies on these data by Madhusudhan & Seager (2011) further supported this picture and also hinted toward a significantly metal-enriched atmosphere.

As these conclusions mainly depended on the 3.6 and 4.5 μm *Spitzer* photometric points, Morley et al. (2017a) re-observed the planet in these two bands with *Spitzer* and presented a new analysis of the combined *Spitzer* data. Both Lanotte et al. (2014) and Morley et al. (2017a) found that the 3.6 μm flux of the planet, obtained from their new observations and data analysis, was significantly lower than the values presented by Stevenson et al. (2010). Forward modeling and retrieval analyses on this revised data suggested that the atmosphere was very rich in metals with metallicities higher than several hundreds times the solar value. The 3.6 μm flux, although fainter than previously thought, was still much higher than expected from thermochemical equilibrium models, suggesting a diminished CH_4 abundance due to a hot interior and the presence of vertical mixing. This hot interior was thought to be potentially due to

tidal heating of the planet's interior, owing to its eccentric orbit. These previous studies made a very compelling case for observing GJ 436b with the more stable and sensitive *JWST* to obtain a higher SNR and a higher resolution spectrum of the planet to further constrain its composition.

In this work, we present the panchromatic eclipse spectrum of GJ 436b obtained with the NIRCam and MIRI instruments aboard *JWST*. Our observations cover wavelengths between 2–12 μm with multiple eclipses of the planet. We also present a modeling analysis of this panchromatic spectrum with both atmospheric retrievals and self-consistent forward models. Our observations and data analysis techniques, along with comparisons with previous *Spitzer* observations, are described in §7.2 and §7.3, respectively. We present our modeling analysis and key results in §7.4. This is followed by a detailed discussion of the results and our conclusions in §7.5 and §7.6, respectively.

7.2 Observations

We observed a total of 8 eclipses of GJ 436b to build up a panchromatic emission spectrum spanning from 2.4 to 12 μm in *JWST* programs 1177 and 1185 as part of the MANATEE survey (e.g. Schlawin et al. 2018). Specifically, we collected 3 eclipses with the NIRCam F322W2 grism, 3 eclipses with the NIRCam F444W grism, and 2 eclipses with the MIRI LRS prism. The observations were collected between 2022-12-07 UT and 2023-12-21 UT, with more observation details listed in Table 7.1. We observed for ∼4.7 hours around the time of mid-eclipse, which occurs at an orbital

phase of 0.5876 due to the eccentricity of the orbit. We allowed ample time (2.65 to 2.74 hours) for any observatory or detector settling (e.g. Bell et al. 2023a; Bouwman et al. 2023) and for measuring the baseline before first contact for the T_{14}=1.02 hour-long eclipse. As discussed in Section 7.7.1, we experimented with a telescope offset to improve 1/f noise (noise that has power spectrum that is inversely proportional to its frequencey – see Schlawin et al. (2020)) in three of the NIRCam observations.

7.3 Data Analysis

We analyzed the data with two independent pipelines used in previous MANATEE publications, `tshirt` and `Eureka!` (e.g. Bell et al. 2023b; Welbanks et al. 2024; Schlawin et al. 2024b; Beatty et al. 2024b). Systematic noise is present in both the NIRCam and MIRI lightcurves, but combining together multiple eclipse observations increases the accuracy of our spectra, which are largely consistent when accounting for this systematic noise.

7.3.1 `tshirt` Reduction and Analysis

We begin with the `_uncal.fits` data products and apply custom processing with modified steps to the `jwst` pipeline, as in previous JWST observations (Ahrer et al. 2023; Bell et al. 2023b). Across all 8 observations, we used JWST version 1.13.4, CRDS version 11.17.15 and CRDS context `jwst_1188.pmap`. For the NIRCam observations, we used a modified version of the JWST pipeline with the reference pixel step replaced by a row-by-row, odd/even, by amplifier (ROEBA) correction using sky pixels instead

of reference pixels for 1/f subtraction (Schlawin et al. 2020). We also used a jump step rejection threshold of 6σ and skipped the dark subtraction step as it can add noise. For MIRI, we used the JWST pipeline's Stage 1 defaults except that we use a jump rejection threshold of 7σ and stop processing after producing `_rateints.fits` data products. We manually divide all integrations by a flat field: `jwst_nircam_flat_0266.fits` for the F322W observations, `jwst_nircam_flat_0313.fits` for the F444W observations and `jwst_miri_flat_0789.fits` for the LRS observations.

We begin extraction of both NIRCam and MIRI data by finding the centroids of a reference image with Gaussian fitting along the spatial direction and then fitting the resulting trace with a third-order polynomial with 3σ clipping. We then performed background subtraction with 3σ clipping along the spatial direction with a linear fit for NIRCam and a mean background for MIRI. The background region for NIRCam was all Y pixels along a column from Y=5 to Y=65 that were more than 7 pixels from the source centroid, rounded to whole pixels. For MIRI, we used all X pixels along a row from X=10 to X=70 that were more than 7 pixels from the source centroid. We extracted the spectra using covariance-weighted optimal extraction (Schlawin et al. 2020), with a full aperture size of 10 pixels for NIRCam and 8 pixels for MIRI. We binned the lightcurves into 20 equally spaced in wavelength bins per NIRCam observation (85 nm/87 px for F322W2 and 63 nm/65 px for F444W) and save these for spectroscopic lightcurve fitting. We binned the lightcurves into 250 nm wavelength bins for MIR LRS, rounded to the nearest pixel.

We first used the MIRI LRS broadband lightcurves to update the planet's

orbital parameters. We used the `Eureka!` reduction described below for the broadband lightcurves, first optimizing and fitting the systematic baseline parameters (a linear coefficient and two exponential constants) for each of the two eclipses separately and then saving the de-trended lightcurves. We then fit both lightcurves simultaneously and derived orbital parameters for use in spectroscopic fitting. For the orbital parameter priors, we use the inclination, a/R_*, eccentricity, argument of periastron and planet-to-star radius ratio from (Bourrier et al. 2018) and the period and time of transit center epoch from (Kokori et al. 2022). We fit for a linear baseline trend and iteratively clip any points more than 5σ from the best-fit lightcurve. The posterior means and standard deviations are listed in Table 7.2. We selected the mean values of the posteriors and fixed the planet's orbital parameters for spectroscopic analysis of both NIRCam and MIRI data.

All NIRCam observations exhibited a steep downward trend seen in other NIRCam lightcurves (e.g. Ahrer et al. 2023; Hu et al. 2024a). These overall trends are correlated with the Focal Plane Array Housing Temperature (FPAH) (Schlawin et al. 2024b). We also find a correlation with the average value of the reference pixels for a given integration. Even when de-trending by these two vectors, significant time-correlated noise is present, so we model the lightcurves with a Gaussian process using `celerite2` (Foreman-Mackey 2018), a linear coefficient for the smoothed FPAH temperature deviation, and a linear coefficient with the average reference pixel value. Similarly, we used a Gaussian Process to model the MIRI LRS lightcurves to account for time-correlated noise. We used `celerite2` and assumed a stochastic harmonic os-

cillator term with a fixed quality factor of Q=0.25. The resulting NIRCam spectra are consistent within error, as is briefly described in Section 7.7.5. Finally, we calculated a weighted average of all eclipse observations per wavelength region (see Table 7.1) and used this averaged spectrum for atmospheric modeling.

7.3.2 `Eureka!` Reduction and Analysis

Our second reduction method for the NIRCam observations used version 0.11.dev446+gf5d684e of the open-source `Eureka!` package (Bell et al. 2022a) with version 1.15.1 of the `jwst` package, and version 11.17.26 of the CRDS package with the context `jwst_1253.pmap`. Meanwhile, for the MIRI observations we used `Eureka!` version 0.11.dev77+g1e43198f.d20240130, `jwst` version 1.13.4, and CRDS version 11.17.15 with context `jwst_1188.pmap`. The `Eureka!` control and parameter files we used are available for download[1], with the important steps and parameters summarized below.

We largely followed the methods of Bell et al. (2023b) for the reduction of the NIRCam data and of Bell et al. (2024a) for the reduction of the MIRI data. For all datasets, we started with the `_uncal.fits` files. In Stage 1, we increased the jump step rejection threshold to 6.0 for the NIRCam observations and 8.0 for the MIRI observations to avoid excessive false positives. For the MIRI data, we also ran the `lastframe` step which removed the last frame from each integration; this frame is often quite noisy for MIRI data and was saturated at some short wavelengths. We did not run the `firstframe` step to remove the first frames from the MIRI data; while it can

[1] Zenodo DOI:10.5281/zenodo.14814183

sometimes be advantageous to remove these noisy frames, GJ 436 is so bright that this would only leave us with three frames per integration, and keeping the noisier first frame resulted in lower overall noise for this particular dataset. In Stage 2, we skipped the `photom` and `extract_1d` steps as these are not needed for time-series observations. In Stage 3, we cropped the frames to a smaller subarray to remove excessively noisy pixels, corrected for the slight curvature in the NIRCam data by shifting the data with integer-pixel movements, and performed column-by-column background subtraction on each integration (after first rotating the MIRI data by 90° so that the trace was oriented similarly to the NIRCam data). We also computed the mean spatial position and PSF-width of the spectral trace in each integration to later use as covariates when fitting the lightcurves. For the MIRI observations, we assumed a constant gain of 3.1 electrons per Data Number, following Bell et al. (2024a). Next, we used the median frame of each observation to construct the spatial profile used by our optimal spectral extraction (Horne 1986) routine, using only the central 9 px, 4 px, and 5 px for NIRCam F322W2, NIRCam F444W, and MIRI LRS, respectively. In Stage 4, we manually masked some bad wavelengths where the pixel-level lightcurves were far noisier than their neighboring pixels, presumably due to unmasked bad pixels in an earlier stage of processing. We then spectrally binned the data and sigma-clipped any remaining severe outliers in the binned lightcurves.

We then fit each spectral lightcurve independently for each of the observations. Our astrophysical model consisted of a `batman` eclipse model, using the same orbital parameters used in the `tshirt` method. Our eclipse model accounted for the

change in light travel time throughout the planet's orbit, assuming a stellar radius of $0.449\,R_{\odot}$ (Bourrier et al. 2018) to convert from relative units to physical units. While ultimately we arrived at a different radius of the star in Section 7.3.4 and thus a different semi-major axis of the planet, the difference in travel time between the two is only 1.4 seconds, far below the $\pm$15 sec timing uncertainty on the combined MIRI secondary eclipse time. Our systematic model consisted of a linear trend in time, a linear decorrelation against changes in the spatial position and PSF-width measured in Stage 3, and a Gaussian Process (GP) with a Matérn-3/2 kernel (as implemented by celerite2; Foreman-Mackey et al. 2017; Foreman-Mackey 2018) as a function of time to account for the impact of any otherwise-unmodelled red noise. Our systematic model for the MIRI observations also included a single exponential ramp as a function of time, following the recommendations of Bell et al. (2024a). Finally, we also included a white-noise multiplier term to account for any additional white noise or error in the estimated gain used in Stage 3. To estimate best-fit values and uncertainties, we used the dynamic nested sampling algorithm (Skilling 2006a) from the `dynesty` package (Speagle 2020) with 121 live points, 'multi' bounds, the 'rwalk' sampler, and a convergence criterion of $d\log\mathcal{Z} = 0.01$, where $\mathcal{Z}$ is the Bayesian evidence. Our NIRCam spectra were quite consistent (1σ) between each of the three visits for each filter, and our MIRI spectra were also quite consistent, with the exception of a small number of wavelength bins that differed by more than 1σ. To compute a 'final' spectrum from the two NIRCam filters, we computed an error-weighted average between the three visits. Since the MIRI LRS spectra differed more significantly between the two visits in a couple of wavelength bins,

we chose to compute our 'final' MIRI spectrum by taking the mean between the two visits, and we inflated the final uncertainties to account for disagreements between the two epochs.

7.3.3 Reduction Comparisons

The top panel of Figure 7.1 shows the full *JWST* panchromatic spectrum of GJ 436b from 2 to 12 μm. Additionally, Figure 7.1 also shows the *Spitzer* photometry presented in Stevenson et al. (2010), Morley et al. (2017a), and Lanotte et al. (2014). Figure 7.1 top panel shows that the *JWST* spectrum agrees with the *Spitzer* measurements in most wavelengths except in the 3.6 μm band. The measured flux of the planet from *JWST* NIRCam is significantly fainter than the flux observed in the *Spitzer* 3.6 μm band.

There is a significant evolution of eclipse depths in the 3.6 μm wavelength band over many different analyses from Stevenson et al. (2010) to this work. While time-evolution of the planet's atmosphere is a possibility, the significant correlated noise present in the *Spitzer* and NIRcam lightcurves instead points to discrepancies in the systematic noise and the correction of it, such as between Stevenson et al. (2010) and Morley et al. (2017a) using the same archival data but newer de-trending techniques. We further discuss the atmospheric implications of the previous versus new 3.6 μm planet flux in Section 7.5.1. The bottom panel of Figure 7.1 compares the spectrum of the planet obtained with two independent data reduction pipelines: `tshirt` and `Eureka!`. It is clear that the two reduction pipelines agree with each other within

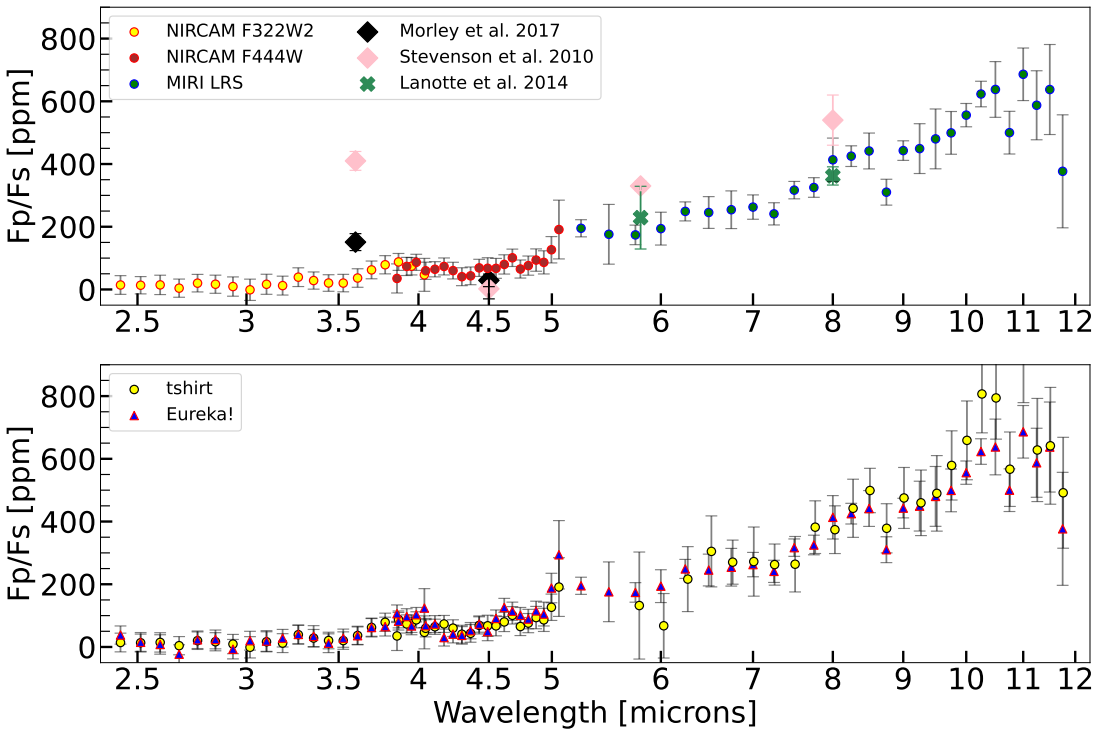

Figure 7.1: **Top panel** shows the panchromatic emission spectrum of GJ 436b observed with *JWST* using three instrument modes – NIRCam F322W2 (yellow points), NIRCam F444W (red points), and MIRI LRS (blue points). The NIRCam data shown here is from the `tshirt` reduction pipeline and the MIRI LRS data is from the `Eureka!` pipeline. The panchromatic spectrum is obtained from the weighted average of individual visits for each instrument mode. The pink diamonds, black diamonds, and green crosses also show photometry of the planet observed with *Spitzer* and analyzed by Stevenson et al. (2010), Morley et al. (2017a), and Lanotte et al. (2014), respectively. **Bottom panel** compares the F_p/F_s spectra derived from the *JWST* observations with two different data reduction pipelines – `tshirt` and `Eureka!`.

the 1σ uncertainty level, and both of them show a disagreement with the 3.6 μm flux measured with *Spitzer*.

7.3.4 Calibrated Stellar Spectrum

For the NIRCam flux-calibrated spectra, we used the commissioning and calibration observations of GSPC P330-E, as in Schlawin et al. (2024b) with program 1076 observation 1 for the F322W2 filter and program 4498 observation 61 for the F444W filter. We used the CALSPEC model `p330e_mod_006.fits` to derive a calibration factor (erg s^{-1} cm^{-2} cm^{-1} per DN s^{-1}) for observations 1185-10 and 1185-11. We used the same trace, aperture size, and background subtraction regions for both GSPC P330-E and GJ 436. Then, we multiplied the observed DN/s by this calibration factor to derive the flux in erg s^{-1} cm^{-2} cm^{-1}.

For the flux-calibrated MIRI/LRS spectrum, we used the `Eureka!` package (Bell et al. 2022a). We began with the Stage 1 outputs from the `Eureka!` methods described above and ran Stage 2 with the `photom` step turned on. Our Stage 3 processing of the flux-calibrated data was largely the same as the lightcurve reduction, although we left the spectra in units of mJy and used the central 9 px when performing optimal spectral extraction to ensure we captured most of the stellar flux and minimized the uncertainties introduced by the `apcorr` reference file. Following a similar method to that of Schlawin et al. (2024b), we also computed flux-calibrated MIRI/LRS spectra of the three early G-type stars HD 37962, HD 106252, and HD 167060 from the absolute flux calibration program JWST-CAL-1538 (P.I. Karl Gordon), and we compared our

flux-calibrated spectra to each star's CALSPEC model (based on the BOSZ grid of Bohlin et al. 2017). We used the mean ratio of the observed to modeled spectra of these calibrator stars to compute a spectroscopic correction factor. Among the flux-calibrator stars, this resulted in 1% deviations from the stars' CALSPEC models. Among other exoplanet-host stars, we found that this method resulted in a ∼2% deviation from BOSZ models around 8–9 microns, while the deviation typically increased to ∼5% at both ends of the LRS wavelength range.

7.3.4.1 Stellar Parameters from *JWST*

We fit our calibrated stellar spectrum from *JWST* with the latest grid of BOSZ stellar atmosphere models (Mészáros et al. 2024). We interpolate the logarithm of the outgoing flux across the BOSZ stellar model grid, with $T_{\rm eff}$ spanning between 3000 K and 5000 K, $log(g)$ between 2-5 (cgs units), metallicity ([M/H]) and C- abundance ([C/M]) between -0.5 and +0.5, α element abundance ([α/M]) between -0.25 and +0.25, and the microturbulence parameter between 0 to 4. We fit the calibrated stellar spectrum with the interpolated grid model fluxes and find that the best-fit parameters are $T_{\rm eff}$= 3648 K, R=0.41 $R_{\odot}$, $log(g)$=4.47, [M/H]=+0.5, [C/M]=-0.5, [α/M]=+0.25, and the microturbulence parameter=3.8. We assume a 2% error in the calibrated stellar fluxes to get these best-fit parameter values. Our fitting analysis underestimates the uncertainty on these parameter values as our method does not account for the interpolation uncertainties in our model fluxes. However, previous analysis have shown that the best-fit parameters remain the same even if these uncertainties are ignored (Zhang

et al. 2021b). Figure 7.14 shows the comparison between the best-fit stellar model and the observed stellar spectrum. We note that fitting the optical photometry for GJ 436 simultaneously with the *JWST* spectrum resulted in extremely poor model fits to the *JWST* spectrum. As this work focuses on the *JWST* emission spectrum of GJ 436b, we therefore only fit the *JWST* stellar spectrum to constrain the host star parameters. We calculate a planet radius of 0.329 $R_{\rm jup}$ for GJ 436b by combining the stellar radius obtained from the *JWST* stellar spectrum with the planet-to-star radius ratio obtained in Bourrier et al. (2018). We use these stellar and planetary parameters throughout the analysis presented in this work.

7.4 Results

7.4.1 Atmospheric Retrievals

We perform two types of atmospheric retrievals on the data – a clear free chemistry retrieval and an isothermal atmosphere retrieval. The goal of the clear free chemistry retrieval is to assess the detection of gases directly from the observed spectrum. On the other hand, we use the isothermal atmosphere retrieval for assessing the average day-side temperature of the planet from the observed spectrum and constraining its Bond albedo and day-to-night side heat recirculation efficiency. We describe our findings from each analysis below in §7.4.1.1 and §7.4.1.2 .

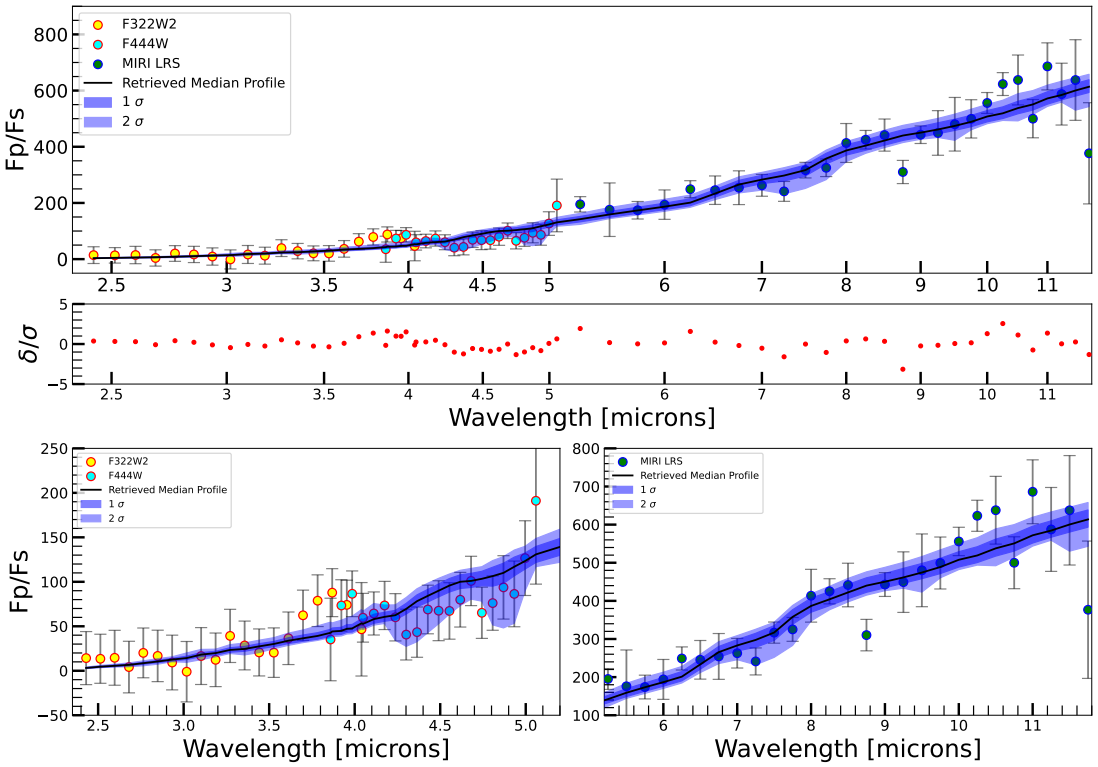

Figure 7.2: The **top panel** shows the median spectral model obtained from the free chemistry retrieval with the solid blue line compared with the *JWST* observations. The 1σ and 2σ envelopes on the model spectra are shown with dark and light blue shaded regions. The **middle panel** shows the residuals of the model fit divided by the errors in the data. The **bottom left** and **bottom right** panels show a zoomed in version of the top panel with comparison of the retrieved models with parts of the spectrum observed with NIRCam and MIRI, respectively.

7.4.1.1 Clear Atmospheric Free Retrieval

We use the 1D `PICASO` atmospheric modeling tool (Batalha et al. 2019; Mukherjee et al. 2023, 2021a) to perform a free chemistry retrieval analysis on the *JWST* spectrum of GJ 436b. We divide the atmosphere in 91 plane-parallel pressure levels (90 layers) with logarithmically spaced pressure intervals between 10^{-8} and 2000 bars. We parametrize the temperature–pressure ($T(P)$) profile in these atmospheric layers using the $T(P)$ profile formulation from Madhusudhan & Seager (2009a) with 6 free parameters. Additionally, we include the volume mixing ratios (VMR) of H_2O, CH_4, CO_2, CO, NH_3, N_2, HCN, C_2H_2, OCS, H_2S, and SO_2 as free parameters as well. The VMR of these gases are assumed to be constant with pressure in our retrieval model. Therefore, our free retrieval model has 17 free parameters in total. The H_2+He VMR is obtained by subtracting the sum of the VMR of all these other gases from 1. We assume a H_2/He fraction of 5.1349 and this ratio is used to divide the H_2+He VMR between H_2 and He VMR. For a given value of all these 17 free parameters, `PICASO` is used to calculate the model thermal emission spectrum. We generate this model spectrum at a resolution of R$\sim$ 60,000 using resampled opacities (see Mukherjee et al. (2024c) for detailed references of used line lists). Our opacities also include collision-induced absorption from H_2-H_2, H_2-He, H_2-N_2, and H_2-CH_4. This higher resolution spectrum is then binned down to the resolution of the observed data.

We use the best-fit BOSZ stellar model described in §7.3.4.1 to compute the $F_{\rm planet}/F_{\rm star}$ from the $F_{\rm planet}$ computed with `PICASO`. We wrap our retrieval model within

the Bayesian nested sampling algorithm PyMultiNest (Feroz et al. 2009a). We perform our retrieval analysis with 2000 live points along with the standard convergence criteria for PyMultiNest. We adopt uniform priors for all the 17 free parameters. The $\log_{10}$(VMR) of the 11 gases included in our retrieval are allowed to vary between -0.5 to -15.5.

Figure 7.2 compares the median retrieved profile with the observed *JWST* spectrum. The spectral envelopes corresponding to the 1σ and 2σ levels are also shown in Figure 7.2. The top panel shows the comparison of the retrieved spectrum with the panchromatic *JWST* spectrum. Residuals of the data from the median retrieved spectrum are also shown in the middle panel of Figure 7.2. The retrieved model fits all the data points within 2σ except two points at 8.8 and 11.8 μm. The bottom left and bottom right panels compare the retrieved models with the segments of the spectrum observed with NIRCam and MIRI LRS data, respectively. The median retrieved model has a reduced-χ^2 value of 0.813. We report the total-χ^2/N as the reduced-χ^2 here and throughout the manuscript, where N is the number of spectral bins.

Figure 7.15 shows the corner plot of all the 17 retrieved parameters which include both 1D posteriors and cross-correlations between all the free parameters. The dashed lines in the posterior distributions mark the median and $\pm1\sigma$ values for each parameter. Figure 7.15 shows that none of the gases are detected from the spectrum at a 3σ or higher significance level. The 2σ constraints on CO_2 abundance are $\log_{10}(CO_2)$=-$3.23^{+2.49}_{-9.93}$, which means that the significance of the presence of CO_2 absorption feature in the spectrum is between 2σ and 3σ level. The 2σ limits on CO and SO_2 abundance

are $\log_{10}(\mathrm{CO})$=-4.53$^{+3.80}_{-10.03}$ and $\log_{10}(\mathrm{SO_2})$=-4.98$^{+2.39}_{-9.35}$, respectively. The retrieved abundances of all other gases are consistent with the lower bounds of our prior within 2σ.

7.4.1.2 Isothermal Atmosphere Retrieval

We also perform another retrieval on the data assuming that the $T(P)$ profile is isothermal. This is essentially a fit to the data assuming that the planet's atmosphere emits like a blackbody. The top panel of Figure 7.3 shows the median retrieved spectrum from this retrieval setup along with the 1σ and 2σ envelope. The reduced-χ^2 of this model fit is 0.88. This reduced-χ^2 value is larger than the value obtained with the non-isothermal $T(P)$ profile retrieval presented in the previous section, but the number of free parameters in this case is 1 compared to 17 in the previous case.

The best-fit blackbody temperature for the spectrum is constrained at $662.8^{+5.0}_{-4.8}$ K. Using our best-fit stellar parameters, we estimate the zero-albedo equilibrium temperature (T_{eq}) for GJ 436b to be 675 K. We use the a/R* constraint from Table 7.2 along with our derived stellar radius and T_{eff} to get this T_{eq}. This T_{eq} was calculated assuming full redistribution of incident stellar heat across both the day and night side of the planet. Comparison between the retrieved blackbody temperature of the day-side from the observed data and the calculated T_{eq} suggests that the day-side of the planet is either very efficiently transporting heat to the night-side achieving a full heat-recirculation like scenario or the day-side is reflecting significant amount of incident stellar irradiation to space, leading to a high Bond albedo.

As we do not observe the night-side of the planet, it is not possible to put strong

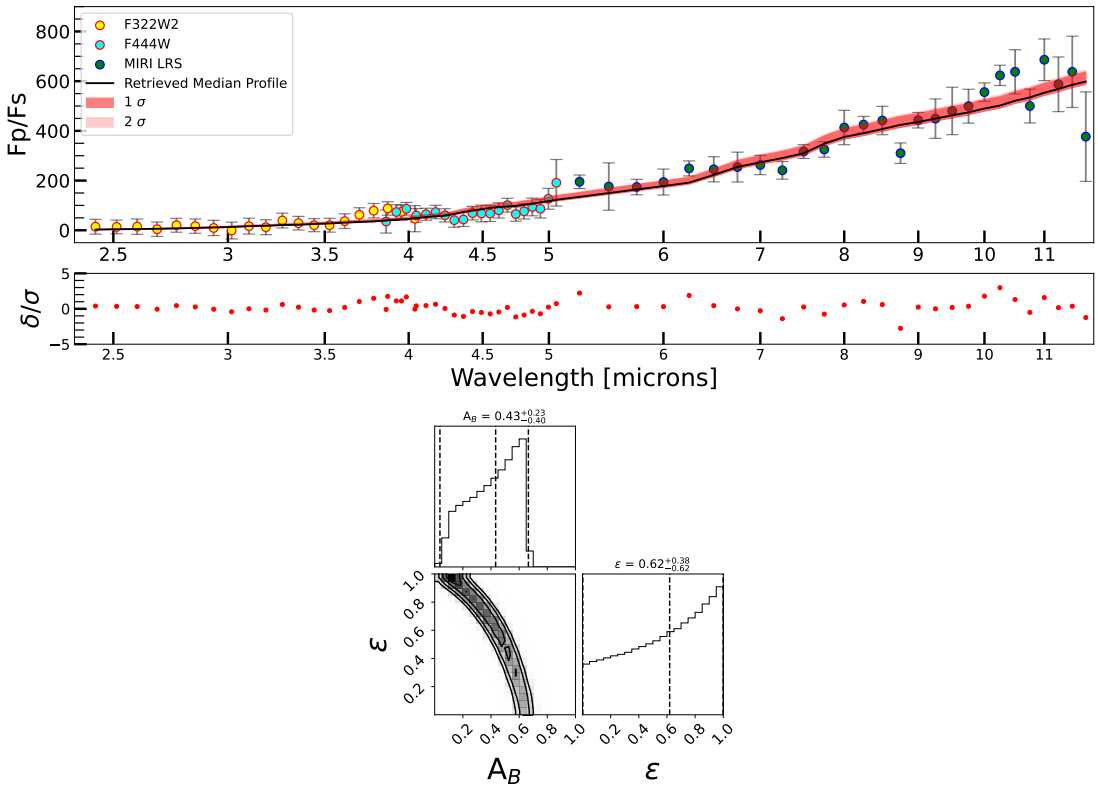

Figure 7.3: The **top panel** shows the median spectrum obtained from the isothermal retrieval with the red solid line compared with the *JWST* spectrum of the planet. The 1σ and 2σ envelopes on the model spectra are shown with dark and light red shaded regions. The **middle panel** shows the residuals of the model fit divided by the errors in the data. The **bottom panel** shows the corner plot between Bond albedo (A_B) and heat recirculation parameter (ϵ) obtained by fitting the day-side blackbody temperature constrained from the isothermal retrieval with the methodology described in Cowan & Agol (2011). The dashed line show the median and 3σ constraints on each parameter.

constraints on both the albedo and the heat recirculation efficiency. However, we use the methodology from Cowan & Agol (2011) to estimate how our measured average day-side temperature influences the albedo–recirculation efficiency parameter space. Figure 7.3 lower panel shows the constraints on the Bond albedo (A_B) and the recirculation efficiency factor $(\epsilon)^2$. The ϵ=1 represents full day-to-night side recirculation and ϵ=0 represents no day-to-night side recirculation. Figure 7.3 lower panel shows that a 3σ upper limit is constrained on the Bond albedo $A_B \leq 0.66$. The ϵ parameter, however, remains unconstrained.

7.4.2 Self-Consistent Models

We also compute a grid of 1D clear radiative–convective–thermochemical equilibrium (RCTE) models using the `PICASO` climate model (Mukherjee et al. 2023). The atmosphere is divided into 91 plane-parallel layers for computing these models. These model layers have logarithmically spaced pressures between 10^{-6} bars and 2000 bars. We vary four different parameters in this model grid including the interal temperature ($T_{\rm int}$), atmospheric metallicity ([M/H]), C/O ratio, and the heat-recirculation factor (`rfacv`). We sample 5 $T_{\rm int}$ values of 60 K, 100 K, 200 K, 300 K, and 400 K. We also sample 10 different [M/H] values between +1.0 and +2.9. We include 6 different C/O values between 0.1× and 1.3× solar, where the assumed solar C/O is 0.458 (Lodders et al. 2009). The heat recirculation factor (`rfacv`) is varied between 0.2 to 1.0 (9 values), where 0.5 represents a full day-to-night side heat recirculation and 1.0 represents

[2]Note that the ϵ from Cowan & Agol (2011) is defined differently from the `rfacv` parameter here.

no day-to-night side heat transport. We include smaller values of `rfacv` than 0.5 to capture the scenario where the day-side of the planet has a higher albedo than predicted by a clear 1D RCTE model. We note that `PICASO` typically uses precomputed chemistry and correlated-k opacity tables to perform RCTE calculations (Mukherjee et al. 2023) and as a result the model grids can only sparsely sample the [M/H] and C/O parameter space. However, we use a version of `PICASO` which is self-consistently coupled to the *photochem* model (Mukherjee et al. 2024b; Wogan 2024) to compute the grid with finer [M/H] and C/O intervals. This version of `PICASO` uses the on-the-fly correlated-k opacity mixing technique (Amundsen et al. 2017; Mukherjee et al. 2022, 2024c) for all atmospheric gases and calculates the chemical abundances of gases with *photochem* self-consistently. This coupling also lets us expand the grid beyond 100×solar metallicity. The model grid has a total of 2700 unique RCTE models.

We also compute a grid of models with disequilibrium chemistry by post-processing the `PICASO` RCTE grid described above with the *photochem* 1D chemical kinetics model (Wogan et al. 2023; Mukherjee et al. 2024b). This grid includes disequilibrium chemistry processes such as quenching of gases due to vertical mixing and photochemistry. It samples all the same parameters and their values as the RCTE grid except for one additional parameter – the vertical eddy diffusion coefficient K_{zz}. We sample three values for K_{zz} – 10^6, 10^8, and 10^{10} cm^{2}s^{-1}. These K_{zz} values span weak to vigorous vertical mixing in the atmosphere (Mukherjee et al. 2022; Phillips et al. 2020).

7.4.2.1 Clear Equilibrium Chemistry Atmospheric Models

We first use the clear self-consistent atmospheric model grid to fit the observed spectrum of the planet. We use a χ^2-minimization based fitting algorithm. We compute the F_{planet}/F_{star} from each unique model of the grid at a resolution of R$\sim$60,000 and then we bin the spectrum to the spectral resolution of the observed data. We compute the χ^2 metric for each of these models and the observed data. Figure 7.4 shows the model with the minimum χ^2 metric with the green colored line. This best-fit clear RCTE grid model has a reduced-χ^2= 1.04.

We further use the χ^2 value of each grid model to construct a corner plot for the grid models. We assign a probability $P = e^{-\chi^2/2}$ to each model of the grid. We use these probabilities as weights to construct the corner plot for the clear RCTE grid of models. Figure 7.16 left plot shows the corner plot obtained from the clear RCTE grid. The best-fit model with the highest likelihood from this grid has a metallicity of [M/H]=+2.7 and a C/O=0.1×solar. The metallicity is constrained to be [M/H]≥+2.7 at 1σ level with these models. The `rfacv` parameter preferred by the observation is 0.6, which corresponds to near full day-to-night recirculation. This `rfacv` value is consistent with the results from the isothermal retrieval presented in §7.4.1.2. The data also prefers $T_{\rm int}$=100 K as the best-fitting model, but Figure 7.16 left panel shows that higher or lower $T_{\rm int}$ values are not completely ruled out. The contribution of various gasses to the best-fit model spectrum are shown (Figure 7.17) and further described in §7.7.10.

7.4.2.2 Clear Disequilibrium Chemistry Atmospheric Models

We use the clear disequilibrium chemistry atmospheric model grid to fit the observed spectrum of the planet as well. We use the same methodology as §7.4.2.1 for fitting the data with this grid. Figure 7.4 shows the model with the minimum χ^2 metric with the red colored line. This best-fit clear disequilibrium chemistry grid model has a reduced-χ^2= 0.78.

We use the χ^2 value of each grid model to construct a corner plot for this grid as well. Figure 7.16 right panel shows the corner plot obtained from the disequilibrium chemistry grid. The model with the highest likelihood has $T_{\rm int}$=100 K, [M/H]=+2.7, and C/O=0.1×solar. The corner plot shows that the disequilibrium chemistry grid suggests substantial probabilities for [M/H]≥+1.9 (1σ lower limit) and [M/H]≥+1.5 (2σ lower limit). This is in contrast with the clear RCTE grid, which prefers an extremely metal-enriched atmosphere ([M/H]≥+2.7 at 1σ level). The best-fit `rfacv` parameter is 0.6, which is also the value preferred by the clear RCTE grid. Similar to the RCTE grid, the probability distribution for `rfacv` is consistent with the full day-to-night recirculation value of 0.5. Figure 7.17 bottom panel shows the contribution of various gasses to the best-fit model spectrum.

7.4.2.3 Cloudy Atmospheric Models

We use the `virga` cloud model (Rooney et al. 2021; Ackerman & Marley 2001b) to compute the cloud structure and optical properties for GJ 436b. We use the $T(P)$ profile from the RCTE model grid as inputs for `virga`. We assume KCl and Na_2S

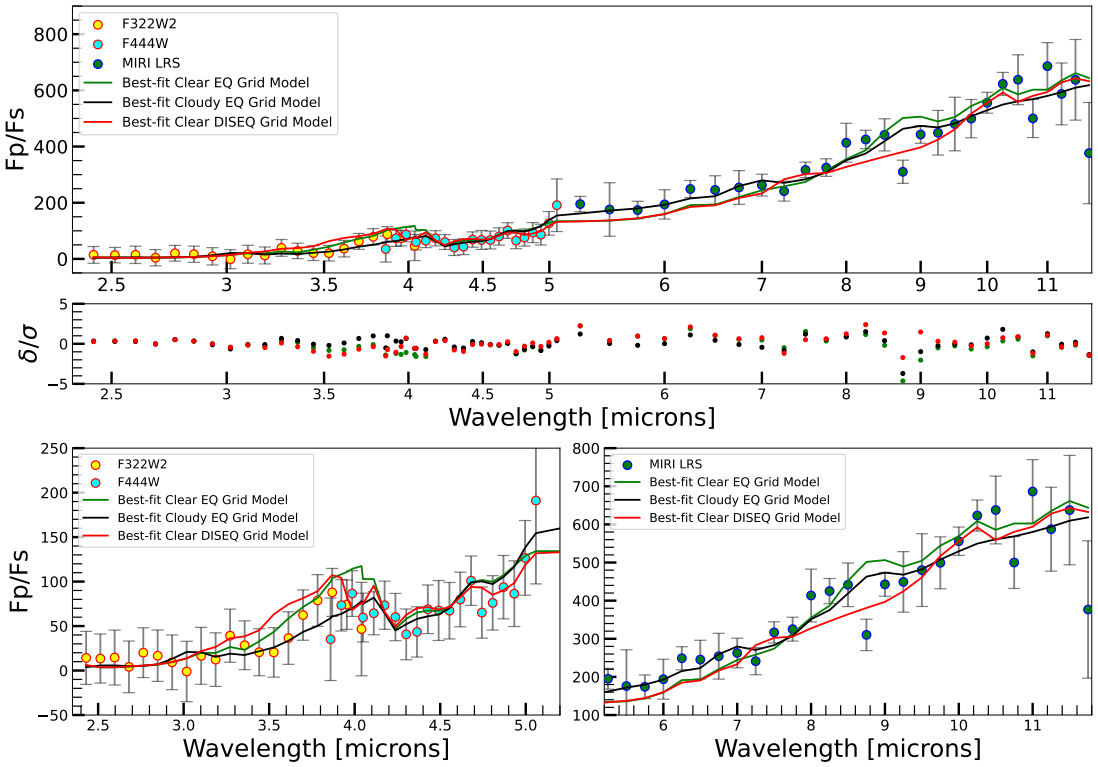

Figure 7.4: The **top panel** shows the comparison of the best-fit clear equilibrium chemistry grid model (green line), clear disequilibrium chemistry grid model (red line), and cloudy equilibrium chemistry grid model (black line) with the *JWST* spectrum of GJ 436b. The **middle panel** shows the residuals of the model fits divided by the errors in the data. Similar to Figure 7.2, the **bottom left** and **bottom right** panels show a zoomed in version of the top panel with comparison of the best-fit grid models with parts of the spectrum observed with NIRCam and MIRI, respectively. The clear and cloudy equilibrium chemistry models are consistent with very elevated metallicities ($\geq$500$\times$solar and $\geq$300$\times$solar at 1σ, respectively), whereas the disequilibrium chemistry models are consistent with metallicities higher than 80$\times$solar.

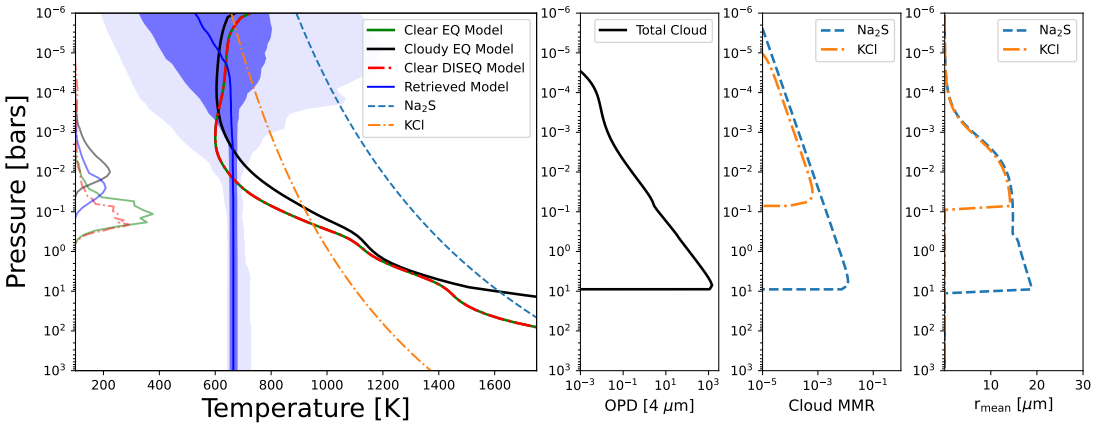

Figure 7.5: The **left most panel** shows the $T(P)$ profile obtained from the clear free chemistry retrieval with the solid blue line along with the 1σ and 2σ envelopes on the $T(P)$ profile. The $T(P)$ profiles of the best-fit model from the clear equilibrium chemistry grid is shown with the green solid line. The $T(P)$ profile from the cloudy equilibrium chemistry grid and clear disequilibrium chemistry grid are also shown with black solid and red dot-dashed lines, respectively. The thermal contribution function from each of these models at 4 μm are also shown on the left side of the panel. The **second column** shows the cloud optical depth per atmospheric layer as a function of pressure at 4 μm for the best-fit cloudy equilibrium chemistry model. The **third column** shows the cloud mass mixing ratio as a function of pressure for the KCl and Na_2S cloud included in the cloudy best-fit model. The **forth column** shows the mean cloud particle sizes in the best-fit model as a function of pressure for KCl and Na_2S.

as condensible species for the planet's atmosphere (Morley et al. 2012). The `virga` cloud model has two physical cloud parameters – the sedimentation efficieny () and the vertical eddy diffusion coefficient (K_{zz}). The parameter is the ratio between the velocity of falling cloud particles and the convective velocity. A lower value, as a result, corresponds to clouds which are more extended in the vertical direction. K_{zz} is the vertical eddy diffusion parameter and is responsible for transporting condensible vapor in the vertical direction and keeping cloud particles aloft. The K_{zz} parameter affects both the vertical cloud structure as well as the cloud particle size distribution. A higher value of K_{zz} can keep bigger cloud particles lofted in the atmosphere (Ackerman & Marley 2001b). We generate a cloudy grid of models by varying both the and the K_{zz} parameter. The is varied between 0.5 and 8, whereas the K_{zz} is varied between 10^9 and 10^{12} cm^2s^{-1}. Note that this cloudy grid of models is not fully self-consistent (i.e., not in radiative–convective equilibrium). We have post-processed our clear atmospheric model grid with clouds instead.

We fit the observed spectrum with this cloudy model grid following the same χ^2 based methodology as outlined in §7.4.2.1. Figure 7.4 shows the best-fit cloudy model spectrum with the black line in the top panel. Comparison of this model spectrum with just the NIRCam and the MIRI data are also shown in the bottom left and right panels of Figure 7.4, respectively. The best-fit cloudy model has a reduced-χ^2 value of 0.64, which is significantly lower than the best-fit clear grid model. Figure 7.16 middle panel shows the corner-plot obtained from fitting the data with the cloudy grid. The best-fit model has a slightly lower metallicity of [M/H]=+2.9 and relatively

higher C/O=1.0×solar than the clear RCTE grid. However, the probability distribution suggests a smaller lower limit on metallicity ([M/H]≥+2.5 at 1σ and [M/H]≥+2.1 at 2σ). The heat recirculation parameter is constrained to be higher with this cloudy grid with `rfacv`=0.7. The additional cloud opacity in these models can absorb significant outgoing infrared flux, thus allowing the day-side of the planet to be hotter than the best-fit clear atmospheric models. The best-fit model has =0.5 and $\log_{10}K_{zz}$=9. This suggests a preference for a vertically extended cloud with moderately sized particles.

Figure 7.5 left most panel shows a comparison between the retrieved $T(P)$ profile from the clear free chemistry retrieval (§7.4.1.1) with the $T(P)$ profile from the best-fit clear equilibrium chemistry atmospheric model (green line), best-fit clear disequilibrium chemistry atmospheric model (dot-dashed red line), and the best-fit cloudy equilibrium chemistry atmospheric model (black line). The condensation curves for KCl and Na_2S are also shown as dotted lines. The thermal contribution function at 4 μm is also shown in the left axis of this panel as a function of pressure for each $T(P)$ profile. The contribution from the cloudy best-fit model comes from the smallest pressures ($\sim$ 0.01 bars) due to the presence of optically thick clouds in the atmosphere. The thermal contribution from the retrieved model with the highest likelihood peaks at around 0.03 bars and the contribution from both the cloud-free grid models peak between 0.1 to 0.3 bars. The three right panels in Figure 7.5 show the cloud properties of the best-fit cloud model. The second column shows the total cloud layer-by-layer optical depth at 4 μm. The base-pressure of the cloud deck is at around $\sim$ 10 bars. The third column shows the cloud mass-mixing ratio (MMR) as a function of pressure for Na_2S and KCl.

The Na_2S cloud base is at a deeper pressure than the KCl cloud deck by a factor of 100. The fourth column shows the mean particle radius of the cloud particles for each condensate as a function of pressure. The particles typically have a mean size between $\sim$ 10-20 μm both for Na_2S and the KCl clouds. We show the effect of cloud and other gaseous absorbers on the best-fit model spectrum in §7.7.10 (Figure 7.17).

7.5 Discussion

7.5.1 From *Spitzer* to *JWST*

The *Spitzer* photometry is clearly discrepant with the *JWST* data, especially in the 3.6 μm region as shown in Figure 7.1. The *Spitzer* photometry has been used over the years to argue that the $T_{\rm int}$ of the planet is considerably higher than predicted by evolutionary models (e.g., Morley et al. 2017a; Madhusudhan & Seager 2011). This has been attributed to tidal heating of the planet owing to its non-zero eccentricity. The *Spitzer* photometry has also led to the conclusion that the planet is very rich in metals, irrespective of whether equilibrium or disequilibrium chemistry is assumed when modeling the data (e.g., Morley et al. 2017a). In this work, we show that our *JWST* observations agree with such high metallicities when equilibrium chemistry is assumed when modeling the *JWST* data with clear or cloudy models. However, if we consider disequilibrium chemistry due to quenching and photochemistry, then the metallicity of the planet derived from the *JWST* data is consistent with [M/H]$\geq$+1.9 at 1σ level and [M/H]$\geq$+1.5 at 2σ level.

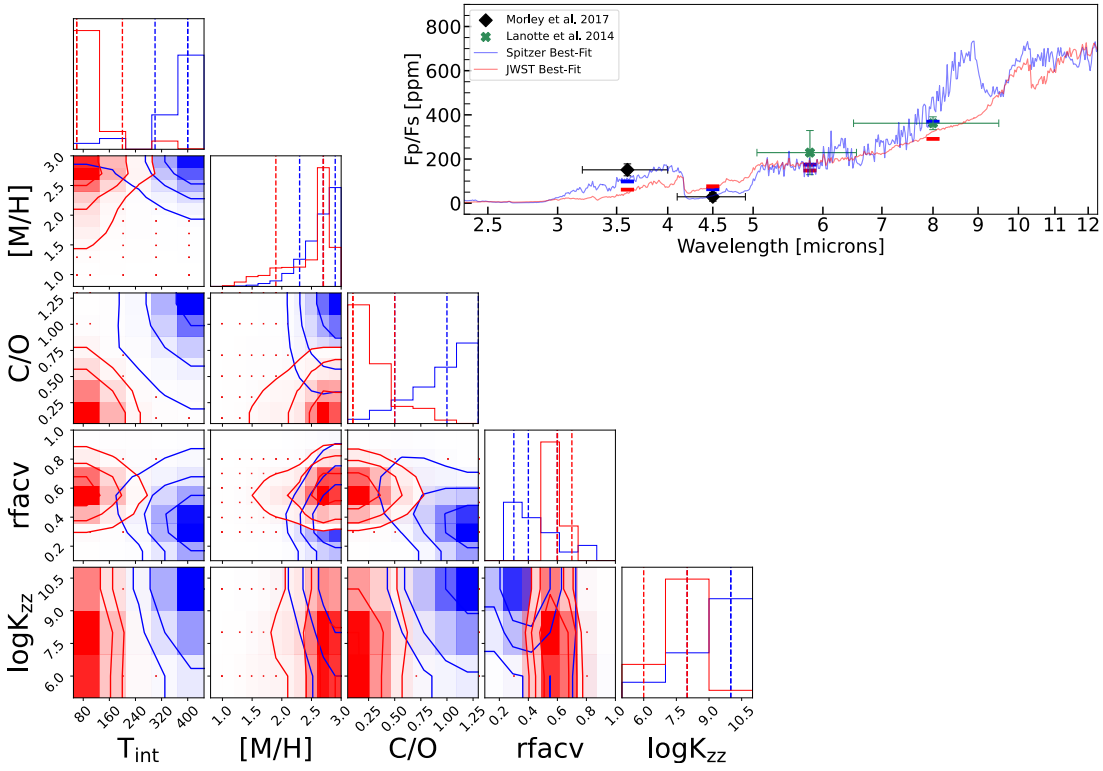

Figure 7.6: The **left panel** shows the corner plot obtained by fitting the *Spitzer* photometry of GJ 436b from Morley et al. (2017a) and Lanotte et al. (2014) with our clear disequilibrium chemistry model grid in blue. The corner plot obtained by fitting the *JWST* data with the same grid has been overplotted in red. The **right panel** compares the *Spitzer* photometry with the best-fit disequilibrium chemistry model in blue and the best-fit model to the *JWST* data in red. The model photometry derived from each model has been shown with blue and red dashes as well. Note that the C/O plotted here is relative to the solar value, where the assumed solar value is 0.458.

In order to asses how the conclusions about the planet have changed from the *Spitzer* photometry to the *JWST* observations, we model both the datasets using our clear disequilibrium chemistry model grid. Figure 7.6 shows a direct comparison between the constraints on the planet parameters obtained from fitting the *Spitzer* observations (from Morley et al. (2017a) and Lanotte et al. (2014)) and those obtained from fitting our new *JWST* observations using our clear disequilibrium chemistry grid. The top right panel shows the *Spitzer* photometry along with the best-fit spectrum to the *Spitzer* data in blue, while the best-fit model to the *JWST* data is shown in red. The corner plot in Figure 7.6 shows the constraints obtained from the *Spitzer* data in blue and the constraints obtained from fitting the *JWST* data in red.

It is clear that constraints obtained by fitting the *Spitzer* data with our disequilibrium chemistry models are consistent with the analysis of Morley et al. (2017a). However, our new *JWST* spectrum prefers a much lower $T_{\rm int}$ value ($\sim$ 60 K) than the archival *Spitzer* data ($T_{\rm int} \geq$ 300 K). The *JWST* data also allows for slightly lower metallicities than the *Spitzer* data. The main reason behind both of these differences is the lower flux around the *Spitzer* 3.6 μm band in the *JWST* data compared to the *Spitzer* data. This low flux in the *JWST* data allows for a colder deeper atmosphere and much more absorption from CH_4 and H_2O in the spectrum compared to the model fits to the *Spitzer* photometry, allowing for a lower $T_{\rm int}$. The *Spitzer* data also shows preference for higher C/O ratios, while the *JWST* data prefers lower C/O ratio values. We further show a direct comparison of the *JWST* lightcurves with previous Spitzer eclipse depth findings in Section 7.7.7.

As a part of our analysis, we also refit the Morley et al. (2017a) Spitzer 3.6 μm eclipse lightcurve - along with two unpublished 3.6 μm eclipses observed as a part of a longer phase curve observation taken in 2018 (PI V. Parmentier, PID 13234). We fit all three eclipse lightcurves using the BLISS-mapping technique following Beatty et al. (2019a). We describe our reduction process in more detail in Section 7.7.7. For consistency with the rest of our analysis, in fitting both the published Morley et al. (2017a) eclipse data and the unpublished eclipse data, we used the system and orbital parameters measured for GJ 436b using the NIRCam data that are listed in Table 2.

Our reanalysis of the Morley et al. (2017a) 3.6 μm eclipse data yields effectively the same eclipse depth: 196 ± 32 ppm in our fitting vs. a depth of 177 ± 31 ppm measured in Morley et al. (2017a). The two unpublished 3.6 μm eclipses, however, show much smaller depths, at -15 ± 69 ppm and 94 ± 65 ppm. We jointly fit both of the unpublished 3.6 μm eclipses using the same eclipse depth for both events, and measured a joint depth of 46 ± 43 ppm. This latter jointly-fit eclipse depth is consistent with the NIRCam eclipse observations and $2.8\,\sigma$ lower than the Morley et al. (2017a) value.

It is likely that the difference in the 3.6 μm eclipse depths between the Morley et al. (2017a) observations and the 2018 phase curve observations is caused by differences in Spitzer's pointing while taking the lightcurves. The image of GJ 436 landed within 0.3 pixels of the IRAC1 sensitivity "sweet spot" during the two phase curve eclipse observations, but GJ 436 was 0.6 pixels away from the "sweet spot" during the earlier Morley et al. (2017a) observations. The Morley et al. (2017a) observations were taken before the implementation of the PCRS Peak-up mode to improve Spitzer's target

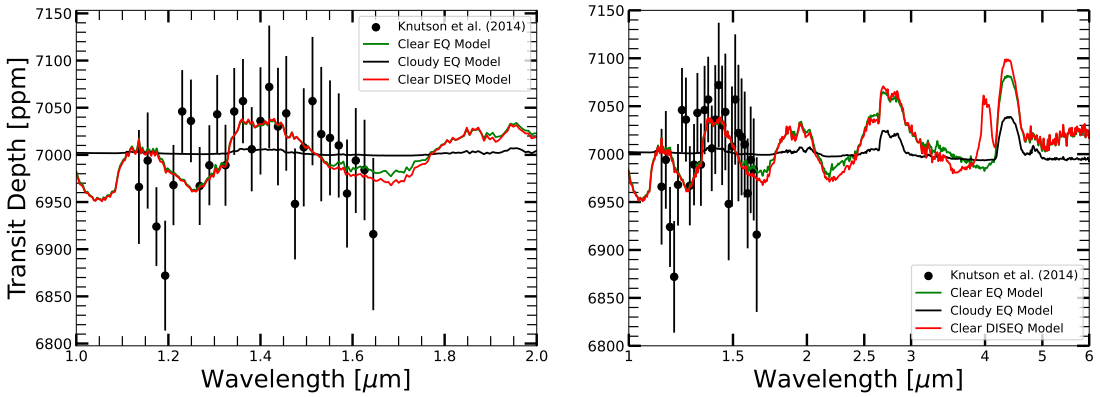

Figure 7.7: Comparison of the transmission spectrum computed from the various best-fit self-consistent models from this work with the HST/WFC3 transmission spectrum observations of GJ 436b. Green and black lines shows the clear and cloudy equilibrium chemistry models, respectively. The red line shows the best-fit clear disequilibrium chemistry model.

acquisition and pointing, which likely accounts for the relatively poor placement of the star in those images. Other repeat observations of exoplanet lightcurves have shown that Spitzer data taken comparably far from the "sweet spot" are not reliable (e.g., Murphy et al. 2023). Thus we consider the lower 3.6 μm eclipse depth of 46 ± 43 ppm measured from jointly fitting the phase curve data to be more likely correct.

7.5.2 Transmission Spectrum of GJ 436b

We also compare the best-fit self-consistent models obtained by analyzing the *JWST* eclipse spectra with the transmission spectra of GJ 436b observed with *HST*/WFC3 by Knutson et al. (2014a). The spectrum was found to be featureless in this wavelength range, which ruled out cloud-free metal-poor atmospheres for GJ 436b. Figure 7.7 shows a comparison of the observed transmission spectra with the best-

fit models from the three flavors of self-consistent models used to analyze the *JWST* eclipse spectrum in this work. The green-line represents the best-fit clear equilibrium chemistry model, which has a metallicity of ∼500×solar. The black line shows the transmission spectrum calculated from the cloudy equilibrium chemistry model, which is also significantly metal-enriched ([M/H]=+2.9 or metallicity= 800×solar) but the cloud deck mutes the features in the transmission spectrum. The red line shows the best-fit clear disequilibrium chemistry model with a metallicity of [M/H]=+2.7 or metallicity= 500×solar. The left panel of Figure 7.7 shows that all the three best-fitting models to the *JWST* emission spectrum also fit the *HST*/WFC3 transmission spectrum well. The right panel of Figure 7.7 shows each of these models and how their transmission spectra differ from each other at longer wavelengths. This shows that future *JWST* transmission spectroscopy observations of the planet at these longer wavelengths are crucial to constrain the metallicity of the planet accurately.

The transmission spectrum of GJ 436b has been observed at high spectral resolution using the CRIRES+ instrument on *VLT* by Grasser et al. (2024). Like the *HST*/WFC3 observations, these CRIRES+ observations also could not detect molecular features from the transmission spectrum. However, these observations were used to rule out metallicities $\leq$ 300×solar and cloud top pressures deeper than 10^{-2} bars. These constraints are consistent with the best-fit cloudy equilibrium chemistry model from the *JWST* eclipse spectrum. The metallicity constraints from the high-resolution observations are also consistent with the metallicity constraints from the clear equilibrium chemistry model and the clear disequilibrium model grids.

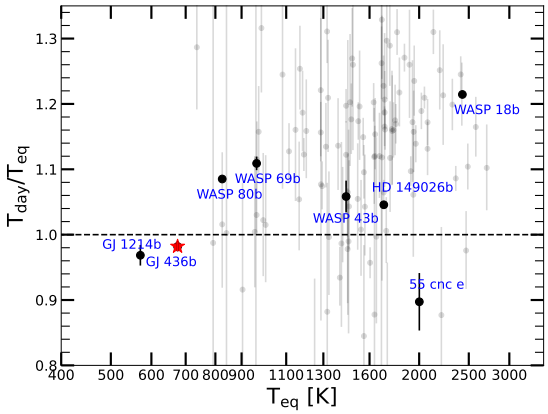

Figure 7.8: The ratio of planets' derived day-side effective/average brightness temperatures and equilibrium temperatures from their *JWST* emission spectroscopy or phase-curve measurements as a function of their equilibrium temperatures is shown. GJ 436b and GJ 1214b are the only two non-terrestrial planets where this ratio is less than or similar to 1. The faded black points show the ratio for the sample of planets presented in Deming et al. (2023). These ratios are computed using the brightness temperature derived from their *Spitzer* 3.6 μm flux in Deming et al. (2023).

7.5.3 Day-side vs. Equilibrium Temperature

Our isothermal retrieval (§7.4.1.2) constrains the day-side blackbody temperature of GJ 436b to be 662.8±5 K. Figure 7.3 shows that this measurement alone cannot break the degeneracy between the Bond albedo (A_B) and the heat-recirculation efficiency factor (ϵ). Our self-consistent modeling analysis of GJ 436b's spectrum shows that the cloudy atmospheric model and the clear disequilibrium chemistry model have the smallest reduced-χ^2 values 0.64 and 0.78, respectively. We compare our constraints on the day-side temperature of GJ 436b with constraints on the day-side effective temperature/average brightness temperature obtained for other exoplanets with *JWST* emission or phase-curve observations (Kempton et al. 2023; Schlawin et al. 2024b; Coulombe et al. 2023; Bell et al. 2024a; Bean et al. 2023; Hu et al. 2024b, Wiser et

al. (private communication)). Figure 7.8 shows this comparison as a function of planet $T_{\rm eq}$ for planets with published *JWST* constraints. 55 Cancri e is the only terrestrial planet in this Figure with constraints from *JWST*. The constraints on the brightness temperature derived from *Spitzer* 3.6 μm observations of planets (Deming et al. 2023) is also shown in Figure 7.8 with faint black points. GJ 1214b and GJ 436b are the only two (non-terrestrial) planets with *JWST* constraints in this Figure that have $T_{\rm day} \leq T_{\rm eq}$. Hotter giant planets with *JWST* observations show hotter dayside temperatures than their $T_{\rm eq}$. Figure 7.8 and Deming et al. (2023) show that this trend holds for the 3.6 μm brightness temperature constraints obtained from *Spitzer* for most planet targets as well. The *JWST* phase curve observations of GJ 1214b were best explained with a high mean molecular weight (or high metallicity) and high albedo atmosphere (Kempton et al. 2023). Our best-fit cloudy model has a Bond albedo of 0.075. Therefore, future phase-curve observations of GJ 436b would be very useful in deciphering why the day-side of GJ 436b appears not to be warmer than it's $T_{\rm eq}$, which is typically not the case for the other hotter giant planets shown in Figure 7.8.

7.6 Conclusions

We present the panchromatic *JWST* emission spectrum of GJ 436b in this work. Multiple eclipses of the planet were observed at wavelengths spanning 2.4–11.9 μm with the *JWST* NIRCam and MIRI LRS instrument modes. We summarize the major findings from this work here:

1. The *JWST* eclipse depths are significantly inconsistent with the latest published *Spitzer* photometric eclipse depths in the 3.6 μm filter. The *JWST* data show less flux from the planet compared to the *Spitzer* observations at these wavelengths. The 4.5 μm band *Spitzer* also shows inconsistency with the *JWST* spectrum, albeit at a much smaller significance.

2. We performed a Bayesian free chemistry retrieval with 17 free parameters on the *JWST* panchromatic spectrum of GJ 436b. We find weak evidence for the presence of a CO_2 absorption feature in the spectrum, at a 2σ significance level. The 1σ constraint on the CO_2 abundance is $\log(CO_2) = -3.23^{+1.66}_{-3.30}$. However, the posteriors of all the 11 gases included in the retrieval are consistent with the lower limit of the applied prior (i.e., log(VMR)=-15.0) at the 3σ significance level.

3. We constrain the day-side temperature of the planet using an isothermal/blackbody retrieval on the *JWST* spectrum. We find that the spectrum is consistent with $T_{\rm day} = 662.8^{+5.0}_{-4.8}$ K, which is comparable to the zero-albedo equilibrium temperature (675 K). We use this measurement of the day-side temperature to explore the Bond albedo (A_B) and day-to-night heat recirculation efficiency (ϵ) parameter space. We find that this measurement cannot break the degeneracy between these two parameters, but we place a 3σ upper limit on the Bond albedo at $A_B \leq 0.66$.

4. We used a cloud-free self-consistent RCTE model grid, computed with the `PICASO` climate model, to fit the *JWST* spectrum of GJ 436b. We find that the best-fit model from this grid has a reduced-χ^2=1.04. The best-fit model has an extremely

metal-rich atmosphere with a metallicity$\geq$500$\times$solar (at 1σ level) and a sub-solar C/O. The best-fit heat-recirculation parameter (`rfacv`) is 0.6, which represents nearly full day-to-night side heat redistribution.

5. We also use a clear disequilibrium chemistry model grid to fit the data, which includes effects like quenching due to vertical mixing and photochemistry. The best-fit model from this grid has a reduced-χ^2=0.78. In contrast with the clear RCTE grid, this grid constrains a lower metallicity lower limit (1σ limit at metallicity$\geq$80$\times$solar). The C/O is found to be sub-solar (0.0458) with this grid. This grid prefers a low $T_{\rm int}$ value ($T_{\rm int}\sim$60 K), which is consistent with expectations from evolutionary models for the planet in the absence of tidal heating of its interior (Fortney et al. 2020).

6. We also use the `VIRGA` cloud model to post-process the `PICASO` equilibrium chemistry models with KCl and Na_2S clouds. The best-fit model from this grid has a reduced-χ^2=0.64. We find that the metallicity is constrained to be metallicity$\geq$300$\times$solar (1σ limit) with this cloudy model grid. This grid also prefers a sub-solar C/O for the planet. The best-fit `rfacv` parameter was found to be 0.7, which is higher than the constraints of the two types of clear atmospheric models used in this work.

7. We re-fit the *Spitzer* photometric observations of GJ 436b with our clear disequilibrium chemistry grid and find that the *JWST* data prefers a much cooler $T_{\rm int}$ and are consistent with lower metallicities than the *Spitzer* photometric data. We

also show that all the best-fit models from our grid are broadly consistent with the *HST*/WFC3 transmission spectrum of the planet.

8. The position of GJ 436b is in the same region of $T_{\rm eq}$ and $\rm T_{day}/T_{eq}$ space (see Figure 7.8) as the cloud-enshrouded planet GJ 1214b (Gao et al. 2023; Kempton et al. 2023; Schlawin et al. 2024c; Ohno et al. 2024). This, along with the non-detection of absorption features in transmission at high spectral resolution (Grasser et al. 2024) and low resolution (Lothringer et al. 2018; Knutson et al. 2014a), is suggestive of a metal-rich opaque cloud-dominated atmosphere that strongly impacts the planet's emission and transmission spectrum. However, additional observations will be required to confirm this suggestion.

7.7 Appendix

7.7.1 Observing Details

We observed GJ 436b for 8 separate eclipses using both the NIRCam and MIRI instruments. A summary of the observing specifications is listed in Table 7.1. The default field points for NIRCam do not include any sky background regions on the leftmost amplifier for the F322W2 filter nor the right amplifier for the F444W filter. We experimented with offsetting the field point by +9.2 arcseconds for the NIRCam F322W2 filter and −5.3 arcseconds for the F444W filter so that more sky background was available for 1/f subtractions on both sides of the source. We found that this did decrease the 1/f noise scatter between integrations. However, this did not mitigate the

significant time-correlated noise present in the NIRCam lightcurves (which dominate the error budget), so the overall eclipse depths were no better constrained with these pointing offsets.

Date (UT)	Program	Obs #	Description	Wave Range	Nint	Ngroup	Readout Pattern	x offset	Duration
YYYY-mm-dd				μm				arcsec	(hr)
2023-01-16	1185	10	F322W2	2.4 - 4.01	7215	3	BRIGHT2	0.0	4.79
2023-04-21	1185	12	F322W2	2.4 - 4.01	7136	3	BRIGHT2	9.2	4.74
2023-12-21	1185	14	F322W2	2.4 - 4.01	7136	3	BRIGHT2	9.2	4.74
2023-01-11	1185	11	F444W	3.88 - 4.98	4597	5	BRIGHT2	0.0	4.79
2022-12-31	1185	13	F444W	3.88 - 4.98	4597	5	BRIGHT2	0.0	4.79
2023-12-07	1185	15	F444W	3.88 - 4.98	4549	5	BRIGHT2	-5.3	4.79
2023-05-26	1177	4	LRS	5.3 - 12	18075	5	FASTR1	0.0	4.79
2023-12-02	1177	5	LRS	5.3 - 12	18075	5	FASTR1	0.0	4.79

Table 7.1: Summary of GJ 436b observations

7.7.2 Orbital Parameters from Broadband Fits

We derive orbital parameters from joint fitting with JWST MIRI and list the posterior values in Table 7.2.

7.7.3 NIRCam De-Trending Models

In our `tshirt` reduction of the NIRCam eclipses, we included 3 components to systematically de-trend the lightcurves: FPAH, reference pixels and a Gaussian process. In the F322W2 lightcurves, the systematic noise dominates over the eclipse depth. Figure 7.9 shows example lightcurves for Observation 1185-14 (F322W2) and Observation 1185-15 (F444W). The long downward trend over the duration of the exposure tracks

Parameter	Value	Unit	Source
Planet-to-Star Radius Ratio, Rp/R*	0.082577 ± 0.00017		Bourrier et al. 2018
Semi-major axis to Stellar Radius Ratio, a/R*	14.60 ± 0.10		MIRI Broadband fit
Inclination, i	86.87 ± 0.04	deg	MIRI Broadband fit
Time of transit center, t_0	2454873.015821 ± 0.000041	d (BJD_{TDB})	MIRI Broadband fit
Time of eclipse center, t_s	2454874.56934 ± 0.00026	d (BJD_{TDB})	MIRI Broadband fit
Local time of transit center, $t_{0,local}$	2460279.78627 ± 0.00024	d (BJD_{TDB})	MIRI Broadband fit
Local time of eclipse center, $t_{s,local}$	2460281.33978 ± 0.00012	d (BJD_{TDB})	MIRI Broadband fit
Orbital Period, P	2.643897528 ± 1.2×10^{-7}	days	MIRI Broadband fit
Orbital Eccentricity, e	0.1634 ± 0.0027		MIRI Broadband fit
Argument of Pericenter, ω	327.31 ± 1.54	deg	MIRI Broadband fit
Orbital Phase of Mid-eclipse	0.58759 ± 0.00010		MIRI Broadband fit

Table 7.2: Summary of GJ 436b Orbital Parameters

with the FPAH, whereas the short timescale behavior correlates with the reference pixel time series (indicating the overall detector bias).

7.7.4 Experiments with Moving the Field Point to Reduce 1/f Noise

1/f noise can be a significant contribution to the broadband lightcurve noise for NIRCam, especially on bright targets. Some of the 1/f noise can be mitigated by row-by-row subtraction of sky background pixels surrounding a source, especially if those sky pixels are located in the same amplifier as the source enabling common-mode P-type semi-conductor Field Effect Transistor (PFET) noise subtraction (Schlawin et al. 2020). The default field points for the NIRCam grism time series cover more than 3 of the detector amplifiers for the F322W2 filter and 2.5 of the detector amplifiers for the F444W filter. As listed in Table 7.1, we experimented with Special Requirement offsets

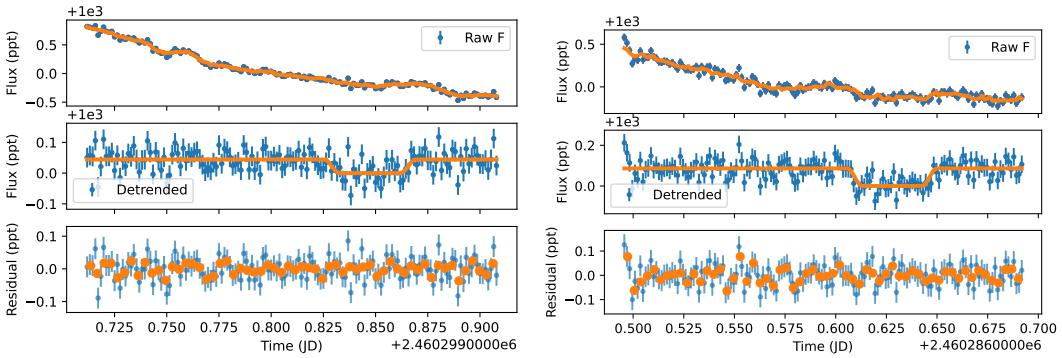

Figure 7.9: *Top:* Example broadband NIRCam lightcurves for observation 1185-14 (F322W2, top left) and Observation 1185-15, (F444W, top right) before and after de-trending, as well as the residuals. In each time panel section, the data are plotted as blue points with error, and the model curve is plotted as an orange line for the raw lightcurve (top) and the de-trended lightcurve (middle). The bottom panel section shows the residuals and a set of 60 equally-spaced time-bins (4.8 minutes apart). *Bottom:* Broadband MIRI LRS lightcurve for Observation 1177-5.

in the detector X direction (observatory V2 axis) to spread sky pixels on either side of the target spectrum for use in 1/f noise subtraction. We found that re-positioning the source did enable subtraction using the first and fourth amplifiers and reduced the noise, more noticeably for the F322W2 filter: 341 ppm for observation 10 before the shift and 215 ppm for observation 12 after the shift, However, the overall benefit of moving the source spectrum was not clear because the large systematic trends, such as in Figure 7.9, were still present and after time-binning, the noise difference was no longer significant as it becomes systematics-dominated.

7.7.5 Comparison Across Separate Eclipses

In our `tshirt` analyses, we found that with our systematic model of NIRCam fluxes (included a Gaussian process for correlated noise), that the individual spectra are

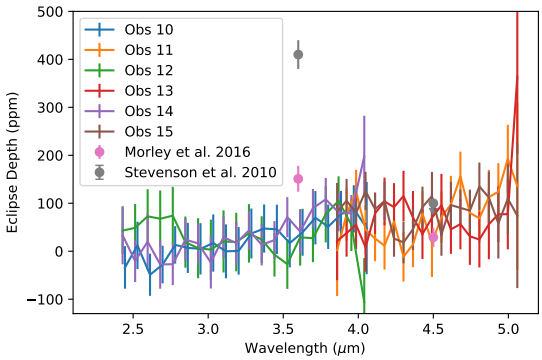

Figure 7.10: Individual eclipse observations with NIRCam as reduced by `tshirt`. The errors, inflated by the Gaussian process fit, give largely consistent spectra.

consistent within errors. We note that the systematic noise modeling resulted in error bars significantly above expectations from photon and read noise. Figure 7.10 shows the individual eclipses of GJ 436b for the `tshirt` reduction for NIRCam.

7.7.6 Correlated Noise in Eclipse Observations

As visible in Figure 7.9, there are significant correlations visible with timescales of ∼0.02 days (i.e., 30 minutes) in the broadband lightcurves, most noticeably in the NIRCam lightcurves where the broadband eclipse depths are less than 100 ppm. As discussed in Section 7.3, we account for correlated noise by fitting lightcurves with a Gaussian Process regression to account for this correlated noise. We also calculate and plot the Allan Variance plots for all broadband lightcurves with the `tshirt` code to illustrate the correlated noise. Figure 7.11 shows the Allan variance curves compared to a $1/\sqrt{N}$ scaling for independent (ie. uncorrelated noise). When using a Gaussian process, the lightcurve residuals generally follow a $1/\sqrt{N}$ law. However, if we remove

the Gaussian Process component, it is clear that correlated noise creates a noise floor in NIRCam with an amplitude of 50-90 ppm. The timescale is also relevant for transits and eclipses because the noise floor enters around the 5-20 minute timescale, which approaches a significant fraction of the 1.02 hour eclipse duration of GJ 436 b. We therefore find it critical to apply a Gaussian Process as part of the lightcurve fitting to assess the impact of correlated noise on the spectrum. Other similarly bright target stars observed with NIRCam that push close to the saturation limit may need to account for correlated noise in a similar manner. We also analyze the residuals of the lightcurves with Lomb Scargle periodograms, as shown in Figure 7.12. While no sharp perdiodic signals appear in the data, there are sometimes excess noise near 80 minutes and 130 minutes, when considering the lightcurve residuals before the GP de-correlations are applied. Further analysis of NIRCam correlated noise will be explored in a future work (Schlawin et al., in prep).

7.7.7 Comparison with Previous Spitzer Observations

To further investigate the disagreement between our NIRCam emission spectrum and previous Spitzer 3.6 μm IRAC photometry (Stevenson et al. 2010; Morley et al. 2017a), we calculated lightcurves from the spectroscopic data that were integrated approximately over the same wavelengths as the Spitzer photometry. We calculated these integrated bandpass photometry from the NIRCam F322W2 and F444W data of Spitzer 3.6 μm and Spitzer 4.5 μm bandpasses, respectively. We calculate approximate photometry with square bandpasses centered on 3.551 and 4.495 μm with widths of 0.75 μm

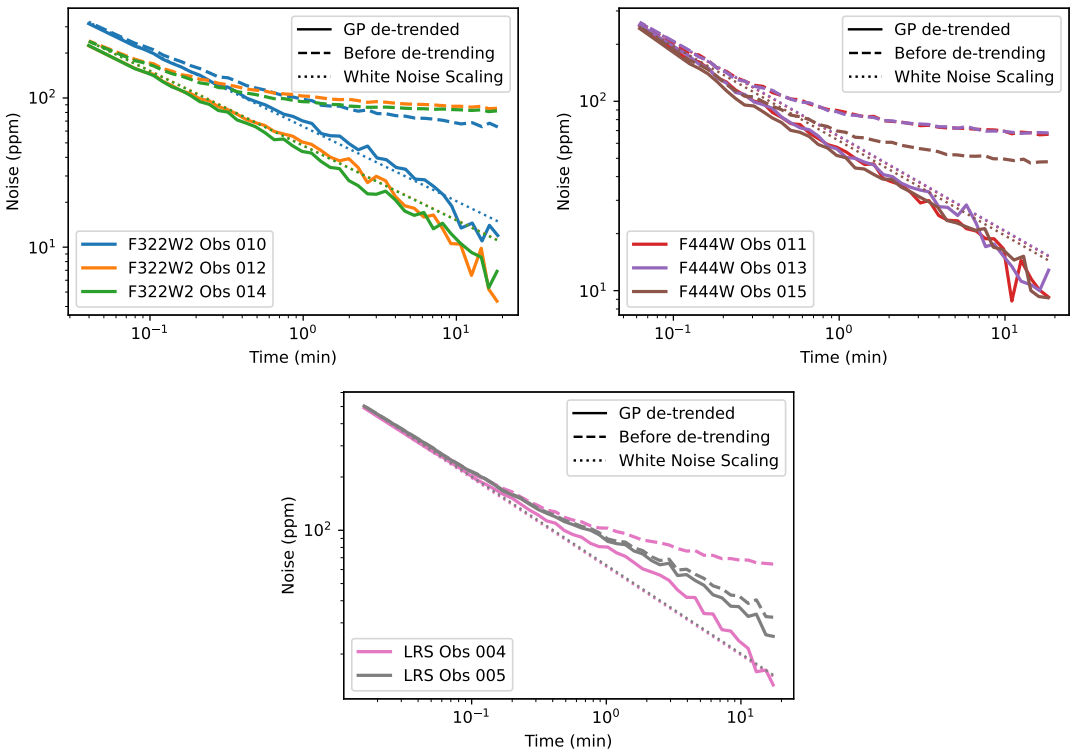

Figure 7.11: Allan Variance Plots of the broadband lightcurves of the 8 observations analyzed by the `tshirt` pipeline (Top Left: F322W2, Top Right: F444W, Bottom: LRS). Significant levels of noise enter at the 100 ppm level, requiring a Gaussian process to mitigate systematics and ensure consistency across independent eclipse observations. The dotted lines ("White Noise Scaling") show the expectation for uncorrelated white noise, which follows $1/\sqrt{N}$ statistics for N data points. The dashed line shows the lightcurve residuals with the Gaussian Process component removed ("Before de-trending"). The solid lines show the lightcurve residuals with the Gaussian Process applied ("GP de-trended").

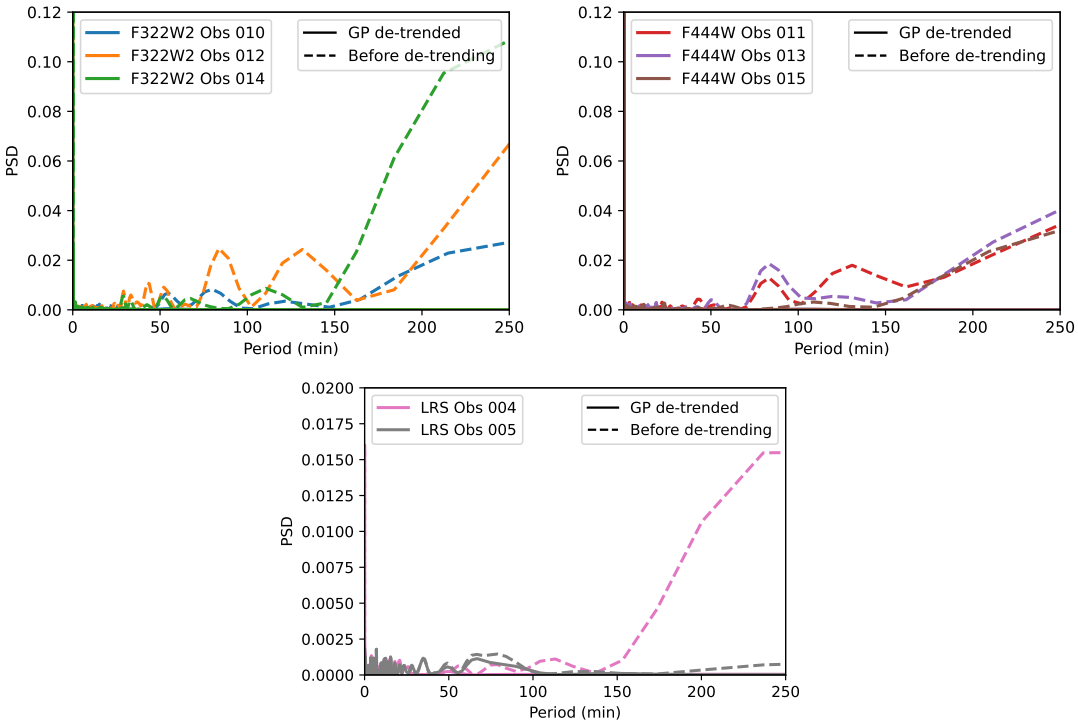

Figure 7.12: Lomb Scargle Periodograms of the broadband lightcurves of the 8 observations analyzed by the `tshirt` pipeline (Top Left: F322W2, Top Right: F444W, Bottom: LRS). There can sometimes be broad periodicities near 80 and 130 minutes, which are mitigated by the Gaussian process. The solid lines show the periodogram of residuals with the Gaussian Process applied ("GP de-trended"). The solid lines show the periodogram of residuals without removing the GP correlated noise ("Before de-trending").

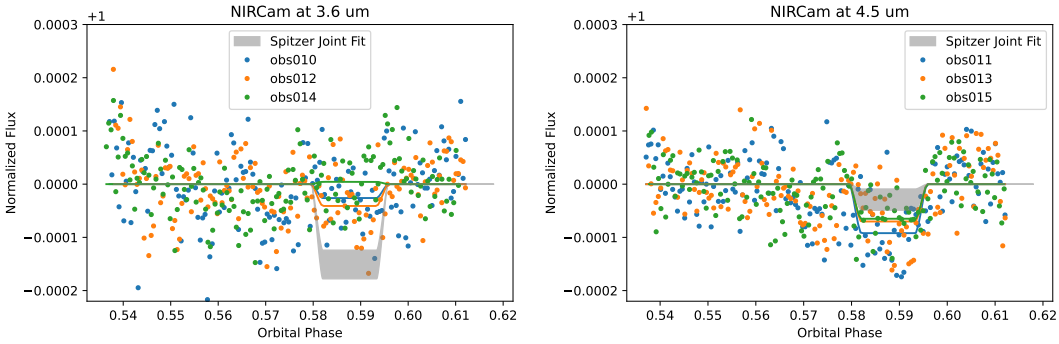

Figure 7.13: We integrated the *JWST* NIRCam bandpass over the same wavelengths as *Spitzer* IRAC1 and IRAC2 bands. The bandpass-integrated photometry for three different eclipses observed with NIRCam F322W2 is considerably shallower than the observed 3.6 μm *Sptizer* photometry (gray posteriors), likely due to uncorrected correlated noise in the *Spitzer* lightcurves. While the *JWST* NIRCam observations contain their own systematics, the modeled eclipses are all in agreement at a much shallower eclipse depth.

and 1.01 μm, respectively. The resulting lightcurves are shown in Figure 7.13 (left) and Figure 7.13 (right). All three synthetic 3.6 μm eclipse observations show significantly shallower eclipses than the reported average Spitzer eclipse depth uncertainty of 151$\pm$27 ppm (Morley et al. 2017a). The 3.6 μm eclipse depths were already revised downward from the first epoch, which was found to be 410$\pm$30 ppm (Stevenson et al. 2010).

To refit the Morley et al. (2017a) 3.6 μm eclipse data and the two unpublished phase curve eclipses, we began our data reduction and photometric extraction process from the basic calibrated data (BCD) images. We first subtracted the background from the images and corrected for bad pixels. We then used the background-subtracted, bad-pixel corrected images to measure the pixel position of GJ 436 in each image using a two-dimensional Gaussian. Note that we used these corrected images only to estimate the background and to measure the position of GJ 436 – we used uncorrected background-

subtracted images for the photometric extraction.

We extracted raw photometry for GJ 436 using a circular extraction aperture centered on the star's position in each image. We used an aperture radius of 2.1 pixels. For reference, the average full-width half-maximum of GJ 436's point spread function was 1.8 pixels. We chose this aperture size by extracting photometry for a range of aperture sizes from 1.8 pixels to 3.0 pixels, fitting the lightcurves, and choosing the aperture that yielded fits with the highest log-likelihoods and the lowest scatter in the residuals. We trimmed the first 5000 data points for each observation to remove residual ramp effects and performed a single round of $5\,\sigma$ clipping to remove outliers.

All three Spitzer lightcurves showed position-dependent flux variations caused by intrapixel effects that are typical for these observations. We used a linear ramp coupled with a Bi-Linear Interpolated Subpixel Sensitivity (BLISS) map (Stevenson et al. 2012) to detrend the Spitzer lightcurves. We used `BATMAN` (Kreidberg 2015a) eclipse models and performed an MCMC fit to the broadband data using the `emcee` (Foreman-Mackey et al. 2013a) Python package. We imposed Gaussian priors on the system and orbital properties of GJ 436b using the values listed in Table 2, and we imposed no prior on the eclipse depth. We also allowed for a background linear slope during the eclipse. We judged the MCMC fitting to have converged by checking the Gelman-Rubin statistic for each parameter was below 1.1, and by visual inspection of the posterior corner plot. We also checked the Gaussianity of the residuals for each of the broadband lightcurve fits using an Anderson-Darling test, and we did not find any significant non-Gaussianity.

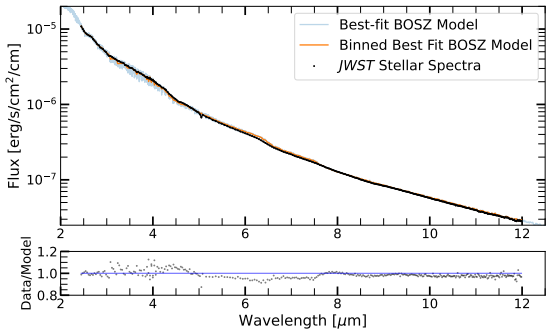

Figure 7.14: Best-fit BOSZ stellar model compared with the flux calibrated stellar spectrum from *JWST* for GJ 436 is shown in the **top panel**. **Bottom panel** shows the ratio between the data and the best-fit model. Deviations of this ratio from 1 indicate missing or additional opacities present in the best-fit model compared to the observed stellar spectrum.

To jointly fit the two phase curve eclipses at the same time we constructed a single, combined, 3.6 μm BLISS map for both eclipses. We then fit the two combined eclipse lightcurves using the same eclipse depth and the same set of planetary parameters - but allowing the linear background trend to differ between the two. This technique has been used previously (Beatty et al. 2019a).

7.7.8 BOSZ model fits to stellar spectrum

Figure 7.14 shows a comparison of the best-fit BOSZ stellar spectrum with the flux calibrated stellar spectrum from our *JWST* observations. The bottom panel of Figure 7.14 shows the ratio between the data and the best-fit model. This ratio deviates from 1 in certain wavelength bands showing missing or required opacities in the best-fit stellar model.

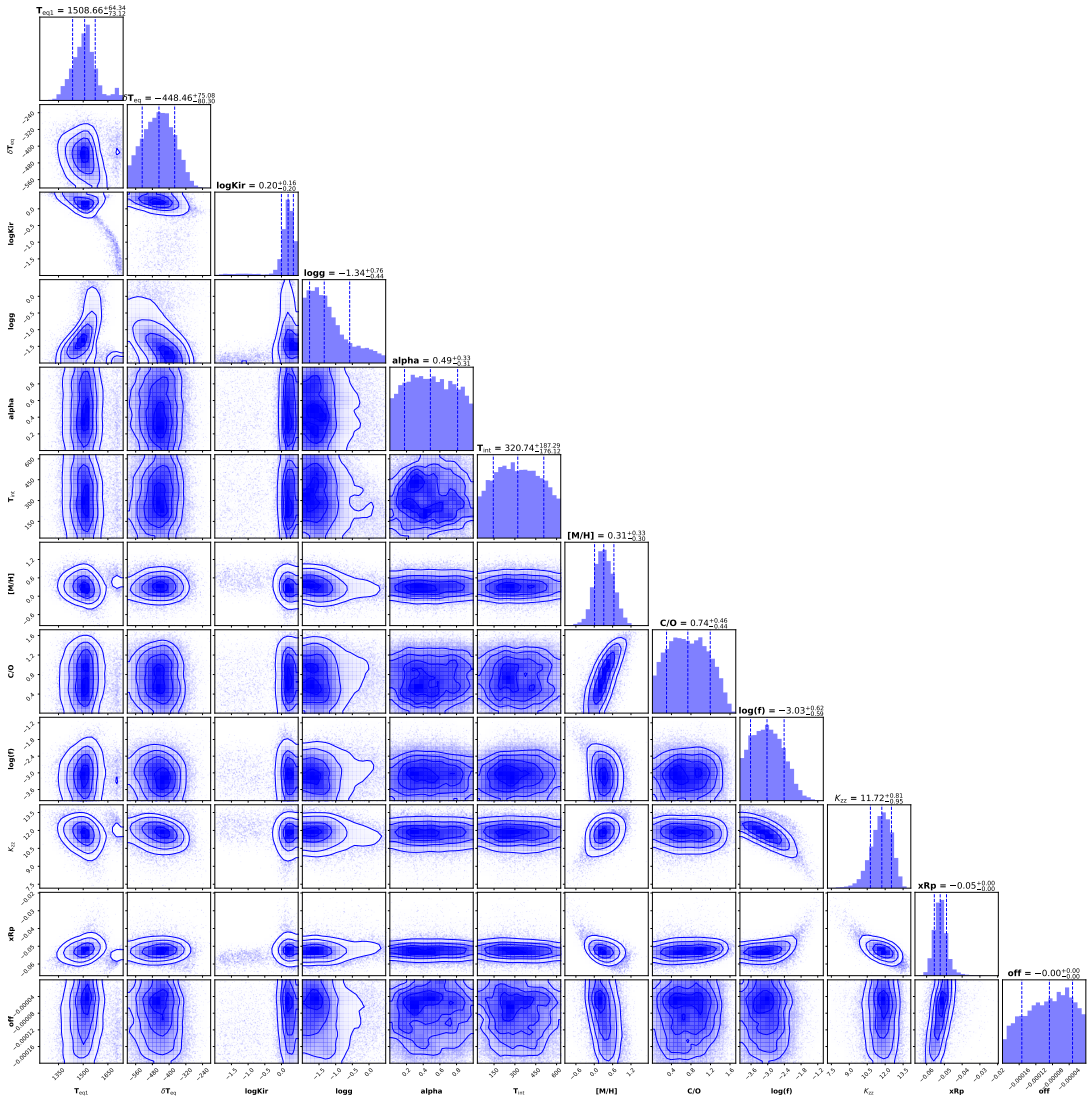

Figure 7.15: The corner plot from the clear free chemistry retrieval on the *JWST* data.

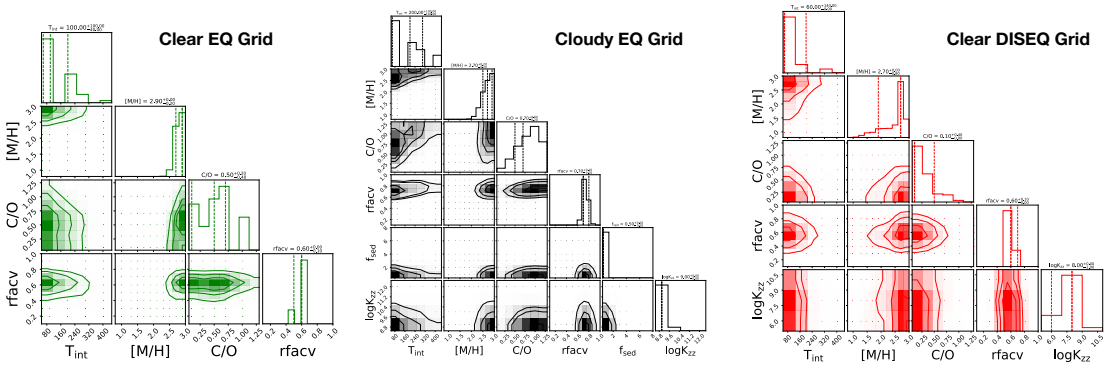

Figure 7.16: The corner plot obtained from the grid fitting exercise from the clear equilibrium chemistry grid is shown in the **left** panel. The corner plot from the cloudy equilibrium chemistry grid and clear disequilibrium chemistry grid are shown in the **middle** and **right** panels, respectively. Note that the C/O shown is relative to the solar value, where the assumed solar C/O is 0.458.

7.7.9 Posterior Distributions from Model Fits

Figure 7.15 shows the corner-plot from the free chemistry retrieval results presented in §7.4.1.1. The corner-plots estimated from the three types of self-consistent model grids presented in §7.4.2 are shown in Figure 7.16. The left, middle, and right panels in Figure 7.16 show the corner-plots obtained from the clear equilibrium chemistry grid, cloudy equilibrium chemistry grid, and clear disequilibrium chemistry grid, respectively. Note that the C/O shown in Figure 7.16 is relative to the solar value, where the assumed solar C/O is 0.458.

7.7.10 Contribution of Absorbers to the Best-fitting Self-consistent Model Spectra

Figure 7.17 shows the contribution of various gases to the best-fitting self-consistent forward models described in §7.4.2. To show how each absorber shapes the

best-fit spectrum, we compare the best-fit model spectrum with the spectrum obtained by removing an absorber from the best-fit model atmosphere. The top panel shows the contributions for the best-fit clear equilibrium chemistry model, where the H_2O, CH_4, and CO_2 are the most prominent absorbers in the spectrum in this model scenario ([M/H]$\sim$+2.7). The middle panel of Figure 7.17 shows the contribution of cloud and gas opacities on the best-fit cloudy equilibrium chemistry model. It is clear that the cloud absorption shapes the best-fit model spectrum to a large extent in this case. CH_4, H_2O, and CO_2 also affect the spectrum, albeit to a much smaller extent compared to the clouds ([M/H]$\sim$+2.9). The bottom panel in Figure 7.17 shows the contribution of various gasses on the best-fit clear disequilibrium chemistry model. In this case, CO_2, SO_2, H_2O, CO, and NH_3 contribute to the best-fit model significantly at different wavelength regions (([M/H]$\sim$+2.7)).

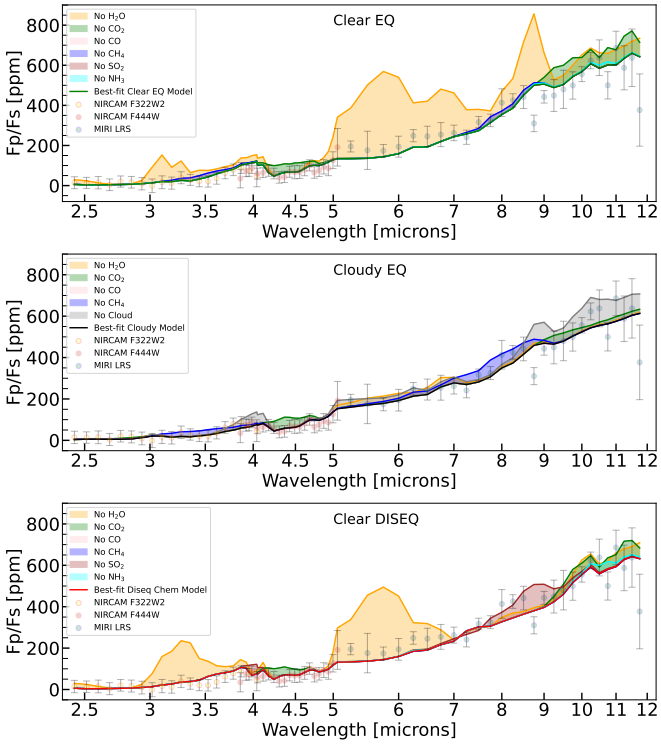

Figure 7.17: The contribution of gases and clouds in shaping the best-fit self-consistent model is shown here for the clear equilibrium chemistry scenario (**top panel**), cloudy equilibrium chemistry scenario (**middle panel**), and clear disequilibrium chemistry scenario (**bottom panel**). The best-fit model in each panel is shown with a solid line – green in the top panel, black in the middle panel, and red in the bottom panel. The contribution of each absorber is shown as the shaded region between the best-fit spectrum and best-fit model without that absorber.

Chapter 8

Cloudy Mornings and Clear Evenings in a Giant Extrasolar World

Aerosols are ubiquitous in the atmospheres of solar system planets (Baines et al. 2009; Sromovsky et al. 2009) and observations of exoplanets have shown that they play a prominent role in their atmospheres too, significantly shaping their observable properties (Sing et al. 2016; Inglis et al. 2024; Miles et al. 2022; Kempton et al. 2023; Wakeford et al. 2017; Gao et al. 2023; Ehrenreich et al. 2020). Their impact on the observable spectra of exoplanet atmospheres is multifaceted, including the muting of gaseous absorption features, the addition of new spectral features and slopes, atmospheric heating or cooling, and alterations to atmospheric chemistry. But our understanding of the nature of atmospheric aerosols, their distribution across the three dimensions of exoplanetary atmospheres, and the atmospheric physical processes governing their properties have remained severely limited. Whether aerosols in highly

irradiated giant exoplanets (or "hot Jupiters") are primarily composed of condensate clouds formed out of complex minerals (clouds hereafter) (Miles et al. 2022; Visscher et al. 2010a; Wakeford & Sing 2015; Gao et al. 2020c; Wakeford et al. 2017) or are made through complex photochemical reactions driven by intense UV irradiation (hazes hereafter)(Porco et al. 2005; Sánchez-Lavega et al. 2020)– is a long-standing question. Mineral clouds formed through condensation have been theorized and observationally probed for few hot Jupiters (Wakeford & Sing 2015; Wakeford et al. 2017; Fortney 2005; Grant et al. 2023; Inglis et al. 2024). But theoretical studies, laboratory experiments, and some observations have found that photochemically produced hazes, in addition to condensation clouds, might play a major role in shaping hot Jupiter atmospheres as well (Steinrueck et al. 2023a; Fleury et al. 2019; **?**; Kempton et al. 2017; Pont et al. 2008; Estrela et al. 2021; Gibson et al. 2012; Carter et al. 2020).

Moreover, multiple physical processes that determine the nature of aerosols in hot Jupiters – 3D atmospheric circulation, aerosol response to 3D temperature structure, and UV irradiation, remain the most uncertain aspects of our understanding of these planets (Steinrueck et al. 2023a; Parmentier et al. 2013a, 2016; Kempton et al. 2017; Lines et al. 2019; Komacek et al. 2019; Christie et al. 2021). Atmospheric circulation can transport aerosols across a significant fraction of the planet's circumference or atmospheric depth (Parmentier et al. 2013a; Lines et al. 2019; Steinrueck et al. 2023a). Aerosols can respond to 3D planetary temperature gradients via evaporation, condensation, and chemical reactions (Parmentier et al. 2016; **?**; Arfaux & Lavvas 2024). Intense stellar UV irradiation can lead to haze formation and their circulation-driven transport

across the planet (Steinrueck et al. 2023a). While significant theoretical advances have been made to understand the influence of such processes on the aerosol properties of hot Jupiters, order of magnitude uncertainties in circulation timescales and aerosol particle sizes, in addition to uncertainty on aerosol composition, are persistent. Direct observational probes of aerosol properties are therefore essential for characterizing exoplanetary aerosols and resolving key uncertainties in atmospheric physics.

Several observational techniques have been employed to address these problems, such as phase-curve observations (Coulombe et al. 2025; Kempton et al. 2023). Though phase-curve measurements at infrared wavelengths can probe the 3D atmospheric structure of exoplanets, thick aerosol coverage can make inferences from phase-resolved emission spectroscopy degenerate between the thermal and cloud structures of the atmosphere. In addition, high-resolution limb-resolving spectroscopy has shown evidence of chemical asymmetry between the limbs of some hot Jupiters (Louden & Wheatley 2015; Ehrenreich et al. 2020; Kesseli & Snellen 2021), which can be due to condensation of gases in the colder nightside of the planet. However, as clouds are not directly probed, alternative physical mechanisms potentially driving the chemical asymmetries have been proposed (Savel et al. 2023, 2022). Therefore, conclusive evidence on whether atmospheric limb inhomogeneities are driven by aerosols or other planetary processes, is still missing.

The *James Webb Space Telescope's (JWST)* extraordinary precision has led to the emergence of a new technique probing the 3D nature of exoplanetary atmospheres– limb-resolving low-resolution transmission spectroscopy (Espinoza et al. 2024; Murphy

et al. 2024b; Fortney et al. 2010). It leverages the transit light curves of exoplanets to measure separate transit depths for the leading morning limb and the trailing evening limb of the planet (Jones & Espinoza 2022; Espinoza & Jones 2021). This technique has revealed temperature difference-driven limb-to-limb asymmetry in two giant exoplanets (Murphy et al. 2024b; Espinoza et al. 2024). Aerosols were not primarily driving these asymmetries at the observed longer wavelengths, as aerosol-driven scattering signatures were lacking. As a result, we have not yet understood the composition of aerosols or resolved the uncertain physical mechanisms driving aerosol physics in giant exoplanets with this technique.

Due to their multifaceted role in influencing exoplanetary atmospheres, the uncertainties in aerosol physics are a key barrier in achieving one of the most fundamental goals of studying exoplanets – understanding the formation and evolution of a wide variety of planetary systems. Measuring the chemical composition of exoplanets by studying their atmospheres and comparing them with the chemical inventory of their host stars has been identified as one of the most promising methods of achieving this (Öberg et al. 2011; Welbanks et al. 2019). However, the key uncertainties in our understanding of atmospheric aerosols in giant planets can cause major biases in their measured chemical composition (Line & Parmentier 2016; Madhusudhan 2019; Mai & Line 2019). Therefore, resolving these uncertainties is crucial for understanding the formation and evolution of giant exoplanets like hot Jupiters. At the same time, constraining the underlying physics is also essential for evaluating the potential to detect biosignatures in smaller terrestrial and sub-Neptune exoplanets where aerosols are nearly

certain to play a significant role (Fauchez et al. 2019; Komacek et al. 2020)—especially with future missions like the Habitable Worlds Observatory.

8.1 Asymmetric Limbs of a sub-Jovian Mass Planet

We have used *JWST*'s NIRISS instrument to observe the transit of hot Jupiter, WASP-94A b, between 0.8-2.8 μm. WASP-94A b orbits a F8-type host star with a mass of 0.456 $M_{Jupiter}$ and a radius of 1.72 $R_{Jupiter}$ (Bonomo et al. 2017; Neveu-VanMalle et al. 2014). We construct a white light curve of the planet's transit between two broadband wavelength channels covering wavelengths of strong H_2O absorption – 0.9-1.2 μm and 1.35-1.5 μm, using the FIREFLy analysis pipeline [1]. To determine whether the limbs of the planet are asymmetric, we test two transit models with different assumed planet shapes– a spherically symmetric model and a model with limb-to-limb asymmetry (Espinoza & Jones 2021; Jones & Espinoza 2022). We fit the light curve in the 0.9-1.2 μm wavelength band with each of these models to constrain the planetary system parameters including the mid-transit time (T_0) from each model. After fixing the T_0 and the other system parameters determined from the 0.9-1.2 μm band light curve through each method to their corresponding values, we refit the 1.35-1.5 μm band white light curve with each model. Fig. 8.1 panel (**A**) shows a comparison of the best-fit light curve obtained from both models with the observed 1.35-1.5 μm band white light curve. We find that the asymmetric limb model is preferred at a 6σ level (ΔBIC=31.23[2],

[1] We use two bands to stop the spherical transit model from compensating for limb asymmetry by varying the T_0, as T_0 in reality should be the same at all wavelengths (see Fig. 8.9).

[2] Bayesian Information Criterion

$\Delta\chi^2_\nu$=0.027[3]) over the spherical planet model, very strongly suggesting that the planet's limbs are asymmetric in radius. The residuals for the asymmetric limb model in panel (**B**) are consistent with zero whereas those of the spherical planet model in panel (**C**) show significant deviations during ingress/egress. We measure the average morning and the evening transit depths of the planet to be 1.176±0.035% and 1.078±0.035%, respectively, from the white light curve between 0.8-2.8 μm, making them different at a 2.8σ level. We note that this difference is significantly higher when measured at each individual spectroscopic channel.

8.2 Transmission Spectrum of the Morning and Evening Limbs

We fit the spectroscopic light curves at a spectral resolution of R∼50 using the asymmetric limb transit model. This allows us to measure the transit depths of the leading morning limb and the trailing evening limb of the planet simultaneously at each wavelength channel producing a transmission spectrum for each limb of the planet. Fig. 8.2 (**C**) and (**D**) panels show the measured transmission spectrum of the trailing evening limb $(R_E/R_S)^2(\lambda)$ and leading morning limb $(R_M/R_S)^2(\lambda)$ of WASP-94A b, respectively. The observing geometry (to scale) is shown in panel (**A**).

[3]Reduced χ^2

8.3 A Cloudy Morning and Clear Evening– Aerosols composed of Clouds and not Hazes

The spectrum of the morning limb shows an increase towards bluer wavelengths, lacking any prominent gas absorption features. The evening limb spectrum shows prominent gas absorption features and no significant slope. The absence of any prominent gas absorption on the morning limb spectrum is a tell-tale signature of high-altitude aerosols. The lack of such significant aerosol-driven obscuration of the evening terminator suggests that the primary aerosols on WASP-94A b are not photochemically produced hazes but clouds produced through gas condensation. As photochemical hazes are produced only on the UV-irradiated permanent dayside of these tidally locked planets, the planet-wide equatorial jets are expected to transport them to the evening terminator before the morning terminator (Kempton et al. 2017; Steinrueck et al. 2023a). As a result, the transmission spectrum of the trailing evening terminator should be equally or more obscured by hazes than the leading morning terminator spectrum. However, the observations indicate the completely opposite scenario, one which is expected from aerosols composed of condensate clouds. Condensate clouds can form in the cooler nightside of the planet and can be circulated downwind to the morning terminator (Lines et al. 2019; Parmentier et al. 2016). They can then be further transported to the much hotter dayside where a large fraction of them might evaporate, making the evening terminator clearer than the morning terminator. We also find that clouds better fit the morning limb spectrum than several haze species at greater than

4σ significance. While observations of two hot Jupiters have detected cloud absorption signatures (Inglis et al. 2024; Grant et al. 2023), it was not clear how important hazes are in hot Jupiter atmospheres. Our observations provide the first definitive empirical evidence to show that aerosols can be predominantly composed of condensate clouds instead of photochemically produced hazes in hot Jupiters like WASP-94A b and condensate clouds can primarily shape their transmission spectrum at both long and short wavelengths.

Host star activity effects have been difficult to disentangle from aerosol properties of planets, as unocculted star spots can mimic the effect of aerosols on their transmission spectrum by producing similar slopes at blue wavelengths (Narrett et al. 2024; Rackham et al. 2019). However, our analysis localizes the aerosols in the planet's atmosphere, yielding prominent H_2O features with nearly no scattering slope in the evening limb and a highly cloud-obscured morning limb. In addition, star-spot/faculae crossing events during the transit can also mimic planetary asymmetries in the transit light curve. As the host star is too hot (F8 spectral type) to have molecular H_2O in its photosphere and we detect H_2O features only in one limb, such an effect is therefore very unlikely to be a contaminant of our detected signal.

8.4 Temperature Differences and Day/Night Cloud Cycling

We employ a Bayesian atmospheric modeling technique, also known as atmospheric retrievals, to theoretically interpret these two transmission spectra simultaneously. We build a 1.5D atmospheric model with two distinct atmospheric structures for the planet limbs that converge in the deep atmosphere (see methods) to calculate the transmission spectrum of both planet limbs. The (**C**) and (**D**) panels of Fig. 8.2 show the best-fit theoretical model obtained by the retrieval along with key atmospheric absorbers shaping the spectrum of the morning and evening limbs. The evening limb spectrum is shaped by prominent H_2O absorption, which we detect with a significance of 10σ. The evening terminator also shows cloud absorption from $\sim$1 mbar pressure. The spectrum of the morning terminator is completely dominated by cloud absorption with nearly no gaseous absorption features, which we detect at a significance of 11σ.

8.4.1 Limb-to-Limb Temperature Difference

We constrain the temperature-pressure ($T(P)$) profiles as well as the cloud properties of both limbs. Panel (**A**) of Fig. 8.3 presents the constraints on the $T(P)$ profiles of each limb along with condensation curves of three mineral cloud species relevant for temperatures of WASP-94A b. The $T(P)$ profile of the evening terminator is significantly hotter than the morning terminator, with a temperature difference of 448 ± 78 K (3σ lower limit of 280 K). As a result, the cloud droplets that are formed and

lofted to the higher altitudes of the colder morning terminator get evaporated in the higher altitudes of the hotter evening terminator. Panel (**A**) shows that the morning limb spectrum probes very low pressures below 0.01 mbars whereas the evening limb spectrum probes higher pressures between 0.01-4 mbars. The $T(P)$ profiles for each terminator of WASP-94A b predicted from 3D general circulation model (GCM) matches well with our measured $T(P)$ profiles, further affirming that the measured temperature difference between the planet limbs is physically plausible.

8.4.2 Cloud Properties of each limb

The (**B**)-(**G**) panels of Fig. 8.3 show the cloud properties of each limb, with the top and bottom panels showing properties of the evening and morning limbs, respectively. The (**B**) and (**C**) panels present the cloud optical depth profiles for each limb, where the evening terminator becomes transparent at smaller pressures than a mbar but the morning terminator remains optically thick up to pressures of $\sim$0.01 mbars. The temperature difference between the planet's limbs drives the day-night cloud cycling, causing drastic difference in the cloud optical depth (i.e., the strength of cloud absorption) between the limbs. This effect causes the evening limb to have prominent H_2O features but the morning limb to be devoid of them. Panels (**D**) and (**E**) show the cloud mass-mixing ratio derived with our model for each cloud species at each limb. Silicate ($MgSiO_3$ here) and iron (Fe) clouds are likely the main components of the clouds for both the limbs. Panel (**G**) shows that the morning limb has cloud particles with mean radius between 0.1-1 μm between the 0.01-1 mbar pressure range. These smaller

cloud particles are responsible for the strong blue-side slope in the morning limb spectrum. Panels (**D**) and (**F**) show that the properties of clouds at pressures deeper than a mbar remain unconstrained in the evening limb because they are below the transit photosphere.

8.4.3 Constraints on Circulation Timescales

The observed distribution of cloud particles is intimately connected to various uncertain circulation timescales in the atmosphere, including the vertical mixing and the horizontal advection timescales. By considering the balance between vertical lifting of cloud particles and their gravitational settling, we constrain the strength of vertical mixing through the 1D vertical eddy diffusion parameter $\log_{10}(K_{zz}) = 11.72 \pm 0.89$ cm^2 s^{-1}. We derive an average K_{zz} profile from the 3D GCM and find that our observational constraints are consistent with the K_{zz} from the upper atmosphere of the GCM. The constrained vertical mixing timescale lies between ∼0.08-5.4 days. If the horizontal advection timescale at 0.01 mbar pressures is much slower than the fastest vertical mixing timescale derived here, then the cloud droplets will be stable at these high altitudes. However, if the horizontal advection timescale is faster than the vertical mixing timescales, then the cloud particles will not be replenished fast enough to be maintained at the high altitudes observed in the morning limb. The 3D GCM suggests that the fastest advection timescales involved in the horizontal transport of the cloud particles from the morning to the evening terminator is achieved within the planet-wide equatorial jet and is typically $\sim$ 1.15-2.2 days. Our nominal GCM model suggests that

the jet spans the latitudes of ±40° for pressures smaller than one bar. This suggests that if the cloud particles trace the wind velocities at lower pressures, then the vertical mixing timescale for the cloud particles should be nearer the lower limit of 0.08 days, as opposed to the upper limit of 5.4 days.

8.5 Effect of Asymmetric Limbs on the Measured Composition of WASP-94A b

In addition to the morning/evening spectrum, we also measure a planet-wide transmission spectrum assuming spherical symmetry. This spectrum is shown along with the evening limb spectrum in Fig. 8.4 (**A**) panel. The features in the spherical spectrum appear muted by a factor of ∼2 compared to the features in the evening limb spectrum (in terms of scale heights). We apply a 1D retrieval model to the spherical spectrum instead of the 1.5D retrieval used for the limb spectra, otherwise maintaining a near identical setup between the two. The constraints on the chemical composition and cloud properties from the limb-resolved spectrum and the spherical spectrum are shown in Fig. 8.4 (**B**)-(**D**). We find that the metallicity of WASP-94A b is constrained at [M/H]=+0.31±0.32 by the asymmetric-limb observations, whereas it is constrained at [M/H]=+1.937±0.073 by the spherical spectrum, showing a 5σ level inconsistency. This suggests that not considering limb asymmetry can lead to severe biases in the measured metal-content of exoplanets, especially when the limb asymmetry is aerosol driven. This bias, as predicted by theoretical studies (Line & Parmentier 2016), stems from the

dilution of gas absorption features in the spherical spectrum, making the features appear compressed. Constraints on C/O[4] from the two spectra, shown in Fig. 8.4 (**C**), are not inconsistent but show very different probability distributions due to the bias introduced by the 1D retrievals on the spherical spectrum. The vertical mixing strength (K_{zz}) is also strongly affected by this bias (panel (**D**)), showing a 2σ level inconsistency. We also find that parameterizing patchy cloud covers within 1D forward models to fit spherical planet spectrum doesn't alleviate these biases. Drawing inferences from limb-resolved spectroscopy instead is necessary.

This bias in measuring chemical compositions and cloud properties is not limited to this planet or similar hot Jupiters, but has far reaching implications for a much wider and diverse population of transiting exoplanets. Fig. 8.4 (**E**) shows the 1.4 μm H_2O amplitude (gray points) measured from *HST*/WFC3[5] transmission spectroscopy observations of a population of transiting exoplanets with varying sizes, masses, and temperatures (Fu et al. 2017). These H_2O amplitudes were measured from the 1D spectrum without considering limb-asymmetries. The black star shows the H_2O amplitude measured from the spherical 1D *JWST* spectrum of WASP-94A b, and it follows the same trend as the WFC3 population with most hot-Jupiters (1000-2000 K) showing similarly sized amplitude features. However, we know that the H_2O feature is highly asymmetric between the two limbs of WASP-94A b and are shown as blue and red stars. The red and blue solid lines in the panels show model predictions of the spherical planet H_2O feature amplitude from fully clear and very cloudy 1D atmospheres, respectively.

[4]Carbon-to-Oxygen ratio
[5]*Hubble Space Telescope*/Wide Field Camera 3

The black dashed line shows the predicted spherical planet H_2O feature amplitude from planet models with one clear and one very cloudy limb like WASP-94A b. The *HST*/WFC3 transit light curves have not been analyzed for limb-asymmetric signals. With day/night cloud cycling established, this implies that the H_2O feature amplitudes of the entire *HST*/WFC3 population of transiting planets can be diluted to varying levels due to limb-asymmetry, potentially severely biasing the composition and cloud properties inferred from this population. These results also further complicate the inferences drawn from the *JWST*/*HST* transmission spectrum of smaller exoplanets such as sub-Neptunes, that are expected to have significant aerosol cover (Kempton et al. 2023; Coulombe et al. 2025). Limb-to-limb asymmetry also needs to be seriously considered while determining the observational scenarios required to detect potential biosignatures from terrestrial planets (e.g., TRAPPIST-1 e) with *JWST* and future missions (Fauchez et al. 2019; Komacek et al. 2020; Tinetti et al. 2022). Therefore, asymmetric planetary limbs need to be empirically probed and theoretically understood for diverse exoplanets to achieve one of the foundational objectives of the field– understanding how diverse planetary systems form and evolve.

8.6 Methods

8.6.1 Data Reduction

We observed WASP-94A b, a sub-Jovian mass exoplanet (Ahrer et al. 2024; Bonomo et al. 2017; Neveu-VanMalle et al. 2014), using the NIRISS instrument aboard

JWST in the Single-Object Slitless-Spectroscopy (SOSS) mode between 11th and 12th October 2024. These observations were taken as part of the cycle 3 GO "Grand Tour" spectroscopic survey program (PID: 5194, PI-Sing). The observations started at 22:36:23 on 11th October UT and continued for 11.51 hours till 09:12:22 on 12th October UT. The observations were obtained with the SUBSTRIP256 subarray and included 3 groups per integration. There were a total of 1458 integrations for a total exposure time of 8.9 hours. The NISRAPID readout setting was used to read out the NIRISS detector.

We use three independent *JWST* data reduction pipelines to analyze these observations – FIREFLy, Eureka!, and Fu. Below, we briefly describe the key data reduction steps performed within each of these pipelines.

8.6.1.1 FIREFLy

The `FIREFLy` data reduction routines have been used to analyze *JWST* NIRSpec observations of several exoplanets over the past few years (Sing et al. 2024; Rustamkulov et al. 2023) and are well described in (Rustamkulov et al. 2022a, 2023; Sing et al. 2024); recently, it has also been upgraded to better handle NIRISS/SOSS observations (Schmidt et al. 2025). We use the `FIREFLy` to analyze the NIRISS/SOSS observations of WASP-94A b, which required the implementation of several additional steps within the analysis pipeline. We have described these steps here.

The `FIREFLy` routines analyze stage zero NIRISS/SOSS data with several custom modifications of the *JWST* calibration pipeline starting from the uncalibrated im-

Parameter	**Unit**	**FIREFLy**	**Eureka!**	**Fu**
$(R_{morning}/R_*)^2$	%	1.176±0.035	1.170 ± 0.036	1.153 ± 0.040
$(R_{evening}/R_*)^2$	%	1.078±0.035	1.092 ± 0.036	1.096 ± 0.039
Period	Days	3.9502 (fixed)	3.950190	3.950190
Transit Time (T_0)-2460595	BJD_{TDB}	0.71518±0.00018	0.71511 ± 0.00019	0.71506±0.00021
a/R_*	-	7.3120±0.019	7.313 ± 0.016	7.3207±0.0190
Impact Parameter b	-	0.150±0.018	0.139 (calculated)	0.141 (calculated)
inclination i	°	88.82 (calculated)	88.91 ± 0.13	88.89±0.17
limb darkening u_+	-	0.3473±0.0071	0.3839 (calculated)	0.351 (calculated)
limb darkening u_-	-	-0.004±0.015	-0.1243 (calculated)	-0.019 (calculated)
limb darkening u_1	-	0.1716 (calculated)	0.1298	0.166±0.0086
limb darkening u_2	-	0.1756 (calculated)	0.2541	0.185±0.0168
ϕ	°	90 (fixed)	90 (fixed)	90 (fixed)

Table 8.1: Constraints on system and planetary parameters from different reduction pipelines from fitting the white light curve for WASP-94A b with the catwoman transit model. The values which are denoted as "calculated" are not fit directly in that particular reduction pipeline but is derived from the median parameter values of related parameters.

ages. One of the major modifications arise in the method of $1/f$ noise removal due to the slitless nature of the SOSS data. `FIREFLy` constructs a custom PSF mask for each observation using a detector count threshold. We used a mask count threshold of 12 ADU for analyzing the observations presented in this paper. This PSF mask is then used to mask the PSF and any background sources across the detector. As described in (Radica et al. 2023), the background is removed from each group by scaling a background template to a region with minimal contamination from the PSF or other sources to a median time series image. With the background subtracted from each group, we used the unmasked regions to subtract the $1/f$ noise in a column-by-column basis at the group level. This step significantly reduces the $1/f$ noise in the data presented here. The background is then re-added before the linearity step is applied. We find the noise is reduced by $\sim$5% using this process compared to only applying a $1/f$ noise subtraction at the integration stage.

To further clean the data, `FIREFLy` employs a static bad pixel cleaning routine by constructing a filter-smoothed median detector image and cleaning pixels from integration that are 7σ outliers from the filter smoothed median image. The cosmic ray hits on the detector are cleaned from each integration using the LA Cosmic technique (van Dokkum 2001). We also perform another cleaning of the cosmic rays using a temporal cleaning method, where a rolling median detector image is created with 11 integrations at a time and 7σ outliers of this rolling median image are cleaned from the respective integrations. At this stage, we perform another $1/f$ noise and background removal at the integration level by creating another custom PSF mask with a 15σ count threshold.

To extract 1D spectrum from the cleaned detector images, we use a full aperture width of 31 pixels. We vary this aperture width through higher and lower values to select this optimum aperture width on the basis of the lowest median absolute deviation (MAD) value for the extracted white light curve of the transit. This MAD value for our case is 76 ppm. The extracted white light curve along with the best-fit asymmetric planet limb model are shown in Fig. 8.5. Fig. 8.6 (**A**) panel shows the wavelength vs. time 2D map of the normalized extracted spectroscopic light curves with `FIREFLy`.

We use the catwoman routine (Jones & Espinoza 2022; Espinoza & Jones 2021) to fit the spectroscopic light curves and the white light curve of WASP-94A b to measure the transmission spectrum of each limb of the planet and to constrain the system parameters of the planet, respectively. We trim the first 10 integrations in all the light curves to allow for detector settling. While fitting the white light curve, we fix the period of the planet to 3.9502 days (Kokori et al. 2023). We vary the transit depths of the morning and evening limbs (($R_{morning}/R_*)^2$ and ($R_{evening}/R_*)^2$), mid-transit time (T_0), a/R_*, impact parameter (b), and the limb darkening coefficients (u_+ and u_-). We assume a quadratic limb darkening law in our transit model. We detrend the white light curve with a linear with time systematics model. We use the `emcee` sampler (Foreman-Mackey et al. 2013b) with 100 walkers and 1000 iterations to fit the white light curve. Table 8.1 summarizes all the free parameters included in our light curve model along with constraints on each from the white light curve. Fig. 8.5 shows the FIREFly fit to the white light curve with the catwoman model.

While fitting the spectroscopic light curves, we fix the T_0, a/R_*, period, and

b to the median values obtained from the white light curve fits. We assume that the planet's rotational axis is perfectly aligned with the orbital axis of the planet (ϕ= 90°), which is expected for a tidally locked planet at such close proximity to its host star. We bin the spectroscopic light curves at a spectral resolution of $R \sim 50$. We allow the morning/evening transit depths, the limb darkening coefficients (u_+ and u_-), and the linear systematics model coefficient to vary while fitting the light curve of each spectroscopic channel with the `emcee` sampler. Fig. 8.6 (**B**) panel shows the wavelength vs. time 2D map of the normalized best-fit model light curves for each spectroscopic channel. Fig. 8.7 (**A**) and (**B**) panels shows a comparison between u_+ and u_- constrained from fitting the spectroscopic light curves with the predicted values from the 3D Stagger-grid from (Magic et al. 2015). The 3D models predict the wavelength-dependence of both the limb darkening parameters well but show a constant offset with the measured values from the light curves. Therefore, we apply an offset of -0.02684 to the model predictions for u_+ and another much smaller offset of -0.007 to the model predictions of u_- to match the measured coefficient values. The stellar models with the applied offsets are shown with dashed lines in (**A**)-(**B**) panels of Fig. 8.7. We fit the spectroscopic light curves again by fixing the limb darkening parameters to this modified stellar model predictions to measure our final transmission spectra for the morning and the evening terminators. The (**C**) and (**D**) panels of Fig. 8.7 show a comparison of the transmission spectrum derived for each limb with free limb darkening coefficients in blue and the fixed limb darkening coefficients in red. These plots show that the features in the spectrum of each limb shows very small sensitivity to each case. We use the spectrum measured with the

fixed limb darkening coefficients for all the analysis presented in this work.

Fig. 8.8 (**A**)-(**D**) panels present Allan variance plots for four randomly selected spectroscopic channels showing that the spectroscopic light curves show negligible correlated noise. The residuals of the model fits to the light curves follow a $1/\sqrt{N}$ type behavior, where N is the bin size. This suggests that the cleaning and model fitting components of our data analysis has been satisfactory.

Extraction of the 2nd Order Spectrum –

We find that the 2nd order trace on the detector is heavily contaminated by three other traces. Fig. 8.10 highlights these traces with red boxes on the detector and shows the tiny wavelength region from which we could reliably recover the 2nd order spectrum with the green box. We could measure the limb-asymmetry spectrum between 0.65-0.7 μm, which is shown in Fig. 8.11. We do not use the 2nd order spectrum for any model inference analysis in this work as it can still be diluted due to contamination, which can cause biases in our inferences.

Extracting 1D spectrum assuming planet is spherical –

We also derive a transmission spectrum of the planet by fitting the spectroscopic light curves with the batman transit model (Kreidberg 2015b), which assumes that the planet is a perfect sphere. Fig. 8.14 shows the spectrum extracted with the batman transit model. Evidence of limb–to–limb asymmetry can be found by fitting for the mid-transit time (T_0) for each spectroscopic channel while fitting the light curves with the batman transit model (Espinoza et al. 2024). The asymmetry in the spectroscopic

light curves due to the asymmetric limbs is then captured by a shifting T_0 in various wavelength regions of strong molecular absorptions (e.g., H_2O absorption bands). The (**A**) panel of Fig. 8.9 shows the fitted T_0 using batman to each spectroscopic light curve. The T_0 signature shows strong correlations with molecular absorption bands such as the H_2O absorption band between 1.35-1.5 μm. The green line in the (**A**) panel of Fig. 8.9 shows the T_0 signature calculated analytically (Murphy et al. 2024a) from the transmission spectrum of the morning and the evening limbs measured with the catwoman transit model. The analytically derived T_0 signature from the spectrum of the two limbs matches the T_0 variations measured by fitting the light curves with a spherical transit model. The (**B**) panel of Fig. 8.9 also shows a comparison of the 1D spherical spectrum calculated by averaging the spectrum of the two terminators with the 1D spherical spectrum derived from fitting the light curves with the batman spherical transit model. The 1D spherical spectrum of the planet derived in these two ways shows an excellent match. The uncertainties on the 1D spectrum derived from the spectrum of the two terminators are larger because of additional parameters involved in fitting the light curves in each spectroscopic channel with the catwoman transit model.

8.6.1.2 Fu Pipeline

The data reduction steps followed were broadly consistent with previous studies using SOSS (Fu et al. 2024). Initially, the data underwent analysis steps in the default JWST pipeline up to the `darkcurrentstep`, then followed by custom group-level background subtraction using the `darkcurrent.fits` files. The spectra PSF was masked

and a column-by-column median subtraction was performed using the unmasked regions. Subsequently, the datasets were processed through the `jumpstep` and `rampfitstep`, yielding `rampfitstep.fits` files.

Next, we performed spectral extraction by identifying the vertical location of the spectral trace in each column through a column-by-column cross-correlation with the spectral PSF. Spectra were extracted using a fixed, 30-pixel-wide aperture centered around this identified spectral trace. Each spectroscopic light curve was further cleaned temporally by removing outliers using a rolling median.

For transit modeling, we first fitted the white light curve with `Catwoman` model (Espinoza & Jones 2021) and the `emcee` sampler (Foreman-Mackey et al. 2013b), incorporating a total of nine free parameters: visit-long slope, constant offset, mid-transit time, R_p, ΔR_p, inclination, and $a/R_\star$. To enhance sampling efficiency and alleviate degeneracy between the limbs radii, the default R_{p1} and R_{p2} parameters are parameterized to R_p and δR_p through $R_{p1} = R_p - \delta R_p/2$ and $R_{p2} = R_p + \delta R_p/2$, where R_{p1} and R_{p2} are the radius of each limb.

The best-fit parameters from the white light curve analysis (mid-transit time, inclination, and $a/R_\star$) were fixed in subsequent spectroscopic channel analyses. Each channel fit included four free parameters: visit-long slope, constant offset, R_p, and ΔR_p. The two quadratic limb darkening parameters are fixed to the `stagger` (Magic et al. 2015) 3D stellar grid values. After fitting, R_p, and δR_p were converted back to R_{p1} and R_{p2}.

8.6.1.3 Eureka!

For the purposes of this analysis, we added NIRISS/SOSS functionality to the pipeline (Bell et al. 2022b). Whenever possible, this newly-developed code makes use of existing functions and follows the same framework as other instrument modes.

In Stage 1, we made no changes to the wrapper around STScI's official software, version 1.15.1 (Bushouse et al. 2024). Unlike other reductions, we did not correct for $1/f$ noise or apply group-level background subtraction at this stage. The resulting *rateints* files were remarkably clean and the final transmission spectrum matches the other reductions; therefore, we determined that these additional steps were unnecessary for this dataset. In Stage 2, we skipped the *photom* step, following standard practices for time-series observations.

In Stage 3, we supplied `PASTASOSS` (Baines et al. 2023a,b) with the NIRISS pupil position reported in the header to compute the trace and 1D wavelength solution for each spectral order. Similar to the other instrument modes, we performed a double-iteration, 4σ outlier rejection of the sky background region (the full frame option is also available) along the time axis and computed a median flux frame that is free of bad pixels. Before we straightened the trace for a given order, we first masked the flux from the other order using the trace computed above and applying the spectral extraction half-width. We then shifted each column by an integer number of pixels to create a roughly-straightened 2D spectrum for each order. Each order's spectrum was centered at the location specified in the control file (ECF). The column-by-column

background subtraction routine operates on each spectral order. For our reduction, we used a background half-width of 22 pixels and a zeroth-order polynomial. We performed both standard and optimal spectral extraction for each order. Here we used a spectral half-width of 17 pixels and used the median frame as our optimal weighting function. In Stage 4, we computed white and spectroscopic light curves for each spectral order.

We fit the Order 1 white light curve (0.86 – 2.80 μm) using the `Catwoman` transit model (Espinoza & Jones 2021) with free quadratic limb darkening parameters, a quadratic baseline in time, and a scatter multiplier term. We estimate uncertainties using `emcee` (Foreman-Mackey et al. 2013b) and display the results in Table 8.1. For the Order 1 spectroscopic fits, we fix the transit time, inclination, and semi-major axis parameters to the best-fit white light curve values. We also apply a fixed limb darkening model using ExoTiC-LD (Grant & Wakeford 2024) and the MPS2 grid (Kostogryz et al. 2022). We tested several resolutions and settled on 59 channels at constant resolving power ($R \sim 50$) for the final fits. For Order 2, there was significant contamination from the nearby stellar companion that biased the measured transmission spectrum.

8.6.1.4 Comparison of spectrum between independent pipelines

Fig. 8.12 shows a comparison of the transmission spectrum of the evening and morning limbs measured with the three pipelines described above. The shape of the spectrum for each limb is consistent between the three pipelines. However, there seems to be an offset between each of them. We find that this offset is purely driven by small differences in the T_0 constrained from the white light curve by each pipeline. Even

though these differences in T_0 between pipelines are within the 1σ error on T_0, they still affect the offset between the morning and evening spectrum as T_0 is fixed to the value constrained from the white light curve while fitting the spectroscopic light curve in each pipeline. Fig. 8.13 shows this effect, where the difference in transit depth at 1.4 μm between the morning and evening terminators from each pipeline shows a direct correlation with the median T_0 obtained by that pipeline. This effect leads to about 200 ppm offset differences between the spectra derived by the three pipelines. To take this offset difference into account within our analysis and interpretation, we allow for the morning spectrum to move by up to 200 ppm offset relative to the evening spectrum in our modeling and Bayesian retrieval analysis. Fig. 8.14 shows a comparison of the spherical spectrum measured with each pipeline and they are found to be consistent with each other.

8.6.2 Modeling

8.6.2.1 Atmospheric Retrievals

Retrievals on the Morning and Evening Transmission Spectrum We use the `PICASO` atmospheric model (Mukherjee et al. 2023; Batalha et al. 2019; Mukherjee et al. 2021a) and the `VIRGA` cloud model (Ackerman & Marley 2001b; Rooney et al. 2021) to perform a 1.5D Bayesian retrieval on the transmission spectrum of the morning and evening limbs of the planet simultaneously. Our retrieval model parametrizes the $T(P)$ profile of both limbs using the $T(P)$ parametrization from (Guillot 2010). This $T(P)$ profile parametrization includes 5 free parameters including $T_{\rm eq}$, $log(\kappa_{\rm IR})$, $log(\gamma)$, α, and

$T_{\rm int}$. We assume that the $T_{\rm int}$ parameter is the same for the morning and the evening limbs, such that the $T(P)$ profiles of both limbs converge to the same temperatures in the deep atmosphere. We also assume that the $log(\kappa_{\rm IR})$, $log(\gamma)$ and α parameters remain the same between both the limbs. We allow the morning and evening limbs to have two different $T_{\rm eq}$ values to account for the temperature difference between the limbs. We simulate the clouds in the morning and evening limbs of the planet's atmosphere using the `VIRGA` model (Rooney et al. 2021; Ackerman & Marley 2001b). The `VIRGA` cloud model simulates the cloud structure of the atmosphere using a balance between turbulent mixing and sedimentation of cloud particles. The model includes two parameters – the cloud sedimentation factor $f_{\rm sed}$ and the vertical eddy diffusion coefficient $K_{\rm zz}$. The $f_{\rm sed}$ parameter is defined as the ratio between the sedimentation velocity of the cloud particles and the velocity of convective mixing. As a result, lower values of $f_{\rm sed}$ lead to more vertically extended cloud decks (Rooney et al. 2021; Ackerman & Marley 2001b). We assume both the morning and the evening limbs have the same $K_{\rm zz}$ and $f_{\rm sed}$ parameter, meaning that the vertical dynamics of cloud particles between the two limbs are not different. We include three cloud forming species relevant to the temperature regime of this planet within our retrievals – $MgSiO_3$, Fe, and MnS with optical constants from (Scott & Duley 1996; Huffman & Wild 1967; Batalha & Marley 2020). We assume thermochemical equilibrium for both the limbs and vary the metallicity ([M/H]) and carbon-to-oxygen ratio (C/O) to calculate the abundances of gases in each limb based on the $T(P)$ profile of the limbs, as WASP-94A b's equilibrium temperature is too hot for disequilibrium chemistry effects to be very important (Mukherjee et al. 2024a). We

include opacities for H_2, H_2O, CO, CO_2, CH_4, H_2S, HCN, N_2, N_2O, and NH_3 in our retrieval with opacity sources listed in (Mukherjee et al. 2024c, 2023). We also include collision-induced opacities for H_2-H_2, He-H_2, and H_2-N_2 collisions. We fit for the radius at 10^{-3} bars of both the limbs simultaneously using the xR_p parameter, which defines the 1 mbar radius as $R = R_p(1 + xR_p)$. Due to the small dependence of the offset between the morning and evening limb spectra on the used T_0 in the data reduction (Fig. 8.13), we allow for a 200 ppm offset between the morning and the evening limb spectrum within our retrieval. Therefore, our retrieval model has 12 free parameters including 6 parameters for $T(P)$ profiles of the limbs, 2 chemical composition related parameters, 2 cloud parameters, 1 radius scaling parameter, and 1 offset parameter.

We use the pyMultiNest sampler (Feroz et al. 2009b) for parameter estimation from the observed spectra. The log-likehood function, $\ln(\mathcal{L})$, in our retrieval is defined as

$$\ln(\mathcal{L}) = -\frac{1}{2}\sum_i \left(\frac{y_i^{morning} + O - f_i^{morning}}{\sigma_i^{morning}} \right)^2 - \frac{1}{2}\sum_i \left(\frac{y_i^{evening} - f_i^{evening}}{\sigma_i^{evening}} \right)^2 \quad (8.1)$$

where $y_i^{morning}$ and $y_i^{evening}$ are the observed transit depth in the i^{th} spectral channel and σ denote their corresponding uncertainties. The $f_i^{evening}$ and $f_i^{morning}$ are the model transit depths from our retrieval model and O is the offset parameter that we have allowed in our retrieval for the spectrum of the morning terminator. We apply uniform priors on all 12 parameters, which is summarized in Table 8.2. We perform our retrievals with 2000 live points and use the custom convergence criteria of the pyMultiNest routine. Fig. 8.16 shows the corner plot obtained from our retrieval, showing the

Parameter	**Units**	**Prior**	**Median**	$\pm 1\sigma$
$T_{\rm eq}$	K	$\mathcal{U}(800, 2100)$	1509	69
$\delta T_{\rm eq}$	K	$\mathcal{U}(0, -600)$	-448	78
$log(\kappa_{\rm IR})$	-	$\mathcal{U}(-2.0, +0.5)$	0.20	0.18
$log(\gamma)$	-	$\mathcal{U}(-2.0, +0.5)$	-1.34	0.61
α	-	$\mathcal{U}(0, 1)$	0.49	0.32
$T_{\rm int}$	K	$\mathcal{U}(30, 630)$	321	183
[M/H]	$\times$solar	$\mathcal{U}(-1.0, +3.0)$	+0.31	0.32
C/O	$\times$0.458	$\mathcal{U}(0.01, 2.0)$	0.74	0.45
$log(f_{\rm sed})$	-	$\mathcal{U}(-4, +1.0)$	-3.0	0.6
$log(K_{\rm zz})$	$\rm cm^2/s$	$\mathcal{U}(7, 14)$	11.72	0.89
xR_p	-	$\mathcal{U}(-0.1, 0)$	-0.0524	0.003
offset	ppm	$\mathcal{U}(-200, 0)$	-87	62

Table 8.2: Parameters in the `PICASO` atmospheric retrieval on the morning and evening limb transmission spectra with the combined morning/evening limb model along with applied priors and constraints.

posterior distribution of various parameters and the correlations between them. The median and 1σ constraint on each parameter is also tabulated in Table 8.2. Fig. 8.15 also shows the median retrieved spectrum for each limb along with $\pm1\sigma$ and $\pm2\sigma$ envelopes. Our constraints on the $T(P)$ profile and the cloud properties of each limb are shown in Fig. 8.3. We note that we do not observe any species-specific cloud absorption feature in our spectrum. But as our observations demonstrate that the aerosols are composed of condensate clouds, we use the cloud species that are relevant for a planet of WASP-94A b's temperature in our analysis. The silicate component of the cloud might be composed of other Si- containing minerals such as fosterite or quartz, but this would have nearly no effect on any major conclusions of this work.

Fig. 8.17 (**A**) and (**B**) shows the contribution function as a function of pressure and wavelength for the evening and morning limb of the planet, respectively. These contribution functions are calculated by the derivative of the wavelength and pressure dependent transmittance values with respect to pressure in the best-fit model from the 1.5D retrieval. These show that the evening limb transmission spectrum is sensitive to pressure ranges between ∼4-0.01 mbars whereas the morning limb transmission spectrum is sensitive to a much lower and narrower pressure range of ∼0.01-0.001 mbars.

Fig. 8.18 shows constraints on the gas abundances obtained from the 1.5D retrievals on each planet limb. The abundance constraints on the evening limb are shown in panel (**A**) whereas panel (**B**) shows the constraints for the colder morning limb. We just detect prominent H_2O features in our transmission spectrum, but the thermochemical equilibrium assumed in our retrieval analysis allows us to predict constraints on the

Parameter	**Units**	**Prior**	**Median**	$\pm 1\sigma$
$T_{\rm eq}$	K	$\mathcal{U}(800, 2100)$	1246	126
$log(\kappa_{\rm IR})$	-	$\mathcal{U}(-2.0, +0.5)$	-0.29	0.74
$log(\gamma)$	-	$\mathcal{U}(-2.0, +0.5)$	-1.36	0.61
α	-	$\mathcal{U}(0, 1)$	0.54	0.32
$T_{\rm int}$	K	$\mathcal{U}(30, 630)$	312	159
[M/H]	$\times$solar	$\mathcal{U}(-1.0, +3.0)$	1.937	0.073
C/O	$\times 0.458$	$\mathcal{U}(0.01, 2.0)$	0.27	0.21
$log(f_{\rm sed})$	-	$\mathcal{U}(-4, +1.0)$	-1.42	0.21
$log(K_{\rm zz})$	$\rm cm^2/s$	$\mathcal{U}(7, 14)$	8.12	0.58
xR_p	-	$\mathcal{U}(-0.1, 0)$	-0.0454	0.0020

Table 8.3: Parameters in the `PICASO` atmospheric retrieval on the spherical transmission spectra with the 1D model along with applied priors and constraints.

other gases too. Even though both limbs of the planet have the same metallicity and C/O constraints, the abundances of individual gases are different between the morning and evening limbs due to different $T(P)$ profiles in each planet limb. For example, a gas like CH_4 will likely be more abundant in the colder morning limb than the hotter evening limb, which can be seen in Fig. 8.18. On the other hand, the abundance of H_2O appears to be uniform across the two planet limbs from Fig. 8.18.

Retrievals on the Spherical Transmission Spectrum with `PICASO` We use `PICASO` to also perform 1D atmospheric retrievals on the transmission spectrum for

WASP-94A b, measured by assuming that the planet is spherically symmetric. The forward model used in this retrieval is very similar to the model used in the simultaneous morning/evening limb model, except that it has just one limb instead of two. As a result, this model has all the same free parameters and priors as the morning/evening limb model except $\delta T_{\rm eq}$ and the offset. Fig. 8.19 and Fig. 8.20 show the retrieved transmission spectrum and the corner plot of the involved parameters, respectively. The priors and constraints on each involved parameters are in Table 8.3.

Patchy Cloud Retrievals on the Spherical Transmission Spectrum with `POSEIDON`

We also use the `POSEIDON` Python package[6] (MacDonald & Madhusudhan 2017; MacDonald 2023) to perform an atmosphere retrieval on our WASP-94A b spherical transmission spectrum with 1D and patchy 2D cloud models. Our atmosphere model assumes background gas consisting of H_2 and He at Solar $He/H_2 = 0.17$ (Asplund et al. ????). We construct atmospheres with 150 layers uniformly spaced in log pressure, ranging from 10^{-7}-100 bar, under hydrostatic equilibrium. We solve hydrostatic equilibrium with the boundary condition that the atmosphere reaches a pressure of 10^{-3} bar at the reference radius. We freely retrieve the $T(P)$ profile following the prescription of (Madhusudhan & Seager 2009b). Our atmosphere model considers the following trace species: CO, CO_2, CH_4, H_2O, SO_2, H_2S, HCN, NH_3, K, and OCS. We assume equilibrium chemistry and retrieve the atmospheric metallicity and C/O ratio. For clouds and aerosols, we use the inhomogeneous cloud and haze parameterization of (MacDonald & Madhusudhan

[6] https://github.com/MartianColonist/POSEIDON, version 1.2.1

2017). Our 1D cloud model assumes a cloud coverage fraction $\phi = 1$, while our 2D patchy cloud model allows it to vary as a free parameter. In total, our 1D cloud model has 12 free parameters: 6 $T(P)$ profile parameters, 3 cloud/haze parameters, and the reference radius, atmospheric metallicity, and C/O ratio, while our patchy 2D cloud model has 13 free parameters: the same as the 1D cloud model, plus the cloud coverage fraction ϕ.

We calculate model spectra in our `POSEIDON` retrievals by solving the equation of radiative transfer in a cylindrical coordinate system for 100 incident stellar rays that are attenuated according to the atmospheric opacity along line-of-sight. We pre-compute our opacities at high resolution, $R = 60,000$, across a grid of temperatures and pressures using the `Cthulhu`[7] Python package (Agrawal & MacDonald 2024). We derive our opacities using the following spectroscopic line lists or measured cross sections: CO (Li2015; (Li et al. 2015)), CO_2 (UCL-4000; (Yurchenko et al. 2020)), CH_4 (MM; (Yurchenko et al. 2024)), H_2O (POKAZATEL; (Polyansky et al. 2018b)), SO_2 (ExoAmes; (Underwood et al. 2016)), H_2S (AYT2; (Azzam et al. 2016)), HCN (Harris; (Barber et al. 2014b)), NH_3 (CoYuTe; (Coles et al. 2019)), K (VALD3; (Ryabchikova et al. 2015)), and OCS (OYT8; (Owens et al. 2024)). We also include continuum collision-induced absorption from H_2-H_2 and H_2-He pairs (Karman et al. 2019) and Rayleigh scattering for all gases (MacDonald & Lewis 2022). We calculate model transmission spectra using opacity sampling on a wavelength grid from 0.8–2.9μm, and we use nested sampling via the `PyMultiNest` (Feroz et al. 2009c; Buchner et al. 2014) Python package with 1000 live

[7] https://github.com/MartianColonist/Cthulhu

points to explore the parameter space for both of our retrievals.

Our POSEIDON retrievals on the spherical transmission spectrum of WASP-94A b find an atmospheric metallicity and C/O ratio that are severely inconsistent with our 1.5D PICASO simultaneous morning/evening limb retrieval. However, the constraints on metallicity ([M/H]=+1.82±0.2) and C/O (C/O=0.28±0.09) obtained with the patchy cloud POSEIDON retrieval on the spherical spectrum are consistent with the constraints from the PICASO 1D retrieval on the spherical spectrum. The retrieved posteriors on metallicity and C/O are shown in the (**B**) and (**C**) panels of Fig. 8.21. Additionally, the cloud coverage fraction we retrieve, $0.93^{+0.04}_{-0.05}$, cannot rule out a fully cloudy atmosphere, in conflict with our observed relatively cloud-free evening limb. The posterior distribution for the cloud coverage fraction is shown in the (**D**) panel of Fig. 8.21. This inconsistency suggests that the use of a cloud coverage fraction as a parameterization of 2D clouds in retrievals on spherical transmission spectra yields inaccurate results, just like 1D retrievals without patchy clouds, in situations like this where there are significant differences in the cloud coverage of one planet limb from the other.

8.6.2.2 3D Atmospheric Global Circulation Models

We use the Met Office Unified Model (UM) general circulation model (GCM) adopting the same fundamental setup as (Drummond et al. 2020b; Zamyatina et al. 2023; Zamyatina et al. ????) to simulate the 3D atmospheric structure of WASP-94A b. The dynamical core of the UM, (ENDGame (Wood et al. ????; Mayne et al. ????a,b)) solves the full deep-atmosphere non-hydrostatic equations of motion using a semi-implicit semi-

Lagrangian scheme on a constant angular grid. The radiative transfer is computed using SOCRATES (Edwards ????; Edwards & Slingo ????; Amundsen et al. 2014; Amundsen et al. ????; Amundsen et al. 2017) which solves the two-stream radiative transfer equations, handling opacities using the equivalent extinction and correlated-k methods. Opacity sources contained in the radiative transfer scheme are absorption due to CO, H_2O, CO_2, HCN, CH_4, NH_3, Li, Na, K, Rb, Cs and collision-induced absorption due to H_2-H_2 and H_2-He together with Rayleigh scattering due to H_2 and He (for further details, see Appendix A of (Zamyatina et al. 2023)). The chemical component of the UM computes the chemical structure and evolution of hot-Jupiter atmospheres, using an "equilibrium" scheme.

We adopt the PHOENIX BT-Settl stellar spectrum (Rajpurohit et al. ????) matching as closely as possible to the system parameters of WASP-94A from (Ahrer et al. 2024). The UM simulations were initialized with a dayside mean pressure-temperature profile from the 1D radiative-convective-chemistry model ATMO (see for example (Tremblin et al. 2015; Drummond et al. 2016; Drummond et al. 2019)) assuming chemical equilibrium for the species in the chemical network from (Venot et al. 2012). We shift the initial pressure-temperature profile by +600 K, which corrects for deep atmosphere thermal inversions as seen in (Drummond et al. 2020b; Zamyatina et al. ????). Deep atmosphere thermal inversions are purely due to initial conditions and are fundamentally unphysical (Drummond et al. 2020b). In this study, we performed one simulation at solar metallicity, using the compositions of (Asplund et al. ????), considering solely the chemistry of the gas phase treated by an "equilibrium" chemical scheme.

The "equilibrium" simulation calculated the chemical abundances using (a) the Gibbs minimization scheme, following the methodology of (Gordon & McBride 1994), for the C-H-O-N chemical species present in the reduced chemical network from (Venot et al. 2019), and (b) the smoothing of the (Burrows & Sharp 1999) transformation boundaries for the alkali metals. The UM employs a height based grid structure. Due to the temperature contrast between the two sides of the atmosphere, the pressure, for a given height, on the dayside and nightside varies over orders of magnitude. Therefore, as material advects between the dayside and nightside, gravity waves are induced, which cascade through the model domain causing numerical instabilities. As a result, to maintain model stability, we limit the minimum pressure in our UM simulation to 1 mbar. The UM simulation evolved for 1000 Earth days until the upper atmosphere ($10^{-3} - 10^{0}$ bars) reached pseudo-equilibrium, judged by the settling of maximum wind velocities, total outgoing top of atmosphere flux and atmospheric kinetic energy. The remaining parameters for our simulations of WASP-94Ab are given in Table 8.4.

Panel (**A**) of Fig. 8.22 shows the zonal-mean zonal advection timescale over the pressure domain of the model. An equatorial jet extends between the latitudes of $\pm 40^{\circ}$, to a maximum depth of 1 bar. This region has a minimum transport timescale of 1.15 days. Surrounding the equatorial jet, a retrograde flow develops with a typical transport timescale an order of magnitude slower than that within the jet. Panel (**C**) of Fig. 8.22 shows the zonal advection timescales at 1 mbar across different longitudes and latitudes as a color map, revealing the circulation pattern in the model. Panel (**B**) of Fig. 8.22 shows the $T(P)$ profile for the two terminators at mid-latitudes of the GCM. A

Parameter	**Value**	**Units**
Inner radius	1.10×10^8	m
Domain height	2.50×10^7	m
Semi-major axis	0.0554	au
Orbital period	3.95	Earth days
Rotation rate	1.84×10^{-5}	$\mathrm{rad\,s^{-1}}$
Surface gravity at inner boundary	4.74	$\mathrm{m\,s^{-2}}$
Specific gas constant	3517.24	$\mathrm{J\,K^{-1}\,kg^{-1}}$
Specific heat capacity	1.30×10^4	$\mathrm{J\,K^{-1}\,kg^{-1}}$
Stellar irradiance	1.46×10^6	$\mathrm{W\,m^{-2}}$
Stellar constant at 1 au	4494.55	$\mathrm{W\,m^{-2}}$
Intrinsic temperature	100	K
Longitude grid resolution	2.5	degrees
Latitude grid resolution	2	degrees
Number of vertical grid levels	66	-

Table 8.4: WASP-94A b parameters used in the UM general circulation model simulations.

temperature difference of 350 K is found between the morning and evening terminators of WASP-94A b at 1 mbar, which agrees well with the temperature difference constrained from the Bayesian retrievals on the limb asymmetric spectrum (448± 78 K). Panel (**D**) shows a color map of the temperature at 1 mbar across different latitudes and longitudes of the model, showing that the evening terminator is hotter than the morning terminator for most of the mid-latitudes surrounding the equatorial region of the planet.

To investigate the cloud distribution at the morning and evening terminators, we post-process condensates, using the cloud-free GCM outputs as inputs for the `VIRGA` cloud model. The $T(P)$ and K_{zz} profiles at each latitude-longitude pair of the GCM were used as inputs to the `VIRGA` model for calculating the cloud distribution. A map of the cloud optical depth at 6 mbar as a function of latitude and longitude is shown in panel (**B**) of Fig. 8.23. The colder $T(P)$ profile of the morning terminator, shown in panel (**B**) of Fig. 8.22, allows formation of Fe, MnS, and $MgSiO_3$ clouds. The enhanced nightside cloud formation can be seen in the increased opacity in panel (**B**) of Fig. 8.23. Condensates in the mid-latitudes of the nightside are transported by the equatorial jet to the morning terminator, resulting in a cloudy morning terminator. However, panel (**B**) of Fig. 8.22 shows that the evening terminator is too hot for these condensates. As a result, the cloud particles are evaporated in the evening terminator causing little cloud opacity in the evening terminator, as shown in panel (**B**) of Fig. 8.23.

Panel (**A**) of Fig. 8.23 shows the globally averaged K_{zz} profile estimated using the RMS of the vertical velocity along isobars and scale heights of the atmosphere. The K_{zz} profile from our GCM simulation is consistent with the constraints from the

retrievals from 1 bar to 1 mbar within 2σ uncertainty on the retrieved value. We also use the analytical prescription in (Parmentier et al. 2013a) to estimate the strength of the K_{zz} parameter. We find that to keep 0.1 ± 1 dex μm cloud particles aloft near a pressure of 0.01 mbar at a temperature of 1500 ± 100 K, the strength of mixing should be $log_{10}(K_{zz}) = 10\pm1$ in cgs units, which is consistent with our finding from both the cloud model and the GCM. Therefore, the vertical mixing at the morning terminator is strong enough to sustain small condensate particles at lower pressures probed by observations of the morning spectrum.

In this work, radiatively active clouds have been omitted due to the computational cost and complexity of coupling a microphysical cloud model with a GCM. The radiative effects of clouds have been studied using the UM in (Lines et al. 2018) and (Lines et al. 2019), using two different cloud models (the latter similar to that used within VIRGA), which both demonstrated the importance of the radiative impact of clouds (alongside, e.g., (Roman & Rauscher 2019)), but produced markedly different cloud structures for the same planet. Therefore, GCM simulations, which include radiatively coupled condensates, are required to further explore the effects of clouds on the temperature and wind structure of WASP-94A b, as well as sensitivities of cloud distribution to model choices.

8.6.2.3 Slope of Morning Limb Transmission Spectrum

We use a parametric model to measure the scattering slope of the morning limb transmission spectrum. Following (Pont et al. 2013; Ohno & Kawashima 2020),

we define the planet radius $R_p(\lambda)$ as,

$$R_p(\lambda) = R_{p0} + H \times S \times \ln\left(\frac{\lambda}{1\mu m}\right) \tag{8.2}$$

where H is the atmospheric pressure scale height, R_{p0} is the baseline planet radius, and S is the slope of the transmission spectrum. We fit the morning limb spectrum of WASP-94A b using this parameterization and assuming H=1460 km. Fig. 8.24 shows constraints on the slope of the spectrum S=-1.33±0.23. Even though we do not use the extracted 2nd order spectrum to determine the slope, Fig. 8.24 panel (**D**) shows that the fit is consistent with the 2nd order spectrum. We find a slope of $S = -1.33 \pm 0.23$ which is significantly smaller than a Rayleigh-scattering slope of $S = -4$. Instead, the slope is close to -1 as expected from grains in the settling regime with a constant mass fraction distribution of sizes (Pont et al. 2013). A constant slope over a wide wavelength range from the SOSS observations can be constraining for cloud and haze models, as many potential aerosol species have expected spectral features within this wavelength range (Wakeford & Sing 2015).

8.6.2.4 Can hazes better fit the morning limb spectrum than clouds?

A morning planet limb heavily obscured by aerosols and a nearly clear evening limb is very difficult to reconcile with a scenario where hazes are the dominant component of aerosols in WASP-94A b. The main reason behind this is because haze precursors are only produced in the highly UV irradiated permanent dayside of the planet. These hazes should be more or equally abundant on the evening terminator of the planet as the morning terminator. The observations of WASP-94A b are instead

consistent with condensate clouds that are formed on the colder planetary nightside and then cycle between a cooler and cloudier morning terminator and a clearer and hotter evening terminator. However, we do not detect any specific cloud absorption feature in the wavelengths covered by our observations. Therefore, we also test whether clouds or other hazes provide a better fit to the morning limb spectrum of WASP-94A b. We use the "Flexible Cloud Layer" [8] functionality of the `VIRGA` cloud model to simulate the effect of various aerosol species on the morning limb transmission spectrum from their refractive indices. This method was previously used to model *JWST* observations and is described in (Schlawin et al. 2024a). This `VIRGA` functionality allows us to populate the atmosphere with arbitrary aerosol species using their real and imaginary refractive indices. We assume a Gaussian particle size distribution for the aerosols with two parameters– the mean particle size ($r_{\rm mean}$), and the standard deviation of the particle size distribution ($\sigma_{\rm r}$). We fix the $\sigma_{\rm r}$, or width of the distribution, to 0.01. This is to populate the atmosphere with a narrow particle size distribution for the aerosols.

The aerosol model that we use for silicate clouds here has three other tunable inputs– the base pressure of the cloud deck ($P_{\rm base}$), a column density of all aerosol particles (ndz), and a scaling parameter for the layer-by-layer aerosol optical depth ($f_{\rm layer}$). The cloud optical depth is set to 0 for pressures larger than $P_{\rm base}$, whereas it is scaled with $e^{-f_{\rm layer} z/H}$ for layers with pressures smaller than $P_{\rm base}$. z/H is an arbitrarily set monotonically increasing number with decreasing pressure. This scaling factor ensures that the cloud optical depth decreases exponentially with increasing altitude above the

[8] https://natashabatalha.github.io/virga/notebooks/9_CustomCloudLayer.html

cloud base, like seen in microphysical cloud simulations (Ackerman & Marley 2001b; Gao & Benneke 2018a; Helling et al. 2020). This custom cloud model therefore has four tunable parameters– ndz, $f_{\rm layer}$, $P_{\rm base}$, and $r_{\rm mean}$ for a given cloud species with input refractive indices.

To simulate haze-like aerosols, we instead use a box-like optical depth profile with two parameters – $P_{\rm base}$ and $P_{\rm top}$. Here, the optical depth profile doesn't decrease with altitude for pressures smaller than $P_{\rm base}$ but remains constant between $P_{\rm base}$ and $P_{\rm top}$. This is to mimic high-altitude hazes in the atmosphere, whose optical depths could show an increase with decreasing pressures due to the comparatively higher prevalence of haze-producing photochemical reactions in the upper atmosphere compared to the deeper planetary atmosphere (Ohno & Kawashima 2020; Gao & Zhang 2020). This parametric model closely mimics the regime of haze formation where the haze distribution in the atmosphere is determined by a balance between haze transport timescale and haze coagulation timescale, as pointed out in (Gao & Zhang 2020).

We use these custom aerosol models to fit the morning limb transmission spectrum with 5 types of aerosols– Titan tholins with refractive indices from (Khare et al. 1984) (haze model), soots with refractive indices from (Lavvas & Koskinen 2017) (haze model), Saturn-like phosphorus hazes with refractive indices from (Noy et al. 1981; Sromovsky et al. 2020; Fletcher et al. 2023) (haze model), 400 K Tholins with refractive indices from (He et al. 2024) (haze model), and enstatite clouds ($MgSiO_3$) with optical constants from (Scott & Duley 1996) (cloud model). We use the same Bayesian sampling method as our retrievals to estimate the free parameters of our aerosol model for

each type of aerosol. As the morning limb spectrum is devoid of prominent gas absorption features, we fix the $T(P)$ profile and chemistry of the atmosphere to the best-fit retrieved model for the morning limb spectrum with our 1.5D retrieval setup.

Fig. 8.25 shows the best-fitting model for the morning limb spectrum from each of these haze/cloud species. The evidence value associated with each aerosol model is also shown in the legend. The model with enstatite clouds shows the highest evidence value of $ln(Z) = -25.1$ compared to the other haze species. The haze model that has the next nearest evidence value ($ln(Z) = -32.1$) to this cloud model is the Tholin haze with optical constants from (He et al. 2024). This suggests that the cloud model is preferred over these other haze species at a significance of 4.15σ or higher. This preference of clouds in addition to the formation-location-circulation argument makes hazes a very unlikely cause of the observed asymmetry in the morning/evening limb spectrum of WASP-94A b. The Bayesian evidence for each aerosol species along with constraints on the model parameters for them are presented in Table 8.5.

8.6.2.5 Atmospheric Mass Loss

The transmission spectrum exhibits excess metastable 1.083 μm helium absorption, though the line profile remains unresolved. Fig. 8.26 illustrates this absorption feature in the transmission spectrum and compares the light curve of the pixel containing the helium feature to a neighboring pixel and the white light curve. We constrain the helium transit depth to 1.17%±0.01% and compare it to the white-light depth of 1.12%±0.02%.

Aerosol Type	Parameter Constraints	ln(Z)	Significance relative to clouds
Clouds ($MgSiO_3$)	ndz=16.0±3.4 $log(P_{\rm base})$=-1.6±1.6 $log(f_{\rm layer})$=0.712± 0.08 $log(r_{\rm mean})$= -4.95± 0.23	-25.1	-
Tholin Haze (Khare et al. (1984))	ndz=10.99±0.82 $log(P_{\rm base})$=-2.61±0.54 $log(P_{\rm top})$=-5.95± 0.06 $log(r_{\rm mean})$= -5.51± 0.17	-35.1	4.85σ (disfavored)
Soot (Lavvas et al. (2017))	ndz=5.93±0.46 $log(P_{\rm base})$=-2.45±0.37 $log(P_{\rm top})$=-6.18± 0.12 $log(r_{\rm mean})$= -4.86±0.11	-32.4	4.23σ (disfavored)
Tholin (400 K, He et al. (2023))	ndz=9.85±0.88 $log(P_{\rm base})$=-2.67±0.53 $log(P_{\rm top})$=-6.00±0.079 $log(r_{\rm mean})$= -5.44± 0.25	-32.1	4.15σ (disfavored)
Saturn like Phosphorus haze	ndz=11.59±0.67 $log(P_{\rm base})$=-2.66±0.56 $log(P_{\rm top})$=-5.977±0.06 $log(r_{\rm mean})$=-5.98±0.20	-33.2	4.44σ (disfavored)

Table 8.5: Comparison of model parameters and Bayesian evidences for various aerosol composition in the morning limb of WASP-94A b. Clouds are the most preferred aerosol. The mean radius $r_{\rm mean}$ reported here is in cm.

Fully resolved metastable helium absorption can be used to constrain atmospheric mass-loss parameters; however, the unresolved nature of the absorption profile from NIRISS SOSS complicates this process. To estimate the mass-loss rate of WASP-94A b, we apply the one-dimensional, isothermal Parker-wind model (Parker 1958) using the p-winds code (version 2.0; (Dos Santos et al. 2022)). p-winds follows the original mass-loss formulation of (Oklopčić & Hirata 2018) with modifications introduced by (Lampón et al. 2021) and (Vissapragada et al. 2022). The code leverages planetary and stellar parameters to fit helium absorption features in the transmission spectrum and derive mass-loss properties, including the mass outflow rate and temperature. For this analysis, we assume a He/H fraction of 10/90 and adopt the high-energy spectral energy distribution (SED) of HD 149026 from the MUSCLES database as a proxy for the high-energy SED of WASP-94A b (France et al. 2016; Youngblood et al. 2016; Loyd et al. 2016; Wilson et al. 2021; Behr et al. 2023). However, given the unresolved absorption line profile in our observations, the mass-loss rate and outflow temperature remain degenerate with each other when fitting an isothermal Parker-wind model to the feature. Fig. 8.26 displays an example best-fit given the constraints placed on the mass-loss parameters discussed above. However, the degeneracy between the mass-loss rate and outflow temperature results in multiple best-fit solutions. The low resolution of this observation, which does not fully resolve the helium triplet feature, leads to a broader line profile to account for the wide helium triplet absorption window. A similar approach was used in the analysis of helium escape in the SOSS spectrum of HAT-P-18b (Fu et al. 2022).

With an estimate of the mass-loss rate, the outflow temperature can be further constrained. (McCreery et al. 2025) used archival helium spectra to estimate the mass-loss efficiency, ε, as defined in the energy-limited mass-loss framework of (Caldiroli et al. 2022):

$$\dot{M} = \frac{3\varepsilon}{4G} \frac{F_{XUV}}{\rho_p} \tag{8.3}$$

For a He/H ratio of 10/90, the efficiency is estimated to be 0.34 ± 0.13 prior to the predicted breakdown of energy-limited mass loss formulations ($F_{XUV}/\rho_p \sim 10^4$) and 0.10 ± 0.06 thereafter. Using Equation 8.3, we constrain WASP-94A b's mass-loss rate to $7.3^{+2.7}_{-2.6} \times 10^{10}$ g/s. Applying p-winds, this corresponds to an estimated outflow temperature of 4000–6000 K. These results align with constraints obtained using the self-consistent hydrodynamics code ATmospheric EScape (ATES) for WASP-94A b (Caldiroli et al. 2021a).

Ground-based, high-resolution spectroscopy is required to resolve the absorption profile and break the degeneracy between mass-loss rate and outflow temperature.

8.6.2.6 Host Star Parameters

The stellar parameters and elemental abundances of WASP-94 A are derived following the methodology of (Reggiani et al. 2022), which integrates photometric and spectroscopic techniques to infer accurate, precise, and self-consistent stellar parameters and abundances. Isochrone analysis utilizes multiwavelength photometry to determine initial stellar parameters, which are iteratively refined via spectroscopy to achieve con-

vergence in effective temperature, surface gravity, and metallicity. This ensures a fully self-consistent approach incorporating both photometry and spectroscopy.

For isochrone fitting, we use the isochrones Python package (Morton 2015) [9], incorporating photometry from Tycho-2 VT and BT (Høg et al. 2000), Gaia DR3 G (Gaia Collaboration et al. 2021), J, H, and K_s from 2MASS (Skrutskie et al. 2006), and CatWISE W1 and W2 (Eisenhardt et al. 2020). We adopt Gaia DR3 parallaxes, with extinction estimates derived from 3D dust maps provided by GTOMO ((Lallement, R. et al. 2022); (Vergely, J. L. et al. 2022)).

For the spectroscopic analysis, we measure equivalent widths (EWs) of Fe I and Fe II absorption lines in an archival ESPRESSO spectrum of WASP-94 A using the REvIEW fitting algorithm [10], with a line list from (Reggiani et al. 2022). We then employ the MOOG wrapper (Ramírez et al. 2014) [11], which uses the fitted EWs and atomic data to minimize inferred FeI and FeII abundances, ensuring independence from reduced equivalent width and excitation potential. The derived stellar parameters are presented in Table 8.6. Uncertainties are estimated by sampling the posterior distributions of $T_{\rm eff}$ and $\log g$ from the isochrone analysis and propagating these through the spectroscopic analysis to assess the range of self-consistent solutions.

To determine elemental abundances of non-iron species, we measure EWs using REvIEW and compute abundances assuming the best-fit stellar parameters from Table 8.6. We then apply non-local thermodynamic equilibrium (NLTE) corrections

[9] https://github.com/timothydmorton/isochrones
[10] https://github.com/madeleine-mckenzie/REvIEW
[11] https://github.com/astroChasqui/q2

Isochrone-based Stellar Parameters		
Parameter	**Value**	**Uncertainty**
Stellar Mass ($M_\odot$)	1.35	± 0.01
Stellar Radius ($R_\odot$)	1.58	± 0.01
Effective Temperature ($T_{\rm eff}$, K)	6140	$^{+80}_{-75}$
Surface Gravity ($\log g$, cm/s^2)	4.17	$^{+0.14}_{-0.13}$
$\log$ Age (Gyr)	9.42	$^{+.04}_{-.02}$
Spectroscopic-based Stellar Parameters		
Parameter	**Value**	**Uncertainty**
[Fe/H] (dex)	.30	± 0.05
ξ(km/s)	1.17	± 0.01

Table 8.6: Isochrone- and spectroscopic-based stellar parameters for WASP-94 A.

by interpolating NLTE correction grids specific to each element and stellar parameter set. Uncertainties are primarily driven by line-to-line scatter. The final abundances, presented in Table 8.7, include only elements with multiple measured lines and reliable, interpolatable NLTE corrections. A full discussion of uncertainty estimation, underlying assumptions, and potential systematics is provided in (Reggiani et al. 2024).

Element ($N_{\mathbf{lines}}$)	**LTE Abundance**	**NLTE Corrected Abundance**
FeI (31)	7.76 ± 0.01	7.71 ± 0.01
FeII (6)	7.77 ± 0.01	7.77 ± 0.01
OI (3)	9.08 ± 0.01	8.72 ± 0.02
CI (5)	8.63 ± 0.05	8.61 ± 0.05
AlI (3)	6.65 ± 0.01	-
BaII (2)	4.30 ± 0.10	4.28 ± 0.10
CaI (3)	6.61 ± 0.02	6.29 ± 0.03
CoI (3)	6.48 ± 0.21	-
CrI (9)	5.93 ± 0.02	-
CrII (5)	5.89 ± 0.01	-
MnI (5)	7.11 ± 0.37	-
NaI (2)	6.56 ± 0.02	6.42 ± 0.02
NiI (16)	6.59 ± 0.02	-
ScI (4)	4.79 ± 0.46	-
SiI (9)	7.82 ± 0.02	7.80 ± 0.02
TiI (10)	5.18 ± 0.02	-
TiII (6)	5.40 ± 0.02	-
VI (3)	4.18 ± 0.03	-
YII (2)	3.34 ± 0.38	-
Abundance Ratios		
Ratio	**Value**	**Uncertainty**
$[Fe/H]_{NLTE}$	0.28	± 0.06
$[C/O]_{NLTE}$	0.12	± 0.05
C/O_{NLTE}	0.78	± 0.10

Table 8.7: LTE and NLTE abundances from the spectroscopic analysis and key abundance ratios for WASP-94 A.

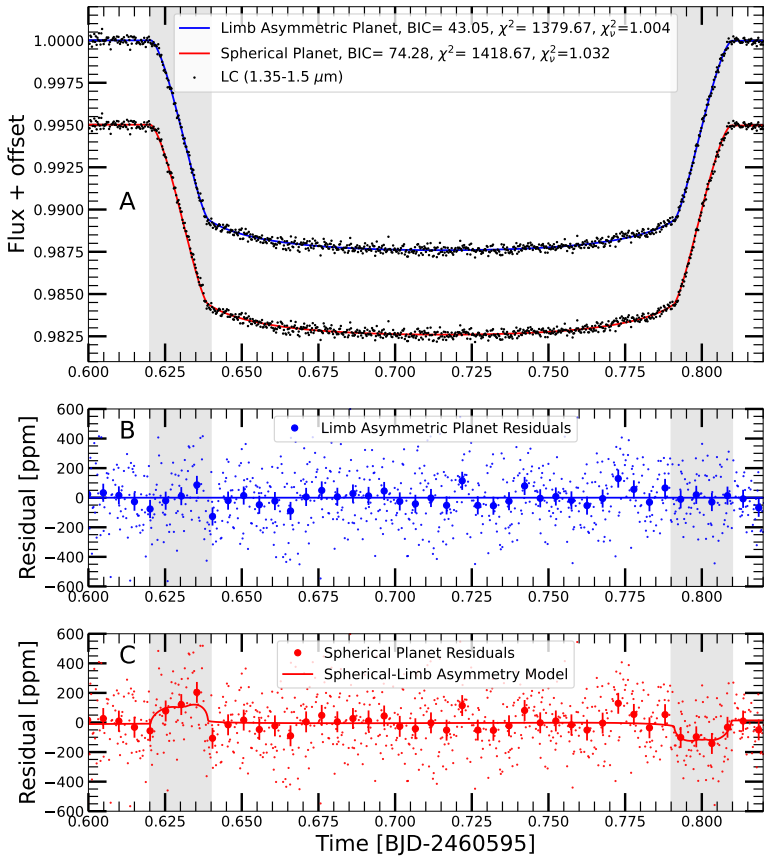

Figure 8.1: **Transit light curves of WASP-94A b show limb asymmetry.** (**A**) shows the broadband light curve between 1.35-1.5 μm with black points. The asymmetric limb planet model fit to the light curve is shown with the blue line and the spherical planet model fit with the red line. The time period of ingress and egress are shown with the shaded gray region. The asymmetric limb model fits the light curve better at a 6σ significance. (**B**) shows the binned (larger points) and unbinned residuals of the asymmetric limb model fit to the data. The residuals are consistently zero. (**C**) shows the binned (larger points) and unbinned residuals of the spherical planet model fit to the data. The residuals are inconsistent with zero during ingress/egress.

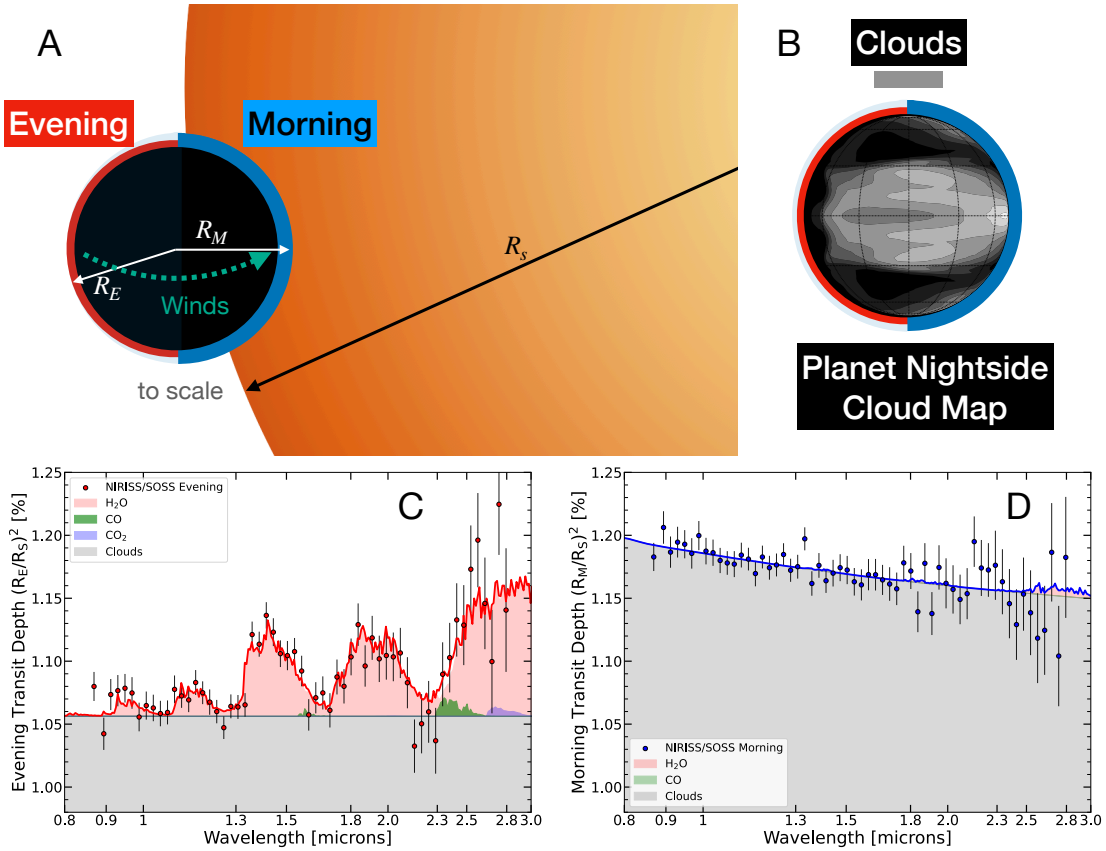

Figure 8.2: **Transmission spectrum of the morning and evening limbs of WASP-94A b**. (**A**) shows the observing geometry of the two limbs of WASP-94A b and its host star (to scale). (**B**) shows the nightside cloud map of WASP-94A b predicted through a 3D general circulation model. (**C**) shows the observed transmission spectrum of the evening terminator of the planet with red points along with the best-fit model. The key atmospheric absorbers shaping the observed spectrum (H_2O, clouds, etc) are shown with the shaded colors. (**D**) shows the observed transmission spectrum of the morning terminator with blue points along with the best-fit model. The spectrum is mainly shaped by cloud scattering as has been shown with the gray shaded region.

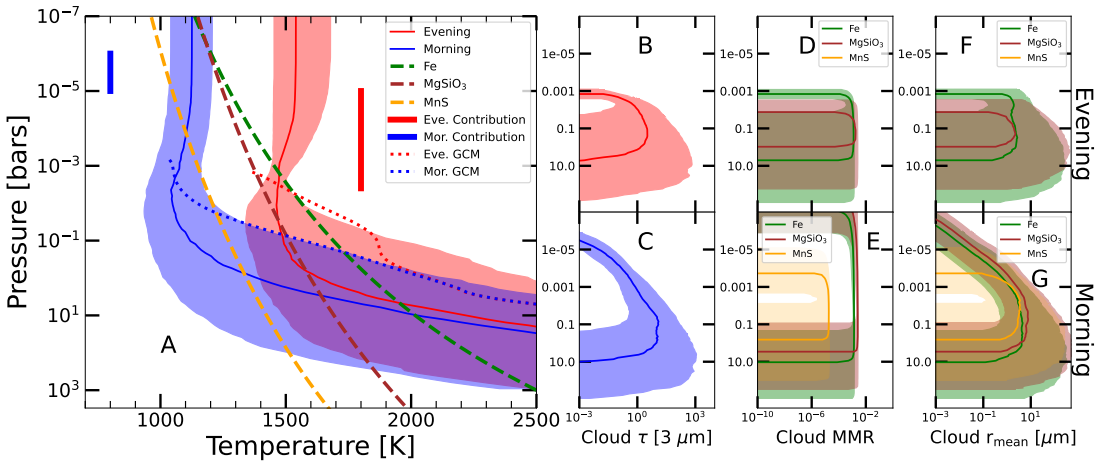

Figure 8.3: **Constrained temperature and cloud structure of the morning and evening limbs.** (**A**) shows the median and 1σ envelopes on the retrieved temperature-pressure profile for the morning and evening terminators in blue and red, respectively. Condensation curves corresponding to $MgSiO_3$, Fe, and MnS clouds are shown with the red, green, and yellow dashed lines, respectively. The $T(P)$ profiles of the two terminators derived from the 3D general circulation model are also shown with dotted lines. The vertical solid red and blue lines show the range of pressures probed by the transmission spectrum of the evening and morning limbs, respectively. (**B**) and (**C**) shows the retrieved cloud optical depth as a function of pressure like (**A**) for the evening and morning terminators , respectively. (**D**) and (**E**) shows the retrieved cloud mass mixing ratio as a function of pressure for the evening and morning terminators, respectively. Mass mixing ratio of Fe, $MgSiO_3$, and MnS are shown with green, brown, and orange shaded regions in both panels, respectively. (**F**) and (**G**) shows the retrieved mean cloud particle radius as a function of pressure for the evening and morning terminators, respectively. Particle sizes of Fe, $MgSiO_3$, and MnS cloud are shown with green, brown, and orange shaded regions in both panels, respectively. (**B**)-(**G**) panels show the same pressure range in the y-axis as (**A**).

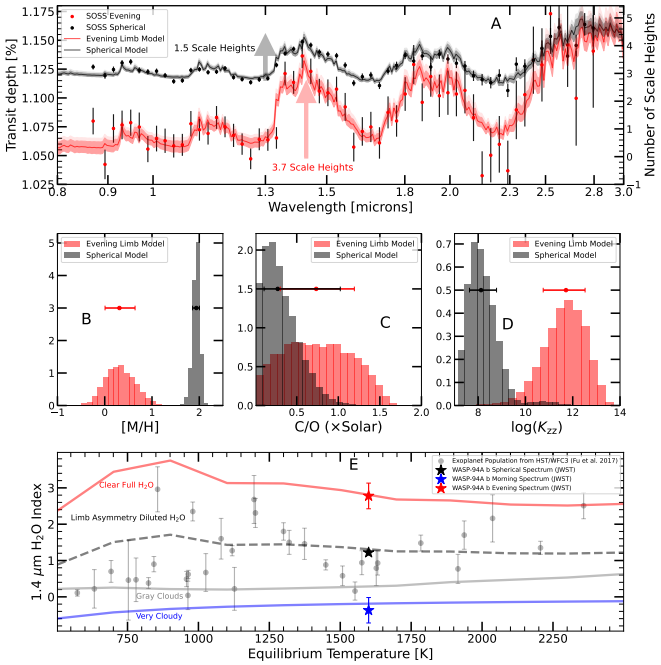

Figure 8.4: **Effect of limb asymmetry on inferred composition of WASP-94A b.** (**A**) shows a comparison of the observed transmission spectrum of the evening terminator of WASP-94A b in red with the 1D spectrum extracted assuming the planet is spherically symmetric in black. The red and black shaded regions show the 1σ envelope on the retrieved model spectrum in each case. The scale height of the spherical spectrum gets artificially muted relative to the scale height of the evening terminator spectrum by more than a factor of $\sim$2 due to very asymmetric limbs of the planet. (**B**) shows the effect of this muting on the inferred metallicity of the planet between the two cases. The metallicity inferred from the spherical spectrum (black) is biased at a 5σ level. (**C**) shows the bias on the posteriors of the inferred C/O ratio. (**D**) shows that the strength of the vertical mixing parameter K_{zz} also gets biased at 2σ level. (**E**) shows a comparison of the 1.4 μm H_2O feature amplitude for a population of exoplanets measured with the *HST*/WFC3 instrument with light gray points. The black point shows the H_2O feature amplitude measured from the spherical spectrum of WASP-94A b while the red and blue points show the H_2O amplitude for the evening and morning terminators, respectively. The red and blue solid lines and the black dashed lines show the H_2O amplitude from atmospheric models for a clear, very cloudy, and limb-asymmetry affected planet, respectively. This shows that these biases are likely to affect a much wider population of exoplanets other than just hot Jupiters.

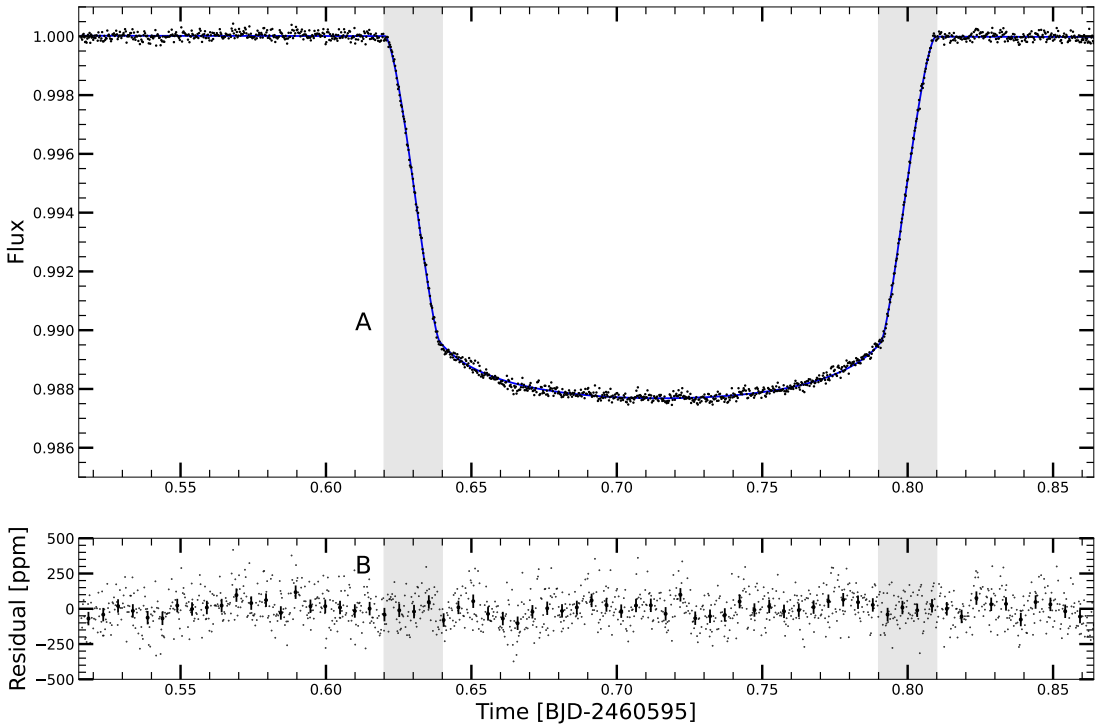

Figure 8.5: **Observed and modeled white light curve**. (**A**) shows the observed white light curve of WASP-94A b from the FIREFLy reduction with black points and the best-fit asymmetric limb model from catwoman is shown with the blue line. (**B**) shows the binned and unbinned residuals of the fit, that have a median absolute deviation of 76 ppm.

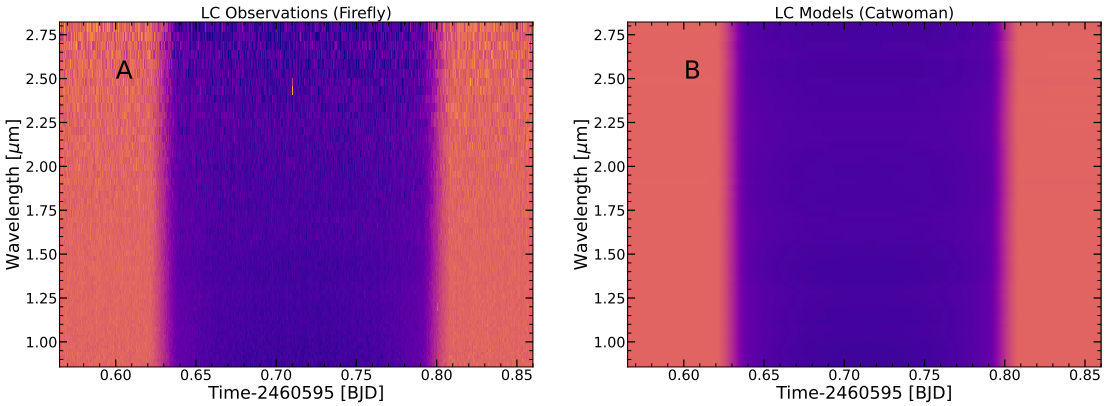

Figure 8.6: **Observed and modeled spectroscopic light curves**. (**A**) shows the observed spectroscopic light curves as a heat map. (**B**) shows the model fits to the spectroscopic light curves as a heat map with FIREFLy.

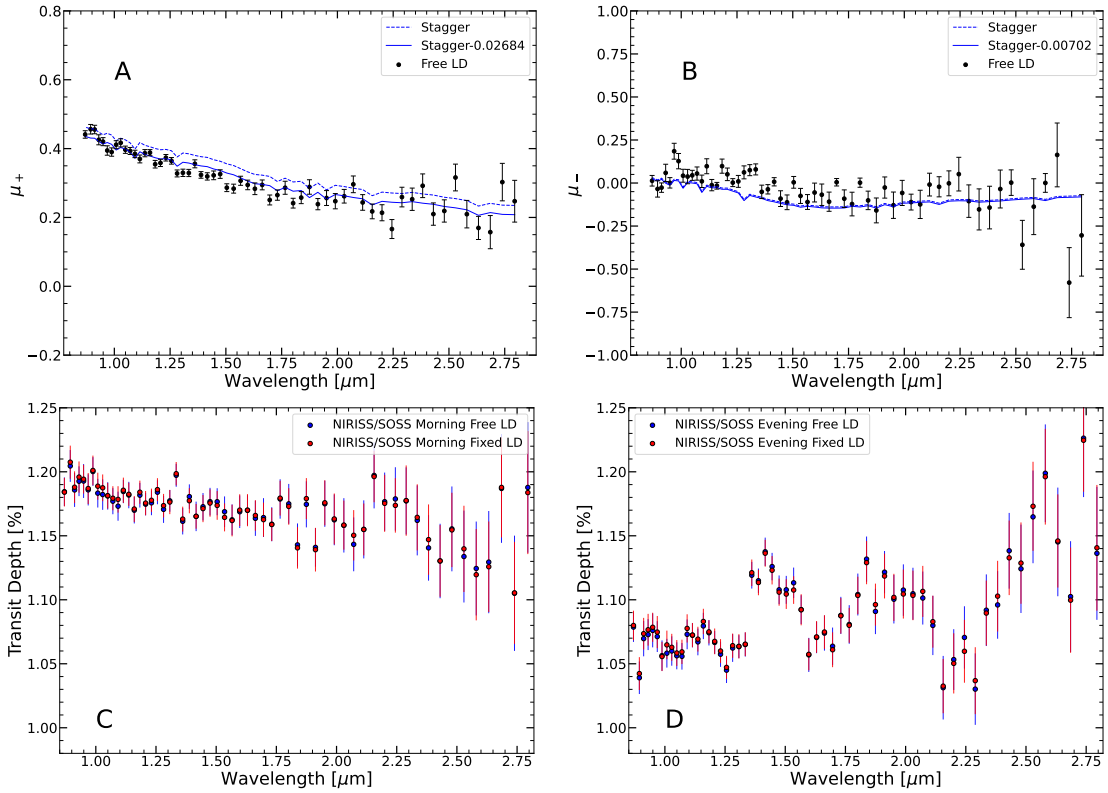

Figure 8.7: **Effect of limb darkening on the transmission spectrum**. (**A**) shows the u_+ parameter when fitted freely for each spectroscopic channel with black points. The u_+ parameter from a 3D stellar model with and without offset are shown with the blue lines. (**B**) shows the same for the u_- parameter. (**C**) and (**D**) show the measured transmission spectrum of the morning and evening limbs, respectively. The blue points in each panel show the spectrum when limb darkening is fitted freely and the red points show the spectrum when limb darkening parameters are fixed to the 3D stellar model+offset.

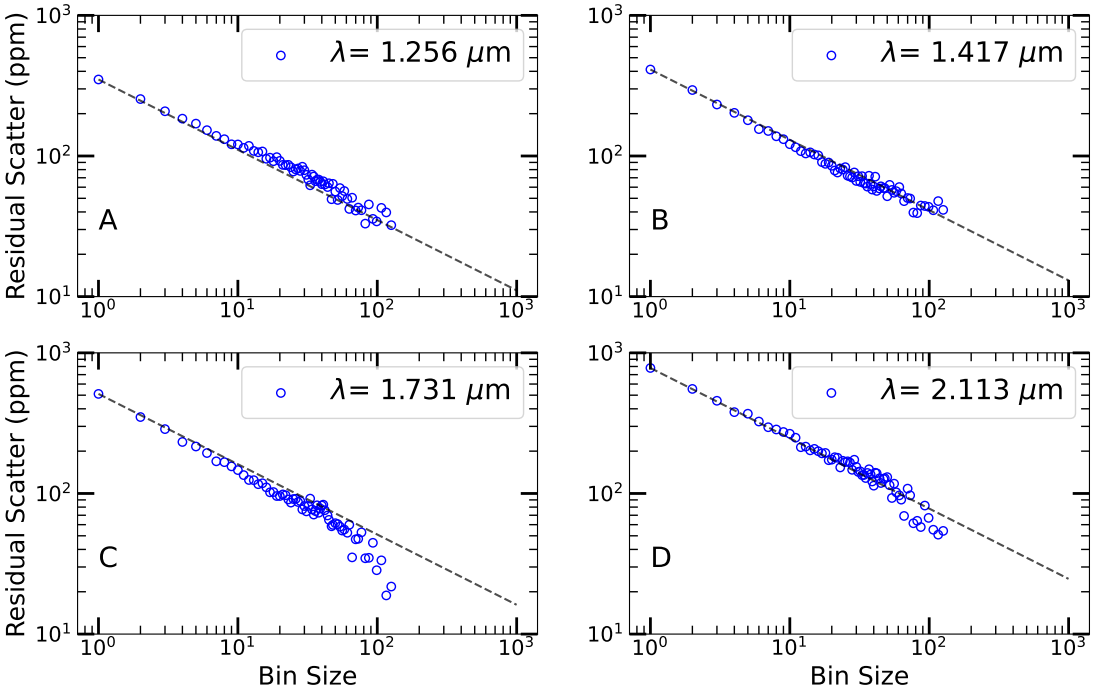

Figure 8.8: **Allan variance plots showing correlated noise behavior in spectroscopic light curves**. (**A**), (**B**), (**C**), and (**D**) show the Allan variance plots for four randomly selected spectroscopic channels. Each plot shows that neglegible correlated noise is present in the spectroscopic light curves.

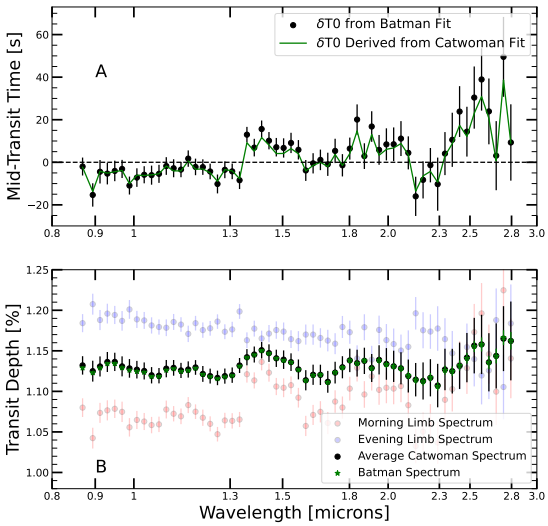

Figure 8.9: **Alternative evidence of limb asymmetry in spectroscopic light curves.** (**A**) shows the mid-transit time (T_0) as a function of wavelength with black points, when all the spectroscopic light curves were fit with the spherical planet model allowing for an independently fitted T_0 for each channel. The fitted T_0 compensates for the limb asymmetry of the planet and thus shows molecular features in H_2O absorption bands. The T_0 spectrum calculated from the measured spectrum of the two limbs of the planet is shown with the green line. (**B**) shows a comparison of the average planet spectrum (green) derived from the spectrum of the two limbs (blue and red) with the spherical planet spectrum extracted with the spherical planet model (black).

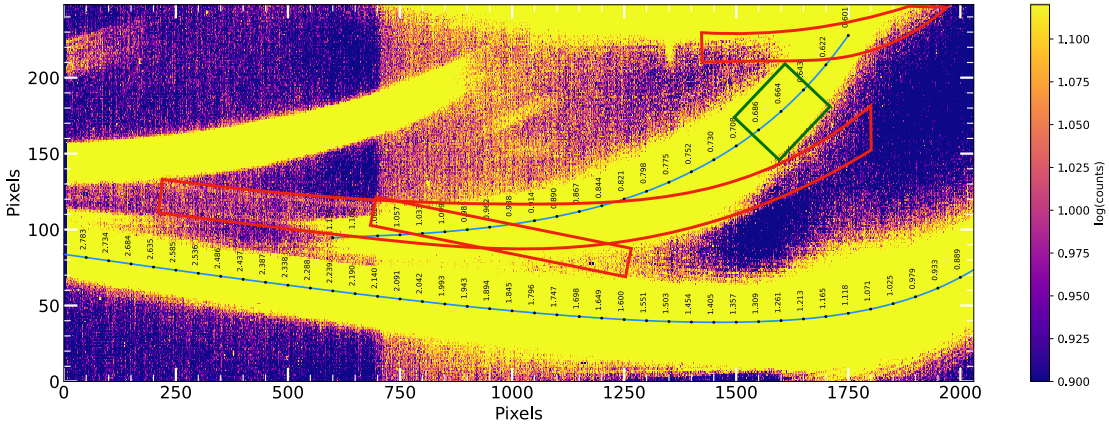

Figure 8.10: **Contamination of the 2nd order trace.** Contamination of the 2nd order trace of the stellar spectrum is highlighted with red boxes on the detector image. The green box is the only small region from which we could reliably extract transmission spectrum. The wavelengths of each region of the 1st and 2nd order trace are marked on the blue line.

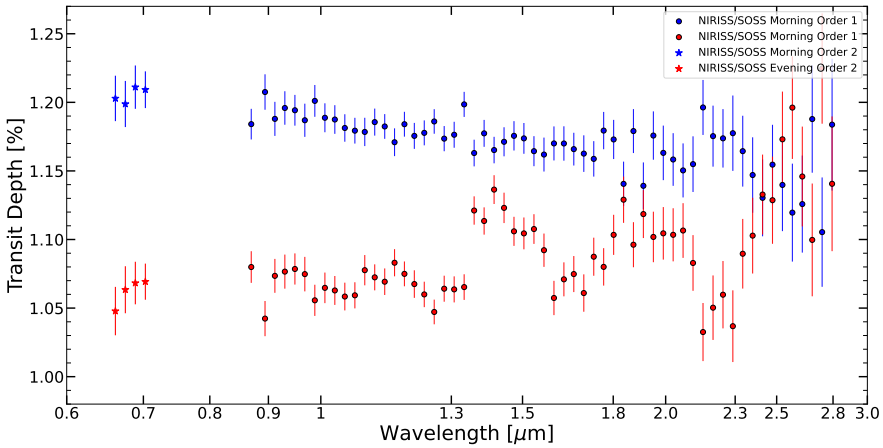

Figure 8.11: **2nd order transmission spectrum.** Extracted 2nd order spectrum is shown with the star points and is compared with the 1st order spectrum of each planet limb (circular points).

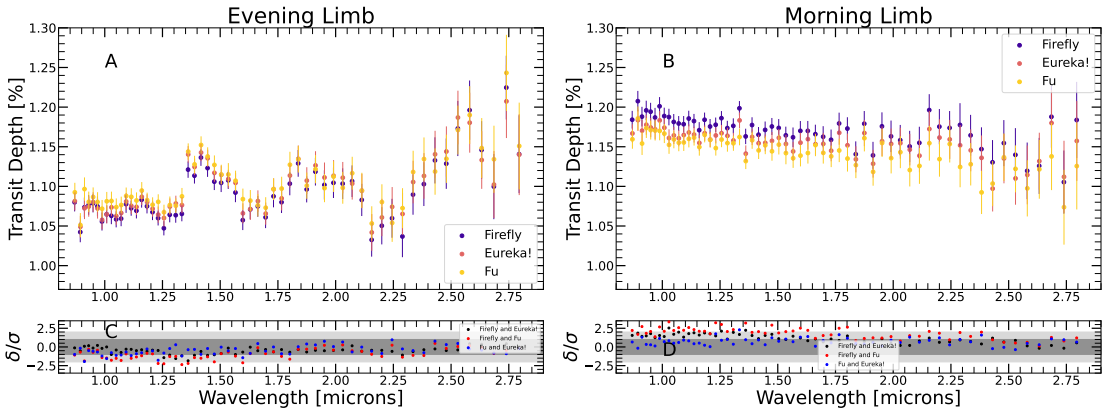

Figure 8.12: **Comparison between spectrum of morning and evening limbs from different reduction pipelines.** (**A**) shows the comparison of the evening limb spectrum measured from three different reduction pipelines – FIREFLy, Eureka!, and Fu. (**B**) shows the same for the morning limb spectrum. (**C**) and (**D**) show the residuals between the spectrum derived from each pipeline for the evening and morning limbs, respectively.

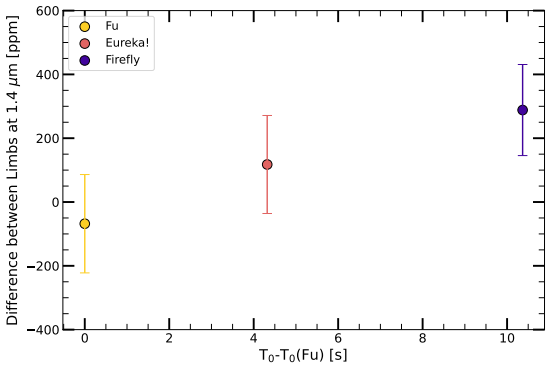

Figure 8.13: **Correlation between mid-transit time and difference in transit depths between limbs.** The difference in the transit depths between the morning and evening limbs at 1.4 μm from the three data reduction pipelines is shown as a function of the constrained mid-transit time from the white light curves from each pipeline. The difference between the mid-transit time from a pipeline and the mid-transit time from the Fu pipeline is plotted in the x-axis. Note that the uncertainty in the constrained T_0 from each pipeline is larger than the difference in T_0 between the pipelines.

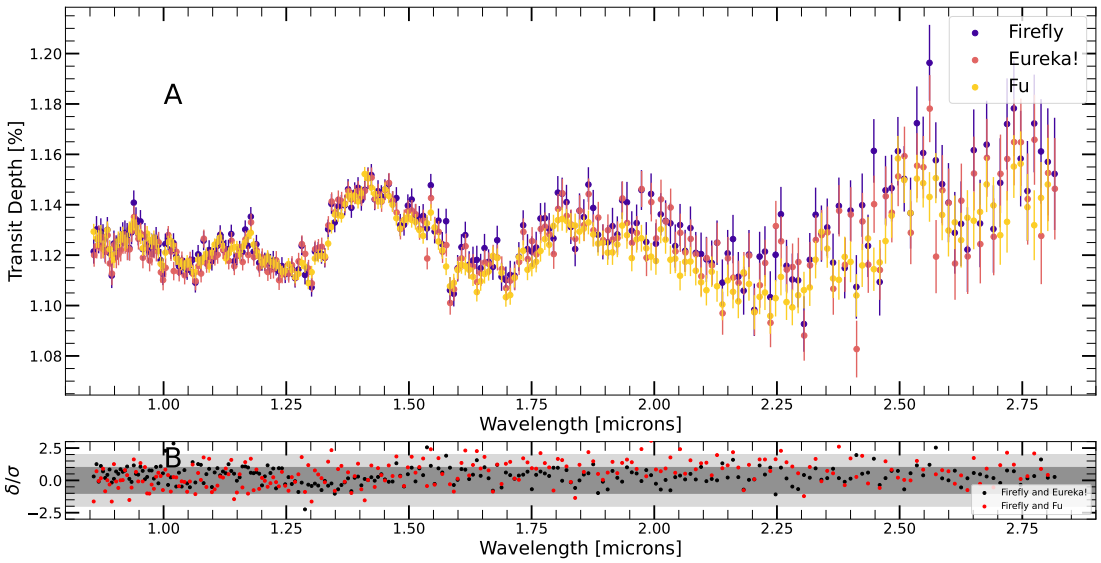

Figure 8.14: **Comparison between spherical planet spectrum between pipelines.** (**A**) shows a comparison between the spectrum measured for the planet assuming a spherical planet model between the three pipelines. (**B**) shows the residuals between the pipelines.

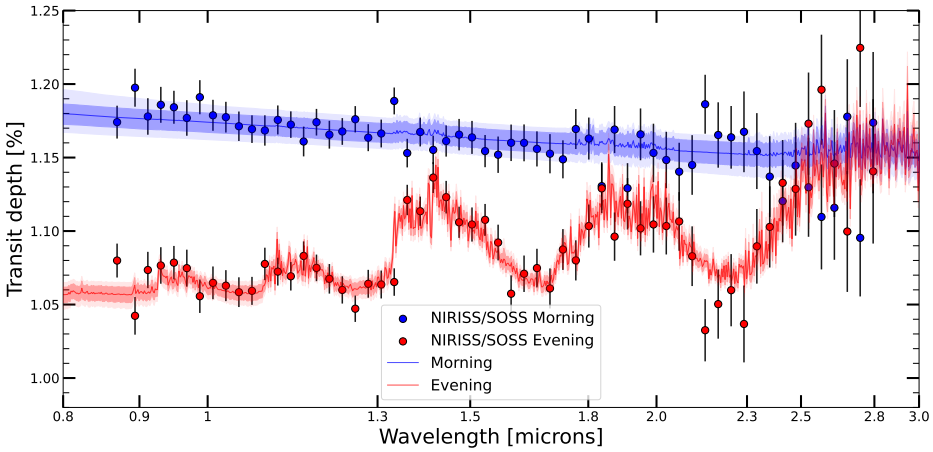

Figure 8.15: **Retrieved spectrum for each planet limb**. The retrieved median spectrum for the evening and morning limbs along with their 1σ and 2σ envelopes are shown in red and blue, respectively. The observed evening and morning spectrum are also shown with red and blue points, respectively.

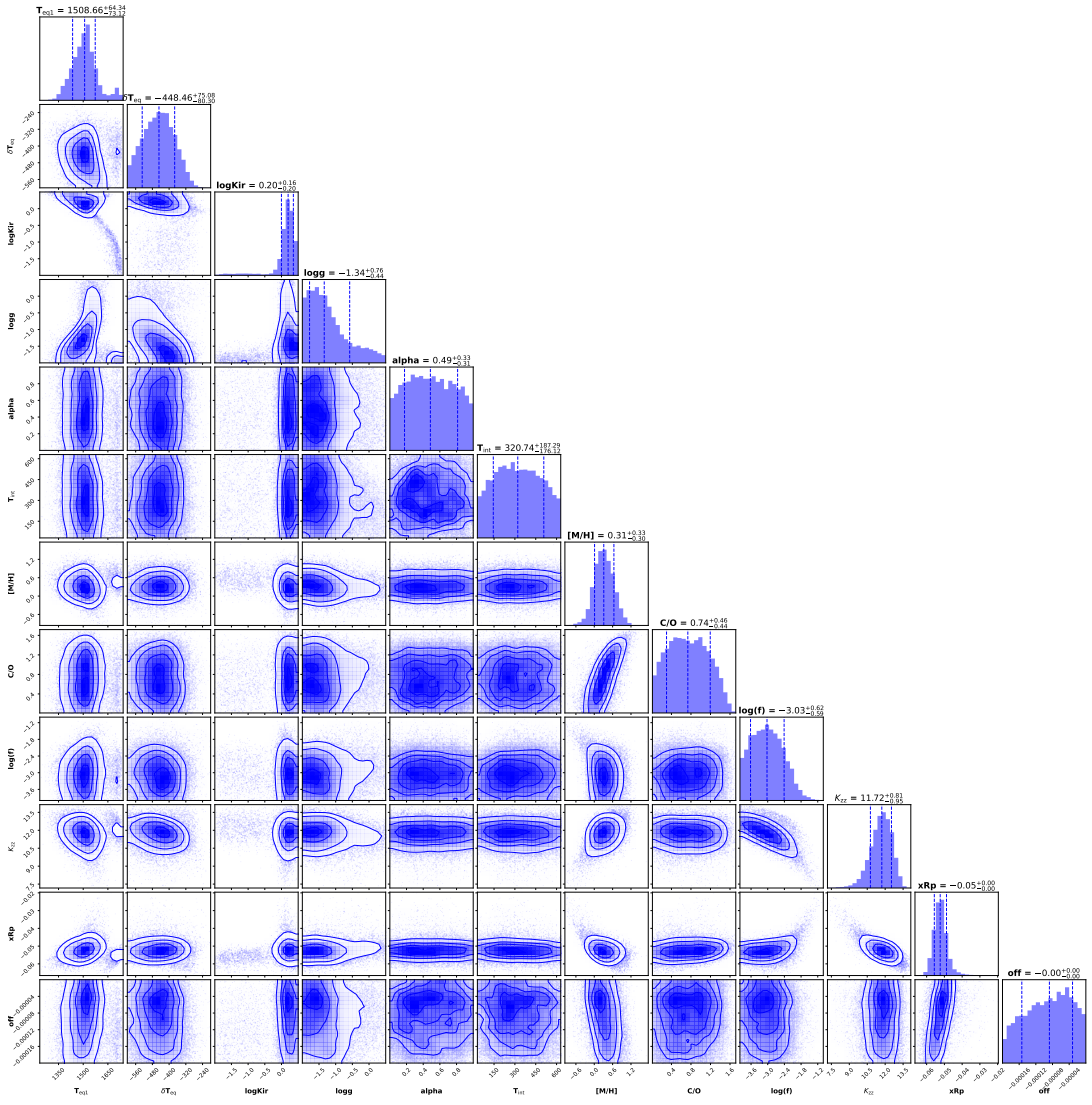

Figure 8.16: **Corner plot for simultaneous retrieval on both limbs**. The posterior distribution for each parameter along with their cross-correlations are shown for the 1.5D simultaneous retrieval on the spectrum of the evening and morning limbs of the planet.

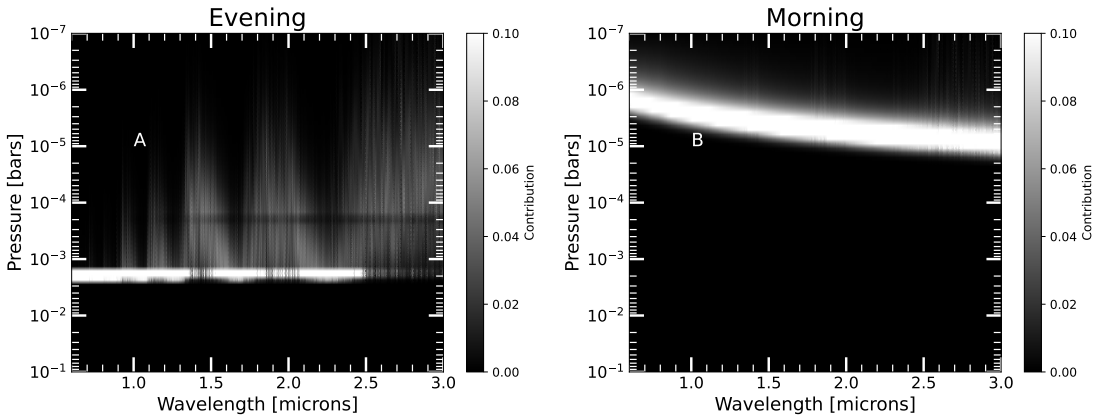

Figure 8.17: **Contribution function for the evening and morning limb spectrum**. (**A**) shows the contribution function as a function of pressure and wavelength from the best-fit 1.5D retrieval model for the evening limb. The contribution function is derived from the derivative of the transmittance with pressure for each wavelength value. (**B**) shows the contribution function for the morning limb spectrum.

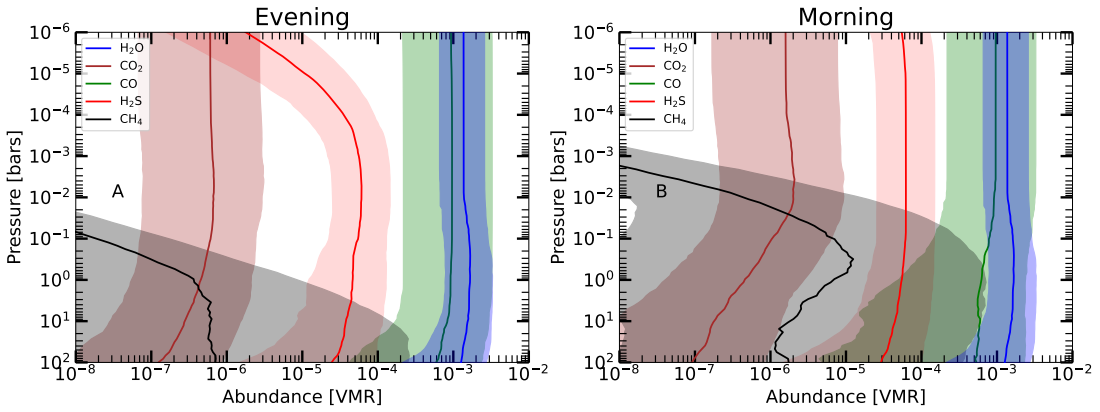

Figure 8.18: **Constraints on Chemical Abundances**. (**A**) shows the constraints on the chemical abundances of various atmospheric gases on the evening limb of the planet. (**B**) shows the constraints on the morning limb. Note that we detect H_2O from the spectrum but the chemical equilibrium assumption allows us to predict the abundance constraints on the other gases.

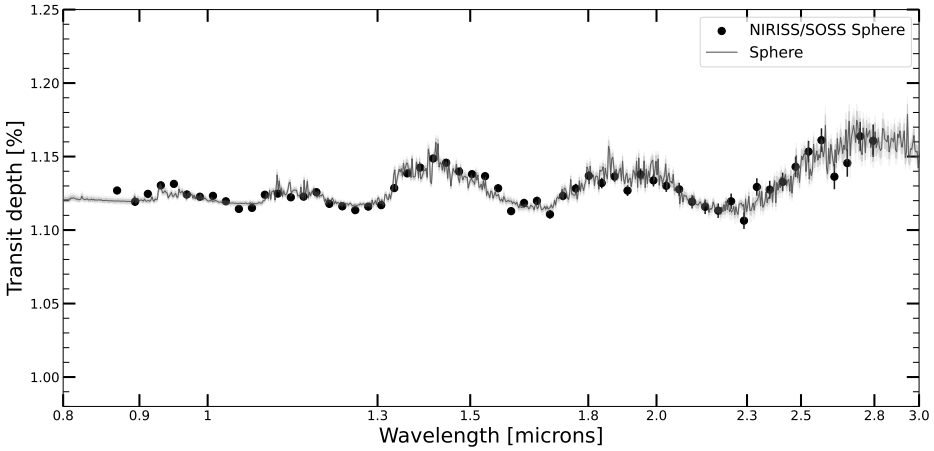

Figure 8.19: **Retrieved spectrum for the spherical planet spectrum**. The retrieved median spectrum for the spherical planet spectrum along with its 1σ and 2σ envelopes are shown in black. The measured spherical planet spectrum is shown with black points.

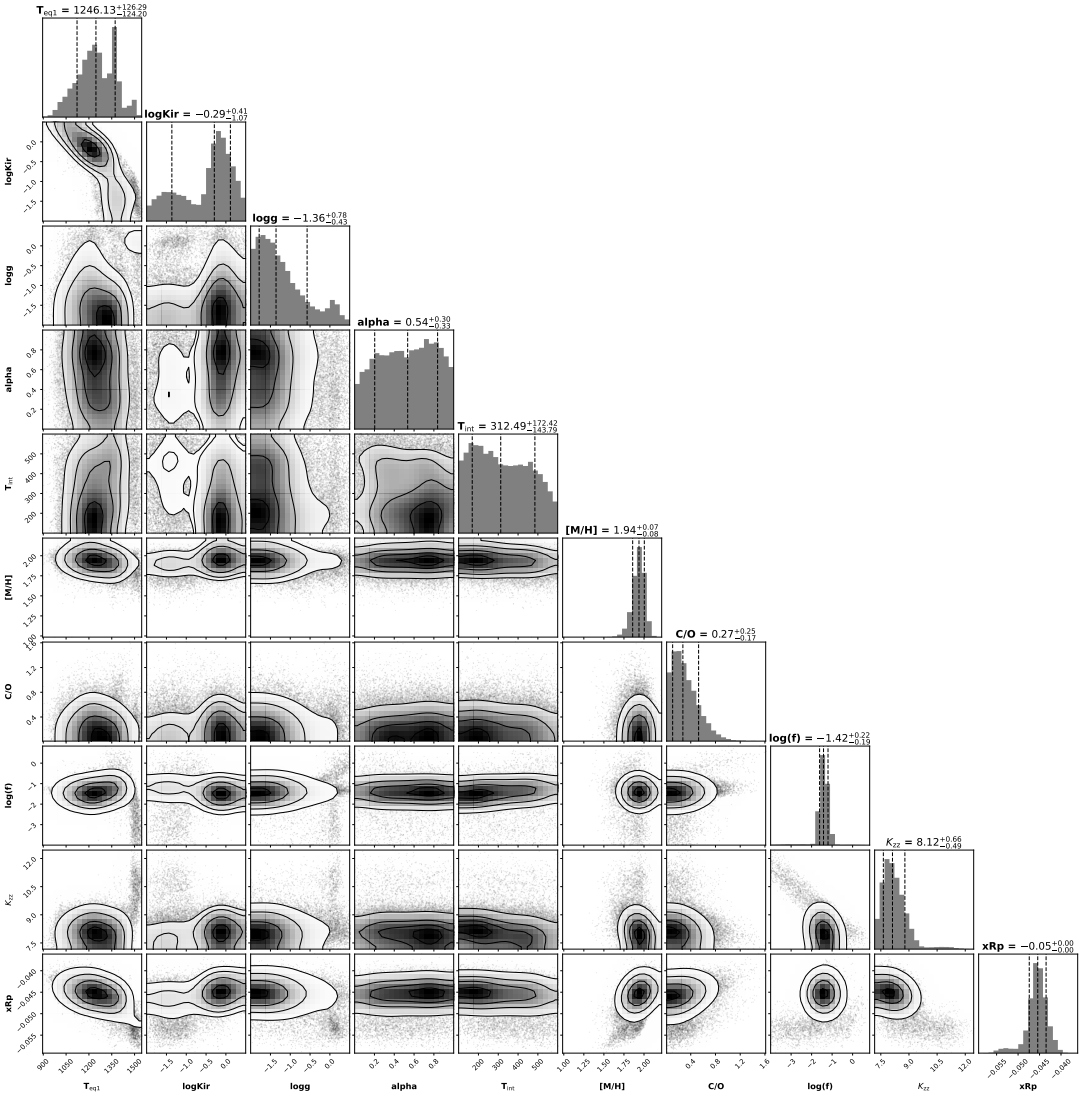

Figure 8.20: **Corner plot for 1D retrieval on the spherical spectrum of the planet**. The posterior distribution for each parameter along with their cross-correlations are shown for the 1D `PICASO` retrieval on the spherical spectrum of the planet.

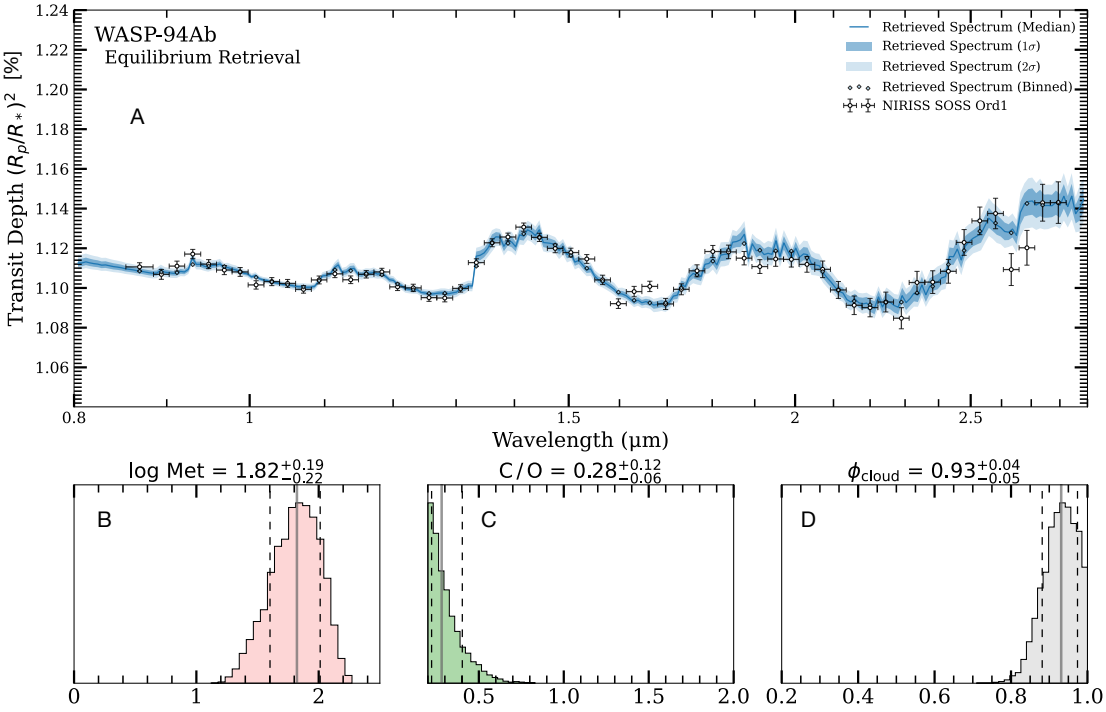

Figure 8.21: **Results of the patchy 2D cloud retrieval with POSEIDON**. (**A**) shows the retrieved median spectrum along with the 1σ and 2σ regions in blue, along with the measured spherical planet spectrum as unfilled black points. (**B**), (**C**), and (**D**) shows histograms of the posterior for the planet's atmospheric metallicity, C/O ratio, and cloud coverage fraction, respectively.

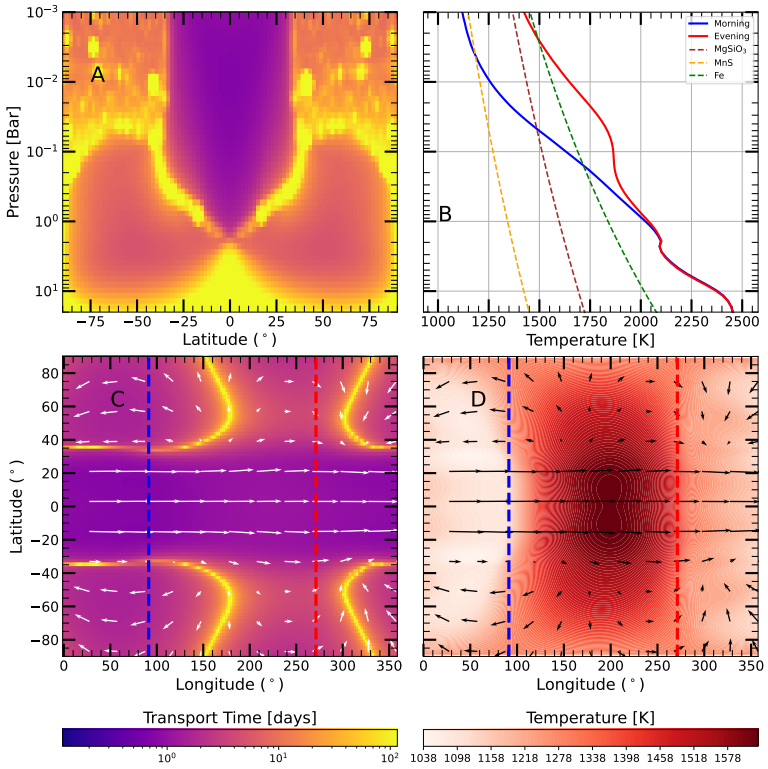

Figure 8.22: **3D atmospheric structure from GCM simulations of WASP-94Ab.** (**A**) shows zonal-mean zonal advective timescale (colour scale) as a function of pressure and latitude. (**B**) shows the $T(P)$ profiles, at latitude 0°, for the morning (blue) and evening (red) terminators. Condensation curves for $MgSiO_3$, Fe, and MnS are also shown with the dashed lines. (**C**) shows the zonal advective timescale at 1 mbar (colour scale) as a function of longitude and latitude. The wind direction is marked with white arrows. (**D**) shows the temperature (colour scale) for an isobaric surface at 1 mbar. All plots are generated with data corresponding to the final day of the simulation, horizontal wind vectors have been over-plotted to aid interpretation.

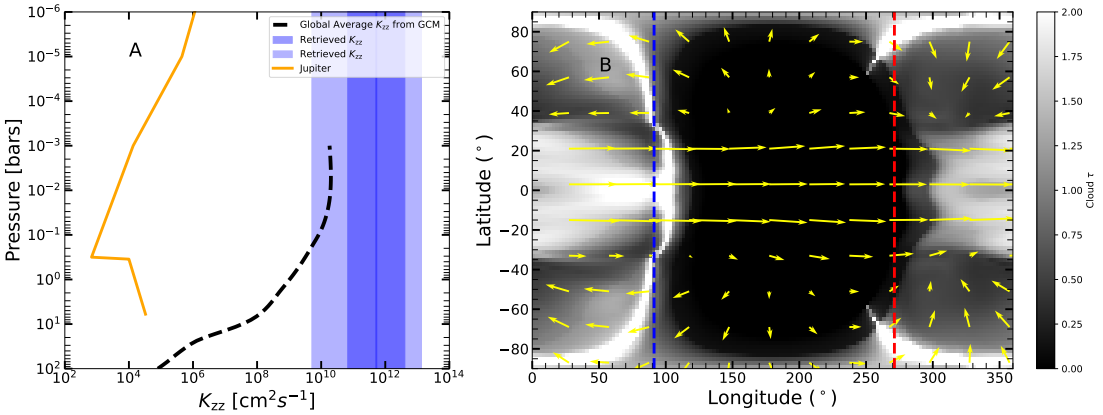

Figure 8.23: **Vertical mixing and cloud properties from GCM simulations of WASP-94A b.** (**A**) shows a comparison of the global mean K_{zz} profile from the GCM (black dashed line) with the constraints on K_{zz} from the limb asymmetry observations shown as the blue shaded region. The measured K_{zz} profile for Jupiter from (Moses et al. 2005) is shown with the orange line. (**B**) shows the cloud optical depth map at 6 mbar obtained by post-processing the GCM with $MgSiO_3$, Fe, and MnS clouds using the `VIRGA` model. The morning terminator appears cloudy while the evening terminator is relatively clear. Wind vectors have been over-plotted to aid interpretation.

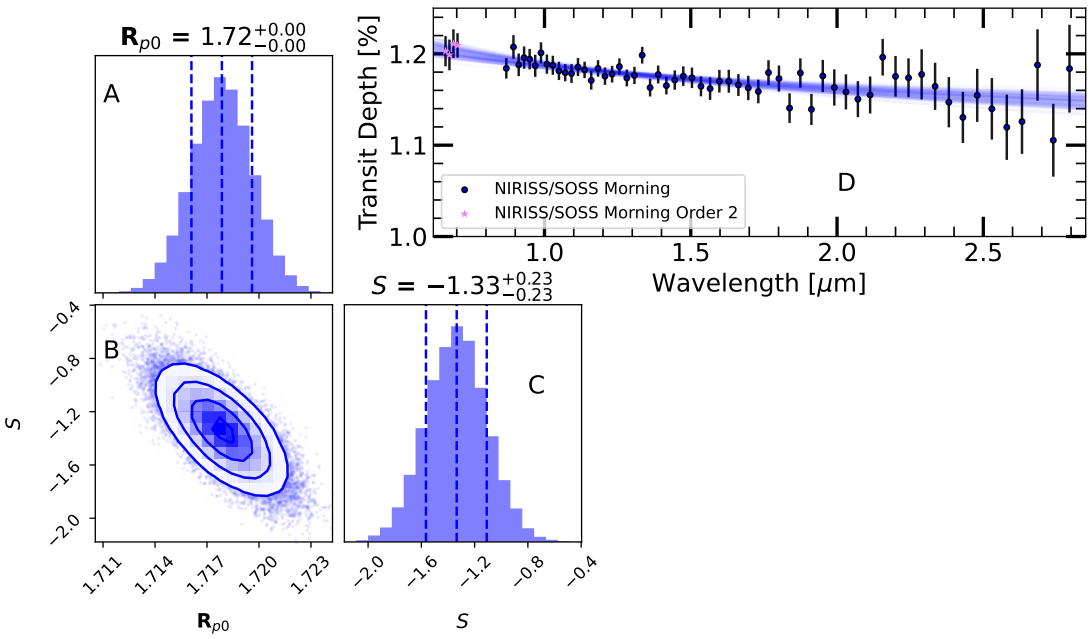

Figure 8.24: **Slope of morning limb spectrum.** The corner plot with panels (**A**), (**B**), and (**C**) show constraints obtained on the slope S of the morning limb transmission spectrum. Panel (**D**) shows the morning limb spectrum with blue points and 500 samples of the fitted parametric model with the blue lines. The order 2 spectrum of the morning limb, which was not used in the fitting, is also shown with the pink star points.

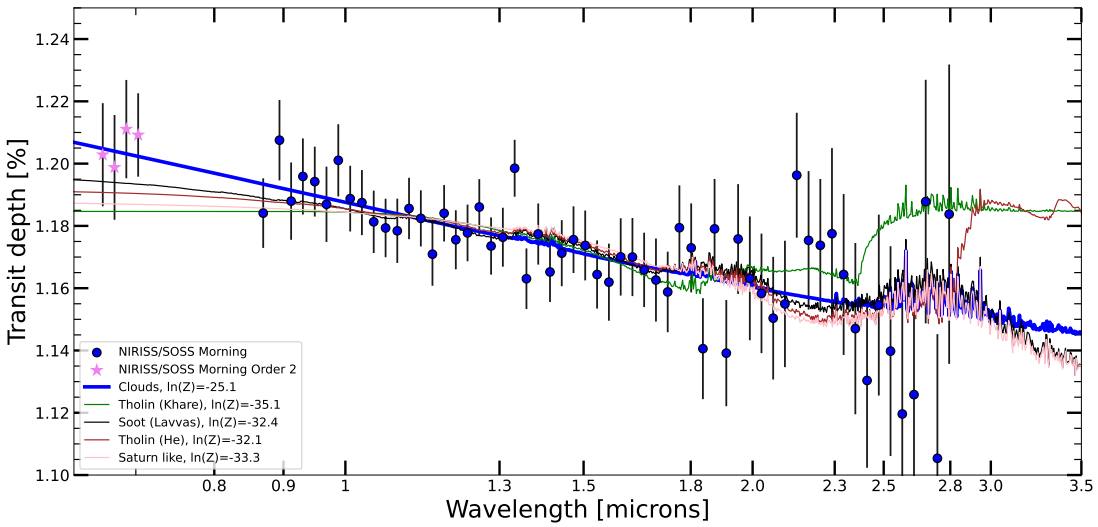

Figure 8.25: **Fit of the morning limb spectrum with various aerosol species.** The blue points show the spectrum of the morning limb. The different colored lines show the best-fit model with that aerosol species to the morning limb spectrum. The logarithm of the Bayesian evidence associated with each aerosol species is also shown in the legend. The cloud model provides the best-fit to the spectrum with the highest evidence. The pink star points show the 2nd order spectrum for the morning limb, which was not used in the fit.

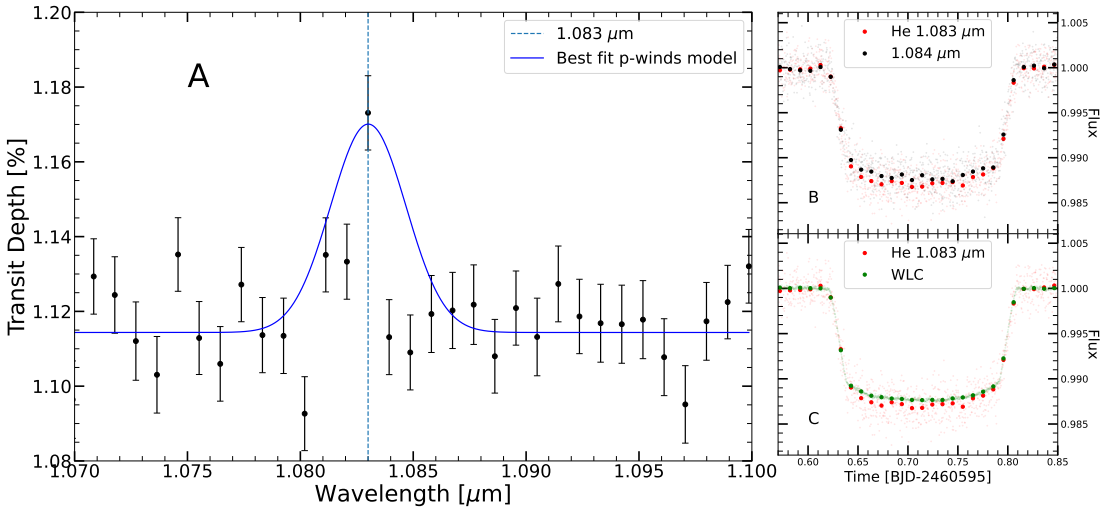

Figure 8.26: **Detection of Helium outflow from WASP-94A b.** (**A**) shows the excess transit depth of WASP-94A b due to metastable He absorption at 1.083 μm with black points. The best-fit model of mass-loss from WASP-94A b's atmosphere is shown with the blue solid line. (**B**) compares the light curve within the He absorption band with the light curve just outside it, showing the excess transit depth at a light curve level. (**C**) compares the light curve within the He absorption band with the white light curve of WASP-94A b.

Chapter 9

Conclusions

A key goal of this thesis was to comprehensively understand the atmospheres of exoplanets and brown dwarfs. The work for this thesis started in fall 2020, more than a year before the launch of *JWST*. The landscape of our understanding of exoplanets and brown dwarfs has changed rapidly since then. This change has happened in two distinct fronts– 1) a large amount of high signal-to-noise empirical evidence (e.g., spectra) has been gathered with *JWST* and other instruments within this period, and 2) this empirical evidence hase completely transformed the key focus areas in theoretical modeling of substellar atmospheres and interiors. To outline this rapid transformation of the field, I summarize the state of our understanding of substellar atmospheres around fall 2020 below, focusing on atmospheric chemistry, clouds, and interiors.

9.1 Where did we stand in 2020?

1. The key physical processes that could affect the chemical state of exoplanet and brown dwarf atmospheres were theoretically explored in the preceeding decade including– thermochemical equilibrium, atmospheric dynamics, photochemistry, and atmosphere-interior interaction (e.g., Visscher et al. 2006; Moses et al. 2011; Tsai et al. 2017; Kite et al. 2016; Fortney et al. 2020). Ground-based and space-based observations of brown dwarfs had long shown signs of chemical disequilibrium due to such processes (e.g., Noll et al. 1997; Sorahana & Yamamura 2012; Griffith & Yelle 1999). However, conclusive empirical evidence on such processes in transiting exoplanet atmospheres was largely missing.

2. Most self-consistent atmospheric models of transiting exoplanets, directly imaged exoplanets, and brown dwarfs assumed thermochemical equilibrium to model the chemical composition of their entire atmospheres (e.g., Marley et al. 2021; Saumon & Marley 2008; Morley et al. 2014a; Fortney et al. 2007; Goyal et al. 2020; Mollière et al. 2015). Very few atmospheric model grids for substellar objects included a self-consistent treatment of disequilibrium chemistry (e.g., Phillips et al. 2020; Drummond et al. 2016) and they showed that such an effect can be very important to model the observational spectra of brown dwarfs and exoplanets.

3. Due to lower signal-to-noise of available observations, atmospheric dynamics and its effect on exoplanet atmospheres and observations was one of the least understood physical aspects (e.g., Parmentier et al. 2013a; Komacek et al. 2019;

Fortney et al. 2020; Phillips et al. 2020). Following early Earth science literature (e.g., Allen et al. 1981), the complex 3D atmospheric dynamical process was commonly parametrized with a single parameter– K_{zz}. This parameter describing the strength of vertical atmospheric dynamics remained uncertain by 6-8 orders of magnitude.

4. Due to lack of precise and panchromatic observations, theoretical models often assumed that the strength of vertical mixing (K_{zz}) is uniform across all pressures (or altitudes) within the atmosphere. There was very recent empirical evidence from Miles et al. (2020) showing that this assumption might not be correct. However, the effect of vertically non-uniform atmospheric dynamics on substellar atmospheres and their spectral observations was unexplored. Even though there were theoretical ideas about the strength of dynamics in the convective atmosphere (e.g., Gierasch & Conrath 1985b; Ackerman & Marley 2001a), theoretical predictions on the strength of dynamics in the radiative atmosphere of exoplanets remained ambiguous.

5. Probing the chemistry of transiting exoplanet atmospheres was theoretically identified as a key way to constrain their interior properties (e.g., Fortney et al. 2020; Agúndez et al. 2014; Morley et al. 2017a). However, theoretical clarity on how the observable chemistry of transiting exoplanets – from gas giants to sub-Neptunes, responds to various key planetary parameters like their equilibrium temperature, metallicity, elemental abundance ratios, interior properties, strength

of atmospheric dynamics, and incident high-energy radiation was lacking. Additionally, the limited signal-to-noise of their transmission spectra was not enough to understand their interiors in most cases.

6. Evidence on spatial non-uniformity in cloud cover or temperature structure in brown dwarfs was present mainly in the form of their observed photometric variability (e.g., Apai et al. 2021; Biller et al. 2013; Buenzli et al. 2012, 2015; Vos et al. 2019; Crossfield et al. 2014). However, distinguishing whether the variability is driven by non-uniform cloud cover or presence of thermal hot- or cold- spots was an open question (e.g., Morley et al. 2014b). Polarized thermal emission from brown dwarfs was theoretically proposed as a probe to distinguish between these scenarios (e.g., Sengupta & Marley 2010; de Kok et al. 2011). Very few detections of such signals were present in the literature, with recent detections from binary brown dwarf pair Luhman 16 A and B being one of the strongest signals (Millar-Blanchaer et al. 2020).

7. 3D GCMs of transiting exoplanets also predicted very non-uniform aerosol cover in their atmospheres (e.g., Parmentier et al. 2016; Lines et al. 2019; Lines et al. 2018). However, direct empirical evidence of such non-uniformity was missing. Additionally, whether aerosols in transiting giant exoplanets like hot Jupiters are composed of mineral clouds formed through condensation or photochemically produced hazes was a major unresolved question (e.g., Kempton et al. 2017).

9.2 Where do we stand today?

This thesis is a half-decade-long attempt to address the uncertainties and unresolved questions highlighted above. I list below the major results from this thesis that have addressed these questions. I also highlight how the status of the field has changed within the 2020-2025 time period.

1. Since the launch of *JWST* in 2021, overwhelming empirical evidence pointing towards the influence of atmospheric dynamics on the observed chemistry of directly imaged planets and transiting exoplanets has been gathered (Miles et al. 2022; Welbanks et al. 2024; Sing et al. 2024; Tsai et al. 2023c). This had exposed several gaps in theoretical atmospheric models that required immediate attention.

2. One unresolved question that needed to be addressed right away was how does atmospheric dynamics affect the chemical and thermal structure of exoplanet atmospheres. The open-sourced `PICASO` 1D radiative-convective equilibrium climate model was developed in Chapter 3 to address this question. Chapter 4 shows that a self-consistent treatment of disequilibrium chemistry driven by vertical atmospheric dynamics has a profound impact on the location of radiative and convective regions in brown dwarf and directly imaged exoplanet atmospheres. Chapter 4 shows that detached radiative regions can form in the atmosphere of high gravity T- type objects with $T_{\rm eff}$ between 500–900 K. These detached radiative zones were found in parts of their deep atmospheres that were otherwise found to be convective in nature from theoretical studies that assumed thermochemical equilibrium

(e.g., Marley et al. 2021).

3. Chapter 4 proposed the formation of these detached radiative regions in late T-type objects as an opportunity to measure the highly uncertain strength of vertical dynamics in the radiative atmospheres of substellar objects with *JWST* spectroscopy. This study also found that the large mismatch between the observed strength of atmospheric mixing and theoretically predicted strength of mixing from convection in Miles et al. (2020) was due to the presence of these deep detached radiative regions, where vertical mixing can be relatively inefficient. These detached radiative regions formed within a very similar $T_{\rm eff}$ interval where the discrepancy was reported in Miles et al. (2020). They also self-consistently disappeared for colder $T_{\rm eff}$, where the observed strength of mixing was also found to be high and consistent with predictions from convection in Miles et al. (2020).

4. Most theoretical models of substellar atmospheres that included a self-consistent treatment of vertical dynamics driven disequilibrium chemistry focused on solar or near-solar composition atmospheres (e.g., Karalidi et al. 2021a; Phillips et al. 2020). Research presented in Chapter 5 shows that both atmospheric metallicity ([M/H]) and strength of vertical dynamics (K_{zz}) have very similar effects on the spectrum of brown dwarfs and directly imaged exoplanets, especially in narrower wavelength bands such as the L and M infrared bands. Therefore, we developed the Sonora Elf Owl grid of self-consistent atmospheric models in Chapter 5. The Elf Owl grid explores a vast parameter space including variations in atmospheric

metallicity, C/O, and K_{zz} in addition to $T_{\rm eff}$ and gravity. By fitting archival observations of T- type brown dwarfs from the AKARI and *Spitzer* telescopes (Sorahana & Yamamura 2012; Suárez & Metchev 2022) with the Elf Owl grid, we reconfirm a several orders of magnitude discrepancy between the observed K_{zz} parameter and the K_{zz} predicted from convective atmospheres for T-dwarfs. This provides further confirmation on the presence of deep detached radiative regions in late T-dwarfs atmospheres, as theoretically predicted in Chapter 4.

5. The detection of SO_2 gas in exoplanet WASP-39 b by the *JWST* transiting planets ERS collaboration (Tsai et al. 2023c; Rustamkulov et al. 2023) showed that including photochemistry within theoretical models of exoplanet atmospheres is critical. Chapter 6 presents a self-consistent coupling between the 1D radiative-convective equilibrium `PICASO` atmosphere model and a 1D chemical kinetics model for exoplanet atmospheres *photochem* (Wogan et al. 2023; Wogan 2024). We have explored how the observable chemistry of transiting exoplanets responds to planetary properties such as their interior heat flux, temperature, composition, and strength of vertical mixing in Chapter 6. We have explored the chemical behavior and transitions in a wide range of planet types including sub-Neptunes, warm giant planets, and hot Jupiters. We have identified key trends in the chemical abundances of various observable gasses and determined the specific gasses that should be targeted to constrain various planetary parameters (like metallicity or interior heat flux) for these different planet types in Chapter 6.

6. Constraints on atmospheric chemistry from *JWST* observations of transiting exoplanets like WASP-107b was leveraged by the community in 2024 to constrain their interior heat flux in addition to their atmospheric metallicity (e.g., Welbanks et al. 2024; Sing et al. 2024). These constraints were critical in measuring the total metal mass fraction of these transiting exoplanets– a major step forward in understanding their formation conditions and evolution. Aiming to reach similar constraints for a warm Neptune-like exoplanet, we present the first panchromatic thermal emission spectrum of GJ 436 b measured using the NIRCam and MIRI instruments aboard *JWST* in Chapter 7. We show that the planet's observed emission is inconsistent with past *Spitzer* measurements (e.g., Morley et al. 2017a; Stevenson et al. 2010), where it appears significantly fainter in the 3.6 μm band than estimated by *Spitzer*. The *JWST* spectrum is mostly consistent with blackbody emission. Our modeling analysis suggests that these new observations no longer require GJ 436b to have a large heat flux from its interior contrary to previous findings with *Spitzer* data. We find weak evidence of CO_2 absorption from the spectrum. It is likely that GJ 436 b's atmosphere is enshrouded in aerosols and is quite rich in metals,, but our observations could not conclusively prove this. Due to various systematic noises in the data, we could not place meaningful constraints on the planet's interior as well.

7. Following the very recent detection of polarized thermal emission from binary brown dwarf pair Luhman 16 A & B, we used a self-consistently cloudy 3D gen-

eral circulation model (GCM) to test whether the detected polarization can be explained by our most advanced model of 3D cloud cover in brown dwarf atmospheres (Tan & Showman 2021). We found that the patchy cloud distribution that is driven by object parameters like $T_{\rm eff}$, $log(g)$, and their rotation rate could match the detected thermal polarization from each object well. We also found that if the real brown dwarf atmosphere hosts a patchy cloud distribution as predicted by our GCM, then a nominal "band-like" cloud model created by latitudinally smoothing the GCM itself couldn't reproduce the polarization from the original GCM. This showed the great influence of small-scale cloud vortices on the disk-integrated thermal polarization signal of substellar objects.

8. *JWST*'s excellent stability has enabled precise light curve measurements for transiting exoplanets. This precision has been leveraged to measure the transit depths of the leading morning limb and the trailing evening limb of tidally locked transiting exoplanets (e.g., Espinoza et al. 2024; Murphy et al. 2024b). In Chapter 8, we have measured separate transmission spectra of the morning and evening limbs of hot Jupiter WASP-94Ab using the NIRISS/SOSS instrument aboard *JWST*. We found that the colder morning limb of WASP-94A b is completely enshrouded in aerosols with negligible gaseous absorption features in its transmission spectrum. Whereas the hotter evening limb spectrum appears to be lacking significant aerosol absorption with large gaseous absorption features due to H_2O. This observation showed that clouds and not photochemically produced hazes can be the major

aerosol component in hot Jupiter atmospheres, as hazes are primarily formed in the planetary dayside and should make the evening limb spectrum appear more or similarly featureless than the morning limb spectrum. This is the opposite scenario than the observations. Clouds, on the other hand, can form on the colder planetary night side and be transported to the colder morning limb (muting its spectrum) before being evaporated on the hotter day side of the planet, leading to a clearer evening limb. The observed morning and evening limb spectrum of WASP-94Ab is consistent with this picture. These observations provided direct empirical evidence on the 3D distribution and composition of aerosols in transiting exoplanet atmospheres.

9. In Chapter 8, we also showed that ignoring such limb-to-limb aerosol asymmetry can lead to $\geq 5\sigma$ level bias in the measured composition (e.g., metallicity) of hot Jupiter exoplanets like WASP-94Ab. This bias is driven by the artificial muting of gas absorption features in a transmission spectrum derived by assuming the planet to be spherically symmetric, if in reality the limbs of the planet are highly asymmetric like in the case of WASP-94Ab. This fundamental effect makes a much larger population of transiting exoplanets susceptible to this limb-asymmetry driven compositional bias including the population of hot Jupiters, warm giant planets, sub-Neptunes, super-Earths, etc. In Chapter 8, we also highlight why this bias forces us to revisit all the conclusions drawn on planet compositions from *HST*/WFC3 observations of transiting exoplanets over the past two

decades, as the WFC3 wavelength band can be especially susceptible to this bias. This is due to the prevalence of aerosol opacities at shorter wavelengths that could make limbs relatively more asymmetric in the WFC3 band and asymmetric limbs were not considered in most *HST*/WFC3 analysis of transiting exoplanets.

Beyond these key results, the state-of-the-art open-sourced theoretical models developed in this thesis have been instrumental in enabling interpretation of *JWST* observations of diverse exoplanets and brown dwarfs, taking us closer to a more comprehensive understanding of these objects. These models have been used extensively for understanding the chemistry and aerosol properties of several transiting exoplanets including giant exoplanets (e.g., Schlawin et al. 2024a; Louie et al. 2025; Cañas et al. 2025; Gagnebin et al. 2024; Madurowicz et al. 2023; Inglis et al. 2024; Radica et al. 2023; Rustamkulov et al. 2023; Feinstein et al. 2022; Alderson et al. 2022; Ahrer et al. 2023; Fu et al. 2025; Valentine et al. 2024; Franson et al. 2024) and smaller sub-Neptunes/super-Earths (e.g., Gao et al. 2023; Wallack et al. 2024; Mukherjee et al. 2025; Alderson et al. 2025; Wogan et al. 2024; Welbanks et al. 2025; Thao et al. 2024; Teske et al. 2025; Alam et al. 2025; Alderson et al. 2024). Additionally, they have also been widely used in the community to understand the *JWST* spectral observations of several T-, Y-, and L- type brown dwarfs and discovering them from wide-ranging datasets (e.g., Kothari et al. 2024; Beiler et al. 2023; Burgasser et al. 2025; Tu et al. 2025; Balmer et al. 2025; Miles et al. 2022; Matthews et al. 2024; Hainline et al. 2024; Lew et al. 2024; Burgasser et al. 2024; Tu et al. 2024).

9.3 Where do we go from here?

While *JWST* has made several ground-breaking discoveries in the field of exoplanets and brown dwarfs, new observations have raised many new science questions, uncovered new physical processes to be understood, and brought upon new technological and observational challenges to be solved. For atmospheric characterization of giant exoplanets, some of the most exciting broad problem areas to be solved in the coming years are– 1) understanding the composition of aerosol in their atmospheres, 2) placing tighter constraints on their 3D thermal structure and overall energetics including albedo, 3) mapping the 3D aerosol patterns of a statistically significant sample of transiting giant exoplanets across a wide range of planetary properties (e.g., $T_{\rm eq}$, gravity, etc), 4) understanding their interior structure and evolution, and 5) constraining metrics that are focused towards connecting their atmospheric observations to their formation/evolutionary scenarios including elemental abundance ratios (e.g., C/O, S/O, etc), metallicities, and isotopic ratios. Spectroscopic and spectral variability observations of transiting and directly imaged giant exoplanets combined with theoretical model advancement both in the 1D and 3D domain will be critical in answering these questions. The extraordinary high signal-to-noise observations and advanced theoretical models of brown dwarf atmospheres will also be a critical resource for understanding giant exoplanet atmospheres and interiors. Therefore, the brown dwarf-exoplanet connection will definitely play a central role in understanding giant exoplanets– both directly imaged and transiting. These efforts are likely to push exoplanet science forward in the next

5-10 years in the *JWST* era.

The landscape for smaller planets, including sub-Neptunes and super-Earths, is starkly different from giant exoplanets today. In contrast to giant exoplanets, we are debating the detection or absence of atmospheres or gaseous absorption features for many of these smaller planets today (e.g., Wallack et al. 2024; Alderson et al. 2024, 2025; Schlawin et al. 2024c). As most of these smaller planets often orbit lower mass stars, several stellar processes including flares, spot-crossings, faculae, etc., pose a major challenge that limits our ability to probe their atmospheres. Some sub-Neptunes have been found to have prominent gas absorption features in their *JWST* transmission spectra (e.g., Madhusudhan et al. 2023; Schmidt et al. 2025; Benneke et al. 2024). However, the theoretical framework to understand sub-Neptune atmospheres and interiors is lagging behind in comparison to the theoretical framework available to understand giant exoplanet atmospheres. Therefore, the key challenges to be overcome to understand these smaller planets are both observational and theoretical in nature. The major questions the community seeks to answer for these smaller planets are – 1) what are their chemical composition? 2) why are they so common? 3) why are sub-Neptunes/super-Earths missing in our own solar system? and 4) can they be potentially habitable? In order to answer these questions, major theoretical advancements are required, including understanding how sub-Neptune interiors interact with their atmospheres. What are the composition and 3D distribution of aerosol in their atmospheres? Are clouds or hazes the dominant aerosol component shaping their atmospheres and observations? What are the specific chemical metrics that can help us in connecting their atmospheric ob-

servations to their formation and evolutionary mechanisms? Answering these questions requires significant effort in laboratory astrophysics, theoretical model development, and observational campaigns. A large portion of exoplanet atmospheric science over the next two decades will likely be focused on pushing today's boundaries along these fronts. It must be emphasized that pursuing most of these science questions will very likely be an effort beyond the *JWST* era and will extend well into the era of the Habitable Worlds Observatory and the Extremely Large Telescopes.

Humanity's age-old quest of finding another home planet and extraterrestrial life led us to stumble upon a treasure trove of diverse worlds about three decades ago. Since then, we have tried to find similarities between these distant worlds and the planets in our own backyard, but this has always led to more delightful surprises and awe about all the other possible ways planets can be made and all the possible forms they can assume. This is a testament to how curiosity and science can elevate humanity in surprising ways and how exoplanet science can take us towards absolutely unforeseen territories in the coming years. I, for one, am ready to take that adventurous ride to the great unknown!

Bibliography

Abe, Y., Abe-Ouchi, A., Sleep, N. H., & Zahnle, K. J. 2011, Astrobiology, 11, 443

Abel, M., Frommhold, L., Li, X., & Hunt, K. L. C. 2011, The Journal of Physical Chemistry A, 115, 6805, pMID: 21207941

Abramowitz, M., & Stegun, I. A. 1970,

Ackerman, A. S., & Marley, M. S. 2001a, ApJ, 556, 872

—. 2001b, ApJ, 556, 872

Ackerman, A. S., & Marley, M. S. 2001, Astrophys. J., 556, 872

Agrawal, A., & MacDonald, R. 2024, The Journal of Open Source Software, 9, 6894

Agúndez, M., Venot, O., Selsis, F., & Iro, N. 2014, ApJ, 781, 68

Ahrer, E., Seidel, J. V., Doyle, L., et al. 2024, MNRAS, 530, 2749

Ahrer, E.-M., Stevenson, K. B., Mansfield, M., et al. 2022, arXiv e-prints, arXiv:2211.10489

—. 2023, Nature, 614, 653

Alam, M. K., Gao, P., Adams Redai, J., et al. 2025, AJ, 169, 15

Alderson, L., Wakeford, H. R., Alam, M. K., et al. 2022, arXiv e-prints, arXiv:2211.10488

Alderson, L., Batalha, N. E., Wakeford, H. R., et al. 2024, AJ, 167, 216

Alderson, L., Moran, S. E., Wallack, N. L., et al. 2025, AJ, 169, 142

Alibert, Y., Mordasini, C., Benz, W., & Winisdoerffer, C. 2005, A&A, 434, 343

Allard, F., Allard, N. F., Homeier, D., et al. 2007a, A&A, 474, L21

Allard, F., Homeier, D., & Freytag, B. 2012a, Philosophical Transactions of the Royal Society of London Series A, 370, 2765

—. 2012b, Philosophical Transactions of the Royal Society of London Series A, 370, 2765

Allard, N. F., Kielkopf, J. F., & Allard, F. 2007b, European Physical Journal D, 44, 507

Allard, N. F., Spiegelman, F., & Kielkopf, J. F. 2016, A&A, 589, A21

Allard, N. F., Spiegelman, F., Leininger, T., & Molliere, P. 2019, A&A, 628, A120

Allen, M., Yung, Y. L., & Waters, J. W. 1981, Journal of Geophysical Research: Space Physics, 86, 3617

Amundsen, D. S., Baraffe, I., Tremblin, P., et al. 2014, A&A, 564, A59

Amundsen, D. S., Tremblin, P., Manners, J., Baraffe, I., & Mayne, N. J. 2017, A&A, 598, A97

Amundsen, D. S., Mayne, N. J., Baraffe, I., et al. ????, 595, A36, publisher: EDP Sciences

Apai, D., Nardiello, D., & Bedin, L. R. 2021, ApJ, 906, 64

Arcangeli, J., Désert, J.-M., Line, M. R., et al. 2018, ApJ, 855, L30

Arfaux, A., & Lavvas, P. 2022, MNRAS, 515, 4753

—. 2024, MNRAS, 530, 482

Artigau, É., Bouchard, S., Doyon, R., & Lafrenière, D. 2009, ApJ, 701, 1534

Asay-Davis, X. S., Marcus, P. S., Wong, M. H., & de Pater, I. 2009, Icarus, 203, 164

Asplund, M., Grevesse, N., Sauval, A. J., & Scott, P. ????, 47, 481, ADS Bibcode: 2009ARA&A..47..481A

Astropy Collaboration, Robitaille, T. P., Tollerud, E. J., et al. 2013, A&A, 558, A33

Astropy Collaboration, Price-Whelan, A. M., Sipőcz, B. M., et al. 2018, AJ, 156, 123

Atreya, S. K., Wong, M. H., Owen, T. C., et al. 1999, Planet. Space Sci., 47, 1243

August, P. C., Bean, J. L., Zhang, M., et al. 2023a, ApJ, 953, L24

—. 2023b, ApJ, 953, L24

Azzam, A. A. A., Tennyson, J., Yurchenko, S. N., & Naumenko, O. V. 2016, Monthly Notices of the Royal Astronomical Society, 460, 4063

Baines, K. H., Delitsky, M. L., Momary, T. W., et al. 2009, Planet. Space Sci., 57, 1650

Baines, K. H., Simon-Miller, A. A., Orton, G. S., et al. 2007, Science, 318, 226

Baines, T., Espinoza, N., Filippazzo, J., & Volk, K. 2023a, arXiv e-prints, arXiv:2311.07769

—. 2023b, arXiv e-prints, arXiv:2311.07771

Bains, W., Pasek, M. A., Ranjan, S., et al. 2023, ACS Earth and Space Chemistry, 7, 1219

Balmer, W. O., Franson, K., Chomez, A., et al. 2025, AJ, 169, 30

Baraffe, I., Homeier, D., Allard, F., & Chabrier, G. 2015, A&A, 577, A42

Barat, S., Désert, J.-M., Vazan, A., et al. 2024, Nature Astronomy, 8, 899

Barber, R. J., Strange, J. K., Hill, C., et al. 2014a, MNRAS, 437, 1828

—. 2014b, MNRAS, 437, 1828

Barber, R. J., Tennyson, J., Harris, G. J., & Tolchenov, R. N. 2006, Monthly Notices of the Royal Astronomical Society, 368, 1087

Bard, A., Kock, A., & Kock, M. 1991, A&A, 248, 315

Bard, A., & Kock, M. 1994, A&A, 282, 1014

Barman, T. S., Hauschildt, P. H., & Allard, F. 2001, ApJ, 556, 885

Barman, T. S., Konopacky, Q. M., Macintosh, B., & Marois, C. 2015, ApJ, 804, 61

Barman, T. S., Macintosh, B., Konopacky, Q. M., & Marois, C. 2011, ApJ, 735, L39

Barstow, J. K., Aigrain, S., Irwin, P. G. J., et al. 2014a, ApJ, 786, 154

—. 2014b, ApJ, 786, 154

Barstow, J. K., Aigrain, S., Irwin, P. G. J., & Sing, D. K. 2017, ApJ, 834, 50

Barstow, J. K., Changeat, Q., Garland, R., et al. 2020, MNRAS, 493, 4884

Barton, E. J., Geller, M. J., & Kenyon, S. J. 2000, ApJ, 530, 660

Barton, E. J., Yurchenko, S. N., & Tennyson, J. 2013, MNRAS, 434, 1469

Batalha, N. 2019, natashabatalha/picaso: Initial Publication Release

Batalha, N., caoimherooney11, & sagnickm. 2020a, natashabatalha/virga: Initial Release

—. 2020b, natashabatalha/virga: Initial Release

Batalha, N., Freedman, R., Lupu, R., & Marley, M. 2020c, Resampled Opacity Database for PICASO v2

Batalha, N., & Marley, M. 2020, Refractive Indices For Virga Exoplanet Cloud Model

Batalha, N. E., Lewis, N. K., Line, M. R., Valenti, J., & Stevenson, K. 2018a, ApJ, 856, L34

Batalha, N. E., & Line, M. R. 2017, AJ, 153, 151

Batalha, N. E., Marley, M. S., Lewis, N. K., & Fortney, J. J. 2019, ApJ, 878, 70

Batalha, N. E., Smith, A. J. R. W., Lewis, N. K., et al. 2018b, Color Classification of Extrasolar Giant Planets: Prospects and Cautions, The authors acknowledge support from the NASA Grant NNG16PJ24C and Grant NNX15AJ80G

—. 2018c, AJ, 156, 158

Batalha, N. M. 2014, Proceedings of the National Academy of Science, 111, 12647

Baudino, J. L., Bézard, B., Boccaletti, A., et al. 2015, A&A, 582, A83

Baudino, J.-L., Mollière, P., Venot, O., et al. 2017, ApJ, 850, 150

Baxter, C., Désert, J.-M., Tsai, S.-M., et al. 2021, A&A, 648, A127

Bean, J. L., Raymond, S. N., & Owen, J. E. 2021, Journal of Geophysical Research: Planets, 126, e2020JE006639, e2020JE006639 2020JE006639

Bean, J. L., Xue, Q., August, P. C., et al. 2023, Nature, 618, 43

Beatty, T. G., Marley, M. S., Gaudi, B. S., et al. 2019a, AJ, 158, 166

—. 2019b, AJ, 158, 166

Beatty, T. G., Welbanks, L., Schlawin, E., et al. 2024a, ApJ, 970, L10

—. 2024b, ApJ, 970, L10

Beer, R. 1975, ApJ, 200, L167

Behr, P. R., France, K., Brown, A., et al. 2023, AJ, 166, 35

Beiler, S., Cushing, M., Kirkpatrick, D., et al. 2023, arXiv e-prints, arXiv:2306.11807

Bell, K. 1980, Journal of Physics B: Atomic and Molecular Physics (1968-1987), 13, 1859

Bell, K. L., & Berrington, K. A. 1987, Journal of Physics B: Atomic and Molecular Physics, 20, 801

Bell, T., Ahrer, E.-M., Brande, J., et al. 2022a, The Journal of Open Source Software, 7, 4503

—. 2022b, The Journal of Open Source Software, 7, 4503

Bell, T. J., Kreidberg, L., Kendrew, S., et al. 2023a, arXiv e-prints, arXiv:2301.06350

Bell, T. J., Welbanks, L., Schlawin, E., et al. 2023b, Nature, 623, 709

—. 2023c, Nature, 623, 709

Bell, T. J., Crouzet, N., Cubillos, P. E., et al. 2024a, Nature Astronomy, arXiv:2401.13027

—. 2024b, Nature Astronomy, 8, 879

Benneke, B., & Seager, S. 2012, ApJ, 753, 100

Benneke, B., Wong, I., Piaulet, C., et al. 2019, ApJ, 887, L14

Benneke, B., Roy, P.-A., Coulombe, L.-P., et al. 2024, arXiv e-prints, arXiv:2403.03325

Bertin, E., & Arnouts, S. 1996, A&AS, 117, 393

Best, W. M. J., Dupuy, T. J., Liu, M. C., Siverd, R. J., & Zhang, Z. 2020, The Ultracool-Sheet: Photometry, Astrometry, Spectroscopy, and Multiplicity for 3000+ Ultracool Dwarfs and Imaged Exoplanets

Best, W. M. J., Liu, M. C., Magnier, E. A., & Dupuy, T. J. 2021, AJ, 161, 42

Best, W. M. J., Magnier, E. A., Liu, M. C., et al. 2018, ApJS, 234, 1

Beuzit, J. L., Vigan, A., Mouillet, D., et al. 2019, A&A, 631, A155

Biller, B. A., Crossfield, I. J. M., Mancini, L., et al. 2013, ApJ, 778, L10

Bittner, D. M., & Bernath, P. F. 2018, VizieR Online Data Catalog, J/ApJS/235/8

Bjoraker, G. L., Larson, H. P., & Kunde, V. G. 1986, Icarus, 66, 579

Bloot, S., Miguel, Y., Bazot, M., & Howard, S. 2023, MNRAS, 523, 6282

Bodenheimer, P., Hubickyj, O., & Lissauer, J. J. 2000, Icarus, 143, 2

Bohlin, R. C., Mészáros, S., Fleming, S. W., et al. 2017, AJ, 153, 234

Bokeh Development Team. 2014,

Boley, A. C. 2009, ApJ, 695, L53

Bolton, S. J., Lunine, J., Stevenson, D., et al. 2017, Space Sci. Rev., 213, 5

Bonomo, A. S., Desidera, S., Benatti, S., et al. 2017, A&A, 602, A107

Bordwell, B., Brown, B. P., & Oishi, J. S. 2018, ApJ, 854, 8

Borucki, W. J., Koch, D., Basri, G., et al. 2010, Science, 327, 977

Borunov, S., Dorofeeva, V., Khodakovsky, I., et al. 1995, Icarus, 113, 460

Bourrier, V., Lovis, C., Beust, H., et al. 2018, Nature, 553, 477

Bouwman, J., Kendrew, S., Greene, T. P., et al. 2023, PASP, 135, 038002

Brande, J., Crossfield, I. J. M., Kreidberg, L., et al. 2024, ApJ, 961, L23

Brooke, T. Y., Knacke, R. F., Encrenaz, T., et al. 1998, Icarus, 136, 1

Buchner, J., Georgakakis, A., Nandra, K., et al. 2014, A&A, 564, A125

Buenzli, E., Marley, M. S., Apai, D., et al. 2015, ApJ, 812, 163

Buenzli, E., Apai, D., Morley, C. V., et al. 2012, ApJ, 760, L31

Burgasser, A. J., Geballe, T. R., Leggett, S. K., Kirkpatrick, J. D., & Golimowski, D. A. 2006, ApJ, 637, 1067

Burgasser, A. J., Marley, M. S., Ackerman, A. S., et al. 2002a, ApJ, 571, L151

—. 2002b, ApJ, 571, L151

Burgasser, A. J., Sheppard, S. S., & Luhman, K. L. 2013, ApJ, 772, 129

Burgasser, A. J., Kirkpatrick, J. D., Cutri, R. M., et al. 2000, ApJ, 531, L57

Burgasser, A. J., Gerasimov, R., Bezanson, R., et al. 2023, arXiv e-prints, arXiv:2308.12107

Burgasser, A. J., Gerasimov, R., Kremer, K., et al. 2024, ApJ, 971, L25

Burgasser, A. J., Schneider, A. C., Meisner, A. M., et al. 2025, ApJ, 982, 79

Burningham, B., Marley, M. S., Line, M. R., et al. 2017, MNRAS, 470, 1177

Burningham, B., Faherty, J. K., Gonzales, E. C., et al. 2021, MNRAS, 506, 1944

Burrows, A., Budaj, J., & Hubeny, I. 2008, ApJ, 678, 1436

Burrows, A., Ram, R. S., Bernath, P., Sharp, C. M., & Milsom, J. A. 2002, The Astrophysical Journal, 577

Burrows, A., & Sharp, C. M. 1999, ApJ, 512, 843

Burrows, A., Sudarsky, D., & Hubeny, I. 2006, ApJ, 640, 1063

Burrows, A., Sudarsky, D., & Lunine, J. I. 2003, The Astrophysical Journal, 596, 587

Burrows, A., Marley, M., Hubbard, W. B., et al. 1997, ApJ, 491, 856

Bushouse, H., Eisenhamer, J., Dencheva, N., et al. 2024, JWST Calibration Pipeline

Butler, R. P., Vogt, S. S., Marcy, G. W., et al. 2004, ApJ, 617, 580

Butler, R. P., Wright, J. T., Marcy, G. W., et al. 2006, The Astrophysical Journal, 646, 505–522

Bézard, B., Lellouch, E., Strobel, D., Maillard, J.-P., & Drossart, P. 2002, Icarus, 159, 95

Cañas, C. I., Lustig-Yaeger, J., Tsai, S.-M., et al. 2025, arXiv e-prints, arXiv:2502.06966

Cahoy, K. L., Marley, M. S., & Fortney, J. J. 2010, ApJ, 724, 189

Calamari, E., Faherty, J. K., Burningham, B., et al. 2022, The Astrophysical Journal, 940, 164

Caldiroli, A., Haardt, F., Gallo, E., et al. 2021a, A&A, 655, A30

—. 2021b, A&A, 655, A30

—. 2022, A&A, 663, A122

Carter, A. L., Nikolov, N., Sing, D. K., et al. 2020, MNRAS, 494, 5449

Casasayas-Barris, N., Orell-Miquel, J., Stangret, M., et al. 2021, A&A, 654, A163

Castelli, F., & Kurucz, R. L. 2004, arXiv Astrophysics e-prints, astro-ph/0405087

Chabrier, G., Baraffe, I., Allard, F., & Hauschildt, P. 2000, ApJ, 542, 464

Chamberlain, J. W., & Hunten, D. M. 1987,

Charbonneau, D., Brown, T. M., Noyes, R. W., & Gilliland, R. L. 2002, ApJ, 568, 377

Charnay, B., Bézard, B., Baudino, J. L., et al. 2018, ApJ, 854, 172

Charnay, B., Blain, D., Bézard, B., et al. 2021, A&A, 646, A171

Chen, J., & Kipping, D. 2016, The Astrophysical Journal, 834, 17

Christie, D. A., Mayne, N. J., Lines, S., et al. 2021, MNRAS, 506, 4500

Cloutier, R., Doyon, R., Bouchy, F., & Hébrard, G. 2018, AJ, 156, 82

Coles, P. A., Yurchenko, S. N., & Tennyson, J. 2019, MNRAS, 490, 4638

Cooper, C. S., & Showman, A. P. 2006, ApJ, 649, 1048

Cooper, C. S., Sudarsky, D., Milsom, J. A., Lunine, J. I., & Burrows, A. 2003, ApJ, 586, 1320

Coppola, C. M., Lodi, L., & Tennyson, J. 2011, MNRAS, 415, 487

Corrales, L. 2015, ApJ, 805, 23

Coulombe, L.-P., Benneke, B., Challener, R., et al. 2023, Nature, 620, 292

Coulombe, L.-P., Radica, M., Benneke, B., et al. 2025, Nature Astronomy, arXiv:2501.14016

Courtin, R. 1999, Planet. Space Sci., 47, 1077

Cowan, N. B., & Agol, E. 2011, ApJ, 729, 54

Crossfield, I. J. M. 2023, ApJ, 952, L18

Crossfield, I. J. M., Biller, B., Schlieder, J. E., et al. 2014, Nature, 505, 654

Currie, T., Biller, B., Lagrange, A., et al. 2023, in Astronomical Society of the Pacific Conference Series, Vol. 534, Protostars and Planets VII, ed. S. Inutsuka, Y. Aikawa, T. Muto, K. Tomida, & M. Tamura, 799

Cushing, M. C., Marley, M. S., Saumon, D., et al. 2008, ApJ, 678, 1372

Cushing, M. C., Kirkpatrick, J. D., Gelino, C. R., et al. 2011, ApJ, 743, 50

Cushing, M. C., Hardegree-Ullman, K. K., Trucks, J. L., et al. 2016, ApJ, 823, 152

Cutri, R. M., Wright, E. L., Conrow, T., et al. 2021, VizieR Online Data Catalog, II/328

Damiano, M., & Hu, R. 2020, The Astronomical Journal, 159, 175

Davenport, B., Kempton, E. M. R., Nixon, M. C., et al. 2025, arXiv e-prints, arXiv:2501.01498

Dawson, R. I., & Johnson, J. A. 2018, ARA&A, 56, 175

de Kok, R. J., Stam, D. M., & Karalidi, T. 2011, ApJ, 741, 59

Deline, A., Hooton, M. J., Lendl, M., et al. 2022, A&A, 659, A74

Deming, D., Harrington, J., Laughlin, G., et al. 2007, ApJ, 667, L199

Deming, D., Line, M. R., Knutson, H. A., et al. 2023, AJ, 165, 104

Demory, B. O., Gillon, M., Barman, T., et al. 2007, A&A, 475, 1125

Demory, B.-O., de Wit, J., Lewis, N., et al. 2013, ApJ, 776, L25

Dickinson, R. E., & Cicerone, R. J. 1986, Nature, 319, 109

Dlugach, J. M., & Yanovitskij, E. G. 1974, Icarus, 22, 66

Dos Santos, L. A., Vidotto, A. A., Vissapragada, S., et al. 2022, A&A, 659, A62

Dressing, C., Adibekyan, V., Akinsanmi, B., et al. 2020, Probing the Atmosphere of a Temperate Transiting Jovian Planet with an Orbital Period of 1.5 Years, HST Proposal

Drummond, B., Carter, A. L., Hébrard, E., et al. 2019, Monthly Notices of the Royal Astronomical Society, 486, 1123

Drummond, B., Tremblin, P., Baraffe, I., et al. 2016, A&A, 594, A69

Drummond, B., Mayne, N. J., Manners, J., et al. 2018, ApJ, 855, L31

Drummond, B., Hébrard, E., Mayne, N. J., et al. 2020a, A&A, 636, A68

—. 2020b, A&A, 636, A68

Dulick, M., Bauschlicher, C. W., J., Burrows, A., et al. 2003, ApJ, 594, 651

Dupuy, T. J., & Kraus, A. L. 2013, Science, 341, 1492

Dupuy, T. J., & Liu, M. C. 2012, ApJS, 201, 19

Dyrek, A., Min, M., Decin, L., et al. 2024, Nature, 625, 51

Dyudina, U., Zhang, X., Li, L., et al. 2016, ApJ, 822, 76

Edwards, J. M. ????, 53, 1921, publisher: American Meteorological Society Section: Journal of the Atmospheric Sciences

Edwards, J. M., & Slingo, A. ????, 122, 689, _eprint: https://onlinelibrary.wiley.com/doi/pdf/10.1002/qj.49712253107

Ehrenreich, D., Bonfils, X., Lovis, C., et al. 2014, A&A, 570, A89

Ehrenreich, D., Lovis, C., Allart, R., et al. 2020, Nature, 580, 597

Eisenhardt, P. R. M., Marocco, F., Fowler, J. W., et al. 2020, ApJS, 247, 69

Ellison, S. L., Patton, D. R., Simard, L., & McConnachie, A. W. 2008, AJ, 135, 1877

Enoch, B., Cameron, A. C., Anderson, D. R., et al. 2011, MNRAS, 410, 1631

Eriksson, S. C., Janson, M., & Calissendorff, P. 2019, A&A, 629, A145

Espinoza, N., & Jones, K. 2021, AJ, 162, 165

Espinoza, N., Steinrueck, M. E., Kirk, J., et al. 2024, Nature, 632, 1017

Esplin, T. L., Luhman, K. L., Cushing, M. C., et al. 2016, ApJ, 832, 58

Esteves, L. J., De Mooij, E. J. W., & Jayawardhana, R. 2015, ApJ, 804, 150

Estrela, R., Swain, M. R., Roudier, G. M., et al. 2021, AJ, 162, 91

Evans, T. M., Pont, F., Sing, D. K., et al. 2013a, ApJ, 772, L16

—. 2013b, ApJ, 772, L16

Fauchez, T. J., Turbet, M., Villanueva, G. L., et al. 2019, ApJ, 887, 194

Fegley, Jr., B., & Lodders, K. 1994, Icarus, 110, 117

Fegley, B., J., & Prinn, R. G. 1985, ApJ, 299, 1067

Fegley, Bruce, J., & Lodders, K. 1996, ApJ, 472, L37

Feinstein, A. D., Radica, M., Welbanks, L., et al. 2022, arXiv e-prints, arXiv:2211.10493

Feng, Y. K., Line, M. R., Fortney, J. J., et al. 2016, ApJ, 829, 52

Feng, Y. K., Robinson, T. D., Fortney, J. J., et al. 2018, The Astronomical Journal, 155, 200

Feng, Y. K., Robinson, T. D., Fortney, J. J., et al. 2018, AJ, 155, 200

Ferland, G. J., Porter, R. L., van Hoof, P. A. M., et al. 2013, Rev. Mexicana Astron. Astrofis., 49, 137

Feroz, F., Hobson, M. P., & Bridges, M. 2009a, MNRAS, 398, 1601

—. 2009b, MNRAS, 398, 1601

—. 2009c, MNRAS, 398, 1601

Fischer, D. A., Marcy, G. W., Butler, R. P., Laughlin, G., & Vogt, S. S. 2002, ApJ, 564, 1028

Fletcher, L. N., King, O. R. T., Harkett, J., et al. 2023, Journal of Geophysical Research (Planets), 128, e2023JE007924

Fleury, B., Gudipati, M. S., Henderson, B. L., & Swain, M. 2019, ApJ, 871, 158

Foreman-Mackey, D. 2018, Research Notes of the American Astronomical Society, 2, 31

Foreman-Mackey, D., Agol, E., Ambikasaran, S., & Angus, R. 2017, AJ, 154, 220

Foreman-Mackey, D., Hogg, D. W., Lang, D., & Goodman, J. 2013a, PASP, 125, 306

—. 2013b, PASP, 125, 306

Fortney, J. J. 2005, MNRAS, 364, 649

Fortney, J. J., Dawson, R. I., & Komacek, T. D. 2021, Journal of Geophysical Research (Planets), 126, e06629

Fortney, J. J., Lodders, K., Marley, M. S., & Freedman, R. S. 2008a, ApJ, 678, 1419

—. 2008b, ApJ, 678, 1419

Fortney, J. J., Marley, M. S., & Barnes, J. W. 2007, ApJ, 659, 1661

Fortney, J. J., Marley, M. S., Lodders, K., Saumon, D., & Freedman, R. 2005, ApJ, 627, L69

Fortney, J. J., Mordasini, C., Nettelmann, N., et al. 2013, ApJ, 775, 80

Fortney, J. J., Shabram, M., Showman, A. P., et al. 2010, ApJ, 709, 1396

Fortney, J. J., Visscher, C., Marley, M. S., et al. 2020, AJ, 160, 288

Fossati, L., Young, M. E., Shulyak, D., et al. 2021, A&A, 653, A52

France, K., Loyd, R. O. P., Youngblood, A., et al. 2016, ApJ, 820, 89

Franson, K., Balmer, W. O., Bowler, B. P., et al. 2024, ApJ, 974, L11

Freedman, R. S., Lustig-Yaeger, J., Fortney, J. J., et al. 2014a, ApJS, 214, 25

—. 2014b, ApJS, 214, 25

Freedman, R. S., Marley, M. S., & Lodders, K. 2008, ApJS, 174, 504

Freytag, B., Allard, F., Ludwig, H. G., Homeier, D., & Steffen, M. 2010, A&A, 513, A19

Fu, G., Deming, D., Knutson, H., et al. 2017, ApJ, 847, L22

Fu, G., Espinoza, N., Sing, D. K., et al. 2022, ApJ, 940, L35

Fu, G., Welbanks, L., Deming, D., et al. 2024, Nature, 632, 752

Fu, G., Stevenson, K. B., Sing, D. K., et al. 2025, arXiv e-prints, arXiv:2501.02081

Fuhr, J. R., Martin, G. A., & Wiese, W. L. 1988, Journal of Physical and Chemical Reference Data, 17

Fulton, B. J., Petigura, E. A., Howard, A. W., et al. 2017, AJ, 154, 109

Gagnebin, A., Mukherjee, S., Fortney, J. J., & Batalha, N. E. 2024, ApJ, 969, 86

Gaia Collaboration. 2020, VizieR Online Data Catalog: Gaia EDR3 (Gaia Collaboration, 2020), VizieR On-line Data Catalog: I/350. Originally published in: 2021A&A...649A...1G; doi:10.5270/esa-1ug

Gaia Collaboration, Brown, A. G. A., Vallenari, A., et al. 2021, AA, 649, A1

Gandhi, S., & Madhusudhan, N. 2017, MNRAS, 472, 2334

Gao, F., Wang, L., Pearson, W. J., et al. 2020a, A&A, 637, A94

Gao, P., & Benneke, B. 2018a, ApJ, 863, 165

—. 2018b, ApJ, 863, 165

Gao, P., Marley, M. S., & Ackerman, A. S. 2018, ApJ, 855, 86

Gao, P., Marley, M. S., Zahnle, K., Robinson, T. D., & Lewis, N. K. 2017, AJ, 153, 139

Gao, P., & Zhang, X. 2020, ApJ, 890, 93

Gao, P., Thorngren, D. P., Lee, E. K. H., et al. 2020b, Nature Astronomy, 4, 951

Gao, P., Thorngren, D. P., Lee, G. K. H., et al. 2020c, Nature Astronomy

Gao, P., Thorngren, D. P., Lee, G. K. H., et al. 2020, Nature Astronomy

Gao, P., Piette, A. A. A., Steinrueck, M. E., et al. 2023, ApJ, 951, 96

Garcia Munoz, A., & Isaak, K. G. 2015, Proceedings of the National Academy of Science, 112, 13461

Gardner, J. P., Mather, J. C., Clampin, M., et al. 2006, Space Sci. Rev., 123, 485

Gaudi, B. S., Seager, S., Mennesson, B., et al. 2020, arXiv e-prints, arXiv:2001.06683

Geballe, T. R., Saumon, D., Golimowski, D. A., et al. 2009, ApJ, 695, 844

Geballe, T. R., Saumon, D., Leggett, S. K., et al. 2001, ApJ, 556, 373

Gharib-Nezhad, E., Iyer, A. R., Line, M. R., et al. 2021a, ApJS, 254, 34

—. 2021b, ApJS, 254, 34

Gharib-Nezhad, E., Marley, M. S., Batalha, N. E., et al. 2021c, ApJ, 919, 21

GharibNezhad, E., Shayesteh, A., & Bernath, P. F. 2013, MNRAS, 432, 2043

Giacobbe, P., Brogi, M., Gandhi, S., et al. 2021, Nature, 592, 205

Gibson, N. P., Aigrain, S., Pont, F., et al. 2012, MNRAS, 422, 753

Gierasch, P. J., & Conrath, B. J. 1985a, Energy conversion processes in the outer planets., ed. G. E. Hunt, 121–146

—. 1985b, in Recent Advances in Planetary Meteorology, ed. G. E. Hunt, 121–146

Gillon, M., Pont, F., Demory, B. O., et al. 2007, A&A, 472, L13

Girardin, F., Artigau, É., & Doyon, R. 2013, ApJ, 767, 61

Gladstone, G. R., Stern, S. A., Ennico, K., et al. 2016, Science, 351, aad8866

Goldman, B., Pitann, J., Zapatero Osorio, M. R., et al. 2009, A&A, 502, 929

Golimowski, D. A., Leggett, S. K., Marley, M. S., et al. 2004, AJ, 127, 3516

Goodwin, D. G., Moffat, H. K., Schoegl, I., Speth, R. L., & Weber, B. W. 2023, Cantera: An Object-oriented Software Toolkit for Chemical Kinetics, Thermodynamics, and Transport Processes, https://www.cantera.org, version 3.0.0

Goody, R. M., & Yung, Y. L. 1989,

Gordon, I. E., Rothman, L. S., Tan, Y., Kochanov, R. V., & Hill, C. 2017, in 72nd International Symposium on Molecular Spectroscopy, TJ08

Gordon, I. E., Rothman, L. S., Hargreaves, R. J., et al. 2022, J. Quant. Spec. Radiat. Transf., 277, 107949

Gordon, S., & McBride, B. J. 1994, Computer Program for Calculation of Complex Chemical Equilibrium Compositions and Applications, Reference Publication 1311, https://www.grc.nasa.gov/WWW/CEAWeb/RP-1311.htm

Gordon, S., & McBride, B. J. 1994, Computer program for calculation of complex chemical equilibrium compositions and applications. Part 1: Analysis,

Goyal, J. M., Mayne, N., Sing, D. K., et al. 2018, MNRAS, 474, 5158

Goyal, J. M., Mayne, N., Drummond, B., et al. 2020, MNRAS, 498, 4680

Grant, D., & Wakeford, H. R. 2024, Journal of Open Source Software, 9, 6816

Grant, D., Lewis, N. K., Wakeford, H. R., et al. 2023, ApJ, 956, L32

Grasser, N., Snellen, I. A. G., Landman, R., Picos, D. G., & Gandhi, S. 2024, A&A, 688, A191

Greenbaum, A. Z., Llop-Sayson, J., Lew, B., et al. 2023, arXiv e-prints, arXiv:2301.11455

Griffith, C. A., & Yelle, R. V. 1999, ApJ, 519, L85

Guillot, T. 2010, A&A, 520, A27

Hainline, K. N., D'Eugenio, F., Sun, F., et al. 2024, ApJ, 975, 31

Hanisch, R. J., & Biemesderfer, C. D. 1989, in BAAS, 780

Hansen, J. E. 1969, Journal of Atmospheric Sciences, 26, 478

—. 1971, Journal of Atmospheric Sciences, 28, 1400

Hansen, J. E., & Travis, L. D. 1974a, Space Sci. Rev., 16, 527

—. 1974b, Space Sci. Rev., 16, 527

Hargreaves, R., Gordon, I., Huang, X., Conway, E., & Rothman, L. 2022, in American Astronomical Society Meeting Abstracts, Vol. 54, American Astronomical Society Meeting Abstracts, 217.01

Hargreaves, R. J., Hinkle, K. H., Bauschlicher, Charles W., J., et al. 2010, AJ, 140, 919

Harris, G. J., Tennyson, J., Kaminsky, B. M., Pavlenko, Y. V., & Jones, H. R. A. 2006, MNRAS, 367, 400

Hatzes, A. P., Cochran, W. D., Endl, M., et al. 2006, A&A, 457, 335

He, C., Radke, M., Moran, S. E., et al. 2024, Nature Astronomy, 8, 182

Helling, C., & Casewell, S. 2014, A&A Rev., 22, 80

Helling, C., Kawashima, Y., Graham, V., et al. 2020, A&A, 641, A178

Helling, C., Oevermann, M., Lüttke, M. J. H., Klein, R., & Sedlmayr, E. 2001, A&A, 376, 194

Helling, C., Tootill, D., Woitke, P., & Lee, G. 2017, A&A, 603, A123

Helling, C., Ackerman, A., Allard, F., et al. 2008, MNRAS, 391, 1854

Heng, K., & Kitzmann, D. 2017, ApJS, 232, 20

Herrero-Illana, R., Privon, G. C., Evans, A. S., et al. 2019, A&A, 628, A71

Hobbs, R., Rimmer, P. B., Shorttle, O., & Madhusudhan, N. 2021, Monthly Notices of the Royal Astronomical Society, 506, 3186

Hoch, K. K. W., Konopacky, Q. M., Theissen, C. A., et al. 2023, AJ, 166, 85

Hoeijmakers, H. J., Ehrenreich, D., Heng, K., et al. 2018, Nature, 560, 453

Hoeijmakers, H. J., Seidel, J. V., Pino, L., et al. 2020, Astronomy & Astrophysics, 641, A123

Høg, E., Fabricius, C., Makarov, V. V., et al. 2000, A&A, 355, L27

Holmberg, M., & Madhusudhan, N. 2024, A&A, 683, L2

Horak, H. G., & Little, S. J. 1965, ApJS, 11, 373

Horne, K. 1986, PASP, 98, 609

Howard, A. W., & Fulton, B. J. 2016, PASP, 128, 114401

Howard, A. W., Marcy, G. W., Johnson, J. A., et al. 2010, Science, 330, 653

Howe, A. R., Burrows, A., & Deming, D. 2017, ApJ, 835, 96

Hu, R. 2019, The Astrophysical Journal, 887, 166

Hu, R. 2021, ApJ, 921, 27

Hu, R., Bello-Arufe, A., Zhang, M., et al. 2024a, Nature, 630, 609

—. 2024b, Nature, 630, 609

Hu, Y.-X., Wielicki, B., Lin, B., et al. 2000, Journal of Quantitative Spectroscopy and Radiative Transfer, 65, 681

Huang, X., Gamache, R. R., Freedman, R. S., Schwenke, D. W., & Lee, T. J. 2014, Journal of Quantitative Spectroscopy and Radiative Transfer, 147, 134

Hubbard, W. B. 1977, Icarus, 30, 305

Hubbard, W. B., Guillot, T., Marley, M. S., et al. 1999, Planet. Space Sci., 47, 1175

Hubeny, I. 1988, Computer Physics Communications, 52, 103

Hubeny, I. 2017, Monthly Notices of the Royal Astronomical Society, 469, 841

Hubeny, I., & Burrows, A. 2007, ApJ, 659, 1458

Hubeny, I., Burrows, A., & Sudarsky, D. 2003, ApJ, 594, 1011

Huffman, D. R., & Wild, R. L. 1967, Physical Review, 156, 989

Hunter, J. D. 2007, Computing in Science & Engineering, 9, 90

Ida, S., & Lin, D. N. C. 2004, ApJ, 604, 388

Ingersoll, A. P. 1969, Journal of the Atmospheric Sciences, 26, 1191

—. 2020, Space Sci. Rev., 216, 122

Inglis, J., Batalha, N. E., Lewis, N. K., et al. 2024, ApJ, 973, L41

Irwin, P. G. J., Bowles, N., Braude, A. S., et al. 2019a, Icarus, 321, 572

Irwin, P. G. J., Fletcher, L. N., Read, P. L., et al. 2016, Icarus, 264, 72

Irwin, P. G. J., Tice, D. S., Fletcher, L. N., et al. 2015, Icarus, 250, 462

Irwin, P. G. J., Toledo, D., Garland, R., et al. 2019b, Icarus, 321, 550

Irwin, P. G. J., Teanby, N. A., de Kok, R., et al. 2008, J. Quant. Spec. Radiat. Transf., 109, 1136

Ishizuka, M., Kawahara, H., Nugroho, S. K., et al. 2021, AJ, 161, 153

Iwabuchi, H., & Suzuki, T. 2009, Journal of Quantitative Spectroscopy and Radiative Transfer, 110, 1926

Iyer, A. R., Line, M. R., Muirhead, P. S., Fortney, J. J., & Gharib-Nezhad, E. 2023, ApJ, 944, 41

Jensen-Clem, R., Millar-Blanchaer, M., Mawet, D., et al. 2016, ApJ, 820, 111

Jensen-Clem, R., Millar-Blanchaer, M. A., van Holstein, R. G., et al. 2020, AJ, 160, 286

John, T. L. 1988, A&A, 193, 189

Jones, K., & Espinoza, N. 2022, Journal of Open Source Software, 7, 2382

Joseph, J. H., Wiscombe, W. J., & Weinman, J. A. 1976, Journal of Atmospheric Sciences, 33, 2452

Karalidi, T., Apai, D., Schneider, G., Hanson, J. R., & Pasachoff, J. M. 2015, ApJ, 814, 65

Karalidi, T., Marley, M., Fortney, J. J., et al. 2021a, ApJ, 923, 269

—. 2021b, ApJ, 923, 269

Karkoschka, E. 1994, Icarus, 111, 174

Karkoschka, E., & Tomasko, M. G. 2011, Icarus, 211, 780

Karman, T., Gordon, I. E., van der Avoird, A., et al. 2019, Icarus, 328, 160

Kataria, T., Showman, A. P., Fortney, J. J., Marley, M. S., & Freedman, R. S. 2014, ApJ, 785, 92

Kataria, T., Sing, D. K., Lewis, N. K., et al. 2016, ApJ, 821, 9

Kawashima, Y., & Ikoma, M. 2018, ApJ, 853, 7

Kawashima, Y., & Min, M. 2021, A&A, 656, A90

Kempton, E. M. R., Bean, J. L., & Parmentier, V. 2017, ApJ, 845, L20

Kempton, E. M. R., Bean, J. L., Louie, D. R., et al. 2018, PASP, 130, 114401

Kempton, E. M. R., Zhang, M., Bean, J. L., et al. 2023, Nature, 620, 67

Kennedy, T. D., Rauscher, E., Malsky, I., Roman, M. T., & Beltz, H. 2025, ApJ, 978, 82

Kesseli, A. Y., & Snellen, I. A. G. 2021, ApJ, 908, L17

Khare, B. N., Sagan, C., Arakawa, E. T., et al. 1984, Icarus, 60, 127

Kirk, J., Ahrer, E.-M., Claringbold, A. B., et al. 2024, arXiv e-prints, arXiv:2410.08116

Kirkpatrick, J. D. 2005, ARA&A, 43, 195

Kirkpatrick, J. D., Cushing, M. C., Gelino, C. R., et al. 2011, ApJS, 197, 19

Kirkpatrick, J. D., Gelino, C. R., Cushing, M. C., et al. 2012, ApJ, 753, 156

Kite, E. S., Fegley, Jr., B., Schaefer, L., & Ford, E. B. 2020, ApJ, 891, 111

Kite, E. S., Fegley, Jr., B., Schaefer, L., & Gaidos, E. 2016, ApJ, 828, 80

Kitzmann, D., & Heng, K. 2018, MNRAS, 475, 94

Kluyver, T., Ragan-Kelley, B., Pérez, F., et al. 2016, in ELPUB, 87–90

Knapp, G. R., Leggett, S. K., Fan, X., et al. 2004, AJ, 127, 3553

Kniazev, A. Y., Vaisanen, P., Mužić, K., et al. 2013, The Astrophysical Journal, 770, 124

Knutson, H. A., Benneke, B., Deming, D., & Homeier, D. 2014a, Nature, 505, 66

Knutson, H. A., Fulton, B. J., Montet, B. T., et al. 2014b, ApJ, 785, 126

Kokori, A., Tsiaras, A., Edwards, B., et al. 2022, ApJS, 258, 40

—. 2023, ApJS, 265, 4

Komacek, T. D., Fauchez, T. J., Wolf, E. T., & Abbot, D. S. 2020, ApJ, 888, L20

Komacek, T. D., Showman, A. P., & Parmentier, V. 2019, The Astrophysical Journal, 881, 152

Komacek, T. D., Showman, A. P., & Parmentier, V. 2019, ApJ, 881, 152

Kostogryz, N., Witzke, V., Shapiro, A., et al. 2022, Astronomy & Astrophysics, 666, A60

Kothari, H., Cushing, M. C., Burningham, B., et al. 2024, ApJ, 971, 121

Kreidberg, L. 2015a, PASP, 127, 1161

—. 2015b, PASP, 127, 1161

—. 2018, in Handbook of Exoplanets, ed. H. J. Deeg & J. A. Belmonte, 100

Kreidberg, L., Line, M. R., Thorngren, D., Morley, C. V., & Stevenson, K. B. 2018, ApJ, 858, L6

Kreidberg, L., Bean, J. L., Désert, J.-M., et al. 2014, Nature, 505, 69

Kuai, L., Natraj, V., Shia, R.-L., Miller, C., & Yung, Y. L. 2010, J. Quant. Spec. Radiat. Transf., 111, 1296

Kuiper, G. P. 1947, ApJ, 106, 251

Lacy, B., & Burrows, A. 2020, The Astrophysical Journal, 892, 151

Lacy, B., & Burrows, A. 2020, ApJ, 892, 151

—. 2023, ApJ, 950, 8

Lacy, B., Shlivko, D., & Burrows, A. 2018, arXiv e-prints, arXiv:1801.08964

—. 2019, AJ, 157, 132

Lallement, R., Vergely, J. L., Babusiaux, C., & Cox, N. L. J. 2022, AA, 661, A147

Lam, S. K., Pitrou, A., & Seibert, S. 2015, in Proceedings of the Second Workshop on the LLVM Compiler Infrastructure in HPC, LLVM '15 (New York, NY, USA: ACM), 7:1–7:6

Lampón, M., López-Puertas, M., Sanz-Forcada, J., et al. 2021, A&A, 647, A129

Lamport, L. 1994, LaTeX: A Document Preparation System, 2nd edn.

Lanotte, A. A., Gillon, M., Demory, B. O., et al. 2014, A&A, 572, A73

Larson, H. P., Fink, U., & Treffers, R. C. 1978, ApJ, 219, 1084

Larson, H. P., Treffers, R. R., & Fink, U. 1977, ApJ, 211, 972

Lavvas, P., & Koskinen, T. 2017, ApJ, 847, 32

Lavvas, P., Koskinen, T., Steinrueck, M. E., García Muñoz, A., & Showman, A. P. 2019, ApJ, 878, 118

Lavvas, P., Lellouch, E., Strobel, D. F., et al. 2021, Nature Astronomy, 5, 289

Lee, E., Dobbs-Dixon, I., Helling, C., Bognar, K., & Woitke, P. 2016, A&A, 594, A48

Lee, E. K. H., Parmentier, V., Hammond, M., et al. 2021a, Monthly Notices of the Royal Astronomical Society, 506, 2695

—. 2021b, Monthly Notices of the Royal Astronomical Society, 506, 2695

Lee, E. K. H., Prinoth, B., Kitzmann, D., et al. ????, 517, 240

Lee, E. K. H., Tan, X., & Tsai, S.-M. 2023, MNRAS, 523, 4477

Lee, G. K. H., Wood, K., Dobbs-Dixon, I., Rice, A., & Helling, C. 2017, A&A, 601, A22

Leggett, S. K., Morley, C. V., Marley, M. S., & Saumon, D. 2015, ApJ, 799, 37

Leggett, S. K., Morley, C. V., Marley, M. S., et al. 2013, ApJ, 763, 130

Leggett, S. K., Tremblin, P., Esplin, T. L., Luhman, K. L., & Morley, C. V. 2017, ApJ, 842, 118

Leggett, S. K., Saumon, D., Marley, M. S., et al. 2012, ApJ, 748, 74

Lenzuni, P., Chernoff, D. F., & Salpeter, E. E. 1991, ApJS, 76, 759

Lew, B. W. P., Roellig, T., Batalha, N. E., et al. 2024, AJ, 167, 237

Lewis, J. S. 1969, Icarus, 10, 365

Li, C., Zhang, X., Kammer, J. A., et al. 2014, Planet. Space Sci., 104, 48

Li, G., Gordon, I. E., Rothman, L. S., et al. 2015, ApJS, 216, 15

Li, G., Gordon, I. E., Rothman, L. S., et al. 2015, The Astrophysical Journal Supplement Series, 216, 15, aDS Bibcode: 2015ApJS..216...15L

Li, L., Zhang, J., Peter, H., et al. 2018, ApJ, 868, L33

Line, M. R., & Parmentier, V. 2016, ApJ, 820, 78

Line, M. R., Vasisht, G., Chen, P., Angerhausen, D., & Yung, Y. L. 2011, ApJ, 738, 32

Line, M. R., Zhang, X., Vasisht, G., et al. 2012, ApJ, 749, 93

Line, M. R., Marley, M. S., Liu, M. C., et al. 2017, ApJ, 848, 83

Lines, S., Mayne, N. J., Manners, J., et al. 2019, MNRAS, 488, 1332

Lines, S., Mayne, N. J., Boutle, I. A., et al. 2018, Astronomy & Astrophysics, 615, A97, publisher: EDP Sciences

Linsky, J. L. 1969, ApJ, 156, 989

Liu, M. C., Dupuy, T. J., & Allers, K. N. 2016, ApJ, 833, 96

Lodders, K. 1999, ApJ, 519, 793

Lodders, K. 2002, The Astrophysical Journal, 577, 974

Lodders, K. 2004, ApJ, 611, 587

—. 2010, in Formation and Evolution of Exoplanets, 157

—. 2019, arXiv e-prints, arXiv:1912.00844

Lodders, K., Palme, H., & Gail, H. P. 2009, Landolt Börnstein, 4B, 712

Lopez, E. D., & Fortney, J. J. 2014, ApJ, 792, 1

Lothringer, J. D., Benneke, B., Crossfield, I. J. M., et al. 2018, AJ, 155, 66

Louden, T., & Wheatley, P. J. 2015, ApJ, 814, L24

Louie, D. R., Mullens, E., Alderson, L., et al. 2025, AJ, 169, 86

Loyd, R. O. P., France, K., Youngblood, A., et al. 2016, ApJ, 824, 102

Lucas, P. W., Tinney, C. G., Burningham, B., et al. 2010, MNRAS, 408, L56

Luhman, K. L. 2013, ApJ, 767, L1

Luhman, K. L., & Esplin, T. L. 2016, AJ, 152, 78

Luna, J. L., & Morley, C. V. 2021, ApJ, 920, 146

Lunine, J. I., Hubbard, W. B., Burrows, A., Wang, Y. P., & Garlow, K. 1989, ApJ, 338, 314

Lupu, R., Freedman, R., Gharib-Nezhad, E., Visscher, C., & Molliere, P. 2021a, Correlated k coefficients for H2-He atmospheres; 196 spectral windows and 1460 pressure-temperature points

—. 2021b, Correlated k coefficients for H2-He atmospheres; 196 spectral windows and 1460 pressure-temperature points

Lupu, R. E., Marley, M. S., Lewis, N., et al. 2016, The Astronomical Journal, 152, 217

Lupu, R. E., Marley, M. S., Lewis, N., et al. 2016, AJ, 152, 217

MacDonald, R. J. 2023, The Journal of Open Source Software, 8, 4873

MacDonald, R. J., & Lewis, N. K. 2022, ApJ, 929, 20

MacDonald, R. J., & Madhusudhan, N. 2017, MNRAS, 469, 1979

MacDonald, R. J., Marley, M. S., Fortney, J. J., & Lewis, N. K. 2018a, ApJ, 858, 69

—. 2018b, ApJ, 858, 69

Macintosh, B., Graham, J. R., Ingraham, P., et al. 2014, Proceedings of the National Academy of Sciences, 111, 12661

Madhusudhan, N. 2012, ApJ, 758, 36

—. 2018, in Handbook of Exoplanets, ed. H. J. Deeg & J. A. Belmonte, 104

Madhusudhan, N. 2019, Annual Review of Astronomy and Astrophysics, 57, 617–663

Madhusudhan, N. 2019, ARA&A, 57, 617

Madhusudhan, N., Agúndez, M., Moses, J. I., & Hu, Y. 2016, Space Sci. Rev., 205, 285

Madhusudhan, N., Amin, M. A., & Kennedy, G. M. 2014, ApJ, 794, L12

Madhusudhan, N., & Burrows, A. 2012, ApJ, 747, 25

Madhusudhan, N., Sarkar, S., Constantinou, S., et al. 2023, ApJ, 956, L13

Madhusudhan, N., & Seager, S. 2009a, ApJ, 707, 24

—. 2009b, ApJ, 707, 24

—. 2011, ApJ, 729, 41

Madurowicz, A., Mukherjee, S., Batalha, N., et al. 2023, AJ, 165, 238

Magic, Z., Chiavassa, A., Collet, R., & Asplund, M. 2015, A&A, 573, A90

Mai, C., & Line, M. R. 2019, ApJ, 883, 144

Malik, M., Kempton, E. M. R., Koll, D. D. B., et al. 2019a, ApJ, 886, 142

Malik, M., Kitzmann, D., Mendonça, J. M., et al. 2019b, AJ, 157, 170

Malik, M., Grosheintz, L., Mendonça, J. M., et al. 2017, AJ, 153, 56

Manabe, S., & Wetherald, R. T. 1967, Journal of the Atmospheric Sciences, 24, 241

Maness, H. L., Marcy, G. W., Ford, E. B., et al. 2007, PASP, 119, 90

Mang, J., Gao, P., Hood, C. E., et al. 2022, arXiv e-prints, arXiv:2202.01355

Manjavacas, E., Miles-Páez, P. A., Zapatero-Osorio, M. R., et al. 2017, Monthly Notices of the Royal Astronomical Society, 468, 3024

Marchese, E., Braito, V., Della Ceca, R., Caccianiga, A., & Severgnini, P. 2012, MNRAS, 421, 1803

Marley, M., Saumon, D., Morley, C., & Fortney, J. 2018a, Sonora 2018: Cloud-free, solar composition, solar C/O substellar atmosphere models and spectra

—. 2018b, Sonora 2018: Cloud-free, solar composition, solar C/O substellar atmosphere models and spectra

Marley, M., Saumon, D., Morley, C., et al. 2021, Sonora Bobcat: cloud-free, substellar atmosphere models, spectra, photometry, evolution, and chemistry

Marley, M. S., Gelino, C., Stephens, D., Lunine, J. I., & Freedman, R. 1999a, ApJ, 513, 879

—. 1999b, ApJ, 513, 879

Marley, M. S., & McKay, C. P. 1999, Icarus, 138, 268

Marley, M. S., & Robinson, T. D. 2015, ARA&A, 53, 279

Marley, M. S., Saumon, D., Cushing, M., et al. 2012, The Astrophysical Journal, 754, 135

Marley, M. S., Saumon, D., & Goldblatt, C. 2010, ApJ, 723, L117

Marley, M. S., Saumon, D., Guillot, T., et al. 1996, Science, 272, 1919

Marley, M. S., Seager, S., Saumon, D., et al. 2002, ApJ, 568, 335

Marley, M. S., & Sengupta, S. 2011, MNRAS, 417, 2874

Marley, M. S., Saumon, D., Visscher, C., et al. 2021, ApJ, 920, 85

Matthews, E. C., Carter, A. L., Pathak, P., et al. 2024, Nature, 633, 789

Mayne, N. J., Baraffe, I., Acreman, D. M., et al. ????a, Using the UM dynamical cores to reproduce idealised 3D flows, 1310.6041 [astro-ph]

—. ????b, 561, A1, publisher: EDP Sciences

Mayor, M., & Queloz, D. 1995, Nature, 378, 355

Mayorga, L. C., Robinson, T. D., Marley, M. S., May, E. M., & Stevenson, K. B. 2021, ApJ, 915, 41

McCreery, P., Dos Santos, L. A., Espinoza, N., Allart, R., & Kirk, J. 2025, The Astrophysical Journal, 980, 125

McKay, C. P. 2014, Proceedings of the National Academy of Science, 111, 12628

McKay, C. P., Pollack, J. B., & Courtin, R. 1989, Icarus, 80, 23

—. 1991, Science, 253, 1118

McKemmish, L. K., Masseron, T., Hoeijmakers, H. J., et al. 2019, MNRAS, 488, 2836

McKemmish, L. K., Yurchenko, S. N., & Tennyson, J. 2016, MNRAS, 463, 771

McKinney, W. 2010, in Proceedings of the 9th Python in Science Conference, ed. S. van der Walt & J. Millman, 51 – 56

Meisner, A. M., Leggett, S. K., Logsdon, S. E., et al. 2023, Exploring the Extremes: Characterizing a New Population of Old and Cold Brown Dwarfs

Ménard, F., Delfosse, X., & Monin, J. L. 2002, A&A, 396, L35

Mendonça, J. M., Tsai, S.-m., Malik, M., Grimm, S. L., & Heng, K. 2018, ApJ, 869, 107

Menou, K. 2019, Monthly Notices of the Royal Astronomical Society: Letters, 485, L98

Menou, K., & Rauscher, E. 2009, ApJ, 700, 887

Mészáros, S., Bohlin, R., Allende Prieto, C., et al. 2024, A&A, 688, A197

Metchev, S. A., Heinze, A., Apai, D., et al. 2015, ApJ, 799, 154

Miles, B. E., Skemer, A. J. I., Morley, C. V., et al. 2020, AJ, 160, 63

Miles, B. E., Biller, B. A., Patapis, P., et al. 2022, arXiv e-prints, arXiv:2209.00620

Miles-Páez, P. A., Pallé, E., & Zapatero Osorio, M. R. 2017, MNRAS, 472, 2297

Miles-Páez, P. A., Zapatero Osorio, M. R., & Pallé, E. 2015, A&A, 580, L12

Miles-Páez, P. A., Zapatero Osorio, M. R., Pallé, E., & Peña Ramírez, K. 2013, A&A, 556, A125

Millar-Blanchaer, M. A., Graham, J. R., Pueyo, L., et al. 2015, ApJ, 811, 18

Millar-Blanchaer, M. A., Girard, J. H., Karalidi, T., et al. 2020, ApJ, 894, 42

Min, M., Hovenier, J. W., & de Koter, A. 2005, A&A, 432, 909

Mingozzi, M., Vallini, L., Pozzi, F., et al. 2018, MNRAS, 474, 3640

Mishchenko, M. I., Travis, L. D., Kahn, R. A., & West, R. A. 1997, J. Geophys. Res., 102, 16831

Mizus, I. I., Alijah, A., Zobov, N. F., et al. 2017, MNRAS, 468, 1717

Mollière, P., van Boekel, R., Dullemond, C., Henning, T., & Mordasini, C. 2015, ApJ, 813, 47

Mollière, P., Molyarova, T., Bitsch, B., et al. 2022a, ApJ, 934, 74

—. 2022b, ApJ, 934, 74

Mordasini, C., & Burn, R. 2024, Reviews in Mineralogy and Geochemistry, 90, 55

Mordasini, C., van Boekel, R., Mollière, P., Henning, T., & Benneke, B. 2016, ApJ, 832, 41

Moreno, J., Torrey, P., Ellison, S. L., et al. 2019, MNRAS, 485, 1320

Morley, C. V., Fortney, J. J., Kempton, E. M. R., et al. 2013, ApJ, 775, 33

Morley, C. V., Fortney, J. J., Marley, M. S., et al. 2012, ApJ, 756, 172

—. 2015, ApJ, 815, 110

Morley, C. V., Fortney, J. J., Marley, M. S., et al. 2015, The Astrophysical Journal, 815, 110

Morley, C. V., Knutson, H., Line, M., et al. 2017a, AJ, 153, 86

—. 2017b, AJ, 153, 86

—. 2017c, AJ, 153, 86

Morley, C. V., Marley, M. S., Fortney, J. J., et al. 2014a, ApJ, 787, 78

—. 2014b, ApJ, 787, 78

Morley, C. V., Skemer, A. J., Allers, K. N., et al. 2018, ApJ, 858, 97

Morley, C. V., Mukherjee, S., Marley, M. S., et al. 2024, arXiv e-prints, arXiv:2402.00758

Morton, T. D. 2015, isochrones: Stellar model grid package, Astrophysics Source Code Library, record ascl:1503.010

Moses, J. I., Allen, M., & Yung, Y. L. 1992, Icarus, 99, 318

Moses, J. I., Armstrong, E. S., Fletcher, L. N., et al. 2015, Icarus, 261, 149

Moses, J. I., Fouchet, T., Bézard, B., et al. 2005, Journal of Geophysical Research (Planets), 110, E08001

Moses, J. I., Madhusudhan, N., Visscher, C., & Freedman, R. S. 2013a, ApJ, 763, 25

—. 2013b, ApJ, 763, 25

Moses, J. I., Tremblin, P., Venot, O., & Miguel, Y. 2021, Experimental Astronomy, arXiv:2103.07023

Moses, J. I., Visscher, C., Fortney, J. J., et al. 2011, ApJ, 737, 15

Moses, J. I., Line, M. R., Visscher, C., et al. 2013c, ApJ, 777, 34

Moses, J. I., Marley, M. S., Zahnle, K., et al. 2016, ApJ, 829, 66

Mukherjee, S., Batalha, N. E., Fortney, J. J., & Marley, M. S. 2023, ApJ, 942, 71

Mukherjee, S., Batalha, N. E., & Marley, M. S. 2021a, ApJ, 910, 158

Mukherjee, S., Fortney, J. J., Batalha, N. E., et al. 2022, ApJ, 938, 107

Mukherjee, S., Fortney, J. J., Jensen-Clem, R., et al. 2021b, ApJ, 923, 113

Mukherjee, S., Fortney, J. J., Wogan, N. F., Sing, D. K., & Ohno, K. 2024a, arXiv e-prints, arXiv:2410.17169

—. 2024b, arXiv e-prints, arXiv:2410.17169

Mukherjee, S., Fortney, J. J., Morley, C. V., et al. 2024c, arXiv e-prints, arXiv:2402.00756

Mukherjee, S., Schlawin, E., Bell, T. J., et al. 2025, ApJ, 982, L39

Mullally, S. E., Debes, J., Cracraft, M., et al. 2024, ApJ, 962, L32

Murphy, M. M., Beatty, T. G., & Apai, D. 2024a, ApJ, 974, 179

Murphy, M. M., Beatty, T. G., Roman, M. T., et al. 2023, AJ, 165, 107

Murphy, M. M., Beatty, T. G., Schlawin, E., et al. 2024b, Nature Astronomy, 8, 1562

Nair, H., Allen, M., Anbar, A. D., Yung, Y. L., & Clancy, R. T. 1994, Icarus, 111, 124

Narrett, I. S., Rackham, B. V., & de Wit, J. 2024, AJ, 167, 107

Nayak, M., Lupu, R., Marley, M. S., et al. 2017a, PASP, 129, 034401

—. 2017b, PASP, 129, 034401

Neininger, N., Guélin, M., Ungerechts, H., Lucas, R., & Wielebinski, R. 1998, Nature, 395, 871

Neveu-VanMalle, M., Queloz, D., Anderson, D. R., et al. 2014, A&A, 572, A49

Niemann, H. B., Atreya, S. K., Bauer, S. J., et al. 2005, Nature, 438, 779

Nikolov, N., Sing, D. K., Burrows, A. S., et al. 2015, MNRAS, 447, 463

Niraula, P., Redfield, S., de Wit, J., et al. 2018, arXiv e-prints, arXiv:1812.09227

Noll, K. S., Geballe, T. R., & Marley, M. S. 1997, ApJ, 489, L87

Noy, N., Podolak, M., & Bar-Nun, A. 1981, J. Geophys. Res., 86, 11985

Öberg, K. I., Murray-Clay, R., & Bergin, E. A. 2011, ApJ, 743, L16

O'Brian, T. R., Wickliffe, M. E., Lawler, J. E., Whaling, W., & Brault, J. W. 1991, Journal of the Optical Society of America B Optical Physics, 8, 1185

Ohno, K. 2024, ApJ, 977, 188

Ohno, K., & Fortney, J. J. 2023a, ApJ, 946, 18

—. 2023b, ApJ, 956, 125

Ohno, K., & Kawashima, Y. 2020, ApJ, 895, L47

Ohno, K., & Okuzumi, S. 2018, ApJ, 859, 34

Ohno, K., Okuzumi, S., & Tazaki, R. 2020, ApJ, 891, 131

Ohno, K., Zhang, X., Tazaki, R., & Okuzumi, S. 2021, ApJ, 912, 37

Ohno, K., Schlawin, E., Bell, T. J., et al. 2024, arXiv e-prints, arXiv:2410.10186

Oklopčić, A., Hirata, C. M., & Heng, K. 2016, ApJ, 832, 30

—. 2017, ApJ, 846, 91

Oklopčić, A. 2019, ApJ, 881, 133

Oklopčić, A., & Hirata, C. M. 2018, ApJ, 855, L11

Oppenheimer, B. R., & Hinkley, S. 2009, ARA&A, 47, 253

Oppenheimer, B. R., Kulkarni, S. R., Matthews, K., & van Kerkwijk, M. H. 1998, ApJ, 502, 932

Ormel, C. W., & Min, M. 2019, A&A, 622, A121

Owens, A., Yurchenko, S. N., & Tennyson, J. 2024, MNRAS, 530, 4004

Parker, E. N. 1958, ApJ, 128, 664

Parmentier, V., Fortney, J. J., Showman, A. P., Morley, C., & Marley, M. S. 2016, ApJ, 828, 22

Parmentier, V., Showman, A. P., & Lian, Y. 2013a, A&A, 558, A91

—. 2013b, A&A, 558, A91

Patten, B. M., Stauffer, J. R., Burrows, A., et al. 2006, ApJ, 651, 502

Pelletier, S., Benneke, B., Ali-Dib, M., et al. 2023, Nature, 619, 491

Pérez, F., & Granger, B. E. 2007, Computing in Science & Engineering, 9

Phillips, M. W., Tremblin, P., Baraffe, I., et al. 2020, A&A, 637, A38

Piaulet-Ghorayeb, C., Benneke, B., Radica, M., et al. 2024, ApJ, 974, L10

Piskorz, D., Buzard, C., Line, M. R., et al. 2018, The Astronomical Journal, 156, 133

Plana, H., Rampazzo, R., Mazzei, P., et al. 2017, MNRAS, 472, 3074

Pollack, J. B., Hubickyj, O., Bodenheimer, P., et al. 1996, Icarus, 124, 62

Pollack, J. B., Rages, K., Baines, K. H., et al. 1986, Icarus, 65, 442

Pollack, J. B., Rages, K., Baines, K. H., et al. 1986, Icarus, 65, 442

Polman, J., Waters, L. B. F. M., Min, M., Miguel, Y., & Khorshid, N. 2023, A&A, 670, A161

Polyansky, O. L., Kyuberis, A. A., Zobov, N. F., et al. 2018a, MNRAS, 480, 2597

—. 2018b, MNRAS, 480, 2597

Pont, F., Knutson, H., Gilliland, R. L., Moutou, C., & Charbonneau, D. 2008, MNRAS, 385, 109

Pont, F., Sing, D. K., Gibson, N. P., et al. 2013, MNRAS, 432, 2917

Pontoppidan, K., Blome, C., Braun, H., et al. 2022, arXiv e-prints, arXiv:2207.13067

Pontoppidan, K. M., Pickering, T. E., Laidler, V. G., et al. 2016, in Observatory Operations: Strategies, Processes, and Systems VI, ed. A. B. Peck, R. L. Seaman, & C. R. Benn, Vol. 9910, International Society for Optics and Photonics (SPIE), 381 – 395

Porco, C. C., Baker, E., Barbara, J., et al. 2005, Nature, 434, 159

Powell, D., Zhang, X., Gao, P., & Parmentier, V. 2018, ApJ, 860, 18

Price, M. J. 1977, Reviews of Geophysics and Space Physics, 15, 227

Prinn, R. G., & Barshay, S. S. 1977, Science, 198, 1031

Pruppacher, H., & Klett, J. 1996, Microphysics of Clouds and Precipitation, Atmospheric and Oceanographic Sciences Library

Prša, A., Harmanec, P., Torres, G., et al. 2016, AJ, 152, 41

Querry, M. R. 1987, Optical constants of minerals and other materials from the millimeter to the ultraviolet

Rackham, B. V., Apai, D., & Giampapa, M. S. 2019, AJ, 157, 96

Radica, M., Welbanks, L., Espinoza, N., et al. 2023, MNRAS, 524, 835

Radica, M., Coulombe, L.-P., Taylor, J., et al. 2024, ApJ, 962, L20

Radigan, J., Jayawardhana, R., Lafrenière, D., et al. 2012, ApJ, 750, 105

Radigan, J., Lafrenière, D., Jayawardhana, R., & Artigau, E. 2014, ApJ, 793, 75

Rajpurohit, A. S., Reylé, C., Allard, F., et al. ????, 556, A15, publisher: EDP Sciences

Ramírez, I., Meléndez, J., Bean, J., et al. 2014, A&A, 572, A48

Ranjan, S., Schwieterman, E. W., Harman, C., et al. 2020, ApJ, 896, 148

Rasio, F. A., & Ford, E. B. 1996, Science, 274, 954

Reggiani, H., Galarza, J. Y., Schlaufman, K. C., et al. 2024, The Astronomical Journal, 167, 45

Reggiani, H., Schlaufman, K. C., Healy, B. F., Lothringer, J. D., & Sing, D. K. 2022, The Astronomical Journal, 163, 159

Ricker, G. R., Winn, J. N., Vanderspek, R., et al. 2014, in Society of Photo-Optical Instrumentation Engineers (SPIE) Conference Series, Vol. 9143, Space Telescopes and Instrumentation 2014: Optical, Infrared, and Millimeter Wave, ed. J. M. Oschmann, Jr., M. Clampin, G. G. Fazio, & H. A. MacEwen, 914320

Robinson, T. D., & Marley, M. S. 2014, ApJ, 785, 158

Robock, A. 2000, Reviews of Geophysics, 38, 191

Roman, M., & Rauscher, E. 2019, ApJ, 872, 1

Romani, P. N., & Atreya, S. K. 1988, Icarus, 74, 424

Rooney, C. M., Batalha, N. E., Gao, P., & Marley, M. S. 2021, arXiv e-prints, arXiv:2110.05903

Rosenthal, L. J., Fulton, B. J., Hirsch, L. A., et al. 2021, ApJS, 255, 8

Roth, A., Parmentier, V., & Hammond, M. 2024, MNRAS, arXiv:2404.09626

Rothman, L. S., Gordon, I. E., Barber, R. J., et al. 2010, Journal of Quantitative Spectroscopy and Radiative Transfer, 111

Rothman, L. S., Gordon, I. E., Babikov, Y., et al. 2013, Journal of Quantitative Spectroscopy and Radiative Transfer, 130

Roy, N., Bundy, K., Nevin, R., et al. 2021, ApJ, 913, 33

Rustamkulov, Z., Sing, D. K., Liu, R., & Wang, A. 2022a, ApJ, 928, L7

Rustamkulov, Z., Sing, D. K., Mukherjee, S., et al. 2022b, arXiv e-prints, arXiv:2211.10487

—. 2023, Nature, 614, 659

Ryabchikova, T., Piskunov, N., Kurucz, R. L., et al. 2015, Physica Scripta, 90, 054005

Sagan, C., & Thompson, W. R. 1984, Icarus, 59, 133

Sainsbury-Martinez, F., Wang, P., Fromang, S., et al. ????, 632, A114, publisher: EDP Sciences

Saitoh, N., Imasu, R., Ota, Y., & Niwa, Y. 2009, Journal of Geophysical Research (Atmospheres), 114, D17305

Sánchez-Lavega, A., García-Muñoz, A., del Río-Gaztelurrutia, T., et al. 2020, Nature Communications, 11, 2281

Sanghavi, S., & Shporer, A. 2018, ApJ, 866, 28

Sanghavi, S., & West, R. 2019, ApJ, 877, 134

Sanghavi, S., West, R., & Jiang, J. 2021, ApJ, 907, 30

Saumon, D., & Marley, M. S. 2008, ApJ, 689, 1327

Saumon, D., Marley, M. S., Abel, M., Frommhold, L., & Freedman, R. S. 2012, ApJ, 750, 74

Saumon, D., Marley, M. S., Cushing, M. C., et al. 2006, ApJ, 647, 552

Saumon, D., Marley, M. S., & Lodders, K. 2003, arXiv e-prints, astro

Savel, A. B., Kempton, E. M. R., Rauscher, E., et al. 2023, ApJ, 944, 99

Savel, A. B., Kempton, E. M. R., Malik, M., et al. 2022, ApJ, 926, 85

Schlawin, E., Greene, T. P., Line, M., Fortney, J. J., & Rieke, M. 2018, AJ, 156, 40

Schlawin, E., Leisenring, J., Misselt, K., et al. 2020, AJ, 160, 231

Schlawin, E., Mukherjee, S., Ohno, K., et al. 2024a, AJ, 168, 104

—. 2024b, arXiv e-prints, arXiv:2406.15543

Schlawin, E., Ohno, K., Bell, T. J., et al. 2024c, ApJ, 974, L33

Schmidt, S. P., MacDonald, R. J., Tsai, S.-M., et al. 2025, arXiv e-prints, arXiv:2501.18477

Schneider, A. C., Cushing, M. C., Kirkpatrick, J. D., & Gelino, C. R. 2016, ApJ, 823, L35

Schneider, A. C., Cushing, M. C., Kirkpatrick, J. D., et al. 2015, ApJ, 804, 92

Schwarz, G. J., Ness, J.-U., Osborne, J. P., et al. 2011, ApJS, 197, 31

Schwenke, D. W. 1998, Faraday Discussions, 109, 321

Scott, A., & Duley, W. W. 1996, ApJS, 105, 401

Scoville, N., Aussel, H., Sheth, K., et al. 2014, ApJ, 783, 84

Seager, S., & Sasselov, D. D. 1998, ApJ, 502, L157

Seidel, J. V., Prinoth, B., Pino, L., et al. 2025, arXiv e-prints, arXiv:2502.12261

Sengupta, S., & Krishan, V. 2001, ApJ, 561, L123

Sengupta, S., & Marley, M. S. 2010, ApJ, 722, L142

—. 2016, ApJ, 824, 76

Sheppard, K. B., Mandell, A. M., Tamburo, P., et al. 2017, ApJ, 850, L32

Showman, A. P., Cooper, C. S., Fortney, J. J., & Marley, M. S. 2008, ApJ, 682, 559

Showman, A. P., Fortney, J. J., Lian, Y., et al. 2009a, ApJ, 699, 564

—. 2009b, ApJ, 699, 564

Showman, A. P., & Polvani, L. M. 2011, ApJ, 738, 71

Showman, A. P., Tan, X., & Parmentier, V. 2020, Space Sci. Rev., 216, 139

Silva, A., Marchesini, D., Silverman, J. D., et al. 2021, ApJ, 909, 124

Sing, D. K. 2018, arXiv e-prints, arXiv:1804.07357

Sing, D. K., Fortney, J. J., Nikolov, N., et al. 2016, Nature, 529, 59

Sing, D. K., Rustamkulov, Z., Thorngren, D. P., et al. 2024, arXiv e-prints, arXiv:2405.11027

Skilling, J. 2006a, Bayesian Analysis, 1, 833, publisher: International Society for Bayesian Analysis

—. 2006b, Bayesian Anal., 1, 833

Skrutskie, M. F., Cutri, R. M., Stiening, R., et al. 2006, AJ, 131, 1163

Smith, B. A., Soderblom, L., Beebe, R. F., et al. 1981, Science, 212, 163

Smith, B. A., Soderblom, L., Batson, R. M., et al. 1982, Science, 215, 504

Smith, M. D. 1998, Icarus, 132, 176

Snook, K. J. 1999, PhD thesis, STANFORD UNIVERSITY

Solomon, P. M., & Vanden Bout, P. A. 2005, ARA&A, 43, 677

Somerville, R. C. J., & Remer, L. A. 1984, J. Geophys. Res., 89, 9668

Sorahana, S., & Yamamura, I. 2012, ApJ, 760, 151

Sorahana, S., & Yamamura, I. 2012, The Astrophysical Journal, 760, 151

Sorensen, C. M., Heinson, Y. W., Heinson, W. R., Maughan, J. B., & Chakrabarti, A. 2017, Atmosphere, 8, 68

Sousa-Silva, C., Al-Refaie, A. F., Tennyson, J., & Yurchenko, S. N. 2014, Monthly Notices of the Royal Astronomical Society, 446, 2337

Southworth, J., Hinse, T. C., Burgdorf, M., et al. 2014, Monthly Notices of the Royal Astronomical Society, 444, 776

Speagle, J. S. 2020, MNRAS, 493, 3132

Speagle, J. S. 2020, Monthly Notices of the Royal Astronomical Society, 493, 3132, aDS Bibcode: 2020MNRAS.493.3132S

Spelman, M. J., & Manabe, S. 1984, J. Geophys. Res., 89, 571

Spergel, D., Gehrels, N., Breckinridge, J., et al. 2013a, arXiv e-prints, arXiv:1305.5422

—. 2013b, arXiv e-prints, arXiv:1305.5422

Spiegel, D. S., & Burrows, A. 2012, ApJ, 745, 174

Spiegel, D. S., Burrows, A., Ibgui, L., Hubeny, I., & Milsom, J. A. 2010, ApJ, 709, 149

sqlite3 Development Team. 2019,

Sromovsky, L. A. 2005, Icarus, 173, 254

Sromovsky, L. A., Baines, K. H., & Fry, P. M. 2020, Icarus, 344, 113398

Sromovsky, L. A., Fry, P. M., Hammel, H. B., et al. 2009, Icarus, 203, 265

Sromovsky, L. A., Fry, P. M., & Kim, J. H. 2011, Icarus, 215, 292

Stamnes, K., Tsay, S.-C., Jayaweera, K., & Wiscombe, W. 1988, Appl. Opt., 27, 2502

Steinrueck, M. E., Koskinen, T., Lavvas, P., et al. 2023a, ApJ, 951, 117

—. 2023b, ApJ, 951, 117

Steinrueck, M. E., Parmentier, V., Showman, A. P., Lothringer, J. D., & Lupu, R. E. 2019, ApJ, 880, 14

Steinrueck, M. E., Showman, A. P., Lavvas, P., et al. 2021, MNRAS, 504, 2783

Stephens, D. C., Leggett, S. K., Cushing, M. C., et al. 2009, ApJ, 702, 154

Stevenson, D. J. 1991, ARA&A, 29, 163

Stevenson, D. J., & Salpeter, E. E. 1977, ApJS, 35, 239

Stevenson, K. B., Harrington, J., Nymeyer, S., et al. 2010, Nature, 464, 1161

Stevenson, K. B., Harrington, J., Fortney, J. J., et al. 2012, ApJ, 754, 136

Stolker, T., Min, M., Stam, D. M., et al. 2017, A&A, 607, A42

STScI Development Team. 2013a, pysynphot: Synthetic photometry software package, ascl:1303.023

—. 2013b, pysynphot: Synthetic photometry software package, Astrophysics Source Code Library, ascl:1303.023

Suárez, G., & Metchev, S. 2022, arXiv e-prints, arXiv:2205.00168

Sudarsky, D., Burrows, A., & Hubeny, I. 2003, ApJ, 588, 1121

Sudarsky, D., Burrows, A., Hubeny, I., & Li, A. 2005, ApJ, 627, 520

Sumlin, B. J., Heinson, W. R., & Chakrabarty, R. K. 2018a, Journal of Quantitative Spectroscopy and Radiative Transfer, 205, 127

—. 2018b, Journal of Quantitative Spectroscopy and Radiative Transfer, 205, 127

Tan, X. 2022, Monthly Notices of the Royal Astronomical Society, 511, 4861

Tan, X., & Showman, A. P. 2019, ApJ, 874, 111

—. 2021, MNRAS, 502, 678

Tan, X., & Showman, A. P. 2021, Monthly Notices of the Royal Astronomical Society, 502, 2198

Tan, X., & Showman, A. P. 2021, MNRAS, 502, 2198

Tata, R., Martín, E. L., Sengupta, S., et al. 2009, A&A, 508, 1423

Taylor, J., Parmentier, V., Line, M. R., et al. 2021, MNRAS, 506, 1309

—. 2020, arXiv e-prints, arXiv:2009.12411

Tennyson, J., & Yurchenko, S. 2018, Atoms, 6, 26

Tennyson, J., Yurchenko, S. N., Al-Refaie, A. F., et al. 2020, J. Quant. Spec. Radiat. Transf., 255, 107228

Teske, J., Batalha, N. E., Wallack, N. L., et al. 2025, AJ, 169, 249

Thao, P. C., Mann, A. W., Feinstein, A. D., et al. 2024, arXiv e-prints, arXiv:2409.16355

The LUVOIR Team. 2019, arXiv e-prints, arXiv:1912.06219

Thelen, A. E., Nixon, C. A., Chanover, N. J., et al. 2019, Icarus, 319, 417

Thomas, G. E., & Stamnes, K. 2002, Radiative Transfer in the Atmosphere and Ocean,

Thorngren, D. P., Fortney, J. J., Murray-Clay, R. A., & Lopez, E. D. 2016, ApJ, 831, 64

Thorngren, D. P., Marley, M. S., & Fortney, J. J. 2019, Research Notes of the AAS, 3, 128

Tice, D. S., Irwin, P. G. J., Fletcher, L. N., et al. 2013, Icarus, 223, 684

Tinetti, G., Eccleston, P., Lueftinger, T., et al. 2022, in European Planetary Science Congress, EPSC2022–1114

Toon, O. B., McKay, C. P., Ackerman, T. P., & Santhanam, K. 1989, J. Geophys. Res., 94, 16287

Toon, O. B., Pollack, J. B., & Sagan, C. 1977, Icarus, 30, 663

Treister, E., Messias, H., Privon, G. C., et al. 2020, ApJ, 890, 149

Tremblin, P., Amundsen, D. S., Mourier, P., et al. 2015, ApJ, 804, L17

Tremblin, P., Chabrier, G., Mayne, N. J., et al. ????, 841, 30, publisher: IOP ADS Bibcode: 2017ApJ...841...30T

Triaud, A. H. M. J., Lanotte, A. A., Smalley, B., & Gillon, M. 2014, MNRAS, 444, 711

Trotta, R. 2008, Contemporary Physics, 49, 71–104

Tsai, S.-M., Lyons, J. R., Grosheintz, L., et al. 2017, ApJS, 228, 20

Tsai, S.-M., Malik, M., Kitzmann, D., et al. 2021, ApJ, 923, 264

Tsai, S.-M., Moses, J. I., Powell, D., & Lee, E. K. H. 2023a, ApJ, 959, L30

Tsai, S.-M., Steinrueck, M., Parmentier, V., Lewis, N., & Pierrehumbert, R. 2023b, MNRAS, 520, 3867

Tsai, S.-M., Lee, E. K. H., Powell, D., et al. 2023c, Nature, 617, 483

Tu, Z., Wang, S., Chen, X., & Liu, J. 2025, ApJ, 980, 230

Tu, Z., Wang, S., & Liu, J. 2024, ApJ, 976, 82

Underwood, D. S., Tennyson, J., Yurchenko, S. N., et al. 2016, MNRAS, 459, 3890

Valdes, F., Gupta, R., Rose, J. A., Singh, H. P., & Bell, D. J. 2004, ApJS, 152, 251

Valentine, D., Wakeford, H. R., Challener, R. C., et al. 2024, AJ, 168, 123

van Dokkum, P. G. 2001, PASP, 113, 1420

van Holstein, R. G., Snik, F., Girard, J. H., et al. 2017, in Society of Photo-Optical Instrumentation Engineers (SPIE) Conference Series, Vol. 10400, Society of Photo-Optical Instrumentation Engineers (SPIE) Conference Series, 1040015

van Holstein, R. G., Stolker, T., Jensen-Clem, R., et al. 2021a, A&A, 647, A21

—. 2021b, A&A, 647, A21

Vanderburg, A., Rappaport, S. A., Xu, S., et al. 2020, Nature, 585, 363

Varghese, A., Ratnasingam, R. P., Vanon, R., Edelmann, P. V. F., & Rogers, T. M. 2023, ApJ, 942, 53

Venot, O., Bounaceur, R., Dobrijevic, M., et al. 2019, A&A, 624, A58

Venot, O., Hébrard, E., Agúndez, M., et al. 2012, A&A, 546, A43

Vergely, J. L., Lallement, R., & Cox, N. L. J. 2022, AA, 664, A174

Villanueva, G. L., Smith, M. D., Protopapa, S., Faggi, S., & Mandell, A. M. 2018, J. Quant. Spec. Radiat. Transf., 217, 86

Vissapragada, S., Knutson, H. A., Greklek-McKeon, M., et al. 2022, AJ, 164, 234

Visscher, C. 2020, Journal of Geophysical Research (Planets), 125, e06526

Visscher, C., & Fegley, Bruce, J. 2005, ApJ, 623, 1221

Visscher, C., Lodders, K., & Fegley, B. 2010, The Astrophysical Journal, 716, 1060

Visscher, C., Lodders, K., & Fegley, Jr., B. 2010a, ApJ, 716, 1060

Visscher, C., Lodders, K., & Fegley, Bruce, J. 2006, ApJ, 648, 1181

—. 2010b, ApJ, 716, 1060

Visscher, C., & Moses, J. I. 2011, ApJ, 738, 72

Visscher, C., Moses, J. I., & Saslow, S. A. 2010c, Icarus, 209, 602

Vogt, F. P. A., Dopita, M. A., Kewley, L. J., et al. 2014, ApJ, 793, 127

Vos, J. M., Faherty, J. K., Gagné, J., et al. 2022, ApJ, 924, 68

Vos, J. M., Biller, B. A., Bonavita, M., et al. 2019, MNRAS, 483, 480

Wakeford, H. R., & Sing, D. K. 2015, A&A, 573, A122

Wakeford, H. R., Visscher, C., Lewis, N. K., et al. 2017, MNRAS, 464, 4247

Waldmann, I. P., Tinetti, G., Rocchetto, M., et al. 2015, ApJ, 802, 107

Wallack, N. L., Batalha, N. E., Alderson, L., et al. 2024, arXiv e-prints, arXiv:2404.01264

Walt, S. v. d., Colbert, S. C., & Varoquaux, G. 2011, Computing in Science & Engineering, 13, 22

Wang, D., Gierasch, P. J., Lunine, J. I., & Mousis, O. 2015, Icarus, 250, 154

Wang, D., Lunine, J. I., & Mousis, O. 2016, Icarus, 276, 21

Webber, M. W., Lewis, N. K., Marley, M., et al. 2015a, ApJ, 804, 94

—. 2015b, ApJ, 804, 94

Welbanks, L., & Madhusudhan, N. 2022, ApJ, 933, 79

Welbanks, L., Madhusudhan, N., Allard, N. F., et al. 2019, ApJ, 887, L20

Welbanks, L., Bell, T. J., Beatty, T. G., et al. 2024, arXiv e-prints, arXiv:2405.11018

Welbanks, L., Nixon, M. C., McGill, P., et al. 2025, arXiv e-prints, arXiv:2504.21788

West, R. A., Strobel, D. F., & Tomasko, M. G. 1986, Icarus, 65, 161

Wildt, R. 1937, ApJ, 86, 321

Wilson, D. J., Froning, C. S., Duvvuri, G. M., et al. 2021, ApJ, 911, 18

Wilzewski, J. S., Gordon, I. E., Kochanov, R. V., Hill, C., & Rothman, L. S. 2016, Journal of Quantitative Spectroscopy and Radiative Transfer, 168, 193

Wiscombe, W. J. 1977, Journal of Atmospheric Sciences, 34, 1408

Wogan, N. 2024, Photochem

Wogan, N. F., Batalha, N. E., Zahnle, K. J., et al. 2024, ApJ, 963, L7

Wogan, N. F., Catling, D. C., Zahnle, K. J., & Lupu, R. 2023, , 4, 169

Woitke, P., Helling, C., & Gunn, O. 2020, A&A, 634, A23

Wolf, E. T., Kopparapu, R., Haqq-Misra, J., & Fauchez, T. J. 2022, The Planetary Science Journal, 3, 7

Wong, M. H., Mahaffy, P. R., Atreya, S. K., Niemann, H. B., & Owen, T. C. 2004, Icarus, 171, 153

Wong, M. L., Fan, S., Gao, P., et al. 2017, Icarus, 287, 110

Wood, N., Staniforth, A., White, A., et al. ????, 140, 1505, _eprint: https://onlinelibrary.wiley.com/doi/pdf/10.1002/qj.2235

Wright, E. L., Mainzer, A., Kirkpatrick, J. D., et al. 2014, AJ, 148, 82

Wright, J. T., Marcy, G. W., Fischer, D. A., et al. 2007, ApJ, 657, 533

Xue, Q., Bean, J. L., Zhang, M., et al. 2024, ApJ, 963, L5

Yadin, B., Veness, T., Conti, P., et al. 2012, MNRAS, 425, 34

Yan, F., Reiners, A., Pallé, E., et al. 2022, A&A, 659, A7

Yelle, R. V., Doose, L. R., Tomasko, M. G., & Strobel, D. F. 1987, Geophys. Res. Lett., 14, 483

Youngblood, A., France, K., Loyd, R. O. P., et al. 2016, ApJ, 824, 101

Yung, Y. L., Drew, W. A., Pinto, J. P., & Friedl, R. R. 1988, Icarus, 73, 516

Yurchenko, S. N., Barber, R. J., & Tennyson, J. 2011, Monthly Notices of the Royal Astronomical Society, 413, 1828

Yurchenko, S. N., Mellor, T. M., Freedman, R. S., & Tennyson, J. 2020, MNRAS, 496, 5282

Yurchenko, S. N., Owens, A., Kefala, K., & Tennyson, J. 2024, MNRAS, 528, 3719

Yurchenko, S. N., & Tennyson, J. 2014, Monthly Notices of the Royal Astronomical Society, 440, 1649

Yurchenko, S. N., Tennyson, J., Barber, R. J., & Thiel, W. 2013, Journal of Molecular Spectroscopy, 291, 69

Zahnle, K., Marley, M. S., Freedman, R. S., Lodders, K., & Fortney, J. J. 2009, ApJ, 701, L20

Zahnle, K., Marley, M. S., Morley, C. V., & Moses, J. I. 2016, ApJ, 824, 137

Zahnle, K. J., & Marley, M. S. 2014, ApJ, 797, 41

Zalesky, J. A., Line, M. R., Schneider, A. C., & Patience, J. 2019, The Astrophysical Journal, 877, 24

Zalesky, J. A., Saboi, K., Line, M. R., et al. 2022, The Astrophysical Journal, 936, 44

Zamyatina, M., Christie, D. A., Hébrard, E., et al. ????, Quenching-driven equatorial

depletion and limb asymmetries in hot Jupiter atmospheres: WASP-96b example, 2402.14535 [astro-ph, physics:physics]

Zamyatina, M., Hébrard, E., Drummond, B., et al. 2023, MNRAS, 519, 3129

Zapatero Osorio, M. R., Béjar, V. J. S., Goldman, B., et al. 2011, ApJ, 740, 4

Zapatero Osorio, M. R., Caballero, J. A., & Béjar, V. J. S. 2005, ApJ, 621, 445

Zeidler, S., Mutschke, H., & Posch, T. 2015, The Astrophysical Journal, 798, 125

Zhang, F., Liu, K., Yang, Q., Wu, K., & Zhao, J.-Q. 2017, Advances in Meteorology, 2017

Zhang, M., Chachan, Y., Kempton, E. M.-R., & Knutson, H. A. 2018, arXiv e-prints, arXiv:1811.11761

Zhang, X. 2020, Research in Astronomy and Astrophysics, 20, 099

Zhang, X., Liang, M. C., Mills, F. P., Belyaev, D. A., & Yung, Y. L. 2012, Icarus, 217, 714

Zhang, X., & Showman, A. P. 2017, ApJ, 836, 73

—. 2018a, ApJ, 866, 1

—. 2018b, ApJ, 866, 1

Zhang, X., West, R. A., Irwin, P. G. J., Nixon, C. A., & Yung, Y. L. 2015, Nature Communications, 6, 10231

Zhang, Z., Liu, M. C., Marley, M. S., Line, M. R., & Best, W. M. J. 2021a, ApJ, 921, 95

—. 2021b, ApJ, 921, 95

Zhang, Z., Mollière, P., Hawkins, K., et al. 2023, arXiv e-prints, arXiv:2309.02488

Zhang, Z., Morley, C. V., Gully-Santiago, M., et al. 2023, Science Advances, 9, eadf8736

Zurlo, A. 2024, arXiv e-prints, arXiv:2404.05797